



CENTRO DE INVESTIGACIÓN Y DE ESTUDIOS AVANZADOS  
DEL INSTITUTO POLITÉCNICO NACIONAL

UNIDAD ZACATENCO  
DEPARTAMENTO DE FÍSICA

“Análisis de Teoría de campo efectiva de sondas de  
precisión a bajas energías en la búsqueda de  
nueva física”

**Tesis que presenta**

**Jesús Alejandro Miranda Hernández**

para obtener el Grado de

Doctor en Ciencias

en la Especialidad de

Física

Director de tesis: Dr. Pablo Roig Garcés

Ciudad de México

Agosto, 2022



CENTER FOR RESEARCH AND ADVANCED STUDIES OF THE NATIONAL  
POLYTECHNIC INSTITUTE

PHYSICS DEPARTMENT

“Effective field theory analyses of low-energy  
precision probes in the search for new  
physics”

**by**

**Jesús Alejandro Miranda Hernández**

In order to obtain the

Doctor of Science

degree, speciality in

Physics

Advisor: Ph. D. Pablo Roig Garcés

Mexico City

August, 2022



# Dedicatoria

Esta tesis está dedicada a:

A mis padres quienes con su amor, paciencia y esfuerzo me han permitido llegar a cumplir hoy un sueño más, gracias por inculcar en mí el ejemplo de esfuerzo y valentía.

A mis abuelos que gracias a sus consejos y palabras de aliento hicieron de mí una mejor persona, y que aunque ya no estén conmigo, de cierta forma siempre me acompañan en todos mis sueños y metas.

Y finalmente, a toda mi familia por su cariño y apoyo incondicional, durante todo este proceso.



# Agradecimientos

Mi profundo agradecimiento a todas las autoridades y personal que integran el Departamento de Física del Cinvestav, por abrirme las puertas y permitirme llevar a cabo todo mi proceso formativo dentro de sus instalaciones.

A los que hicieron posible este trabajo de tesis doctoral. Mi más grande y sincero agradecimiento al Dr. Pablo Roig por plantearme los temas de investigación que comprenden esta tesis, por su esfuerzo, paciencia y dedicación, y sobre todo por tomarse el tiempo de hablar conmigo siempre que lo necesitaba. A los Dres. Pablo Sánchez y Sergi González por su valiosa colaboración. A los Dres. David Delepine y Mauro Napsuciale por su valioso apoyo que me permitió adentrarme y enamorarme del área.

De igual manera, mis agradecimientos a los Dres. Eduard De La Cruz, Iván Heredia, Jaime Santoyo, Josué De Santiago y Sergi González, quienes fungieron como sinodales de esta tesis, por su tiempo y valiosos comentarios.

Agradezco al Consejo Nacional de Ciencia y Tecnología (CONACYT) por el apoyo otorgado durante estos cuatro años para la obtención del grado de Doctor en Ciencias en la especialidad de Física.

Finalmente quiero expresar mi agradecimiento a mis amigos y compañeros, Miguel Jiménez, Fabiola Zavala, Guadalupe Sarabia, Christian Medina, Haydee Hernández, Fabiola Fortuna, Lourdes Merino, Rafael Ramírez, Arantza Zavala, Rodrigo Felipe, Miguel Sandoval, Ubaldo Cavazos, Josué Romero, Gael De La Cruz, Carolina Barboza, Javier Rendón, Marcela Marín, Enrique Ramírez, Iván Pacheco, Marcela García, Gonzalo Sánchez, Giovany Cruz, Edgar López, Marco Ayala y muchos otros que probablemente olvidé mencionar.



# Resumen

El Modelo Estándar de física de partículas (ME) es una de las teorías más exitosas de la física. Sin embargo, hay algunos problemas que el SM no puede resolver, en particular, la materia oscura, la energía oscura y las masas de neutrinos. Dada la falta de evidencia directa de Nueva Física (NF) en el LHC hasta el momento, se puede recurrir a pruebas de precisión a baja energía donde una cantidad permitida dentro del ME se mide con un nivel de precisión que podría revelar pequeñas desviaciones entre la teoría y el experimento, y así indicar la presencia de física más allá del modelo estándar. Para ello, es obligatorio contar con cálculos precisos dentro del ME y una forma independiente de modelo que nos permita estudiar los efectos de nueva física. Lo primero se ha logrado gracias a los esfuerzos de varios grupos en todo el mundo, mientras que el segundo se puede conseguir trabajando en un marco de teoría de campo efectivo.

Este trabajo se divide en tres partes. En primer lugar, estudiamos el efecto de las interacciones de NF en las desintegraciones hadrónicas del tau, lo cual nos permitió obtener límites competitivos para interacciones no estándar a través de un ajuste global. En segundo lugar, revisamos las correcciones electromagnéticas y de ruptura de isospin para los decaimientos de  $\tau^- \rightarrow \pi^- \pi^0 \nu_\tau$  utilizados como input para las contribuciones de dos piones a la polarización del vacío hadrónico (a LO) del momento magnético anómalo del muón. Y finalmente, evaluamos la contribución de mesones axiales a la estructura hiperfina (HFS) del hidrógeno muónico.



# Abstract

The Standard Model of particle physics (SM) is one of the most successful theories in physics. However, there are some problems that the SM cannot address, e.g. dark matter, dark energy, and neutrino masses, among others. Given the lack of direct evidence of New Physics at the LHC so far, one can turn to a low-energy precision test where a quantity allowed within the SM is measured at a level of precision that could reveal tiny deviations between theory and experiment and then signal the presence of BSM dynamics. For this industry, it is mandatory to have precise SM computations and a model-independent way to study the BSM signal. The former was achieved thanks to the efforts of several groups worldwide, while the second can be attained in an Effective field theory framework.

This work is divided into three parts. Firstly, we study the effect of NP interactions in hadronic tau decays getting competitive constraints on these non-standard interactions through a global fit. Secondly, we revisit the electromagnetic and isospin-breaking correction to  $\tau^- \rightarrow \pi^- \pi^0 \nu_\tau$  decays used as input to the two-pion contributions to the hadronic vacuum polarization (at LO) of the muon anomalous magnetic moment. And finally, we evaluate the axial-vector contribution to the hyperfine splitting (HFS) in muonic hydrogen.



# List of Publications

## Peer-reviewed Journal Publications

1. Effective-field theory analysis of the  $\tau^- \rightarrow \pi^- \pi^0 \nu_\tau$  decays.  
J.A. Miranda, & P. Roig  
Published in: JHEP 11 (2018) 038, e-Print: 1806.09547 [hep-ph].
2. Effective-field theory analysis of the  $\tau^- \rightarrow K^-(\eta^{(\prime)}, K^0) \nu_\tau$  decays.  
Sergi González-Solís, Alejandro Miranda, Javier Rendón, & Pablo Roig  
Published in: Phys.Rev.D 101 (2020) 3, 034010, e-Print: 1911.08341 [hep-ph].
3. Exclusive hadronic tau decays as probes of non-SM interactions.  
Sergi González-Solís, Alejandro Miranda, Javier Rendón, & Pablo Roig  
Published in: Phys.Lett.B 804 (2020) 135371, e-Print: 1912.08725 [hep-ph].
4. New  $\tau$ -based evaluation of the hadronic contribution to the vacuum polarization piece of the muon anomalous magnetic moment.  
J.A. Miranda, & P. Roig  
Published in: Phys.Rev.D 102 (2020) 114017, e-Print: 2007.11019 [hep-ph].
5. Axial-vector exchange contribution to the hyperfine splitting.  
Alejandro Miranda, Pablo Roig, Pablo Sánchez-Puertas  
Published in: Phys.Rev.D 105 (2022) 1, 016017, e-Print: 2110.11366 [hep-ph].

## Peer-reviewed Conference Publications

1. Low-energy limit of SMEFT applied to  $\tau^- \rightarrow \pi\pi^0\nu_\tau$  decays.

J.A. Miranda Hernández

Published in: PoS LHCP2019 (2019) 029, Contribution to: LHCP 2019, 029.

2. Isospin-breaking corrections to  $\tau \rightarrow \pi\pi\nu_\tau$  decays and the muon  $g - 2$ .

J.A. Miranda Hernández

Published in: PoS CHARM2020 (2020) 043, Contribution to: CHARM 2020, 043,  
e-Print: 2109.07538 [hep-ph].

3. Axial-vector contributions to the HFS of muonic hydrogen.

J.A. Miranda Hernández, Pablo Roig, Pablo Sánchez-Puertas

Published in: Suplemento de la Revista Mexicana de Física 3 (2022) 2 020719, 1-6.  
Contribution to: 35th Annual Meeting of the DPyC-SMF, MSPF 2021.



# Contents

<b>Dedicatoria</b>	<b>i</b>
<b>Agradecimientos</b>	<b>ii</b>
<b>Resumen</b>	<b>iii</b>
<b>Abstract</b>	<b>iv</b>
<b>List of Publications</b>	<b>v</b>
<b>Abbreviations and nomenclature</b>	<b>xxx</b>
<b>Preface</b>	<b>xxxi</b>
<b>1 Theoretical framework</b>	<b>1</b>
1.1 Standard Model . . . . .	1
1.1.1 Particle content in the Standard Model. . . . .	1
1.1.2 Constructing the Lagrangian of the Electroweak Model . . . . .	3
1.1.3 Standard Model of Elementary Particles. . . . .	5
1.2 Higgs mechanism . . . . .	8
1.3 Lagrangian after SSB . . . . .	10
1.3.1 The Yukawa sector and the mixing matrix . . . . .	14
1.4 Quantum Chromodynamics . . . . .	19
1.4.1 Running coupling . . . . .	20

1.4.2	Quark masses . . . . .	22
1.5	Effective Field Theory . . . . .	23
1.5.1	EFT expansion . . . . .	23
1.5.2	Fermi Theory of Weak Interactions . . . . .	25
1.5.3	SMEFT . . . . .	28
1.5.4	EFT below $M_W$ . . . . .	30
1.5.5	Principles of Effective Field Theory . . . . .	31
1.6	Chiral Perturbation Theory . . . . .	32
1.6.1	Chiral symmetry . . . . .	32
1.6.2	Effective chiral Lagrangian at lowest order . . . . .	34
1.6.3	Pseudoscalar meson masses at the lowest order . . . . .	38
1.6.4	ChPT at $\mathcal{O}(p^4)$ . . . . .	40
1.6.5	Higher-order corrections . . . . .	43
1.7	Dispersion theory . . . . .	46
1.7.1	Analyticity . . . . .	46
1.7.2	Unitarity . . . . .	48
1.7.3	Omnès formalism . . . . .	51
<b>2</b>	<b>Tau physics</b>	<b>54</b>
2.1	Introduction . . . . .	54
2.2	Lepton decays . . . . .	55
2.3	Lepton universality . . . . .	58
2.4	Lorentz structure of the charged current . . . . .	60
2.4.1	Model-dependent interpretation . . . . .	66
2.5	Hadronic decays . . . . .	66
2.5.1	Two-body semileptonic decays . . . . .	67
2.5.2	Decays into two hadrons . . . . .	68

<b>3</b>	<b>Effective-field theory analysis of the <math>\tau^- \rightarrow \pi^- \pi^0 \nu_\tau</math> decays</b>	<b>79</b>
3.1	Introduction . . . . .	79
3.2	Effective theory analysis of $\tau^- \rightarrow \nu_\tau \bar{u} d$ . . . . .	81
3.3	Semileptonic $\tau$ decay amplitude . . . . .	83
3.4	Hadronization of the scalar, vector and tensor currents . . . . .	84
3.5	Decay Observables . . . . .	89
3.5.1	Dalitz plot . . . . .	90
3.5.2	Angular distribution . . . . .	92
3.5.3	Decay rate . . . . .	96
3.5.4	Forward-backward asymmetry . . . . .	97
3.5.5	Limits on $\hat{\epsilon}_S$ and $\hat{\epsilon}_T$ . . . . .	99
3.6	Summary and conclusions . . . . .	103
<b>4</b>	<b>Effective-field theory analysis of the <math>\tau^- \rightarrow K^- \eta^{(\prime)} \nu_\tau</math> decays</b>	<b>106</b>
4.1	Introduction . . . . .	106
4.2	Effective field theory analysis and decay amplitude of $\tau^- \rightarrow \nu_\tau \bar{u} s$ . . . . .	109
4.3	Hadronization of the scalar, vector and tensor currents . . . . .	111
4.4	Decay observables . . . . .	115
4.4.1	Dalitz plot . . . . .	116
4.4.2	Angular distribution . . . . .	121
4.4.3	Decay rate . . . . .	122
4.4.4	Forward-backward asymmetry . . . . .	123
4.4.5	Limits on $\hat{\epsilon}_S$ and $\hat{\epsilon}_T$ . . . . .	125
4.5	Conclusions . . . . .	129
<b>5</b>	<b>Global Fit of non-standard interactions in exclusive semileptonic tau decays</b>	<b>131</b>
5.1	Introduction . . . . .	131
5.2	SMEFT Lagrangian and decay rate . . . . .	134



5.3	Two-meson form factors . . . . .	136
5.4	New Physics bounds from $\Delta\mathbf{S} = \mathbf{0}$ decays . . . . .	140
5.5	New Physics bounds from $ \Delta S  = 1$ decays . . . . .	143
5.6	New Physics bounds from a global fit to both $\Delta S = 0$ and $ \Delta S  = 1$ sectors .	146
5.7	Conclusions . . . . .	148
<b>6</b>	<b>Hadronic contribution to the vacuum polarization of the muon anomalous magnetic moment</b>	<b>151</b>
6.1	Introduction . . . . .	151
6.2	Theoretical calculations of $a_\mu$ . . . . .	152
6.2.1	QED contributions . . . . .	152
6.2.2	EW contributions . . . . .	153
6.2.3	HVP contributions . . . . .	155
6.2.4	HLbL contribution . . . . .	160
6.2.5	The SM prediction for $a_\mu$ . . . . .	163
6.3	Data-driven calculations of HVP . . . . .	164
6.3.1	Hadronic cross sections at low energies . . . . .	165
6.3.2	Tensions in hadronic data . . . . .	176
6.3.3	Use of hadronic tau decay data . . . . .	182
<b>7</b>	<b>Isospin-breaking corrections to <math>\tau^- \rightarrow \pi^- \pi^0 \nu_\tau</math> decays and the muon <math>g - 2</math></b>	<b>191</b>
7.1	Introduction . . . . .	191
7.2	$\tau^- \rightarrow \pi^- \pi^0 \gamma \nu_\tau$ decays . . . . .	194
7.2.1	Amplitude . . . . .	194
7.2.2	Theoretical framework . . . . .	196
7.2.3	Vector Form Factors . . . . .	197
7.2.4	Axial-Vector Form Factors . . . . .	200
7.2.5	SD constraints . . . . .	202
7.3	Radiative corrections for hadronic vacuum polarization . . . . .	207

7.3.1	Radiative decay . . . . .	216
7.4	IB corrections to $\mathbf{a}_\mu^{HVP,LO\pi\pi}$ . . . . .	224
7.5	Conclusions . . . . .	238
<b>8</b>	<b>Lamb shift and hyperfine splitting in muonic hydrogen</b>	<b>239</b>
8.1	Introduction . . . . .	239
8.2	Nuclear effects in hydrogen-like atoms . . . . .	243
8.3	Theory updates and future $\mu\mathbf{H}$ . . . . .	244
8.3.1	Lamb shift in $\mu\mathbf{H}$ . . . . .	244
8.3.2	Hyperfine splitting in $\mu\mathbf{H}$ . . . . .	247
8.4	New Physics searches . . . . .	252
<b>9</b>	<b>Axial-vector contributions to the HFS of muonic hydrogen</b>	<b>254</b>
9.1	Introduction . . . . .	254
9.2	$A \rightarrow \ell^+\ell^-$ decays . . . . .	255
9.3	The contribution to the HFS . . . . .	259
9.4	Model results . . . . .	261
9.4.1	One-resonance saturation . . . . .	262
9.4.2	Two-resonance saturation . . . . .	264
9.5	Results and conclusions . . . . .	266
<b>A</b>	<b><math>F_T(s)</math> including resonances as explicit degrees of freedom</b>	<b>269</b>
<b>B</b>	<b>Chiral ward Identities among four- and five-point Green functions</b>	<b>273</b>
<b>C</b>	<b>Amplitude for the <math>\tau^- \rightarrow \pi^-\pi^-\gamma\nu_\tau</math> decays</b>	<b>275</b>
C.1	Anomaly . . . . .	279
C.2	$R_\chi T$ contributions . . . . .	280
<b>D</b>	<b>Magnetic dipole moment of the <math>\rho</math> meson</b>	<b>296</b>

<b>E</b>	<b>Pseudoscalar resonances in radiative di-pion tau decay</b>	<b>298</b>
E.1	Mixing . . . . .	299
<b>F</b>	<b>Virtual corrections to di-meson tau decays</b>	<b>302</b>
<b>G</b>	<b>Fit of leading odd-intrinsic parity resonance couplings to the <math>\mathcal{O}(p^6)</math> LECs</b>	<b>305</b>
<b>H</b>	<b>Kinematics of four body tau decays</b>	<b>307</b>
H.1	$\tau^-(P) \rightarrow \pi^-(p_-)\pi^0(p_0)\gamma(k)\nu_\tau(q)$ kinematics . . . . .	307
<b>I</b>	<b>Vector Form Factors in radiative di-pion tau decays</b>	<b>312</b>
<b>J</b>	<b>Axial Form Factors in radiative di-pion tau decays</b>	<b>325</b>
<b>K</b>	<b>Axial structure of the nucleon</b>	<b>339</b>
K.1	The coupling of $P$ to the nucleon . . . . .	340
K.2	The coupling of $A$ to the nucleon . . . . .	343
K.2.1	Antisymmetric tensor field ( $A^{\mu\nu}$ ) . . . . .	343
K.2.2	Proca field ( $\hat{A}_\mu$ ) . . . . .	344
K.2.3	Effective coupling in $B\chi PT$ . . . . .	347
K.2.4	Coupling axial-vector to two photons . . . . .	349
K.2.5	$\langle N(\mathbf{p}')   \mathbf{J}_{em}^\mu \mathbf{J}_{em}^\nu   N(\mathbf{p}) \rangle$ . . . . .	349
K.3	Goldberger-Treiman (GT) relation . . . . .	356
K.4	$P \rightarrow \ell\ell$ decays . . . . .	357
K.4.1	Pseudoscalar meson exchange . . . . .	359
<b>L</b>	<b>Transition form factors</b>	<b>365</b>
<b>M</b>	<b>Higher-order effects in the non-relativistic potential</b>	<b>368</b>

# List of Tables

1.1	Matter content of the Standard Model. Upperindex <sup>0</sup> means these fields are in the flavor basis. . . . .	2
1.2	Comparison between degrees of freedom in unitary and renormalizable gauge (11 in both). . . . .	10
1.3	Dimension-six operators other than the four-fermion ones [1]. . . . .	29
1.4	Four-fermion operators [1]. . . . .	30
1.5	Phenomenological determination of the renormalized couplings $L_i^r(M_\rho)$ from $\mathcal{O}(p^4)$ and $\mathcal{O}(p^6)$ $\chi$ PT analyses, and from lattice simulations. The fifth and sixth columns show the R $\chi$ T predictions without and with short-distance information, respectively. Values labeled with † have been used as inputs [2].	45
2.1	Average values of some tau parameters [3]. . . . .	57
2.2	Experimental determinations of the ratios $g_\ell/g_{\ell'}$ [4]. . . . .	59
2.3	Experimental bounds at 90% C.L. for the leptonic $\mu$ -decay couplings [3]. . . . .	64
2.4	Michel parameters [3]. The last column assumes identical couplings for $\ell = e, \mu$ . $\xi_{\mu \rightarrow e}$ refers to the product $\xi_{\mu \rightarrow e} \mathcal{P}_\mu$ , where $\mathcal{P}_\mu \approx 1$ is the longitudinal polarization of the $\mu$ from $\pi$ decay. . . . .	65
2.5	Experimental bounds at 95% C.L. for the leptonic $\tau$ -decay couplings [3]. . . . .	65
2.6	Cabibbo-allowed hadronic $\tau$ branching ratios [5], $h^\pm$ stands for $\pi^\pm$ or $K^\pm$ . . . . .	77
2.7	Cabibbo-suppressed hadronic $\tau$ branching ratios [5], $h^\pm$ stands for $\pi^\pm$ or $K^\pm$ . . . . .	77

3.1	Constraints on the scalar and tensor couplings obtained (at three standard deviations) through the limits on the current branching ratio measurements and the hypothetical case where this value be measured by Belle II with a three times smaller error. Theory errors are included. . . . .	101
4.1	Constraints on the scalar and tensor couplings obtained (at three standard deviations) through the limits on the current branching ratio measurements. Theory errors are included. . . . .	128
6.1	Summary of the contributions to $a_\mu^{SM}$ . Adapted from Ref. [6]. . . . .	163
6.2	Contributions to $10^{10} \cdot a_\mu^{HVP,LO}[\pi\pi](\tau)$ and $10^2 \cdot \mathcal{B}_{\pi^-\pi^0}^{CVC}$ from the IB corrections [6]. Corrections shown correspond to the Gounaris-Sakurai (GS) parameterization [7]. The total uncertainty includes the difference with Kühn-Santamaria (KS) parameterization quoted as $\delta(\text{GS} - \text{KS})$ . . . . .	188
7.1	Operators contributing at $\mathcal{O}(p^6)$ to the vector and axial-vector form factors.	205
7.2	Branching ratios $\text{Br}(\tau^- \rightarrow \pi^- \pi^0 \gamma \nu_\tau)$ for different values of $E_\gamma^{cut}$ . The second column corresponds to the complete Bremsstrahlung and the third and fourth to the $\mathcal{O}(p^4)$ contributions. . . . .	218
7.3	Branching ratios $\text{Br}(\tau^- \rightarrow \pi^- \pi^0 \gamma \nu_\tau)$ for different $E_\gamma^{cut}$ values at $\mathcal{O}(p^6)$ . . . .	218
7.4	Contributions to $\Delta a_\mu^{HVP,LO}$ in units of $10^{-11}$ using the dispersive representation of the form factor. From the two evaluations labelled $\mathcal{O}(p^4)$ , the left(right) one corresponds to $F_V = \sqrt{2}F(F_V = \sqrt{3}F)$ . . . . .	226
7.5	Contributions to $\Delta a_\mu^{HVP,LO}$ in units of $10^{-11}$ using the GP parametrization of the form factor. From the two evaluations labelled $\mathcal{O}(p^4)$ , the left(right) one corresponds to $F_V = \sqrt{2}F(F_V = \sqrt{3}F)$ . . . . .	226
7.6	Contributions to $\Delta a_\mu^{HVP,LO}$ in units of $10^{-11}$ using the DR form factor as the reference one. . . . .	228

7.7	IB-corrected $a_\mu^{HVP,LO}[\pi\pi, \tau]$ in units of $10^{-10}$ using the measured mass spectrum by Belle with $B_{\pi\pi} = (25.24 \pm 0.01 \pm 0.39)\%$ . Different approximation to $G_{EM}(s)$ are displayed in the various columns. The last three of them show the results at $\mathcal{O}(p^6)$ and their differences overestimate the error at this order. The error of the $\mathcal{O}(p^4)$ prediction (obtained with $F_V = \sqrt{2}F$ ) can be quantified from its difference with the SD value (corresponding to the $\mathcal{O}(p^6)$ contribution using only SD constraints). . . . .	233
7.8	IB-corrected $a_\mu^{HVP,LO}[\pi\pi, \tau]$ in units of $10^{-10}$ using the measured mass spectrum by ALEPH with $B_{\pi\pi} = (25.471 \pm 0.097 \pm 0.085)\%$ . The rest is as in Table 7.7. . . . .	234
7.9	IB-corrected $a_\mu^{HVP,LO}[\pi\pi, \tau]$ in units of $10^{-10}$ using the measured mass spectrum by CLEO with $B_{\pi\pi} = (25.36 \pm 0.44)\%$ . The rest is as in Table 7.7. . .	234
7.10	IB-corrected $a_\mu^{HVP,LO}[\pi\pi, \tau]$ in units of $10^{-10}$ using the measured mass spectrum by OPAL with $B_{\pi\pi} = (25.46 \pm 0.17 \pm 0.29)\%$ . The rest is as in Table 7.7. . . . .	235
7.11	IB-corrected $a_\mu^{HVP,LO}[\pi\pi, \tau]$ in units of $10^{-10}$ at $\mathcal{O}(p^4)$ . The first error is related to the systematic uncertainties on the mass spectrum, and also include contributions from the $\tau$ -mass and $V_{ud}$ uncertainties. The second error arises from $B_{\pi\pi^0}$ and $B_e$ , and the third error from the isospin-breaking corrections. . . . .	235
7.12	IB-corrected $a_\mu^{HVP,LO}[\pi\pi, \tau]$ in units of $10^{-10}$ at $\mathcal{O}(p^6)$ . The rest is as in Table 7.11. . . . .	235
8.1	Determinations of the proton Zemach radius $r_{Z_p}$ , in units of fm [8]. . . . .	249

9.1	Branching fraction for $f_1 \rightarrow e^+e^-$ decays in units of $10^{-9}$ with the different form factors outlined in appendix L (ideal mixing case). In particular the first three columns correspond to models incorporating a vector meson mass $m_V = 0.77$ GeV, whereas the last three columns have effective masses around 1 GeV, illustrating the relevance of the intermediate $V\gamma$ state. For reference, this branching ratio is $< 9.4 \times 10^{-9}$ at 90% confidence level [9]. . . . .	258
9.2	The results for $A_1(0)/[\alpha^2 B_{2S}(0,0)]$ for $\ell = \mu$ . For simplicity, we take ideal mixing in VMD models, implying that $m_V = 0.77$ GeV $\simeq m_{\rho,\omega}$ for $a_1, f_1$ and $m_V = m_\phi$ for the $f_1'$ . . . . .	263
9.3	Results for the HFS of muonic hydrogen. The central values for the $g_{ANN}$ couplings are those from ideal mixing, eq. (9.24). The second column displays results from OPE column in table 9.2, including as an additional uncertainty the difference with other models therein (see details in the text). The final two columns include uncertainties from $A_1(0)$ , $g_{ANN}$ , $B_{2S}$ , $m_A$ and an additional uncertainty from the mixing within brackets (see details in the text). . . . .	264
9.4	The contributions from the ground and first excited states contribution to the HFS (errors not included, see details in the text). The results compare to those in table 9.3. The first resonance contribution is enhanced with respect to table 9.3 as a result of the $g_{ANN}$ coupling, whereas the first excited states partially damp this effect. . . . .	266

# List of Figures

1.1	Summary of measurements of $\alpha_s$ as a function of the energy scale $Q$ [3]. The respective degree of QCD perturbation theory used in the extraction of $\alpha_s$ is indicated in brackets (NLO: next-to-leading order; NNLO: next-to-next-to-leading-order; NNLO+res: NNLO matched to a resummed calculation; N <sup>3</sup> LO: next-to-NNLO).	21
1.2	Integration of the $W$ boson out from the electroweak theory yields the Fermi effective interaction, which is exemplified here for the muon decay. . . . .	26
1.3	Symbolic representation of the Cauchy contour in the complex $s$ plane. Reprinted from Ref. [10]. . . . .	47
1.4	Graphical representation of the discontinuity relation for pion form factors, where the black disc represents the form factor, while the gray disc represents the pion-pion scattering $T$ -matrix, projected onto the appropriate partial wave. Reprinted from Ref. [10]. . . . .	50
1.5	Illustrative representation of the inhomogeneous unitarity relation in Eq. (1.137): the homogeneous term similar to a form factor unitarity relation (left), plus the projection of a typical diagram representing crossed-channel dynamics (right), giving rise to the inhomogeneous Omnès problem. The double line renders a heavy particle with its three-body decay partial wave represented by the blue dot, the single lines illustrate the three outgoing decay products that rescatter elastically (red dots). Reprinted from Ref. [10]. . . . .	52
2.1	Feynman diagrams for $\mu^- \rightarrow e^- \bar{\nu}_e \nu_\mu$ and $\tau^- \rightarrow X^- \nu_\tau$ ( $X^- = e^- \bar{\nu}_e, \mu^- \bar{\nu}_\mu, d\bar{u}, s\bar{u}$ ).	55
2.2	Relation between $\mathcal{B}_e$ and $\tau_\tau$ . The diagonal band corresponds to Eq. (2.8). . . . .	58



2.3	Pion form factor from ALEPH [11] and CLEO [12] $\tau$ data (left) and $e^+e^- \rightarrow \pi^+\pi^-$ [13] and $e^-\pi^- \rightarrow e^-\pi^-$ [14] data (right), compared to theory [15–17]. The red dashed line is the prediction from Eq. (2.43). . . . .	71
2.4	Pion form factor extracted from Belle $\tau^- \rightarrow \pi^-\pi^0\nu_\tau$ data [18]. The curves correspond to the different approximations, including $\rho$ , $\rho'$ and $\rho''$ [19]. The BaBar $e^+e^- \rightarrow \pi^+\pi^-\gamma$ measurement [20,21] shows a clear signal of the $\rho'''$ and the isoscalar $\omega$ state. . . . .	72
2.5	The $\tau^- \rightarrow K_S\pi^-\nu_\tau$ spectrum measured by the Belle collaboration [22]. The solid line corresponds to the fit in Ref. [23,24], which includes a R $\chi$ T description of $F_V^{K\pi}(s)$ with two resonances and $F_S^{K\pi}(s)$ from Ref. [25–27]. The scalar and $K^*(1410)$ correspond to the dotted and dash-dotted lines, respectively. . . . .	74
3.1	Modulus and phase, $ F_T(s) $ (left) and $\delta_T(s)$ (right), of the tensor form factor, $F_T(s)$ , corresponding to Eq. (3.15). . . . .	89
3.2	Dalitz plot distribution $ \overline{\mathcal{M}} _{00}^2$ in the SM, Eq. (3.18): Differential decay distribution for $\tau^- \rightarrow \pi^-\pi^0\nu_\tau$ in the (s,t) variables (left). The right-hand figure shows the differential decay distribution in the (s, $\cos\theta$ ) variables, Eq. (3.21). The Mandelstam variables, s and t, are normalized to $M_\tau^2$ . . . . .	93
3.3	Dalitz plot distribution for $\tilde{\Delta}(\hat{e}_S, \hat{e}_T)$ , (3.20), in the $\tau^- \rightarrow \pi^-\pi^0\nu_\tau$ decays: left-hand side corresponds to Eq. (3.18) and right-hand side corresponds to the differential decay distribution in the (s, $\cos\theta$ ) variables, both with ( $\hat{e}_S = 1.31, \hat{e}_T = 0$ ). The Mandelstam variables, s and t, are normalized to $M_\tau^2$ . . . . .	93
3.4	Dalitz plot distribution for $\tilde{\Delta}(\hat{e}_S, \hat{e}_T)$ , (3.20), in the $\tau^- \rightarrow \pi^-\pi^0\nu_\tau$ decays: left-hand side corresponds to Eq. (3.18) and right-hand side corresponds to the differential decay distribution in the (s, $\cos\theta$ ) variables, both with ( $\hat{e}_S = 0, \hat{e}_T = -0.014$ ). The Mandelstam variables, s and t, are normalized to $M_\tau^2$ . . . . .	94

3.5	Dalitz plot distribution for $\tilde{\Delta}(\hat{\epsilon}_S, \hat{\epsilon}_T)$ , (3.20), in the $\tau^- \rightarrow \pi^- \pi^0 \nu_\tau$ decays: left-hand side corresponds to Eq. (3.18) and right-hand side corresponds to the differential decay distribution in the $(s, \cos \theta)$ variables, both with $(\hat{\epsilon}_S = 0.008, \hat{\epsilon}_T = 0)$ . The Mandelstam variables, s and t, are normalized to $M_\tau^2$ . . . . .	94
3.6	Dalitz plot distribution for $\tilde{\Delta}(\hat{\epsilon}_S, \hat{\epsilon}_T)$ , (3.20), in the $\tau^- \rightarrow \pi^- \pi^0 \nu_\tau$ decays: left-hand side corresponds to Eq. (3.18) and right-hand side corresponds to the differential decay distribution in the $(s, \cos \theta)$ variables, both with $(\hat{\epsilon}_S = 0, \hat{\epsilon}_T = -0.001)$ . The Mandelstam variables, s and t, are normalized to $M_\tau^2$ . . . . .	95
3.7	The $\pi^0 \pi^-$ hadronic invariant mass distribution for the SM (solid line) and $\hat{\epsilon}_S = 1.31, \hat{\epsilon}_T = 0$ (dashed line), $\hat{\epsilon}_S = 0, \hat{\epsilon}_T = -0.014$ (dotted line). Axes units are given in GeV powers and the decay distributions are normalized to the tau decay width. . . . .	97
3.8	The forward-backward asymmetry in the $\tau^- \rightarrow \pi^- \pi^0 \nu_\tau$ decay as a function of the $\pi\pi$ energy for the SM case. The low-energy region is shown in the left plot and remaining energy range is represented in the right plot. . . . .	98
3.9	Forward-asymmetry for $\hat{\epsilon}_S = 1.31, \hat{\epsilon}_T = 0$ (dashed line) compared to the SM prediction (solid line). The left plot shows the low-energy region and the right plot includes the remaining energy range. . . . .	98
3.10	Normalized difference with respect to the SM for the forward-backward asymmetry ( $\Delta A_{FB}$ ) in the case of scalar interactions (left plot, with $\hat{\epsilon}_S = 0.008, \hat{\epsilon}_T = 0$ ) and tensor interactions (right plot, $\hat{\epsilon}_T = -0.001, \hat{\epsilon}_S = 0$ ). . . . .	99
3.11	$\Delta$ as a function of $\hat{\epsilon}_S$ for $\hat{\epsilon}_T = 0$ (left-hand) and $\hat{\epsilon}_T$ for $\hat{\epsilon}_S = 0$ (right-hand) for $\tau^- \rightarrow \pi^- \pi^0 \nu_\tau$ decays. Horizontal lines represent the values of $\Delta$ according to the current measurement and theory error (at three standard deviations) of the branching ratio (dashed line) and the hypothetical case of this value being measured by Belle-II with three times reduced error (dotted line). . . . .	99

3.12	Constraints on the scalar and tensor couplings obtained from $\Delta(\tau^- \rightarrow \pi^- \pi^0 \nu_\tau)$ using the Belle measurement and the theory uncertainty (at three standard deviations) of the branching ratio. The left-hand plot shows the constraints obtained from current data. On the right-hand plot we show a magnification of the top part of this ellipse, where the solid line represents the upper limit on $\hat{\epsilon}_S$ and $\hat{\epsilon}_T$ , while the dashed lines intend to illustrate the effect of a possible threefold improvement in the measurement at the Belle-II experiment. . . . .	101
4.1	Normalized absolute value of the tensor form factor $F_T^{K\eta^{(\prime)}}(s)$ given in Eq. (4.17) (left), for $s_{\text{cut}} = 4 \text{ GeV}^2$ (dotted line), $9 \text{ GeV}^2$ (dashed line) and $s_{\text{cut}} \rightarrow \infty$ (solid line), and tensor form factor phase $\delta_T^{K\eta^{(\prime)}}(s)$ (right). . . . .	113
4.2	Dalitz plot distribution in the SM, $ \overline{\mathcal{M}}(0,0) ^2$ in Eq. (4.30), for $\tau^- \rightarrow K^- \eta \nu_\tau$ (left) and $\tau^- \rightarrow K^- \eta' \nu_\tau$ (right) in the $(s, t)$ variables. The figures of the lower row show the differential decay distribution in the $(s, \cos \theta)$ variables, Eq. (4.33). The $s$ and $t$ variables are normalized to $m_\tau^2$ . . . . .	118
4.3	Dalitz plot distribution of $\tilde{\Delta}(\hat{\epsilon}_S, \hat{\epsilon}_T)$ in Eq. (4.32) for $\tau^- \rightarrow K^- \eta \nu_\tau$ with $(\hat{\epsilon}_S = -0.38, \hat{\epsilon}_T = 0)$ (left panels) and $(\hat{\epsilon}_S = 0, \hat{\epsilon}_T = 0.085)$ (right panels). The lower row shows the differential decay distribution in the $(s, \cos \theta)$ variables, Eq. (4.33). The $s$ and $t$ variables are normalized to $m_\tau^2$ . . . . .	119
4.4	Dalitz plot distribution of $\tilde{\Delta}(\hat{\epsilon}_S, \hat{\epsilon}_T)$ in Eq. (4.32) for $\tau^- \rightarrow K^- \eta' \nu_\tau$ with $(\hat{\epsilon}_S = -0.20, \hat{\epsilon}_T = 0)$ (left panels) and $(\hat{\epsilon}_S = 0, \hat{\epsilon}_T = 14.9)$ (right panels). The lower row show the differential decay distribution in the $(s, \cos \theta)$ variables, Eq. (4.33). The $s$ and $t$ variables are normalized to $m_\tau^2$ . . . . .	120
4.5	Left: $K^- \eta$ invariant mass distribution in the SM (solid line), and for $\hat{\epsilon}_S = -0.38, \hat{\epsilon}_T = 0$ (dashed line) and $\hat{\epsilon}_S = 0, \hat{\epsilon}_T = 0.085$ (dotted line). Right: $K^- \eta'$ invariant mass distribution in the SM (solid line), and for $\hat{\epsilon}_S = -0.20, \hat{\epsilon}_T = 0$ (dashed line) and $\hat{\epsilon}_S = 0, \hat{\epsilon}_T = 14.9$ (dotted line). Units in axes units are given in GeV powers and the decay distributions are normalized to the tau decay width. . . . .	123

4.6	Left: Forward-backward asymmetry for the decay $\tau^- \rightarrow K^- \eta \nu_\tau$ in the SM (solid line), and for $\hat{e}_S = -0.38$ , $\hat{e}_T = 0$ (dashed line), and $\hat{e}_T = 0.085$ , $\hat{e}_S = 0$ (dotted line). Right: Forward-backward asymmetry for the decay $\tau^- \rightarrow K^- \eta' \nu_\tau$ in the SM (solid line), and for $\hat{e}_S = -0.20$ , $\hat{e}_T = 0$ (dashed line), and $\hat{e}_T = 14.9$ , $\hat{e}_S = 0$ (dotted line). . . . .	124
4.7	$\Delta$ as a function of $\hat{e}_S$ for $\hat{e}_T = 0$ (left-hand) and $\hat{e}_T$ for $\hat{e}_S = 0$ (right-hand) for the decay $\tau^- \rightarrow K^- \eta \nu_\tau$ . Horizontal lines represent the values of $\Delta$ according to the current measurement and theory errors (at three standard deviations) of the branching ratio (dashed line). . . . .	126
4.8	$\Delta$ as a function of $\hat{e}_S$ for $\hat{e}_T = 0$ (left plot) and $\hat{e}_T$ for $\hat{e}_S = 0$ (right plot) for the decay $\tau^- \rightarrow K^- \eta' \nu_\tau$ . Horizontal lines represent the values of $\Delta$ according to the current measurement and theory errors (at three standard deviations) of the branching ratio (dashed line). . . . .	127
4.9	Constraints on the scalar and tensor couplings obtained from $\Delta(\tau^- \rightarrow K^- \eta \nu_\tau)$ (left plot) and $\Delta(\tau^- \rightarrow K^- \eta' \nu_\tau)$ (right plot) using, respectively, the measured branching ratio (at three standard deviations) and the upper limits of the branching ratio at 90% C.L. . . . .	127
5.1	Belle measurement of the modulus squared of the pion vector form factor [18] as compared to our fits [28]. . . . .	138
5.2	Belle $\tau^- \rightarrow K_S \pi^- \nu_\tau$ (red solid circles) [22] and $\tau^- \rightarrow K^- \eta \nu_\tau$ (green solid squares) [29] measurements as compared to our best fit results in [30] (solid black and blue lines, respectively) obtained from a combined fit to both data sets. The small scalar contributions are represented by black and blue dashed lines. . . . .	139
6.1	SM contributions to $a_\mu$ . The diagrams shown (from left to right) correspond to the one-loop QED diagram, the one-loop EW diagram involving $Z$ -boson exchange, the leading-order HVP diagram and HLbL contributions. Reprinted from Ref. [31]. . .	153

6.2	Five-loop QED diagrams. The overall QED contribution to $a_\mu$ involves 12 672 diagrams. The straight and wavy lines denote lepton and photon propagators, respectively. Reprinted from Ref. [32]. . . . .	154
6.3	One-loop EW Feynman diagrams. Reprinted from Ref. [6]. . . . .	154
6.4	HVP Feynman diagrams at LO and NLO (a)-(c). The gray blobs refer to hadronic VP while the white one refers to leptonic VP. Reprinted from Ref. [6]. . . . .	155
6.5	Contributions to the total hadronic cross section (expressed as the hadronic R-ratio, $R(s) = \sigma_{\text{had}}(s)/(4\pi\alpha^2/(3s))$ ) from different final states below $\sqrt{s} \sim 2$ GeV. The total hadronic cross section is depicted in light blue and each final state is included as a new layer on top in decreasing order of the size of its contribution to $a_\mu^{\text{HVP LO}}$ . Reprinted from Ref. [33]. . . . .	156
6.6	Results for $(a_\mu^{\text{SM}} - a_\mu^{\text{EXP}}) \cdot 10^{10}$ when $a_\mu^{\text{HVP LO}}$ is taken from several lattice [34–46] and data-driven [47–50] estimates. The filled dark blue circles are lattice results [34–41] that are included in the lattice average in Ref. [6], which is indicated by the light-blue band. The unfilled dark blue circles are those results not included in the averages [42–46, 51]. The red squares show results from data-driven estimation of $a_\mu^{\text{HVP LO}}$ , where filled squares are those included in the merged data-driven result [47, 48] and unfilled are not [49, 50]. The purple triangle shows a hybrid result where noisy lattice data at very short and long distances are replaced by $e^+e^- \rightarrow$ hadrons data [40]. The yellow band indicates the “no New Physics” scenario, where $a_\mu^{\text{HVP LO}}$ results are large enough to bring $a_\mu^{\text{SM}}$ into agreement with experiment. The grey band in the center of the yellow one indicates the projected experimental uncertainty from the Fermilab Muon $g - 2$ experiment. Reprinted from Ref. [31]. .	159
6.7	HLbL Feynman diagram at LO. The shaded blob represents all possible intermediate hadronic states. Reprinted from Ref. [46]. . . . .	161
6.8	CMD-2 [52, 53] (left) and SND [54] (right) data for $e^+e^- \rightarrow \pi^+\pi^-$ in the $\rho$ region. Reprinted from Ref. [55]. . . . .	167

6.9	The KLOE $e^+e^- \rightarrow \pi^+\pi^-$ measurement in the $\rho$ region obtained in three experimental configurations [56–58]. Adapted from Ref. [58]. . . . .	168
6.10	BABAR results [20,21] using the large-angle ISR method: $e^+e^- \rightarrow \mu^+\mu^-$ compared to NLO QED (top) and $e^+e^- \rightarrow \pi^+\pi^-$ from threshold to 3 GeV utilizing the $\pi\pi/\mu\mu$ ratio (bottom). Reprinted from Ref. [21]. . . . .	169
6.11	Results from BESIII (left, reprinted from Ref. [59]) and CLEO-c (right, reprinted from Ref. [60]) on $e^+e^- \rightarrow \pi^+\pi^-$ in the $\rho$ region using large-angle detected ISR photons. . . . .	170
6.12	Cross sections for $e^+e^- \rightarrow K_S K_L$ measured by SND [61] (upper left), and $e^+e^- \rightarrow K^+K^-$ by CMD-2 [62], SND [61], and BABAR [63] (upper right), and BABAR over a wider energy range (bottom). Reprinted from Refs. [61,63]. . . . .	171
6.13	The $\omega$ resonance in the $\pi^+\pi^-\pi^0$ mode from CMD-2. Reprinted from Ref. [64]. . .	173
6.14	Multi-pion cross sections results. Top left: $\pi^+\pi^-\pi^0$ from BABAR [65], SND [66, 67], and previous experiments. Top right: $2\pi^+2\pi^-$ BABAR [68,69] and elderly experiments. Bottom: $\pi^+\pi^-2\pi^0$ from BABAR [70] and older experiments (left), and $2\pi^+2\pi^-\pi^0$ from BABAR [71] (right). Reprinted from Refs. [67,69–71]. . . . .	174
6.15	Results from BABAR [71,72], CMD-2 [73], and SND [74] on the cross sections for $e^+e^- \rightarrow \eta\pi^+\pi^-$ (left), and from CMD-3 [75] for $e^+e^- \rightarrow \eta\pi^+\pi^-\pi^0$ (right). Reprinted from Refs. [72,75]. . . . .	174
6.16	BABAR results [76–80] on the cross sections for $e^+e^- \rightarrow K\bar{K}\pi$ (top row) and $e^+e^- \rightarrow K\bar{K}\pi\pi$ (second and third rows). Reprinted from Ref. [81]. . . . .	175
6.17	The total hadronic $e^+e^-$ annihilation cross section ratio $R$ as a function of $\sqrt{s}$ [81]. Inclusive measurements from BES [82–84] and KEDR [85–87] are depicted as data points, while the sum of exclusive channels from this analysis is given by the narrow blue bands. The prediction from massless pQCD is also shown (solid red line). Reprinted from Ref. [48]. . . . .	176

6.18	The $\pi^+\pi^-$ cross section from the KLOE combination compared to the BABAR, CMD-2, SND, and BESIII data points in the 0.6 – 0.9 GeV range [88]. The KLOE combination is represented by the yellow band. The uncertainties shown are the diagonal and systematic uncertainties added in quadrature. Reprinted from Ref. [88].	177
6.19	The $\pi^+\pi^-$ cross section from KLOE combination, BABAR, CMD-2, SND, and BESIII in the $\rho - \omega$ interference region [88]. Reprinted from Ref. [88]. . . . .	178
6.20	Comparison of results for $a_\mu^{\text{HVP}}[\pi\pi]$ evaluated between 0.6 GeV and 0.9 GeV for the different experiments. Reprinted from Ref. [6]. . . . .	179
6.21	Ratios of cross sections [88] from KLOE-2012 to KLOE-2008 (top left), KLOE-2010 to KLOE-2008 (top right), and KLOE-2012 to KLOE-2010 (bottom). The uncommon systematic uncertainties in the respective ratios are indicated by the green bands. Reprinted from Ref. [6]. . . . .	180
6.22	Top left: ratio of SND-2020 $\pi^+\pi^-$ cross section values to form factor fit. Top right: ratio of older SND and CMD-2 cross sections to new SND fit. Bottom: akin ratios for BABAR (left) and KLOE-2008 and KLOE-2010 (right). Reprinted from Ref. [89].	181
6.23	Top left: bare cross sections for $e^+e^- \rightarrow K^+K^-$ . Top right: comparison between individual $e^+e^- \rightarrow K^+K^-$ cross sections measurements from BABAR [63], CMD-2 [62], CMD-3 [90], SND [61], and the HVPTools combination. Bottom: local scale factor vs. CM energy applied to the combined $K^+K^-$ cross section uncertainty to account for inconsistency in the individual measurements. Reprinted from Ref. [48].	183
6.24	Comparison of IB corrections used by Davier et al. [7] and by F. Jegerlehner [91]. The different plots correspond to FSR (top left), $1/G_{\text{EM}}$ (top right), $\beta_0^3(s)/\beta_-^3(s)$ ratio term (middle left), the effect of the $\rho$ mass and width difference in the $ F_0/F_- $ term (middle right), the effect of the $\rho - \omega$ interference in the $ F_0/F_- $ term (bottom left), and the total corrections (bottom right). The difference between the open blue points and the solid black one in the last plot come from the $\rho - \gamma$ mixing corrections proposed in Ref. [91]. Reprinted from Ref. [92]. . . . .	186

6.25	Relative comparison between the combined $\tau$ after the IB corrections and $e^+e^- \rightarrow \pi^+\pi^-$ spectral function contributions. Reprinted from Ref. [93]. . . . .	189
6.26	The measured branching ratios for $\tau^- \rightarrow \pi^-\pi^0\nu_\tau$ decays compared to the predictions from the $e^+e^- \rightarrow \pi^+\pi^-$ spectral functions, after applying the IB corrections. The long and short vertical error bands represent the $\tau$ and $e^+e^-$ averages, respectively. Reprinted from Ref. [7]. . . . .	190
6.27	Same as Fig. 6.25, apart from the $\rho-\gamma$ mixing correction proposed in Ref. [91] has been applied to the $\tau$ data. . . . .	190
7.1	One-resonance exchange contributions from the $R\chi T$ to the vector form factors of the $\tau^- \rightarrow \pi^-\pi^0\gamma\nu_\tau$ decays. . . . .	198
7.2	Two-resonance exchange contributions from the $R\chi T$ to the vector form factors of the $\tau^- \rightarrow \pi^-\pi^0\gamma\nu_\tau$ decays. . . . .	198
7.3	Three-resonance exchange contributions from the $R\chi T$ to the vector form factors of the $\tau^- \rightarrow \pi^-\pi^0\gamma\nu_\tau$ decays. . . . .	198
7.4	Anomalous diagrams contributing to the axial tensor amplitude $A^{\mu\nu}$ at $\mathcal{O}(p^4)$ . 200	
7.5	One-resonance exchange contributions from the $R\chi T$ to the axial-vector form factors of the $\tau^- \rightarrow \pi^-\pi^0\gamma\nu_\tau$ decays. . . . .	201
7.6	Two-resonance exchange contributions from the $R\chi T$ to the axial-vector form factors of the $\tau^- \rightarrow \pi^-\pi^0\gamma\nu_\tau$ decays. . . . .	201
7.7	Three-resonance exchange contributions from the $R\chi T$ to the axial-vector form factors of the $\tau^- \rightarrow \pi^-\pi^0\gamma\nu_\tau$ decays. . . . .	201



7.8	Correction function $G_{EM}^{(0)}(s)$ in Eq. (7.51a) (blue dashed line). The solid line shows the $G_{EM}(s)$ function neglecting the structure-dependent part (SI), i.e. by taking $v_1 = v_2 = v_3 = v_4 = a_1 = a_2 = a_3 = a_4 = 0$ , the dashed and dotted lines are the $\mathcal{O}(p^4)$ $G_{EM}(s)$ function (with either $F_V = \sqrt{2}F$ or $F_V = \sqrt{3}F$ constraints). The blue shaded region is the full $\mathcal{O}(p^6)$ contribution, including (overestimated) uncertainties. The left-hand side plot corresponds to the dispersive parametrization [19] while the right-hand side corresponds to the Guerrero-Pich parametrization [15] of the form factor (the latter was used in Ref. [94]). . . . .	216
7.9	Modulus and phase of the pion vector form factor, $f_+(s)$ . The solid line corresponds to the dispersive representation used in Ref. [19] while the dashed line corresponds to the Guerrero-Pich parametrization [15] employed by Ref. [94].	219
7.10	The $\pi^-\pi^0$ hadronic invariant mass distribution for the $\tau^- \rightarrow \pi^-\pi^0\gamma\nu_\tau$ decays for $E_\gamma^{cut} = 100$ MeV (black), $E_\gamma^{cut} = 200$ MeV (brown), $E_\gamma^{cut} = 300$ MeV (blue), $E_\gamma^{cut} = 400$ MeV (gray) and $E_\gamma^{cut} = 500$ MeV (red) using only the Bremsstrahlung (SI) contribution. . . . .	220
7.11	The $\pi^-\pi^0$ hadronic invariant mass distributions for $E_\gamma^{cut} = 300$ MeV. The solid and dashed lines represent the $\mathcal{O}(p^4)$ corrections using $F_V = \sqrt{3}F$ and $F_V = \sqrt{2}F$ , respectively. The dotted line stands for the Bremsstrahlung contribution (SI). . . . .	221
7.12	The $\pi^-\pi^0$ hadronic invariant mass distributions for $E_\gamma^{cut} = 300$ MeV. The solid and dashed line represent the $\mathcal{O}(p^4)$ corrections using $F_V = \sqrt{3}F$ and $F_V = \sqrt{2}F$ , respectively. The dotted line represents the Bremsstrahlung contribution (SI). The dotdashed red line corresponds to using only SD constraints at $\mathcal{O}(p^6)$ and the blue shaded region overestimates the corresponding uncertainties. . . . .	221

7.13	Photon energy distribution for the $\tau^- \rightarrow \pi^- \pi^0 \gamma \nu_\tau$ decays normalized with the non-radiative decay width. The dotted line represents the Bremsstrahlung contribution. The solid and dashed lines represent the $\mathcal{O}(p^4)$ corrections using $F_V = \sqrt{3}F$ and $F_V = \sqrt{2}F$ , respectively. The dotdashed red line corresponds to using only SD constraints at $\mathcal{O}(p^6)$ (with overestimated uncertainties in the blue shaded area). . . . .	222
7.14	Branching ratio for the $\tau^- \rightarrow \pi^- \pi^0 \gamma \nu_\tau$ decays as a function of $E_\gamma^{cut}$ . The dotted line represents the Bremsstrahlung contribution, the solid line and dashed line represent the $\mathcal{O}(p^4)$ corrections using $F_V = \sqrt{3}F$ and $F_V = \sqrt{2}F$ , respectively. The dotdashed red line is the $\mathcal{O}(p^6)$ contribution using only SD constraints and neglecting all other couplings. The blue shaded region overestimates the $\mathcal{O}(p^6)$ uncertainties. . . . .	222
7.15	Predictions for the branching ratio at $\mathcal{O}(p^6)$ for a sample of 1000 points, with $E_{cut} = 100, 300, \text{ and } 500 \text{ MeV}$ from top to bottom. . . . .	223
7.16	Ratio of the form factors (FF1) for $\theta_{\rho\omega} = (-3.5 \pm 0.7) \times 10^{-3} \text{ GeV}^2$ . The solid line represents the mean value. . . . .	229
7.17	Full IB correction factor $R_{IB}(s)$ for the different orders of approximation in $G_{EM}(s)$ using the central values given in (FF1). The blue region corresponds to the (overestimated) corrections at $\mathcal{O}(p^6)$ in $G_{EM}(s)$ . . . . .	229
7.18	Comparison between the different data sets from BaBar (above) and KLOE (below) with $\Delta\Gamma_{\pi\pi\gamma} = 1.5 \text{ MeV}$ (left-hand) and $\Delta\Gamma_{\pi\pi\gamma} = 0.45 \text{ MeV}$ (right-hand) for FF1 and FF2, respectively. The blue region corresponds to the experimental error on $\sigma_{\pi\pi(\gamma)}$ . The solid and dashed lines represent the contributions with $F_V = \sqrt{3}F$ and $F_V = \sqrt{2}F$ at $\mathcal{O}(p^4)$ , respectively. The dotted line is the SI contribution. The red line depicts the envelope of $G_{EM}(s)$ at $\mathcal{O}(p^6)$ , that overestimates the uncertainty at this order. The blue dotdashed line is the $\mathcal{O}(p^6)$ contribution using only SD constraints. . . . .	232

7.19	Comparison between the experimental values of $a_\mu$ from BNL [95] and FNAL [96] with respect to the Muon $g - 2$ Theory Initiative recommended value [6], the lattice QCD calculation from the BMW collaboration [43] and our results [97]. . . . .	237
8.1	Selection of recent proton charge radius determinations [8]. The band corresponds to the $\mu H$ '13 value. The references are (from top to bottom): CODATA [98–100], muonic atoms [101–103], $H$ spectroscopy [99,104–108], $ep$ scattering [109–114], dispersive analysis of $ep$ scattering [115–118]. . . . .	241
8.2	Deuteron charge radius determinations [8]. The results here correspond to: CODATA [98,99], $ed$ scattering [119], $\mu D$ spectroscopy [101,120,121], $H - D$ isotopic shift and $\mu H$ Lamb shift [102], $D$ spectroscopy [122]. . . . .	242
8.3	Main corrections in $\mu H$ . Here, the cyan blobs represent the finite-size effects, thin and thick lines the muon and proton, respectively. . . . .	243
8.4	(A) Formation of $\mu H$ in highly excited states and subsequent cascade with emission of “prompt” $K_{\alpha,\beta,\gamma^*}$ . (B) Laser excitation of the $2S - 2P$ transition with subsequent decay to the ground state with $K_\alpha$ emission. (C) $2S$ and $2P$ energy levels. The measured transitions $\nu_s$ and $\nu_t$ are indicated along with the Lamb shift, $2S$ -HFS, and $2P$ -Pine and hyperfine splitting. Reprinted from Ref. [102]. . . . .	245
8.5	Correlation between the Zemach and charge radius of the proton. . . . .	249
8.6	Experimental values and theoretical predictions for the $1S$ and $2S$ HFS in $H$ and $\mu H$ [8]. . . . .	252
9.1	The leading contribution to $A \rightarrow \ell^+ \ell^-$ decays (left). The axial-vector meson contribution to the $\ell^- p \rightarrow \ell^- p$ amplitude relevant to the HFS (right). The grey blob includes structure-dependent axial-photon-photon interactions. . . . .	256
9.2	The Zemach radius ( $r_Z$ ) from the references in the text and this work. The blue band represents the average from Refs. [123–126]. . . . .	268
A.1	Modulus and phase, $ F_T(s) $ (left) and $\delta_T(s)$ (right), of the tensor form factor, $F_T(s)$ , corresponding to the description explained in this appendix. . . . .	272

C.1	Feynman diagrams for the $\tau^- \rightarrow \pi^- \pi^0 \nu_\tau \gamma$ decays. . . . .	275
C.2	Bremsstrahlung off the charged-pion. . . . .	276
C.3	Anomalous diagrams for the transition $W^- (P - q) \rightarrow \pi^- (p_-) \pi^0 (p_0) \gamma (k)$ contributing to the axial tensor amplitude $A^{\mu\nu}$ . . . . .	279
C.4	$\rho$ and $a_1$ exchange diagrams for the model at $\mathcal{O}(p^4)$ . . . . .	283
C.5	Diagrams that receives contribution from $X^{\mu\nu}$ . . . . .	285
H.1	The $\tau^- \rightarrow \pi^- \pi^0 \gamma \nu_\tau$ decay in the $\tau$ -lepton rest frame. . . . .	307
H.2	Projection of the kinematic region for the non-radiative decay $\mathcal{R}^{III}$ (gray) and the radiative decay $\mathcal{R}^{IV} = \mathcal{R}^{IV/III} \cup \mathcal{R}^{III}$ (black and gray) onto the $su$ -plane. $\mathcal{R}^{IV/III}$ (black) is the kinematic region which is only accessible to the radiative decay. . . . .	311
K.1	Two photon exchange vertex. . . . .	350
K.2	Contributions to the $P \rightarrow \ell\ell$ decays via a $P$ coupling to $\gamma\gamma$ . . . . .	358
K.3	Muon-proton interaction produced by a pseudoscalar exchange. . . . .	359

# Abbreviations and nomenclature

## Nomenclature

EFT Effective Field Theory.

QFT Quantum Field Theory.

ChiPT [ $\chi$ PT] Chiral Perturbation Theory.

R $\chi$ T Resonance Chiral Theory.

HVP Hadronic Vacuum Polarization.

SD Structure-Dependent.

SI Structure-Independent.

HFS Hyperfine Splitting.

# Preface

The standard model is a quantum field theory [127–129] that describes the strong, weak, and electromagnetic interaction, and it has been tested with unprecedented accuracy. Despite its success, the SM is unable to explain the neutrino mass, the matter-antimatter asymmetry, the dark matter content in our universe, the accelerated expansion of the universe, and it doesn't include gravity. Although many BSM theories have been proposed to address these issues, plenty of them predict new particles at scales far beyond any current and planned experiment.

An effective field theory (EFT) provides us with the perfect framework to look up possible departures from the SM in a model-independent way, for instance, the SMEFT [1, 130] is the EFT of the SM that realizes its symmetries linearly, where the heavy new physics is decoupled [131], and all the information about the fundamental theory is already contained in the Wilson coefficients. Direct searches at colliders have set constraints on the mass scale of new particles above a few TeVs.

Given the lack of direct evidence of new particles at the LHC so far, the study of precision observables such as the  $W$  mass, the Higgs mass, flavor observables, and  $(g-2)_\mu$  would allow disentangling new physics effects. The muon anomalous magnetic moment,  $a_\mu = (g_\mu - 2)/2$ , is one of the most precise quantities that provides a stringent test of the SM and a window to physics beyond the SM (BSM). A long-standing deviation between theory and experiment about 3–4 standard deviations has been observed. The difference between the combination of the latest measurements from FNAL [96] and the previous one at Brookhaven [95] with respect to the latest SM prediction [6] increases the significance at  $4.2\sigma$ .

Chiral perturbation theory <sup>1</sup> and dispersion relations give an excellent description of the hadronic process at low-energies, where QCD becomes non-perturbative and any computation from first-principles is not feasible. Nevertheless, there have been several improvements on the lattice QCD estimations (see [134] for further details).

The thesis is structured as follows: the theoretical framework implemented in this thesis, which includes concepts on QCD, EFT, ChPT and dispersion relations is presented in Chapter 1. In Chapter 2, we highlight the relevance of the leptonic  $\tau$  decays in the search of New Physics and test of LU. Besides, we briefly describe the experimental and theoretical progress of the hadronic tau decays. In Chapter 3, analogously to leptonic  $\tau$  decays we study the Lorentz structure of the  $\tau^- \rightarrow \pi^- \pi^0 \nu_\tau$  decays through an EFT analysis that includes the most general structure allowed by the symmetries of the SM. In addition, we investigate the sensitivity of some observables to non-standard interactions. In Chapter 4, as before we explore the susceptibility to NP in the  $\tau^- \rightarrow K^- \eta^{(\prime)} \nu_\tau$  decays. In Chapter 5, we implement a global analysis of strangeness-conserving and -changing exclusive hadronic tau decays into one and two pseudoscalar mesons. Given the theoretical and experimental improvements of the muon anomalous magnetic moment, we discuss the SM estimation of  $a_\mu$  and the input used for the data-driven approach in Chapter 6. In Chapter 7, we review the isospin-breaking and electromagnetic corrections to the  $\tau^- \rightarrow \pi^- \pi^0 \nu_\tau$  decays, which are used as an input to the two-pion contributions to the hadronic vacuum polarization (at LO) of the anomalous magnetic moment ( $a_\mu$ ). An overview of the status of the Lamb shift and hyperfine splitting in muonic hydrogen is discussed in Chapter 8. In Chapter 9, we focus on the axial-vector contributions to the hyperfine splitting in muonic hydrogen.

---

<sup>1</sup>A nice review of ChiPT is given in [132, 133].

# Chapter 1

## Theoretical framework

### 1.1 Standard Model

The standard model of particle physics is the most successful quantum field theory in describing three of the four fundamental interactions of electromagnetic, weak and strong type. Each one of its predictions has been verified, showing an impressive agreement between theory and experiment.

#### 1.1.1 Particle content in the Standard Model.

The particles and fields content of the Standard Model [127–129] (SM) consists of 12 fermions (spin=1/2), 4 vector gauge bosons (spin=1), and a scalar Higgs boson (spin=0).

There are two types of fermions: leptons and quarks. These are:

- 3 charged leptons ( $e, \mu, \tau$ );
- 3 neutrinos ( $\nu_e, \nu_\mu, \nu_\tau$ ) (or  $\nu_1, \nu_2, \nu_3$ );
- 6 quarks of different flavors.

Every quark can have one of three possible colors. Each fermion has 2 degrees of freedom e.g., it can have spin up or spin down, or be left- or right-handed. Every fermion particle in



the SM has an antiparticle,  $f \neq \bar{f}$ , the latter has not yet been verified for neutrinos, which could be Majorana particles. Traditionally, fermions are known as matter fields, and bosons as force fields (they are the mediators of SM interactions).

The SM has the following boson fields:

- 8 vector (spin=1) gluons;
- 4 vectors (spin=1) electroweak bosons:  $\gamma$ ,  $Z$ ,  $W^\pm$ ;
- 1 scalar (spin=0) Higgs boson.

Gluons and photons are massless and have 2 degrees of freedom (polarizations),  $Z$  and  $W$  bosons are massive and have 3 degrees of freedom (polarizations). Massive or massless refers to the presence or absence of a corresponding mass term in the SM Lagrangian.

Gluons and electroweak (EW) bosons are gauge bosons, their interactions with fermions are fixed by certain symmetries of the SM Lagrangian. Electrically neutral bosons ( $H$ ,  $\gamma$ ,  $Z$  and gluons) coincide with their antiparticles e.g.,  $\gamma \equiv \bar{\gamma}$ . Each one of the 8 gluons carries both a color and an anticolor. All this is summarized in Table 1.1.

$q_i$	$SU(3)_C$	$SU(2)_L$	$U(1)_Y$	$Q = T_3 + Y$
$u_{mL}^0$	3	2	$+\frac{1}{6}$	$+\frac{2}{3}$
$d_{mL}^0$	3	2	$+\frac{1}{6}$	$-\frac{1}{3}$
$u_{mR}^0$	3	1	$+\frac{2}{3}$	$+\frac{2}{3}$
$d_{mR}^0$	3	1	$-\frac{1}{3}$	$-\frac{1}{3}$
$\ell_{mL}^0$	1	2	$-\frac{1}{2}$	-1
$\nu_{mL}^0$	1	2	$-\frac{1}{2}$	0
$\ell_{mR}^0$	1	1	-1	-1
$W^\pm$	1	3	0	$\pm 1$
$Z$	1	3	0	0
$\gamma$	1	1	0	0
$H$	1	2	$+\frac{1}{2}$	0
$g$	8	1	0	0

Table 1.1: Matter content of the Standard Model. Upperindex  $^0$  means these fields are in the flavor basis.

## 1.1.2 Constructing the Lagrangian of the Electroweak Model

With all fields discussed above, it is possible to build the most general renormalizable Lagrangian invariant under  $SU(2)_L \times U(1)_Y$ . Given that the symmetry  $SU(3)_C$  commutes with the  $SU(2)_L$  factor and the fact that the color symmetry is exact, we can ignore color indices and terms including gluons.

Working in natural units ( $\hbar = c = 1$ ) in a  $(1 + 3)$ -dimensional space, we can see that  $[\psi] = E^{3/2}$ ,  $[X] = E^1$  and  $[\phi] = E^1$  where  $X = W^i, B$ . For the theory to be renormalizable we must include all operators  $\hat{\mathcal{O}}^{(i)}$  with  $i \leq 4$ , that can be built with the SM fields, that is

$$\mathcal{L} = \sum_{i=0}^4 \alpha_i \hat{\mathcal{O}}^{(i)} = \alpha_0 \hat{\mathcal{O}}^{(0)} + \alpha_2 \hat{\mathcal{O}}^{(2)} + \alpha_3 \hat{\mathcal{O}}^{(3)} + \alpha_4 \hat{\mathcal{O}}^{(4)}, \quad (1.1)$$

where  $[\alpha_i] = E^{4-i}$  and  $[\mathcal{O}] = E^i$ .

We will see now which could be these operators:

- For  $i = 0$ ,  $\mathcal{O}^{(0)}$  must be dimension zero, so the only possibility corresponds to a constant. These terms are negligible working in flat spaces but become important in curved spaces.
- For  $i = 1$ , the only possibility is including a boson field, since they are of mass dimension 1, although these terms would not be invariant under  $SU(2)_L \times U(1)_Y$ , so there are not operators with  $i = 1$ .
- For  $i = 2$ , the only possibility corresponds to mass terms of the boson fields. For the gauge fields, these terms are forbidden since they are not invariant, while for the scalar fields they are allowed. In the scalar field case this term appears in the potential  $V(\phi)$ .
- For  $i = 3$ , there are several possibilities. On one side, there are the mass terms of the fermion fields,

$$\bar{\psi}\psi = \bar{\psi}_L\psi_R + \bar{\psi}_R\psi_L, \quad (1.2)$$

since  $\psi_L$  is  $SU(2)_L$  doublet and  $\psi_R$  is  $SU(2)_L$  singlet, these terms are not gauge in-

variant. A term of the form  $\phi^\dagger \partial^\mu \phi$  would not be a relativistic invariant. The last possibility corresponds to couplings between three boson fields  $X^3, X^2\phi, X\phi^2$  and  $\phi^3$  which are not invariant under  $SU(2) \times U(1)$ .  $X\phi^2$  terms are generated in the theory after promoting the global symmetry to a local one, while the  $X^3$  arise because the non-abelian nature of the gauge fields.

- There are more possibilities for  $i=4$ . The kinetic term of the fermion fields

$$\bar{\psi}\gamma^\mu\partial_\mu\psi = \bar{\psi}_L\gamma^\mu\partial_\mu\psi_L + \bar{\psi}_R\gamma^\mu\partial_\mu\psi_R, \quad (1.3)$$

is invariant as it does not mix chiral components. The scalar field kinetic term,  $(\partial_\mu\phi)^\dagger\partial^\mu\phi$  is  $SU(2) \times U(1)$  invariant. A term of the type  $\phi^\dagger\Box\phi$ , where  $\Box \equiv \partial_\mu\partial^\mu$ , would be redundant. The kinetic term for the  $X$  gauge fields which is  $SU(2)$  invariant corresponds to  $\langle X_{\mu\nu}X^{\mu\nu} \rangle = \frac{1}{2}X_{\mu\nu}^iX_i^{\mu\nu}$ , where

$$X_{\mu\nu} \equiv \tau^i X_{\mu\nu}^i, \quad X_{\mu\nu}^i = \partial_\mu X_\nu^i - \partial_\nu X_\mu^i - g f_{ijk} X_\mu^j X_\nu^k, \quad (1.4)$$

$f_{ijk}$  being the group structure constant. For the  $X = B$  case, the kinetic term,  $B_{\mu\nu}B^{\mu\nu}$  with  $B_{\mu\nu} = \partial_\mu B_\nu - \partial_\nu B_\mu$ , is  $U(1)_Y$  invariant. Terms of the form  $(\partial_\mu X)X^2$  are not relativistic invariants. Another possibility includes the coupling between 4 gauge boson fields, the  $X^4$  terms are not invariant by themselves, but are already included in the kinetic terms.  $X^3\phi$  and  $X\phi^3$  are not invariant. Even though the term  $X^2\phi^2$  is not invariant, it appears when promoting the global symmetry to a local one. The term including the coupling between four scalar fields  $\phi^4$  is invariant under  $SU(2)_L$ . Lastly, it is possible to construct a term which is  $SU(2)_L \times U(1)_Y$  invariant of the form  $\psi^2\phi$ , in the simplest case, only a complex scalar doublet of  $SU(2)_L$  is needed. This requires a left-handed and a right-handed fermion field,  $\bar{\psi}_L\phi\psi_R$  or  $\bar{\psi}_L\gamma^5\phi\psi_R$ .

### 1.1.3 Standard Model of Elementary Particles.

The Standard Model is based on the local gauge symmetry group  $G = SU(3)_C \times SU(2)_L \times U(1)_Y$ . The  $SU(3)_C$  factor (QCD) has gauge couplings  $g_s$  and eight gauge bosons (gluons)  $G^i$ ,  $i = 1 \cdots 8$ . This part is not chiral, and acts over color indices of the left- and right-handed quarks  $q_{r\alpha}$ , where  $\alpha = 1, 2, 3$  stands for color and  $r$  for flavor. QCD is not broken spontaneously, so the gluons do not acquire mass.

On the other hand, the electroweak  $SU(2)_L \times U(1)_Y$  factor is chiral. The  $SU(2)_L$  group has gauge couplings  $g$ , gauge bosons  $W^i$  ( $i = 1, 2, 3$ ), and acts only over the flavor indices of left-handed fermions. This leads to the Fermi weak charged current interactions, and also includes a neutral  $W^3$  boson associated with a fermion phase symmetry. The abelian factor  $U(1)$  has gauge couplings  $g'$  and a gauge boson  $B$ . This is also chiral, acting over L and R fermions but with different hypercharge. After spontaneous symmetry breaking (SSB),  $SU(2)_L \times U(1)_Y$  is broken to a single  $U(1)_Q$ , incorporating  $QED$  with the photon, which is a linear combination of  $W^3$  and  $B$ . The orthogonal combination ( $Z$ ), as well as  $W^\pm$ , acquire mass.

The Standard Model Lagrangian is

$$\mathcal{L} = \mathcal{L}_{gauge} + \mathcal{L}_f + \mathcal{L}_\phi + \mathcal{L}_{Yuk}, \quad (1.5)$$

including the gauge, fermion, Higgs and Yukawa sectors of the theory. There are additional terms: ghosts and gauge-fixing, entering the quantization, which are not shown above. Gauge terms are

$$\mathcal{L}_{gauge} = -\frac{1}{4}G_{\mu\nu}^i G^{\mu\nu i} - \frac{1}{4}W_{\mu\nu}^i W^{\mu\nu i} - \frac{1}{4}B_{\mu\nu} B^{\mu\nu}, \quad (1.6)$$

where the field-strength tensors of  $SU(3)_C$ ,  $SU(2)_L$ , and  $U(1)_Y$  are, respectively

$$G_{\mu\nu}^i = \partial_\mu G_\nu^i - \partial_\nu G_\mu^i - g_s f_{ijk} G_\mu^j G_\nu^k, \quad i, j, k = 1 \cdots 8; \quad (1.7a)$$

$$W_{\mu\nu}^i = \partial_\mu W_\nu^i - \partial_\nu W_\mu^i - g f_{ijk} W_\mu^j W_\nu^k, \quad i, j, k = 1 \cdots 3; \quad (1.7b)$$

$$B_{\mu\nu} = \partial_\mu B_\nu - \partial_\nu B_\mu. \quad (1.7c)$$

These include kinetic terms of the gauge bosons as well as self-interacting terms of three and four points for the  $G^i$  and  $W^i$ . The abelian gauge boson  $U(1)$  does not have self-interactions. The fermion part of the Standard Model involves  $F = 3$ , where  $F$  is the number of quark and lepton families. Each family consists of

$$\text{L Doublets : } q_{mL}^0 = \begin{pmatrix} u_m^0 \\ d_m^0 \end{pmatrix}_L, \quad \ell_{mL}^0 = \begin{pmatrix} \nu_m^0 \\ \ell_m^{-0} \end{pmatrix}_L, \quad (1.8a)$$

$$\text{R Singlets : } u_{mR}^0, d_{mR}^0, e_{mR}^{-0}, \nu_{mR}^0, \quad (1.8b)$$

wherein the chiral fields L are  $SU(2)$  doublets and the R fields are singlets. Upperindex  $^0$  means these fields are weak eigenstates, i.e., with definite gauge transformation properties, and the elements of each doublet transforming under  $SU(2)_L$ , and  $m = 1, 2, 3$  labelling the family. After SSB, these mix in the mass eigenstate basis. Quarks  $u^0$  and  $d^0$  have electric charges  $2/3$  and  $-1/3$  (in terms of the electron charge), respectively. There are  $2F = 6$  quark flavors. Each of them carries a color index  $u_{mL,R\alpha}^0$  or  $d_{mL,R\alpha}^0$ . Groups  $SU(2)_L$  and  $SU(3)_C$  commute, in such a way that QCD conserves flavor, and viceversa. Leptons  $e^-$  and  $\nu^0$  are color singlets and have electric charges  $-1$  and  $0$ . Although there are not R neutrinos in the Standard Model, these are required in various models to give neutrinos a mass. Here we have considered R neutrinos simply as  $SU(2)_L$  singlets. All these fields but  $\nu_{mR}^0$  carry weak hypercharge  $Y$ , defined in our convention by

$$Y = Q - T_L^3, \quad (1.9)$$

where  $T_L^3$  is the third  $SU(2)_L$  generator and  $Q$  is the electric charge.

$SU(2)_L$  and  $U(1)_Y$  representations are chiral.  $\mathcal{L}_f$  consists entirely of kinetic terms,

$$\begin{aligned} \mathcal{L}_f = \sum_{m=1}^F & \left( \bar{q}_{mL}^0 i \not{D} q_{mL}^0 + \bar{\ell}_{mL}^0 i \not{D} \ell_{mL}^0 \right. \\ & \left. + \bar{u}_{mR}^0 i \not{D} u_{mR}^0 + \bar{d}_{mR}^0 i \not{D} d_{mR}^0 + \bar{e}_{mR}^0 i \not{D} e_{mR}^0 + \bar{\nu}_{mR}^0 i \not{D} \nu_{mR}^0 \right), \end{aligned} \quad (1.10)$$

for an arbitrary number of fermion families,  $F$ .

The Higgs part of the SM Lagrangian is

$$\mathcal{L}_\phi = (D^\mu \phi)^\dagger D_\mu \phi - V(\phi), \quad (1.11)$$

where  $\phi \equiv \begin{pmatrix} \phi^+ \\ \phi^0 \end{pmatrix}$  is a complex doublet scalar Higgs field [135–137]. The covariant derivative is

$$D_\mu \phi = \left( \partial_\mu + \frac{ig}{2} \vec{\tau} \cdot \vec{W}_\mu + \frac{ig'}{2} B_\mu \right) \phi. \quad (1.12)$$

The modulus squared of the covariant derivative acting on  $\phi$  generates interactions between the gauge boson and the Higgs fields.  $V(\phi)$  is the corresponding Higgs potential. Invariance under  $SU(2)_L \times U(1)_Y$  and renormalizability restrict  $V$  to be

$$V(\phi) = +\mu^2 \phi^\dagger \phi + \lambda (\phi^\dagger \phi)^2, \quad \mu^2 < 0. \quad (1.13)$$

The term  $\mathcal{L}_{Yuk}$  represents Yukawa couplings among fermions and the Higgs doublet, which are necessary to generate fermion masses through the SSB of chiral gauge symmetries. For  $F$  fermion families, we have

$$\begin{aligned} \mathcal{L}_{Yuk} = - \sum_{m,n=1}^F & \left[ \Gamma_{mn}^u \bar{q}_{mL}^0 \tilde{\phi} u_{nR}^0 + \Gamma_{mn}^d \bar{q}_{mL}^0 \phi d_{nR}^0 \right. \\ & \left. + \Gamma_{mn}^e \bar{\ell}_{mL}^0 \phi e_{nR}^0 + \Gamma_{mn}^\nu \bar{\ell}_{mL}^0 \tilde{\phi} \nu_{nR}^0 \right] + h.c., \end{aligned} \quad (1.14)$$

Left-handed fermion fields  $\psi_i = \begin{pmatrix} \nu_i \\ \ell_i^- \end{pmatrix}$  and  $\begin{pmatrix} u_i \\ d_i \end{pmatrix}$ , of the  $i$ -th lepton family, transform as doublets under  $SU(2)_L$ , where  $d'_i \equiv \sum_j V_{ij} d_j$ , and  $V$  is the Cabibbo-Kobayashi-Maskawa (CKM) [138, 139] mixing matrix. Right-handed fields are  $SU(2)$  singlets. In the minimal model there are three lepton families and a complex Higgs doublet  $\phi \equiv \begin{pmatrix} \phi^+ \\ \phi^0 \end{pmatrix}$ .

## 1.2 Higgs mechanism

It is convenient to write  $\phi$  in an Hermitian basis

$$\phi = \begin{pmatrix} \phi^+ \\ \phi^0 \end{pmatrix} = \begin{pmatrix} \frac{1}{\sqrt{2}} (\phi_1 + i\phi_2) \\ \frac{1}{\sqrt{2}} (\phi_3 + i\phi_4) \end{pmatrix}, \quad (1.15)$$

where  $\phi_i = \phi_i^\dagger$  is an hermitian field. In this basis, the Higgs potential takes the form

$$V(\phi) = \frac{1}{2}\mu^2 \left( \sum_{i=1}^4 \phi_i^2 \right) + \frac{1}{4}\lambda \left( \sum_{i=1}^4 \phi_i^2 \right)^2. \quad (1.16)$$

This potential is  $O(4) \sim SU(2) \times SU(2)$  invariant. This is an example of an accidental symmetry; the most general potential consistent with the gauge symmetry  $SU(2) \times U(1)$  and renormalizability displays a larger symmetry group.

We can choose axes as follows  $\langle 0 | \phi_i | 0 \rangle = 0$ ,  $i = 1, 2, 4$  y  $\langle 0 | \phi_i | 0 \rangle = \nu$ . In such a way that

$$\phi \rightarrow \langle 0 | \phi | 0 \rangle \equiv v = \frac{1}{\sqrt{2}} \begin{pmatrix} 0 \\ \nu \end{pmatrix}, \quad (1.17)$$

$$V(\phi) \rightarrow V(v) = \frac{1}{2}\mu^2\nu^2 + \frac{1}{4}\lambda\nu^4,$$

which has to be minimized with respect to  $\nu$ . There are two possibilities, for  $\mu^2 > 0$  the minimum corresponds to  $\nu = 0$  and, therefore, the symmetry is not broken therein. On the

other hand, for  $\mu < 0$  the  $\nu = 0$  point is unstable, and the minimum occurs for  $\nu \neq 0$ , breaking the  $SU(2) \times U(1)$  symmetry. This gives as solution  $\nu = \sqrt{\frac{-\mu^2}{\lambda}}$ .

Now we turn to the  $\mu^2 < 0$  case, for which the Higgs doublet is replaced, in first approximation, by its vacuum expectation value,  $\text{vev} (v)$ . Generators corresponding to  $T^1$ ,  $T^2$  and  $T^3 - Y$  are broken,

$$\begin{aligned} T^1 v &= \frac{\sigma^1}{2} \frac{1}{\sqrt{2}} \begin{pmatrix} 0 \\ \nu \end{pmatrix} = \frac{1}{2\sqrt{2}} \begin{pmatrix} \nu \\ 0 \end{pmatrix} \neq 0, \\ T^2 v &= \frac{\sigma^2}{2} \frac{1}{\sqrt{2}} \begin{pmatrix} 0 \\ \nu \end{pmatrix} = \frac{-i}{2\sqrt{2}} \begin{pmatrix} \nu \\ 0 \end{pmatrix} \neq 0, \\ (T^3 - Y)v &= \left( \frac{\sigma^3}{2} - \mathbf{Y} \right) \frac{1}{\sqrt{2}} \begin{pmatrix} 0 \\ \nu \end{pmatrix} = \frac{-1}{\sqrt{2}} \begin{pmatrix} 0 \\ \nu \end{pmatrix} \neq 0, \end{aligned} \tag{1.18}$$

while  $Qv = (T^3 + Y)v = 0$ , given that the vacuum is electrically neutral, so that  $U(1)_Q$  of electromagnetism is not broken, and  $SU(2)_L \times U(1)_Y \rightarrow U(1)_Q$ .

Thus, the vacuum is only invariant under  $Q = T^3 + Y$ , and the SSB of the three other generators gives three Goldstone bosons, spinless and massless particles, which appear as longitudinal polarizations of the gauge bosons  $W^\pm = (W^1 \mp iW^2)/\sqrt{2}$  and  $Z^0$ . The unbroken generator ( $Q$ ) warrants there is a massless gauge boson, the photon. This process is the spontaneous symmetry breaking.

It is generally useful to rewrite the  $\phi$  field in terms of a new set of variables using the Kibble transformation,

$$\phi = \frac{1}{\sqrt{2}} \exp \left[ i \sum_{i=1}^3 \xi^i T^i \right] \begin{pmatrix} 0 \\ \nu \end{pmatrix}, \tag{1.19}$$

where the  $T^i$  are the three broken generators  $T^1$ ,  $T^2$  and  $T^3 - Y$ , and  $H$  is an hermitian scalar field, the physical *Higgs boson*. Hermitian  $\xi^i$  fields are the Goldstone bosons.

These only appear through derivatives, and disappear in the physical spectrum of the gauge



theory. It is useful to work in the unitary gauge,

$$\phi \rightarrow \phi' = \exp \left[ -i \sum \xi^i T^i \right] \phi = \frac{1}{\sqrt{2}} \begin{pmatrix} 0 \\ \nu + H \end{pmatrix}, \quad \tilde{\phi} \rightarrow \frac{1}{\sqrt{2}} \begin{pmatrix} \nu + H \\ 0 \end{pmatrix}, \quad (1.20)$$

together with the corresponding transformations of the other fields. Unitary gauge is the simplest to show the matter content of the theory, because Goldstone bosons disappear and only physical degrees of freedom survive. Sometimes it is better to work in other gauges since they facilitate computations at higher orders (loops). Table 1.2 compares the degrees of freedom in the unitary ('physical') and renormalizable gauges.

Unitary gauge	Renormalizable gauge
0 Goldstone Bosons 3 massive gauge bosons ( $W^\pm, Z$ ) with 3 polarizations (2 T and 1 L) 1 massless Gauge Boson ( $\gamma$ ) with 2 transverse polarizations (T)	3 Goldstone Bosons 4 massless gauge bosons ( $W^i, B$ ) with 2 transverse polarizations (T)

Table 1.2: Comparison between degrees of freedom in unitary and renormalizable gauge (11 in both).

### 1.3 Lagrangian after SSB

The kinetic term of the Higgs sector in the unitary gauge takes the following form

$$(D_\mu \phi)^\dagger D^\mu \phi = \frac{1}{2} \begin{pmatrix} 0 & \nu \end{pmatrix} \left[ \frac{g}{2} \tau^i W_\mu^i + \frac{g'}{2} B_\mu \right]^2 \begin{pmatrix} 0 \\ \nu \end{pmatrix} + \dots \quad (1.21)$$

We can rewrite it using the relation

$$\tau^i W^i = \tau^3 W^3 + \sqrt{2} \tau^+ W^+ + \sqrt{2} \tau^- W^-, \quad (1.22)$$

where

$$W^\pm = \frac{W^1 \mp iW^2}{\sqrt{2}}, \quad \tau^\pm = \frac{\tau^1 \pm \tau^2}{2}, \quad (1.23)$$

which yields

$$\begin{aligned} & \frac{g^2 \nu^2}{4} W^{+\mu} W_\mu^- + \frac{1}{2}(g^2 + g'^2) \frac{\nu^2}{4} \left[ \frac{-g' B_\mu + g W_\mu^3}{\sqrt{g^2 + g'^2}} \right]^2 \\ & \equiv M_W^2 W^{+\mu} W_\mu^- + \frac{M_Z^2}{2} Z^\mu Z_\mu, \end{aligned} \quad (1.24)$$

where  $W^\pm$  are the charged gauge bosons mediating weak charged current interactions, and

$$Z \equiv \frac{-g' B + g W^3}{\sqrt{g^2 + g'^2}} = -\sin \theta_W B + \cos \theta_W W^3 \quad (1.25)$$

is a massive vector gauge boson mediating the weak interactions predicted by the  $SU(2) \times U(1)$  symmetry, where  $\theta_W$  is the weak mixing angle, defined by

$$\tan \theta_W \equiv \frac{g'}{g}, \quad \sin \theta_W = \frac{g'}{\sqrt{g^2 + g'^2}}, \quad \cos \theta_W = \frac{g}{\sqrt{g^2 + g'^2}}. \quad (1.26)$$

The linear combination of  $B$  and  $W^3$  orthogonal to  $Z$  is the photon ( $\gamma$ ), whose field

$$A = \cos \theta_W B + \sin \theta_W W^3, \quad (1.27)$$

remains massless.

After SSB, the Lagrangian including the Higgs sector is

$$\begin{aligned} \mathcal{L}_\phi &= (D^\mu \phi)^\dagger D_\mu \phi - V(\phi) \\ &= M_W^2 W^{+\mu} W_\mu^- \left(1 + \frac{H}{\nu}\right)^2 + \frac{1}{2} M_Z^2 Z^\mu Z_\mu \left(1 + \frac{H}{\nu}\right)^2 \\ &\quad + \frac{1}{2} (\partial_\mu H)^2 - V(\phi), \end{aligned} \quad (1.28)$$

where the Higgs potential after SSB becomes

$$V(\phi) \rightarrow -\frac{\mu^4}{4\lambda} - \mu^2 H^2 + \lambda\nu H^3 + \frac{\lambda}{4} H^4. \quad (1.29)$$

Eq. (1.28) describes the interactions of massive gauge bosons,  $W^\pm$  and  $Z$ , with the Higgs boson, which are  $ZZH$ ,  $W^+W^-Z$ ,  $ZZH^2$  and  $W^+W^-H^2$ . The Lagrangian includes a kinetic term for the Higgs and a corresponding mass term in the potential has been generated, predicting  $M_H^2 = -2\mu^2 = 2\lambda\nu^2$ .

On the other side, the Lagrangian for the fermion field after SSB is

$$\begin{aligned} \mathcal{L}_F &= \sum_i \bar{\psi}_i \left[ i\not{\partial} - m_i \left( 1 + \frac{gH}{2M_W} \right) \right] \psi_i \\ &\quad - \frac{g}{2\sqrt{2}} \sum_i \bar{\psi}_i \gamma^\mu (1 - \gamma^5) (T^+ W_\mu^+ + T^- W_\mu^-) \psi_i \\ &\quad - e \sum_i q_i \bar{\psi}_i \gamma^\mu \psi_i A_\mu \\ &\quad - \frac{g}{2 \cos \theta_W} \sum_i \bar{\psi}_i \gamma^\mu (g_V^i - g_A^i \gamma^5) \psi_i Z_\mu. \end{aligned} \quad (1.30)$$

In this expression,  $e = g \sin \theta_W$  is the positron electric charge. The Yukawa coupling between  $H$  and  $\psi_i$  in the first term of  $\mathcal{L}_f$ , diagonal in the minimal model, is  $g m_i / 2M_W$ . Gauge boson masses in the EW sector are given (at tree level) by

$$M_H = \sqrt{2\lambda}v, \quad (1.31a)$$

$$M_W = \frac{1}{2}gv = \frac{ev}{2 \sin \theta_W}, \quad (1.31b)$$

$$M_Z = \frac{1}{2}\sqrt{g^2 + g'^2}v = \frac{ev}{2 \sin \theta_W \cos \theta_W} = \frac{M_W}{\cos \theta_W}, \quad (1.31c)$$

$$M_\gamma = 0. \quad (1.31d)$$

From them, it can be shown that the limit  $g' \rightarrow 0$  leads to  $M_Z = M_W$ . This is because the  $O(4)$  global symmetry of the potential in Eq. (1.16) is broken to  $O(3) \sim SU(2)$  after SSB. This *custodial* symmetry (of global type) is respected by the  $SU(2)$  gauge interactions in

eq. (1.21) for  $g' = 0$ , such that  $M_{W^\pm} = M_{W^3} = M_Z$ . Custodial  $SO(3)$  symmetry warrants that the coefficient  $\nu^2$  be the same for the  $W^\pm$  and  $Z$  mass terms, even for  $g \neq 0$ , implying  $M_W = M_Z \cos \theta_W$ . Since this relation has been verified experimentally with great accuracy, any alternative model of SSB must involve global custodial  $SU(2)$  symmetry to keep it.

The second term in  $\mathcal{L}_f$  represents the weak charged current interaction, where  $T^+$  and  $T^-$  are the weak isospin raising and lowering operators. For instance, the coupling of a  $W$  to an electron and a neutrino is

$$-\frac{e}{2\sqrt{2}\sin\theta_W} \left[ W_\mu^- \bar{e} \gamma^\mu (1 - \gamma^5) \nu_e + W_\mu^+ \bar{\nu}_e \gamma^\mu (1 - \gamma^5) e \right]. \quad (1.32)$$

For momenta small compared to  $M_W$ , this term gives rise to an effective four-fermion local interaction with strength encoded in the Fermi constant, given by  $G_F/\sqrt{2} = 1/2v^2 = g^2/8M_W^2$ .  $CP$  is incorporated in the EW SM by means of a single physical phase in  $V_{ij}$ .

The third term in  $\mathcal{L}_f$  describes electromagnetic interactions (QED), and the last one is the neutral current weak interaction. Their vector and axial-vector couplings are

$$g_V^i \equiv t_{3L}(i) - 2q_i \sin^2 \theta_W, \quad (1.33a)$$

$$g_A^i \equiv t_{3L}(i), \quad (1.33b)$$

where  $t_{3L}(i)$  is the weak isospin of the  $i$  fermion ( $+1/2$  for  $u_i$  and  $\nu_i$ ;  $-1/2$  for  $d_i$  and  $e_i$ ) and  $q_i$  is the electric charge of  $\psi_i$  in units of  $e$ .

The first term in eq. (1.30) also gives masses to fermions and, in presence of right-handed neutrinos, gives neutrinos a Dirac mass, as well.

$SU(2)$  gauge kinetic terms produce self-interactions among three and four fields

$$\begin{aligned}
\mathcal{L}_{WWB} = & -ig \cos \theta_W \left\{ (\partial_\rho Z_\nu) W_\mu^+ W_\sigma^- [g^{\rho\mu} g^{\nu\sigma} - g^{\rho\sigma} g^{\mu\nu}] + (\partial_\rho W_\mu^+) Z_\nu W_\sigma^- [g^{\rho\sigma} g^{\mu\nu} - g^{\rho\nu} g^{\mu\sigma}] \right. \\
& \left. + (\partial_\rho W_\sigma^-) Z_\nu W_\mu^+ [g^{\rho\nu} g^{\mu\sigma} - g^{\rho\mu} g^{\nu\sigma}] \right\} \\
& - ig \sin \theta_W \left\{ (\partial_\rho A_\nu) W_\mu^+ W_\sigma^- [g^{\rho\mu} g^{\nu\sigma} - g^{\rho\sigma} g^{\mu\nu}] + (\partial_\rho W_\mu^+) A_\nu W_\sigma^- [g^{\rho\sigma} g^{\mu\nu} - g^{\rho\nu} g^{\mu\sigma}] \right. \\
& \left. + (\partial_\rho W_\sigma^-) A_\nu W_\mu^+ [g^{\rho\nu} g^{\mu\sigma} - g^{\rho\mu} g^{\nu\sigma}] \right\}
\end{aligned} \tag{1.34}$$

and

$$\begin{aligned}
\mathcal{L}_{W^4} = & \frac{g^2}{4} \left[ W_\mu^+ W_\nu^+ W_\sigma^- W_\rho^- \mathcal{Q}^{\mu\nu\rho\sigma} - 2 \cos^2 \theta_W W_\mu^+ Z_\nu Z_\sigma W_\rho^- \mathcal{Q}^{\mu\rho\nu\sigma} \right. \\
& \left. - 4 \sin \theta_W \cos \theta_W W_\mu^+ A_\nu Z_\sigma W_\rho^- \mathcal{Q}^{\mu\rho\nu\sigma} - 2 \sin^2 \theta_W W_\mu^+ A_\nu A_\sigma W_\rho^- \mathcal{Q}^{\mu\rho\nu\sigma} \right],
\end{aligned} \tag{1.35}$$

where

$$\mathcal{Q}_{\mu\nu\rho\sigma} \equiv 2g_{\mu\nu}g_{\rho\sigma} - g_{\mu\rho}g_{\nu\sigma} - g_{\mu\sigma}g_{\nu\rho}. \tag{1.36}$$

### 1.3.1 The Yukawa sector and the mixing matrix

We will study now in more detail the Yukawa sector, which is responsible for generating the mass terms after SSB. Working in the unitary gauge for the  $\phi$  and  $\tilde{\phi}$  fields, one obtains, for  $F$  families

$$\begin{aligned}
-\mathcal{L}_{Yuk} = & \sum_{m,n=1}^F \bar{u}_{mL}^0 \Gamma_{mn}^u \left( \frac{\nu + H}{\sqrt{2}} \right) u_{nR}^0 + (d, e, \nu) + h.c. \\
= & \bar{u}_L^0 (M^u + h^u H) u_R^0 + (d, e, \nu) + h.c.,
\end{aligned} \tag{1.37}$$

where  $u_L^0 = (u_{1L}^0 u_{2L}^0 \cdots u_{FL}^0)^T$  is a column vector with  $F$  components, and similarly for  $u_R^0$ . In this expression  $M^u$  is an  $F \times F$  matrix,

$$M_{mn}^u = \Gamma_{mn}^u \frac{\nu}{\sqrt{2}}, \quad (1.38)$$

induced by the SSB, and

$$h^u = \frac{M^u}{\nu} = \frac{gM^u}{2M_W} \quad (1.39)$$

is the matrix of Yukawa couplings. Given that  $\Gamma_{mn}^u$  does not need to be diagonal, Hermitian or symmetric, it is necessary to diagonalize  $M$  by means of a unitary transformation defined by  $A_L$  and  $A_R$ , acting on the left- and right-handed fermion fields, respectively. Then,  $A_L^{u\dagger} M^u A_R^u = M_D^u$  is a diagonal matrix with real non-negative eigenvalues corresponding to the up-type quark masses (u). Similarly, we denote the  $h^u$  eigenvalues as  $h_i$  with  $i = u, c, t$  for  $F = 3$ . Likewise, the mass matrices for down-type quarks and leptons can be diagonalized by

$$A_L^{d\dagger} M^d A_R^d = M_D^d \quad A_L^{\ell\dagger} M^\ell A_R^\ell = M_D^\ell. \quad (1.40)$$

Fields in the mass eigenbasis can be rewritten as  $u_{L,R} = A_{L,R}^{u\dagger} u_{L,R}^0$ ,  $d_{L,R} = A_{L,R}^{d\dagger} d_{L,R}^0$  and  $\ell_{L,R} = A_{L,R}^{\ell\dagger} \ell_{L,R}^0$ , in such a way that  $\bar{u}_L^0 M^u u_R^0 = \bar{u}_L M_D^u u_R$ .

For the quarks case, eigenvalues in  $M_D^{u,d}$  are the bare masses in the QCD Lagrangian.

Unitary matrices  $A_{L,R}$  can be built from the fact that  $MM^\dagger$  and  $M^\dagger M$  are hermitian. From the previous relations, the following can be shown

$$\hat{A}_L^{u\dagger} M^u M^{u\dagger} \hat{A}_L^u = \hat{A}_R^{u\dagger} M^{u\dagger} M^u \hat{A}_R^u = M_D^2 = \begin{pmatrix} m_{u_1}^2 & 0 & 0 & 0 \\ 0 & m_{u_2}^2 & 0 & 0 \\ 0 & 0 & m_{u_3}^2 & 0 \\ 0 & 0 & 0 & \ddots \end{pmatrix}, \quad (1.41)$$

so then  $\hat{A}_{L,R}^u$  and their eigenvalues can be obtained with basic techniques. Given the hermiticity of  $MM^\dagger$  and  $M^\dagger M$ , eigenvalues of  $m_{u_r}^2$  are real and their eigenvectors are orthogonal,

$m_{u_r}^2 > 0$  holding as well. Nonetheless, these matrices are not unique,  $A_{L,R}^u$  is only determined up to phases. In this way, in addition to  $A_{L,R}^u$  as solution of Eq. (1.41), also  $A_L^u \equiv \hat{A}_L^u K_L^u$  and  $A_R^u \equiv \hat{A}_R^u K_R^u$  solves it, where

$$K_{L,R}^u = \begin{pmatrix} \exp[i\phi_{1L,R}^u] & 0 & 0 & 0 \\ 0 & \exp[i\phi_{2L,R}^u] & 0 & 0 \\ 0 & 0 & \exp[i\phi_{3L,R}^u] & 0 \\ 0 & 0 & 0 & \ddots \end{pmatrix} \quad (1.42)$$

are diagonal matrices with arbitrary non-observable phases. Usual methodology consists in choosing  $K_L^u$  such that all non-physical phases can be removed from the CKM matrix, then one can choose the phase in  $K_R^u$  so that  $m_r^u$  be real and non-negative. On the other hand,  $A_R^u$  matrices are non-observable in the SM but this does not need to be the case in some of its extensions.

With these results, the Lagrangian including kinetic terms for the fermions and the Yukawa sector can be written

$$\mathcal{L}_\psi = \sum_r \bar{\psi}_r \left[ i\not{\partial} - m_r \left( 1 + \frac{H}{\nu} \right) \right] \psi_r, \quad (1.43)$$

where the sum runs over all fermions, quarks and charged leptons. This expression corresponds to the first term in the Lagrangian of Eq. (1.30), using the relation  $\nu = 2M_W/g$ .

If now we consider the second term of Eq. (1.30), which corresponds to the weak charged current Lagrangian, it can be written as

$$\begin{aligned} \mathcal{L}_W &= -\frac{g}{2\sqrt{2}} \sum_i \bar{\psi}_i \gamma^\mu (1 - \gamma^5) (T^+ W_\mu^+ + T^- W_\mu^-) \psi_i, \\ &= -\frac{g}{2\sqrt{2}} (J_W^\mu W_\mu^- + J_W^{\mu\dagger} W_\mu^+), \end{aligned} \quad (1.44)$$

where the  $J_W^{\mu\dagger}$  and  $J_W^\mu$  are defined by

$$\begin{aligned} J_W^\mu &= \sum_{m=1}^F \left[ \bar{\nu}_m^0 \gamma^\mu (1 - \gamma^5) e_m^0 + \bar{u}_m^0 \gamma^\mu (1 - \gamma^5) d_m^0 \right], \\ J_W^{\mu\dagger} &= \sum_{m=1}^F \left[ \bar{e}_m^0 \gamma^\mu (1 - \gamma^5) \nu_m^0 + \bar{d}_m^0 \gamma^\mu (1 - \gamma^5) u_m^0 \right], \end{aligned} \quad (1.45)$$

in the flavor eigenbasis. Rewriting these currents in the mass eigenbasis yields

$$\begin{aligned} J_W^\mu &= 2\bar{\nu}_L \gamma^\mu V_\ell e_L + 2\bar{u}_L \gamma^\mu V_q d_L, \\ J_W^{\mu\dagger} &= 2\bar{e}_L \gamma^\mu V_\ell^\dagger \nu_L + 2\bar{d}_L \gamma^\mu V_q^\dagger u_m^0, \end{aligned} \quad (1.46)$$

where  $u_L, d_L, e_L$ , and  $\nu_L$  are  $F$  component vector columns. The unitary quark mixing matrix,  $V_q \equiv A_L^{u\dagger} A_L^d$ , describes the misalignment between the flavor and weak eigenbasis for the *up*- and *down*-type quarks.  $V_\ell$  is its analog for the lepton case, the PMNS matrix, which is essential in the description of neutrino oscillations and other processes sensitive to neutrino masses. For processes insensitive to them one can simply take  $V_\ell = \mathcal{I}$ .

For a complex  $F \times F$  matrix, there are  $2F^2$  real parameters describing it,  $F^2$  moduli and  $F^2$  phases. However,  $V_q$  is unitary, implying  $F(F+1)/2$  restrictions on the moduli and  $F(F-1)/2$  conditions on the phases. We recall that not all these phases are observable, according to the  $K_L^{u,d}$  matrices. In this way, we can choose  $K_L^{u,d}$  freely to remove  $2F-1$  phase differences in  $V_q$ , so that there are

$$(F-1)^2 = \frac{F(F-1)}{2} + \frac{(F-1)(F-2)}{2} \quad (1.47)$$

observable parameters,  $F(F-1)/2$  of them are rotation angles and the remaining  $(F-1)(F-2)/2$  are *CP* violating phases. From this relation,  $F > 2$  is needed for violating *CP*. For  $F = 3$  one has  $V_q = V_{CKM}$ , with three mixing angles and a *CP* violating phase.



The third term in Eq. (1.30), corresponds to the QED Lagrangian,

$$\begin{aligned}\mathcal{L}_Q &= -e \sum_i q_i \bar{\psi}_i \gamma^\mu \psi_i A_\mu \\ &= -e J_Q^\mu A_\mu,\end{aligned}\tag{1.48}$$

where  $A_\mu$  is the photon field and

$$\begin{aligned}J_Q^\mu &= \sum_r q_r \bar{\psi}_r^0 \gamma^\mu \psi_r^0 = \sum_{m=1}^F \left[ \frac{2}{3} \bar{u}_m^0 \gamma^\mu u_m^0 - \frac{1}{3} \bar{d}_m^0 \gamma^\mu d_m^0 - \bar{e}_m^0 \gamma^\mu e_m^0 \right] \\ &\equiv \frac{2}{3} \bar{u}^0 \gamma^\mu u^0 - \frac{1}{3} \bar{d}^0 \gamma^\mu d^0 - \bar{e}^0 \gamma^\mu e^0,\end{aligned}\tag{1.49}$$

rewriting this expression in the mass eigenbasis yields

$$J_Q^\mu = \frac{2}{3} \bar{u} \gamma^\mu u - \frac{1}{3} \bar{d} \gamma^\mu d - \bar{e} \gamma^\mu e,\tag{1.50}$$

so that  $J_Q^\mu$  is diagonal in flavor.

The last term corresponds to the neutral weak current

$$\begin{aligned}\mathcal{L}_Z &= -\frac{g}{2 \cos \theta_W} \sum_i \bar{\psi}_i \gamma^\mu \left( g_V^i - g_A^i \gamma^5 \right) \psi_i Z_\mu \\ &= -\frac{g}{2 \cos \theta_W} J_Z^\mu Z_\mu,\end{aligned}\tag{1.51}$$

where  $Z_\mu$  is a massive neutral boson. The neutral weak current is

$$\begin{aligned}J_Z^\mu &= \sum_r \bar{\psi}_r^0 \gamma^\mu \left[ t_{rL}^3 (1 - \gamma^5) - 2q_r \sin^2 \theta_W \right] \psi_r^0 \\ &= \sum_r t_{rL}^3 \bar{\psi}^0 \gamma^\mu (1 - \gamma^5) \psi_r^0 - 2 \sin^2 \theta_W J_Q^\mu,\end{aligned}\tag{1.52}$$

summing over all fermion content. Working with the SM fields,

$$\begin{aligned}J_Z^\mu &= \bar{u}_L^0 \gamma^\mu u_L^0 - \bar{d}_L^0 \gamma^\mu d_L^0 + \bar{\nu}_L^0 \gamma^\mu \nu_L^0 - \bar{e}_L^0 \gamma^\mu e_L^0 - 2 \sin^2 \theta_W J_Q^\mu \\ &= \bar{u}_L \gamma^\mu u_L - \bar{d}_L \gamma^\mu d_L + \bar{\nu}_L \gamma^\mu \nu_L - \bar{e}_L \gamma^\mu e_L - 2 \sin^2 \theta_W J_Q^\mu,\end{aligned}\tag{1.53}$$

showing that the neutral weak current is also diagonal in flavor. These results agree with the observations of flavor-changing neutral current processes (FCNC), which are very suppressed since they are forbidden at tree level and need to occur through loops, an additional suppression coming from the GIM [140] mechanism (owing to the unitarity of the CKM matrix).

## 1.4 Quantum Chromodynamics

Quantum chromodynamics (QCD), the gauge theory that describes the strong interactions of colored quarks and gluons, is the  $SU(3)$  component of the  $SU(3) \times SU(2) \times U(1)$  Standard Model. The QCD Lagrangian is given by

$$\mathcal{L} = \sum_q \bar{\psi}_{q,a} \left( i\gamma^\mu \partial_\mu \delta_{ab} - g_s \gamma^\mu t_{ab}^C \mathcal{A}_\mu^C - m_q \delta_{ab} \right) \psi_{q,b} - \frac{1}{4} F_{\mu\nu}^A F_A^{\mu\nu}, \quad (1.54)$$

where repeated indices are summed over. The  $\psi_{q,a}$  are quark-field spinors for a quark of flavor  $q$  and mass  $m_q$ , with a color index  $a$  that runs from  $a = 1$  to  $N_C = 3$ . Quarks are said to be in the fundamental representation of the  $SU(3)$  color group.

The  $A_\mu^C$  correspond to the gluon fields, with  $C$  running from 1 to  $N_C^2 - 1 = 8$ . Gluons transform under the adjoint representation of the  $SU(3)$  color group. The  $t_{ab}^C$ , which correspond to eight  $3 \times 3$  matrices, are the generators of the  $SU(3)$  group and are related to the Gell-Mann matrices by  $t_{ab}^C = \lambda_{ab}^C/2$ . They encode the fact that a gluon's interaction with a quark rotates the quark's color in  $SU(3)$  space. The  $g_s$  term (or  $\alpha_s = \frac{g_s^2}{4\pi}$ ) is the QCD running coupling. Apart from quark masses, which have electroweak origin (and the scale  $\Lambda^{QCD}$ , generated by quantum corrections and giving hadrons' characteristic mass scale), it is the only fundamental parameter of QCD. Lastly, the field tensor  $F_{\mu\nu}^A$  is given by

$$F_{\mu\nu}^A = \partial_\mu \mathcal{A}_\nu^A - \partial_\nu \mathcal{A}_\mu^A - g_s f_{ABC} \mathcal{A}_\mu^B \mathcal{A}_\nu^C \quad [t^A, t^B] = i f_{ABC} t^C, \quad (1.55)$$

where the  $f_{ABC}$  are the structure constants of the  $SU(3)$  group.

Neither quarks nor gluons are observed as free particles. Hadrons are color-singlet combinations of quark, anti-quarks and gluons.

Ab-initio predictive methods for QCD include lattice gauge theory and perturbative expansions in the coupling. The Feynman rules of QCD imply a quark-antiquark-gluon ( $q\bar{q}g$ ) vertex, a 3-gluon vertex both proportional to  $g_s$ , and a 4-gluon vertex proportional to  $g_s^2$ . A list of Feynman rules and examples can be found in Refs. [141–145].

There is a freedom for an additional CP-violating term to be present in the QCD Lagrangian,  $\theta \frac{\alpha_s}{8\pi} F_{\mu\nu}^A \tilde{F}^{A\mu\nu}$ , where  $\theta$  is an extra free parameter, and  $\tilde{F}^{A\mu\nu}$  is the dual of the gluon field tensor,  $\frac{1}{2}\epsilon_{\mu\nu\rho\sigma} F^{A\rho\sigma}$ , with  $\epsilon_{\mu\nu\sigma\rho}$  being the fully antisymmetric Levi-Civita symbol. Experimental limits on ultracold neutrons [146, 147] and atomic mercury [148] constrain the QCD vacuum angle to be  $|\theta| \lesssim 10^{-10}$ . Further discussions can be found in Refs. [3, 149].

### 1.4.1 Running coupling

In the frame of perturbative QCD (pQCD), predictions from observable are expressed in terms of the renormalized coupling  $\alpha_s(\mu_R)$ , a function of an (unphysical) renormalization scale  $\mu_R$ . If  $\mu_R$  is taken close to the scale of the momentum transfer  $Q$  in a given process, then  $\alpha_s(\mu_R^2 \simeq Q^2)$  is indicative of the effective strength of the strong interaction in that process.

The coupling satisfies the next renormalization group equation (RGE):

$$\mu_R^2 \frac{d\alpha_s}{d\mu_R^2} = \beta(\alpha_s) = -(b_0\alpha_s^2 + b_1\alpha_s^3 + b_2\alpha_s^4 + \dots), \quad (1.56)$$

where  $b_0 = (11C_A - 4n_f T_R)/(12\pi) = (33 - 2n_f)/(12\pi)$  is the 1-loop  $\beta$ -function coefficient,  $b_1 = (17C_A^2 - n_f T_R(10C_A + 6C_F))/(24\pi^2) = (153 - 19n_f)/(24\pi^2)$  is the 2-loop coefficient and  $b_2 = (2857 - \frac{5033}{9}n_f + \frac{325}{27}n_f^2)/(128\pi^3)$  is the 3-loop coefficient for the  $SU(3)$  values of  $T_R = T_F = \frac{1}{2}$ ,  $C_A = N_C = 3$  and  $C_F = \frac{N_C^2 - 1}{2N_C} = \frac{4}{3}$ . Here  $n_f$  is the number of quark flavors. The 4-loop coefficient,  $b_3$ , can be found in Refs. [150, 151], while the 5-loop coefficient,  $b_4$ , is in Refs. [152–156]. The  $b_2$  and  $b_3$  coefficients (and subsequent) are renormalization-scheme-dependent and are given here in the modified minimal subtraction scheme ( $\overline{\text{MS}}$ ) [157], which

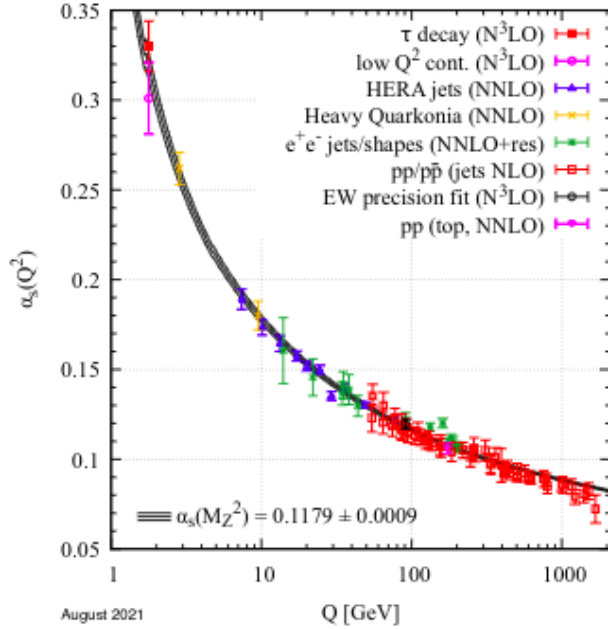


Figure 1.1: Summary of measurements of  $\alpha_s$  as a function of the energy scale  $Q$  [3]. The respective degree of QCD perturbation theory used in the extraction of  $\alpha_s$  is indicated in brackets (NLO: next-to-leading order; NNLO: next-to-next-to-leading-order; NNLO+res: NNLO matched to a resummed calculation; N<sup>3</sup>LO: next-to-NNLO).

is the most used scheme in QCD.

The minus sign in Eq. (1.56) is the origin of Asymptotic Freedom [158, 159], i.e. the fact that the strong coupling becomes weak for processes involving large momentum transfers (“hard processes”). In the 0.1–1 TeV range,  $\alpha_s \sim 0.1$ , while the theory is strongly interacting for scales around and below 1 GeV.

Many experimental observables are used to determine  $\alpha_s$ . A number of recent determinations are collected in Ref. [160]. Further discussions and considerations on determinations of  $\alpha_s$  can also be found in Refs. [161–163]. A summary for the results of  $\alpha_s(Q^2)$  obtained at discrete energy scales  $Q$ , now also including those based just on NLO QCD, is shown in Fig. 1.1. Thanks to the results from the Tevatron and from the LHC, the energy scales, at which  $\alpha_s$  is determined, now extend up to almost 2 TeV.

## 1.4.2 Quark masses

Free quarks have never been observed, which is understood as a result of a long-distance, confining property of the strong QCD force: up, down, strange, charm and bottom quarks all *hadronize*, i.e. become part of a meson or baryon, on a timescale  $\sim 1/\Lambda^{QCD}$ ; and, on the other hand, the top quark decays before it has time to hadronize. This feature makes it challenging to define what a quark mass is, for that one needs to adopt a specific prescription. A perturbatively defined prescription is the pole mass,  $m_q$ , which corresponds to the position of the divergence of the propagator. This is close to the physical picture of mass. Nonetheless, it suffers from a badly behaved perturbative series which makes it ambiguous to an amount related to  $\Lambda^{QCD}$  [164–166] when it is related to observable quantities. An alternative is the  $\overline{\text{MS}}$  mass,  $\bar{m}_q(\mu_R^2)$ , which depends on the renormalization scale  $\mu_R$ .

For the masses of heavier quarks, one quotes either the pole mass or the  $\overline{\text{MS}}$  mass evaluated at a scale equal to the mass,  $\bar{m}_q(\bar{m}_q^2)$ ; light quark masses are often quoted in the  $\overline{\text{MS}}$  scheme at a scale  $\mu_R \sim 2 \text{ GeV}$ . A series that starts as  $m_q = \bar{m}_q(\bar{m}_q^2) \left(1 + \frac{4\alpha_s(\bar{m}_q^2)}{3\pi} + \mathcal{O}(\alpha_s^2)\right)$  relates the pole and  $\overline{\text{MS}}$  masses, while the scale-dependence of  $\overline{\text{MS}}$  masses is given at leading order by

$$\mu_R^2 \frac{d\bar{m}_q(\mu_R^2)}{d\mu_R^2} = \left[ -\frac{\alpha_s(\mu_R^2)}{\pi} + \mathcal{O}(\alpha_s^2) \right] \bar{m}_q(\mu_R^2). \quad (1.57)$$

A more detailed discussion can be found in Ref. [167] and references therein.

In perturbative QCD computations of scattering processes, one neglects (i.e. sets to zero) the masses of all quarks, whose mass is significantly smaller than the momentum transfer in the process. Further details about perturbative calculations are summarized in the section “Quantum Chromodynamics” in Ref. [3].

## 1.5 Effective Field Theory

Effective field theories are a powerful tool to describe low-energy physics, where low is defined with respect to some energy scale  $\Lambda$ . They only take explicitly into account the relevant degrees of freedom i.e., those states with  $m \ll \Lambda$ , while the heavier excitations with  $M \gg \Lambda$  are integrated out from the action. Thus, the information about the heavier degrees of freedom is contained in the couplings of the resulting low-energy Lagrangian. While effective field theories include an infinite number of terms, renormalizability is not a problem in view of the fact that, at any order in the energy expansion, the low energy theory is specified by a finite number of couplings, which permits an order-by-order renormalization. In most of beyond-SM theories that have been considered to date, reduction to the SM at low energies proceeds via decoupling of heavy particles with masses of order  $\Lambda$  or larger. At the perturbative level, this decoupling is described by the Appelquist-Carazzone theorem [131].

The theoretical basis of effective field theory (EFT) [168] can be written as a theorem [169, 170]

*For a given set of asymptotic states, perturbation theory with the most general Lagrangian containing all terms allowed by the assumed symmetries will yield the most general  $S$ -matrix elements consistent with analyticity, perturbative unitarity, cluster decomposition and assumed symmetries.*

The interested reader is referred to various reviews [168, 171, 172] for a broader survey of the subject.

### 1.5.1 EFT expansion

The EFT Lagrangian has an expansion in powers of the operator dimension

$$\mathcal{L}_{\text{EFT}} = \sum_{\mathcal{D} \geq 0, i} \frac{c_i^{(\mathcal{D})} O_i^{(\mathcal{D})}}{\Lambda^{\mathcal{D}-d}} = \sum_{\mathcal{D} \geq 0} \frac{\mathcal{L}_{\mathcal{D}}}{\Lambda^{\mathcal{D}-d}}, \quad (1.58)$$

where  $O_i^{(\mathcal{D})}$  are the allowed operators of dimension  $\mathcal{D}$ . All operators of dimension  $\mathcal{D}$  are combined into the dimension  $\mathcal{D}$  Lagrangian  $\mathcal{L}_{\mathcal{D}}$ . In Eq. (1.58) the sum does not end when

$\mathcal{D} = d$ , but includes operators of arbitrarily high dimension. A scale  $\Lambda$  is introduced so that the coefficients  $c_i^{(\mathcal{D})}$  are dimensionless.  $\Lambda$  represents the short-distance scale at which new physics occurs, but what is really relevant for theoretical calculations and experimental measurements is the product  $c_{\mathcal{D}} \Lambda^{d-\mathcal{D}}$ , not  $c_{\mathcal{D}}$  and  $\Lambda^{d-\mathcal{D}}$  separately.  $\Lambda$  is a suitable tool that makes it clear how to organize the EFT expansion.

When  $d = 4$ ,

$$\mathcal{L}_{\text{EFT}} = \mathcal{L}_{\mathcal{D} \leq 4} + \frac{\mathcal{L}_5}{\Lambda} + \frac{\mathcal{L}_6}{\Lambda^2} + \dots \quad (1.59)$$

$\mathcal{L}_{\text{EFT}}$  is given by an infinite series of terms of increasing operator dimension, and must be treated as an expansion in powers of  $1/\Lambda$ . If you try and sum terms to all orders, you violate the EFT power counting rules, and the EFT breaks down.

At energies below  $\Lambda$ , the behaviour of the different operators is determined by their dimension. We can distinguish three types of operators:

- Relevant ( $\mathcal{D} < 4$ )
- Marginal ( $\mathcal{D} = 4$ )
- Irrelevant ( $\mathcal{D} > 4$ )

The interactions induced by the Fermi Hamiltonian in Eq. (1.60), which are dimension  $\mathcal{D} = 6$ , are suppressed by two powers of  $M_W$ , and are thus *irrelevant*. They are called *irrelevant* since their effects are suppressed by powers of  $E/\Lambda$  and are thus small at low energies. However, this does not mean they are not important. Indeed, they usually contain the compelling information about the underlying dynamics at higher scales.

The four-fermion interactions are important as they generate the leading contributions to flavour-changing processes or to low-energy neutrino scattering. Nonetheless, if the mass of the  $W$  and  $Z$  bosons were  $10^{16}$  GeV, any signal of the weak interaction would have never been observed.

As opposed, a coupling of positive mass dimension gives rise to effects which become large at energies much smaller than the scale of this coupling. Therefore, operators of dimension less than four are called *relevant*, since they become more important at lower energies.

In a four-dimensional relativistic field theory, the number of possible *relevant* operators is quite low:

- $\mathcal{D} = 0$ : The unit operator,
- $\mathcal{D} = 2$ : Boson mass terms ( $\phi^2$ ),
- $\mathcal{D} = 3$ : Fermion mass terms ( $\bar{\psi}\psi$ ) and cubic scalar interactions ( $\phi^3$ ).

At very high energies ( $E \gg m$ ), finite mass effects are negligible, nevertheless they become *relevant* when the energy scale is comparable to their mass.

Dimension-four operators are also important at all energy scales and are called *marginal* operators. They are between relevant and irrelevant operators since quantum effects could modify their scaling behaviour on either side.  $\phi^4$ , the QED and QCD interactions, and the Yukawa  $\bar{\psi}\psi\phi$  interactions are well-known examples of *marginal* operators.

As long as there is a large mass gap between the energy scale being analyzed and the scale of any heavier states (i.e.  $m, E \ll M$ ), the effects induced by *irrelevant* operators are always suppressed by powers of  $E/M$ , and can usually be neglected. The resulting EFT is called *renormalizable* and only contains *relevant* and *marginal* operators. Its predictions are valid up to  $E/M$  corrections, that can be calculated to the desired precision (marked by the experimental uncertainty).

## 1.5.2 Fermi Theory of Weak Interactions

The Fermi theory of weak interactions [173] is an EFT for weak interactions at energies below  $W$  and  $Z$  masses. It is a low-energy EFT constructed from the SM fields.

In the SM, weak decays proceed at lowest order through the exchange of a  $W^\pm$  boson between two fermionic left-handed currents (except for the heavy quark *top* which decays



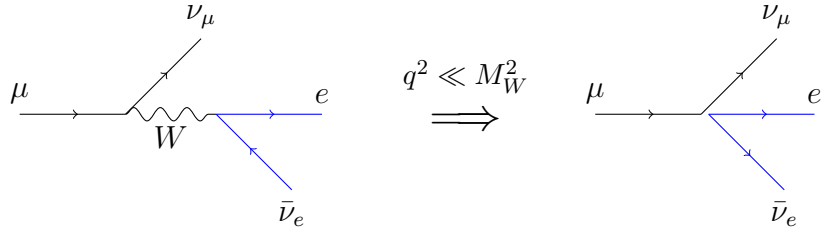


Figure 1.2: Integration of the  $W$  boson out from the electroweak theory yields the Fermi effective interaction, which is exemplified here for the muon decay.

into a real  $W^+$  and a *bottom* quark). The momentum transfer conveyed by the intermediate  $W$  is very small compared to  $M_W$ . Thus, the vector-boson propagator is reduced to a contact interaction (see Fig. 1.2):

$$\mathcal{H}_{\text{eff}} = \frac{G_F}{\sqrt{2}} \mathcal{J}_\mu \mathcal{J}^{\mu\dagger}, \quad (1.60)$$

where

$$\mathcal{J}_\mu = \sum_{ab} \bar{u}_a \gamma_\mu (1 - \gamma_5) V_{ab} d_b + \sum_{\ell} \bar{\nu}_\ell \gamma_\mu (1 - \gamma_5) \ell, \quad (1.61)$$

with  $V_{ab}$  the Cabibbo-Kobayashi-Maskawa mixing matrix <sup>1</sup>, and

$$\frac{G_F}{\sqrt{2}} = \frac{g^2}{8M_W^2} \quad (1.62)$$

is the so-called Fermi coupling constant.

Since it is not possible to produce a physical  $W$  boson at low energies ( $E \ll M_W$ ), the  $W$  field does not have to be included in the theory. The transition amplitudes, that correspond to the weak decays of leptons and quarks, are well described by the effective Hamiltonian in Eq. (1.60), which contains dimension-six operators and, then, a coupling of dimension  $-2$  (in powers of energy). The relation between the effective coupling and the parameters ( $g, M_W$ ) of the underlying electroweak theory (*matching condition*) is established by Eq. (1.62).

<sup>1</sup>For simplicity, the 4-fermion Hamiltonian in Eq. (1.60) is written in terms of the flavor-eigenstate basis of neutrinos, nonetheless they can be also expressed in the mass-eigenstate ( $\nu_1, \nu_2, \nu_3$ ) through the PMNS mixing matrix [174, 175].

Expanding the  $W$  propagator in powers of  $q^2/M_W^2$ , one would get fermionic operators of higher dimensions, which generate corrections to Eq. (1.60). With a precision better than  $m_f^2/M_W^2$ , where  $m_f$  is the mass of the decaying fermion, we can neglect these contributions.

Considering the leptonic decay  $\ell \rightarrow \ell' \nu_{\ell'} \nu_{\ell}$ , the decay width is then given by:

$$\Gamma(\ell \rightarrow \ell' \nu_{\ell'} \nu_{\ell}) = \frac{G_F^5 m_{\ell'}^5}{192\pi^3} f\left(\frac{m_{\ell'}^2}{m_{\ell}^2}\right), \quad (1.63)$$

where  $f(x) = 1 - 8x + 8x^3 - x^4 - 12x^2 \log x$ . The global mass dependence,  $\Gamma \sim G_F^2 m_{\ell'}^5$ , results from the dimension of the Fermi coupling since  $\Gamma$  must have dimension 1. Additionally, there is a three-body phase space factor of  $1/(4\pi)^3$ , in consequence, the explicit calculation needs to take into account a global factor of  $1/3$  and a function  $f(m_{\ell'}^2/m_{\ell}^2)$  containing the dependence on the final lepton mass.

The Fermi constant is obtained from  $\mu$  decays; thus, Eq. (1.63) gives a parameter-free prediction for the leptonic  $\tau$  decays. Therefore, the  $m_{\ell'}^5$  dependence of the decay width implies the following relation

$$\text{Br}(\tau^- \rightarrow e^- \bar{\nu}_e \nu_{\tau}) = \tau_{\tau} \cdot \Gamma(\tau^- \rightarrow e^- \bar{\nu}_e \nu_{\tau}) = \frac{m_{\tau}^5 \tau_{\tau}}{m_{\mu}^5 \tau_{\mu}} \simeq 17.77\%, \quad (1.64)$$

which is comparable with the experimental value  $(17.811 \pm 0.041)\%$  [5].

The effective Hamiltonian can also be used to study the low-energy neutrino scattering off either quarks or leptons. A similar dimensional argument forces the cross-section to scale with energy as

$$\sigma_{\nu} \sim G_F^2 s, \quad (1.65)$$

where  $s$  is the squared of the total energy in the center-of-mass frame. This behaviour eventually points out to the failure of the EFT, at energy scales where the  $W$  boson becomes dynamical.

### 1.5.3 SMEFT

Provided that the Standard Model leaves many questions unanswered, a solution involving some physics beyond the standard model (BSM), which may include new heavy particles with masses  $M \gg v$  much above the scale of electroweak symmetry breaking ( $v \simeq 246$  GeV), is around the corner. While at present we do not know the UV theory, we can construct its low-energy effective theory - the so-called SMEFT - by extending the familiar Standard Model Lagrangian with higher-dimensional local operators built out of Standard Model fields [1, 130, 176–178]:

$$\mathcal{L}_{\text{SMEFT}} = \mathcal{L}_{\text{SM}} + \sum_{n \geq 1} \sum_i \frac{C_i^{(n)}}{M^n} \mathcal{O}_i^{(n)}. \quad (1.66)$$

These new operators  $\mathcal{O}_i^{(n)}$ , with mass dimension  $\mathcal{D} = 4 + n$  must respect the symmetries of the SM, such as Lorentz invariance and gauge invariance. In this framework, there is an infinite set of operators, but there exists only a finite set of dimension  $\mathcal{D}$  operators, and the contributions of these operators to any given observable are suppressed by powers of  $(v/M)^{\mathcal{D}-4}$  relative to the contributions of the operators of the SM (there are processes which are first possible beyond the SM, at  $\mathcal{D} > 4$ , like lepton and/or baryon number violation). The lowest-order operators contributing to Eq. (1.66) will be discussed below.

#### Dimension 5 operators

Imposing the SM gauge symmetry constraints on dimension-5 operators leaves out just a single one [130], up to Hermitian conjugation and flavor assignments. This contribution can be written as

$$Q_{\nu\nu} = \epsilon_{jk} \epsilon_{mn} \varphi^j \varphi^m (\ell_p^k)^T C \ell_r^n \equiv (\tilde{\varphi}^\dagger \ell_p)^T C (\tilde{\varphi}^\dagger \ell_r), \quad (1.67)$$

where  $C$  is the charge conjugation matrix.  $Q_{\nu\nu}$  violates the lepton number by two units. After the electroweak symmetry breaking, it generates neutrino masses and mixings. Neither  $\mathcal{L}_{\text{SM}}^{(4)}$  nor the dimension-six terms can do the job (this is only possible at odd dimensions).

## Dimension 6 operators

All the independent dimension-six operators that are allowed by the SM gauge symmetries are showed in Tabs. 1.3 and 1.4. Dirac indices are always contracted within the brackets, and not displayed. The same is true for the isospin and color indices in the upper part of Table 1.4. In the lower-left block of that table, color indices are still contracted within brackets, while the isospin ones are made explicit. Color indices are displayed only for operators violating the baryon number  $B$  in the lower-right block of Table 1.4. All the other operators in Tables 1.3 and 1.4 are both  $B$  and  $L$  conserving.

$X^3$		$\varphi^6$ y $\varphi^4 D^2$		$\psi^2 \varphi^3$	
$Q_G$	$f^{ABC} G_{\mu\nu}^A G_{\nu\rho}^B G_{\rho\mu}^C$	$Q_\varphi$	$(\varphi^\dagger \varphi)^3$	$Q_{e\varphi}$	$(\varphi^\dagger \varphi)(\bar{\ell}_p e_r \varphi)$
$Q_{\tilde{G}}$	$f^{ABC} \tilde{G}_{\mu\nu}^A G_{\nu\rho}^B G_{\rho\mu}^C$	$Q_{\varphi\Box}$	$(\varphi^\dagger \varphi)\Box(\varphi^\dagger \varphi)$	$Q_{u\varphi}$	$(\varphi^\dagger \varphi)(\bar{q}_p u_r \tilde{\varphi})$
$Q_W$	$\epsilon^{IJK} W_{\mu\nu}^I W_{\nu\rho}^J W_{\rho\mu}^K$	$Q_{\varphi D}$	$(\varphi^\dagger D^\mu \varphi)^*(\varphi^\dagger D_\mu \varphi)$	$Q_{d\varphi}$	$(\varphi^\dagger \varphi)(\bar{q}_p d_r \varphi)$
$Q_{\tilde{W}}$	$\epsilon^{IJK} \tilde{W}_{\mu\nu}^I W_{\nu\rho}^J W_{\rho\mu}^K$				
$X^2 \varphi^2$		$\psi^2 X \varphi$		$\psi^2 \varphi^2 D$	
$Q_{\varphi G}$	$\varphi^\dagger \varphi G_{\mu\nu}^A G^{A\mu\nu}$	$Q_{eW}$	$(\bar{\ell}_p \sigma^{\mu\nu} e_r) \tau^I \varphi W_{\mu\nu}^I$	$Q_{\varphi\ell}^{(1)}$	$(\varphi^\dagger i \overleftrightarrow{D}_\mu \varphi)(\bar{\ell}_p \gamma^\mu \ell_r)$
$Q_{\varphi \tilde{G}}$	$\varphi^\dagger \varphi \tilde{G}_{\mu\nu}^A G^{A\mu\nu}$	$Q_{eB}$	$(\bar{\ell}_p \sigma^{\mu\nu} e_r) \varphi B_{\mu\nu}$	$Q_{\varphi\ell}^{(3)}$	$(\varphi^\dagger i \overleftrightarrow{D}_\mu^I \varphi)(\bar{\ell}_p \tau^I \gamma^\mu \ell_r)$
$Q_{\varphi W}$	$\varphi^\dagger \varphi W_{\mu\nu}^I W^{I\mu\nu}$	$Q_{uG}$	$(\bar{q}_p \sigma^{\mu\nu} T^A u_r) \tilde{\varphi} G_{\mu\nu}^A$	$Q_{\varphi e}$	$(\varphi^\dagger i \overleftrightarrow{D}_\mu \varphi)(\bar{e}_p \gamma^\mu e_r)$
$Q_{\varphi \tilde{W}}$	$\varphi^\dagger \varphi \tilde{W}_{\mu\nu}^I W^{I\mu\nu}$	$Q_{uW}$	$(\bar{q}_p \sigma^{\mu\nu} u_r) \tau^I \tilde{\varphi} W_{\mu\nu}^I$	$Q_{\varphi q}^{(1)}$	$(\varphi^\dagger i \overleftrightarrow{D}_\mu^I \varphi)(\bar{q}_p \gamma^\mu q_r)$
$Q_{\varphi B}$	$\varphi^\dagger \varphi B_{\mu\nu} B^{\mu\nu}$	$Q_{uB}$	$(\bar{q}_p \sigma^{\mu\nu} u_r) \tilde{\varphi} B_{\mu\nu}$	$Q_{\varphi q}^{(3)}$	$(\varphi^\dagger i \overleftrightarrow{D}_\mu^I \varphi)(\bar{q}_p \tau^I \gamma^\mu q_r)$
$Q_{\varphi \tilde{B}}$	$\varphi^\dagger \varphi \tilde{B}_{\mu\nu} B^{\mu\nu}$	$Q_{dG}$	$(\bar{q}_p \sigma^{\mu\nu} T^A d_r) \varphi G_{\mu\nu}^A$	$Q_{\varphi u}$	$(\varphi^\dagger i \overleftrightarrow{D}_\mu \varphi)(\bar{u}_p \gamma^\mu u_r)$
$Q_{\varphi WB}$	$\varphi^\dagger \tau^I \varphi W_{\mu\nu}^I B^{\mu\nu}$	$Q_{dW}$	$(\bar{q}_p \sigma^{\mu\nu} d_r) \tau^I \varphi W_{\mu\nu}^I$	$Q_{\varphi d}$	$(\varphi^\dagger i \overleftrightarrow{D}_\mu^I \varphi)(\bar{d}_p \gamma^\mu d_r)$
$Q_{\varphi \tilde{W}B}$	$\varphi^\dagger \tau^I \varphi \tilde{W}_{\mu\nu}^I B^{\mu\nu}$	$Q_{dB}$	$(\bar{q}_p \sigma^{\mu\nu} d_r) \varphi B_{\mu\nu}$	$Q_{\varphi ud}$	$(\varphi^\dagger i \overleftrightarrow{D}_\mu \varphi)(\bar{u}_p \gamma^\mu d_r)$

Table 1.3: Dimension-six operators other than the four-fermion ones [1].

All the bosonic operators ( $X^3$ ,  $X^2 \varphi^2$ ,  $\varphi^6$  y  $\varphi^4 D^2$ ) are Hermitian. Those containing  $\tilde{X}_{\mu\nu}$  are  $CP$ -odd, while the remaining ones are  $CP$ -even. For the operators containing fermions, Hermitian conjugation is equivalent to transposition of generation indices in each of the fermionic currents in classes  $(\bar{L}L)(\bar{L}L)$ ,  $(\bar{R}R)(\bar{R}R)$ ,  $(\bar{L}L)(\bar{R}R)$ , and  $\psi^2 \varphi^2 D^2$  (except for  $Q_{\varphi ud}$ ).

If  $CP$  is defined in the weak eigenstate basis then  $Q_{(-)}^- Q^\dagger$  are  $CP$ -odd (-even) for all the fermionic operators. However,  $CP$ -violation by any of those operators requires a non-

$(\bar{L}L)(\bar{L}L)$		$(\bar{R}R)(\bar{R}R)$		$(\bar{L}L)(\bar{R}R)$	
$Q_{\ell\ell}$	$(\bar{\ell}_p\gamma_\mu\ell_r)(\bar{\ell}_s\gamma^\mu\ell_t)$	$Q_{ee}$	$(\bar{e}_p\gamma_\mu e_r)(\bar{e}_s\gamma^\mu e_t)$	$Q_{\ell\ell}$	$(\bar{\ell}_p\gamma_\mu\ell_r)(\bar{e}_s\gamma^\mu e_t)$
$Q_{qq}^{(1)}$	$(\bar{q}_p\gamma_\mu q_r)(\bar{q}_s\gamma^\mu q_t)$	$Q_{uu}$	$(\bar{u}_p\gamma_\mu u_r)(\bar{u}_s\gamma^\mu u_t)$	$Q_{\ell e}$	$(\bar{\ell}_p\gamma_\mu\ell_r)(\bar{u}_s\gamma^\mu u_t)$
$Q_{qq}^{(3)}$	$(\bar{q}_p\gamma_\mu\tau^I q_r)(\bar{q}_s\gamma^\mu\tau^I q_t)$	$Q_{dd}$	$(\bar{d}_p\gamma_\mu d_r)(\bar{d}_s\gamma^\mu d_t)$	$Q_{\ell d}$	$(\bar{\ell}_p\gamma_\mu\ell_r)(\bar{d}_s\gamma^\mu d_t)$
$Q_{\ell q}^{(1)}$	$(\bar{\ell}_p\gamma_\mu\ell_r)(\bar{q}_s\gamma^\mu q_t)$	$Q_{eu}$	$(\bar{e}_p\gamma_\mu e_r)(\bar{u}_s\gamma^\mu u_t)$	$Q_{qe}$	$(\bar{q}_p\gamma_\mu q_r)(\bar{e}_s\gamma^\mu e_t)$
$Q_{\ell q}^{(3)}$	$(\bar{\ell}_p\gamma_\mu\tau^I\ell_r)(\bar{q}_s\gamma^\mu\tau^I q_t)$	$Q_{ed}$	$(\bar{e}_p\gamma_\mu e_r)(\bar{d}_s\gamma^\mu d_t)$	$Q_{qu}^{(1)}$	$(\bar{q}_p\gamma_\mu q_r)(\bar{u}_s\gamma^\mu u_t)$
		$Q_{ud}^{(1)}$	$(\bar{u}_p\gamma_\mu u_r)(\bar{d}_s\gamma^\mu d_t)$	$Q_{qu}^{(8)}$	$(\bar{q}_p\gamma_\mu T^A q_r)(\bar{u}_s\gamma^\mu T^A u_t)$
		$Q_{ud}^{(8)}$	$(\bar{u}_p\gamma_\mu T^A u_r)(\bar{d}_s\gamma^\mu T^A d_t)$	$Q_{qd}^{(1)}$	$(\bar{q}_p\gamma_\mu q_r)(\bar{d}_s\gamma^\mu d_t)$
				$Q_{qd}^{(8)}$	$(\bar{q}_p\gamma_\mu T^A q_r)(\bar{d}_s\gamma^\mu T^A d_t)$
$(\bar{L}R)(\bar{R}L)$ y $(\bar{L}R)(\bar{L}R)$		$B$ -violating			
$Q_{\ell edq}$	$(\bar{\ell}_p^j e_r)(\bar{d}_s q_t^j)$	$Q_{duq}$	$\epsilon^{\alpha\beta\gamma}\epsilon_{jk}[(d_p^\alpha)^T C u_r^\beta][(q_s^{\gamma j})^T C \ell_t^k]$		
$Q_{quqd}^{(1)}$	$(\bar{q}_p^j u_r)\epsilon_{jk}(\bar{q}_s^k d_t)$	$Q_{qqqu}$	$\epsilon^{\alpha\beta\gamma}\epsilon_{jk}[(q_p^{\alpha j})^T C q_r^{\beta k}][(u_s^\gamma)^T C e_t]$		
$Q_{quqd}^{(8)}$	$(\bar{q}_p^j T^A u_r)\epsilon_{jk}(\bar{q}_s^k T^A d_t)$	$Q_{qqqq}$	$\epsilon^{\alpha\beta\gamma}\epsilon_{jn}\epsilon_{km}[(q_p^{\alpha j})^T C q_r^{\beta k}][(q_s^{\gamma m})^T C \ell_t^n]$		
$Q_{\ell equ}^{(1)}$	$(\bar{\ell}_p^j e_r)\epsilon_{jk}(\bar{q}_s^k u_t)$	$Q_{duu}$	$\epsilon^{\alpha\beta\gamma}[(d_p^\alpha)^T C u_r^\beta][(u_s^\gamma)^T C e_t]$		
$Q_{\ell equ}^{(3)}$	$(\bar{\ell}_p^j \sigma_{\mu\nu} e_r)\epsilon_{jk}(\bar{q}_s^k \sigma^{\mu\nu} u_t)$				

Table 1.4: Four-fermion operators [1].

vanishing imaginary part of the corresponding Wilson coefficient.

Including the entries in Tables 1.3 and 1.4, there are 15 bosonic operators, 19 single-fermionic-current ones, and 25  $B$ -conserving four-fermion ones, which give a total of  $15+19+25 = 59$  independent dimension-six operators [1], while  $B$ -conservation is imposed. Thanks to the use of the equations of motion and Fierz identities the total number of dimension-six operators in Ref. [130] is reduced from 80 to 59 due to the redundancy of some operators.

### 1.5.4 EFT below $M_W$

Below the electroweak scale, one can write a low energy effective theory (LEFT) with quark and lepton fields, and only QCD and QED gauge fields. The operators have been classified in Refs. [179,180], see also Ref. [172]. The fact that  $SU(2)$  gauge invariance is no longer a requirement, implies that there are several new types of operators beyond those in SMEFT.

The complete renormalization group equations up to dimension-six have been worked out for LEFT [179,180]. Since the theory has dimension-five operators, there exist non-linear terms from two insertions of dimension-five operators for the dimension-six running. Various

pieces of the calculation have been studied before [181–192].

### 1.5.5 Principles of Effective Field Theory

The basic ingredients needed to build an EFT can be summarized as follows [168]:

1. Dynamics at low energies (large distances) does not depend on details of dynamics at high energies (short distances).
2. Choose the appropriate description of the important physics at the considered scale. If there are large energy gaps, put to zero (infinity) the light (heavy) scales, i.e.,

$$0 \longrightarrow m \gg E \gg M \longleftarrow \infty. \quad (1.68)$$

Finite corrections induced by these scales can be incorporated as perturbations.

3. Non-local heavy-particle exchanges are replaced by a tower of local (non-renormalizable) interactions among the light particles.
4. The EFT describes the low-energy physics, to a given accuracy  $\epsilon$ , in terms of a finite set of parameters:

$$(E/M)^{(d_i-4)} \gtrsim \epsilon \leftrightarrow d_i \lesssim 4 + \frac{\log(1/\epsilon)}{\log(M/E)}. \quad (1.69)$$

5. The EFT has the same infrared (but different ultraviolet) behaviour than the underlying fundamental theory.
6. The only remnants of the high-energy dynamics are in the low-energy couplings and in the symmetry of the EFT.

## 1.6 Chiral Perturbation Theory

Since at low energies the strong coupling constant,  $g_s$  becomes large, a perturbative description of QCD in terms of quarks and gluons is no longer valid. In order to describe the dynamics of QCD at low energies, an effective field theory description known as Chiral Perturbation Theory ( $\chi PT$ ) [169, 193, 194], which is based on chiral symmetry, emerges as a successful and powerful tool. The theory is predictive up to some low-energy constants fitted from observables. For that reason, Lattice becomes the only truly *ab initio* nonperturbative method to solve QCD at low energies. Further details can be found in Refs. [2, 132, 133, 195–199].

### 1.6.1 Chiral symmetry

In the absence of quark masses, the QCD Lagrangian with  $N_f$  ( $N_f = 2$  or  $3$ ) massless quarks  $q = (u, d, \dots)^T$

$$\mathcal{L}_{\text{QCD}}^0 = -\frac{1}{4}G_{\mu\nu}^a G_a^{\mu\nu} + i\bar{q}_L \gamma^\mu D_\mu q_L + i\bar{q}_R \gamma^\mu D_\mu q_R, \quad (1.70)$$

has a global symmetry

$$\underbrace{SU(N_f)_L \otimes SU(N_f)_R}_{\text{chiral group } G} \otimes U(1)_V \otimes U(1)_A.$$

At the effective hadronic level, the quark number symmetry  $U(1)_V$  is realized as baryon number. The axial  $U(1)_A$  is not a symmetry at the quantum level because of the Abelian anomaly [200–202]. Therefore, this Lagrangian is invariant under independent *global*  $G \equiv$  transformations of the left- and right-handed quarks in flavor space:

$$q_L \xrightarrow{G} g_L q_L, \quad q_R \xrightarrow{G} g_R q_R, \quad g_{L,R} \in SU(N_f)_{L,R}. \quad (1.71)$$

The Noether currents associated with the chiral group  $G$  are <sup>2</sup>:

---

<sup>2</sup> $\lambda_a$  are Gell-Mann's matrices with  $\text{Tr}(\lambda_a \lambda_b) = 2\delta_{ab}$ .

$$J_X^{a\mu} = \bar{q}_X \gamma^\mu \frac{\lambda_a}{2} q_X, \quad (X = L, R; \quad a = 1, \dots, 8), \quad (1.72)$$

and the corresponding Noether charges  $Q_X^a = \int d^3x J_X^{a0}(x)$  satisfy the familiar commutation relations

$$[Q_X^a, Q_Y^b] = i\delta_{XY} f_{abc} Q_X^c, \quad (1.73)$$

which were the beginning of the Current Algebra methods of the sixties.

The chiral symmetry, which should be approximately good in the light quark sector ( $u, d, s$ ), is nonetheless not seen in the hadronic spectrum. Even though hadrons can be nicely organized in  $SU(3)_V$  representations, degenerate multiplets with opposite parity do not exist. Furthermore, the octet of pseudoscalar mesons is much lighter than all the other hadronic states. Concerning this experimental evidence, the ground state of the theory (the vacuum) should not be symmetric under the chiral group. Thus, the  $SU(3)_L \otimes SU(3)_R$  symmetry spontaneously breaks down to  $SU(3)_{L+R}$  and, in compliance with Goldstone's theorem [203], an octet of pseudoscalar bosons appears in the theory.

If we now consider a Noether charge  $Q$  and assume the existence of an operator  $O$  satisfying

$$\langle 0|[Q, O]|0\rangle \neq 0; \quad (1.74)$$

this can only be possible if  $Q|0\rangle \neq 0$ . Thus, Goldstone's theorem tells us that there is a massless state  $|G\rangle$  in a manner that

$$\langle 0|J^0|G\rangle\langle G|O|0\rangle \neq 0. \quad (1.75)$$

The quantum numbers of the Goldstone boson are determined by those of  $J^0$  and  $O$ . The quantity in the left-hand side of Eq. (1.74) is known as the order parameter of the spontaneous symmetry breakdown.

Given the fact that there exists eight broken axial generators of the chiral group,  $Q_A^a = Q_R^a - Q_L^a$ , there should be eight pseudoscalar Goldstone bosons  $|G^a\rangle$ , which can be linked



with the eight lightest hadronic states ( $\pi^+$ ,  $\pi^-$ ,  $\pi^0$ ,  $\eta$ ,  $K^+$ ,  $K^-$ ,  $K^0$  and  $\bar{K}^0$ ); the explicit breaking of the global symmetry of the QCD Lagrangian produced by the quark-mass matrix is responsible for their small masses. Hence,  $O^a$  must be a pseudoscalar operator, and the simplest possibility is  $O^a = \bar{q}\gamma_5\lambda_a q$ , which satisfies

$$\langle 0|[Q_A^a, \bar{q}\gamma_5\lambda_b q]|0\rangle = -\frac{1}{2}\langle 0|\bar{q}\{\lambda_a, \lambda_b\}q|0\rangle = -\frac{2}{3}\delta_{ab}\langle 0|\bar{q}q|0\rangle. \quad (1.76)$$

Therefore, the quark condensate

$$\langle 0|\bar{u}u|0\rangle = \langle 0|\bar{d}d|0\rangle = \langle 0|\bar{s}s|0\rangle \neq 0 \quad (1.77)$$

is the natural order parameter of Spontaneous Chiral Symmetry Breaking (SCSB).

## 1.6.2 Effective chiral Lagrangian at lowest order

Given that there is a mass gap between the pseudoscalar octet and the rest of the hadronic spectrum, it is possible to build an effective field theory that contains only Goldstone modes. The main assumption is the pattern of SCSB:

$$G \equiv SU(3)_L \otimes SU(3)_R \xrightarrow{\text{SCSB}} H \equiv SU(3)_V. \quad (1.78)$$

Denoting  $\phi^a$  ( $a = 1, \dots, 8$ ) the coordinates representing the Goldstone fields in the coset space  $G/H$ , and choosing a coset representative  $\bar{\xi}(\phi) \equiv (\xi_L(\phi), \xi_R(\phi)) \in G$ , the change of the Goldstone coordinates under a chiral transformation  $g \equiv (g_L, g_R) \in G$  reads

$$\xi_L(\phi) \xrightarrow{G} g_L \xi_L(\phi) h^\dagger(\phi, g), \quad \xi_R(\phi) \xrightarrow{G} g_R \xi_R(\phi) h^\dagger(\phi, g), \quad (1.79)$$

where  $h(\phi, g) \in H$  is a compensating transformation which is needed to recover the corresponding coset  $\bar{\xi}$ ; in general,  $h$  depends both on  $\phi$  and  $g$ . Since the transformation  $h(\phi, g)$  appears in both sectors, left and right (this two can be related by a parity transformation, which leaves  $H$  invariant), we can eliminate it by combining the two chiral relations in Eq. (1.79):

$$U(\phi) \xrightarrow{G} g_R U(\phi) g_L^\dagger, \quad U(\phi) \equiv \xi_R(\phi) \xi_L^\dagger(\phi). \quad (1.80)$$

Besides, we can take a canonical choice of coset representative in order that  $\xi_R(\phi) = \xi_L^\dagger(\phi) \equiv u(\phi)$ . The  $3 \times 3$  unitary matrix

$$U(\phi) = u(\phi)^2 = \exp\{i\sqrt{2}\Phi/f\} \quad (1.81)$$

allows a very convenient parametrization of the Goldstone fields

$$\Phi(x) \equiv \frac{\vec{\lambda}}{\sqrt{2}} \cdot \vec{\phi} = \begin{pmatrix} \frac{1}{\sqrt{2}}\pi^0 + \frac{1}{\sqrt{6}}\eta_8 & \pi^+ & K^+ \\ \pi^- & -\frac{1}{\sqrt{2}}\pi^0 + \frac{1}{\sqrt{6}}\eta_8 & K^0 \\ K^- & \bar{K}^0 & -\frac{2}{\sqrt{6}}\eta_8 \end{pmatrix}, \quad (1.82)$$

where  $f$  is the decay constant of the pseudo-Goldstone bosons in the chiral limit ( $m_u = m_d = m_s = 0$ ), and  $\eta_8$  is the octet component of the  $\eta$  meson.

Although  $U(\phi)$  transforms linearly under the chiral group, the induced transformation on the Goldstone field  $\vec{\phi}$  is highly non-linear.

The recipe to get a low-energy effective Lagrangian is the same, we write the most general Lagrangian involving the matrix  $U(\phi)$ , which is consistent with chiral symmetry. The Lagrangian is organized in terms of increasing powers of momentum (or, equivalently, increasing number of derivatives) and since parity conservation requires an even number of derivatives, this can be written as:

$$\mathcal{L}_{\text{eff}}(U) = \sum_n \mathcal{L}_{2n}. \quad (1.83)$$

At low energies, the terms with a minimum number of derivatives will dominate.

Since  $U$  is a unitarity matrix ( $UU^\dagger = I$ ), the leading-order Lagrangian is given by

$$\mathcal{L}_2 = \frac{f^2}{4} \langle \partial_\mu U \partial^\mu U^\dagger \rangle, \quad (1.84)$$

where  $\langle \dots \rangle$  denotes the trace in flavor space. Expanding  $U(\phi)$  in powers of  $\phi$ , one obtains the Goldstone kinetic terms plus a tower of interactions involving an increasing number of

pseudoscalars.

The effective field theory technique becomes much more powerful when the couplings to external classical fields are introduced. An extended QCD Lagrangian, with quark couplings to external Hermitian matrix-valued fields  $v_\mu$ ,  $a_\mu$ ,  $s$  and  $p$ , can be written as:

$$\mathcal{L}_{QCD} = \mathcal{L}_{QCD}^0 + \bar{q}\gamma^\mu (v_\mu + \gamma_5 a_\mu) q - \bar{q} (s - i\gamma_5 p) q, \quad (1.85)$$

The external fields will allow us to compute the effective realization of general Green functions of quark currents in a very straightforward way. Besides, they can be used to include the electromagnetic and semileptonic weak interactions, and the explicit chiral symmetry breaking through the quark masses:

$$\begin{aligned} r_\mu &\equiv v_\mu + a_\mu = -e\mathcal{Q}A_\mu, \\ \ell_\mu &\equiv v_\mu - a_\mu = -e\mathcal{Q}A_\mu - \frac{e}{\sqrt{2}\sin\theta_W} (W_\mu^\dagger T_+ + h.c.), \\ s &= \mathcal{M}, \\ p &= 0, \end{aligned} \quad (1.86)$$

where  $\mathcal{Q}$  and  $\mathcal{M}$  denote the quark-charge and quark-mass matrices, respectively,

$$\mathcal{Q} = \frac{1}{3}\text{diag}(2, -1, -1), \quad \mathcal{M} = \text{diag}(m_u, m_d, m_s), \quad (1.87)$$

and  $T_+$  is a  $3 \times 3$  matrix which contains the relevant Cabibbo-Kobayashi-Maskawa factors

$$T_+ = \begin{pmatrix} 0 & V_{ud} & V_{us} \\ 0 & 0 & 0 \\ 0 & 0 & 0 \end{pmatrix}. \quad (1.88)$$

The Lagrangian in Eq. (1.85) is invariant under the following set of *local*  $SU(3)_L \otimes SU(3)_R$  transformations:

$$\begin{aligned} q_L &\rightarrow g_L q_L, & q_R &\rightarrow g_R q_R, & s + ip &\rightarrow g_R (s + ip) g_L^\dagger, \\ \ell_\mu &\rightarrow g_L \ell_\mu g_L^\dagger + ig_L \partial_\mu g_L^\dagger, & r_\mu &\rightarrow g_R R_\mu g_R^\dagger + ig_R \partial_\mu g_R^\dagger. \end{aligned} \quad (1.89)$$

Restricting ourselves to this symmetry, we can build a generalized effective Lagrangian for the Goldstone bosons, in the presence of external sources. Local invariance forces the gauge fields  $v_\mu, a_\mu$  to appear only through the covariant derivatives

$$D_\mu U = \partial_\mu U - ir_\mu U + iU\ell_\mu, \quad D_\mu U^\dagger = \partial_\mu U^\dagger + iU^\dagger r_\mu - i\ell_\mu U^\dagger, \quad (1.90)$$

and through the field strength tensors

$$F_L^{\mu\nu} = \partial^\mu \ell^\nu - \partial^\nu \ell^\mu - i[\ell^\mu, \ell^\nu], \quad F_R^{\mu\nu} = \partial^\mu r^\nu - \partial^\nu r^\mu - i[r^\mu, r^\nu]. \quad (1.91)$$

At leading order in momenta, the most general effective Lagrangian, which is consistent with Lorentz invariance and (local) chiral symmetry, is given by [193, 194]

$$\mathcal{L}_2 = \frac{f^2}{4} \langle D_\mu U D^\mu U^\dagger + \chi U^\dagger + \chi^\dagger U \rangle, \quad (1.92)$$

where  $\chi = 2B_0(s + ip)$ , and  $B_0$  is a constant, which, like  $f$ , is not fixed by symmetry requirements alone.

The external field technique provides a powerful tool for computing the chiral Noether currents. The Green functions are obtained as functional derivatives of the generating functional  $Z[v, a, s, p]$ , defined via the path-integral formula

$$\exp[iZ] = \int \mathcal{D}q \mathcal{D}\bar{q} \mathcal{D}G_\mu \exp \left[ i \int d^4x \mathcal{L}_{QCD} \right] = \int \mathcal{D}U \exp \left[ i \int d^4x \mathcal{L}_{eff} \right]. \quad (1.93)$$

At lowest order in momenta, the generating functional reduces to the classical action  $S_2 = \int d^4x \mathcal{L}_2$ ; for that reason, the currents can be trivially computed by taking the appropriate derivatives with respect to the external fields:

$$\begin{aligned} J_L^\mu &= \bar{q}_L \gamma^\mu q_L \doteq \frac{\delta S_2}{\delta \ell_\mu} = \frac{i}{2} f^2 D^\mu U^\dagger U = \frac{f}{\sqrt{2}} D^\mu \Phi - \frac{i}{2} \left( \Phi \overleftrightarrow{D}^\mu \Phi \right) + \mathcal{O}(\Phi^3/f), \\ J_R^\mu &= \bar{q}_R \gamma^\mu q_R \doteq \frac{\delta S_2}{\delta r_\mu} = \frac{i}{2} f^2 D^\mu U U^\dagger = -\frac{f}{\sqrt{2}} D^\mu \Phi - \frac{i}{2} \left( \Phi \overleftrightarrow{D}^\mu \Phi \right) + \mathcal{O}(\Phi^3/f). \end{aligned} \quad (1.94)$$

At  $\mathcal{O}(p^2)$ ,  $f$  is equal to the pion decay constant,  $f = f_\pi = 92.2 \text{ MeV}$ , which is defined as

$$\langle 0 | (J_A^\mu)^{12} | \pi^+ \rangle \equiv i\sqrt{2}f_\pi p^\mu. \quad (1.95)$$

Likewise, when a derivative with respect to the external scalar and pseudoscalar sources is taken,

$$\begin{aligned} \bar{q}_L^j q_R^i &\doteq -\frac{\delta S_2}{\delta (s - ip)^{ji}} = -\frac{f^2}{2} B_0 U(\vec{\phi})_{ij}, \\ \bar{q}_R^j q_L^i &\doteq -\frac{\delta S_2}{\delta (s + ip)^{ji}} = -\frac{f^2}{2} B_0 U^\dagger(\vec{\phi})_{ij}, \end{aligned} \quad (1.96)$$

a relation between the quark condensate and the constant  $B_0$  is established

$$\langle 0 | \bar{q}^j q^i | 0 \rangle = -f^2 B_0 \delta^{ij}. \quad (1.97)$$

The Goldstone bosons, which are parameterized by the matrix  $U(\phi)$ , correspond to the zero-energy excitations over this vacuum condensate.

### 1.6.3 Pseudoscalar meson masses at the lowest order

When  $s = \mathcal{M}$  and  $p = 0$ , the non-derivative piece of the Lagrangian generates a quadratic mass term for the pseudoscalar bosons, plus  $\Phi^{2n}$  interactions proportional to the quark masses. With this, one finds:

$$\frac{f^2}{4} 2B_0 \langle \mathcal{M}(U + U^\dagger) \rangle = B_0 \left\{ \langle \mathcal{M}\Phi^2 \rangle + \frac{1}{6f^2} \langle \mathcal{M}\Phi^4 \rangle + \mathcal{O}\left(\frac{\Phi^6}{f^4}\right) \right\}. \quad (1.98)$$

The computation of the trace in the quadratic term provides the relation between the masses of the physical mesons and the quark masses:

$$\begin{aligned} M_{\pi^\pm}^2 &= 2\hat{m}B_0, & M_{\pi^0}^2 &= 2\hat{m}B_0 - \epsilon + \mathcal{O}(\epsilon^2), \\ M_{K^\pm}^2 &= (m_u + m_s)B_0, & M_{K^0}^2 &= (m_d + m_s)B_0, \\ M_{\eta_s}^2 &= \frac{2}{3}(\hat{m} + 2m_s)B_0 + \epsilon + \mathcal{O}(\epsilon^2), \end{aligned} \quad (1.99)$$

with

$$\hat{m} = \frac{1}{2}(m_u + m_d), \quad \epsilon = \frac{B_0 (m_u - m_d)^2}{4 (m_s - \hat{m})}. \quad (1.100)$$

Thanks to the chiral symmetry, the meson masses squared are proportional to a single power of the quark masses, the proportionality constant is related to the vacuum quark condensate [204]:

$$f_\pi^2 M_{\pi^\pm}^2 = -\hat{m} \langle 0 | \bar{u}u + \bar{d}d | 0 \rangle. \quad (1.101)$$

By factorizing the proportionality factor  $B_0$ , the relations in Eq. (1.99) imply the old Current-Algebra mass ratios [204, 205],

$$\frac{M_{\pi^\pm}^2}{2\hat{m}} = \frac{M_{K^+}^2}{m_u + m_s} = \frac{M_{K^0}^2}{m_d + m_s} \approx \frac{3M_{\eta_s}^2}{2\hat{m} + 4m_s}, \quad (1.102)$$

and, up to  $\mathcal{O}(m_u - m_d)$  corrections, the Gell-Mann-Okubo [206, 207] mass relation,

$$3M_{\eta_s}^2 = 4M_K^2 - M_\pi^2. \quad (1.103)$$

Since the absolute values of the quark masses are short-distance parameters that depend on QCD renormalization conventions, chiral symmetry cannot fix them by itself. The renormalization scale and scheme dependence cancels out in the products  $m_q \bar{q}q \sim m_q B_0$ , which are the relevant combinations determining the pseudoscalar masses. Fortunately,  $\chi$ PPT provides information about quark mass ratios, which does not depend upon  $B_0$  (i.e., QCD is flavor blind). When the tiny  $\mathcal{O}(\epsilon)$  is neglected, one gets the following relations:

$$\begin{aligned} \frac{m_d - m_u}{m_d + m_u} &= \frac{(M_{K^0}^2 - M_{K^+}^2) - (M_{\pi^0}^2 - M_{\pi^+}^2)}{M_{\pi^0}^2} = 0.29, \\ \frac{m_s - \hat{m}}{2\hat{m}} &= \frac{M_{K^0}^2 - M_{\pi^0}^2}{M_{\pi^0}^2} = 12.6. \end{aligned} \quad (1.104)$$

In the first equation, the electromagnetic pion mass-squared difference has been subtracted to account for the virtual photon contribution to the meson self-energies. In the chiral limit ( $m_{u,d,s} = 0$ ), this correction is proportional to the square of the meson charge

and its the same for  $K^+$  and  $\pi^+$  (this result is known as Dashen's theorem [208]). These relations imply the quark mass ratios advocated by Weinberg [205]:

$$m_u : m_d : m_s = 0.55 : 1 : 20.3. \quad (1.105)$$

Thus, quark mass corrections are governed by the strange quark mass  $m_s$ , which is much larger than  $m_u$  and  $m_d$ . The light-quark mass difference  $m_d - m_u$  is not small compared with the individual up and down quark masses. Given the fact that isospin-breaking effects are dominated by the small ratio  $(m_d - m_u)/m_s$ , isospin then turns out to be a very good symmetry.

The  $\mathcal{O}(p^2)$  chiral Lagrangian encodes all the Current-Algebra results obtained in the sixties [209, 210]. The pattern of SCSB in Eq. (1.78) and the explicit breaking, which is incorporated by the QCD quark masses, are corroborated by these successful phenomenological predictions. Aside from its elegant simplicity, the EFT formalism provides a powerful technique to estimate higher-order corrections in a systematic way.

#### 1.6.4 ChPT at $\mathcal{O}(p^4)$

At next-to-leading order in momenta,  $\mathcal{O}(p^4)$ , the calculation of the generating functional  $Z[v, a, s, p]$  involves three elements:

1. The most general effective Lagrangian of  $\mathcal{O}(p^4)$ ,  $\mathcal{L}_4$ , to be considered at tree level.
2. One-loop graphs with the lowest-order Lagrangian  $\mathcal{L}_2$ .
3. The Wess-Zumino (1971)-Witten (1983) functional to account for the chiral anomaly.

#### $\mathcal{O}(p^4)$ Lagrangian

At  $\mathcal{O}(p^4)$ , the most general Lagrangian invariant under parity, charge conjugation and the local chiral transformations in Eq. (1.89), reads [194]

$$\begin{aligned}
\mathcal{L}_4 = & L_1 \langle D_\mu U^\dagger D^\mu U \rangle^2 + L_2 \langle D_\mu U^\dagger D_\nu U \rangle \langle D^\mu U^\dagger D^\nu U \rangle + L_3 \langle D_\mu U^\dagger D^\mu U D_\nu U^\dagger D^\nu U \rangle \\
& + L_4 \langle D_\mu U^\dagger D^\mu U \rangle \langle U^\dagger \chi + \chi^\dagger U \rangle + L_5 \langle D_\mu U^\dagger D^\mu U (U^\dagger \chi + \chi^\dagger U) \rangle \\
& + L_6 \langle U^\dagger \chi + \chi^\dagger U \rangle^2 + L_7 \langle U^\dagger \chi - \chi^\dagger U \rangle^2 + L_8 \langle \chi^\dagger U \chi^\dagger U + U^\dagger \chi U^\dagger \chi \rangle \\
& - i L_9 \langle F_R^{\mu\nu} D_\mu U D_\nu U^\dagger + F_L^{\mu\nu} D_\mu U^\dagger D_\nu U \rangle + L_{10} \langle U^\dagger F_R^{\mu\nu} U F_{L\mu\nu} \rangle \\
& + H_1 \langle F_{R\mu\nu} F_R^{\mu\nu} + F_{L\mu\nu} F_L^{\mu\nu} \rangle + H_2 \langle \chi^\dagger \chi \rangle.
\end{aligned} \tag{1.106}$$

The terms proportional to  $H_1$  and  $H_2$  do not contain the pseudoscalar fields and are then not directly measurable. Thus, at  $\mathcal{O}(p^4)$  we need ten additional coupling constants  $L_i$  to determine the low-energy behavior of the Green functions. These constants parameterize our ignorance about the details of the underlying QCD dynamics. In principle, all the chiral couplings are calculable functions of  $\Lambda_{\text{QCD}}$  and the heavy-quark masses, which can be analysed with lattice simulations. Nevertheless, at this moment, our main source of information about these couplings is still low-energy phenomenology. At this order, the elastic  $\pi\pi$  and  $\pi K$  scattering amplitudes are sensible to  $L_{1,2,3}$ . The two-derivative couplings  $L_{4,5}$  generate mass corrections to the meson decay constants (and mass-dependent wavefunction renormalizations), while the pseudoscalar meson masses are modified by the non-derivative terms  $L_{6,7,8}$ .  $L_9$  is mostly responsible for the charged-meson electromagnetic radius and  $L_{10}$  only contributes to amplitudes with at least two external vector or axial-vector fields, such as the radiative semileptonic decay  $\pi \rightarrow e\nu_e\gamma$ .

## The chiral anomaly

Under an infinitesimal chiral transformation

$$g_L = 1 + i(\alpha - \beta) + \dots, \quad g_R = 1 + i(\alpha + \beta) + \dots, \tag{1.107}$$

with  $\alpha = \alpha_a T^a$  and  $\beta = \beta_a T^a$ , the anomalous change of the generating functional is given by [211]:

$$\delta Z[v, a, s, p] = -\frac{N_C}{16\pi^2} \int d^4x \langle \beta(x) \Omega(x) \rangle, \tag{1.108}$$



where  $N_C = 3$  is the number of QCD colors,

$$\Omega(x) = \epsilon^{\mu\nu\sigma\rho} \left[ v_{\mu\nu} v_{\sigma\rho} + \frac{4}{3} \nabla_\mu a_\nu \nabla_\sigma a_\rho + \frac{2}{3} i \{v_{\mu\nu}, a_\sigma a_\rho\} + \frac{8}{3} i a_\sigma v_{\mu\nu} a_\rho + \frac{4}{3} a_\mu a_\nu a_\sigma a_\rho \right] \quad (1.109)$$

with  $\epsilon_{0123} = +1$ , and

$$v_{\mu\nu} = \partial_\mu v_\nu - \partial_\nu v_\mu - i[v_\mu, v_\nu], \quad \nabla_\mu a_\nu = \partial_\mu a_\nu - i[v_\mu, a_\nu]. \quad (1.110)$$

$\Omega(x)$  only depends on the external fields  $v_\mu$  and  $a_\mu$ , which have been assumed to be traceless. This anomalous variation of  $Z$  is an  $\mathcal{O}(p^4)$  effect in the chiral counting. Up to this point, we have imposing chiral symmetry to construct the effective ChPT Lagrangian. Given that chiral symmetry is explicitly violated by the anomaly at the fundamental QCD level, one needs to include an additional functional  $Z_A$  with the property that its change under a chiral gauge transformation yields Eq. (1.108). This functional was first constructed by Wess and Zumino [212], and reformulated in a nice geometrical way by Witten [213]. The WZW action is then given by

$$S[U, \ell, r]_{WZW} = - \frac{iN_C}{240\pi^2} \int d\sigma^{ijklm} \langle \Sigma_i^L \Sigma_j^L \Sigma_k^L \Sigma_l^L \Sigma_m^L \rangle - \frac{iN_C}{48\pi^2} \int d^4x \epsilon_{\mu\nu\alpha\beta} (W(U, \ell, r)^{\mu\nu\alpha\beta} - W(1, \ell, r)^{\mu\nu\alpha\beta}), \quad (1.111)$$

$$W(U, \ell, r)_{\mu\nu\alpha\beta} = \left\langle U \ell_\mu \ell_\nu \ell_\alpha U^\dagger r_\beta + \frac{1}{4} U \ell_\mu U^\dagger r_\nu U \ell_\alpha U^\dagger r_\beta + i U \partial_\mu \ell_\nu \ell_\alpha U^\dagger r_\beta + i \partial_\mu r_\nu U \ell_\alpha U^\dagger r_\beta - i \Sigma_\mu^L \ell_\nu U^\dagger r_\alpha U \ell_\beta + \Sigma_\mu^L U^\dagger \partial_\nu r_\alpha U \ell_\beta - \Sigma_\mu^L \Sigma_\nu^L U^\dagger r_\alpha U \ell_\beta + \Sigma_\mu^L \ell_\nu \partial_\alpha \ell_\beta + \Sigma_\mu^L \partial_\nu \ell_\alpha \ell_\beta - i \Sigma_\mu^L \ell_\nu \ell_\alpha \ell_\beta + \frac{1}{2} \Sigma_\mu^L \ell_\nu \Sigma_\alpha^L \ell_\beta - i \Sigma_\mu^L \Sigma_\nu^L \Sigma_\alpha^L \ell_\beta \right\rangle - (L \leftrightarrow R), \quad (1.112)$$

where

$$\Sigma_\mu^L = U^\dagger \partial_\mu U, \quad \Sigma_\mu^R = U \partial_\mu U^\dagger, \quad (1.113)$$

and  $(L \leftrightarrow R)$  stands for the interchanges  $U \leftrightarrow U^\dagger$ ,  $\ell_\mu \leftrightarrow r_\mu$  and  $\Sigma_\mu^L \leftrightarrow \Sigma_\mu^R$ . The integration in the first term of equation (1.111) is over a five-dimensional manifold whose

boundary is four-dimensional Minkowski space. The integrand is a surface term; thus both the first and second terms of  $S_{WZW}$  are  $\mathcal{O}(p^4)$ , in compliance with the chiral counting rules.

The effects induced by the anomaly are completely calculable due to their short-distance origin. The translation from the fundamental quark-gluon level to the effective chiral level is unaffected by hadronization problems. The anomalous action in Eq. (1.111) has no free parameters. The most general solution to the anomalous variation (Eq. (1.108)) of the QCD generating functional is given by the WZW action plus the most general chiral-invariant Lagrangian.

The anomaly term does not get renormalized. Thus, quantum loops insertions of the WZW action generate higher-order divergences that obey the standard Weinberg's power counting and correspond to chiral invariant structures. These are renormalized by the LECs of the corresponding  $\chi$ PT operators.

Since a Levi-Civita pseudotensor is present, the anomaly functional gives rise to interactions that break the intrinsic parity. These vertices are absent in the LO and NLO  $\chi$ PT Lagrangians because chiral symmetry only allows for odd-parity invariant structures starting at  $\mathcal{O}(p^6)$ . So, the WZW functional breaks an accidental symmetry of the  $\mathcal{O}(p^2)$  and  $\mathcal{O}(p^4)$  chiral Lagrangians, giving the leading contributions to processes with an odd number of pseudoscalars.

### 1.6.5 Higher-order corrections

The structure of the  $\mathcal{O}(p^6)$   $\chi$ PT Lagrangian has also been studied. It contains  $90 + 4$  independent chiral structures of even intrinsic parity (without Levi-Civita pseudotensors) [214], the last four involving external sources only, and 23 operators of odd intrinsic parity [215,216]:

$$\mathcal{L}_6 = \sum_{i=1}^{94} C_i O_i^{p^6} + \sum_{i=1}^{23} \tilde{C}_i \tilde{O}_i^{p^6}. \quad (1.114)$$

The complete renormalization of the  $\chi$ PT generating functional has been achieved at two-loop level [214], which determines the renormalization group equations for the renormalized  $\mathcal{O}(p^6)$  LECs.

$\chi$ PT is an expansion in powers of momenta over some typical hadronic scale  $\Lambda_\chi$ , associated with the SCSB, which can be expected to be of the order of the (light-quark) resonance masses. The variation of the loop amplitudes under a rescaling of  $\mu$  provides a natural order-of-magnitude estimate of the SCSB scale:  $\Lambda_\chi \sim 4\pi f_\pi \sim 1.2 \text{ GeV}$  [217, 218].

At  $\mathcal{O}(p^2)$ , the  $\chi$ PT Lagrangian is able to describe all QCD Green functions with only two parameters,  $f$  and  $B_0$ , an impressive achievement. Nonetheless, with  $p \lesssim M_K (M_\pi)$ , we expect  $\mathcal{O}(p^4)$  contributions to the LO amplitudes at the level of  $p^2/\Lambda_\chi^2 \lesssim 20\%$  (2%). Aiming to increase the accuracy of the  $\chi$ PT predictions beyond this level, the inclusion of NLO corrections is required, which introduces ten additional unknown LECs. Many more free parameters ( $90 + 23$ ) are needed to account for  $\mathcal{O}(p^6)$  contributions. In consequence, the predictive power of the effective theory is reduced when the precision is increased.

The present knowledge of the  $\mathcal{O}(p^4)$  LECs ( $L_i$ ) is summarized in Table 1.5. The numbers correspond to the renormalized couplings, at a scale  $\mu = M_\rho$ . The second column shows the LECs extracted from  $\mathcal{O}(p^4)$  phenomenological analyses [219], without any estimate of the uncertainties produced by the missing higher-order contributions. The third column shows the results obtained from a global  $\mathcal{O}(p^6)$  fit [219], which includes some theoretical priors on the unknown  $\mathcal{O}(p^6)$  LECs. Since the number of parameters is increased at NNLO, the  $\mathcal{O}(p^6)$  values should be taken with care, however they can give a good estimation of the potential uncertainties. The  $\mathcal{O}(p^6)$  determination of  $L_{10}^r(M_\rho)$  has been directly extracted from hadronic tau decay data [220]. In contrast, the fourth column displays the results of lattice simulations with  $2 + 1 + 1$  dynamical fermions by the HPQCD collaboration [221]. Analogously, the results with  $2 + 1$  fermions were obtained by the MILC collaboration [222], while their errors are larger. A similar compilation of LECs for the  $n_f = 2$  theory can be obtained in Refs. [219, 223].

The numbers reported in the table are in good agreement with the expected size of the couplings  $L_i$  in terms of the scale of SCSB:

$$L_i \sim \frac{f_\pi^2/4}{\Lambda_\chi} \sim \frac{1}{4(4\pi)^2} \sim 2 \cdot 10^{-3}, \quad (1.115)$$

$i$	$L_i^r(M_\rho) \times 10^3$				
	$\mathcal{O}(p^4)$ [219]	$\mathcal{O}(p^6)$ [219]	<i>Lattice</i> [221]	$R\chi T$ [224]	$R\chi T_{SD}$ [225, 226]
1	$1.0 \pm 0.1$	$0.53 \pm 0.06$		0.6	0.9
2	$1.6 \pm 0.2$	$0.81 \pm 0.04$		1.2	1.8
3	$-3.8 \pm 0.3$	$-3.07 \pm 0.20$		-2.8	-4.8
4	$0.0 \pm 0.3$	0.3 (fixed)	$0.09 \pm 0.34$	0.0	0.0
5	$1.2 \pm 0.1$	$1.01 \pm 0.06$	$1.19 \pm 0.25$	$1.2^\dagger$	1.1
6	$0.0 \pm 0.4$	$0.14 \pm 0.05$	$0.16 \pm 0.20$	0.0	0.0
7	$-0.3 \pm 0.2$	$-0.34 \pm 0.09$		-0.3	-0.3
8	$0.5 \pm 0.2$	$0.47 \pm 0.10$	$0.55 \pm 0.15$	$0.5^\dagger$	0.4
9	$6.9 \pm 0.7$	$5.9 \pm 0.4$		$6.9^\dagger$	7.1
10	$-5.2 \pm 0.1$	$-4.1 \pm 0.4$		-5.8	-5.3

Table 1.5: Phenomenological determination of the renormalized couplings  $L_i^r(M_\rho)$  from  $\mathcal{O}(p^4)$  and  $\mathcal{O}(p^6)$   $\chi$ PT analyses, and from lattice simulations. The fifth and sixth columns show the  $R\chi T$  predictions without and with short-distance information, respectively. Values labeled with  $\dagger$  have been used as inputs [2].

where the normalization of  $\mathcal{L}_2$  and  $\Lambda_\chi \sim 4\pi f_\pi$  have been taken as references. Hence, all  $\mathcal{O}(p^4)$  couplings have the right order of magnitude, which implies a good convergence of the momentum expansion below the resonance region, i.e., for  $p < M_\rho$ . Nonetheless, this table shows a clear hierarchy with some couplings being large while others seem compatible with zero.

## 1.7 Dispersion theory

Dispersive techniques are powerful, model-independent methods based on the fundamental principles of analyticity (the mathematical manifestation of causality) and unitarity (a consequence of probability conservation). By exploiting nonperturbative relations between amplitudes, they allow for a resummation of rescattering effects between final-state particles, in contrast to a strictly perturbative  $\chi PT$  expansion in which such effects would be treated order-by-order only. Dispersion theory, coupled with  $\chi PT$ , then allows one to extend the  $\chi PT$  effective description of strong dynamics from low energy to an intermediate-energy range where resonances start to appear.

### 1.7.1 Analyticity

Let us take as an example a form factor  $F(s)$ , which is a function of a single Mandelstam variable  $s$ . In several cases, these form factors are real below some threshold,  $s < s_{\text{th}}$ , while above threshold,  $s > s_{\text{th}}$ , they have both real and imaginary parts, the latter due to the propagation of on-shell intermediate states. Analyticity allows us to relate the real part of the form factor to its discontinuity or imaginary part. In order to completely exploit these properties one needs to analytically continue  $s$  into the complex plane where the discontinuity is represented as a branch cut along the positive real axis, for  $s > s_{\text{th}}$ , see Fig. 1.3. The form factor is then a complex-valued function  $F(s)$  of complex argument  $s$ , which has the following properties:

1.  $F(s)$  is real along the real axis for  $s < s_{\text{th}}$ , and
2.  $F(s)$  is analytic in the entire complex plane except along the branch cut.

The sign of the imaginary part of  $F(s)$  along the cut is fixed by the convention  $F(s + i\epsilon) = \text{Re}F(s) + i\text{Im}F(s)$ , where  $\epsilon$  is a positive infinitesimal quantity.

Starting from the Cauchy's integral formula

$$F(s) = \frac{1}{2\pi i} \oint_C ds' \frac{F(s')}{s' - s}, \quad (1.116)$$

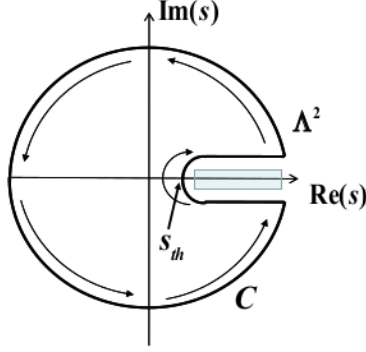


Figure 1.3: Symbolic representation of the Cauchy contour in the complex  $s$  plane. Reprinted from Ref. [10].

and performing the integral on the contour in Fig. 1.3, one obtains

$$\begin{aligned}
 F(s) &= \frac{1}{2\pi i} \left( \int_{s_{th}}^{\Lambda^2} ds' \frac{F(s' + i\epsilon) - F(s' - i\epsilon)}{s' - s} + \int_{|s'|=\Lambda^2} ds' \frac{F(s')}{s' - s} \right) \\
 &= \frac{1}{2\pi i} \left( \int_{s_{th}}^{\Lambda^2} ds' \frac{\text{disc}F(s')}{s' - s} + \int_{|s'|=\Lambda^2} ds' \frac{F(s')}{s' - s} \right).
 \end{aligned} \tag{1.117}$$

When the Schwartz's reflection is applied,  $F(z^*) = F(z)$ , one gets

$$\text{disc}F(s) = F(s + i\epsilon) - F(s - i\epsilon) = F(s + i\epsilon) - F^*(s + i\epsilon) = 2i\text{Im}F(s + i\epsilon), \tag{1.118}$$

and then

$$F(s) = \frac{1}{\pi} \int_{s_{th}}^{\Lambda^2} ds' \frac{\text{Im}F(s')}{s' - s - i\epsilon} + \frac{1}{2\pi i} \int_{|s'|=\Lambda^2} ds' \frac{F(s')}{s' - s}. \tag{1.119}$$

Now, if the second integral vanishes in the limit  $\Lambda \rightarrow \infty$ , we obtain an unsubtracted dispersion relation:

$$F(s) = \frac{1}{\pi} \int_{s_{th}}^{\infty} ds' \frac{\text{Im}F(s')}{s' - s - i\epsilon}. \tag{1.120}$$

This relation is very powerful: it implies that the form factor  $F(s)$  can be reconstructed anywhere in the complex plane provided we know its absorptive part along the branching cut, which is in turn given by unitarity.

In addition to the unsubtracted dispersion relation, if  $F(s)$  does not approach zero fast enough at infinity, more subtractions can be performed at  $s = s_0 < s_{\text{th}}$ . Applying one subtraction,

$$F(s) - F(s_0) = \frac{1}{\pi} \int_{s_{\text{th}}}^{\Lambda^2} ds' \frac{\text{Im}F(s')}{s' - s - i\epsilon} + \frac{1}{2\pi i} \int_{|s'|=\Lambda^2} ds' \frac{F(s')}{s' - s} - \left( \frac{1}{\pi} \int_{s_{\text{th}}}^{\Lambda^2} ds' \frac{\text{Im}F(s')}{s' - s_0} + \frac{1}{2\pi i} \int_{|s'|=\Lambda^2} ds' \frac{F(s')}{s' - s_0} \right) \quad (1.121)$$

one obtains

$$F(s) = F(s_0) + \frac{s - s_0}{\pi} \int_{s_{\text{th}}}^{\Lambda^2} \frac{ds'}{s' - s_0} \frac{\text{Im}F(s')}{s' - s - i\epsilon} + \frac{s - s_0}{2\pi i} \int_{|s'|=\Lambda^2} ds' \frac{F(s')}{(s' - s_0)(s' - s)}. \quad (1.122)$$

Now, the last expression contains one more power of  $s'$  in the denominator, which ensures a better convergence when  $\Lambda \rightarrow \infty$ . In that case, one obtains the once-subtracted dispersion relation:

$$F(s) = F(s_0) + \frac{s - s_0}{\pi} \int_{s_{\text{th}}}^{\infty} \frac{ds'}{s' - s_0} \frac{\text{Im}F(s')}{s' - s - i\epsilon}. \quad (1.123)$$

The  $n$ -times-subtracted dispersion relation at  $s = s_0$  is given by

$$F(s) = P_n(s - s_0) + \frac{(s - s_0)^n}{\pi} \int_{s_{\text{th}}}^{\infty} \frac{ds'}{(s' - s_0)^n} \frac{\text{Im}F(s')}{s' - s - i\epsilon}, \quad (1.124)$$

where  $P_n(s - s_0)$  is a polynomial of power  $n - 1$  in  $(s - s_0)$ . It is possible to perform subtractions in different points given that they are on the real axis to the left of the branch cut.

## 1.7.2 Unitarity

Unitarity is a fundamental property of the  $S$ -matrix:

$$S^\dagger S = 1. \quad (1.125)$$

The decomposition of the  $S$ -matrix into the identity and the nontrivial scattering matrix  $T$ ,  $S = 1 + iT$ , implies

$$-i(T - T^\dagger) = T^\dagger T. \quad (1.126)$$

When this relation is sandwiched between initial and final states and a complete set of intermediate states is inserted on the right-hand side, we arrive at the well-known optical theorem

$$\text{Im}T_{fi} = \frac{1}{2} \sum_n (2\pi)^4 \delta^{(4)}(P_n - P_i) T_{nf}^* T_{ni}, \quad (1.127)$$

where time-reversal invariance has been assumed and  $\langle f|T|i\rangle \equiv (2\pi)^4 \delta^{(4)}(P_f - P_i) T_{fi}$ .

Considering the scattering of two incoming and two outgoing particles, and assuming that we are in an energy region where only elastic final-state rescattering is allowed. Thus, from Eq. (1.127), the only intermediate state is  $|n\rangle = |f\rangle$  and the completeness sum reduces to an integral over the intermediate momenta:

$$\text{Im}T_{fi} = \frac{(2\pi)^4}{2S} \int \frac{d^3q_1 d^3q_2}{2E_1(2\pi)^3 2E_2(2\pi)^3} \delta^{(3)}(p_i - q_1 - q_2) T_{ff}^* T_{fi}. \quad (1.128)$$

The symmetry factor  $S$  is 2 for indistinguishable particles and 1 otherwise. Here,  $q_i = (E_i, \mathbf{q}_i)$  denotes the on-shell four-momenta of the two intermediate particles, and the total initial and final four-momenta are  $p_i = K + k' = p_f = p + p' = (\sqrt{s}, \mathbf{0})$  in the center-of-mass frame. Defining  $\theta$  ( $\theta'$ ) as the angle between  $\mathbf{p}$  and  $\mathbf{k}$  ( $\mathbf{q}_1$ ) the three-momenta, and integrating over the delta function, the following relation is found

$$\text{Im}T_{fi}(s, \theta) = \frac{1}{8(2\pi)^2 S} \frac{|\mathbf{q}_1|}{\sqrt{2}} \int T_{ff}^*(s, \theta') T_{fi}(s, \theta'') d\Omega, \quad (1.129)$$

where  $d\Omega \equiv \sin\theta' d\theta' d\phi$  and  $|\mathbf{q}_1| = \sqrt{s/4 - m_\pi^2}$  as an example of an intermediate state of two pions. A unitarity relation similar to that in Eq. (1.129) results also when we consider a production amplitude or a form factor that produces the final state  $f$  in the elastic regime.

Let us take a look at the pion form factor, which is an essential ingredient throughout the development of this thesis. This is defined as

$$\langle \pi^+(p') \pi^-(p) | j_\mu(0) | 0 \rangle = (p' - p)_\mu F_\pi^V(s), \quad (1.130)$$



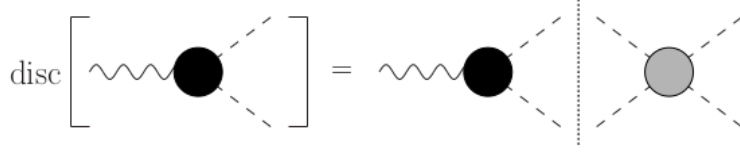


Figure 1.4: Graphical representation of the discontinuity relation for pion form factors, where the black disc represents the form factor, while the gray disc represents the pion-pion scattering  $T$ -matrix, projected onto the appropriate partial wave. Reprinted from Ref. [10].

where

$$j_\mu = \frac{2}{3}\bar{u}\gamma_\mu u - \frac{1}{3}\bar{d}\gamma_\mu d - \frac{1}{3}\bar{s}\gamma_\mu s \quad (1.131)$$

denotes the electromagnetic vector current for the light quarks. The unitarity relation in Eq. (1.129) becomes

$$\text{Im}F_\pi^V(s) = \sigma(s) \left(t_{J=1}^{I=1}\right)^* F_\pi^V(s) \times \theta(s - 4m_\pi^2), \quad (1.132)$$

where  $\sigma(s) = \sqrt{1 - 4m_\pi^2/s}$ , and  $t_{J=1}^{I=1}(s)$  is the  $\pi\pi$   $P$ -wave isospin  $I = 1$  scattering amplitude. The Eq. (1.132) is depicted in Fig. 1.4. If the unitarity relation to  $t_1^1(s)$  is now applied, we find

$$\text{Im}t_1^1(s) = \sigma(s) |t_1^1(s)|^2 \times \theta(s - 4m_\pi^2). \quad (1.133)$$

Since  $t_1^1(s)$  can be written as  $t_1^1(s) = |t_1^1(s)| e^{i\delta_1^1(s)}$ , the Eq. (1.133) leads to

$$|t_1^1(s)| = \frac{\sin \delta_1^1(s)}{\sigma(s)}; \quad (1.134)$$

when this expression is used in Eq. (1.132), we get

$$\text{Im}F_\pi^V(s) = \sin \delta_1^1(s) e^{-i\delta_1^1(s)} F_\pi^V(s) \times \theta(s - 4m_\pi^2). \quad (1.135)$$

Writing  $F_\pi^V(s) = |F_\pi^V(s)| e^{i\phi_V(s)}$ , where  $\phi_V$  is the phase of the vector form factor, then the unitary equation implies  $\phi_V = \delta_1^1(s)$  which means that unitarity forces the phase of the

form factor to be equal to the  $\pi\pi$  (elastic) scattering phase. This is the well-known Watson theorem [227] that holds only in the elastic region.

### 1.7.3 Omnès formalism

The solution to the form factor in Eq. (1.132) is easily obtained in terms of the so-called Omnès function  $\Omega_1^1(s)$  [228],

$$F_\pi^V(s) = R(s)\Omega_1^1(s), \quad \Omega_1^1(s) = \exp\left\{\frac{s}{\pi} \int_{4m_\pi^2}^{\infty} ds' \frac{\delta_1^1(s')}{s'(s' - s - i\epsilon)}\right\}, \quad (1.136)$$

where  $R(s)$  is a function free of right-hand cuts up to the first inelastic threshold. At low energies,  $R(s)$  can be approximated by a polynomial whose coefficients need to be determined by other means, e.g., by matching to chiral perturbation theory near  $s = 0$ . The Omnès function is completely given in terms of the appropriate pion-pion phase shift, which is particularly useful thanks to the excellent information on pion-pion scattering at our disposal [229–232]. The Omnès function then represents the exact resummation of elastic two-body rescattering to all orders. For instance, the pion vector  $F_\pi^V(s)$  as extracted from  $\tau^- \rightarrow \pi^- \pi^0 \nu_\tau$  decays [18] can be described very well up to  $\sqrt{s} = 1 \text{ GeV}$  by Eq. (1.136) with a linear polynomial  $R(s) = 1 + \alpha_V s$ . At higher energies, the nonlinear effects of higher, inelastic ( $\rho'$ ,  $\rho''$ ) resonances become important [233]. For the pion vector form factor measured in  $e^+e^- \rightarrow \pi^+\pi^-$  [21, 53, 54, 57–59], the isospin-violating mixing effect with the  $\omega$ -meson needs to be taken into account [234]. More refined representations parameterizing inelastic effects beyond roughly 1 GeV have employed conformal polynomials instead, which also allows for better high-energy asymptotic behavior of the form factor [235–237]. Eqs. (1.132) and (1.136) have also been generalized and employed frequently to describe coupled channels, e.g.,  $\pi\pi \leftrightarrow \bar{K}K$  scalar form factors [238–245], by promoting the Omnès function to a matrix with a coupled-channel  $T$ -matrix as input. Nevertheless, the coupled-channels description does not permit a compact closed form as in Eq. (1.136).

In order to describe more complicated amplitudes such as four-point functions, a more complex unitarity relation needs to be considered due to the presence of left-hand cuts.

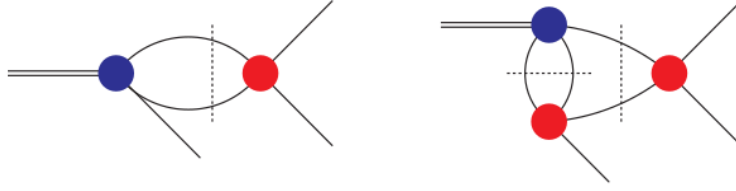


Figure 1.5: Illustrative representation of the inhomogeneous unitarity relation in Eq. (1.137): the homogeneous term similar to a form factor unitarity relation (left), plus the projection of a typical diagram representing crossed-channel dynamics (right), giving rise to the inhomogeneous Omnès problem. The double line renders a heavy particle with its three-body decay partial wave represented by the blue dot, the single lines illustrate the three outgoing decay products that rescatter elastically (red dots). Reprinted from Ref. [10].

These are a consequence of crossing symmetry and unitarity in the crossed channel: for example, the pion-pion scattering amplitude possesses not only a cut in the  $s$ -channel for  $s > 4m_\pi^2$ , but also for  $t, u \geq 4m_\pi^2$ . Therefore, after projection onto  $s$ -channel partial waves, the crossed-channel unitarity cuts translate into another discontinuity on the negative axis for  $s \leq 0$ . Separating right- and left-hand cuts into individual functions  $f_J^I(s)$  and  $\hat{f}_J^I(s)$  of ( $s$ -channel) isospin  $I$  and angular momentum  $J$ , the unitarity condition in Eq. (1.132) yields

$$\text{Im} f_J^I(s) = \sin \delta_J^I(s) e^{-i\delta_J^I(s)} \left( f_J^I(s) + \hat{f}_J^I(s) \right) \theta(s - 4m_\pi^2), \quad (1.137)$$

where the *inhomogeneity*,

$$\hat{f}_J^I(s) = \sum_{n, I', J'} \int_{-1}^{+1} d \cos \theta \cos^n \theta c_n^{II'JJ'} f_{J'}^{I'}(t(s, \cos \theta)), \quad (1.138)$$

is then a consequence of the singularities in the  $t$ - and  $u$ -channels, and ensues from their projection onto the  $s$ -channel partial wave. Here,  $c_n^{II'JJ'}$  are process-dependent coefficients and  $t(s, \cos \theta)$  is the appropriate crossed-channel Mandelstam variable as a function of the energy squared  $s$  and scattering angle  $\theta$ . Fig. 1.5 shows the two terms on the right-hand side of Eq. (1.137), which represents the inhomogeneous Omnès problem.

Given that both  $f_J^I(s)$  and the Omnès function  $\Omega_J^I(s)$  are analytic on the whole complex plane except on the real axis when  $s > s_{\text{th}}$ ,  $g_J^I(s) = f_J^I(s)/\Omega_J^I(s)$  has the same analytic properties. The imaginary part of  $g_J^I(s)$  on the upper rim of the cut can be computed:

$$\begin{aligned}
\text{Im}g_J^I(s) &= \frac{\text{Im}f_J^I(s)\text{Re}\Omega_J^I(s) - \text{Re}f_J^I(s)\text{Im}\Omega_J^I(s)}{|\Omega_J^I(s)|^2} = \frac{\text{Im}f_J^I(s)\Omega_J^I(s) - f_J^I(s)\text{Im}\Omega_J^I(s)}{|\Omega_J^I(s)|^2} \\
&= \frac{\left(f_J^I(s) + \hat{f}_J^I(s)\right) e^{-i\delta_J^I(s)} \sin \delta_J^I(s) \Omega_J^I(s) - f_J^I(s) \Omega_J^I(s) e^{-i\delta_J^I(s)} \sin \delta_J^I(s)}{|\Omega_J^I(s)|^2} \quad (1.139) \\
&= \frac{\hat{f}_J^I(s) \sin \delta_J^I(s)}{|\Omega_J^I(s)|}.
\end{aligned}$$

Thus, the solution of the inhomogeneous Omnès problem is given by the  $n$ -times subtracted dispersion relation for  $g_J^I(s)$  solved for  $f_J^I(s)$ ,

$$f_J^I(s) = \Omega_J^I(s) \left( P_n(s - s_0) + \frac{(s - s_0)^n}{\pi} \int_{s_{\text{th}}}^{\infty} ds' \frac{\hat{f}_J^I(s) \sin \delta_J^I(s)}{|\Omega_J^I(s)| (s' - s_0)^n (s' - s - i\epsilon)} \right). \quad (1.140)$$

The inhomogeneous Omnès problem provides a possible dispersion-theoretical description of three-body decays in the form of Khuri-Treiman equations <sup>3</sup> [246, 247].

---

<sup>3</sup>A detailed description for the  $\eta \rightarrow 3\pi$  decay can be found in Ref. [10].

# Chapter 2

## Tau physics

### 2.1 Introduction

The  $\tau$  lepton was discovered in 1975 by Martin Lewis Perl [248] at the Stanford Positron Electron Asymmetric Rings (SPEAR) in SLAC, although it was anticipated previously by Yung-su Tsai [249]. Since then, it has been a subject of extensive experimental analyses. The tau lepton belongs to the third generation and decays into particles belonging to the first and second generations (except to the charm quark). These leptons are excellent probes to perform SM precision tests and look up New Physics. The structure of the Electroweak gauge sector has been successfully measured at the level of 0.1 to 1%, corroborating the SM. Moreover, the hadronic  $\tau$  decays turn out to be a unique laboratory to investigate the strong interaction at low energy, since the *tau* is the only massive enough lepton that can decay into hadrons. Tau decay data is especially useful to obtain a precise determination of the QCD coupling, the mixing matrix CKM element  $|V_{us}|$ , and the strange quark mass.

Leptonic tau decays have been measured with an astonishing precision. This allows to study the effects produced by additional non-standard interactions to the SM through extensions in the effective theory that include the coupling with both spinless and tensor sources. In Chapters 3 and 4, we scrutinize the  $\tau^- \rightarrow \pi^- \pi^0 \nu_\tau$  and  $\tau^- \rightarrow K^- \eta^{(\prime)} \nu_\tau$  decays, respectively, in a similar way to the analyses in Refs. [250, 251] for the  $\pi \eta^{(\prime)}$  and  $(K\pi)^-$  decay

modes. Subsequently, in Chapter 5, we perform a global analysis of strangeness-conserving and -changing exclusive hadronic tau decays into one and two pseudoscalar mesons. But before that, in this chapter, we will review some well-known facts about (semi-)leptonic tau decays.

## 2.2 Lepton decays

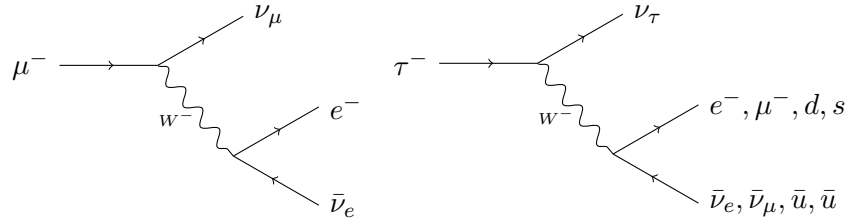


Figure 2.1: Feynman diagrams for  $\mu^- \rightarrow e^- \bar{\nu}_e \nu_\mu$  and  $\tau^- \rightarrow X^- \nu_\tau$  ( $X^- = e^- \bar{\nu}_e, \mu^- \bar{\nu}_\mu, d\bar{u}, s\bar{u}$ ).

The decays of the charged leptons,  $\mu^\pm$  and  $\tau^\pm$ , stem through the  $W$ -exchange diagrams in Fig. 2.1, with the SM Lagrangian for charged-current interactions given by:

$$\mathcal{L}_{cc} = -\frac{g}{2\sqrt{2}} W_\mu^\dagger \left\{ \sum_\ell \bar{\nu}_\ell \gamma^\mu (1 - \gamma^5) \ell + \bar{u} \gamma^\mu (1 - \gamma^5) (V_{ud} d + V_{us} s) \right\} + h.c. \quad (2.1)$$

The momentum transfer bore by the intermediate  $W^\pm$  is very small compared to  $M_W$ . For that reason, the  $W$ -propagator shrinks to a point and can be well approximated through a local four-fermion interaction governed by the Fermi coupling constant  $\frac{G_F}{\sqrt{2}} = \frac{g^2}{8M_W^2}$ . The leptonic decay width can be written as:

$$\Gamma_{\ell \rightarrow \ell'} \equiv \Gamma[\ell^- \rightarrow \ell' \bar{\nu}_{\ell'} \nu_\ell] = \frac{G_{\ell'\ell}^2 m_\ell^5}{192\pi^3} f\left(\frac{m_{\ell'}^2}{m_\ell^2}\right) \left(1 + \delta_{RC}^{\ell'\ell}\right), \quad (2.2)$$

where  $f(x) = 1 - 8x + 8x^3 - x^4 - 12x^2 \log x$ , and [252–262]

$$\delta_{RC}^{\ell'\ell} = \frac{\alpha}{2\pi} \left[ \frac{25}{4} - \pi^2 + \mathcal{O}\left(\frac{m_{\ell'}^2}{m_\ell^2}\right) \right] + \dots \quad (2.3)$$

which take into account radiative QED corrections up to  $\mathcal{O}(\alpha^2)$ . Here,  $\delta_{RC}^{\ell\ell}$  includes inclusively additional photons or lepton pairs. Higher-order electroweak corrections and the non-local structure of the  $W$  propagator, are incorporated into the effective coupling [263,264]

$$G_{\ell\ell}^2 = \left[ \frac{g^2}{4\sqrt{2}M_W^2} (1 + \Delta r) \right]^2 \left[ 1 + \frac{3}{5} \frac{m_\ell^2}{M_W^2} + \frac{9}{5} \frac{m_{\ell'}^2}{M_W^2} + \mathcal{O}\left(\frac{m_{\ell'}^4}{M_W^2 m_\ell^2}\right) \right], \quad (2.4)$$

so that  $G_{e\mu}$  coincides with the Fermi coupling defined in the  $V - A$  theory. Here,  $g$  is the  $SU(2)_L$  gauge coupling constant and  $\Delta r$  is the electroweak correction introduced by Sirlin in Ref. [265].

The Fermi coupling is defined by the muon lifetime, given that  $\tau_\mu^{-1} = \Gamma[\mu^- \rightarrow e^- \bar{\nu}_e \nu_\mu(\gamma)]$ . The MuLan collaboration has achieved a precision of 1.0 parts per million in the measurement of  $\tau_\mu$  [266], which is 15 times more precise than any previous experiment. It is the most accurate particle lifetime ever measured and, in consequence, the world averaged,  $\tau_\mu = 2.1969811(22) \cdot 10^{-6} s$  [3], is dominated by this measurement. In addition to the electron and muon masses,  $m_e = 0.5109989461(31) \text{ MeV}$  and  $m_\mu = 105.6583745(24) \text{ MeV}$  [3], it implies

$$G_F \equiv G_{e\mu} = (1.1663787 \pm 0.0000006) \cdot 10^{-5} \text{ GeV}^{-2}. \quad (2.5)$$

Thanks to its much heavier mass, the  $\tau$  lepton has various final states which are kinematically allowed i.e.  $\tau^- \rightarrow e^- \bar{\nu}_e \nu_\tau$ ,  $\tau^- \rightarrow \mu^- \bar{\nu}_\mu \nu_\tau$ ,  $\tau^- \rightarrow d\bar{u} \nu_\tau$  and  $\tau^- \rightarrow s\bar{u} \nu_\tau$ . The universality of the  $W$  couplings predicted by the SM implies that all these decay modes have equal amplitudes (when final fermion masses and QCD interactions are neglected), with an additional  $N_C |V_{uD}|$  factor ( $D = d, s$ ) for the semileptonic channels<sup>1</sup>. Regarding the unitarity of the quark mixing matrix,  $|V_{ud}|^2 + |V_{us}|^2 = 1 - |V_{ub}|^2 \approx 1$ , the lowest-order estimation for the  $\tau$  lifetime is given by

$$\tau_\tau \equiv \frac{1}{\Gamma(\tau)} \approx \left\{ \Gamma(\mu) \left( \frac{m_\tau}{m_\mu} \right)^5 [2 + N_C (|V_{ud}|^2 + |V_{us}|^2)] \right\}^{-1} \approx \frac{1}{5} \tau_\mu \left( \frac{m_\mu}{m_\tau} \right)^5 = 3.3 \cdot 10^{-13} \text{ s}, \quad (2.6)$$

while their branching fractions are expected to be approximately ( $\ell = e, \mu$ )

---

<sup>1</sup> $N_C$  refers to the number of colors.

$$\mathcal{B}_\ell \equiv \text{Br}(\tau^- \rightarrow \ell^- \bar{\nu}_\ell \nu_\tau) \simeq \frac{1}{5} = 20\%, \quad \frac{\Gamma(\tau^- \rightarrow \nu_\tau + \text{hadrons})}{\Gamma(\tau^- \rightarrow \nu_\tau e^- \bar{\nu}_e)} \simeq N_C = 3. \quad (2.7)$$

We can see the agreement between theory and experiment in Table 2.1, which provides strong evidence for the color degree of freedom. An additional enhancement of about 20% in the hadronic  $\tau$  decay width is due to the missing QCD corrections ( $\sim \mathcal{O}(\frac{\alpha_S}{\pi})$ ) which are responsible for the numerical differences.

$m_\tau$	$(1776.86 \pm 0.12) \text{ MeV}$
$\tau_\tau$	$(290.3 \pm 0.5) \cdot 10^{-15} \text{ s}$
$\text{Br}(\tau^- \rightarrow e^- \bar{\nu}_e \nu_\tau)$	$(17.82 \pm 0.04)\%$
$\text{Br}(\tau^- \rightarrow \mu^- \bar{\nu}_\mu \nu_\tau)$	$(17.39 \pm 0.04)\%$
$\mathcal{B}_\mu/\mathcal{B}_e$	$0.9762 \pm 0.0028$
$\text{Br}(\tau^- \rightarrow \pi^- \nu_\tau)$	$(10.82 \pm 0.05)\%$
$\text{Br}(\tau^- \rightarrow K^- \nu_\tau)$	$(6.96 \pm 0.1) \cdot 10^{-3}$

Table 2.1: Average values of some tau parameters [3].

Using the measured value of  $G_F$  in  $\mu$  decays, final fermion masses and taking into account higher-order corrections, a precise relation between the  $\tau$  lifetime and the leptonic branching ratios is provided by Eq. (2.2)

$$\mathcal{B}_e = \frac{\mathcal{B}_\mu}{0.972564 \pm 0.000004} = \frac{\tau_\tau}{(1632.6 \pm 0.6) \cdot 10^{-15} \text{ s}}. \quad (2.8)$$

The error in the previous expression is dominated by the uncertainty of  $m_\tau$ , which highlights its sensitivity to the value of the  $\tau$  mass.

The predicted value of  $\mathcal{B}_\mu/\mathcal{B}_e$  is in fair agreement with the measured ratio in Table 2.1 ( $1.3\sigma$ )<sup>2</sup>. In Fig. 2.2 we can see that the relation between  $\mathcal{B}_e$  and  $\tau_\tau$  is well satisfied by the current data.

Taking into account the relation in Eq. (2.8), the values of  $\mathcal{B}_e$ ,  $\mathcal{B}_\mu$  and  $\tau_\tau$  can be combined to determine the electronic branching ratios within the SM, i.e., assuming lepton universality (LU):

<sup>2</sup>The precise BaBar measurement,  $\mathcal{B}_\mu/\mathcal{B}_e = 0.9725 \pm 0.0039$  [267], is responsible for this small difference, which is  $1.8\sigma$  away from the theoretical prediction. Before this data, the previous world-average was in perfect agreement with the SM value.



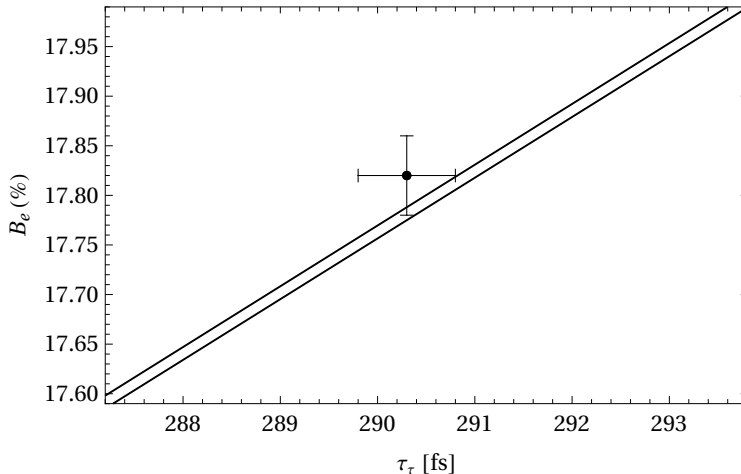


Figure 2.2: Relation between  $\mathcal{B}_e$  and  $\tau_\tau$ . The diagonal band corresponds to Eq. (2.8).

$$\mathcal{B}_e^{uni} = (17.817 \pm 0.023)\%. \quad (2.9)$$

The leptonic branching fractions and the lifetime of the tau are known with a precision of 0.2%. The precise Belle measurement,  $\tau_\tau = (290.17 \pm 0.53 \pm 0.33) \cdot 10^{-15} \text{ s}$  [268], dominates the world-average  $\tau_\tau = (290.3 \pm 0.5) \cdot 10^{-15} \text{ s}$  [3].

The  $\tau$  mass is only known at the  $10^{-4}$  level. Making an energy scan of  $\sigma(e^+e^- \rightarrow \tau^+\tau^-)$  around the  $\tau^+\tau^-$  production threshold [269–271], the BES-III collaboration found  $m_\tau = 1776.91 \pm 0.12_{-0.13}^{+0.10} \text{ MeV}$  [272] with an accuracy of 0.1 MeV. Recently the Belle II collaboration released their first measurements of the mass of the  $\tau$  lepton using the pseudomass method in a blinded analysis procedure,  $m_\tau = 1777.28 \pm 0.75 \pm 0.33$  [273], which is in good agreement with the present world-average [3].

## 2.3 Lepton universality

In the SM all left-handed leptons are accommodated in  $SU(2)_L$  doublets with identical couplings to the  $W$  boson, i.e.,  $g_e = g_\mu = g_\tau \equiv g$ . Comparing the measurements of (semi)leptonic decay widths which only differ in the lepton flavor, it is possible to test experimentally this statement. The  $\mathcal{B}_\mu/\mathcal{B}_e$  ratio constrains  $|g_\mu/g_e|$ , while  $\mathcal{B}_e/\tau_\tau$  provides information on  $|g_\tau/g_\mu|$ .

The results are summarized in Table 2.2, together with the constraints obtained from  $\pi$ ,  $K$  and  $W$  decays.

	$\Gamma_{\tau \rightarrow \mu} / \Gamma_{\tau \rightarrow e}$	$\Gamma_{\pi \rightarrow \mu} / \Gamma_{\pi \rightarrow e}$	$\Gamma_{K \rightarrow \mu} / \Gamma_{K \rightarrow e}$	$\Gamma_{K \rightarrow \pi \mu} / \Gamma_{K \rightarrow \pi e}$	$\Gamma_{W \rightarrow \mu} / \Gamma_{W \rightarrow e}$
$ g_\mu / g_e $	1.0018(14)	1.0021(16)	0.9978(20)	1.0010(25)	0.996(10)
	$\Gamma_{\tau \rightarrow e} / \Gamma_{\mu \rightarrow e}$	$\Gamma_{\tau \rightarrow \pi} / \Gamma_{\pi \rightarrow \mu}$	$\Gamma_{\tau \rightarrow K} / \Gamma_{K \rightarrow \mu}$	$\Gamma_{W \rightarrow \tau} / \Gamma_{K \rightarrow \pi e}$	
$ g_\tau / g_\mu $	1.0011(15)	0.9962(27)	0.9858(70)	1.034(13)	
	$\Gamma_{\tau \rightarrow \mu} / \Gamma_{\mu \rightarrow e}$	$\Gamma_{W \rightarrow \tau} / \Gamma_{W \rightarrow e}$			
$ g_\tau / g_e $	1.0030(15)	1.031(13)			

Table 2.2: Experimental determinations of the ratios  $g_\ell / g_{\ell'}$  [4].

The  $\tau$  determination of  $|g_\mu / g_e|$  is as precise ( $\sim 15\%$ ) as the one obtained from  $\pi_{\ell 2}$  decays and comparable accuracies have been reached with  $K_{\ell 2}$  and  $K_{\ell 3}$ . The ratios

$$R_{P \rightarrow e/\mu} \equiv \frac{\Gamma[P^- \rightarrow e^- \bar{\nu}_e(\gamma)]}{\Gamma[P^- \rightarrow \mu^- \bar{\nu}_\mu(\gamma)]} = \left| \frac{g_e}{g_\mu} \right|^2 \frac{m_e^2}{m_\mu^2} \left( \frac{1 - m_e^2/m_P^2}{1 - m_\mu^2/m_P^2} \right)^2 (1 + \delta R_{P \rightarrow e/\mu}), \quad P = \pi, K, \quad (2.10)$$

have been calculated and measured with high accuracy. Because of the  $V - A$  structure of the charged currents in the SM, the leptonic decay rate of a pseudoscalar meson is helicity suppressed, which makes these ratios excellent probes of new-physics interactions. The radiative corrections  $\delta R_{P \rightarrow e/\mu}$  involve a summation of leading QED logarithms  $\alpha^n \log^n(m_\mu/m_e)$  [274, 275] and a systematic two-loop calculation of  $\mathcal{O}(e^2 p^4)$  effects within Chiral Perturbation Theory [193, 194]. Comparing the SM predictions [276, 277]

$$R_{\pi \rightarrow e/\mu}^{SM} = (1.2352 \pm 0.0001) \cdot 10^{-4}, \quad R_{K \rightarrow e/\mu}^{SM} = (2.477 \pm 0.001) \cdot 10^{-5}, \quad (2.11)$$

and the experimental  $R_{\pi \rightarrow e/\mu}$  [278–283] and  $R_{K \rightarrow e/\mu}$  ratios [284–289],

$$R_{\pi \rightarrow e/\mu} = (1.2327 \pm 0.0023) \cdot 10^{-4}, \quad R_{K \rightarrow e/\mu} = (2.488 \pm 0.009) \cdot 10^{-5}, \quad (2.12)$$

we can see a good agreement between them,  $\sim 1.1 \sigma$  for  $R_{\pi \rightarrow e/\mu}$  and  $\sim 1.2 \sigma$  for  $R_{K \rightarrow e/\mu}$ <sup>3</sup>.

<sup>3</sup>The results quoted in Table 2.2 were obtained using a previous estimation of  $R_{\pi \rightarrow e/\mu}$ ,  $R_{\pi \rightarrow e/\mu} = (1.230 \pm 0.004) \cdot 10^{-4}$ .

The decay modes  $\tau^- \rightarrow \pi^- \nu_\tau$  and  $\tau^- \rightarrow K^- \nu_\tau$  can be used to test universality through the ratios

$$R_{\tau/P} \equiv \frac{\Gamma[\tau^- \rightarrow P^- \nu_\tau]}{\Gamma[P^- \rightarrow \mu^- \bar{\nu}_\tau]} = \left| \frac{g_\tau}{g_\mu} \right|^2 \frac{m_\tau^3}{2m_P m_\mu^2} \left( \frac{1 - m_P^2/m_\tau^2}{1 - m_\mu^2/m_P^2} \right)^2 (1 + \delta R_{\tau/P}), \quad (2.13)$$

where a rough estimate of the size of the relative corrections was given in [274, 290–292]:

$$\delta R_{\tau/\pi} = (0.16 \pm 0.14)\%, \quad \delta R_{\tau/K} = (0.90 \pm 0.22). \quad (2.14)$$

The outcome for the  $|g_\tau/g_\mu|$  ratios in Table 2.2 was obtained using these numbers. A recent improved evaluation of  $\delta R_{\tau/P}$  [293, 294] yields  $\delta R_{\tau/\pi} = (0.18 \pm 0.57)\%$  and  $\delta R_{\tau/K} = (0.97 \pm 0.58)\%$  which imply  $|g_\tau/g_\mu|_\pi = 0.9964 \pm 0.0038$  and  $|g_\tau/g_\mu|_K = 0.9857 \pm 0.0078$ , compatible with LU at  $0.9\sigma$  and  $1.8\sigma$ , respectively.

## 2.4 Lorentz structure of the charged current

Thanks to the high statistics, the leptonic decays  $\ell^- \rightarrow \ell'^- \bar{\nu}_{\ell'} \nu_\ell$  allow us to study the Lorentz structure of the decay amplitudes through the analysis of the energy and angular distribution of the final charged lepton, which can be complemented with polarization information when available.

The most general, local, derivative-free, lepton-number conserving, four-lepton interaction Hamiltonian, which is consistent with locality and Lorentz invariance [295–302],

$$\mathcal{H} = 4 \frac{G_{\ell\ell}}{\sqrt{2}} \sum_{n,\epsilon,\omega} g_{\epsilon\omega}^n \left[ \bar{\ell} \Gamma^n (\nu_{\ell'})_\sigma \right] \left[ (\bar{\nu}_\ell)_\lambda \Gamma_n \ell_\omega \right], \quad (2.15)$$

contains ten complex coupling constants, and since a common phase is arbitrary, there are nineteen independent real parameters which could be different for each leptonic decay. The chiralities of the corresponding fermions are labeled by the subindices  $\epsilon, \omega, \sigma, \lambda$ , and  $n = S, V, T$  corresponds to the type of interaction, i.e., scalar ( $\Gamma^S = \mathcal{I}$ ), vector ( $\Gamma^V = \gamma^\mu$ ), and tensor ( $\Gamma^T = \sigma^{\mu\nu}/\sqrt{2}$ ). The chiralities of neutrinos are uniquely determined once  $n, \epsilon, \omega$  are given. By factoring out  $G_{\ell\ell}$  the coupling constants  $g_{\epsilon\omega}^n$  are normalized to [300]

$$1 = \frac{1}{4} \left( |g_{RR}^S|^2 + |g_{RL}^S|^2 + |g_{LR}^S|^2 + |g_{LL}^S|^2 \right) + 3 \left( |g_{RL}^T|^2 + |g_{LR}^T|^2 \right) + \left( |g_{RR}^V|^2 + |g_{RL}^V|^2 + |g_{LR}^V|^2 + |g_{LL}^V|^2 \right). \quad (2.16)$$

Hence,  $|g_{\epsilon\omega}^S| \leq 2$ ,  $|g_{\epsilon\omega}^V| \leq 1$ , and  $|g_{\epsilon\omega}^T| \leq 1/\sqrt{3}$ . The probabilities for the decay of an  $\omega$ -handed  $\ell^-$  into an  $\epsilon$ -handed daughter lepton is given by [300]

$$Q_{\epsilon\omega} = \frac{1}{4} |g_{\epsilon\omega}^S|^2 + |g_{\epsilon\omega}^V|^2 + 3(1 - \delta_{\epsilon\omega}) |g_{\epsilon\omega}^T|^2. \quad (2.17)$$

In the SM,  $|g_{LL}^V|^2 = 1$  and all other vanish,  $|g_{\epsilon\omega}^n|^2 = 0$ .

Given an initial lepton with polarization  $\mathcal{P}_\ell$ , the final charged-lepton distribution in the decaying-lepton rest frame is usually parameterized as [296–298]

$$\frac{d^2\Gamma_{\ell \rightarrow \ell'}}{dx d\cos\theta} = \frac{m_\ell \omega^4}{2\pi^3} G_{\ell'\ell}^2 \sqrt{x^2 - x_0^2} \left\{ F(x) - \frac{1}{3} \xi \mathcal{P}_\ell \sqrt{x^2 - x_0^2} \cos\theta A(x) \right\}, \quad (2.18)$$

where  $\theta$  is the angle between the  $\ell^-$  spin and the final charged-lepton momentum,  $\omega \equiv (m_{\ell'}^2 + m_\ell^2)/2m_\ell$  is the maximum  $\ell'^-$  energy for massless neutrinos,  $x \equiv E_{\ell'}/\omega$  is the reduced energy,  $x_0 \equiv m_{\ell'}/\omega$  and

$$F(x) = x(1-x) + \frac{2}{9} \rho (4x^2 - 3x - x_0^2) + \eta x_0 (1-x), \quad (2.19a)$$

$$A(x) = 1 - x + \frac{2}{3} \delta \left( 4x - 4 + \sqrt{1 - x_0^2} \right). \quad (2.19b)$$

For an unpolarized lepton  $\ell$ , the distribution is described by the so-called Michel [295] parameters  $\rho$  and  $\eta$ . When the initial lepton polarization is known, we have two additional parameters,  $\xi$  and  $\delta$ . If the polarization of the final charged-lepton is also known, 5 additional independent parameters ( $\xi', \xi'', \eta'', \alpha', \beta'$ ) appear [3]. In the SM,  $\rho = \delta = 3/4$ ,  $\eta = \eta'' = \alpha' = \beta' = 0$  and  $\xi = \xi' = \xi'' = 1$ .

The total decay rate for massless neutrinos can be written as [302]

$$\Gamma_{\ell \rightarrow \ell'} = \frac{\hat{G}_{\ell'\ell}^2 m_\ell^5}{192\pi^3} f \left( m_{\ell'}/m_\ell \right) \left( 1 + \delta_{RC}^{\ell'\ell} \right), \quad (2.20)$$

where

$$\hat{G}_{\ell\ell} \equiv G_{\ell\ell} \sqrt{1 + 4\eta \frac{m_{\ell'}}{m_{\ell}} \frac{g(m_{\ell'}^2/m_{\ell}^2)}{f(m_{\ell'}^2/m_{\ell}^2)}}, \quad (2.21)$$

$g(z) = 1 + 9z - 9z^2 - z^3 + 6z(1+z) \log z$ , and the radiative corrections  $\delta_{RC}^{\ell\ell}$  in the SM have been included. Assuming that the SM produces the dominant contribution to the decay rate, any additional higher-order correction beyond the Hamiltonian in Eq. (2.15) would be a subleading effect.

The Fermi coupling  $G_F$ , which is measured in  $\mu$  decay, corresponds to the normalization  $G_{e\mu}$ . The ratios defined previously,  $\mathcal{B}_{\mu}/\mathcal{B}_e$  and  $\mathcal{B}_e \tau_{\mu}/\tau_{\tau}$ , that allow us to test lepton universality, also probe the ratios  $\hat{G}_{\mu\tau}/\hat{G}_{e\tau}$  and  $\hat{G}_{e\tau}/\hat{G}_{e\mu}$ , respectively. According to Eq. (2.21) the experimental determination of  $G_{e\mu}$  is sensitive to the uncertainty in  $\eta_{\mu \rightarrow e}$ .

In terms of the  $g_{e\omega}^n$  couplings, the parameters in Eqs. (2.18) and (2.19) are:

$$\rho = \frac{3}{4}(\beta^+ + \beta^-) + (\gamma^+ + \gamma^-), \quad (2.22a)$$

$$\xi = 3(\alpha^- - \alpha^+) + (\beta^- - \beta^+) + \frac{7}{3}(\gamma^+ - \gamma^-), \quad (2.22b)$$

$$\xi\delta = \frac{3}{4}(\beta^- - \beta^+) + (\gamma^+ - \gamma^-), \quad (2.22c)$$

$$\eta = \frac{1}{2} \text{Re} \left[ g_{LL}^V g_{RR}^{S*} + g_{RR}^V g_{LL}^{S*} + g_{LR}^V (g_{RL}^{S*} + 6g_{RL}^{T*}) + g_{RL}^V (g_{LR}^{S*} + 6g_{LR}^{T*}) \right], \quad (2.22d)$$

where [303]

$$\alpha^+ \equiv |g_{RL}^V|^2 + \frac{1}{16}|g_{RL}^S + 6g_{RL}^T|^2, \quad \alpha^- \equiv |g_{LR}^V|^2 + \frac{1}{16}|g_{LR}^S + 6g_{LR}^T|^2, \quad (2.23a)$$

$$\beta^+ \equiv |g_{RR}^V|^2 + \frac{1}{4}|g_{RR}^S|^2, \quad \beta^- \equiv |g_{LL}^V|^2 + \frac{1}{4}|g_{LL}^S|^2, \quad (2.23b)$$

$$\gamma^+ \equiv \frac{3}{16}|g_{RL}^S - 2g_{RL}^T|^2, \quad \gamma^- \equiv \frac{3}{16}|g_{LR}^S - 2g_{LR}^T|^2, \quad (2.23c)$$

are positive-definite combinations of decay constants, that correspond to a final right-handed ( $\alpha^+, \beta^+, \gamma^+$ ) or left-handed ( $\alpha^-, \beta^-, \gamma^-$ ) lepton. The normalization in Eq. (2.16) can be written as  $\alpha^+ + \alpha^- + \beta^+ + \beta^- + \gamma^+ + \gamma^- = 1$ . In terms of these parameters, the

probabilities  $Q_{\epsilon\omega}$  are:

$$Q_{LL} = \beta^- = \frac{1}{4} \left( -3 + \frac{16}{3}\rho - \frac{1}{3}\xi + \frac{16}{9}\xi\delta + \xi' + \xi'' \right), \quad (2.24a)$$

$$Q_{RR} = \beta^+ = \frac{1}{4} \left( -3 + \frac{16}{3}\rho + \frac{1}{3}\xi - \frac{16}{9}\xi\delta - \xi' + \xi'' \right), \quad (2.24b)$$

$$Q_{LR} = \alpha^- + \gamma^- = \frac{1}{4} \left( 5 - \frac{16}{3}\rho + \frac{1}{3}\xi - \frac{16}{9}\xi\delta + \xi' - \xi'' \right), \quad (2.24c)$$

$$Q_{LR} = \alpha^+ + \gamma^+ = \frac{1}{4} \left( 5 - \frac{16}{3}\rho - \frac{1}{3}\xi + \frac{16}{9}\xi\delta - \xi' - \xi'' \right). \quad (2.24d)$$

Upper bounds on any of these probabilities translate into corresponding limits for all couplings with the given chiralities. The following relations are particularly useful:

$$Q_{\ell_R} \equiv Q_{RR} + Q_{LR} = \frac{1}{2} \left( 1 + \frac{1}{3}\xi - \frac{16}{3}\xi\delta \right), \quad (2.25a)$$

$$Q_{\ell'_R} \equiv Q_{RR} + Q_{RL} = \frac{1}{2} (1 - \xi'). \quad (2.25b)$$

Thus, the total probability for the decay of an initial right-handed lepton is characterized by  $\xi$  and  $\xi\delta$ , while a single polarization parameter fixes the probability to decay into a final right-handed lepton. Other convenient positive-definite quantities are:

$$\frac{3}{2}\beta^+ + 2\gamma^- = \rho - \xi\delta, \quad (2.26a)$$

$$Q_{LR} + Q_{RL} = \frac{1}{2} \left( 5 - \frac{16}{3}\rho - \xi'' \right). \quad (2.26b)$$

The first one supplies direct bounds on  $|g_{RR}^V|$ ,  $|g_{RR}^S|$  and  $|g_{LR}^S - 2g_{LR}^T|$ , and shows that  $\rho \geq \xi\delta$ . A precise measurement of the polarization parameter  $\xi''$  would imply upper limits on all couplings  $g_{\epsilon\omega}^n$  with  $\epsilon \neq \omega$  through the second identity.

In the case of  $\mu$  decay, where a precise measurement of the  $\mu$  and  $e$  polarizations exist, there are upper bounds [300] on  $Q_{RR}$ ,  $Q_{LR}$  and  $Q_{RL}$ , and a lower limit on  $Q_{LL}$ , which can be translated to upper bounds on the 8 couplings  $|g_{RR}^n|$ ,  $|g_{LR}^n|$  and  $|g_{RL}^n|$ . The  $\mu$  and  $e$  measurements do not permit to determine  $|g_{LL}^S|$  and  $|g_{LL}^V|$  separately [300, 304]. However, a lower limit on  $|g_{LL}^V|$  is obtained in the inverse muon decay since  $\sigma(\nu_\mu e^- \rightarrow \mu^- \nu_e) \propto |g_{LL}^V|^2$  [300]. Since the  $\nu_\mu$  helicity in pion decay is experimentally well known [305, 306],

$|2h_{\nu_\mu} + 1| < 0.0041$  (90% C.L.) [307], the  $|g_{LL}^S|$  contribution to  $\sigma(\nu_\mu e^- \rightarrow \mu^- \nu_e)$  is negligible; the  $\mu$ -decay constraints suppress the contributions from other  $g_{e\omega}^n$  couplings [308]. Setting a lower bound on  $|g_{LL}^V|$ , the relation  $Q_{LL}$  gives the upper limit  $|g_{LL}^S|^2 < 4(1 - |g_{LL}^V|^2)$ . In Table 2.3 the present 90% C.L. bounds on the  $\mu$ -decay couplings [309–314] are summarized. All these bounds show nicely that the  $\mu$ -decay transition amplitude is indeed of the predicted  $V - A$  type.

$ g_{RR}^S  < 0.035$	$ g_{LR}^S  < 0.050$	$ g_{RL}^S  < 0.412$	$ g_{LL}^S  < 0.550$
$ g_{RR}^V  < 0.017$	$ g_{LR}^V  < 0.023$	$ g_{RL}^V  < 0.104$	$ g_{LL}^V  > 0.960$
$ g_{RR}^T  \equiv 0$	$ g_{LR}^T  < 0.015$	$ g_{RL}^T  < 0.103$	$ g_{LL}^T  \equiv 0$
$ g_{LR}^S + 6g_{LR}^T  < 0.143$	$ g_{LR}^S + 2g_{LR}^T  < 0.108$	$ g_{LR}^S - 2g_{LR}^T  < 0.070$	
$ g_{RL}^S + 6g_{RL}^T  < 0.418$	$ g_{RL}^S + 2g_{RL}^T  < 0.417$	$ g_{RL}^S - 2g_{RL}^T  < 0.418$	
$Q_{RR} + Q_{LR} < 8.2 \cdot 10^{-4}$			

Table 2.3: Experimental bounds at 90% C.L. for the leptonic  $\mu$ -decay couplings [3].

Since the  $\tau$  lifetime is shorter, the experimental determination of the  $\tau$  decay parameters must be different from the muon one. The measurements of the  $\tau$  polarization and the parameters  $\xi$  and  $\delta$  are still possible because the spins of the  $\tau^+ \tau^-$  pair produced in  $e^+ e^-$  annihilation are strongly correlated [249, 315–325]. The use of beam polarization was employed by the SLD Collaboration [326]. Nevertheless, the polarization of the final charged lepton in the  $\tau$  decay has never been measured. For instance, this could be done by stopping the muons and detecting their decay products of the  $\tau^- \rightarrow \mu^- \bar{\nu}_\mu \nu_\tau$  decay [322]. Another possibility is to use radiative decays,  $\tau^- \rightarrow \ell^- \bar{\nu}_\ell \nu_\tau \gamma$  ( $\ell = e, \mu$ ) [327], since the distribution of the photons emitted by the daughter lepton is sensitive to the lepton polarization. Although the measurement of the inverse decay would be very helpful, this is far from reach. There are also interesting prospects from the five-lepton tau decay,  $\tau \rightarrow \ell \ell' \ell^{(\prime)} \nu_\tau \bar{\nu}_{\ell^{(\prime)}}$ , which shows a big sensitivity to new physics in one of its Michel parameters [328] (Denis Epifanov, private communication).

In Table 2.4 we can see the experimental status on the  $\tau$ -decay Michel parameters [326, 329–343] together with the more accurate values measured in  $\mu$  decay [3, 309–311, 344–350].

The 95% C.L. bounds on the  $\tau$ -decay couplings are shown in Table 2.5.

	$\mu^- \rightarrow e^- \bar{\nu}_e \nu_\mu$	$\tau^- \rightarrow \mu^- \bar{\nu}_\mu \nu_\tau$	$\tau^- \rightarrow e^- \bar{\nu}_e \nu_\tau$	$\tau^- \rightarrow \ell^- \bar{\nu}_\ell \nu_\tau$
$\rho$	$0.74979 \pm 0.00026$	$0.763 \pm 0.020$	$0.747 \pm 0.010$	$0.745 \pm 0.008$
$\eta$	$0.057 \pm 0.034$	$0.094 \pm 0.073$	—	$0.013 \pm 0.020$
$\xi$	$1.0009^{+0.0016}_{-0.0007}$	$1.030 \pm 0.059$	$0.994 \pm 0.040$	$0.985 \pm 0.030$
$\xi\delta$	$0.7511^{+0.0012}_{-0.0006}$	$0.778 \pm 0.037$	$0.734 \pm 0.028$	$0.746 \pm 0.021$
$\xi'$	$1.00 \pm 0.04$	—	—	—
$\xi''$	$0.65 \pm 0.36$	—	—	—

Table 2.4: Michel parameters [3]. The last column assumes identical couplings for  $\ell = e, \mu$ .  $\xi_{\mu \rightarrow e}$  refers to the product  $\xi_{\mu \rightarrow e} \mathcal{P}_\mu$ , where  $\mathcal{P}_\mu \approx 1$  is the longitudinal polarization of the  $\mu$  from  $\pi$  decay.

$\tau^- \rightarrow e^- \bar{\nu}_e \nu_\tau$			
$ g_{RR}^S  < 0.70$	$ g_{LR}^S  < 0.99$	$ g_{RL}^S  < 2.01$	$ g_{LL}^S  < 2.01$
$ g_{RR}^V  < 0.17$	$ g_{LR}^V  < 0.13$	$ g_{RL}^V  < 0.52$	$ g_{LL}^V  < 1.005$
$ g_{RR}^T  \equiv 0$	$ g_{LR}^T  < 0.082$	$ g_{RL}^T  < 0.51$	$ g_{LL}^T  \equiv 0$
$\tau^- \rightarrow \mu^- \bar{\nu}_\mu \nu_\tau$			
$ g_{RR}^S  < 0.72$	$ g_{LR}^S  < 0.95$	$ g_{RL}^S  < 2.01$	$ g_{LL}^S  < 2.01$
$ g_{RR}^V  < 0.18$	$ g_{LR}^V  < 0.12$	$ g_{RL}^V  < 0.52$	$ g_{LL}^V  < 1.005$
$ g_{RR}^T  \equiv 0$	$ g_{LR}^T  < 0.079$	$ g_{RL}^T  < 0.51$	$ g_{LL}^T  \equiv 0$

Table 2.5: Experimental bounds at 95% C.L. for the leptonic  $\tau$ -decay couplings [3].

Assuming LU, the leptonic decay ratios  $\mathcal{B}_\mu/\mathcal{B}_e$  and  $\mathcal{B}_e \tau_\mu/\tau_\tau$  bring limits on the low-energy parameter  $\eta$ .  $\hat{G}_{\mu\tau}$  provides the best sensitivity [351] since the term proportional to  $\eta$  is not suppressed by the  $m_e/m_\ell$  factor. Using the world-average value of  $\mathcal{B}_\mu/\mathcal{B}_e$ , it is possible to determine  $\eta_{\tau \rightarrow \ell} = 0.016 \pm 0.013$ , which only assumes  $e/\mu$  universality. This value is more accurate than the  $\mu \rightarrow e$  and  $\tau \rightarrow \mu$  shown in Table 2.4. A  $\eta$  value different from zero would point out that there are at least two distinct couplings with opposite chiralities for the charged leptons. Assuming the  $V - A$  coupling  $g_{LL}^V$  to be dominant, the second one would be a scalar couplings  $g_{RR}^S$ . The  $\eta_{\tau \rightarrow \ell}$  value implies,  $-0.019 < \text{Re}[g_{RR}^S] < 0.083$  at 95% C.L. since at leading order in new physics contributions,  $\eta \approx \text{Re}[g_{RR}^S]/2$ .



### 2.4.1 Model-dependent interpretation

Since the sensitivity of the current  $\tau$  data is not good enough to set strong constraints from a completely general analysis of the four-fermion Hamiltonian. However, more stringent limits can be obtained assuming a particular model. For instance, in the framework of a two Higgs doublet model, the measurements correspond to a limit of  $m_{H^\pm} > 1.9 \text{ GeV} \times \tan \beta$  on the mass of the charged Higgs boson, or a limit of 253 GeV on the mass of the second  $W$  boson in left-right symmetric models for arbitrary mixing (both 95% C.L.). See [302, 352–354].

For interactions mediated by a  $W$  boson, the hadronic decay modes  $\tau^- \rightarrow h^- \nu_\tau$  can be used to test the structure of the  $\tau \nu_\tau W$  vertex, if one assumes the SM coupling of the  $W$  to the light quarks. In that case, the Hamiltonian contains only two vector couplings  $g_\lambda$ , with  $\lambda$  being the  $\tau$  (and  $\nu_\tau$ ) chirality, where  $|g_L|^2 + |g_R|^2 = 1$ . The  $\mathcal{P}_\tau$  dependent part of the decay amplitude is proportional to  $\xi_h = |g_L|^2 - |g_R|^2$ , which plays a role analogous to the leptonic decay constant  $\xi$ . This parameter,  $\xi_h$ <sup>4</sup>, determines the mean  $\nu_\tau$  helicity times a factor  $-2$ . The study of  $\tau^+ \tau^-$  decay correlations in leptonic-hadronic and hadronic-hadronic decay modes, using the  $\pi$ ,  $\rho$ , and  $a_1$  hadronic final states [326, 329, 330, 332–341, 355–361], implies  $\xi_h = 0.995 \pm 0.007$  [3]. This suggests  $|g_L| > 0.995$  and  $|g_R| < 0.10$  at 95% C.L.

## 2.5 Hadronic decays

Since the  $\tau$  is the only known lepton massive enough that can decay into hadrons, its semileptonic decays provide us with a clean laboratory to test QCD at low-energies and investigate the hadronic weak currents. The  $\tau^- \rightarrow H^- \nu_\tau$  decay probes the matrix element of the left-handed charged current between the vacuum and the final hadronic state  $H^-$ ,

$$\langle H^- | (V_{ud}^* \bar{d} + V_{us}^* \bar{s}) \gamma^\mu (1 - \gamma^5) u | 0 \rangle. \quad (2.27)$$

The semileptonic  $\tau$  decays allow us to study the properties of both vector and axial-vector currents for Cabibbo-allowed or Cabibbo-suppressed final states [362], contrary to

---

<sup>4</sup> $\xi = 1$  in the SM.

the well-known process  $e^+e^- \rightarrow \gamma^* \rightarrow \text{hadrons}$ .

The matrix element of the vector charged current is related to the isovector part of the  $e^+e^-$  annihilation cross section into hadrons through an isospin rotation, which evaluate the hadronic matrix element of the  $I = 1$  component of the electromagnetic current,

$$\langle V^0 | (\bar{u}\gamma^\mu u - \bar{d}\gamma^\mu d) | 0 \rangle. \quad (2.28)$$

The  $\tau \rightarrow V^- \nu_\tau$  decay can be written as an integral over the  $e^+e^- \rightarrow V^0$  cross section [249, 363]:

$$R_{\tau \rightarrow V} \equiv \frac{\Gamma(\tau^- \rightarrow V^- \nu_\tau)}{\Gamma_{\tau \rightarrow e}} = \frac{3 \cos^2 \theta_C}{2\pi\alpha^2 m_\tau^2} S_{EW} \int_0^{m_\tau^2} ds \left(1 - \frac{s}{m_\tau^2}\right)^2 \left(1 + \frac{2s}{m_\tau^2}\right) s \sigma_{e^+e^- \rightarrow V^0}^{I=1}(s), \quad (2.29)$$

where  $S_{EW}$  are the short-distance electroweak corrections that include a next-to-leading order resummation of large logarithms [256, 364, 365]. A comparison among the available data on  $e^+e^- \rightarrow V^0$ , the corresponding  $\tau^- \rightarrow V^- \nu_\tau$  decay width and the invariant-mass distribution [366–371] could help us to improve our understanding of the non-perturbative QCD. The  $e^+e^-$  data contains an additional isoscalar ( $I = 0$ ) component, which is not present in  $\tau$  decays and needs to be subtracted in Eq. (2.29). The general form factors characterizing the hadronic amplitudes can be extracted from Dalitz-plot distributions of the final hadrons [372, 373]. A detailed analysis of these processes gives a very valuable data basis to confront with theoretical models.

### 2.5.1 Two-body semileptonic decays

The matrix elements for the  $\tau^- \rightarrow \pi^- \nu_\tau$  and  $\tau^- \rightarrow K^- \nu_\tau$  decays are given by

$$\langle \pi^-(p) | \bar{d}\gamma^\mu \gamma^5 u | 0 \rangle = -i\sqrt{2} f_\pi p^\mu, \quad \langle K^-(p) | \bar{s}\gamma^\mu \gamma^5 u | 0 \rangle = -i\sqrt{2} f_K p^\mu, \quad (2.30)$$

where  $f_\pi$  and  $f_K$  are the decay constants, which are already known from the measured  $\pi^- \rightarrow \mu^- \nu_\mu$  and  $K^- \rightarrow \mu^- \nu_\mu$  decays, and lattice QCD. The  $\tau$  decay width can be predicted

accurately using Eq. (2.13). As shown in Table 2.2, these predictions are in good agreement with the measured values, and yield a quite precise test of charged-current universality.

Additionally, the ratio of the measured  $\tau^- \rightarrow K^- \nu_\tau$  and  $\tau^- \rightarrow \pi^- \nu_\tau$  decay widths can be used to extract information about the ratio of the hadronic matrix elements:

$$\frac{|V_{us}|f_K}{|V_{ud}|f_\pi} = \frac{m_\tau^2 - m_\pi^2}{m_\tau^2 - m_K^2} \left\{ \frac{\text{Br}(\tau^- \rightarrow K^- \nu_\tau)}{\text{Br}(\tau^- \rightarrow \pi^- \nu_\tau)} \frac{1 + \delta R_{\tau/\pi}}{1 + \delta R_{\tau/K}} \frac{1}{1 + \delta R_{K/\pi}} \right\}^{1/2} = 0.2737 \pm 0.0021, \quad (2.31)$$

which uses the radiative corrections in Eq. (2.14), and the corrections to the meson decay ratio  $R_{K/\pi} = \Gamma(K^- \rightarrow \mu^- \bar{\nu}_\mu) / \Gamma(\pi^- \rightarrow \mu^- \bar{\nu}_\mu)$ :

$$\delta R_{K/\pi} = -(0.0069 \pm 0.0017) - (0.0044 \pm 0.0015) = -(0.0113 \pm 0.0023), \quad (2.32)$$

where the first number is of electromagnetic origin [374, 375], the second one is related to the strong isospin-breaking corrections [374], and  $f_K$  and  $f_\pi$  denote the meson decay constants in the isospin-limit. From  $R_{K/\pi}$  [374], it is found  $(|V_{us}|f_K) / (|V_{ud}|f_\pi) = 0.2760(4)$  [376] which is consistent with the result in Eq. (2.31). Taking into account the lattice average  $f_K/f_\pi = 1.1932(21)$  [377] and  $V_{ud} = 0.97370(14)$  [3, 378], one obtains a determination of the Cabbibo mixing <sup>5</sup>:

$$\frac{|V_{us}|}{|V_{ud}|} = \begin{cases} 0.2294 \pm 0.0018 \\ 0.2313 \pm 0.0005 \end{cases} \quad |V_{us}| = \begin{cases} 0.2234 \pm 0.0018 & (\tau \rightarrow K/\pi) \\ 0.2252 \pm 0.0005 & (K/\pi \rightarrow \mu) \end{cases}. \quad (2.33)$$

## 2.5.2 Decays into two hadrons

The decay into two pseudoscalar mesons,  $\tau^- \rightarrow P^- P^0 \nu_\tau$ , is mediated by the vector current. The amplitude for the  $\tau^-(P) \rightarrow P^-(p_-) P^0(p_0) \nu_\tau(q)$  decays is given by

$$\mathcal{M}_0 = \frac{G_F V_{uD} \sqrt{S_{EW}}}{\sqrt{2}} H_\nu(p_-, p_0) \bar{u}(q) \gamma^\nu (1 - \gamma^5) u(P). \quad (2.34)$$

the hadronic matrix element can be written as

$$H^\nu(p_-, p_0) = C_V F_+(t) Q^\nu + C_S \frac{\Delta_-^0}{t} q^\nu F_0(t), \quad t = q^2, \quad (2.35)$$

---

<sup>5</sup>This has been updated in Ref. [293] to  $\frac{|V_{us}|}{|V_{ud}|} = 0.2288 \pm 0.0020$ ,  $|V_{us}| = 0.2220 \pm 0.0018$  at 2.1 and 2.6 $\sigma$  from unitarity, respectively.

where  $q^\nu = (p_- + p_0)^\nu$ ,  $Q^\nu = (p_- - p_0)^\nu - \frac{\Delta_{-0}}{t} q^\nu$  and  $\Delta_{ij} = m_i^2 - m_j^2$ .  $F_+(t)$  and  $F_0(t)$  are the vector and scalar form factors.  $C_V$  and  $C_S$  are the Clebsch–Gordan (CG) coefficients:

$$\begin{aligned} C_V^{\pi^-\pi^0} &= C_S^{\pi^-\pi^0} = \sqrt{2}, & C_V^{K^-K^0} &= C_S^{K^-K^0} = -1, \\ C_V^{K^-\pi^0} &= C_S^{K^-\pi^0} = \frac{1}{\sqrt{2}}, & C_V^{\pi^-\bar{K}^0} &= C_S^{\pi^-\bar{K}^0} = -1. \end{aligned}$$

Thus, the spin-averaged squared amplitude follows as

$$\begin{aligned} \overline{|\mathcal{M}_0|^2} &= 2G_F^2 |V_{uD}|^2 S_{EW} \left\{ C_S^2 |F_0(t)|^2 D_0^{h^-h^0}(t, u) + C_S C_V \text{Re}[F_+(t)F_0^*(t)] D_{+0}^{h^-h^0}(t, u) \right. \\ &\quad \left. + C_V^2 |F_+(t)|^2 D_+^{h^-h^0}(t, u) \right\}, \end{aligned} \quad (2.36)$$

where we have defined  $F_{+/0}(t, u) = F_{+/0}(t) + \delta F_{+/0}(t, u)$ , and  $\delta F_0(t, u) \equiv \delta F_+(u) + \frac{t}{\Delta_{-0}} \delta F_-(u)$ . The expressions for  $D_0^{h^-h^0}(t, u)$ ,  $D_{+0}^{h^-h^0}(t, u)$  and  $D_+^{h^-h^0}(t, u)$  are given by:

$$\begin{aligned} D_+^{h^-h^0}(t, u) &= \frac{m_\tau^2}{2} (m_\tau^2 - t) + 2m_0^2 m_-^2 - 2u(m_\tau^2 - t + m_0^2 + m_-^2) + 2u^2 \\ &\quad + \frac{\Delta_{-0}}{t} m_\tau^2 (2u + t - m_\tau^2 - 2m_0^2) + \frac{\Delta_{-0}^2}{t^2} \frac{m_\tau^2}{2} (m_\tau^2 - t), \end{aligned} \quad (2.37)$$

$$D_0^{h^-h^0}(t, u) = \frac{\Delta_{-0}^2 m_\tau^4}{2t^2} \left( 1 - \frac{t}{m_\tau^2} \right), \quad (2.38)$$

$$D_{+0}^{h^-h^0}(t, u) = \frac{\Delta_{-0} m_\tau^2}{t} \left( 2u + t - m_\tau^2 - 2m_0^2 + \frac{\Delta_{-0}}{t} (m_\tau^2 - t) \right). \quad (2.39)$$

The differential decay width in the tau rest frame is

$$\frac{d^2\Gamma}{dt du} = \frac{1}{32(2\pi)^3 m_\tau^3} \overline{|\mathcal{M}_0|^2}, \quad (2.40)$$

where  $t = (p_- + p_0)^2$  is the invariant mass and  $u = (P - p_-)^2 = (p_0 + q)^2$ . The physical region is limited by  $(m_- + m_0)^2 \leq t \leq m_\tau^2$  and  $u^-(t) \leq u \leq u^+(t)$ ,

$$u^\pm(t) = \frac{1}{2t} \left\{ 2t(m_\tau^2 + m_0^2 - t) - (m_\tau^2 - t)(t + m_-^2 - m_0^2) \pm (m_\tau^2 - t) \sqrt{\lambda(t, m_-^2, m_0^2)} \right\}, \quad (2.41)$$

and  $\lambda(x, y, z) = x^2 + y^2 + z^2 - 2xy - 2xz - 2yz$ .

The invariant mass distribution is obtained integrating upon the  $u$  variable

$$\begin{aligned} \frac{d\Gamma}{dt} &= \frac{G_F^2 S_{EW} |V_{uD}|^2 m_\tau^3}{768\pi^3 t^3} \left( 1 - \frac{t}{m_\tau^2} \right)^2 \lambda^{1/2}(t, m_-^2, m_0^2) \left\{ C_V^2 |F_+(t)|^2 \left( 1 + \frac{2t}{m_\tau^2} \right) \lambda(t, m_-^2, m_0^2) \right. \\ &\quad \left. + 3C_S^2 \Delta_{-0}^2 |F_0(t)|^2 \right\}, \end{aligned} \quad (2.42)$$

Long-distance electromagnetic corrections and isospin-breaking contributions are channel dependent and have been only studied in a model-dependent way for the  $\pi\pi$  [7, 94, 97, 379] and  $K\pi$  [380, 381] final states.

$$\tau^- \rightarrow \pi^- \pi^0 \nu_\tau$$

It is well known that in the isospin-limit the two-pion final state does not receive scalar contributions. For that reason, this kind of decays are governed by the so-called pion form factor  $F_\pi(s) \equiv F_V^{\pi\pi}(s)$ . In recent years there was a huge effort to improve our understanding of  $F_\pi(s)$  [15–17, 218, 382–384] using analyticity, unitarity and some properties of QCD, such as chiral symmetry [132, 133, 198] and the short-distance asymptotic behaviour [224–226, 385–387]. For instance, all these requirements are complied using the following expression for the pion form factor [15]

$$F_\pi(s) = \frac{M_\rho^2}{M_\rho^2 - s - iM_\rho\Gamma_\rho(s)} \exp\left\{-\frac{s}{96\pi^2 f_\pi^2} \text{Re}[A(s)]\right\}, \quad (2.43)$$

where

$$A(s) \equiv \log \frac{m_\pi^2}{M_\rho^2} + 8 \frac{m_\pi^2}{s} - \frac{5}{3} + \sigma_\pi^3 \log \left( \frac{\sigma_\pi + 1}{\sigma_\pi - 1} \right) \quad (2.44)$$

contains the one-loop chiral logarithms [194], that account for the final-state interaction (FSI) of the two pions,  $\sigma_\pi \equiv \sqrt{1 - 4m_\pi^2/s}$  and the off-shell  $\rho$  width is given by  $\Gamma_\rho(s) = \theta(s - 4m_\pi^2) \sigma_\pi^3 M_\rho s / (96\pi f_\pi^2)$  [15, 383].

In the large- $N_C$  limit [388–390], the pion form factor is described by an infinite sum of narrow-width vector resonance contributions [226, 391, 392]. In Eq. (2.43) only the lightest  $\rho$  state, which dominates below 1 GeV, has been taken into account. As a consequence of the conservation of the electromagnetic current, we have the normalization  $F_\pi(0) = 1$ , while the SD properties of QCD demand the form factor to vanish at infinite momentum. The large- $N_C$  propagator is dressed with pion loop corrections subleading in  $1/N_C$  in such a way that a Taylor expansion in powers of  $s/M_\rho^2$  reproduces the one-loop  $\chi$ PT prediction at low-energies. It is possible to implement a resummation of the one-loop chiral logarithms

through an Omnès exponential [228] to comply with the constraints from analyticity and unitarity. By a Dyson summation, the absorptive part of these corrections is reabsorbed into the  $\rho$  width in order to regulate the resonance pole. All these ingredients extend the validity domain of the  $\chi$ PT prediction in Eq. (2.43). The theoretical prediction, which only hinges on three parameters:  $M_\rho$ ,  $m_\pi$  and  $f_\pi$ , is compared with the data in Fig. 2.3. The agreement is also extended to negative values of  $s$ , where the  $e^- \pi^-$  elastic data sits.

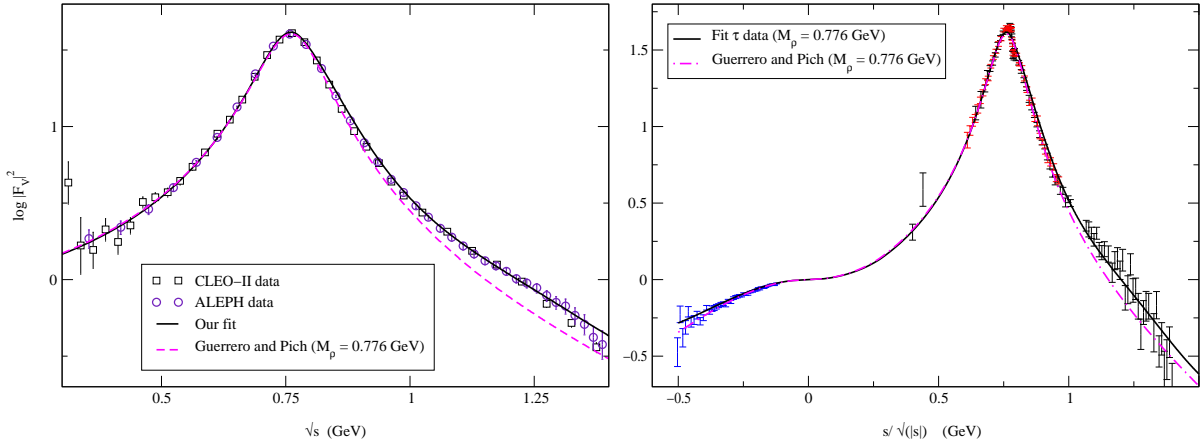


Figure 2.3: Pion form factor from ALEPH [11] and CLEO [12]  $\tau$  data (left) and  $e^+e^- \rightarrow \pi^+\pi^-$  [13] and  $e^- \pi^- \rightarrow e^- \pi^-$  [14] data (right), compared to theory [15–17]. The red dashed line is the prediction from Eq. (2.43).

One can easily include the modifications due to kaon loops, heavier  $\rho$  resonance contributions and additional NLO corrections in  $1/N_C$ ; the precision of this approximation can be improved by including more free parameters at the cost of decreasing its predictive power [16, 17, 218, 382, 384], which gives a better description of the  $\rho'$  around 1.2 GeV (continuous line in Fig. 2.3). Belle has reported a clear signal for the  $\rho''(1700)$  resonance in  $\tau^- \rightarrow \pi^- \pi^0 \nu_\tau$  decays [18]. A fit to the Belle data, which includes the  $\rho'$  and  $\rho''$  states [19], is shown in Fig. (2.4).

The  $\tau^- \rightarrow \pi^- \pi^0 \nu_\tau$  decay amplitude is related to the isovector component of  $\sigma(e^+e^- \rightarrow \pi^+\pi^-)$  through an isospin rotation. For that reason, the pion form factor can be extracted using both datasets. Over the years, there have been discrepancies between the different experimental measurements that may be due to the underestimation of systematic uncer-

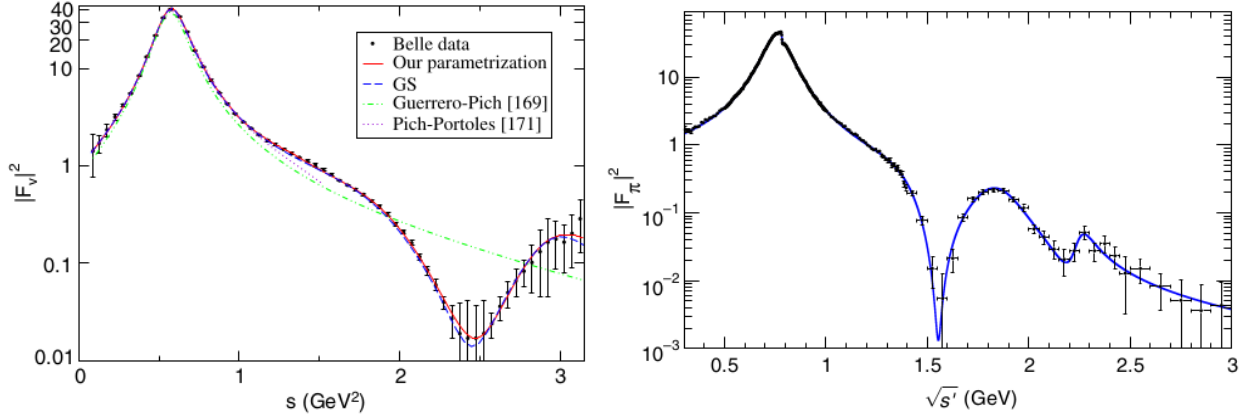


Figure 2.4: Pion form factor extracted from Belle  $\tau^- \rightarrow \pi^- \pi^0 \nu_\tau$  data [18]. The curves correspond to the different approximations, including  $\rho$ ,  $\rho'$  and  $\rho''$  [19]. The BaBar  $e^+e^- \rightarrow \pi^+\pi^-\gamma$  measurement [20,21] shows a clear signal of the  $\rho'''$  and the isoscalar  $\omega$  state.

tainties. The amplitude measured in  $e^+e^-$  experiments [13, 20, 21, 52–54, 56–58, 393–396] is slightly lower than those from  $\tau$  decays [11, 12, 18, 397], and this discrepancy cannot be fully explained through the calculation of isospin-violating effects [7, 94, 379]. Additionally to the direct energy scan adopted in most  $e^+e^-$  measurements, some recent experiments utilize the so-called radiative return method in order to extract  $\sigma(e^+e^- \rightarrow \pi^+\pi^-)$  from the  $e^+e^- \rightarrow \pi^+\pi^-\gamma$  data, checking different ranges of  $\pi^+\pi^-$  invariant masses via the radiated photon (initial state radiation, ISR) [398–405]. The BaBar data [20, 21], that uses this method, has reduced the tension with  $\tau$ -decay measurements, nevertheless the discrepancies persevere with the KLOE data for  $e^+e^- \rightarrow \pi^+\pi^-\gamma$  [56–58, 395].

Using the isospin-breaking corrections in Refs. [7, 94, 379], the prediction from  $e^+e^-$  data is  $\text{Br}(\tau^- \rightarrow \pi^- \pi^0 \nu_\tau) = (24.94 \pm 0.25)\%$  [406], which is  $2.1\sigma$  smaller than the world average from  $\tau$  decay measurements,  $\text{Br}(\tau^- \rightarrow \pi^- \pi^0 \nu_\tau) = (25.49 \pm 0.09)\%$  [3]. The BaBar data exhibits a discrepancy of about  $1.2\sigma$  while that of KLOE differs from the direct measurements by  $2.7\sigma$  [406]. The computation of the isospin-breaking corrections to this channel is the main focus of Chapter 7, which are also an essential ingredient for the estimation of the hadronic vacuum polarization contribution to the muon  $g - 2$  from  $\tau$  data.

$$\tau^- \rightarrow (K\pi)^- \nu_\tau$$

Unlike the  $\pi\pi$  channel, the  $\tau^- \rightarrow K^- \pi^0 \nu_\tau$  and  $\tau^- \rightarrow \bar{K}^0 \pi^- \nu_\tau$  decays receive contributions from two form factors because of the masses of the final state pseudoscalars. The vector and scalar form factors are also probed in  $K_{\ell 3}$  decays, but the tau ones are sensitive to a different and broader region, where the light-flavored resonances play a key role.

A detailed analysis of these processes can be found in [23, 24, 380, 407–411]. The vector form factor  $F_V^{K\pi}(s)$  can be obtained in a similar way to the pion form factor, whereas the scalar one  $F_S^{K\pi}(s)$  uses additional information from  $K\pi$  scattering data through dispersion relations [25–27, 412–414]. A comparison between the Belle  $\tau^- \rightarrow K_S \pi^- \nu_\tau$  measurement [22, 415] and a theoretical fit using the R $\chi$ T description of  $F_V^{K\pi}(s)$  with two resonances [23, 24] is shown in Fig. 2.5. The scalar component gives a small contribution to the total decay width,  $\text{Br}[\tau^- \rightarrow \nu_\tau (K\pi)_{S\text{-wave}}] = (3.88 \pm 0.19) \cdot 10^{-4}$ , but it is sizeable near the threshold. The dominant contribution comes from the  $K^*(892)$  followed by the  $K^*(1410)$ , which induces a small correction at higher invariant mass. The Belle data shows a bump at 0.682–0.705 GeV (points 5, 6 and 7) that cannot be explained by the theoretical description<sup>6</sup> and, as a consequence, it is not included in the fit; this bump seems to be absent in the BaBar data [419].

The slope and curvature of the vector form factor can be extracted through a fit to the  $\tau^- \rightarrow K_S \pi^- \nu_\tau$  spectrum, with a precision comparable to that in  $K_{\ell 3}$ , and it is also possible to predict the  $\tau^- \rightarrow K^- \pi^0 \nu_\tau$  and  $\tau^- \rightarrow \bar{K}^0 \pi^- \nu_\tau$  branching ratios [23, 24, 380, 409–411]. A combined fit to  $\tau^- \rightarrow K_S \pi^- \nu_\tau$  and  $K_{\ell 3}$  data, that utilizes a dispersive parameterization of the two form factors, and includes electromagnetic and isospin-breaking corrections, gives [380]:

$$\text{Br}[\tau^- \rightarrow \bar{K}^0 \pi^- \nu_\tau]_{\text{th}} = (0.8566 \pm 0.0299)\%, \quad \text{Br}[\tau^- \rightarrow K^- \pi^0 \nu_\tau]_{\text{th}} = (0.4707 \pm 0.0181)\%. \quad (2.45)$$

These are slightly larger than the current experimental world averages,  $\text{Br}[\tau^- \rightarrow \bar{K}^0 \pi^- \nu_\tau]_{\text{th}} =$

---

<sup>6</sup>Although many devoted analysis [23, 30, 251, 380, 409–411, 416, 417] have signalled these three points as controversial, there is a work by L.A. Jiménez and G. Toledo [418], which is able to describe these data points due to the effect of the longitudinal correction to the  $K^*(892)$  propagator by a flavor symmetry breaking on  $F_S^{K\pi}(s)$ .



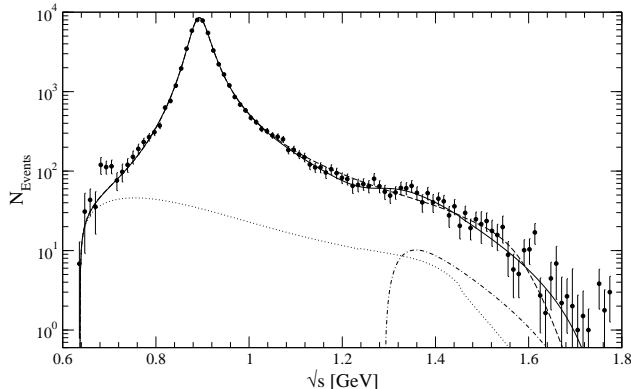


Figure 2.5: The  $\tau^- \rightarrow K_S \pi^- \nu_\tau$  spectrum measured by the Belle collaboration [22]. The solid line corresponds to the fit in Ref. [23, 24], which includes a R $\chi$ T description of  $F_V^{K\pi}(s)$  with two resonances and  $F_S^{K\pi}(s)$  from Ref. [25–27]. The scalar and  $K^*(1410)$  correspond to the dotted and dash-dotted lines, respectively.

$(0.838 \pm 0.014)\%$  and  $\text{Br}[\tau^- \rightarrow K^- \pi^0 \nu_\tau]_{\text{th}} = (0.433 \pm 0.015)\%$  [3], corroborating an earlier observation made in Ref. [23, 24]. This effect has a significant impact on the  $V_{us}$  determination.

This channel provides valuable information about  $CP$  violation, which is an essential ingredient to explain the presence of the baryon asymmetry in the universe [420]. Although earlier searches did not find evidence for  $CP$  violation [421, 422], a recent result by the BaBar collaboration [423],

$$A_{CP}^{\tau, \text{exp}} = -3.6(2.3)(1.1) \cdot 10^{-3}, \quad (2.46)$$

disagrees with the SM prediction,  $A_{CP}^{\tau, \text{SM}} = 3.32(6) \cdot 10^{-3}$ , which is driven by the  $K^0 - \bar{K}^0$  mixing [424, 425]. The discrepancy between theory and experiment is slightly increased ( $\sim 2.8\sigma$ ) when the experimental conditions corresponding to the reconstruction of the  $K_S$  at the B-factory are taken into account [426], which yields  $A_{CP}^{\tau, \text{SM}} = 3.6(1) \cdot 10^{-3}$ . This tension could be considered a hint for beyond the Standard Model (BSM) physics. In Refs. [251, 427], an explanation using a new tensor interaction in terms of BSM originating in the ultraviolet was ruled out.

The  $\tau^- \rightarrow K^- \eta^{(\prime)} \nu_\tau$  decays have been studied in Ref. [428]. These decay channels are very

suppressed. The  $\tau^- \rightarrow K^- \eta \nu_\tau$  channel has been measured at the  $B$  factories [29, 429–432] with an average  $\text{Br}[\tau^- \rightarrow K^- \eta \nu_\tau] = (1.55 \pm 0.08) \cdot 10^{-4}$  [3], while for the  $K^- \eta'$  mode there is only an upper limit,  $\text{Br}[\tau^- \rightarrow K^- \eta \nu_\tau] < 2.4 \cdot 10^{-6}$  [433].

### $\tau^- \rightarrow \pi^- \eta \nu_\tau$

The final state of  $\pi\eta$  has  $I^G = 1^-$  and  $J^P = 0^+$  or  $1^-$  for  $S$  and  $P$  wave, respectively. For that reason, any observation of these decays would indicate either a  $G$ -parity violation since the Cabibbo-allowed vector current has even  $G$ -parity [434], or a new physics contribution that incorporates second-class currents [435, 436]. In the SM, these decays can proceed via the isospin violation provided by the light quarks mass difference  $m_u - m_d$  or through electromagnetic contributions, which make them very suppressed [437–439] and increase its sensitivity to new scalar or tensor interactions [250, 438, 440]. At LO in  $\chi$ PT the coupling to the vector current is dominated by the well-known  $\pi^0 - \eta$  mixing, which predicts a constant and equal vector and scalar form factors:

$$F_V^{\pi\eta}(s)_{LO} = F_S^{\pi\eta}(s)_{LO} = \frac{\sqrt{3} (m_u - m_d)}{4 (m_s - \hat{m})} \approx 0.99 \cdot 10^{-2}, \quad (2.47)$$

where  $\hat{m} = (m_u + m_d)/2$ . This result is enhanced by the NLO chiral corrections and electromagnetic contributions. It is possible to extract both form factors at  $s = 0$  in a simple and very elegant way from the ratio  $F_V^{K^- \pi^0}(0)/F_V^{\bar{K}^0 \pi^-}(0)$  [441]. Using the  $K_{\ell 3}$  information [442], a very precise prediction of the  $\pi\eta$  form factors at  $s = 0$  can be found [443]:

$$F_V^{\pi\eta}(0) = F_S^{\pi\eta}(0) = (1.49 \pm 0.23) \cdot 10^{-2}. \quad (2.48)$$

Using this as an input, together with the  $\chi$ PT constraints, it is feasible to estimate the two form factors in the relevant kinematical domain through a dispersive representation, implying the following branching ratio [443]:

$$\text{Br}[\tau^- \rightarrow \pi^- \eta \nu_\tau] = (0.48_{-0.20}^{+0.30}) \cdot 10^{-5}. \quad (2.49)$$

This number, which is governed by the scalar contribution, is a factor 20 smaller than

the current experimental upper bound <sup>7</sup>:  $\text{Br}[\tau^- \rightarrow \pi^- \eta \nu_\tau] < 9.9 \cdot 10^{-5}$  (95% CL) [429]. Many predictions exist already in the literature which differ by one to two orders of magnitude [438–441, 445, 446]. For instance, the  $R\chi T$  prediction of Ref. [447] for this decay mode is  $\sim 1.7 \cdot 10^{-5}$  (see also Ref. [448]). With a branching ratio of  $4.4 \cdot 10^{-5}$ , the  $\tau^- \rightarrow \pi^- \eta \nu_\tau$  decay could be observed with a significance of  $2.6\sigma$  at Belle II [449]. A somewhat better bound exists for the  $\pi^- \eta'$  mode:  $\text{Br}[\tau^- \rightarrow \pi^- \eta' \nu_\tau] < 4.0 \cdot 10^{-6}$  (90% CL) [433], in which the  $R\chi T$  prediction is  $[1 \cdot 10^{-7}, 1 \cdot 10^{-6}]$  [447].

### Higher-multiplicity decays

Modes with high multiplicity require a richer dynamical structure and provide a very valuable experimental window into the non-perturbative hadronization of the QCD currents. Nevertheless, the inclusion of three or more final-state hadrons is not an easy task. At tree level, there are several computations in  $R\chi T$  for tau decays into three mesons, and some final states with four pseudoscalars, but the chiral loop corrections are not yet implemented, except for  $\tau \rightarrow 3\pi\nu_\tau$  [450] and  $\tau \rightarrow 4\pi\nu_\tau$  [451], at very low  $q^2$ . These predictions correspond to the limit of large- $N_C$ ; the only subleading contribution in the  $1/N_C$  expansion that is taken into account is the finite width of the hadronic resonances. Despite the limitations of the  $R\chi T$  approximations, these results provide a direct connection with the fundamental QCD theory and are a good starting point to analyse the measured observables.

The first exhaustive studies of  $\tau^- \rightarrow \pi^+ \pi^- \pi^- \nu_\tau$  and  $\tau^- \rightarrow \pi^0 \pi^0 \pi^- \nu_\tau$  were made in [369, 452]. A  $R\chi T$  analysis was later performed in Refs. [453, 454], which includes a theoretical description of the measured [317, 358, 359, 397, 455–457]  $J^P = 1^+$  structure functions [372, 373]. The  $\tau^- \rightarrow (3\pi)^- \nu_\tau$  decay amplitude contains two interfering contributions, that corresponds to the exchange of the two identical final state pions and causing a parity-violating angular asymmetry [317, 369, 458]. This makes possible to determine the sign of the  $\nu_\tau$  helicity to be  $-1$  [356–361].

Exhaustive analyses were carried out for other decay modes such as  $\tau \rightarrow K \bar{K} \pi \nu_\tau$  [459] and

---

<sup>7</sup>This mode was once claimed to have been observed with a surprisingly large branching fraction,  $\text{Br} = (5.1 \pm 1.5)\%$  [444], however this was not confirmed by other experiments.

$X^-$	$\text{Br}(\tau^- \rightarrow X^- \nu_\tau)$ [%]	References	$X^-$	$\text{Br}(\tau^- \rightarrow X^- \nu_\tau)$ [%]	References
$\pi^-$	$(10.808 \pm 0.053)$	Ref. [397]	$\pi^- \pi^+ \pi^-$ (ex. $K^0, \omega$ )	$(8.981 \pm 0.052)$	Ref. [397]
$\pi^- \pi^0$	$(25.486 \pm 0.090)$	Ref. [397]	$\pi^- \pi^+ \pi^- \pi^0$ (ex. $K^0, \omega$ )	$(2.743 \pm 0.071)$	
$\pi^- 2\pi^0$ (ex. $K^0$ )	$(9.245 \pm 0.099)$	Ref. [397]	$h^- h^+ h^- 2\pi^0$ (ex. $K^0, \omega, \eta$ )	$(0.0979 \pm 0.0356)$	
$\pi^- 3\pi^0$ (ex. $K^0$ )	$(1.040 \pm 0.071)$	Ref. [397]	$h^- h^+ h^- 3\pi^0$	$(0.0212 \pm 0.0030)$	Ref. [474]
$h^- 4\pi^0$ (ex. $K^0, \eta$ )	$(0.1118 \pm 0.0391)$	Ref. [397]	$\pi^- K^- K^+$	$(0.1434 \pm 0.0027)$	Refs. [475–478]
$K^- K^0$	$(0.1486 \pm 0.0034)$	Refs. [479–483]	$\pi^- K^- K^+ \pi^0$	$(0.0061 \pm 0.0018)$	Refs. [475, 484]
$K^- K^0 \pi^0$	$(0.1499 \pm 0.0070)$	Refs. [479, 480, 482, 483]	$3h^- 2h^+$ (ex. $K^0$ )	$(0.0828 \pm 0.0031)$	Refs. [397, 485–489]
$\pi^- K_S^0 K_S^0$	$(0.0235 \pm 0.0006)$	Refs. [479, 482, 483, 490]	$3h^- 2h^+ \pi^0$ (ex. $K^0$ )	$(0.0164 \pm 0.0011)$	Refs. [397, 474, 487, 489]
$\pi^- K_S^0 K_L^0$	$(0.1048 \pm 0.0247)$	Ref. [479]	$\pi^- \pi^0 \eta$	$(0.1386 \pm 0.0072)$	Refs. [29, 430, 432]
$\pi^- K_L^0 K_L^0$	$(0.0235 \pm 0.0006)$		$\pi^- \omega$	$(1.947 \pm 0.065)$	
$\pi^- K^0 \bar{K}^0 \pi^0$	$(0.0354 \pm 0.0119)$		$h^- \pi^0 \omega$	$(0.4069 \pm 0.0419)$	Ref. [430]
$a_1^- (\rightarrow \pi^- \gamma)$	$(0.0400 \pm 0.0200)$	Ref. [397]			

$\text{Br}(\tau^- \rightarrow X^- \nu_\tau) = (61.80 \pm 0.11)\%$

Table 2.6: Cabibbo-allowed hadronic  $\tau$  branching ratios [5],  $h^\pm$  stands for  $\pi^\pm$  or  $K^\pm$ .

$X^-$	$\text{Br}(\tau^- \rightarrow X^- \nu_\tau)$ [%]	References	$X^-$	$\text{Br}(\tau^- \rightarrow X^- \nu_\tau)$ [%]	References
$K^-$	$(0.6957 \pm 0.0096)$	Ref. [480, 491–493]	$K^- \eta$	$(0.0155 \pm 0.0008)$	Ref. [29, 429–431]
$K^- \pi^0$	$(0.4322 \pm 0.0148)$	Ref. [480, 491, 494, 495]	$K^- \pi^0 \eta$	$(0.0048 \pm 0.0012)$	Ref. [29, 496]
$K^- 2\pi^0$ (ex. $K^0$ )	$(0.0634 \pm 0.0219)$	Ref. [480, 491]	$\pi^- \bar{K}^0 \eta$	$(0.0094 \pm 0.0015)$	Ref. [29, 496]
$K^- 3\pi^0$ (ex. $K^0, \eta$ )	$(0.0465 \pm 0.0213)$	Ref. [480]	$K^- \omega$	$(0.0410 \pm 0.0092)$	Ref. [484]
$\pi^- \bar{K}^0$	$(0.8375 \pm 0.0139)$	Ref. [480, 482, 497, 498]	$K^- \phi (\phi \rightarrow K \bar{K})$	$(0.0044 \pm 0.0016)$	
$\pi^- \bar{K}^0 \pi^0$	$(0.3810 \pm 0.0129)$	Refs. [479, 480, 482, 497]	$K^- \pi^- \pi^+$ (ex. $K^0, \omega$ )	$(0.2924 \pm 0.0068)$	
$\pi^- \bar{K}^0 2\pi^0$ (ex. $K^0$ )	$(0.0234 \pm 0.0231)$	Refs. [499]	$K^- \pi^- \pi^+ \pi^0$ (ex. $K^0, \omega, \eta$ )	$(0.0387 \pm 0.0142)$	
$\bar{K}^0 h^- h^+ h^-$	$(0.0222 \pm 0.0202)$	Refs. [479]			

$\text{Br}(\tau^- \rightarrow X_S^- \nu_\tau) = (2.908 \pm 0.048)\%$

Table 2.7: Cabibbo-suppressed hadronic  $\tau$  branching ratios [5],  $h^\pm$  stands for  $\pi^\pm$  or  $K^\pm$ .

$\tau \rightarrow K 2\pi \nu_\tau$  [460], which include both vector and axial-vector currents, and  $\tau \rightarrow \eta' 2\pi \nu_\tau$  [461], which is dominated by the vector current (up to small isospin-breaking effects). The results in Ref. [459] for the  $\tau \rightarrow K \bar{K} \pi \nu_\tau$  decays agree with those in Ref. [462], where the vector contribution dominates this mode, but are at odds with the results in Refs. [463, 464] that suggest a larger axial component. Disentangling the two contributions would require a precise experimental determination of the hadronic invariant-mass distribution. The vector-currents amplitudes for these decays can be also evaluated using the corresponding  $e^+e^-$  annihilation processes [465].  $R\chi T$  currents were coded [466, 467] in the Monte Carlo Generator TAUOLA [468, 469] and are available for public use.

More involved transitions, namely  $e^+e^- \rightarrow 3\pi$  [465],  $\tau \rightarrow 4\pi \nu_\tau$  and  $e^+e^- \rightarrow 4\pi$  [451, 470], and radiative tau decays with one-meson in the final state [471–473] were also studied using the  $R\chi T$  techniques.

## Experimental status

A huge effort is underway to understand the rich pattern of hadronic tau decay modes [3,5]. The current world averages for the Cabibbo-allowed and -suppressed branching ratios are shown in Tables 2.6 and 2.7, using the “47 basis quantities” defined by the Heavy Flavor Averaging Group (HFAG) [5]. They used a total of 171 measurements to fit 135 quantities subject to 88 constraints. The fit has a  $\chi^2/\text{d.o.f} = 134/124$ , which corresponds to a confidence level  $\text{CL} = 24.56\%$ . Summing all the fitted branching ratios, leptonic and hadronic final states, a unitarity residual is obtained [5]:

$$1 - \sum_j \text{Br}(\tau \rightarrow X_j \nu_\tau) = (0.0684 \pm 0.1068)\%, \quad (2.50)$$

which is consistent with 0 within the experimental uncertainty. A unitarity constraint was not used in the fit.

The expected high-statistics data samples that will be accumulated by the Belle-II detector will lead to a new era of precision in  $\tau$  physics [500]. B-Factory experiments such as BaBar, Belle and Belle-II, and future prospects at Super Tau Charm Factory, LHC, EIC and FCC-ee experiments have the potential to discover New Physics via charged lepton flavor violation in the  $\tau$  sector [501]. A nice summary of the progress made by the  $\tau$  physics community and future prospects can be found in Ref. [502].

# Chapter 3

## Effective-field theory analysis of the

## $\tau^- \rightarrow \pi^- \pi^0 \nu_\tau$ decays

### 3.1 Introduction

Early studies of nuclear beta decays and, particularly, the problem of apparent non-conservation of energy and violation of the spin-statistics theorem lead to Pauli's postulation of the neutrino. Soon after, Fermi proposed a theory [503] describing these decays which was inspired by QED's vector current interaction which, however, was of a local current-current type. This was the first step towards establishing the V-A nature of the weak force and understanding its maximal parity violation. Now the original Fermi theory is regarded as one of the possible contributions of dimension six effective operators to these decays and it constitutes the basis for effective field theories. In this spirit, not only nuclear beta decays, but also purely leptonic lepton decays, pion decays into a lepton and its corresponding neutrino and also strangeness-changing meson and baryon decays involving a lepton charged current can be studied in a coherent and comprehensive way with direct connection to the underlying theory at some TeVs [187, 192, 504–512]. Thus, it is possible to obtain bounds on non-standard charged current interactions from either of these processes that can be compared among them (assuming lepton universality if necessary). As a result, quite generic New Physics

(NP) is restricted in absence of deviations from the Standard Model (SM) predictions. In the event of any such departures appearing, one would expect them to point to the underlying new dynamics, as (nuclear) beta and muon decays did with the  $W$  mass value (provided the coupling intensity can be estimated from some symmetry argument) and its left-handed couplings.

In Ref. [250] we put forward that semileptonic tau decays are also an interesting scenario in this respect. Particularly, our study of the  $\tau^- \rightarrow \pi^-(\eta/\eta')\nu_\tau$  decays [250] showed that they could be competitive with superallowed nuclear beta decays in restricting scalar non-standard interactions. Our aim in this work is to extend our previous analysis to the  $\tau^- \rightarrow \pi^-\pi^0\nu_\tau$  decays, which should not be sensitive to NP charged current scalar interactions (as generally, they are very suppressed by the small isospin breaking effects giving rise to them in this decay channel [379]) but could instead be very competitive restricting charged-current tensor interactions. The recent letter [512] also addresses this question.

Only if the SM input (and particularly the hadronization) to the considered decays is well under control one can actually set bounds on NP effective couplings. This is the case for the vector and -to a lesser extent- the scalar interactions (where we will follow the treatment in Refs. [513] and [19], respectively) but only a theory-driven approach is possible for the tensor form factor (where we will complement our previous work [250] guided by Refs. [427] and [514]). In all cases it is desirable to fulfill the requirements imposed by the approximate chiral symmetry of QCD, which are automatically enforced in its low-energy effective field theory, Chiral Perturbation Theory ( $\chi PT$ ) [169, 193, 194]. If possible, it is also convenient to use dispersion relations to warrant analyticity and comply with unitarity, at least in the elastic region (for the  $\pi\pi$  system it amounts to  $\sim 1$  GeV). Within this formalism, known short-distance QCD constraints [515, 516] can also be satisfied. In the absence of data (as it the case for the tensor form factor) enlarging the domain of applicability of  $\chi PT$  coupled to tensor sources [517, 518] by including resonances as explicit degrees of freedom [224, 225] could seem useful, although we showed [519] it is not the case here.

This chapter is organized as follows: in section 3.2 we present the basics for an effective

field theory treatment of the considered decays. In section 3.3 the different contributions to the matrix element are identified and the participant meson form factors defined. These are the subject of section 3.4, with a special focus on the tensor form factor. With all SM contributions fixed, we perform a phenomenological study in search for NP signatures, examining the hadron spectrum and branching ratio, the Dalitz plot distributions and the forward-backward asymmetry in section 3.5. The conclusions of this research are summarized in section 3.6.

## 3.2 Effective theory analysis of $\tau^- \rightarrow \nu_\tau \bar{u}d$

For low-energy charged current processes, the effective Lagrangian with  $SU(2) \otimes U(1)$  invariant dimension six operators <sup>1</sup> reads [504, 505]

$$\mathcal{L}^{(eff)} = \mathcal{L}_{SM} + \frac{1}{\Lambda^2} \sum_i \alpha_i \mathcal{O}_i \quad \rightarrow \quad \mathcal{L}_{SM} + \frac{1}{v^2} \sum_i \hat{\alpha}_i \mathcal{O}_i, \quad (3.1)$$

with  $\hat{\alpha}_i = (v^2/\Lambda^2)\alpha_i$  the dimensionless multi-TeV NP couplings.

If we particularize it for the  $\mathcal{O}(1 \text{ GeV})$  semileptonic strangeness and lepton-flavor conserving <sup>2</sup> charged current transitions involving any lepton ( $\ell = e, \mu, \tau$ ) and only left-handed neutrino fields, the following Lagrangian is obtained (where subscripts L(R) stand for left-(right-)handedness)

$$\begin{aligned} \mathcal{L}_{CC} = & -\frac{4G_F}{\sqrt{2}} \left[ (1 + [v_L]_{\ell\ell}) \bar{\ell}_L \gamma_\mu \nu_{\ell L} \bar{u}_L \gamma^\mu d_L + [v_R]_{\ell\ell} \bar{\ell}_L \gamma_\mu \nu_{\ell L} \bar{u}_R \gamma^\mu d_R \right. \\ & + [s_L]_{\ell\ell} \bar{\ell}_R \nu_{\ell L} \bar{u}_R d_L + [s_R]_{\ell\ell} \bar{\ell}_R \nu_{\ell L} \bar{u}_L d_R \\ & \left. + [t_L]_{\ell\ell} \bar{\ell}_R \sigma_{\mu\nu} \nu_{\ell L} \bar{u}_R \sigma^{\mu\nu} d_L \right] + h.c. . \end{aligned} \quad (3.2)$$

In the previous equation  $G_F$  is the tree-level definition of the Fermi constant and  $\sigma^{\mu\nu} \equiv i[\gamma^\mu, \gamma^\nu]/2$ . The SM Lagrangian is recovered setting  $v_{L,R} = s_{L,R} = t_L = 0$ . Heavy degrees

<sup>1</sup>See in Refs. [1, 130] the most general effective Lagrangian including SM fields.

<sup>2</sup>An EFT framework study of strangeness-changing processes is carried out in Refs. [507, 509, 510].



of freedom (H,  $W^\pm$  and  $Z$  bosons plus  $c$ ,  $b$  and  $t$  quarks) have been integrated out to obtain Eq. (3.2). The effective couplings  $v_{L,R}$ ,  $s_{L,R}$  and  $t_L$  generated by the NP can be taken real since we are only interested in  $CP$  conserving quantities <sup>3</sup>.

Although observables are renormalization scale and scheme independent, this scale independence comes after the cancellation of the scale dependence of the effective couplings ( $v_{L,R}$ ,  $s_{L,R}$  and  $t_L$ ) by the corresponding scale dependence of the hadronic matrix elements. These encode the amplitude for the quark current to produce/annihilate the measured hadrons. As it conventional, we select  $\mu = 2 \text{ GeV}$  as the renormalization scale.

It is advantageous to shift our basis for the spin-zero currents so that the new ones have defined parity. This is achieved by means of introducing  $\epsilon_S = s_L + s_R$  and  $\epsilon_P = s_L - s_R$ . Although the other elements in the basis of currents remain unmodified, we also rename them to avoid any confusion between both bases:  $\epsilon_{R,L} = v_{L,R}$  and  $\epsilon_T = t_L$ .

One can proceed with  $\ell = e, \mu, \tau$  in full generality (which may be profitable if lepton universality is an approximate symmetry). We focus now on the tau case (and omit the corresponding flavor subindex in the following), in such a way that the corresponding semileptonic effective Lagrangian is:

$$\begin{aligned} \mathcal{L}_{CC} = & -\frac{G_F}{\sqrt{2}} V_{ud} (1 + \epsilon_L + \epsilon_R) \{ \bar{\tau} \gamma_\mu (1 - \gamma^5) \nu_\tau \bar{u} [\gamma^\mu - (1 - 2\hat{\epsilon}_R) \gamma^\mu \gamma^5] d \\ & + \bar{\tau} (1 - \gamma^5) \nu_\tau \bar{u} (\hat{\epsilon}_S - \hat{\epsilon}_P \gamma^5) d \\ & + 2\hat{\epsilon}_T \bar{\tau} \sigma_{\mu\nu} (1 - \gamma^5) \nu_\tau \bar{u} \sigma^{\mu\nu} d \} + h.c., \end{aligned} \quad (3.3)$$

where  $\hat{\epsilon}_i \equiv \epsilon_i / (1 + \epsilon_L + \epsilon_R)$  for  $i = R, S, P, T$ . From this expression it is easily seen that, working at linear order in the  $\hat{\epsilon}_i$ , one is insensitive to non-standard spin-one charged current interactions because the overall dependence on  $\epsilon_L + \epsilon_R$  cannot be isolated, as it is subsumed in the determination of  $G_F$ . That is, conveniently normalized rates cancel the overall factor  $(1 + \epsilon_L + \epsilon_R)$  in the previous equation. We note that, at linear order in the  $\hat{\epsilon}_i$ 's, these agree with Ref. [505].

---

<sup>3</sup>Appendix A in Ref. [505] provides with these couplings as functions of the  $\hat{\alpha}_i$  couplings.

### 3.3 Semileptonic $\tau$ decay amplitude

From now on, we will study the semileptonic  $\tau^- \rightarrow \pi^-(P_{\pi^-}) \pi^0(P_{\pi^0}) \nu_\tau(P')$  decays, where pions parity determines that only scalar, vector and tensor currents contribute. The decay amplitude reads<sup>4</sup>

$$\begin{aligned} \mathcal{M} &= \mathcal{M}_V + \mathcal{M}_S + \mathcal{M}_T \\ &= \frac{G_F V_{ud} \sqrt{S_{EW}}}{\sqrt{2}} (1 + \epsilon_L + \epsilon_R) \left[ L_\mu H^\mu + \hat{\epsilon}_S L H + 2\hat{\epsilon}_T L_{\mu\nu} H^{\mu\nu} \right], \end{aligned} \quad (3.4)$$

where the following lepton currents were introduced:

$$L_\mu = \bar{u}(P') \gamma^\mu (1 - \gamma^5) u(P), \quad (3.5a)$$

$$L = \bar{u}(P') (1 + \gamma^5) u(P), \quad (3.5b)$$

$$L_{\mu\nu} = \bar{u}(P') \sigma_{\mu\nu} (1 + \gamma^5) u(P). \quad (3.5c)$$

The scalar ( $H$ ), vector ( $H^\mu$ ) and tensor ( $H^{\mu\nu}$ ) hadron matrix elements entering Eq. (3.4) can be decomposed using Lorentz invariance and discrete QCD symmetries in terms of a number of allowed Lorentz structures times the corresponding form factors, which are scalar functions encoding the hadronization procedure. Specifically, these are

$$H = \langle \pi^0 \pi^- | \bar{d} u | 0 \rangle \equiv F_S(s), \quad (3.6a)$$

$$H^\mu = \langle \pi^0 \pi^- | \bar{d} \gamma^\mu u | 0 \rangle = C_V Q^\mu F_+(s) + C_S \left( \frac{\Delta_{\pi^- \pi^0}}{s} \right) q^\mu F_0(s), \quad (3.6b)$$

$$H^{\mu\nu} = \langle \pi^0 \pi^- | \bar{d} \sigma^{\mu\nu} u | 0 \rangle = i F_T(s) (P_{\pi^0}^\mu P_{\pi^-}^\nu - P_{\pi^-}^\mu P_{\pi^0}^\nu). \quad (3.6c)$$

In the previous equations, the momentum of the meson system is  $q^\mu = (P_{\pi^-} + P_{\pi^0})^\mu$ , with  $s = q^2$ . We also introduced  $Q^\mu = (P_{\pi^-} - P_{\pi^0})^\mu + (\Delta_{\pi^0 \pi^-} / s) q^\mu$ , and  $\Delta_{\pi^0 \pi^-} = m_{\pi^0}^2 - m_{\pi^-}^2$ .

---

<sup>4</sup>As in Ref. [250], we take the short-distance electroweak radiative corrections encoded in  $S_{EW}$  [256, 274, 364, 365, 520–523] as a global factor in Eq. (3.4). Although  $S_{EW}$  does not affect the scalar and tensor contributions, the error of this approximation is negligible and renders simpler expressions than proceeding otherwise.

Clebsch-Gordan flavor coefficients are  $C_S = C_V = \sqrt{2}$  for this decay channel.

The  $F_S(s)$  and  $F_0(s)$  form factors can be related by taking the divergence of the vector current via

$$F_S(s) = C_S \frac{\Delta_{\pi^-\pi^0}}{(m_d - m_u)} F_0(s). \quad (3.7)$$

As in Ref. [250], the scalar contribution can be absorbed into the vector current amplitude.

This can be achieved by replacing

$$C_S \frac{\Delta_{\pi^-\pi^0}}{s} \longrightarrow C_S \frac{\Delta_{\pi^-\pi^0}}{s} \left[ 1 + \frac{s \hat{\epsilon}_S}{m_\tau(m_d - m_u)} \right], \quad (3.8)$$

in Eq. (3.6b).

Obtaining the  $F_0(s)$ ,  $F_+(s)$  and  $F_T(s)$  form factors is discussed in the following section.

### 3.4 Hadronization of the scalar, vector and tensor currents

Lorentz invariance, together with the discrete symmetries of the strong interactions, determine Eqs. (3.6a) to (3.6c). QCD dynamics is encoded in these hadron matrix elements, although it is not possible to determine them using the Lagrangian of the underlying theory unambiguously. Nevertheless, QCD properties are useful in restricting this hadronic input. On the one hand, it is desirable to keep the properties derived from the (very approximate) chiral symmetry of low-energy QCD and from asymptotic strong interactions, where known. On the other, using dispersion relations is ideal to warrant the correct analytic structure of the amplitudes and to comply with unitarity (at least in the elastic region). These properties will be exploited in what follows, as we will briefly review.

As shown in Ref. [513], the scalar form factor  $F_0(s)$  can be determined in an essentially model-independent way in the low-energy region, though it does not involve resonance contributions to first order in isospin breaking. The S-wave  $\pi^-\pi^0$  system must have isospin

$I = 2$ . Watson's final-state interactions theorem [524] ensures that -in the elastic region- the phase of the di-meson form factor with definite angular momentum ( $L$ ) and isospin ( $I$ ) coincides with the corresponding meson-meson scattering phase shift having the same  $L$  and  $I$  values ( $L = 0$  and  $I = 2$  in our case, so this phase shift is  $\delta_0^2(s)$  according to the usual notation). Neglecting inelastic effects (that is a good approximation up to  $s \sim 1 \text{ GeV}^2$  in this case), the required di-pion scalar form factor can be obtained [513] by means of a phase dispersive representation ( $F_0(0) = 1$  has been used)

$$F_0(s) = \exp \left\{ \frac{s}{\pi} \int_{4m_\pi^2}^{\infty} ds' \frac{\delta_0^2(s')}{s'(s' - s - i\epsilon)} \right\}, \quad (3.9)$$

since the phase shift  $\delta_0^2(s)$  has been measured [525, 526].  $|F_0(s)|$  and  $\delta_0^2(s)$  are plotted in the upper panel of Fig. 12 in Ref. [513]. As expected, there is no hint of resonance dynamics in  $F_0(s)$ .

The vector form factor,  $F_+(s)$ , is known with great accuracy, both theoretically and experimentally. In absence of new-physics interactions, it can be extracted directly from  $\tau^- \rightarrow \pi^- \pi^0 \nu_\tau$  data (since the scalar form factor is negligible up to second-order isospin-violating corrections [379], which are tiny). The di-pion invariant mass spectrum in these decays has been most precisely measured by the Belle Collaboration [365] (it was earlier obtained by the CLEO [12], and ALEPH [397] and OPAL [527] LEP collaborations).  $F_+(s)$  can also be accessed -through a CVC violating correction [94, 379]- via  $e^+e^- \rightarrow \pi^+\pi^-$  cross-section data at low energies, which has been measured very precisely by BaBar [20], BES-III [59], CMD-2 [53], KLOE-2 [88] and SND [52, 54]. Finally, in the elastic region ( $s \lesssim 1 \text{ GeV}^2$ ),  $F_+(s)$  is related via unitarity with the spin-one isospin-one  $\pi\pi$  scattering amplitude, for which accurate measurements have been performed [528–530]. All previous measurements correspond to the  $s > 0$  region,  $e^- \pi$  scattering [14] probes  $F_+(s < 0)$ .

Theoretically,  $F_+(s)$  is well-constrained at low-energies by  $\chi PT$  [169, 193, 194] and in the asymptotic regime by short-distance QCD results [515, 516]. In the intermediate energy ( $\mathcal{O}(1) \text{ GeV}$ ) region, resonance dynamics is needed to interpolate between the two former

limits. An adequate tool to connect all energy ranges taking advantage of analyticity and unitarity constraints on  $F_+(s)$  are the dispersion relations, which have been employed widely in this context (see i. e. Ref. [19] and references therein). We will not discuss at length the procedure here, but only recall that an excellent description of the data can be achieved with three subtractions (one is used to set  $F_+(0) = 1$ )

$$F_+(s) = \exp \left[ \alpha_1 s + \frac{\alpha_2}{2} s^2 + \frac{s^3}{\pi} \int_{4m_\pi^2}^{\infty} ds' \frac{\delta_1^1(s')}{(s')^3 (s' - s - i\epsilon)} \right], \quad (3.10)$$

being  $\alpha_{1,2}$  the remaining subtraction constants, to be fitted to low-energy data, and  $\delta_1^1(s)$  the relevant phase shift. In Ref. [19],  $\delta_1^1(s)$  is given (below the  $\rho'$  resonance region), in terms of the  $\rho(770)$  pole position and the pion decay constant,  $F_\pi$ . Its description in the  $[M_{\rho'} \lesssim \sqrt{s} \leq M_\tau]$  interval depends on the  $\rho'$  and  $\rho''$  properties. We will use this framework in what follows. The central values of the modulus and phase of  $F_+(s)$  are plotted and compared to data in Figs. 1 and 2 in Ref. [19]. We will use the best fit results corresponding to case III in this reference, which includes first-order isospin breaking corrections. Both statistical and systematic uncertainties on  $F_+(s)$  are taken into account throughout our numerical analysis.

Although it is difficult to constrain the hadronization of the tensor current, Eq. (3.6c), from first principles, this would be desirable as it turns out that the  $\tau^- \rightarrow \pi^- \pi^0 \nu_\tau$  decays have the potential to set competitive bounds on (non-standard) charged current tensor interactions. This is in contrast with the  $\tau^- \rightarrow \pi^- \eta^{(\prime)} \nu_\tau$  decays explored in Ref. [250], which are competitive for new scalar contributions but not for tensor ones, which justified using leading-order  $\chi PT$  results for Eq. (3.6c) in that analysis. Unfortunately, there is no experimental data that can guide us in building  $F_T(s)$ , so we will rely only on theory to accomplish this task.

Since  $s$  can vary from the two-pion threshold up to  $M_\tau^2$ , light resonances contribution (giving the energy dependence of the form factor) should be included in a refined analysis, as we intend. We show in the appendix of Ref. [519] that, for  $F_T(s)$ , it is not convenient

to extend the energy range of applicability of  $\chi PT$  by including the resonances as explicit degrees of freedom, in the so-called Resonance Chiral Theory [224]. Instead, it will be more appropriate to use a dispersive construction of  $F_T(s)$  taking advantage of unitarity constraints on its phase [427].  $F_T(0)$  will be studied within  $\chi PT$  in the following.

The lowest-order  $\chi PT$  Lagrangian with tensor sources, which is  $\mathcal{O}(p^4)$  in the chiral counting [518], includes only four operators. Among them, only the one with coefficient  $\Lambda_2$  contributes to the studied decays:

$$\mathcal{L} = \Lambda_1 \langle t_+^{\mu\nu} f_{+\mu\nu} \rangle - i\Lambda_2 \langle t_+^{\mu\nu} u_\mu u_\nu \rangle + \dots \quad (3.11)$$

In the preceding equation,  $t_+^{\mu\nu} = u^\dagger t^{\mu\nu} u^\dagger + u t^{\mu\nu\dagger} u$  and  $\langle \dots \rangle$  means a flavor space trace. Operators in Eq. (3.11) are built with chiral tensors [531], with three of them entering the displayed operators:

- $u_\mu = i \left[ u^\dagger (\partial_\mu - i r_\mu) u - u (\partial_\mu - i \ell_\mu) u^\dagger \right]$ , which includes the left- and right-handed sources,  $\ell_\mu$  and  $r_\mu$ .
- The chiral tensor sources  $t^{\mu\nu}$  and its adjoint, and
- $f_+^{\mu\nu} = u F_L^{\mu\nu} u^\dagger + u^\dagger F_R^{\mu\nu} u$ , including the left- and right-handed field-strength tensors,  $F_L^{\mu\nu}$  and  $F_R^{\mu\nu}$ , given in terms of  $\ell^\mu$  and  $r^\mu$ .

Let us recall the non-linear representation of the pseudo Goldstone bosons, given by  $u = \exp \left[ \frac{i}{\sqrt{2}F} \phi \right]$  [532, 533], where (for two flavors)

$$\phi = \begin{pmatrix} \frac{\pi^0}{\sqrt{2}} & \pi^+ \\ \pi^- & -\frac{\pi^0}{\sqrt{2}} \end{pmatrix}, \quad (3.12)$$

$F$  being the pion decay constant in the chiral limit,  $F \sim F_\pi \sim 92$  MeV. All resonance multiplets considered below have analogous flavor structure to Eq. (3.12).

The tensor source ( $\bar{t}^{\mu\nu}$ ) is related to its chiral projections ( $t^{\mu\nu}$  and  $t^{\mu\nu\dagger}$ ) by means of [518]

$$t^{\mu\nu} = P_L^{\mu\nu\lambda\rho} \bar{t}_{\lambda\rho}, \quad 4P_L^{\mu\nu\lambda\rho} = (g^{\mu\lambda}g^{\nu\rho} - g^{\mu\rho}g^{\nu\lambda} + i\epsilon^{\mu\nu\lambda\rho}), \quad (3.13)$$

where  $\bar{\Psi}\sigma_{\mu\nu}\bar{t}^{\mu\nu}\Psi$  is the tensor quark current.

From Eq. (3.11) it can be shown [250] that, in the limit of isospin symmetry <sup>5</sup>,

$$i \left\langle \pi^- \pi^0 \left| \frac{\delta \mathcal{L}_{\chi PT}^{\mathcal{O}(p^4)}}{\delta \bar{t}_{\alpha\beta}} \right| 0 \right\rangle = \frac{\sqrt{2}\Lambda_2}{F^2} (p_{\pi^-}^\alpha p_{\pi^0}^\beta - p_{\pi^0}^\alpha p_{\pi^-}^\beta). \quad (3.14)$$

We show in Appx. A that it is not convenient to include the energy-dependence of the tensor form factor by extending  $\chi PT$  [169, 193, 194] including resonances [224, 225].

Ref. [514] evaluated  $f_T(0) = 2m_\pi F_T(0)$  on the lattice. Their result,  $f_T(0) = 0.195 \pm 0.010$  yields  $\Lambda_2 = (12.0 \pm 0.6)$  MeV, that we will use in the following. This value of  $\Lambda_2$  is roughly a factor three smaller than the prediction for  $\Lambda_1$  obtained using short-distance QCD properties [517],  $\Lambda_1 = (33 \pm 2)$  MeV. Since both operators displayed in Eq. (3.11) have the same chiral counting order, one would have guessed  $\Lambda_2 \sim \Lambda_1$ , resulting in an overestimation of  $\Lambda_2$ , as in Ref. [250] <sup>6</sup>.

We will follow Ref. [427] and obtain  $F_T(s)$  using again a phase dispersive representation. As shown in Ref. [427], the tensor form factor phase equals the vector form factor phase,  $\delta_T(s) = \delta_+(s)$ , in the elastic region. We will use the previous equation also above the onset of inelasticities in our dispersion relation

$$\frac{F_T(s)}{F_T(0)} = \exp \left\{ \frac{s}{\pi} \int_{4m_\pi^2}^{\infty} ds' \frac{\delta_T(s')}{s'(s' - s - i\epsilon)} \right\}, \quad (3.15)$$

and fix  $F_T(0) = \frac{\sqrt{2}\Lambda_2}{F^2}$  according to the leading-order  $\chi PT$  result. We plot in figure 3.1 the modulus and phase of  $F_T(s)$  obtained using Eq. (3.15). The different curves on the left

<sup>5</sup>Since  $F_T(s)$ , as given by Eq. (3.14), is purely real and the sign of  $\Lambda_2$  was unknown, a factor  $i$  was absorbed redefining  $F_T(s)$  in Ref. [250]. As we consider a non-vanishing tensor form factor phase (see Eq.(3.15) and related discussion), we will not follow this procedure in the present analysis.

<sup>6</sup>Fortunately, since the  $\tau^- \rightarrow \eta^{(\prime)}\pi^-\nu_\tau$  decays are quite insensitive to tensor interactions, this does not change the limits obtained in this paper for  $\hat{\epsilon}_S$ .

panel are obtained for  $s_{max} = M_\tau^2$ , 4 and 9 GeV<sup>2</sup> <sup>7</sup> and we will take this range for  $F_T(s)$  as an estimate of our corresponding error (our plots will be given for  $s_{max} = 4$  GeV<sup>2</sup> in the following). We neglect the uncertainty associated to our ignorance on the inelasticities affecting  $\delta_T(s)$  (see the related discussion in Ref. [427]), which are small below  $\sqrt{s} = 1.3$  GeV.

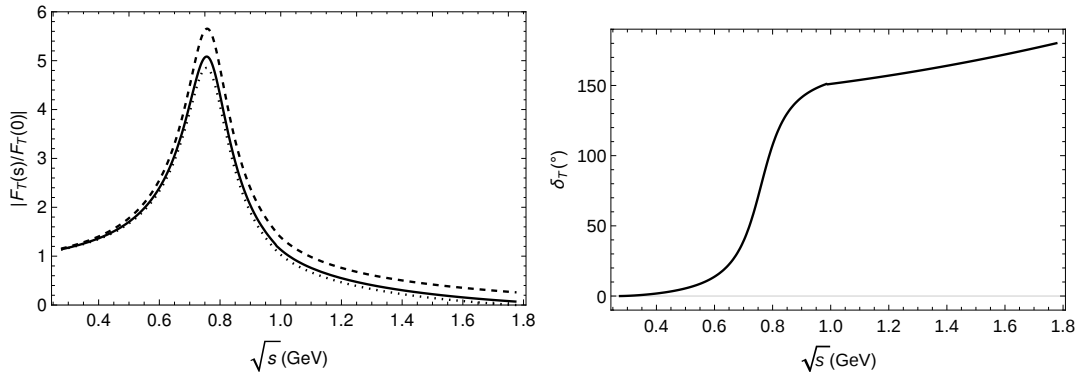


Figure 3.1: Modulus and phase,  $|F_T(s)|$  (left) and  $\delta_T(s)$  (right), of the tensor form factor,  $F_T(s)$ , corresponding to Eq. (3.15).

### 3.5 Decay Observables

In order to study possible NP effects in these decays, one should use not only the hadronic spectrum and branching ratio, but also Dalitz plot distributions and the measurable forward-backward asymmetry. In this section, we focus in the study of the possible effects of the non-standard effective couplings described in section 3.2 in these  $\tau^- \rightarrow \pi^- \pi^0 \nu_\tau$  decay observables. We will start with the Dalitz plots (which should contain more dynamical information, as no integration over any of the two independent kinematical variables has been performed) and move later on to (partially) integrated observables: differential decay rate as function of the di-meson invariant mass, forward-backward asymmetry and, finally, branching ratio.

<sup>7</sup>The parameter  $s_{max}$  corresponds to the cutoff of the dispersive integral. The unphysical dependence on it is a consequence of the dispersion relation (3.15) being once-subtracted. Additional subtractions would reduce the artificial dependence on  $s_{max}$ . However, since we lack low-energy information to fix these subtraction constants, we cannot follow this procedure. Taking this into account, we restrict the  $s_{max}$  values in the previously quoted range.



The differential decay width of the  $\tau^- \rightarrow \pi^- \pi^0 \nu_\tau$  decays, in the  $\tau$  lepton rest frame, is

$$\frac{d^2\Gamma}{ds dt} = \frac{1}{32(2\pi)^3 M_\tau^3} \overline{|\mathcal{M}|^2}, \quad (3.16)$$

where  $\overline{|\mathcal{M}|^2}$  represents the unpolarized spin-averaged squared matrix element,  $s$  being the  $\pi^0 \pi^-$  system invariant mass, limited in the interval  $(m_{\pi^0} + m_{\pi^-})^2 \leq s \leq M_\tau^2$  and  $t = (p' + p_{\pi^0})^2 = (p - p_{\pi^-})^2$  with  $t^-(s) \leq t \leq t^+(s)$ , where

$$t^\pm(s) = \frac{1}{2s} \left[ 2s(M_\tau^2 + m_{\pi^0}^2 - s) - (M_\tau^2 - s)(s + m_{\pi^-}^2 - m_{\pi^0}^2) \pm (M_\tau^2 - s) \sqrt{\lambda(s, m_{\pi^-}^2, m_{\pi^0}^2)} \right], \quad (3.17)$$

and  $\lambda(x, y, z) = x^2 + y^2 + z^2 - 2xy - 2xz - 2yz$  is the usual Kallen function.

### 3.5.1 Dalitz plot

Including possible non-standard weak charged current interactions, the unpolarized spin-averaged squared amplitude yields <sup>8</sup>

$$\overline{|\mathcal{M}|^2} = \frac{G_F^2 |V_{ud}|^2 S_{EW}}{s^2} (1 + \epsilon_L + \epsilon_R)^2 [M_{00} + M_{++} + M_{0+} + M_{T+} + M_{T0} + M_{TT}], \quad (3.18)$$

---

<sup>8</sup>We note a typo writing the corresponding equation, (22), of Ref. [250], where the factor 2 should not appear. All subsequent expressions and the numerical results of Ref. [250] are not affected by this typo.

where the scalar, vector and tensor squared amplitudes are  $M_{00}$ ,  $M_{++}$  and  $M_{TT}$ , respectively. Their corresponding interferences are denoted  $M_{0+}$ ,  $M_{T+}$ ,  $M_{T0}$ . All these read <sup>9</sup>

$$\begin{aligned}
M_{0+} &= 2C_V C_S m_\tau^2 \text{Re} [F_+(s)F_0^*(s)] \Delta_{\pi^-\pi^0} \left( 1 + \frac{s\hat{\epsilon}_S}{m_\tau(m_d - m_u)} \right) \\
&\quad \times \left\{ s \left( m_\tau^2 - s - 2t + \Sigma_{\pi^-\pi^0} \right) - m_\tau^2 \Delta_{\pi^-\pi^0} \right\}, \\
M_{T+} &= 4C_V \hat{\epsilon}_T m_\tau^3 s \text{Re} [F_T(s)F_+^*(s)] \left( 1 - \frac{s}{m_\tau^2} \right) \lambda(s, m_{\pi^-}^2, m_{\pi^0}^2), \\
M_{T0} &= 4C_S \Delta_{\pi^-\pi^0} \hat{\epsilon}_T m_\tau s \text{Re} [F_T(s)F_0^*(s)] \left( 1 + \frac{s\hat{\epsilon}_S}{m_\tau(m_d - m_u)} \right) \\
&\quad \times \left\{ s \left( m_\tau^2 - s - 2t + \Sigma_{\pi^-\pi^0} \right) - m_\tau^2 \Delta_{\pi^-\pi^0} \right\}, \\
M_{00} &= C_S^2 (\Delta_{\pi^-\pi^0})^2 m_\tau^4 \left( 1 - \frac{s}{m_\tau^2} \right) |F_0(s)|^2 \left( 1 + \frac{s\hat{\epsilon}_S}{m_\tau(m_d - m_u)} \right)^2, \\
M_{++} &= C_V^2 |F_+(s)|^2 \left\{ m_\tau^4 (s - \Delta_{\pi^-\pi^0})^2 - m_\tau^2 s [s(s + 4t) - 2\Delta_{\pi^-\pi^0} (s + 2t - \Sigma_{\pi^-\pi^0}) + (\Delta_{\pi^-\pi^0})^2] \right. \\
&\quad \left. + 4m_{\pi^-}^2 s^2 (m_{\pi^0}^2 - t) + 4s^2 t (s + t - m_{\pi^0}^2) \right\}, \\
M_{TT} &= 4\hat{\epsilon}_T^2 |F_T(s)|^2 s^2 \left\{ m_{\pi^-}^4 (m_\tau^2 - s) - 2m_{\pi^-}^2 (m_\tau^2 - s) (s + 2t - m_{\pi^0}^2) - m_{\pi^0}^4 (3m_\tau^2 + s) \right. \\
&\quad \left. + 2m_{\pi^0}^2 [(s + m_\tau^2)(s + 2t) - 2m_\tau^4] - s [(s + 2t)^2 - m_\tau^2 (s + 4t)] \right\},
\end{aligned} \tag{3.19}$$

where the familiar definitions  $\Delta_{\pi^-\pi^0} = m_{\pi^-}^2 - m_{\pi^0}^2$  and  $\Sigma_{\pi^-\pi^0} = m_{\pi^-}^2 + m_{\pi^0}^2$  were employed. Noteworthy, the scalar form factor is always suppressed by  $\Delta_{\pi^-\pi^0}$ , which is tiny, in the previous equations for  $M_{00}$ ,  $M_{T0}$  and  $M_{0+}$ . This makes its effect negligible even for  $|\hat{\epsilon}_S| \sim 1$  (radiative pion decay limits  $|\hat{\epsilon}_S| \lesssim 0.01$  and, under the reasonable assumption of lepton flavor universality, this limit should also apply for the tau flavor considered here).

We now turn to analyze possible NP signatures in Dalitz plots distributions. The left panel of figure 3.2 shows the squared matrix element  $|\overline{\mathcal{M}}|_{00}^2$  in the (s,t) plane, which is obtained using the SM predictions for  $\tau^- \rightarrow \pi^-\pi^0\nu_\tau$  form factors [19, 513]. The  $\rho(770)$

---

<sup>9</sup>Comparing Eqs. (3.6a) to (3.6c) to their analogs in Ref. [250], it can be verified that Eqs. (3.19) agree with the corresponding expressions in Ref. [250].

meson dominance of the dynamics is clearly seen in this plot.

In order to better appreciate the modifications induced by non-vanishing  $\hat{\epsilon}_{S,T}$  in Dalitz plots, we introduce the observable

$$\tilde{\Delta}(\hat{\epsilon}_S, \hat{\epsilon}_T) = \frac{\left| |\mathcal{M}(\hat{\epsilon}_S, \hat{\epsilon}_T)|^2 - |\mathcal{M}(0, 0)|^2 \right|}{|\mathcal{M}(0, 0)|^2}. \quad (3.20)$$

In the left panel of figures 3.3 and 3.4,  $\tilde{\Delta}(\hat{\epsilon}_S, \hat{\epsilon}_T)$  (3.20) is shown for two representative values of the set of  $(\hat{\epsilon}_S, \hat{\epsilon}_T)$  parameters that are consistent with the  $\text{Br}(\tau^- \rightarrow \pi^- \pi^0 \nu_\tau)$  (obtaining these limits will be discussed in subsection 3.5.5). Although  $\mathcal{O}(1)$  effects are seen in fig. 3.3, these are not realistic since two-pion tau decays are almost insensitive to  $\hat{\epsilon}_S$ . Indeed, when  $\hat{\epsilon}_S$  is taken from more adequate processes [250, 504, 505, 512], the left panel of fig. 3.5 shows that only a measurement of  $\tilde{\Delta}$  with  $\lesssim 1\%$  uncertainty could distinguish these new physics effects. In the left plot of fig. 3.4 (with  $(\hat{\epsilon}_S = 0, \hat{\epsilon}_T = -0.014)$ ) the deviations with respect to the SM are around 15% in a given region, but the left plot in figure 3.6 (obtained using our best fit value for  $\hat{\epsilon}_T$  in section 3.5.5) reduces the size of this signal to a 1% effect. These  $\mathcal{O}(1\%)$  effects would be difficult to measure, even at Belle-II [500]. Our uncertainties do not affect the conclusions drawn in this paragraph.

### 3.5.2 Angular distribution

The hadronic mass and angular distributions are also modified by the generic new effective interactions that we are studying and can have different sensitivity to  $\hat{\epsilon}_S$  and  $\hat{\epsilon}_T$ . The rest frame of the hadronic system is convenient for this analysis. It is defined by  $\vec{p}_{\pi^-} + \vec{p}_{\pi^0} = \vec{p}_\tau - \vec{p}_\nu = 0$ . In this frame, the charged particle energies are given by  $E_\tau = (s + M_\tau^2)/2\sqrt{s}$  and  $E_{\pi^-} = (s + m_{\pi^-}^2 - m_{\pi^0}^2)/2\sqrt{s}$ . The measurable angle  $\theta$  between these two particles can be obtained from the invariant  $t$  variable by means of  $t = m_{\pi^-}^2 + m_\tau^2 - 2E_\tau E_{\pi^-} + 2|\vec{p}_{\pi^-}| |\vec{p}_\tau| \cos \theta$ , with  $|\vec{p}_a| = \sqrt{E_a^2 - m_a^2}$  for  $a = \pi^-, \tau^-$ .

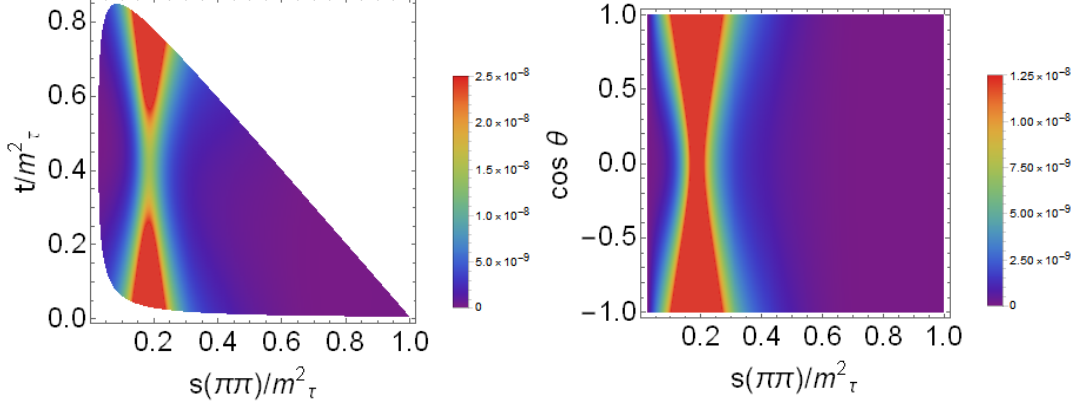


Figure 3.2: Dalitz plot distribution  $\overline{|\mathcal{M}|^2}_{00}$  in the SM, Eq. (3.18): Differential decay distribution for  $\tau^- \rightarrow \pi^- \pi^0 \nu_\tau$  in the  $(s, t)$  variables (left). The right-hand figure shows the differential decay distribution in the  $(s, \cos \theta)$  variables, Eq. (3.21). The Mandelstam variables,  $s$  and  $t$ , are normalized to  $M_\tau^2$ .

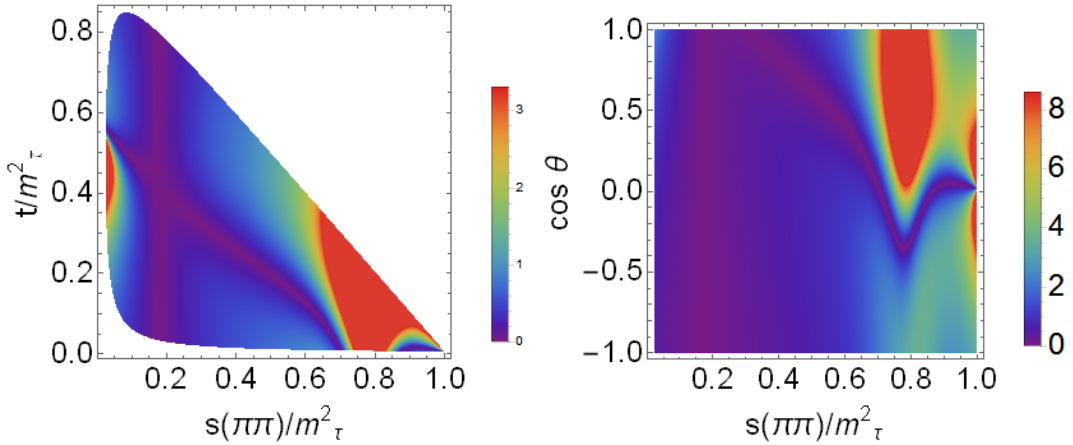


Figure 3.3: Dalitz plot distribution for  $\tilde{\Delta}(\hat{e}_S, \hat{e}_T)$ , (3.20), in the  $\tau^- \rightarrow \pi^- \pi^0 \nu_\tau$  decays: left-hand side corresponds to Eq. (3.18) and right-hand side corresponds to the differential decay distribution in the  $(s, \cos \theta)$  variables, both with  $(\hat{e}_S = 1.31, \hat{e}_T = 0)$ . The Mandelstam variables,  $s$  and  $t$ , are normalized to  $M_\tau^2$ .

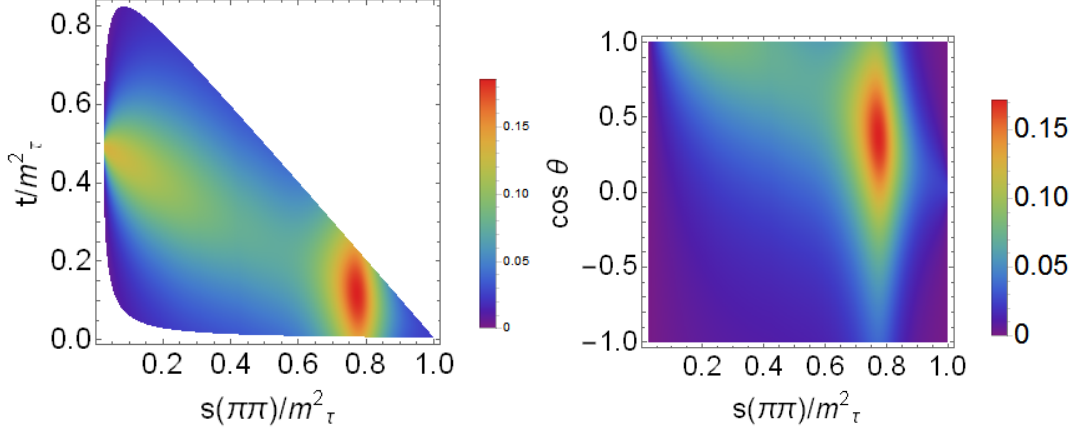


Figure 3.4: Dalitz plot distribution for  $\tilde{\Delta}(\hat{\epsilon}_S, \hat{\epsilon}_T)$ , (3.20), in the  $\tau^- \rightarrow \pi^- \pi^0 \nu_\tau$  decays: left-hand side corresponds to Eq. (3.18) and right-hand side corresponds to the differential decay distribution in the  $(s, \cos \theta)$  variables, both with  $(\hat{\epsilon}_S = 0, \hat{\epsilon}_T = -0.014)$ . The Mandelstam variables,  $s$  and  $t$ , are normalized to  $M_\tau^2$ .

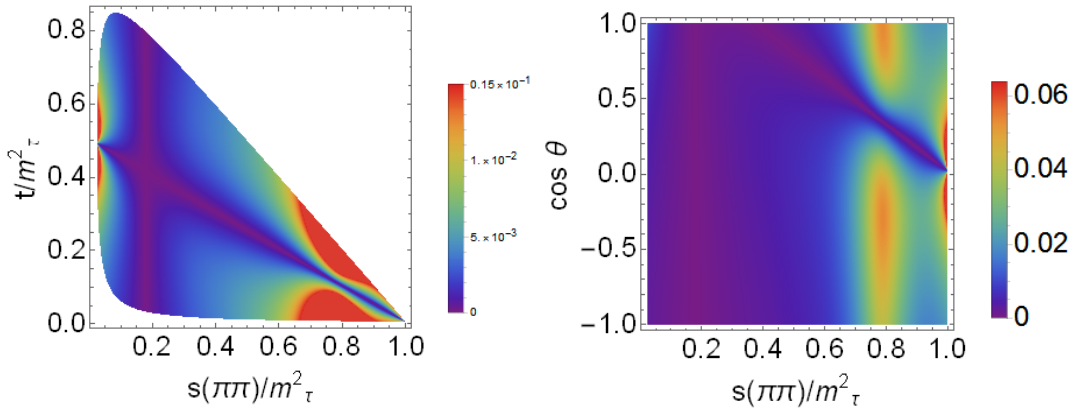


Figure 3.5: Dalitz plot distribution for  $\tilde{\Delta}(\hat{\epsilon}_S, \hat{\epsilon}_T)$ , (3.20), in the  $\tau^- \rightarrow \pi^- \pi^0 \nu_\tau$  decays: left-hand side corresponds to Eq. (3.18) and right-hand side corresponds to the differential decay distribution in the  $(s, \cos \theta)$  variables, both with  $(\hat{\epsilon}_S = 0.008, \hat{\epsilon}_T = 0)$ . The Mandelstam variables,  $s$  and  $t$ , are normalized to  $M_\tau^2$ .

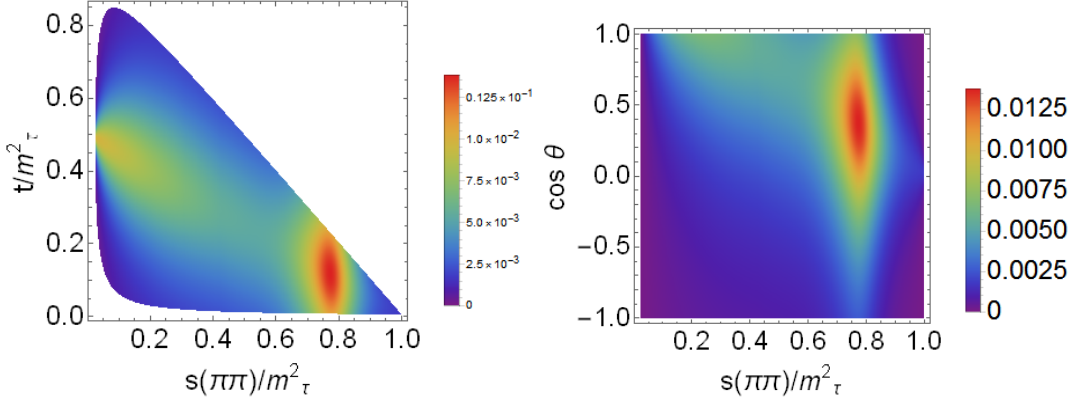


Figure 3.6: Dalitz plot distribution for  $\tilde{\Delta}(\hat{\epsilon}_S, \hat{\epsilon}_T)$ , (3.20), in the  $\tau^- \rightarrow \pi^- \pi^0 \nu_\tau$  decays: left-hand side corresponds to Eq. (3.18) and right-hand side corresponds to the differential decay distribution in the  $(s, \cos \theta)$  variables, both with  $(\hat{\epsilon}_S = 0, \hat{\epsilon}_T = -0.001)$ . The Mandelstam variables,  $s$  and  $t$ , are normalized to  $M_\tau^2$ .

The Dalitz decay distribution in the  $(s, \cos \theta)$  variables, for general  $\hat{\epsilon}_S$  and  $\hat{\epsilon}_T$  reads

$$\begin{aligned}
\frac{d^2\Gamma}{d\sqrt{s}d\cos\theta} &= \frac{G_F^2 |V_{ud}|^2 S_{EW}}{128\pi^3 m_\tau} (1 + \epsilon_L + \epsilon_R)^2 \left(\frac{m_\tau^2}{s} - 1\right)^2 |\vec{p}_{\pi^-}| \left\{ C_S^2 (\Delta_{\pi^- \pi^0})^2 |F_0(s)|^2 \right. \\
&\quad \times \left(1 + \frac{s\hat{\epsilon}_S}{m_\tau(m_d - m_u)}\right)^2 + 16|\vec{p}_{\pi^-}|^2 s^2 \left| \frac{C_V}{2m_\tau} F_+(s) + \hat{\epsilon}_T F_T(s) \right|^2 \\
&\quad + 4|\vec{p}_{\pi^-}|^2 s \left(1 - \frac{s}{m_\tau^2}\right) \cos^2 \theta \left[ C_V^2 |F_+(s)|^2 - 4s\hat{\epsilon}_T^2 |F_T(s)|^2 \right] - 4C_S \Delta_{\pi^- \pi^0} |\vec{p}_{\pi^-}| \sqrt{s} \cos \theta \\
&\quad \left. \times \left(1 + \frac{s\hat{\epsilon}_S}{m_\tau(m_d - m_u)}\right) \left[ C_V \text{Re} [F_0(s)F_+^*(s)] + \frac{2s\hat{\epsilon}_T}{m_\tau} \text{Re} [F_T(s)F_0^*(s)] \right] \right\}, \tag{3.21}
\end{aligned}$$

which coincides with the SM result when these two effective NP couplings are set to zero.

The right panel of figure 3.2 shows Eq. (3.21) for  $\pi^- \pi^0$  in the SM case. In the right panel of figures 3.3 and 3.4 the  $(s, \cos \theta)$  distributions for  $\tilde{\Delta}(\hat{\epsilon}_S, \hat{\epsilon}_T)$ , (3.20), are plotted; for the same representative values of  $(\hat{\epsilon}_S, \hat{\epsilon}_T)$  used in order to obtain the left panel of these figures. Again for non-standard scalar interactions, the large effect seen in the left panel of fig. 3.3 is unrealistic and it will be challenging to measure the reduced effect ( $\lesssim 6\%$ ) of fig. 3.5 at Belle-II [500]. For tensor interactions, the deviation from the SM depicted in the right plot of fig. 3.4 could be measurable, but this is not the case for the effect seen in the right plot

of figure 3.6 ( $\lesssim 1\%$ ), obtained using our preferred value for  $\hat{\epsilon}_T$ . Again, our uncertainties do not affect the preceding discussion.

### 3.5.3 Decay rate

The di-pion invariant mass distributions is obtained integrating upon the  $t$  variable in Eq. (3.16)

$$\begin{aligned} \frac{d\Gamma}{ds} = & \frac{G_F^2 |V_{ud}|^2 m_\tau^3 S_{EW}}{384\pi^3 s} (1 + \epsilon_L + \epsilon_R)^2 \left(1 - \frac{s}{m_\tau^2}\right)^2 \lambda^{1/2}(s, m_{\pi^0}^2, m_{\pi^-}^2) \\ & \times \left[ X_{VA} + \hat{\epsilon}_S X_S + \hat{\epsilon}_T X_T + \hat{\epsilon}_S^2 X_{S^2} + \hat{\epsilon}_T^2 X_{T^2} \right], \end{aligned} \quad (3.22)$$

where

$$X_{VA} = \frac{1}{2s^2} \left[ 3|F_0(s)|^2 C_S^2 \Delta_{\pi^-\pi^0}^2 + |F_+(s)|^2 C_V^2 \left(1 + \frac{2s}{m_\tau^2}\right) \lambda(s, m_{\pi^0}^2, m_{\pi^-}^2) \right], \quad (3.23a)$$

$$X_S = \frac{3}{s m_\tau} |F_0(s)|^2 C_S^2 \frac{\Delta_{\pi^-\pi^0}^2}{m_d - m_u}, \quad (3.23b)$$

$$X_T = \frac{6}{s m_\tau} \text{Re} \left[ F_T(s) F_+^*(s) \right] C_V \lambda(s, m_{\pi^0}^2, m_{\pi^-}^2), \quad (3.23c)$$

$$X_{S^2} = \frac{3}{2m_\tau^2} |F_0(s)|^2 C_S^2 \frac{\Delta_{\pi^-\pi^0}^2}{(m_d - m_u)^2}, \quad (3.23d)$$

$$X_{T^2} = \frac{4}{s} |F_T(s)|^2 \left(1 + \frac{s}{2m_\tau^2}\right) \lambda(s, m_{\pi^0}^2, m_{\pi^-}^2). \quad (3.23e)$$

Again, the SM limit is recovered with  $\epsilon_{L,R} = \hat{\epsilon}_{S,T} = 0$ . Figure 3.7 plots the invariant mass distribution of the di-pion system for  $\tau^- \rightarrow \pi^-\pi^0\nu_\tau$  decays. It is almost impossible to distinguish the case of tensor interactions from the SM curve and, although some departure is seen for non-standard scalar interactions, it goes away when realistic values on  $|\hat{\epsilon}_S| \sim 10^{-2}$  [250, 504, 505] are considered.

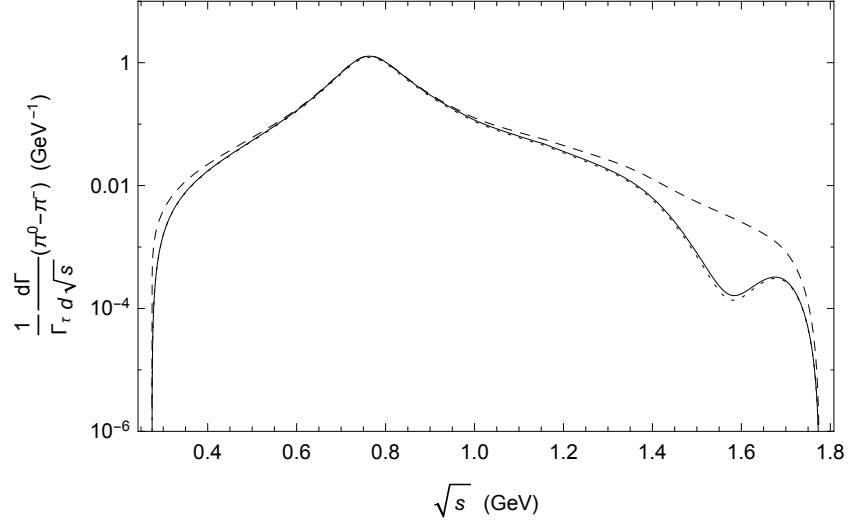


Figure 3.7: The  $\pi^0\pi^-$  hadronic invariant mass distribution for the SM (solid line) and  $\hat{\epsilon}_S = 1.31, \hat{\epsilon}_T = 0$  (dashed line),  $\hat{\epsilon}_S = 0, \hat{\epsilon}_T = -0.014$  (dotted line). Axes units are given in GeV powers and the decay distributions are normalized to the tau decay width.

### 3.5.4 Forward-backward asymmetry

The forward-backward asymmetry is defined [513] by

$$\mathcal{A}_{\pi\pi}(s) = \frac{\int_0^1 d\cos\theta \frac{d^2\Gamma}{dsd\cos\theta} - \int_{-1}^0 d\cos\theta \frac{d^2\Gamma}{dsd\cos\theta}}{\int_0^1 d\cos\theta \frac{d^2\Gamma}{dsd\cos\theta} + \int_{-1}^0 d\cos\theta \frac{d^2\Gamma}{dsd\cos\theta}}. \quad (3.24)$$

We can obtain it for  $\tau^- \rightarrow \pi^-\pi^0\nu_\tau$  decays plugging in Eq. (3.21) into Eq. (3.24) and integrating upon the  $\cos\theta$  variable,

$$\begin{aligned} \mathcal{A}_{\pi\pi}(s) = & \frac{-3C_S\sqrt{\lambda(s, m_{\pi^-}^2, m_{\pi^0}^2)}}{2s^2[X_{VA} + \hat{\epsilon}_S X_S + \hat{\epsilon}_T X_T + \hat{\epsilon}_S^2 X_{S^2} + \hat{\epsilon}_T^2 X_{T^2}]} \left(1 + \frac{s\hat{\epsilon}_S}{m_\tau(m_d - m_u)}\right) \Delta_{\pi^-\pi^0} \\ & \times \left\{ C_V \text{Re}[F_0(s)F_+^*(s)] + \frac{2s\hat{\epsilon}_T}{m_\tau} \text{Re}[F_T(s)F_0^*(s)] \right\}, \end{aligned} \quad (3.25)$$

where, again, the SM forward-backward asymmetry is recovered for  $\epsilon_{R,L} = \hat{\epsilon}_{S,T} = 0$ . This reference case is plotted in figure 3.8, which agrees with the prediction in Ref. [513] (this asymmetry was first studied in Ref. [534]). This observable is plotted in fig. 3.9 for an unrealistically large value of  $\hat{\epsilon}_S$ , for which there is a large deviation with respect to the SM



case. Since such large departures disappear for reasonable values of  $\hat{\epsilon}_{S,T}$ , in order to enhance the sensitivity to new physics effects, we define the observable (odd under  $\hat{\epsilon}_S \leftrightarrow -\hat{\epsilon}_S$ )

$$\Delta A_{FB} = A_{FB}(s, \hat{\epsilon}_S, \hat{\epsilon}_T) - A_{FB}(s, 0, 0), \quad (3.26)$$

which is plotted in figs. 3.10. Even by using this observable it does not seem possible to evidence non-vanishing  $\hat{\epsilon}_{S,T}$  using the forward-backward asymmetry.

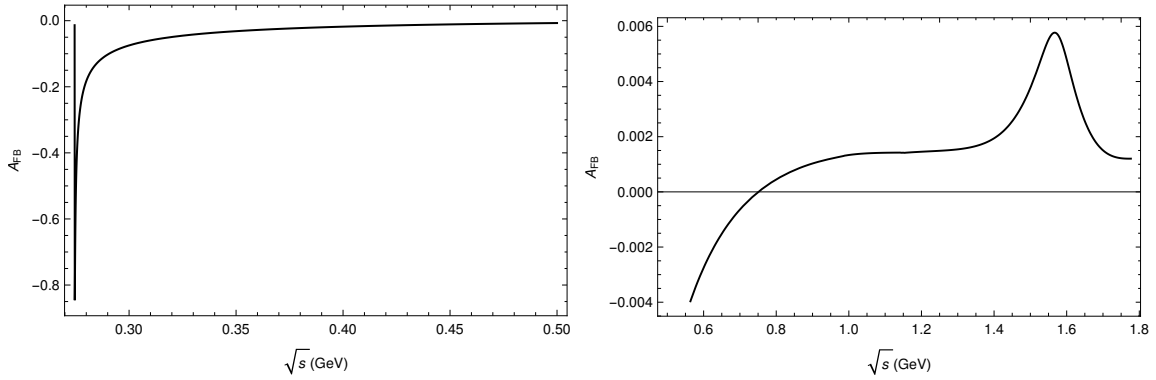


Figure 3.8: The forward-backward asymmetry in the  $\tau^- \rightarrow \pi^- \pi^0 \nu_\tau$  decay as a function of the  $\pi\pi$  energy for the SM case. The low-energy region is shown in the left plot and remaining energy range is represented in the right plot.

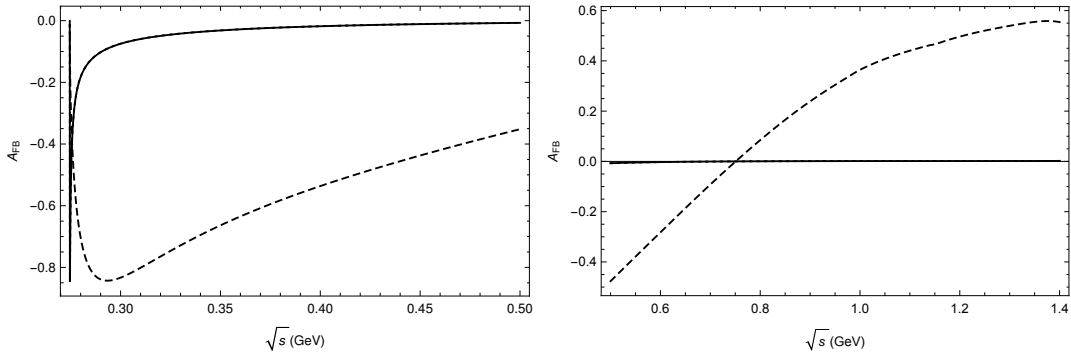


Figure 3.9: Forward-asymmetry for  $\hat{\epsilon}_S = 1.31, \hat{\epsilon}_T = 0$  (dashed line) compared to the SM prediction (solid line). The left plot shows the low-energy region and the right plot includes the remaining energy range.

As advanced before,  $\mathcal{A}_{\pi\pi}(s)$  in Eq. (3.25) is a good observable for finding non-standard scalar interactions: despite its numerator is suppressed by the small value of  $\Delta_{\pi-\pi^0}$ , its

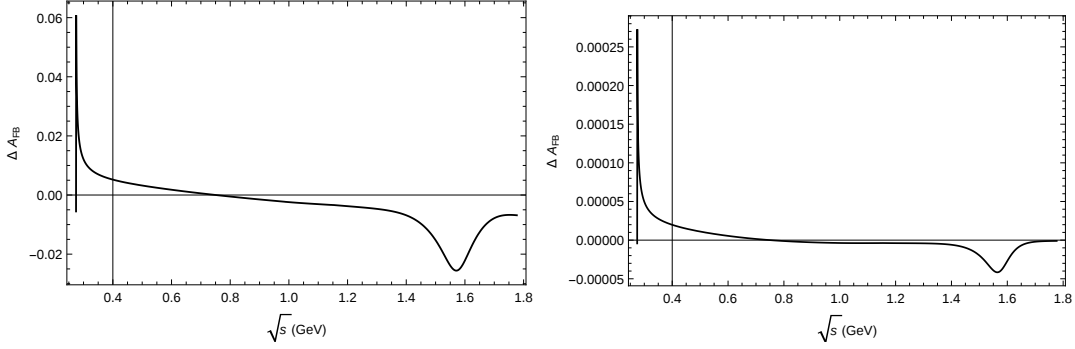


Figure 3.10: Normalized difference with respect to the SM for the forward-backward asymmetry ( $\Delta A_{FB}$ ) in the case of scalar interactions (left plot, with  $\hat{\epsilon}_S = 0.008, \hat{\epsilon}_T = 0$ ) and tensor interactions (right plot,  $\hat{\epsilon}_T = -0.001, \hat{\epsilon}_S = 0$ ).

denominator is further suppressed by the dependence of  $X_{S^2}$  on  $\Delta_{\pi^-\pi^0}^2$ , which enhances the sensitivity of this forward-backward asymmetry to scalar contributions. However, as just observed, if the strict limits on  $|\hat{\epsilon}_S|$  obtained in other low-energy processes are applied, even  $\mathcal{A}_{\pi\pi}(s)$  happens to be unable of evidencing this kind of NP contributions.

### 3.5.5 Limits on $\hat{\epsilon}_S$ and $\hat{\epsilon}_T$

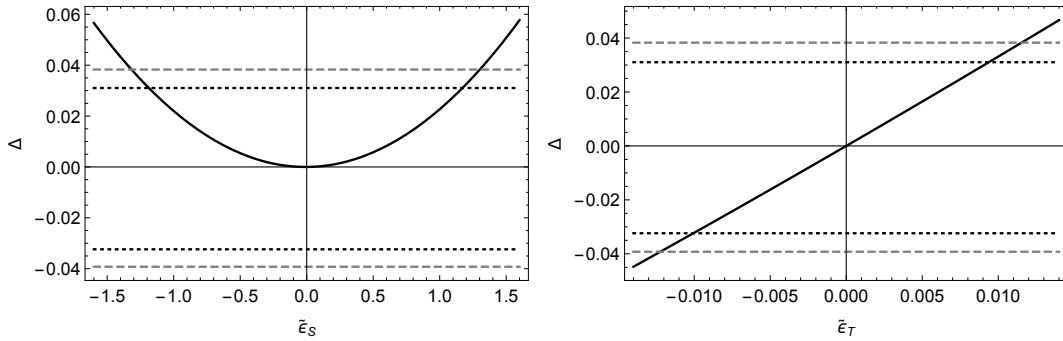


Figure 3.11:  $\Delta$  as a function of  $\hat{\epsilon}_S$  for  $\hat{\epsilon}_T = 0$  (left-hand) and  $\hat{\epsilon}_T$  for  $\hat{\epsilon}_S = 0$  (right-hand) for  $\tau^- \rightarrow \pi^-\pi^0\nu_\tau$  decays. Horizontal lines represent the values of  $\Delta$  according to the current measurement and theory error (at three standard deviations) of the branching ratio (dashed line) and the hypothetical case of this value being measured by Belle-II with three times reduced error (dotted line).

The  $\tau^- \rightarrow \pi^-\pi^0\nu_\tau$  decay width can be obtained integrating the invariant mass distribution, using the expressions for the form factors [19,513]. Since the total decay width depends

on the effective couplings, this process branching ratio sets bounds on  $\hat{\epsilon}_S$  and  $\hat{\epsilon}_T$ . For that, we compare the decay rate ( $\Gamma$ ) for  $\tau^- \rightarrow \pi^- \pi^0 \nu_\tau$  in the presence of non-vanishing NP effective couplings with respect to the one ( $\Gamma^0$ ) obtained by neglecting them (SM case). Using the best fit results of case III in Ref. [19], we obtain a value of  $\Gamma_0$  which corresponds to the branching ratio  $(25.53 \pm 0.24)\%$ , in excellent agreement with the PDG value of  $(25.49 \pm 0.09)\%$ . Integrating Eq. (3.22) we get the relative shift produced by NP contributions as follows

$$\Delta \equiv \frac{\Gamma - \Gamma^0}{\Gamma^0} = \alpha \hat{\epsilon}_S + \beta \hat{\epsilon}_T + \gamma \hat{\epsilon}_S^2 + \delta \hat{\epsilon}_T^2, \quad (3.27)$$

for whose coefficients we get:  $\alpha = 3.5 \times 10^{-4}$ ,  $\beta = 3.3_{-0.4}^{+0.6}$ ,  $\gamma = 2.2 \times 10^{-2}$ ,  $\delta = 4.7_{-1.0}^{+2.0}$ . The relative error of the coefficients  $\alpha$  and  $\gamma$  due to our uncertainties is  $\leq 2\%$ . Eq. (3.27) is a quadratic function of the effective scalar and tensor couplings, which can be used to explore the sensitivity of  $\tau^- \rightarrow \pi^- \pi^0 \nu_\tau$  decays to non-standard scalar and tensor interactions. We will do this in two steps. Firstly, we can make the analysis for one vanishing and one non-vanishing coupling. This is shown in figure 3.11 where we represent with horizontal lines the current experimental limits on  $\Delta$  (at three standard deviations) and use Eq. (3.27) to translate this information into bounds for  $\hat{\epsilon}_S$  and  $\hat{\epsilon}_T$ . According to this procedure, we get the following constraint  $-1.33 \leq \hat{\epsilon}_S \leq 1.31$  with  $\hat{\epsilon}_T = 0$  and  $[-0.79, -0.57] \cup [-1.4, 1.3] \cdot 10^{-2}$  as the allowed region for  $\hat{\epsilon}_T$  with  $\hat{\epsilon}_S = 0$  (at three standard deviations). The previous results were used to estimate the values of  $\hat{\epsilon}_S$  and  $\hat{\epsilon}_T$  which were employed in the preceding subsections:  $\hat{\epsilon}_S \sim 1.31$  and  $\hat{\epsilon}_T \sim -0.014$ <sup>10</sup>. The dotted lines illustrate how the limits would evolve for an error reduced by a factor three, which could be achieved at Belle-II (the theory error is not assumed to decrease in this exercise).

Then, we can also fix joint constraints on the scalar and tensor effective interactions assuming both  $\hat{\epsilon}_S$  and  $\hat{\epsilon}_T$  non-vanishing and using again Eq. (3.27) as before. This result is shown in figure 3.12, where the limits on the scalar and tensor couplings are contained inside an ellipse in the  $\hat{\epsilon}_S - \hat{\epsilon}_T$  plane. As a rough estimate of the possible impact of Belle-II data

---

<sup>10</sup>The value  $\hat{\epsilon}_T \sim -0.001$  could seem a bit too small, compared to the intervals just given. However, we will see later in this section that the fits to the di-pion mass spectrum justify such an estimate.

we repeat the exercise of assuming a threefold error improvement with respect to Belle-I. The dashed lines of the figure 3.12 (right panel) are illustrative of this effect.

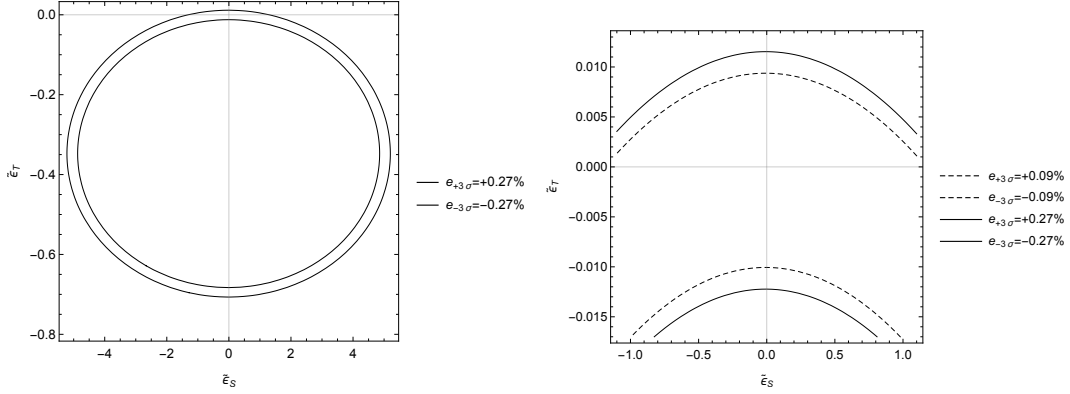


Figure 3.12: Constraints on the scalar and tensor couplings obtained from  $\Delta(\tau^- \rightarrow \pi^- \pi^0 \nu_\tau)$  using the Belle measurement and the theory uncertainty (at three standard deviations) of the branching ratio. The left-hand plot shows the constraints obtained from current data. On the right-hand plot we show a magnification of the top part of this ellipse, where the solid line represents the upper limit on  $\hat{\epsilon}_S$  and  $\hat{\epsilon}_T$ , while the dashed lines intend to illustrate the effect of a possible threefold improvement in the measurement at the Belle-II experiment.

Table 3.1 summarizes the constraints on the scalar and tensor effective couplings that can be obtained (at three standard deviations) from the Belle measurement of the branching ratio for  $\tau^- \rightarrow \pi^- \pi^0 \nu_\tau$  decays (including theory errors). The bottom part of Table 3.1 illustrates the bounds that could be achieved with a threefold reduction of the uncertainty at Belle-II.

$\Delta$ limits	$\hat{\epsilon}_S (\hat{\epsilon}_T = 0)$	$\hat{\epsilon}_T (\hat{\epsilon}_S = 0)$	$\hat{\epsilon}_S$	$\hat{\epsilon}_T$
Belle	$[-1.33, 1.31]$	$[-0.79, -0.57] \cup [-1.4, 1.3] \cdot 10^{-2}$	$[-5.2, 5.2]$	$[-0.79, 0.013]$
3-fold improved measurement	$[-1.20, 1.18]$	$[-0.79, -0.57] \cup [-1.1, 1.1] \cdot 10^{-2}$	$[-5.1, 5.1]$	$[-0.78, 0.011]$

Table 3.1: Constraints on the scalar and tensor couplings obtained (at three standard deviations) through the limits on the current branching ratio measurements and the hypothetical case where this value be measured by Belle II with a three times smaller error. Theory errors are included.

Next we consider fits to the data reported by Belle [365] for the normalized spectrum  $(1/N_{\pi\pi})(dN_{\pi\pi}/ds)$  and integrated branching ratio using the function <sup>11</sup>

$$\frac{1}{\Gamma(\hat{\epsilon}_S, \hat{\epsilon}_T)} \frac{d\Gamma(s, \hat{\epsilon}_S, \hat{\epsilon}_T)}{ds}. \quad (3.28)$$

When fitting  $\hat{\epsilon}_S$  and  $\hat{\epsilon}_T$  to Belle data in order to search for non-standard interactions, we are assuming that our description of  $\Gamma_0$  (based on Ref. [19]) is a reliable estimate of the corresponding SM prediction (including theoretical uncertainties). Thus, we examine whether it is possible or not to improve the agreement of the SM prediction with data by means of non-vanishing new physics scalar or tensor interactions.

If both  $\hat{\epsilon}_S$  and  $\hat{\epsilon}_T$  are fitted, bounds of order one on  $\hat{\epsilon}_S$  and of order 0.1 on  $\hat{\epsilon}_T$  are obtained. Because of this unrealistic bounds for  $\hat{\epsilon}_S$ , which hinder the extraction of  $\hat{\epsilon}_T$ , in our reference fits we restrict  $|\hat{\epsilon}_S| < 0.8 \times 10^{-2}$  [504, 505] and fit only  $\hat{\epsilon}_T$ . In this case we find  $\hat{\epsilon}_T = (-1.3_{-2.2}^{+1.5}) \cdot 10^{-3}$ , which shows a small preference (0.9 sigma) for charged current tensor interactions. We believe, however, that it is interesting to check this conclusion with more precise measurements of these decays and scrutinizing  $F_+(s)$ , hopefully with improved knowledge on the inelastic effects on  $F_T(s)$ .

A caveat is, of course, in order: although chiral symmetry (at low energies) and the use of dispersion relations together with precise measurements (especially useful outside the  $\chi PT$  regime of applicability) makes us confident on our knowledge of the vector two-pion form factor,  $F_+(s)$ , one should be very cautious before claiming evidence for NP from this type of analysis <sup>12</sup>. Provided a hint for an anomaly appears, different investigations should be performed to test it: it may be worth considering a dispersive coupled-channel analysis of the two-pion and two-kaon vector form factors [535–538], one should analyze along these lines the compatibility between the  $F_+(s)$  form factor measured by Belle and the  $L = 1 = I$   $\pi\pi$  scattering amplitude...

<sup>11</sup>All discussed uncertainties are considered in our fits.

<sup>12</sup>In the case of  $\tau^- \rightarrow \pi^-(\eta/\eta')\nu_\tau$  decays [250] this would be noticeably more difficult: although the hadronization of the vector current is given again in terms of the precisely-known two-pion vector form factor, the dominant scalar contribution is subject to large uncertainties still [447].

We can finally compare the constraints in tables 3.1 and the best fit results to the di-pion spectrum with those obtained in Ref. [505]. For this, we need to assume lepton universality because our decays involve the tau lepton, while their analysis involves electron and muon flavors. According to Refs. [250,504,505], it is clear  $\tau^- \rightarrow \pi^- \pi^0 \nu_\tau$  decays cannot be competitive setting constraints on the non-standard scalar interactions. Our three sigma upper limit (using current data) is  $|\hat{e}_S| < 1.3$  while the limit from the radiative pion decays  $\pi \rightarrow e\nu\gamma$  is  $|\hat{e}_S| < 0.8 \times 10^{-2}$  (at 90% C.L.). Conversely, our best fit result,  $\hat{e}_T = (-1.3_{-2.2}^{+1.5}) \cdot 10^{-3}$ , is competitive in the case of tensor interactions since the limit reported in [504, 505] is  $|\hat{e}_T| < 0.1 \times 10^{-2}$  (at 90% C.L.). Notwithstanding, we find that the measured branching ratio only limits  $\hat{e}_T \in [-0.79, -0.57] \cup [-1.4, 1.3] \cdot 10^{-2}$  (at three sigma), which is not competitive with the previous value. Our results in this work and in Ref. [250] are compatible with those in Ref. [512] (which also analyze semileptonic tau decays in this context):  $\hat{e}_S = (-0.6 \pm 1.5) \cdot 10^{-2}$ ,  $\hat{e}_T = (-0.04 \pm 0.46) \cdot 10^{-2}$ . It must be noted that the analysis in Ref. [250] does not include theory errors, which explains the smaller uncertainties quoted therein for  $\hat{e}_S$ . In this work, our bounds using only the measured branching ratio are less restrictive than those in Ref. [512], and we can only achieve stronger limits with our fit to both the branching ratio and spectrum (using the error band for  $\Gamma_0$  obtained in Ref. [19] and restricting  $|\hat{e}_S| \lesssim 1 \times 10^{-2}$ ). In the light of more precise and diverse measurements of the  $\tau^- \rightarrow \pi^- \pi^0 \nu_\tau$  decays, improved theory analysis shall be needed to pursue cornering new physics with these decays.

### 3.6 Summary and conclusions

We have considered the  $\tau^- \rightarrow \pi^- \pi^0 \nu_\tau$  decays in the presence of generic New Physics effective interactions up to dimension-six operators, assuming left-handed neutrinos and that the new dynamics scale is in the multi-TeV range. Within this setting, we have paid particular attention to the hadron matrix elements, which are needed SM inputs in order to set bounds on the non-standard scalar and tensor couplings,  $\hat{e}_S$  and  $\hat{e}_T$ , respectively (we recall that it

is not possible to restrict spin-one non-standard interactions in the considered processes). For this, we have employed previous results using dispersion relations for the scalar [513], vector [19] and tensor [427] form factors implementing the known chiral constraints at low energies and QCD asymptotics at short distances, according to data. For the tensor form factor, since no experimental information is available, we have pursued a purely theoretical determination of its leading chiral behaviour using Chiral Perturbation Theory. In this work, we improved over our previous treatment of the tensor form factor where only leading-order chiral predictions were considered and unitarity constraints were ignored [250], motivated here by the fact that di-pion tau decays constitute an excellent arena to set competitive limits on  $\hat{e}_T$ . Lattice QCD results [514] allowed determining the only leading low-energy constant of the tensor form factor, permitting a direct access to  $\hat{e}_T$ .

Within this framework, we have set bounds on  $\hat{e}_S$  and  $\hat{e}_T$  using the measured Belle branching ratio, through our observable  $\Delta$ . This procedure yields quite competitive limits with the world-best bounds for the tensor case (that we have thus used in the remaining analysis), but quite poor (unrealistic assuming some reasonable approximate lepton universality holds for them) in the scalar case, which is a consequence of its suppression in all considered observables (but the forward-backward asymmetry) by the tiny difference between charged and neutral pion masses squared. Because of this feature, we have assumed  $\hat{e}_S$  limits similar to those obtained in light quark beta and  $\tau^- \rightarrow \pi^-(\eta/\eta')\nu_\tau$  decays in the remaining analysis.

As a result of our study, it turns out that Dalitz plot distributions (both in the Mandelstam variables  $s$  and  $t$  and also replacing  $t$  by the angle between the two charged particles) are not very sensitive to non-zero realistic values of  $\hat{e}_S$  and  $\hat{e}_T$ , as it also happens with the forward-backward asymmetry. Apparently, the hadronic invariant mass distribution is not sensitive either to charged-current tensor interactions. However, a fit to Belle data on this observable (limiting  $|\hat{e}_S| \lesssim 1 \times 10^{-2}$  and with  $\Gamma_0$  fixed -within errors- previously) hints for a slight preference for non-zero  $\hat{e}_T$ . Therefore, it is very worth measuring with extreme precision the di-pion invariant mass distribution in  $\tau^- \rightarrow \pi^-\pi^0\nu_\tau$  decays at Belle-II, as it will serve to further restrict  $\hat{e}_T$  and this way offer complementary information to other low-energy

processes in the searches for non-standard charged current interactions. This effort would need to come together with both a tight scrutiny of the dominant vector form factor SM prediction and measurements of Dalitz distributions and forward-backward asymmetry.



# Chapter 4

## Effective-field theory analysis of the $\tau^- \rightarrow K^- \eta^{(\prime)} \nu_\tau$ decays

In this chapter we study the effect of NP interactions in the  $\tau^- \rightarrow K^- \eta^{(\prime)} \nu_\tau$  decays through an effective field theory analysis which is complementary to another semileptonic tau decays analysis, the  $\pi\pi$  [519] and the  $\pi\eta^{(\prime)}$  [250] channels for the strangeness conserving and the  $K\pi$  [251] channel for the strangeness changing charged current transitions.

### 4.1 Introduction

Hadronic tau decays provide an important source of experimental information about QCD at low and intermediate energies. These decays have the advantage of containing hadrons in the final state thus avoiding the complications arising from having them in the initial state as well. At the exclusive level, they can be used to understand specific properties of pions, kaons,  $\eta$  and  $\eta'$  mesons, and the interactions among them. So far, we have a good knowledge over decays into a pair of pseudoscalar mesons, the Standard Model (SM) input of which is encoded in terms of hadronic form factors. An ideal roadmap to describe meson form factors would require a model-independent approach demanding a full knowledge of QCD in both its perturbative and non-perturbative regimes, knowledge not yet unraveled. An

alternative to such enterprise would pursue a synergy between theoretical calculations and experimental data. In this respect, dispersion relations are a powerful tool to direct oneself towards a model-independent description of meson form factors. For example, the analyses of the decays  $\pi^-\pi^0$  [15,16,19,28] and  $K_S\pi^-$  [23,24,30,409,410], carried out by exploiting the synergy between Resonance Chiral Theory [224] and dispersion theory, are found to be in a nice agreement with the rich data provided by the experiments. Accord with experimental measurements is also found for the  $K^-K_S$  [28] and  $K^-\eta$  [30,428] decay modes, although higher-quality data on these processes is required to constrain the corresponding theories or models.

Several recent works [250,251,512,519] have put forward that semileptonic tau decays offer also an interesting scenario to set bounds on non-standard weak charged current interactions complementary to other low-energy semileptonic probes considered before, such nuclear beta decays, purely leptonic lepton, pion and kaon decays or hyperon decays (see e.g. Refs. [187, 192,504–511,539]). The aim of this chapter is to extent the analysis in Chapter 3 for the  $\tau^- \rightarrow \pi^-\pi^0\nu_\tau$  decays [519] along with previous analyses for the  $\tau^- \rightarrow (K\pi)^-\nu_\tau$  [251] and  $\tau^- \rightarrow \pi^-\eta^{(\prime)}\nu_\tau$  [250] decays, which were studied using the most general effective Lagrangian for weak charge current interactions up to dimension six on several phenomenological interesting observables, to the  $\tau^- \rightarrow K^-(\eta^{(\prime)}, K^0)\nu_\tau$  decays <sup>1</sup>.

On the theory side, a controlled theoretical determination, with a robust error band, of the corresponding form factors within the SM is required in order to increase the accuracy of the search for non-standard interactions. At present, we have such a knowledge for the vector and -to a great extent- the scalar form factors, but there are no experimental data that can help us constructing the tensor form factor and, therefore, it will be built under theoretical considerations only.

On the experimental side, our study is presently limited by the following facts: *i*) for the decay  $\tau^- \rightarrow K^-K^0\nu_\tau$ , while the PDG reports a branching ratio of  $1.486(34) \times 10^{-3}$  [541], no measurement of the corresponding decay spectrum has been released by the *B*-

---

<sup>1</sup>Although the  $\tau^- \rightarrow K^-K^0\nu_\tau$  decays will not be discussed in this thesis, the interested reader is referred to Ref. [540] for detailed description of the methods and results for the  $K^-K^0$  decay mode.

factories; *ii*) the associated errors of the brother process  $\tau^- \rightarrow K^- K_S \nu_\tau$  BaBar data [481] are still relatively large; *iii*) unfolding detector effects has not been performed for the  $\tau^- \rightarrow K^- \eta \nu_\tau$  Belle data [29]<sup>2</sup>; *iv*) and, finally, the decay  $\tau^- \rightarrow K^- \eta' \nu_\tau$  has not been detected yet, although an upper limit at the 90% confidence level was placed by BaBar [433]. We will not thus attempt to extract new physics bounds from the corresponding experimental data as competitive as those coming from other low-energy probes, like the ones mentioned before, but rather explore the size of the deviations from the SM predictions that one could expect in these decay channels. For these reasons, we hope that our paper strengthens the case for a (re)analysis, with a larger data sample, of the  $K^- K^0$ ,  $K^- K_S$  and  $K^- \eta$  decay spectra and encourage experimental groups to measure the  $K^- \eta'$  decay mode. All this should be well within the reach of Belle-II [500], and of other future  $Z$ , tau-charm and  $B$ -factories where new measurements should be possible.

This chapter is organized as follows. The theoretical framework is given in section 4.2 where we briefly present the effective Lagrangian and discuss the different effective weak currents contributing to the decays. The hadronic matrix element and the participant form factors are also defined in this section. The latter are the matter subject of section 4.3, where we pay special attention to the tensor form factor. In section 4.4, we discuss the different interesting phenomenological observables i.e. decay spectra and branching ratio, Dalitz plot distributions and the forward-backward asymmetry, that can help us setting bounds on non-SM interactions. We derive these bounds in section 4.4.5. Finally, our conclusions are presented in section 4.5.

---

<sup>2</sup>This decay was also measured by BaBar [429]. However, the person in charge of the analysis left the field and the data file was lost, unfortunately.

## 4.2 Effective field theory analysis and decay amplitude of $\tau^- \rightarrow \nu_\tau \bar{u} s$

The effective Lagrangian including dimension-six operators, that describes semileptonic  $\tau^- \rightarrow \nu_\tau \bar{u} s$  strangeness-changing charged current transitions with left-handed neutrinos, can be written as [250, 251, 519, 542]:

$$\begin{aligned} \mathcal{L}_{CC} = & -\frac{G_F}{\sqrt{2}} V_{us} (1 + \epsilon_L + \epsilon_R) \left\{ \bar{\tau} \gamma_\mu (1 - \gamma^5) \nu_\tau \bar{u} \left[ \gamma^\mu - (1 - 2\hat{\epsilon}_R) \gamma^\mu \gamma^5 \right] s \right. \\ & \left. + \bar{\tau} (1 - \gamma^5) \nu_\tau \bar{u} (\hat{\epsilon}_S - \hat{\epsilon}_P \gamma^5) s + 2\hat{\epsilon}_T \bar{\tau} \sigma_{\mu\nu} (1 - \gamma^5) \nu_\tau \bar{u} \sigma^{\mu\nu} s \right\} + h.c. , \end{aligned} \quad (4.1)$$

where  $G_F$  is the tree-level definition of the Fermi constant. In Eq. (4.1), we have defined  $\hat{\epsilon}_i = \epsilon_i / (1 + \epsilon_L + \epsilon_R)$  for  $i = R, S, P, T$ , with  $\epsilon_{L,R}$  and  $\epsilon_i$  being effective couplings characterizing NP that can be taken real since we are only interested in  $CP$  conserving quantities. Needless to say, if we put them to zero i.e.  $\epsilon_{L,R} = \hat{\epsilon}_{R,S,P,T} = 0$ , we recover the SM Lagrangian. This factorized form of Eq. (4.1) is useful as long as conveniently normalized rates allow to cancel the overall factor  $(1 + \epsilon_L + \epsilon_R)$ . Note that since  $\epsilon_i = \hat{\epsilon}_i$  at linear order in  $\hat{\epsilon}'_i s$ , we may use  $\epsilon_i$  instead of  $\hat{\epsilon}_i$  when comparing to works which use the former instead of the latter [505]. A more detailed derivation of the Lagrangian of Eq. (4.1) can be found above in Chapter 3 or in Refs. [250, 251, 519].

The decay amplitude for  $\tau^- (P) \rightarrow K^- (p_K) \eta^{(\prime)} (p_{\eta^{(\prime)}}) \nu_\tau (P')$  that arises from the Lagrangian in Eq. (4.1) contains a vector ( $V$ ), an scalar ( $S$ ) and a tensor ( $T$ ) contribution. The resulting amplitude can be expressed as<sup>3</sup>

$$\begin{aligned} \mathcal{M} &= \mathcal{M}_V + \mathcal{M}_S + \mathcal{M}_T \\ &= \frac{G_F V_{us} \sqrt{S_{EW}}}{\sqrt{2}} (1 + \epsilon_L + \epsilon_R) \left[ L_\mu H^\mu + \hat{\epsilon}_S L H + 2\hat{\epsilon}_T L_{\mu\nu} H^{\mu\nu} \right], \end{aligned} \quad (4.2)$$

---

<sup>3</sup>The short-distance electroweak radiative corrections encoded in  $S_{EW}$  [365], do not affect the scalar and tensor contributions. However, the error made by taking  $\sqrt{S_{EW}}$  as an overall factor in Eq. (4.2) is negligible.

where the leptonic currents are defined by:

$$L_\mu = \bar{u}(P')\gamma_\mu(1 - \gamma^5)u(P), \quad (4.3)$$

$$L = \bar{u}(P')(1 + \gamma^5)u(P), \quad (4.4)$$

$$L_{\mu\nu} = \bar{u}(P')\sigma_{\mu\nu}(1 + \gamma^5)u(P). \quad (4.5)$$

The scalar  $H$ , vector ( $H^\mu$ ) and tensor ( $H^{\mu\nu}$ ) hadronic matrix elements in Eq. (4.2) can be decomposed in terms of allowed Lorentz structures and a number of form factors encoding the hadronization procedure as

$$H = \langle K^-\eta^{(\prime)}|\bar{s}u|0\rangle \equiv F_S^{K^-\eta^{(\prime)}}(s), \quad (4.6)$$

$$H^\mu = \langle K^-\eta^{(\prime)}|\bar{s}\gamma^\mu u|0\rangle = C_{K^-\eta^{(\prime)}}^V Q^\mu F_+^{K^-\eta^{(\prime)}}(s) + C_{K^-\eta^{(\prime)}}^S \left(\frac{\Delta_{K\pi}}{s}\right) q^\mu F_0^{K^-\eta^{(\prime)}}(s), \quad (4.7)$$

$$H^{\mu\nu} = \langle K^-\eta^{(\prime)}|\bar{s}\sigma^{\mu\nu}u|0\rangle = iF_T^{K^-\eta^{(\prime)}}(s)(p_{\eta^{(\prime)}}^\mu p_K^\nu - p_K^\mu p_{\eta^{(\prime)}}^\nu), \quad (4.8)$$

where  $q^\mu = (p_K + p_{\eta^{(\prime)}})^\mu$ ,  $Q^\mu = (p_{\eta^{(\prime)}} - p_K)^\mu + (\Delta_{K\eta^{(\prime)}}/s)q^\mu$ ,  $s = q^2$  and  $\Delta_{ij} = m_i^2 - m_j^2$ , and with the Clebsch-Gordan coefficients:  $C_{K\eta^{(\prime)}}^V = -\sqrt{\frac{3}{2}}$ ,  $C_{K\eta}^S = -\frac{1}{\sqrt{6}}$  and  $C_{K\eta'}^S = \frac{2}{\sqrt{3}}$ . The divergence of the vector current Eq. (4.7) relates the form factors  $F_S(s)$  and  $F_0(s)$  via

$$F_S(s) = \frac{C_{K\eta^{(\prime)}}^S \Delta_{K\pi}}{m_s - m_u} F_0^{K\eta^{(\prime)}}(s). \quad (4.9)$$

As in Refs. [250, 251, 519, 542], the scalar and vector contributions in Eqs. (4.6) and Eq. (4.7), respectively, can be treated jointly by doing the following replacement

$$C_{K\eta^{(\prime)}}^S \frac{\Delta_{K\pi}}{s} \rightarrow C_{K\eta^{(\prime)}}^S \frac{\Delta_{K\pi}}{s} \left(1 + \frac{s \hat{\epsilon}_S}{m_\tau(m_s - m_u)}\right), \quad (4.10)$$

in Eq. (4.7). The parametrization of the three independent form factors i.e.,  $F_0(s)$ ,  $F_+(s)$  and  $F_T(s)$ , will be discussed in the next section.

### 4.3 Hadronization of the scalar, vector and tensor currents

It is fundamental to have good control over the scalar, vector and tensor form factors since they are used as SM inputs for binding the non-standard interactions. The frame approach to describe the  $K^-\eta^{(\prime)}$  vector form factor is the following. They are calculated within the context of Resonance Chiral Theory taking into account the effects of the  $K^*(892)$  and the  $K^*(1410)$  vector resonances, and are connected to the  $K\pi$  vector form factor through  $F_+^{K\eta^{(\prime)}}(s) = \cos\theta_P(\sin\theta_P)F_+^{K\pi}(s)$  [428], where  $\theta_P$  is the  $\eta$ - $\eta'$  mixing angle in the octet-singlet basis. We will then discuss the exemplify case of the  $K\pi$  vector form factor and take  $\theta_P = (-13.3 \pm 0.5)^\circ$  [543]. For our analysis, we follow the representation outlined in Ref. [410]. The thrice subtracted dispersion relation reads

$$F_+^{K\pi}(s) = F_+^{K\pi}(0) \exp \left[ \alpha_1 \frac{s}{m_\pi^2} + \frac{1}{2} \alpha_2 \frac{s^2}{m_\pi^4} + \frac{s^3}{\pi} \int_{s_{K\pi}}^{s_{\text{cut}}} ds' \frac{\delta_+^{K\pi}(s')}{(s')^3 (s' - s - i0)} \right], \quad (4.11)$$

where  $s_{K\pi} = (m_K + m_\pi)^2$  is the threshold of the  $K\pi$  system, while the value of  $F_+^{K\pi}(0)$  is extracted from  $|V_{us}F_+^{K^-\pi^0}(0)| = 0.2165(2)$  [541], and  $\alpha_1$  and  $\alpha_2$  are two subtraction constants that are related to the low-energy expansion of the form factor. The use of a three-times subtracted dispersion relation reduces the high-energy contribution of the integral where the phase is less well-known. In Eq.(4.11),  $s_{\text{cut}}$  is a cut-off whose value is fixed from the requirement that the fitted parameters are compatible within errors with the case  $s_{\text{cut}} \rightarrow \infty$ . In Refs. [30,410], the value of  $s_{\text{cut}} = 4 \text{ GeV}^2$  was found to satisfy this criterion, and variations of  $s_{\text{cut}}$  were used to estimate the associated systematic error. For the input phase  $\delta_+^{K\pi}(s)$  we use

$$\delta_+^{K\pi}(s) = \tan^{-1} \left[ \frac{\text{Im} \tilde{f}_+^{K\pi}(s)}{\text{Re} \tilde{f}_+^{K\pi}(s)} \right], \quad (4.12)$$

where  $\tilde{f}_+^{K\pi}(s)$  is taken to be of the form [410]

$$\tilde{f}_+^{K\pi}(s) = \frac{m_{K^*}^2 - \kappa_{K^*} \tilde{H}_{K\pi}(0) + \gamma s}{D(m_{K^*}, \gamma_{K^*})} - \frac{\gamma s}{D(m_{K^{*'}}, \gamma_{K^{*'}})}, \quad (4.13)$$

where we have included two resonances, the  $K^* = K^*(892)$  and the  $K^{*' } = K^*(1410)$ . The denominators in Eq. (4.13) are

$$D(m_n, \gamma_n) \equiv m_n^2 - s - \kappa_n \text{Re}[H_{K\pi}(s)] - im_n \gamma_n(s), \quad (4.14)$$

where

$$\kappa_n = \frac{192\pi F_K F_\pi \gamma_n}{\sigma_{K\pi}^3(m_n^2) m_n}, \quad \gamma_n(s) = \gamma_n \frac{s}{m_n^2} \frac{\sigma_{K\pi}^3(s)}{\sigma_{K\pi}^3(m_n^2)}, \quad (4.15)$$

and with the two-body phase-space factor given by  $\sigma_{K\pi}(s) = 2q_{K\pi}(s)/\sqrt{s}$  where

$$q_{K\pi}(s) = \frac{1}{2\sqrt{s}} \lambda^{1/2}(s, m_K^2, m_\pi^2) \theta(s - (m_K + m_\pi)^2). \quad (4.16)$$

The scalar one-loop integral function  $H_{K\pi}(s)$  is defined below Eq. (3) of Ref. [24], however removing the factor  $1/F_\pi^2$  which cancels if  $\kappa_n$  is expressed in terms of the unphysical width  $\gamma_n$ . For our analysis, we use the results of the reference fit in Ref. [30] jointly with the systematic uncertainty obtained as explained along the lines of the same reference. One limitation of Eq. (4.11) is that the  $1/s$  asymptotic fall-off of the form factor [544] it is not guaranteed because the subtraction constants are fixed from a fit to experimental data. However, we have checked that our form factor parametrization is indeed a decreasing function of  $s$  (apart from the  $K^*(892)$  and  $K^*(1410)$  peak structures) within the entire range where we apply it.

Regarding the  $K\eta^{(\prime)}$  scalar form factors, we employ the well-established results of Ref. [412] derived from a dispersive analysis with three channels ( $K\pi, K\eta, K\eta'$ )<sup>4</sup>.

As was already pointed out in Chapter 3, the tensor form factor is one of the most difficult inputs to be reliably estimated since there are no experimental data that can help constructing  $F_T^{K\eta^{(\prime)}}(s)$ . Therefore, we shall rely again on theoretical considerations only.

---

<sup>4</sup>We are very grateful to Matthias Jamin and José Antonio Oller for providing us their solutions in tables.

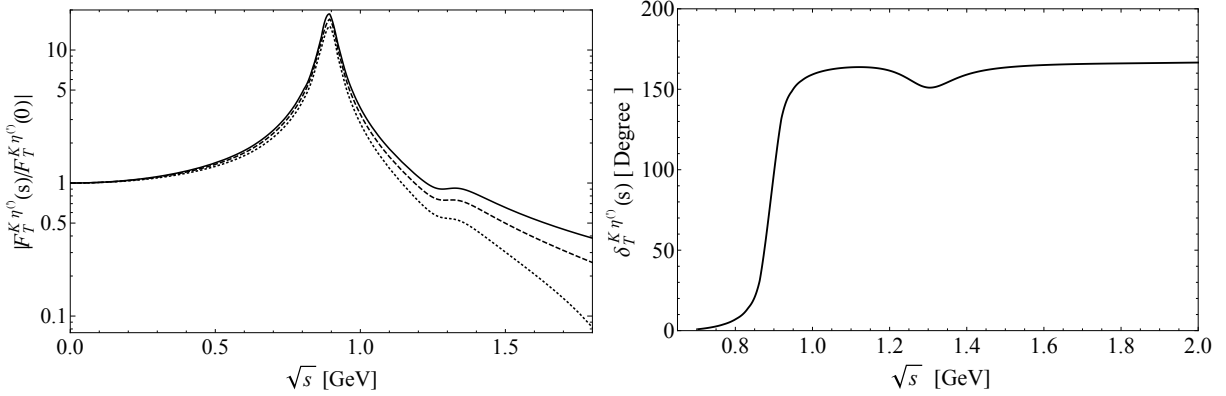


Figure 4.1: Normalized absolute value of the tensor form factor  $F_T^{K\eta^{(\prime)}}(s)$  given in Eq. (4.17) (left), for  $s_{\text{cut}} = 4 \text{ GeV}^2$  (dotted line),  $9 \text{ GeV}^2$  (dashed line) and  $s_{\text{cut}} \rightarrow \infty$  (solid line), and tensor form factor phase  $\delta_T^{K\eta^{(\prime)}}(s)$  (right).

The key observation is that the tensor form admits an Omnès dispersive representation [251, 427, 519]

$$F_T^{K\eta^{(\prime)}}(s) = F_T^{K\eta^{(\prime)}}(0) \exp \left[ \frac{s}{\pi} \int_{s_{K\pi}}^{s_{\text{cut}}} ds' \frac{\delta_T^{K\eta^{(\prime)}}(s')}{s'(s' - s - i0)} \right], \quad (4.17)$$

where in the elastic region, the phase of the tensor form factor equals the  $P$ -wave phase of the  $K\pi$  vector form factor i.e.  $\delta_T^{K\eta^{(\prime)}}(s) = \delta_+^{K\pi}(s)$ , with  $\delta_+^{K\pi}(s)$  extracted from Eq. (4.12). We will assume the previous relations also hold above the onset of inelasticities until  $m_\tau^2$  where we guide smoothly the tensor phase to  $\pi$  as in Ref. [28] to ensure the asymptotic  $1/s$  behavior dictated by perturbative QCD [544]. Lacking of precise low-energy information, we do not increase the number of subtractions in Eq. (4.17), which, in turn, would reduce the importance of the higher-energy part of the integral, but rather cut the integral at different values of  $s_{\text{cut}}$  and take the differing results as an estimate of our theoretical systematic uncertainty for the results presented in section 4.4.5. In Fig. 4.1, we show the tensor form factor phase  $\delta_T^{K\eta^{(\prime)}}(s)$  (right panel) together with the (normalized) absolute value of the tensor form factor (left panel) for the cases  $s_{\text{cut}} = 4, 9 \text{ GeV}^2$  and  $s_{\text{cut}} \rightarrow \infty$ , which is taken as the baseline hypothesis. The value of the normalization  $F_T^{K\eta^{(\prime)}}(0)$  required in Eq. (4.17) can be estimated within ChPT as explained in the following. The lowest-order ChPT Lagrangian



with tensor sources is of  $\mathcal{O}(p^4)$  in the chiral counting and reads [518]

$$\mathcal{L} = \Lambda_1 \langle t_+^{\mu\nu} f_{+\mu\nu} \rangle - i\Lambda_2 \langle t_+^{\mu\nu} u_\mu u_\nu \rangle + \Lambda_3 \langle t_+^{\mu\nu} t_{\mu\nu}^+ \rangle + \Lambda_4 \langle f_+^{\mu\nu} \rangle^2, \quad (4.18)$$

where  $t_+^{\mu\nu} = u^\dagger t^{\mu\nu} u^\dagger + u t^{\mu\nu\dagger} u$  includes the tensor source and its adjoint, and  $\langle \dots \rangle$  stands for a flavor space trace. Only terms proportional to  $\Lambda_2$  contribute to the decays we are considering. The chiral tensors entering Eq. (4.18) are given by:  $u_\mu = i [u^\dagger (\partial_\mu - i r_\mu) u - u (\partial_\mu - i l_\mu) u^\dagger]$ , where  $l_\mu$  and  $r_\mu$  are the left- and right-handed sources, and  $f_+^{\mu\nu} = u F_L^{\mu\nu} u^\dagger + u^\dagger F_R^{\mu\nu} u$ , that includes the left- and right-handed field-strength tensors for  $l_\mu$  and  $r_\mu$ ,  $F_{L,R}^{\mu\nu}$ . The non-linear representation of the pseudo-Goldstone bosons is given by  $u = \exp \left[ \frac{i}{\sqrt{2}F} \phi \right]$  [532, 533], where

$$\phi = \begin{pmatrix} \frac{\pi^3 + \eta_q}{\sqrt{2}} & \pi^+ & K^+ \\ \pi^- & \frac{-\pi^3 + \eta_q}{\sqrt{2}} & K^0 \\ K^- & \bar{K}^0 & \eta_s \end{pmatrix}, \quad (4.19)$$

where  $\eta_q = C_q \eta + C_{q'} \eta'$  and  $\eta_s = -C_s \eta + C_{s'} \eta'$  are the light and strange quark components of the  $\eta$  and  $\eta'$  mesons, respectively.  $\pi^3$  coincides with the  $\pi^0$  when the isospin-breaking terms are neglected. The constants describing the mixing between  $\eta_q$  and  $\eta_s$  states are given by [545, 546]

$$\begin{aligned} C_q &\equiv \frac{F_\pi}{\sqrt{3} \cos(\theta_8 - \theta_0)} \left( \frac{\cos \theta_0}{f_8} - \frac{\sqrt{2} \sin \theta_8}{f_0} \right), & C_{q'} &\equiv \frac{F_\pi}{\sqrt{3} \cos(\theta_8 - \theta_0)} \left( \frac{\sqrt{2} \cos \theta_8}{f_0} + \frac{\sin \theta_0}{f_8} \right), \\ C_s &\equiv \frac{F_\pi}{\sqrt{3} \cos(\theta_8 - \theta_0)} \left( \frac{\sqrt{2} \cos \theta_0}{f_8} + \frac{\sin \theta_8}{f_0} \right), & C_{s'} &\equiv \frac{F_\pi}{\sqrt{3} \cos(\theta_8 - \theta_0)} \left( \frac{\cos \theta_8}{f_0} - \frac{\sqrt{2} \sin \theta_0}{f_8} \right), \end{aligned} \quad (4.20)$$

and for the corresponding mixing parameters we use [547, 548]

$$\theta_8 = (-21.2 \pm 1.9)^\circ, \quad \theta_0 = (-6.9 \pm 2.4)^\circ, \quad (4.21)$$

$$f_8 = (1.27 \pm 0.02) F_\pi, \quad f_0 = (1.14 \pm 0.05) F_\pi, \quad (4.22)$$

with  $F_\pi = 92.2 \text{ MeV}$  being the pion decay constant.

The tensor source ( $\bar{t}^{\mu\nu}$ ) is related to its chiral projections ( $t^{\mu\nu}$  and  $t^{\mu\nu\dagger}$ ) by [518]

$$t^{\mu\nu} = P_L^{\mu\nu\lambda\rho} \bar{t}_{\lambda\rho}, \quad 4P_L^{\mu\nu\lambda\rho} = (g^{\mu\lambda}g^{\nu\rho} - g^{\mu\rho}g^{\nu\lambda} + i\epsilon^{\mu\nu\lambda\rho}), \quad (4.23)$$

where  $\bar{\Psi}\sigma_{\mu\nu}\bar{t}^{\mu\nu}\Psi$  is the tensor quark current. Taking the functional derivative of eq. (4.18) with respect to the tensor source  $\bar{t}_{\mu\nu}$ , we get

$$\left\langle K^- \eta \left| \frac{\delta \mathcal{L}_{\chi PT}^4}{\delta \bar{t}_{\mu\nu}} \right| 0 \right\rangle = i \left( \frac{C_q}{\sqrt{2}} + C_s \right) \frac{\Lambda_2}{F_\pi^2} (p_\eta^\mu p_K^\nu - p_K^\mu p_\eta^\nu), \quad (4.24)$$

$$\left\langle K^- \eta' \left| \frac{\delta \mathcal{L}_{\chi PT}^4}{\delta \bar{t}_{\mu\nu}} \right| 0 \right\rangle = i \left( \frac{C_{q'}}{\sqrt{2}} - C_{s'} \right) \frac{\Lambda_2}{F_\pi^2} (p_{\eta'}^\mu p_K^\nu - p_K^\mu p_{\eta'}^\nu). \quad (4.25)$$

An estimation of  $F_T^{K\pi}(0) = 2m_\pi F_T(0)$  on the lattice was obtained in Ref. [514]. Their result  $F_T^{K\pi}(0) = 0.417 \pm 0.015$ , together with the fact that

$$F_T^{K^- \eta}(0) = \left( \frac{C_q}{\sqrt{2}} + C_s \right) \frac{\Lambda_2}{F_\pi^2}, \quad (4.26)$$

$$F_T^{K^- \eta'}(0) = \left( \frac{C_{q'}}{\sqrt{2}} - C_{s'} \right) \frac{\Lambda_2}{F_\pi^2}, \quad (4.27)$$

yields  $\Lambda_2 = (11.1 \pm 0.4) \text{ MeV}$ , that we will use for our analysis. This value is consistent within one sigma with the one employed for the  $\pi\pi$  channel in Chapter 3 and in Ref. [519].

## 4.4 Decay observables

Now, we focus on the possible NP effects, characterized by the effective weak couplings described in section 4.2, in the following  $\tau^- \rightarrow K^- \eta^{(\prime)} \nu_\tau$  decay observables: Dalitz plots, angular and decay distributions, and the forward-backward asymmetry. The doubly differential decay width for  $\tau^- \rightarrow K^- \eta^{(\prime)} \nu_\tau$ , in the rest frame of the tau lepton, is given by

$$\frac{d^2\Gamma}{ds dt} = \frac{1}{32 (2\pi)^3 m_\tau^3} \overline{|\mathcal{M}|^2}, \quad (4.28)$$

where  $\overline{|\mathcal{M}|^2}$  is the unpolarized spin-averaged squared matrix element,  $s$  is the invariant mass of the  $K^-\eta^{(\prime)}$  system, limited in the interval  $(m_{\eta^{(\prime)}} + m_K)^2 \leq s \leq m_\tau^2$ , and  $t = (P' + p_{\eta^{(\prime)}})^2 = (P - p_K)^2$  with kinematic boundaries given by  $t^-(s) \leq t \leq t^+(s)$ , with

$$t^\pm(s) = \frac{1}{2s} \left[ 2s m_{\eta^{(\prime)}}^2 + (m_\tau^2 - s)(s + m_{\eta^{(\prime)}}^2 - m_K^2) \pm (m_\tau^2 - s) \sqrt{\lambda(s, m_{\eta^{(\prime)}}^2, m_K^2)} \right], \quad (4.29)$$

and where  $\lambda(x, y, z) = x^2 + y^2 + z^2 - 2xy - 2xz - 2yz$  is the usual Kallen function.

#### 4.4.1 Dalitz plot

The unpolarized spin-averaged squared amplitude yields

$$\overline{|\mathcal{M}|^2} = \frac{G_F^2 |V_{us}|^2 S_{EW}}{s^2} (1 + \epsilon_L + \epsilon_R)^2 \{M_{00} + M_{++} + M_{0+} + M_{T+} + M_{T0} + M_{TT}\}, \quad (4.30)$$

where  $M_{00}$ ,  $M_{++}$  and  $M_{TT}$  are, respectively, the scalar, vector and tensor amplitudes, whereas  $M_{0+}$ ,  $M_{T+}$  and  $M_{T0}$  are their corresponding interferences. These expressions are given by:

$$M_{0+} = -2C_{K\eta^{(\prime)}}^S C_{K\eta^{(\prime)}}^V m_\tau^2 \text{Re} \left[ f_+^{K\eta^{(\prime)}}(s) f_0^{*K\eta^{(\prime)}}(s) \right] \Delta_{K\pi} \left( 1 + \frac{s \hat{\epsilon}_S}{m_\tau (m_s - m_u)} \right) \\ \times \left\{ s \left( m_\tau^2 - s - 2t + \Sigma_{K\eta^{(\prime)}} \right) - m_\tau^2 \Delta_{K\eta^{(\prime)}} \right\}, \quad (4.31a)$$

$$M_{T+} = -4C_{K\eta^{(\prime)}}^V \hat{\epsilon}_T m_\tau^3 s \text{Re} \left[ f_T^{K\eta^{(\prime)}}(s) f_+^{*K\eta^{(\prime)}}(s) \right] \left( 1 - \frac{s}{m_\tau^2} \right) \lambda \left( s, m_{\eta^{(\prime)}}^2, m_k^2 \right), \quad (4.31b)$$

$$M_{T0} = 4C_{K\eta^{(\prime)}}^S \hat{\epsilon}_T \Delta_{K\pi} m_\tau s \text{Re} \left[ f_T^{K\eta^{(\prime)}}(s) f_0^{*K\eta^{(\prime)}}(s) \right] \left( 1 + \frac{s \hat{\epsilon}_S}{m_\tau (m_s - m_u)} \right) \\ \times \left\{ s \left( m_\tau^2 - s - 2t + \Sigma_{K\eta^{(\prime)}} \right) - m_\tau^2 \Delta_{K\eta^{(\prime)}} \right\}, \quad (4.31c)$$

$$M_{00} = \left( C_{K\eta^{(\prime)}}^S \right)^2 \Delta_{K\pi}^2 m_\tau^4 \left( 1 - \frac{s}{m_\tau^2} \right) \left| f_0^{K\eta^{(\prime)}}(s) \right|^2 \left( 1 + \frac{s \hat{\epsilon}_S}{m_\tau (m_s - m_u)} \right)^2, \quad (4.31d)$$

$$M_{++} = \left( C_{K\eta^{(\prime)}}^V \right)^2 \left| f_+^{K\eta^{(\prime)}}(s) \right|^2 \left\{ m_\tau^4 \left( s - \Delta_{K\eta^{(\prime)}} \right)^2 + 4m_k^2 s^2 \left( m_{\eta^{(\prime)}}^2 - t \right) + 4s^2 t \left( s + t - m_{\eta^{(\prime)}}^2 \right) \right. \\ \left. - m_\tau^2 s \left[ s(s + 4t) - 2\Delta_{K\eta^{(\prime)}} \left( s + 2t - 2m_{\eta^{(\prime)}}^2 \right) + \Delta_{K\eta^{(\prime)}}^2 \right] \right\}, \quad (4.31e)$$

$$M_{TT} = 4\hat{\epsilon}_T^2 \left| f_T^{K\eta^{(\prime)}}(s) \right|^2 s^2 \left\{ m_K^4 \left( m_\tau^2 - s \right) - m_{\eta^{(\prime)}}^4 \left( 3m_\tau^2 + s \right) - s \left[ (s + 2t)^2 - m_\tau^2 (s + 4t) \right] \right. \\ \left. + 2m_{\eta^{(\prime)}}^2 \left[ (s + 2t) \left( s + m_\tau^2 \right) - 2m_\tau^4 \right] - 2m_K^2 \left( m_\tau^2 - s \right) \left( s + 2t - m_{\eta^{(\prime)}}^2 \right) \right\}, \quad (4.31f)$$

where we have defined  $\Delta_{PQ} = m_P^2 - m_Q^2$  and  $\Sigma_{PQ} = m_P^2 + m_Q^2$ .

In order to study possible NP signatures in Dalitz plots distributions, we introduce the following observable [519]

$$\tilde{\Delta}(\hat{e}_S, \hat{e}_T) = \frac{|\overline{|\mathcal{M}(\hat{e}_S, \hat{e}_T)|^2} - \overline{|\mathcal{M}(0, 0)|^2}|}{|\overline{|\mathcal{M}(0, 0)|^2}}, \quad (4.32)$$

which measures deviations between non-SM (either  $\hat{e}_S \neq 0$  or  $\hat{e}_T \neq 0$ , or both  $\hat{e}_{S,T} \neq 0$ ) and SM ( $\hat{e}_{S,T} = 0$ ) interactions.

Firstly, the Dalitz plot distributions in the SM in the  $(s, t)$  variables for the decays  $\tau^- \rightarrow K^- \eta \nu_\tau$  (upper-left plot) and  $\tau^- \rightarrow K^- \eta' \nu_\tau$  (upper-right plot) are depicted in Fig.4.2. As it can be seen from these plots, there is no evidence for a meson resonance production and only the  $K^*(892)$ -and to lesser extent- the  $K^*(1410)$ , and  $K^0(1430)$  tails can be appreciated for the  $K\eta$  and  $K\eta'$  decay channels, respectively.

Secondly, we turn to analyze possible NP signatures by allowing non-zero values of either  $\hat{e}_S$  or  $\hat{e}_T$ . In Fig. 4.3, first row, we show the observable  $\tilde{\Delta}(\hat{e}_S, \hat{e}_T)$  in Eq. (4.32) for the decay  $\tau^- \rightarrow K^- \eta \nu_\tau$  for two representative values of the set of effective couplings  $(\hat{e}_s, \hat{e}_T)$ , that we anticipated from our results in section 4.4.5, that are consistent with the measured branching ratio. For the left plots of the figure we use  $(\hat{e}_S = -0.38, \hat{e}_T = 0)$  and thus the variations with respect to the SM occur due to  $M_{0+}$  and  $M_{00}$  in Eq. (4.31), while for the right ones we employ  $(\hat{e}_S = 0, \hat{e}_T = 0.085)$  with NP effects entering through  $M_{T+}$ ,  $M_{T0}$  and  $M_{TT}$  in Eq. (4.31). As one can observe, the variations of scalar nature are in general small and occur close to the  $s$  minimum, i.e. near the  $K\eta$  threshold and  $t/m_\tau^2 \sim 0.47$ , and for  $s/m_\tau^2 \sim 0.66$ , while the tensor contributions yield a sizable signal starting near the  $K\eta$  threshold and populate the diagonal of the Dalitz plot decreasingly. However, these contributions arise in zones with very suppressed probability in the SM (see upper-left plot in Fig. 4.2) and will thus be very challenging to identify.

In the case of  $\tau^- \rightarrow K^- \eta' \nu_\tau$ , shown in Fig. 4.4, we take, respectively,  $(\hat{e}_S = -0.20, \hat{e}_T = 0)$  and  $(\hat{e}_S = 0, \hat{e}_T = 14.9)$  for the left- and right-plots and the corresponding variations in the

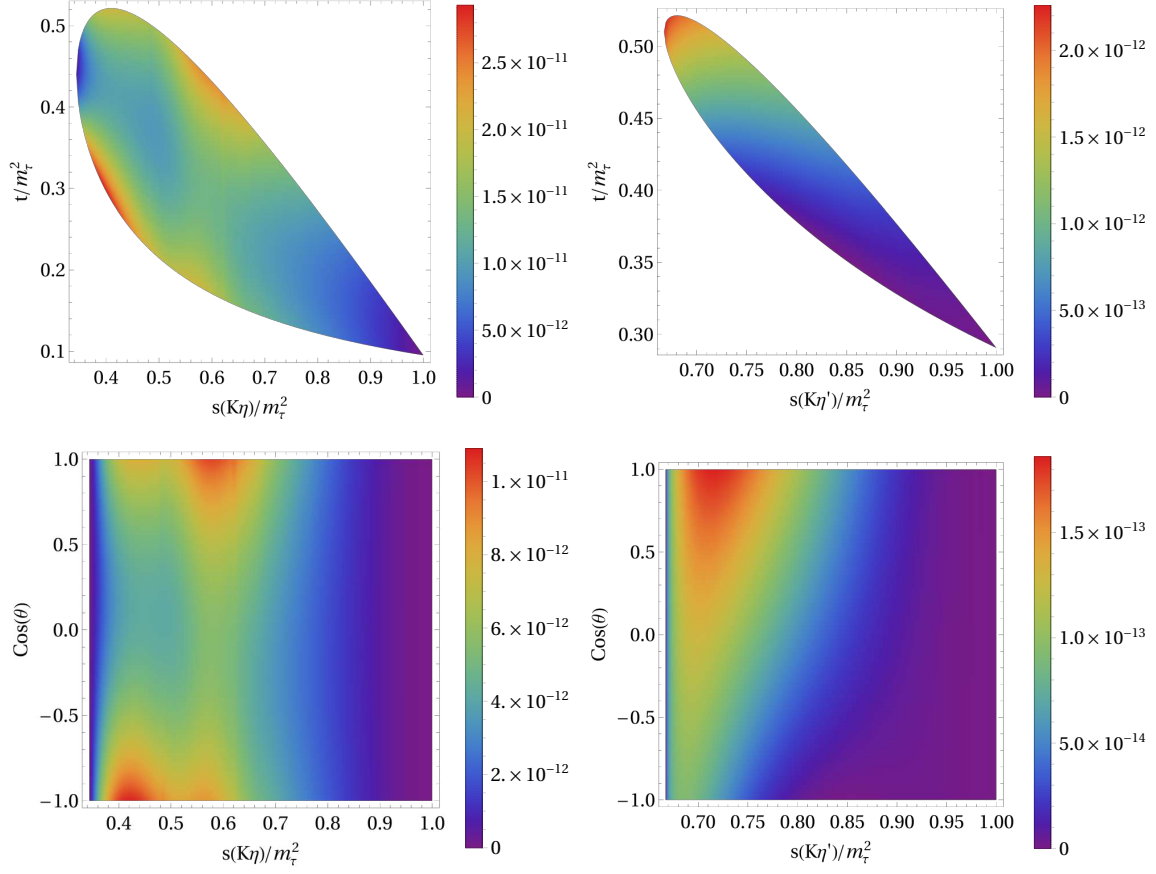


Figure 4.2: Dalitz plot distribution in the SM,  $|\overline{\mathcal{M}(0,0)}|^2$  in Eq. (4.30), for  $\tau^- \rightarrow K^- \eta \nu_\tau$  (left) and  $\tau^- \rightarrow K^- \eta' \nu_\tau$  (right) in the  $(s, t)$  variables. The figures of the lower row show the differential decay distribution in the  $(s, \cos \theta)$  variables, Eq. (4.33). The  $s$  and  $t$  variables are normalized to  $m_\tau^2$ .

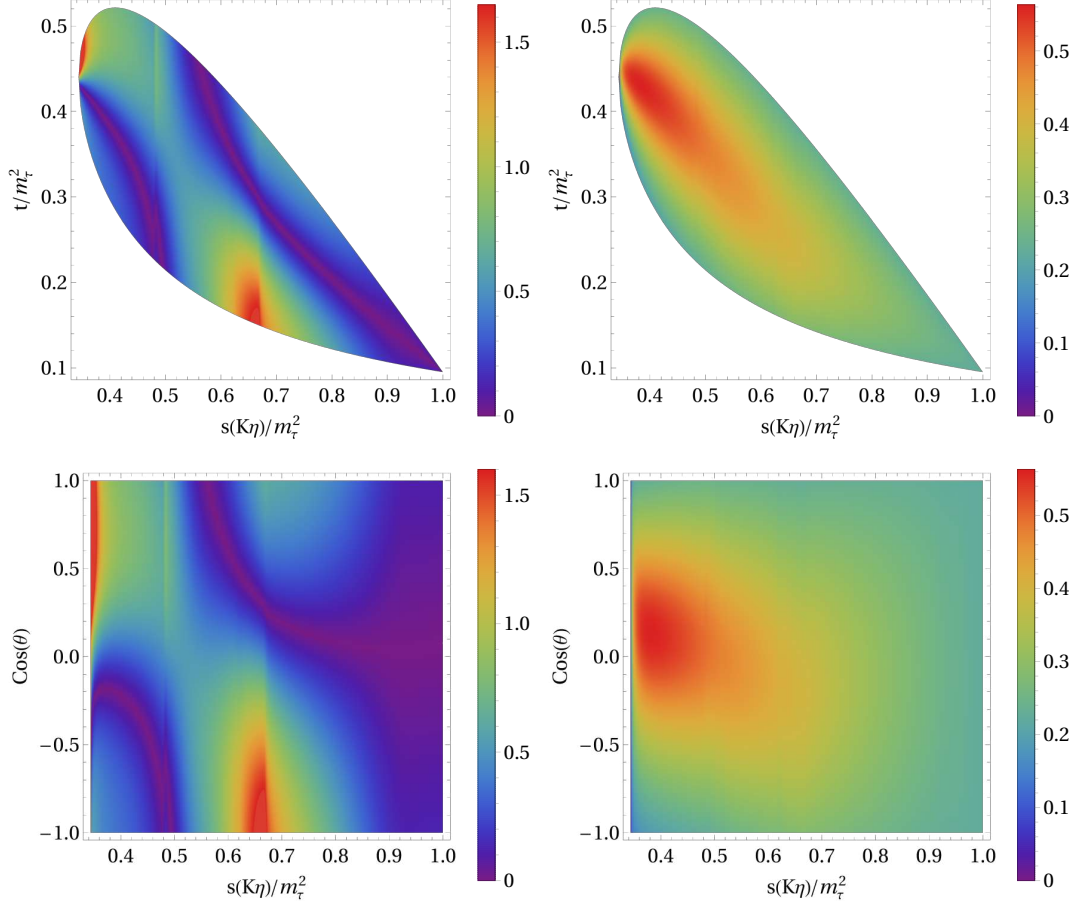


Figure 4.3: Dalitz plot distribution of  $\tilde{\Delta}(\hat{\epsilon}_S, \hat{\epsilon}_T)$  in Eq. (4.32) for  $\tau^- \rightarrow K^- \eta \nu_\tau$  with  $(\hat{\epsilon}_S = -0.38, \hat{\epsilon}_T = 0)$  (left panels) and  $(\hat{\epsilon}_S = 0, \hat{\epsilon}_T = 0.085)$  (right panels). The lower row shows the differential decay distribution in the  $(s, \cos \theta)$  variables, Eq. (4.33). The  $s$  and  $t$  variables are normalized to  $m_\tau^2$ .

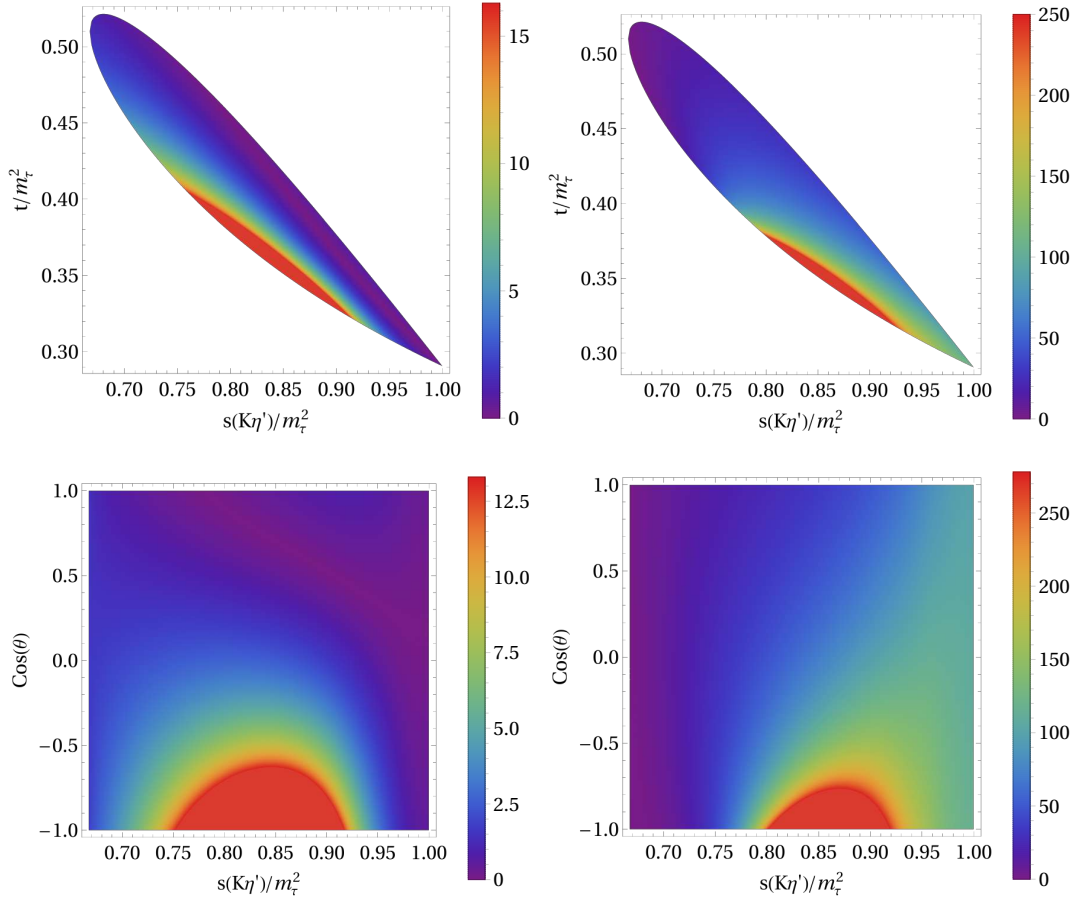


Figure 4.4: Dalitz plot distribution of  $\tilde{\Delta}(\hat{\epsilon}_S, \hat{\epsilon}_T)$  in Eq. (4.32) for  $\tau^- \rightarrow K^- \eta' \nu_\tau$  with  $(\hat{\epsilon}_S = -0.20, \hat{\epsilon}_T = 0)$  (left panels) and  $(\hat{\epsilon}_S = 0, \hat{\epsilon}_T = 14.9)$  (right panels). The lower row show the differential decay distribution in the  $(s, \cos \theta)$  variables, Eq. (4.33). The  $s$  and  $t$  variables are normalized to  $m_\tau^2$ .

Dalitz plot distribution are seen in a reduced and similar region close to  $s/m_\tau^2 \sim 0.85$  and  $t/m_\tau^2 \sim 0.35$ . Again, compared to the SM (see upper-right plot in Fig. 4.2), these effects appear in a zone of small probability density and will be therefore difficult to be measured.

If we had used another set of values of effective couplings e.g. [509], we would have obtained qualitatively similar results.

## 4.4.2 Angular distribution

The hadronic mass and angular distributions are also modified by the inclusion of the NP interactions that we are studying. It is convenient to work in the rest frame of the hadronic  $K\eta^{(\prime)}$  system defined by  $\vec{p}_K + \vec{p}_{\eta^{(\prime)}} = \vec{p}_\tau - \vec{p}_{\nu_\tau} = 0$ . In this frame, the tau lepton and kaon energies are given by  $E_\tau = (s+m_\tau^2)/2\sqrt{s}$  and  $E_K = (s+m_K^2-m_{\eta^{(\prime)}}^2)/2\sqrt{s}$ , and the measurable angle  $\theta$  between these two particles can be obtained from the invariant  $t$  variable through  $t = m_\tau^2 + m_K^2 - 2E_\tau E_K + 2|\vec{p}_K||\vec{p}_\tau| \cos\theta$ , where  $|\vec{p}_K| = \sqrt{E_K^2 - m_K^2}$  and  $|\vec{p}_\tau| = \sqrt{E_\tau^2 - m_\tau^2}$ .

The decay distribution in the  $(s, \theta)$  variables is given by:

$$\begin{aligned} \frac{d^2\Gamma}{d\sqrt{s}d\cos\theta} &= \frac{G_F^2|V_{us}|^2S_{EW}}{128\pi^3m_\tau}(1+\epsilon_L+\epsilon_R)^2\left(\frac{m_\tau^2}{s}-1\right)^2|\vec{p}_K|\left\{(C_{K\eta^{(\prime)}}^S)^2(\Delta_{K\pi})^2|F_0^{K\eta^{(\prime)}}(s)|^2\right. \\ &\times\left(1+\frac{s\hat{\epsilon}_S}{m_\tau(m_s-m_u)}\right)^2+16|\vec{p}_K|^2s^2\left|\frac{C_{K\eta^{(\prime)}}^V}{2m_\tau}F_+^{K\eta^{(\prime)}}(s)-\hat{\epsilon}_T F_T^{K\eta^{(\prime)}}(s)\right|^2 \\ &+4|\vec{p}_K|^2s\left(1-\frac{s}{m_\tau^2}\right)\cos^2\theta\left[(C_{K\eta^{(\prime)}}^V)^2|F_+^{K\eta^{(\prime)}}(s)|^2-4s\hat{\epsilon}_T^2|F_T^{K\eta^{(\prime)}}(s)|^2\right] \\ &+4C_{K\eta^{(\prime)}}^S\Delta_{K\pi}|\vec{p}_K|\sqrt{s}\cos\theta\left(1+\frac{s\hat{\epsilon}_S}{m_\tau(m_s-m_u)}\right) \\ &\times\left[C_{K\eta^{(\prime)}}^V\text{Re}[F_0^{K\eta^{(\prime)}}(s)F_+^{*K\eta^{(\prime)}}(s)]-\frac{2s\hat{\epsilon}_T}{m_\tau}\text{Re}[F_T^{K\eta^{(\prime)}}(s)F_0^{*K\eta^{(\prime)}}(s)]\right]\left.\right\}, \quad (4.33) \end{aligned}$$

which coincides with the SM result [428] when the effective couplings of new interactions are set to zero.

The SM Dalitz plot distribution in the  $(s, \cos\theta)$  variables is shown, for the same set of effective couplings discussed previously, in the second row of Fig. 4.2 for the  $K^-\eta$  (left) and  $K^-\eta'$  (right) decay modes.

The effects of non-SM interactions on the angular distributions is displayed in the second row of Figs. 4.3 and 4.4 for the  $K^-\eta$  and  $K^-\eta'$  decay modes, respectively. For the  $K^-\eta$  channel, the enhanced region near the  $K\eta$  threshold in the  $(s, t)$  upper-left diagram (the one close to  $s$  minimum) is slightly enhanced in a limited region ( $\cos\theta > 0$ ) as it can be seen on the lower-left plot of Fig. 4.3, while NP tensor contributions show that the enhanced area



for large  $t$  translates to nearly minimum values of  $\cos\theta$  as it can be observed on the plots of the right. For the  $K^-\eta'$  system, both NP scalar and tensor contributions have similar effects in the  $(s, \cos\theta)$  plot. These are given in Fig. 4.4 by the red sunshine area centered at  $s/m_\tau^2 \sim 0.85$ . Altogether, we conclude that possible deviations from the SM patterns in near future data will be hard to disentangle in  $(s, \cos\theta)$  Dalitz plot analyses.

### 4.4.3 Decay rate

Integrating Eq. (4.28) upon the  $t$  variable we obtain the  $K\eta^{(\prime)}$  invariant mass distribution

$$\begin{aligned} \frac{d\Gamma}{d\sqrt{s}} &= \frac{G_F^2 |V_{us} F_+^{K\eta^{(\prime)}}(0)|^2 m_\tau^3 S_{EW}}{192\pi^3 \sqrt{s}} (1 + \epsilon_L + \epsilon_R)^2 \left(1 - \frac{s}{m_\tau^2}\right)^2 \lambda^{1/2}(s, m_{\eta^{(\prime)}}^2, m_K^2) \\ &\times \left[ X_{VA} + \hat{\epsilon}_S X_S + \hat{\epsilon}_T X_T + \hat{\epsilon}_S^2 X_{S^2} + \hat{\epsilon}_T^2 X_{T^2} \right], \end{aligned} \quad (4.34)$$

where

$$X_{VA} = \frac{(C_{K\eta^{(\prime)}}^V)^2}{2s^2} \left[ 3|\tilde{F}_0^{K\eta^{(\prime)}}(s)|^2 \Delta_{K\eta^{(\prime)}}^2 + |\tilde{F}_+^{K\eta^{(\prime)}}(s)|^2 \left(1 + \frac{2s}{m_\tau^2}\right) \lambda(s, m_{\eta^{(\prime)}}^2, m_K^2) \right], \quad (4.35)$$

$$X_S = \frac{3}{s m_\tau} (C_{K\eta^{(\prime)}}^V)^2 |\tilde{F}_0^{K\eta^{(\prime)}}(s)|^2 \frac{\Delta_{K\eta^{(\prime)}}^2}{m_s - m_u}, \quad (4.36)$$

$$X_T = -\frac{6}{s m_\tau} C_{K\eta^{(\prime)}}^V \frac{\text{Re}[F_T^{K\eta^{(\prime)}}(s) F_+^{*K\eta^{(\prime)}}(s)]}{|f_+^{K\eta^{(\prime)}}(0)|^2} \lambda(s, m_{\eta^{(\prime)}}^2, m_K^2), \quad (4.37)$$

$$X_{S^2} = \frac{3}{2 m_\tau^2} (C_{K\eta^{(\prime)}}^V)^2 |\tilde{F}_0^{K\eta^{(\prime)}}(s)|^2 \frac{\Delta_{K\eta^{(\prime)}}^2}{(m_s - m_u)^2}, \quad (4.38)$$

$$X_{T^2} = \frac{4}{s} \frac{|F_T^{K\eta^{(\prime)}}(s)|^2}{|F_+^{K\eta^{(\prime)}}(0)|^2} \left(1 + \frac{s}{2 m_\tau^2}\right) \lambda(s, m_{\eta^{(\prime)}}^2, m_K^2). \quad (4.39)$$

In Eq. (4.34) we use  $|V_{us} F_+^{K^-\eta}(0)| = |V_{us} F_+^{K^-\pi^0}(0) \cos\theta_P|$  and  $|V_{us} F_+^{K^-\eta'}(0)| = |V_{us} F_+^{K^-\pi^0}(0) \sin\theta_P|$ , with  $|V_{us} F_+^{K^-\pi^0}(0)| = 0.2165(2)$  [541]. Notice that if one takes  $\epsilon_{L,R} = \hat{\epsilon}_{S,T} = 0$  we recover the SM result from Eq. (2.8) of Ref. [428]. The decay distribution in terms of the  $K\eta$  and  $K\eta'$  invariant mass is given, respectively, on the left-and right-plots of Fig. 4.5 for the rep-

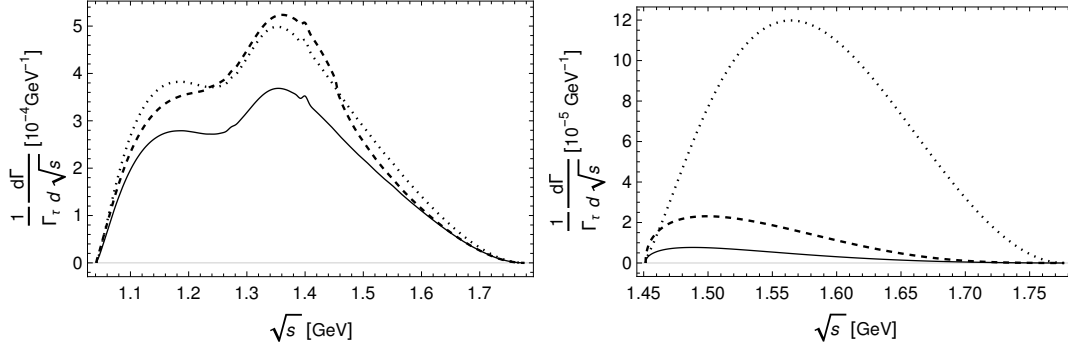


Figure 4.5: Left:  $K^-\eta$  invariant mass distribution in the SM (solid line), and for  $\hat{e}_S = -0.38$ ,  $\hat{e}_T = 0$  (dashed line) and  $\hat{e}_S = 0$ ,  $\hat{e}_T = 0.085$  (dotted line). Right:  $K^-\eta'$  invariant mass distribution in the SM (solid line), and for  $\hat{e}_S = -0.20$ ,  $\hat{e}_T = 0$  (dashed line) and  $\hat{e}_S = 0$ ,  $\hat{e}_T = 14.9$  (dotted line). Units in axes units are given in GeV powers and the decay distributions are normalized to the tau decay width.

representative values of the effective couplings. For the decay  $\tau^- \rightarrow K^-\eta\nu_\tau$ , it can be observed that the deviations with respect to the SM result (solid line) are sizable in the entire energy region of the decay spectrum. For the  $\tau^- \rightarrow K^-\eta'\nu_\tau$  decay spectrum, we predict a SM branching ratio of  $\text{BR}_{\text{SM}} \simeq 1.03 \times 10^{-6}$ . This value is found to be totally in line with [428] and respects the current experimental upper bound  $\text{BR}_{\text{exp}} < 2.4 \times 10^{-6}$  at 90 % C.L. [541]. In this regard, a measurement of this decay mode will be very welcome to further constrain the SM hadronic inputs, a requirement for searches of non-SM interactions. This measurement should be feasible at Belle-II [500].

#### 4.4.4 Forward-backward asymmetry

The forward-backward asymmetry for the hadronic  $K^-\eta^{(\prime)}$  system is defined in analogy to the previous di-meson modes we have studied [250, 251, 519]

$$\mathcal{A}_{K\eta^{(\prime)}}(s) = \frac{\int_0^1 d\cos\theta \frac{d^2\Gamma}{ds d\cos\theta} - \int_{-1}^0 d\cos\theta \frac{d^2\Gamma}{ds d\cos\theta}}{\int_0^1 d\cos\theta \frac{d^2\Gamma}{ds d\cos\theta} + \int_{-1}^0 d\cos\theta \frac{d^2\Gamma}{ds d\cos\theta}}. \quad (4.40)$$

Inserting Eq. (4.33) into the previous expression and integrating upon the  $\cos\theta$  variable

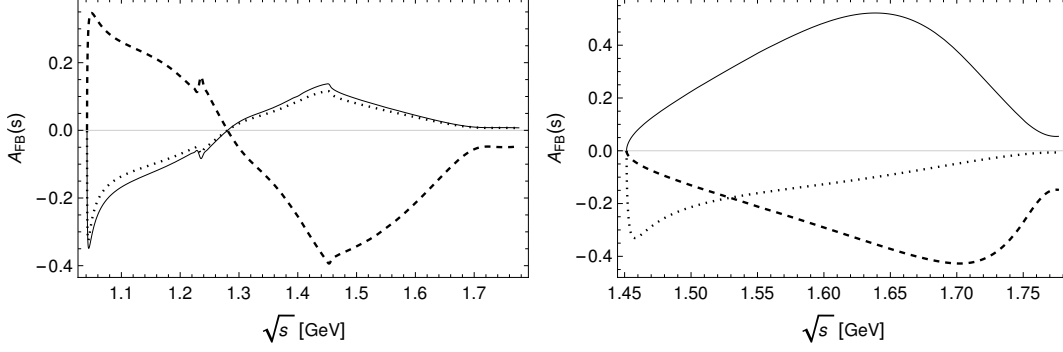


Figure 4.6: Left: Forward-backward asymmetry for the decay  $\tau^- \rightarrow K^- \eta \nu_\tau$  in the SM (solid line), and for  $\hat{\epsilon}_S = -0.38$ ,  $\hat{\epsilon}_T = 0$  (dashed line), and  $\hat{\epsilon}_T = 0.085$ ,  $\hat{\epsilon}_S = 0$  (dotted line). Right: Forward-backward asymmetry for the decay  $\tau^- \rightarrow K^- \eta' \nu_\tau$  in the SM (solid line), and for  $\hat{\epsilon}_S = -0.20$ ,  $\hat{\epsilon}_T = 0$  (dashed line), and  $\hat{\epsilon}_T = 14.9$ ,  $\hat{\epsilon}_S = 0$  (dotted line).

we obtain its analytical expression

$$\begin{aligned}
\mathcal{A}_{K\eta^{(\prime)}}(s) &= \frac{3C_{K\eta^{(\prime)}}^S \Delta_{K\pi} \sqrt{\lambda(s, m_{\eta^{(\prime)}}^2, m_K^2)}}{2s^2 |F_+^{K\eta^{(\prime)}}(0)|^2 [X_{VA} + \hat{\epsilon}_S X_S + \hat{\epsilon}_T X_T + \hat{\epsilon}_S^2 X_{S^2} + \hat{\epsilon}_T^2 X_{T^2}]} \\
&\times \left( 1 + \frac{s\hat{\epsilon}_S}{m_\tau(m_s - m_u)} \right) \left\{ C_{K\eta^{(\prime)}}^V \text{Re}[F_0^{K\eta^{(\prime)}}(s) F_+^{*K\eta^{(\prime)}}(s)] \right. \\
&\left. - \frac{2s\hat{\epsilon}_T}{m_\tau} \text{Re}[F_T^{K\eta^{(\prime)}}(s) F_0^{*K\eta^{(\prime)}}(s)] \right\}. \tag{4.41}
\end{aligned}$$

The forward-backward asymmetry in the SM case i.e.  $\hat{\epsilon}_{S,T} = 0$ , corresponds to the solid line in Fig. 4.6 for the decays  $K^- \eta$  (left plot) and  $K^- \eta'$  (right plot). For the  $K^- \eta$  mode, it should not be difficult to measure a non-zero (negative) value near the  $K^- \eta$  threshold.  $\mathcal{A}_{K\eta}$  increases with  $s$ , crosses zero at around 1.28 GeV and reaches its maximum near 1.45 GeV, when it decreases up to the upper kinematical limit. For the  $K\eta'$  case, the forward-backward asymmetry is a positive increasing observable from the  $K\eta'$  threshold until around 1.64 GeV where it has a plateau and decreases afterwards.

In these figures, we also display the results arising from considering non-SM scalar and tensor interactions. For the  $K^- \eta$  channel, one observes that the tensor case (dotted line) overlaps with the SM prediction thus being difficult to unveil its possible effects from the SM contribution. On the contrary, for non-SM scalar interactions (dashed line),  $\mathcal{A}_{K\eta}$  flips sign

with respect to the SM slightly before 1.3 GeV and it gets larger in magnitude as  $s$  increases. If it is possible to measure this observable eventually, this would ease the identification of NP contributions in  $\mathcal{A}_{K\eta}$ . The non-standard scalar contribution to the forward-backward asymmetry of the  $K\eta'$  decay mode is negative and has, to great extent, the same size than the SM ones but with opposite sign. The NP tensor contribution, also negative, has a clear non-zero value near threshold and then becomes a decreasing function until the kinematical upper limit of  $\sqrt{s}$ . It is clear then that noticeable differences with respect to the SM contribution will be appreciated for quite large values of the new effective couplings.

#### 4.4.5 Limits on $\hat{\epsilon}_S$ and $\hat{\epsilon}_T$

Integrating the invariant mass distribution Eq. (4.34) upon the  $s$  variable one obtains the total decay width which, in turn, depends on the NP effective couplings  $\hat{\epsilon}_{S,T}$ . One can therefore use the experimental branching ratio to set bounds on  $\hat{\epsilon}_{S,T}$ . For this purpose, we compare the decay width as obtained by including non-SM interactions, and that we denote by  $\Gamma$ , with respect to the SM width,  $\Gamma^0$ , obtained by neglecting NP interactions i.e. setting  $\hat{\epsilon}_{S,T} = 0$ . The relative shift produced by the NP contributions is better accounted for through the following observable:

$$\Delta \equiv \frac{\Gamma - \Gamma^0}{\Gamma^0} = \alpha \hat{\epsilon}_S + \beta \hat{\epsilon}_T + \gamma \hat{\epsilon}_S^2 + \delta \hat{\epsilon}_T^2. \quad (4.42)$$

The numerical values of the coefficients  $\alpha, \beta, \gamma$  and  $\delta$  for the processes under consideration are found to be:  $\alpha = 0.85_{-0.09}^{+0.05}$ ,  $\beta = 3.7_{-1.3}^{+1.2}$ ,  $\gamma = 4.3_{-0.9}^{+0.6}$  and  $\delta = 3.9_{-2.2}^{+3.0}$  for the  $K^-\eta$  decay channel;  $\alpha = 24.2_{-2.7}^{+1.5}$ ,  $\beta = -0.26_{-0.24}^{+0.17}$ ,  $\gamma = 175.9_{-36.6}^{+23.3}$  and  $\delta = 0.10_{-0.09}^{+0.28}$  for the  $K^-\eta'$  mode. The errors carried by the previous coefficients come from the uncertainty associated to the corresponding form factors (see section 4.3). Eq. (4.42) is a quadratic function of the effective scalar and tensor couplings that can be used to explore the sensitivity of the corresponding decays to the effects of non-SM interactions. As in Refs. [250,251,519], we will do this in two different ways. Firstly, we set one of the couplings to zero and obtain bounds for the other,

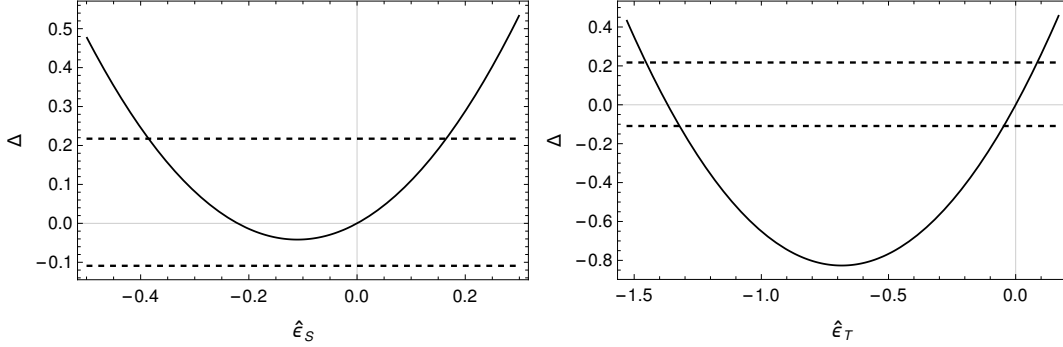


Figure 4.7:  $\Delta$  as a function of  $\hat{e}_S$  for  $\hat{e}_T = 0$  (left-hand) and  $\hat{e}_T$  for  $\hat{e}_S = 0$  (right-hand) for the decay  $\tau^- \rightarrow K^- \eta \nu_\tau$ . Horizontal lines represent the values of  $\Delta$  according to the current measurement and theory errors (at three standard deviations) of the branching ratio (dashed line).

and vice versa. The result is shown in Figs. 4.7 and 4.8 for the two decays concerning us, respectively. In these figures, the horizontal lines represent the current experimental limits on  $\Delta$  (at three standard deviations), and the resulting bounds for the effective couplings are found to be

$$-0.38 \leq \hat{e}_S \leq 0.16, \quad \hat{e}_T = 0, \quad (4.43)$$

$$\hat{e}_S = 0, \quad \hat{e}_T = [-1.4, -0.7] \cup [-0.047, 0.085], \quad (4.44)$$

from the decay  $\tau^- \rightarrow K^- \eta \nu_\tau$  ( $BR_{\text{exp}} = 1.55(8) \times 10^{-4}$  [541]), and

$$-0.20 \leq \hat{e}_S \leq 0.05, \quad \hat{e}_T = 0, \quad (4.45)$$

$$\hat{e}_S = 0, \quad -7.6 \leq \hat{e}_T \leq 14.9, \quad (4.46)$$

from the transition  $\tau^- \rightarrow K^- \eta' \nu_\tau$  ( $BR_{\text{exp}} < 2.4 \times 10^{-6}$  at 90% C.L. [541]).

Secondly, we have also set constraints on these couplings from the general case where both are non-vanishing using Eq. (4.42) as before. These results are graphically represented by ellipses in the  $\hat{e}_S$ - $\hat{e}_T$  plane in Fig. 4.9 for the two decay channels under consideration.

Altogether, our results for the bounds in the scalar and tensor effective couplings  $\hat{e}_S$

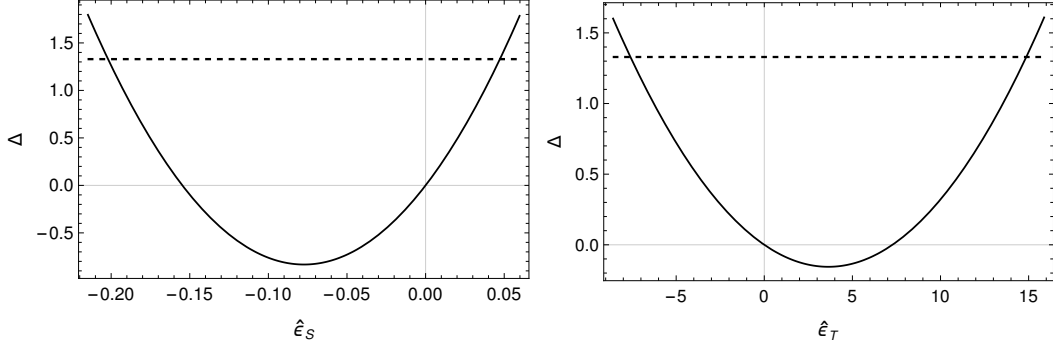


Figure 4.8:  $\Delta$  as a function of  $\hat{e}_S$  for  $\hat{e}_T = 0$  (left plot) and  $\hat{e}_T$  for  $\hat{e}_S = 0$  (right plot) for the decay  $\tau^- \rightarrow K^- \eta' \nu_\tau$ . Horizontal lines represent the values of  $\Delta$  according to the current measurement and theory errors (at three standard deviations) of the branching ratio (dashed line).

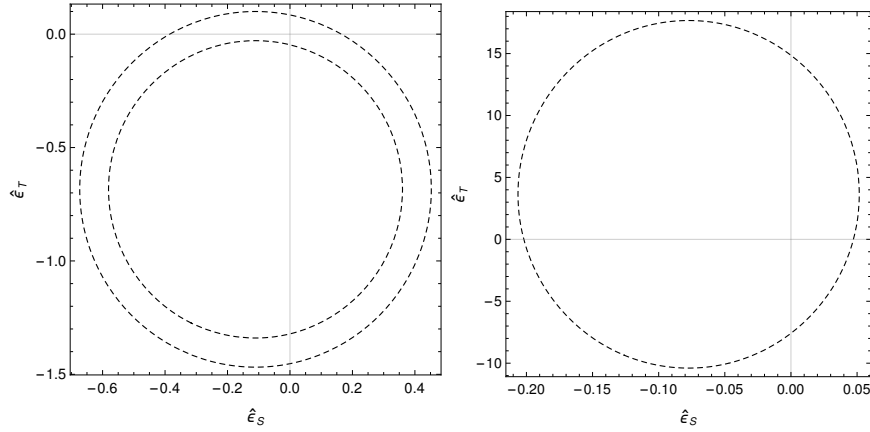


Figure 4.9: Constraints on the scalar and tensor couplings obtained from  $\Delta(\tau^- \rightarrow K^- \eta \nu_\tau)$  (left plot) and  $\Delta(\tau^- \rightarrow K^- \eta' \nu_\tau)$  (right plot) using, respectively, the measured branching ratio (at three standard deviations) and the upper limits of the branching ratio at 90% C.L.

Decay channel	$\hat{\epsilon}_S (\hat{\epsilon}_T = 0)$	$\hat{\epsilon}_T (\hat{\epsilon}_S = 0)$	$\hat{\epsilon}_S$	$\hat{\epsilon}_T$
$\tau^- \rightarrow K^- \eta \nu_\tau$ [542]	$[-0.38, 0.16]$	$[-1.4, -0.7] \cup [-4.7, 8.5] \cdot 10^{-2}$	$[-0.7, 0.5]$	$[-1.5, 0.1]$
$\tau^- \rightarrow K^- \eta' \nu_\tau$ [542]	$[-0.20, 0.05]$	$[-7.6, 14.9]$	$[-0.21, 0.05]$	$[-10.4, 17.7]$
$\tau^- \rightarrow K^- K^0 \nu_\tau$ [542]	$[-0.12, -0.08] \cup [0.08, 0.12]$	$[-0.12, -0.06] \cup [0.92, 0.99]$	$[-0.2, 0.2]$	$[-0.12, 0.98]$
$\tau^- \rightarrow \pi^- \pi^0 \nu_\tau$ [519]	$[-1.33, 1.31]$	$[-0.79, -0.57] \cup [-1.4, 1.3] \cdot 10^{-2}$	$[-5.2, 5.2]$	$[-0.79, 0.013]$
$\tau^- \rightarrow (K\pi)^- \nu_\tau$ [251]	$[-0.57, 0.27]$	$[-0.059, 0.052] \cup [0.60, 0.72]$	$[-0.89, 0.58]$	$[-0.07, 0.72]$
$\tau^- \rightarrow \pi^- \eta \nu_\tau$ [250]	$[-8.3, 3.9] \cdot 10^{-3}$	$[-0.43, 0.39]$	$[-0.83, 0.37] \cdot 10^{-2}$	$[-0.55, 0.50]$
$\tau^- \rightarrow \pi^- \eta' \nu_\tau$ [250]	$[-1.13, 0.68] \cdot 10^{-2}$	$ \hat{\epsilon}_T  < 11.4$	$[-1.13, 0.67] \cdot 10^{-2}$	$[-11.9, 11.9]$

Table 4.1: Constraints on the scalar and tensor couplings obtained (at three standard deviations) through the limits on the current branching ratio measurements. Theory errors are included.

and  $\hat{\epsilon}_T$  that can be obtained at three standard deviations from the current experimental measurement are gathered in Table 4.1. The constraints on the scalar coupling obtained from the  $K^- \eta$  decay channel is quite symmetric while the tensor coupling has a mild preference for  $\hat{\epsilon}_T < 0$ . The allowed region has the same size for both. Limits on the scalar coupling from the  $K^- \eta'$  mode favor slightly  $\hat{\epsilon}_S < 0$  while the constraints on the tensor one are much weaker in this case.

In this table, we also compare the results of this work with the constraints we have obtained in previous analyses from the  $\pi^- \pi^0$  [519],  $K^- K^0$  [540, 542],  $(K\pi)^-$  [251, 540] and  $\pi^- \eta^{(\prime)}$  [250] decay channels. The constraints for the scalar couplings are found to be more precise than those obtained from the di-pion mode, competitive with the limits set from the  $(K\pi)^-$  decays, and weaker than the bounds coming from the decays  $\pi^- \eta^{(\prime)}$ . For the tensor couplings, we notice that the  $K\eta'$  channel gives a much looser limits than the decays with  $K\eta$  and  $K^- K^0$ . The allowed region of the last two, in turn, is similar than that obtained in previous analyses but for  $\pi^- \eta'$ , which is not competitive restricting tensor interactions.

As a final exercise, we have also determined the effective couplings from a  $\chi^2$  function in the following way:

$$\chi^2 = \left( \frac{\text{BR}_{K^- \eta}^{\text{th}} - \text{BR}_{K^- \eta}^{\text{exp}}}{\sigma_{\text{BR}_{K^- \eta}^{\text{exp}}}} \right)^2 + \left( \frac{\text{BR}_{K^- K^0}^{\text{th}} - \text{BR}_{K^- K^0}^{\text{exp}}}{\sigma_{\text{BR}_{K^- K^0}^{\text{exp}}}} \right)^2, \quad (4.47)$$

where  $\text{BR}_{K^- \eta}^{\text{exp}}$  and  $\sigma_{\text{BR}_{K^- \eta}^{\text{exp}}}$ , and  $\text{BR}_{K^- K^0}^{\text{exp}}$  and  $\sigma_{\text{BR}_{K^- K^0}^{\text{exp}}}$ , are the measured branching ratio and the corresponding uncertainties of the  $K^- \eta$  and  $K^- K^0$  decay mode, and  $\text{BR}_{K^- \eta}^{\text{th}}$  and

$\text{BR}_{K^-K^0}^{\text{th}}$  are the analogue theoretical expressions obtained upon integrating Eq. (4.34). The  $\chi^2$  function defined above depends solely on  $\hat{\epsilon}_S$  and  $\hat{\epsilon}_T$ . Using the experimental value given below Eq. (4.44) and the branching fraction of the  $\tau^- \rightarrow K^- K^0 \nu_\tau$  decay ( $\text{BR}_{\text{exp}} = 1.486(34) \cdot 10^{-3}$  [541]), we obtain the constraints:

$$\hat{\epsilon}_S = 0.088_{-0.056}^{+0.035}, \quad \hat{\epsilon}_T = 0.015_{-0.066}^{+0.056}, \quad (4.48)$$

where variations up to  $3\sigma$  of the measured branching ratios have been taken into account.

Comparing our results with bounds obtained from other low-energy probes, our previous limits are not competitive with semileptonic kaon decays,  $\hat{\epsilon}_S = (-3.9 \pm 4.9) \times 10^{-4}$  and  $\hat{\epsilon}_T = (0.5 \pm 5.2) \times 10^{-3}$  [509], while they are similar than those obtained from hyperon decays [507], where  $|\hat{\epsilon}_S| < 4 \times 10^{-2}$  and  $|\hat{\epsilon}_T| < 5 \times 10^{-2}$  are found at a 90% C.L.<sup>5</sup>. Concerning the results of Ref. [512], obtained also from hadronic tau decays (strangeness-conserving transitions only), our corresponding limits are less precise. However, the use of all available data of all possible di-meson tau decays (see Table 4.1) could allow us improve the knowledge in this respect. Such analysis is presented in the next chapter.

## 4.5 Conclusions

Hadronic tau lepton decays remain to be an advantageous tool for the investigation of the hadronization of QCD currents in the non-perturbative regime of the strong interaction. In this paper, we have studied the decays  $\tau^- \rightarrow K^- \eta^{(\prime)} \nu_\tau$  in the presence of non-Standard Model scalar and tensor interactions. We have focused our analysis on setting bounds on the corresponding New Physics couplings from the current experimental measurements of these decays. This has been possible due to the satisfactory knowledge we have on the necessary Standard Model hadronic input, the form factors. For the description of the participating

---

<sup>5</sup>For the comparison, we need to assume lepton universality because our study involves the tau lepton, while theirs electrons and muons. Given the smallness of possible lepton universality violations, this is enough for current precision. We have also assumed that the corresponding CKM matrix elements do not change under NP interactions, which is the case if  $\epsilon(lud) = \epsilon(lus)$  [549].



vector and scalar form factors, we have employed previous results based on constraints from Chiral Perturbation Theory supplemented by dispersion relations and experimental data. On the contrary, there are no experimental data to help us constructing the required tensor form factor and, therefore, it has been described under theoretical arguments solely. Within this framework, we have set limits (see Table 4.1) on the non-standard scalar and tensor couplings,  $\hat{\epsilon}_S$  and  $\hat{\epsilon}_T$ , respectively, using the measured branching ratios, and have studied their effects on different phenomenological observables including Dalitz plot and angular distributions, the decay rate and the forward-backward asymmetry. The present analysis completes our series of dedicated studies of two-meson tau decays [250, 251, 519] that have shown the complementary role that tau decays can play in restricting non-standard interactions. Despite our bounds on the NP couplings are not as precise as those placed, for example, from semileptonic kaon decays [509], and the corresponding effects are very challenging to identify, we hope our works can serve as a motivation for the experimental tau physics groups at Belle-II to measure the different observables we have discussed.

# Chapter 5

## Global Fit of non-standard interactions in exclusive semileptonic tau decays

In this chapter we perform a global fit using exclusive semileptonic tau decays for one and two pseudoscalar mesons, as a outcome we get powerful constraints on non-standard interactions.

### 5.1 Introduction

The  $\tau$  lepton is the only known lepton heavy enough ( $m_\tau = 1.77686$  GeV [541]) to decay into hadrons; the  $\sim 65\%$  of its partial width contains hadrons in the final state. In the Standard Model (SM), hadronic tau decays proceed through the exchange of  $W^\pm$  bosons which couple the  $\tau$  and the generated neutrino  $\nu_\tau$  together with a quark-antiquark pair that subsequently hadronizes. Such decays thus offer an advantageous laboratory to study low-energy effects of the strong interactions under clean conditions [4] since half of the process is purely electroweak and, therefore, free of uncertainties at the required precision. At the inclusive level, these decays allow to extract fundamental parameters of the SM, most importantly the strong coupling  $\alpha_S$  [550,551], but also the CKM quark-mixing matrix

element  $|V_{us}|$  [380, 552, 553] and the mass of the strange quark at high precision [554–560]. On the other hand, exclusive hadronic decays can be used to learn specific properties of the hadrons involved and the interactions among them. These can be classified according to the number of hadrons in the final state. The simple one-meson transitions  $\tau^- \rightarrow P^- \nu_\tau$  ( $P = \pi, K$ ) are very well-known due to the precise determinations of the pion and kaon decays constants obtained by the Lattice collaborations [377]. At present, we also have a very good knowledge on the decays into a pair of mesons, the SM input of which is encoded in terms of hadronic form factors. An ideal road map to describe meson form factors would require a model-independent approach demanding a full knowledge of QCD in both its perturbative and non-perturbative regimes, knowledge not yet unraveled. An alternative to such enterprise would pursue a synergy between theoretical calculations and experimental data. In this respect, dispersion relations are a powerful tool to direct oneself towards a model-independent description of meson form factors. For example, the analyses of the decays  $\pi^- \pi^0$  [15, 16, 19, 28] and  $K_S \pi^-$  [23, 24, 30, 409, 410], carried out by exploiting the synergy between Resonance Chiral Theory [224] and dispersion theory, are found to be in a nice agreement with the rich data provided by the experiments. Accord with experimental measurements is also found for the  $K^- K_S$  [28] and  $K^- \eta$  [30, 428] decay modes, although higher-quality data on these processes is required to constrain the corresponding theories or models, while the predictions for the isospin-violating  $\pi^- \eta^{(\prime)}$  channels [447, 513] respect the current experimental upper bounds. The latter are very challenging processes for Belle-II [500]. Higher-multiplicity decay modes involve a richer dynamical structure but accounting for the strong rescattering effects is not an easy task when three or more hadrons are present.

So far, all experimental results with the  $\tau$  lepton are found to be in accord with the SM, with the exception of the  $2.6\sigma(2.4\sigma)$  deviation from lepton flavour universality in  $|g_\tau/g_\mu|(|g_\tau/g_e|)$  from  $W^- \rightarrow \tau^- \bar{\nu}_\tau$  [541, 561]<sup>1</sup>, of the BaBar measurement of the CP asymmetry in  $\tau^- \rightarrow K_S \pi^- \nu_\tau$ ,  $A_{CP} = -3.6(2.3)(1.1) \times 10^{-3}$  [423], which is  $2.8\sigma$  off the SM prediction,  $A_{CP} = 3.6(1) \times 10^{-3}$  [426], and of the anomalous excess of  $\tau$  production observed in some  $B$

---

<sup>1</sup>See also Ref. [562], where the authors show that a NP explanation of this tension is not very plausible. This anomaly disappeared after the ATLAS [563] and CMS [564] measurements.

decays. As seen, these effects are not statistically large. However, the increased sensitivities of the most recent experiments yield interesting limits on possible New Physics contributions in the hadronic tau sector.

Several recent works [250,251,512,519,542] have put forward that semileptonic tau decays are not only a clean QCD laboratory but also offer an interesting scenario to set bounds on non-standard weak charged current interactions complementary to the traditional low-energy semileptonic probes such nuclear beta decays, purely leptonic lepton, pion and kaon decays or hyperon decays (see e.g. Refs. [187,192,504–511,539]).

The aim of the present work is to close the circle by extending our previous individual analyses of the decays  $\tau^- \rightarrow \pi^- \pi^0 \nu_\tau$  [519],  $\tau^- \rightarrow (K\pi)^- \nu_\tau$  [251],  $\tau^- \rightarrow K^- (K^0, \eta^{(\prime)}) \nu_\tau$  [542] and  $\tau^- \rightarrow \pi^- \eta^{(\prime)} \nu_\tau$  [250], carried out using the low-energy limit of the Standard Model Effective Field Theory Lagrangian (SMEFT) [1,130] up to dimension six, to a global analysis of the strangeness-conserving ( $\Delta S=0$ ) and strangeness-changing ( $|\Delta S|=1$ ) semileptonic exclusive tau decays into one and two pseudoscalar mesons. The main advantage of this EFT framework is that experimental measurements and their implications for New Physics can be compared unambiguously either at low energies or at the high LHC energies in a model-independent way [512].

We can anticipate that the bounds for the NP couplings that we get in this work (in the  $\overline{\text{MS}}$  scheme at the scale  $\mu = 2 \text{ GeV}$ ), obtained from all data available on exclusive  $\tau$  decays only, are competitive and found to be in line with those of Ref. [512], which were obtained analyzing data including both exclusive and inclusive decays. This agreement represents a good consistency test between exclusive and inclusive determinations.

On the theory side, a controlled theoretical determination, with a robust error band, of the corresponding form factors within the SM is required in order to increase the accuracy of the search for non-standard interactions. At present, we have such a knowledge for the vector and -to a great extent- the scalar form factors, but there are no experimental data that can help us constructing the tensor form factor and, therefore, it has to be built under theoretical considerations only.

The fantastic possibilities offered by the Belle-II experiment [500], and other future  $Z$ , tau-charm and  $B$ -factories, to study  $\tau$  physics and low multiplicity final states with high precision make these studies of timely interest.

This chapter is organized as follows. The theoretical framework is given in section 5.2 where we briefly present the effective Lagrangian for weak charge current interactions involving light flavours up to dimension six, assuming left-handed neutrinos. The expressions for the one-and two-meson partial decay width to be used in our fits are also defined in this section. The description of the corresponding form factors is the subject of section 5.3. In sections 5.4 and 5.5 we perform fits to the strangeness-conserving ( $\Delta S=0$ ) and changing ( $|\Delta S|=1$ ) transitions, respectively, and set bounds on the New Physics effective couplings. A global fit to both sectors i.e. ( $|\Delta S|=0$  and 1), is performed in section 5.6. Finally, our conclusions are presented in section 5.7.

## 5.2 SMEFT Lagrangian and decay rate

We start out writing the low-energy limit of the Standard Model Effective Field Theory Lagrangian including dimension six operators that describes semileptonic  $\tau^- \rightarrow \nu_\tau \bar{u} D$  strangeness-conserving ( $D = d$ ) or strangeness-changing ( $D = s$ ) charged current transitions with left-handed neutrinos. Such Lagrangian reads [504, 505]:

$$\begin{aligned} \mathcal{L}_{CC} = & -\frac{G_F V_{uD}}{\sqrt{2}} \left[ (1 + \epsilon_L^\tau) \bar{\tau} \gamma_\mu (1 - \gamma^5) \nu_\tau \cdot \bar{u} \gamma^\mu (1 - \gamma^5) D \right. \\ & + \epsilon_R^\tau \bar{\tau} \gamma_\mu (1 - \gamma^5) \nu_\tau \cdot \bar{u} \gamma^\mu (1 + \gamma^5) D \\ & + \bar{\tau} (1 - \gamma^5) \nu_\tau \cdot \bar{u} (\epsilon_S^\tau - \epsilon_P^\tau \gamma^5) D \\ & \left. + \epsilon_T^\tau \bar{\tau} \sigma_{\mu\nu} (1 - \gamma^5) \nu_\tau \bar{u} \sigma^{\mu\nu} (1 - \gamma^5) D \right] + h.c. , \end{aligned} \quad (5.1)$$

where  $\sigma^{\mu\nu} = i[\gamma^\mu, \gamma^\nu]/2$ ,  $G_F$  is the tree-level definition of the Fermi constant and  $\epsilon_i$  ( $i = L, R, S, P, T$ ) are effective couplings characterizing NP. These can be complex, although we

will assume them real in first approximation since we are only interested in  $CP$  conserving quantities<sup>2</sup>. The product  $G_F V_{uD}$  in Eq. (5.1) denotes that its determination from the super-allowed nuclear Fermi  $\beta$  decays carries implicitly a dependence on  $\epsilon_L^e$  and  $\epsilon_R^e$  that is given by [509]

$$G_F \tilde{V}_{uD}^e = G_F (1 + \epsilon_L^e + \epsilon_R^e) V_{uD}, \quad (5.2)$$

and that we use for our analysis. Setting the coefficients  $\epsilon_i = 0$ , one recovers the SM Lagrangian.

The simplest semileptonic decays that can be calculated with the low-energy effective Lagrangian of Eq. (5.1) are the one-meson decay modes  $\tau^- \rightarrow P^- \nu_\tau$  ( $P = \pi, K$ ). The expression for the  $\tau^- \rightarrow \pi^- \nu_\tau$  decay rate reads

$$\Gamma(\tau^- \rightarrow \pi^- \nu_\tau) = \frac{G_F^2 |\tilde{V}_{ud}^e|^2 f_\pi^2 m_\tau^3}{16\pi} \left(1 - \frac{m_\pi^2}{m_\tau^2}\right)^2 (1 + \delta_{\text{em}}^{\tau\pi} + 2\Delta^{\tau\pi} + \mathcal{O}(\epsilon_i^\tau)^2 + \mathcal{O}(\delta_{\text{em}}^{\tau\pi} \epsilon_i^\tau)), \quad (5.3)$$

where  $f_\pi$  is the pion decay constant, the quantity  $\delta_{\text{em}}^{\tau\pi}$  accounts for the electromagnetic radiative corrections and the term  $\Delta^{\tau\pi}$  contains the tree-level NP corrections that arise from the Lagrangian in Eq. (5.1)<sup>3</sup> that are not absorbed in  $\tilde{V}_{ud}^e$ . For the channel  $\tau^- \rightarrow K^- \nu_\tau$ , the decay rate is that of Eq. (5.3) but replacing  $\tilde{V}_{ud}^e \rightarrow \tilde{V}_{us}^e$ ,  $f_\pi \rightarrow f_K$ ,  $m_\pi \rightarrow m_K$ , and  $\delta_{\text{em}}^{\tau\pi}$  and  $\Delta^{\tau\pi}$  by  $\delta_{\text{em}}^{\tau K}$  and  $\Delta^{\tau K}$ , respectively.

The amplitude for two-meson decays  $\tau^- \rightarrow (PP')^- \nu_\tau$  that arises from the Lagrangian in Eq. (5.1) contains a vector, an scalar and a tensor contribution. The structure of the amplitude, including a detailed definition of the corresponding hadronic matrix element, can be found in our previous works i.e in Ref. [519] for  $\pi^- \pi^0$ , in Ref. [251] for the  $(K\pi)^-$  system, and in Ref. [542] for the cases  $K^-(K^0, \eta^{(\prime)})$ , and we therefore have decided not repeat it here once again.

The resulting partial decay width for two-meson decays is given by (the variable  $s$  is the

---

<sup>2</sup>The only coupling sensitive to an imaginary part is  $\epsilon_S^\tau$  from the decay  $\tau^- \rightarrow \pi^- \eta \nu_\tau$  [512] that we do not consider in this work for lack of data.

<sup>3</sup>In Eq. (5.3) we have expanded up to linear order on the  $\epsilon_i^\tau$  couplings.

invariant mass of the corresponding two-meson system):

$$\begin{aligned} \frac{d\Gamma}{ds} = & \frac{G_F^2 |\tilde{V}_{uD}^e|^2 m_\tau^3 S_{EW}}{384\pi^3 s} \left(1 - \frac{s}{m_\tau^2}\right)^2 \lambda^{1/2}(s, m_P^2, m_{P'}^2) \\ & \times \left[ (1 + 2(\epsilon_L^\tau - \epsilon_L^e + \epsilon_R^\tau - \epsilon_R^e)) X_{VA} + \epsilon_S^\tau X_S + \epsilon_T^\tau X_T + (\epsilon_S^\tau)^2 X_{S^2} + (\epsilon_T^\tau)^2 X_{T^2} \right], \end{aligned} \quad (5.4)$$

where

$$\begin{aligned} X_{VA} = & \frac{1}{2s^2} \left\{ 3 \left(C_{PP'}^S\right)^2 |F_0^{PP'}(s)|^2 \Delta_{PP'}^2 + \left(C_{PP'}^V\right)^2 |F_+^{PP'}(s)|^2 \left(1 + \frac{2s}{m_\tau^2}\right) \lambda(s, m_P^2, m_{P'}^2) \right\}, \\ X_S = & \frac{3}{s m_\tau} \left(C_{PP'}^S\right)^2 |F_0^{PP'}(s)|^2 \frac{\Delta_{PP'}^2}{m_d - m_u}, \\ X_T = & \frac{6}{s m_\tau} C_{PP'}^V \operatorname{Re} \left[ F_T^{PP'}(s) \left(F_+^{PP'}(s)\right)^* \right] \lambda(s, m_P^2, m_{P'}^2), \\ X_{S^2} = & \frac{3}{2m_\tau^2} \left(C_{PP'}^S\right)^2 |F_0^{PP'}(s)|^2 \frac{\Delta_{PP'}^2}{(m_d - m_u)^2}, \\ X_{T^2} = & \frac{4}{s} |F_T^{PP'}(s)|^2 \left(1 + \frac{s}{2m_\tau^2}\right) \lambda(s, m_P^2, m_{P'}^2), \end{aligned} \quad (5.5)$$

with  $C_{PP'}^V$  and  $C_{PP'}^S$  being the corresponding Clebsch-Gordan coefficients and where we have defined  $\Delta_{PP'} = m_P^2 - m_{P'}^2$ . In Eq. (5.4),  $S_{EW} = 1.0201$  [365] resums the short-distance electroweak corrections and the function  $\lambda(x, y, z) = x^2 + y^2 + z^2 - 2xy - 2xz - 2yz$  is the usual Kallen function.

The functions  $F_0^{PP'}(s)$ ,  $F_+^{PP'}(s)$  and  $F_T^{PP'}(s)$  in Eq. (5.5) are, respectively, the scalar, the vector and the tensor form factors, and their respective parametrizations is the subject of the next section.

### 5.3 Two-meson form factors

In this section, we provide a brief overview of the description of the scalar, vector and tensor form factors that we employ in our analysis. It is fundamental to have good control over

them since they are used as SM inputs for binding the non-standard interactions. We will not discuss them here at length but rather provide a compilation of the main formulae to make this work self-contained.

To describe the pion vector form factor we follow the representation outlined in Ref. [28], and briefly summarized below for the convenience of the reader, and write a thrice subtracted dispersion relation

$$F_+^{\pi\pi}(s) = \exp \left[ \alpha_1 s + \frac{\alpha_2}{2} s^2 + \frac{s^3}{\pi} \int_{4m_\pi^2}^{s_{\text{cut}}} \frac{ds'}{(s')^3} \frac{\phi(s')}{(s' - s - i0)} \right], \quad (5.6)$$

where  $\alpha_1$  and  $\alpha_2$  are two subtraction constants that can be related to the slope and curvature appearing in the low-energy expansion of the form factor. The use of a three-times subtracted dispersion relation reduces the high-energy contribution of the integral where the phase is less well-known. In Eq. (5.6),  $s_{\text{cut}}$  is a cut-off whose value is fixed from the requirement that the fitted parameters are compatible within errors with the case  $s_{\text{cut}} \rightarrow \infty$ . The value of  $s_{\text{cut}} = 4 \text{ GeV}^2$  was found to satisfy this criterion [28], and variations of  $s_{\text{cut}}$  were used to estimate the associated systematic error. For the input phase  $\phi(s)$  we use [28]

$$\phi(s) = \begin{cases} \delta_1^1(s) & 4m_\pi^2 \leq s < 1 \text{ GeV}^2, \\ \psi(s) & 1 \text{ GeV}^2 \leq s < m_\tau^2, \\ \psi_\infty(s) & m_\tau^2 \leq s. \end{cases} \quad (5.7)$$

This phase consists in matching smoothly at 1 GeV the phase  $\psi(s)$ , that we will explain in the following, to the phase-shift  $\delta_1^1(s)$  solution of the Roy equations of Ref. [231]. We thus exploit Watson's theorem [227]<sup>4</sup>. The phase  $\delta_1^1(s)$  encodes the physics of the  $\rho$ -meson, it is totally general and provides a phase which perfectly agrees with the  $P$ -wave  $\pi\pi$  experimental data within the elastic region. For  $\psi(s)$ , we use a physically motivated parametrization that contains the physics of the inelastic regime until  $m_\tau^2$ . This phase can be extracted from the

---

<sup>4</sup>Watson's theorem applied to the pion vector form factor tells us that the form factor phase equals that of the two-pion scattering within the elastic region.



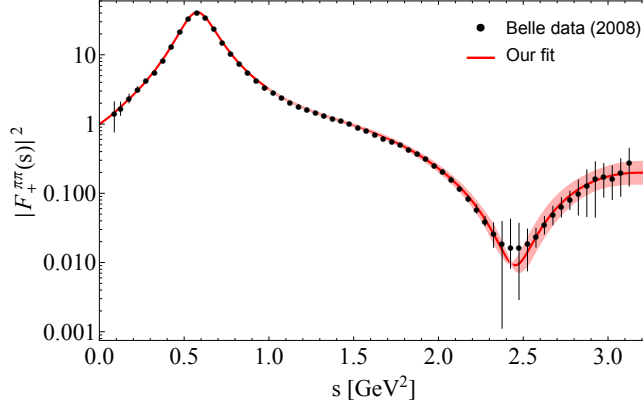


Figure 5.1: Belle measurement of the modulus squared of the pion vector form factor [18] as compared to our fits [28].

relation

$$\tan \psi(s) = \frac{\text{Im} f_+^{\pi\pi}(s)}{\text{Re} f_+^{\pi\pi}(s)}, \quad (5.8)$$

where  $f_+^{\pi\pi}(s)$  includes the contributions from the excited resonances  $\rho'$  and  $\rho''$  that cannot be neglected. The expression of  $f_+^{\pi\pi}(s)$  that we use for our study is given by Eq.(17) of Ref. [28]. Finally, for the high-energy region, we guide smoothly the phase to  $\pi$  at  $m_\tau^2$  ( $\psi_\infty(s)$ ) to ensure the correct asymptotic  $1/s$  fall-off of the form factor [544]<sup>5</sup>.

Armed with this parametrization, in [28] we have analyzed the high-statistics Belle data [18] on the pion vector form factor. The outcome that better illustrates the resulting analysis, and that we use for this work, is displayed in Fig. 5.1, where the red error band denotes the statistical fit uncertainty<sup>6</sup>.

The corresponding vector form factors for the  $(K\pi)^-$ ,  $K^-K^0$  and  $K^-\eta^{(\prime)}$  systems can be obtained following a similar dispersive procedure. We do not show here the explicit expressions that we use for our analysis but rather provide a graphical account of their applications (of some) against the Belle  $\tau^- \rightarrow K_S\pi^-\nu_\tau$  (red solid circles) [22] and  $\tau^- \rightarrow K^-\eta\nu_\tau$  (green solid squares) [29] experimental data (Fig. 5.2) and refer the interested reader to Refs. [28,30,410,428], where they are derived and explained in detail. As seen, the  $K_S\pi^-$

<sup>5</sup>In fact, this behavior it is not guaranteed because the subtraction constants in Eq. (5.6) are fixed from a fit to data. However, we have checked that our form factor is indeed a decreasing function of  $s$  (apart from the resonance peak structures) within the entire range where we apply it.

<sup>6</sup>In [28], we have also estimated potential systematic uncertainties.

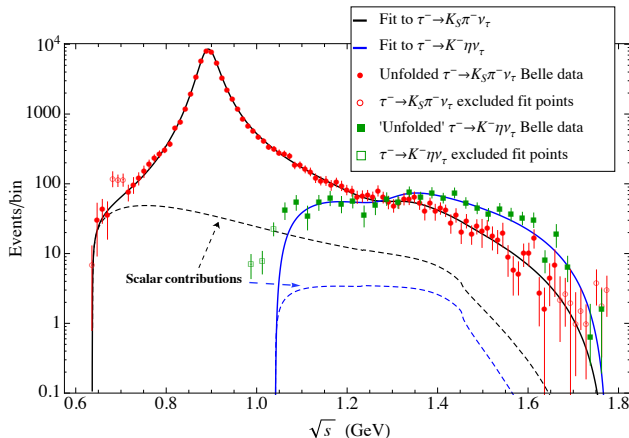


Figure 5.2: Belle  $\tau^- \rightarrow K_S \pi^- \nu_\tau$  (red solid circles) [22] and  $\tau^- \rightarrow K^- \eta \nu_\tau$  (green solid squares) [29] measurements as compared to our best fit results in [30] (solid black and blue lines, respectively) obtained from a combined fit to both data sets. The small scalar contributions are represented by black and blue dashed lines.

spectrum is dominated by the  $K^*(892)$  resonance, whose peak is neatly visible, followed by a mild shoulder due to the heavier  $K^*(1410)$ . There is no such a clear peak structure for the  $K^- \eta$  channel as a consequence of the interplay between both  $K^*$  resonances. In all, satisfactory agreement with data is seen for all data points.

Regarding the scalar form factors we take: the phase dispersive representation of the  $\pi^- \pi^0$  scalar form factor from Ref. [513] while for the  $K^- K^0$  ones, we use the results of Refs. [565–567]<sup>7</sup>. These were obtained after the unitarization, based on the method of  $N/D$ , of the complete one-loop calculation of the strangeness conserving scalar form factors within  $U(3)$  ChPT. Finally, for the  $K\pi$  and  $K\eta^{(\prime)}$  scalar form factors, we employ the well-established results of Ref. [412] derived from a dispersive analysis with three coupled channels ( $K\pi, K\eta, K\eta'$ )<sup>8</sup>. As one can observe in Fig. 5.2, the  $K\pi$  scalar form factor contribution, although small, is important to describe the data immediately above threshold, while the  $K\eta$  one is irrelevant for the decay distribution.

We next turn to the tensor form factor. This is the most difficult input to be reliably

<sup>7</sup>We thank very much Zhi-Hui Guo for providing us tables with the unitarized  $\pi\eta$ ,  $\pi\eta'$  and  $K^0 \bar{K}^0$  scalar form factors. We translate the result of  $K^0 \bar{K}^0$  to the  $K^- K^0$  concerning us through  $F_0^{K^- K^0}(s) = -F_0^{K^0 \bar{K}^0}(s)/\sqrt{2}$ .

<sup>8</sup>We are very grateful to Matthias Jamin and Jose Antonio Oller for providing us their solutions in tables.

estimated since there are no experimental data that can help its construction. Therefore, we shall rely on theoretical considerations only. The key observation is that the tensor form factor admits an Omnès dispersive representation [251, 427, 519, 542, 568]. We thus write the general two-meson ( $PP'$ ) tensor form factor as

$$F_T^{PP'}(s) = F_T^{PP'}(0) \exp \left[ \frac{s}{\pi} \int_{s_{\text{th}}}^{s_{\text{cut}}} \frac{ds'}{s'} \frac{\delta_T^{PP'}(s')}{(s' - s - i0)} \right], \quad (5.9)$$

where  $s_{\text{th}} = (m_P + m_{P'})^2$  is the corresponding two-meson production threshold, and where in the elastic region, the phase of the tensor form factor equals the  $P$ -wave phase of the corresponding vector one i.e.  $\delta_T^{PP'}(s) = \delta_+^{PP'}(s)$ . We will assume the previous relations also hold above the onset of inelasticities until  $m_\tau^2$  where we guide smoothly the tensor phase to  $\pi$  as in Ref. [28] to ensure the asymptotic  $1/s$  behavior dictated by perturbative QCD [544]. Lacking precise low-energy information, we do not increase the number of subtractions, which, in turn, would reduce the importance of the higher-energy part of the integral, but rather cut the integral at different values of  $s_{\text{cut}}$  e.g.  $s_{\text{cut}} = 4,9 \text{ GeV}^2$ , and consider the difference with respect to the case  $s_{\text{cut}} \rightarrow \infty$ , that we take as a baseline hypothesis, as an estimate of our (uncontrolled) theoretical systematic uncertainty for the results presented in the following sections. For the required normalization  $F_T^{PP'}(0)$ , we take the corresponding ChPT based results derived in [251, 519, 542] obtained with the use of the corresponding determination on the lattice [514]. In these references, a graphical account of the energy-dependence of the tensor form factors is also shown.

## 5.4 New Physics bounds from $\Delta S = 0$ decays

We start with the individual analysis of the decay mode with lowest multiplicity,  $\tau^- \rightarrow \pi^- \nu_\tau$ . Taking the decay rate given in Eq. (5.3) and using  $f_\pi = 130.2(8) \text{ MeV}$  from the lattice<sup>9</sup> [377] together with  $\delta_{\text{em}}^{\tau\pi} = 1.92(24)\%$ , obtained from a combination of the values given in Refs.

---

<sup>9</sup>The pion decay constant determined from data cannot be employed as it may be contaminated with NP effects.

[277, 291, 569], and the PDG reported values [541] for:  $|\tilde{V}_{ud}^e| = 0.97420(21)$  from nuclear  $\beta$  decays, the measured branching ratio  $BR(\tau^- \rightarrow \pi^- \nu_\tau) = 10.82(5)\%$ ,  $m_\pi = 0.13957061(24)$  GeV,  $m_\tau = 1.77686(12)$  GeV,  $\Gamma_\tau = 2.265 \times 10^{-12}$  GeV and  $G_F = 1.16637(1) \times 10^{-5}$  GeV $^{-2}$ , we get the constraint:

$$\epsilon_L^\tau - \epsilon_L^e - \epsilon_R^\tau - \epsilon_R^e - \frac{m_\pi^2}{m_\tau(m_u + m_d)} \epsilon_P^\tau = (-0.12 \pm 0.68) \times 10^{-2}, \quad (5.10)$$

where the uncertainty is dominated by  $f_\pi$ , followed by the error of branching ratio and the radiative corrections uncertainty. The central value in Eq. (5.10) shows a slight difference with respect to the result of [512],  $(-0.15 \pm 0.67) \times 10^{-2}$ , that we may attribute to a different numerical input.

We next perform a simultaneous fit to one and two meson strangeness-conserving exclusive hadronic tau decays. For our analysis, we consider the following observables: the high-statistics  $\tau^- \rightarrow \pi^- \pi^0 \nu_\tau$  experimental data reported by the Belle collaboration [18], including both the normalized unfolded spectrum and the branching ratio, and the branching ratios of the decay  $\tau^- \rightarrow K^- K^0 \nu_\tau$  and of the one-meson  $\tau^- \rightarrow \pi^- \nu_\tau$  transition. The  $\chi^2$  function to be minimized in our fits is

$$\begin{aligned} \chi^2 = & \sum_k \left( \frac{\bar{N}_k^{\text{th}} - \bar{N}_k^{\text{exp}}}{\sigma_{\bar{N}_k^{\text{exp}}}} \right)^2 + \left( \frac{BR_{\pi\pi}^{\text{th}} - BR_{\pi\pi}^{\text{exp}}}{\sigma_{BR_{\pi\pi}^{\text{exp}}}} \right)^2 \\ & + \left( \frac{BR_{KK}^{\text{th}} - BR_{KK}^{\text{exp}}}{\sigma_{BR_{KK}^{\text{exp}}}} \right)^2 + \left( \frac{BR_{\tau\pi}^{\text{th}} - BR_{\tau\pi}^{\text{exp}}}{\sigma_{BR_{\tau\pi}^{\text{exp}}}} \right)^2, \end{aligned} \quad (5.11)$$

where  $\bar{N}_k^{\text{th}}$  relates the decay rate of Eq. (5.4) for  $\tau^- \rightarrow \pi^- \pi^0 \nu_\tau$  to the normalized distribution of the measured number of events through

$$\frac{1}{N_{\text{events}}} \frac{dN_{\text{events}}}{ds} = \frac{1}{\Gamma(\epsilon_i^\tau, \epsilon_j^e)} \frac{d\Gamma(s, \epsilon_i^\tau, \epsilon_j^e)}{ds} \Delta^{\text{bin}}, \quad (5.12)$$

where  $N_{\text{events}}$  is the total number of measured events and  $\Delta^{\text{bin}}$  is the bin width.  $\bar{N}_k^{\text{exp}}$  and  $\sigma_{\bar{N}_k^{\text{exp}}}$  in Eq. (5.11) are, respectively, the experimental number of events and the corresponding uncertainties in the  $k$ -th bin. The unfolded distribution measured by Belle is available in 62 equally distributed bins with bin width of 0.05 GeV<sup>2</sup>. The second, third and fourth terms in the  $\chi^2$  function Eq. (5.11) are data points that are used as a constraint of the branching ratios of  $\tau^- \rightarrow \pi^- \pi^0 \nu_\tau$  ( $BR_{\pi\pi}^{\text{exp}} = 25.49(9)\%$ ), of  $\tau^- \rightarrow K^- K^0 \nu_\tau$  ( $BR_{KK}^{\text{exp}} = 1.486(34) \times 10^{-3}$ ) and of  $\tau^- \rightarrow \pi^- \nu_\tau$  ( $BR_{\tau\pi}^{\text{exp}} = 10.82(5)\%$ ) [541].

The bounds for the non-SM effective couplings resulting from the global fit are found to be (in the  $\overline{\text{MS}}$  scheme at scale  $\mu = 2$  GeV)

$$\begin{pmatrix} \epsilon_L^\tau - \epsilon_L^e + \epsilon_R^\tau - \epsilon_R^e \\ \epsilon_R^\tau + \frac{m_\pi^2}{2m_\tau(m_u+m_d)} \epsilon_P^\tau \\ \epsilon_S^\tau \\ \epsilon_T^\tau \end{pmatrix} = \begin{pmatrix} 0.5 \pm 0.6_{-1.8}^{+2.3} \pm 0.2_{-0.1}^{+0.2} \pm 0.4 \\ 0.3 \pm 0.5_{-0.9}^{+1.1} \pm 0.1_{-0.0}^{+0.1} \pm 0.2 \\ 9.7_{-0.6}^{+0.5} \pm 21.5_{-0.1}^{+0.0} \pm 0.2 \\ -0.1 \pm 0.2_{-1.4}^{+1.1} \pm 0.0_{-0.1}^{+0.0} \pm 0.2 \end{pmatrix} \times 10^{-2}, \quad (5.13)$$

with  $\chi^2/\text{d.o.f.} \sim 0.6$ , and where the first error is the statistical fit uncertainty while the associated (statistical) correlation matrix ( $\rho_{ij}$ ) is

$$\rho_{ij} = \begin{pmatrix} 1 & 0.684 & -0.493 & -0.545 \\ & 1 & -0.337 & -0.372 \\ & & 1 & 0.463 \\ & & & 1 \end{pmatrix}. \quad (5.14)$$

The second error in Eq. (5.13) is the dominant one and comes from the theoretical uncertainty associated to the pion vector form factor (cf. Fig. 5.1), while the third and fourth ones are systematic uncertainties coming, respectively, from the error of the quark masses and from the uncertainty associated to the corresponding tensor form factors. The systematic errors, here and hereafter, have been obtained by taking the difference of the central values that are obtained while varying the corresponding inputs with respect to the reported central fit values.

Comparing our limits<sup>10</sup> in Eq. (5.13) with the bounds,  $\epsilon_S^\mu = (-0.039 \pm 0.049) \times 10^{-2}$  and  $\epsilon_T^\mu = (0.05 \pm 0.52) \times 10^{-2}$  [509], obtained from semileptonic kaon decays involving muons, and with those from hyperon decays [507], where  $|\epsilon_S| < 4 \times 10^{-2}$  and  $|\epsilon_T| < 5 \times 10^{-2}$  are found at a 90% C.L., we conclude that while it is impossible to compete with the limits on  $\epsilon_S$  coming from  $K_{\ell 3}$  decays, our analysis yields a very competitive constraint on the coupling  $\epsilon_T$ .

Our results are in accord with those of [512]<sup>11</sup>, which were obtained through a combination of inclusive and exclusive (strangeness-conserving) tau decays, but for the limit on the coefficient  $\epsilon_S^\tau$ . Ours is much weaker, but still compatible within errors with, the bounds set in [250, 512], since we are not using the  $\tau^- \rightarrow \pi^- \eta \nu_\tau$  decay in the global fit for lack of experimental measurements. The differing bound on  $\epsilon_S$  obtained with and without the  $\pi \eta$  mode increases the interest of its measurement and demands improved theoretical understanding accordingly.

## 5.5 New Physics bounds from $|\Delta S| = 1$ decays

The lowest multiplicity strangeness-changing tau decay is  $\tau^- \rightarrow K^- \nu_\tau$ , which can be used to restrict the combination of the couplings of the left-hand side of Eq. (5.10), but replacing  $m_d \rightarrow m_s$  and  $m_\pi \rightarrow m_K$  and with the  $\epsilon$ 's corresponding to  $u \rightarrow s$  transitions<sup>12</sup>. Using the lattice calculation of  $f_K = 155.7(7)$  MeV [377], the radiative corrections  $\delta_{\text{em}}^{\tau K} = 1.98(31)\%$  from Refs. [277, 291, 569] and  $|\tilde{V}_{us}^e| = 0.2231(7)$ ,  $BR(\tau^- \rightarrow K^- \nu_\tau) = 6.96(10) \times 10^{-3}$  and

<sup>10</sup>For the comparison, here and throughout the rest of the paper, we need to assume lepton universality because our study involves the tau lepton, while theirs electrons and muons. Given the smallness of possible lepton universality violations, this is enough for current precision. We have also assumed that the corresponding CKM matrix elements do not change under NP interactions, which is the case if  $\epsilon(lud) = \epsilon(lus)$  [549].

<sup>11</sup>We would like to notice that our fit to  $\Delta S = 0$  processes is not sensitive to the coefficients  $\epsilon_P^\tau$  and  $\epsilon_R^\tau$  individually but rather to a combination of them (given by the second row in Eq. (5.13)). However, as we will see in section 5.6, one can still fit them separately if one performs a global fit including strangeness-changing decays. This is also the case in the next section.

<sup>12</sup>In the chiral limit  $\epsilon_P^\tau$  is the same as in Eq. (5.10).

$m_K = 0.493677(16)$  GeV from the PDG [541] as numerical inputs, we obtain the constraint:

$$\epsilon_L^\tau - \epsilon_L^e - \epsilon_R^\tau - \epsilon_R^e - \frac{m_K^2}{m_\tau(m_u + m_s)} \epsilon_P^\tau = (-0.41 \pm 0.93) \times 10^{-2}. \quad (5.15)$$

where the error is dominated by  $f_K$  and  $|V_{us}|$  followed by the branching ratio and the radiative corrections uncertainty.

Analogously to the previous section, we next analyze strangeness-changing exclusive transitions with one and two mesons in the final state simultaneously. In particular, we fit the  $\tau^- \rightarrow K_S \pi^- \nu_\tau$  Belle spectrum [22]<sup>13</sup> including the measured branching ratio,  $BR_{K\pi}^{\text{exp}} = 0.404(2)(13)\%$ , as experimental datum to constrain the fit. The PDG branching ratio [541] of the decays  $\tau^- \rightarrow K^- \eta \nu_\tau$  ( $BR_{K\eta}^{\text{exp}} = 1.55(8) \times 10^{-4}$ )<sup>14</sup> and  $\tau^- \rightarrow K^- \nu_\tau$  ( $BR_{\tau K}^{\text{exp}} = 6.96(10) \times 10^{-3}$ ) are also added as external restrictions to the fit. The decay  $\tau^- \rightarrow K^- \eta' \nu_\tau$  has not been detected yet, there is only an upper limit at the 90% confidence level placed by BaBar [433] and we therefore have decided to not include it in our analysis. Hence, the  $\chi^2$  function to be minimized in this case is chosen to be

$$\begin{aligned} \chi^2 = & \sum_k \left( \frac{\bar{N}_k^{\text{th}} - \bar{N}_k^{\text{exp}}}{\sigma_{\bar{N}_k^{\text{exp}}}} \right)^2 + \left( \frac{BR_{K\pi}^{\text{th}} - BR_{K\pi}^{\text{exp}}}{\sigma_{BR_{K\pi}^{\text{exp}}}} \right)^2 \\ & + \left( \frac{BR_{K\eta}^{\text{th}} - BR_{K\eta}^{\text{exp}}}{\sigma_{BR_{K\eta}^{\text{exp}}}} \right)^2 + \left( \frac{BR_{\tau K}^{\text{th}} - BR_{\tau K}^{\text{exp}}}{\sigma_{BR_{\tau K}^{\text{exp}}}} \right)^2, \end{aligned} \quad (5.16)$$

where now  $\bar{N}_k^{\text{th}}$  refers to the  $K_S \pi^-$  decay mode and its expression is given by

$$\frac{dN_{\text{events}}}{d\sqrt{s}} = \frac{N_{\text{events}}}{\Gamma(\epsilon_i^\tau, \epsilon_j^e)} \frac{d\Gamma(\sqrt{s}, \epsilon_i^\tau, \epsilon_j^e)}{d\sqrt{s}} \Delta^{\text{bin}}. \quad (5.17)$$

<sup>13</sup>We thank the Belle collaboration, in particular S. Eidelman, D. Epifanov and B. Shwartz, for providing their data and for useful discussions.

<sup>14</sup>While the  $\tau^- \rightarrow K^- \eta \nu_\tau$  decay spectrum has been measured by Belle [29], unfolding detector effects has not been performed and we therefore have decided to include only the branching ratio in our study.

The number of events is  $N_{\text{events}} = 53113.21$ , the bin width is  $\Delta^{\text{bin}} = 11.5$  MeV [22] and the number of fitted data points is 86 for the spectrum<sup>15</sup>, together with the respective branching ratios used as a constraint: thus 89 data points in total.

In this case, the limits for the NP effective couplings are found to be (in the  $\overline{\text{MS}}$  scheme at scale  $\mu = 2$  GeV)

$$\begin{pmatrix} \epsilon_L^\tau - \epsilon_L^e + \epsilon_R^\tau - \epsilon_R^e \\ \epsilon_R^\tau + \frac{m_K^2}{2m_\tau(m_u+m_s)}\epsilon_P^\tau \\ \epsilon_S^\tau \\ \epsilon_T^\tau \end{pmatrix} = \begin{pmatrix} 0.5 \pm 1.5 \pm 0.3 \\ 0.4 \pm 0.9 \pm 0.2 \\ 0.8_{-0.9}^{+0.8} \pm 0.3 \\ 0.9 \pm 0.7 \pm 0.4 \end{pmatrix} \times 10^{-2}, \quad (5.18)$$

where the first error is the statistical fit uncertainty while the second one is a systematic uncertainty due to the tensor form factor. Differently to Eq. (5.18), the uncertainty associated to the kaon vector form factor and to the quark masses is negligible.

The (statistical) correlation matrix associated to the results of Eq. (5.18) is

$$\rho_{ij} = \begin{pmatrix} 1 & 0.854 & -0.147 & 0.437 \\ & 1 & -0.125 & 0.373 \\ & & 1 & -0.055 \\ & & & 1 \end{pmatrix}, \quad (5.19)$$

with  $\chi^2/\text{d.o.f.} \sim 0.9$ .

Notice that  $\rho_{12}$  in Eq. (5.19) is large (it was also the largest element in Eq. (5.14)). As we will see in section 5.6, where we will perform a global fit to both  $\Delta S = 0$  and  $|\Delta S| = 1$  sectors and obtain both  $\epsilon_R^\tau$  and  $\epsilon_P^\tau$  independently, this is due to the strong correlation between  $\epsilon_R^\tau$  and  $\epsilon_P^\tau$ .

The limits obtained from the  $|\Delta S| = 1$  transitions in Eq. (5.18) serve as a consistency

---

<sup>15</sup>The points corresponding to bins 5,6 and 7 are difficult to bring into accord with theoretical parametrizations, even when non-standard interactions are considered [251], and have been excluded from the minimization. The first point has not been included either, since the centre of the bin lies below the  $K_S\pi^-$  production threshold. We have furthermore excluded data corresponding to bin numbers larger than 90 following a suggestion from the experimentalists.



check upon comparison with those of Eq. (5.13) from the  $\Delta S = 0$  ones. As one can observe, the results of the first and second lines in Eq. (5.18) are found to be in line with those from Eq. (5.13). As for the central value of the coefficient  $\epsilon_S^T(\epsilon_T^r)$  from the  $|\Delta S| = 1$  sector, it has decreased(increased) by about one order of magnitude with respect to the  $\Delta S = 0$  one; the  $\epsilon_S^T$  coupling is now more competitive while  $\epsilon_T^r$  has changed sign. We can anticipate, however, that the global fit in section 5.6 benefits from  $\epsilon_T$  from the  $\Delta S = 0$  decays and from  $\epsilon_S$  from the  $|\Delta S| = 1$  ones.

## 5.6 New Physics bounds from a global fit to both $\Delta S = 0$ and $|\Delta S| = 1$ sectors

In this section, we close our exploratory analysis by performing a global fit to both  $\Delta S = 0$  and  $|\Delta S| = 1$  sectors simultaneously. The participant  $|V_{ud}|$  and  $|V_{us}|$  elements of the CKM matrix to be used in this case are not independent but rather correlated according to [377]

$$\frac{|V_{us}|}{|V_{ud}|} = 0.2313(5). \quad (5.20)$$

For our analysis, we take  $|V_{us}| = 0.2231(7)$  [541] and extract  $|V_{ud}|$  through Eq. (5.20).

The  $\chi^2$  function to be minimized in the global fit includes all the quantities in Eqs. (5.11) and (5.16) that were used for the individual analysis of the  $\Delta S = 0$  and  $|\Delta S| = 1$  transitions, respectively. The resulting limits for the NP effective couplings are (in the  $\overline{\text{MS}}$  scheme at

scale  $\mu = 2 \text{ GeV}$ )

$$\begin{pmatrix} \epsilon_L^\tau - \epsilon_L^e + \epsilon_R^\tau - \epsilon_R^e \\ \epsilon_R^\tau \\ \epsilon_P^\tau \\ \epsilon_S^\tau \\ \epsilon_T^\tau \end{pmatrix} = \begin{pmatrix} 2.9 \pm 0.6 & +1.0 & \pm 0.6 & \pm 0.0 & \pm 0.4 & +0.2 & -0.3 \\ 7.1 \pm 4.9 & +0.5 & -1.5 & +1.2 & \pm 0.2 & +40.9 & -14.1 \\ -7.6 \pm 6.3 & \pm 0.0 & -1.6 & +1.7 & \pm 0.0 & +19.0 & -53.6 \\ 5.0 & +0.7 & +0.8 & +0.2 & \pm 0.0 & +1.1 & -0.6 \\ -0.5 \pm 0.2 & +0.8 & \pm 0.0 & \pm 0.0 & \pm 0.6 & \pm 0.1 & \end{pmatrix} \times 10^{-2}, \quad (5.21)$$

where the first error is the statistical error resulting from the fit, the second one comes from the uncertainty on the pion vector form factor, the third error corresponds to the CKM elements  $|V_{ud}|$  and  $|V_{us}|$ , the fourth one is due to the radiative corrections  $\delta_{\text{em}}^{\tau\pi}$  and  $\delta_{\text{em}}^{\tau K}$ , the fifth estimates the (uncontrolled) systematic uncertainty associated to the tensor form factor, while the sixth, and last error, is due to the errors of the quark masses.

The (statistical) correlation matrix associated to the limits of Eq. (5.21) is

$$\mathcal{A} = \begin{pmatrix} 1 & 0.055 & 0.000 & -0.279 & -0.394 \\ & 1 & -0.997 & -0.015 & -0.022 \\ & & 1 & 0.000 & 0.000 \\ & & & 1 & 0.243 \\ & & & & 1 \end{pmatrix}, \quad (5.22)$$

with  $\chi^2/\text{d.o.f.} \sim 1.38$ .

As anticipated in the previous section, the combined fit yields an independent determination of the couplings  $\epsilon_R^\tau$  and  $\epsilon_P^\tau$  which, in turn, carry a large statistical (and systematic) error. This originates in the fact that these parameters are almost 100% correlated (cf. Eq. (5.22)). For the combination of the couplings of the first line in Eq. (5.21), our limits are competitive and within errors with [512]. Regarding  $\epsilon_S^\tau$ , our limit is not competitive and disagrees with the values of Refs. [250,512], where a constraint for  $\epsilon_S^\tau$  was placed from the isospin-violating decay  $\tau^- \rightarrow \pi^- \eta \nu_\tau$ . We do not take into account this channel here since it has not been mea-

sured yet; only an upper bound exists. Finally, our bound for  $\epsilon_T^\tau$  is competitive and found to be in agreement with [512, 519]. We would like to note that the uncertainty associated to the CKM elements dominates the error of those coefficients in Eq. (5.21) for what we get competitive bounds. Therefore, future lattice results can result in tighter constraints. After the completion of this work, Ref. [570] appeared, analysing both the strangeness-changing and -conserving sectors. A very interesting study of solutions to the unitarity puzzle in the  $u$  quark couplings is given therein.

Our limits on the NP effective couplings Eq. (5.21) can be translated into bounds on the corresponding NP scale  $\Lambda$  through the relation

$$\Lambda \sim v (V_{uD}\epsilon_i)^{-1/2}, \quad (5.23)$$

where  $v = (\sqrt{2}G_F)^{-1/2} \sim 246$  GeV. Our bounds can probe scales as high as  $\sim \mathcal{O}(5)$  TeV, which are quite restricted compared to the energy scale probed in semileptonic kaon decays i.e.  $\mathcal{O}(500)$  TeV [509].

## 5.7 Conclusions

This work highlights that hadronic tau lepton decays remain to be not only a privileged tool for the investigation of the hadronization of QCD currents but also offer an interesting scenario as New Physics probes.

In this work, we have performed a global analysis of strangeness-conserving ( $\Delta S = 0$ ) and strangeness-changing ( $|\Delta S| = 1$ ) exclusive hadronic  $\tau$  decays into one and two mesons. From the current experimental measurements of the corresponding decay spectra and/or branching ratios, we have set bounds on the NP effective couplings of the low-energy (dimension six) Standard Model Effective Field Theory Lagrangian. This has been possible due to a controlled theoretical determination of the necessary Standard Model hadronic input i.e. the form factors. For the description of the corresponding vector and scalar form factors, we have employed previous results, based on constraints from Chiral Perturbation Theory

supplemented by dispersion relations, that show a nice agreement with the rich experimental data provided by the experiments. On the other hand, as there is no experimental data that can help us constructing the corresponding tensor form factors, they have been built under theoretical arguments only.

In general, our bounds on the NP couplings, Eqs. (5.13), (5.18) and (5.21), are competitive. This is specially the case for the combination of couplings  $\epsilon_L^\tau - \epsilon_L^\epsilon + \epsilon_R^\tau - \epsilon_R^\epsilon$ , which is found to be in accord with the constraints placed from a combination of inclusive and exclusive (strangeness-conserving) tau decays [512], and for  $\epsilon_T^\tau$ , that can even compete with the constraints set by the theoretically cleaner  $K_{\ell 3}$  decays (for the comparison, lepton flavor universality is assumed as mentioned throughout the main text). Our separate fits to both  $\Delta S = 0$  and  $|\Delta S| = 1$  decays reflect that we are not sensitive to the coefficients  $\epsilon_P^\tau$  and  $\epsilon_R^\tau$  individually but rather to a combination of them. It is still possible to fit them separately performing a global fit to both  $\Delta S = 0$  and  $|\Delta S| = 1$  sectors simultaneously. However, they carry a large error bar whose origin stems from the very strong correlation between them. As for  $\epsilon_S^\tau$ , it is impossible to compete with the limits coming from  $K_{\ell 3}$  decays. Our limit, however, is found to be much weaker than previous constraints from tau decays. This is due to the fact that, for lack of experimental data, the decay  $\tau^- \rightarrow \pi^- \eta \nu_\tau$  has not been taken into account in our analysis. These different bounds on  $\epsilon_S^\tau$  obtained with and without the  $\pi\eta$  mode thus increase the interest of its measurement and demands refined theoretical descriptions accordingly.

Our study is presently limited by the fact that the Standard Model form factors, the input parameters of which have been fitted to data previously, may have absorbed some NP information, if this is in the data. We have tried to address this drawback through fits where not only the NP effective couplings are treated as free parameters to fit but also the Standard Model input parameters entering the corresponding form factors. In doing so, we have too many free parameters to fit and found no sensitivity to the NP couplings. This is indeed interesting to prove in the future, with a higher-quality data, but at present is not feasible. We thus hope our work can serve to encourage the experimental tau physics groups

at Belle-II to measure these decays with higher accuracy.

# Chapter 6

## Hadronic contribution to the vacuum polarization of the muon anomalous magnetic moment

### 6.1 Introduction

The muon ( $\mu^-$ ), like the much lighter electron ( $e^-$ ) or the much heavier tau ( $\tau^-$ ) particle, is one of the 3 known charged leptons: elementary spin 1/2 fermions of electric charge  $-1$  (in units of the positron charge  $e$ ). Each of the leptons has its positively charged antiparticle, the positron  $e^+$ , the  $\mu^+$  and the  $\tau^+$ , respectively, as required by any local relativistic quantum field theory [571]. One of the most precisely measured quantities in particle physics is the muon anomalous magnetic moment ( $a_\mu$ )<sup>1</sup>. A long-standing discrepancy between theory and experiment about 3 – 4 standard deviations has been observed.

The agreement between the latest measurement performed at Fermilab National Accelerator Laboratory (FNAL) Muon  $g - 2$  Experiment [96] with the previous one at Brookhaven

---

<sup>1</sup>Only  $a_e$  is more precise, its measurements allow to fix  $\alpha(0)$ .

[95], allows to combine them and get

$$a_\mu^{\text{Exp}} = 116\,592\,061(41) \times 10^{-11} \quad (0.35 \text{ ppm}).$$

The latest SM prediction [6] is

$$a_\mu^{\text{SM}} = 116\,591\,810(43) \times 10^{-11} \quad (0.37 \text{ ppm}).$$

Therefore, the difference,  $\Delta a_\mu = a_\mu^{\text{Exp}} - a_\mu^{\text{SM}} = (251 \pm 59) \times 10^{-11}$ , increases the significance to  $4.2\sigma$ . This deviation from the Standard Model could be a sign of New Physics around the corner.

In this chapter, we will discuss briefly the SM contributions to  $a_\mu$ , and a description of the data used as input in the data-driven computation of the HVP contribution. Further details can be found in the White Paper (WP) of the Muon  $g - 2$  Theory Initiative [6] or in the several reviews concerning this topic (e.g. Refs. [31, 572, 573]).

## 6.2 Theoretical calculations of $a_\mu$

The prediction of the anomalous magnetic moment in the SM is determined from the sum of all sectors of the SM [31]:

$$a_\mu^{\text{SM}} = a_\mu^{\text{QED}} + a_\mu^{\text{EW}} + a_\mu^{\text{HVP}} + a_\mu^{\text{HLbL}}, \quad (6.1)$$

where  $a_\mu^{\text{QED}}$  are the QED contributions,  $a_\mu^{\text{EW}}$  are the electro-weak (EW) contributions,  $a_\mu^{\text{HVP}}$  are the hadronic vacuum polarization (HVP) contributions and  $a_\mu^{\text{HLbL}}$  are due to contributions from hadronic light-by-light (HLbL) scattering, see Fig. 6.1.

### 6.2.1 QED contributions

The QED contributions to  $a_\mu$  include those from leptons and photons alone and have been completely calculated up to five-order. All contributions up to and including four-loop have

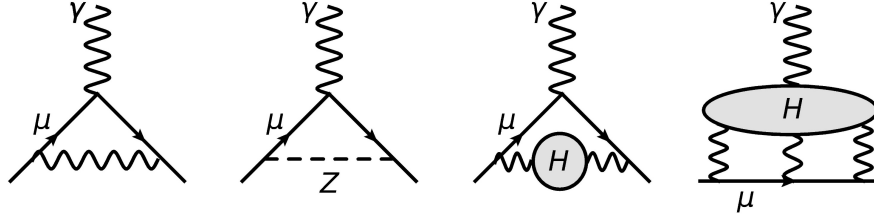


Figure 6.1: SM contributions to  $a_\mu$ . The diagrams shown (from left to right) correspond to the one-loop QED diagram, the one-loop EW diagram involving  $Z$ -boson exchange, the leading-order HVP diagram and HLbL contributions. Reprinted from Ref. [31].

been determined and verified by different groups, from both numerical and analytical calculations [6]. The four-loop universal contribution has been calculated analytically with an impressive precision ( $\sim 1100$  digits) [574] and is consistent with the numerical computations [575]. The overall five-loop contribution, which includes 12 672 Feynman diagrams, has been calculated numerically [32, 576] with independent cross checks [577–580]. The five-loop Feynman diagrams are shown in Fig. 6.2. The value for the QED contribution is then

$$a_\mu^{\text{QED}} = 116\,584\,718.931(104) \cdot 10^{-11}, \quad (6.2)$$

where the given error is the quadrature sum of errors because of the  $\tau$ -lepton mass, four-loop QED, five-loop QED, an estimate of the six-loop QED [6, 32, 576] and the fine-structure constant  $\alpha$  [581].

## 6.2.2 EW contributions

Diagrams that contain at least one of the EW bosons ( $W$ ,  $Z$ , or Higgs) comprise the EW contributions to  $a_\mu$ . The one-loop Feynman diagrams are depicted in Fig. 6.3. These sorts of contributions may include QED and hadronic effects, but no EW processes enter in the estimation of the QED, HVP and HLbL parts. Thanks to the masses of the EW bosons, the EW contributions are highly suppressed. These have been computed up to two-loop and the three-loop contributions have been estimated [582, 583].

The value for  $a_\mu^{\text{EW}}$  is [6, 582, 583]

$$a_\mu^{\text{EW}} = 153.6(1.0) \cdot 10^{-11}, \quad (6.3)$$



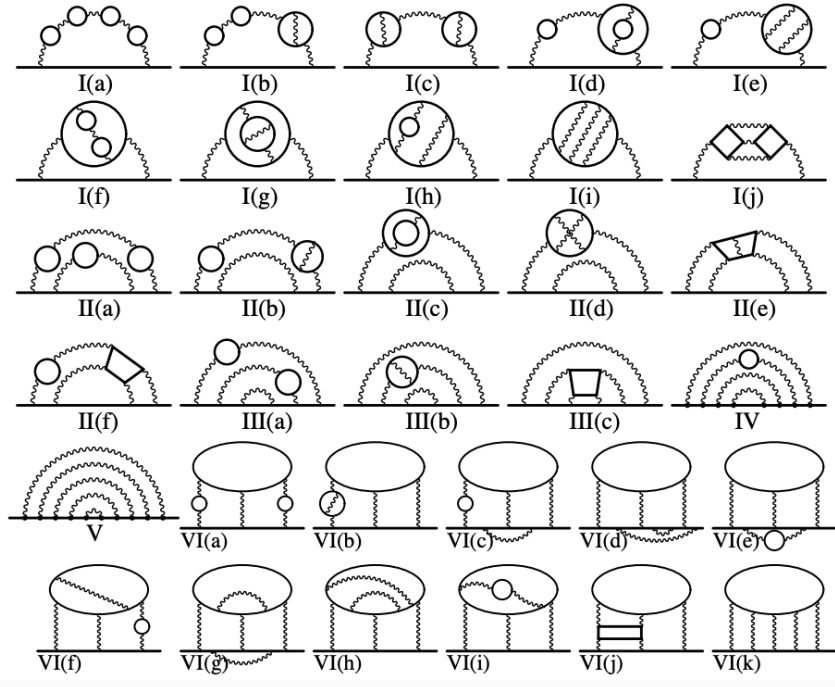


Figure 6.2: Five-loop QED diagrams. The overall QED contribution to  $a_\mu$  involves 12 672 diagrams. The straight and wavy lines denote lepton and photon propagators, respectively. Reprinted from Ref. [32].

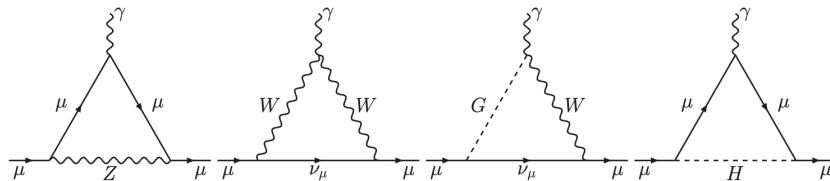


Figure 6.3: One-loop EW Feynman diagrams. Reprinted from Ref. [6].

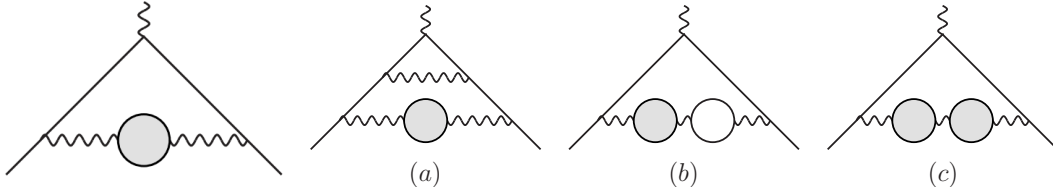


Figure 6.4: HVP Feynman diagrams at LO and NLO (a)-(c). The gray blobs refer to hadronic VP while the white one refers to leptonic VP. Reprinted from Ref. [6].

where the uncertainty involves the two-loop hadronic effects, neglected two-loop terms, and unknown three-loop contributions. The non-perturbative hadronic insertions that enter at two loops significantly govern the uncertainty of the EW contributions and are small compared to the HVP or HLbL sector uncertainties, due to the EW suppression.

### 6.2.3 HVP contributions

The contributions in the third diagram in Fig. 6.1 account for the so-called HVP contributions. This sector can be estimated from data-driven approaches, using measured  $e^+e^- \rightarrow$  hadrons data as input into dispersion relations, or from Lattice QCD.

#### Data-driven HVP

The HVP contribution can be computed utilizing a combination of all  $e^+e^- \rightarrow$  hadrons cross section data,  $\sigma_{had}(s) \equiv \sigma^0(e^+e^- \rightarrow \text{hadrons} + (\gamma))$ , which is inclusive of final state radiation effects and where the superscript ‘0’ indicates the cross section is bare, i.e. excluding all vacuum polarization effects. The LO and NLO HVP contributions are shown in Fig. 6.4.

More than 35 exclusive hadronic channels (final states) from different experimental collaboration must be combined (Fig. 6.5). Hadronic cross-section data are either obtained from direct scan measurements (for instance, CMD-2, SND, KEDR) or via the method of radiative return (for instance, BaBar, KLOE, BESIII), see below for more details. The combinations of data are accomplished channel-by-channel to determine individual contributions to  $a_\mu^{\text{HVP}}$ , which are then summed. These combinations are not trivial, since the combined result needs to be an accurate representation of the differing data and their uncertainties.

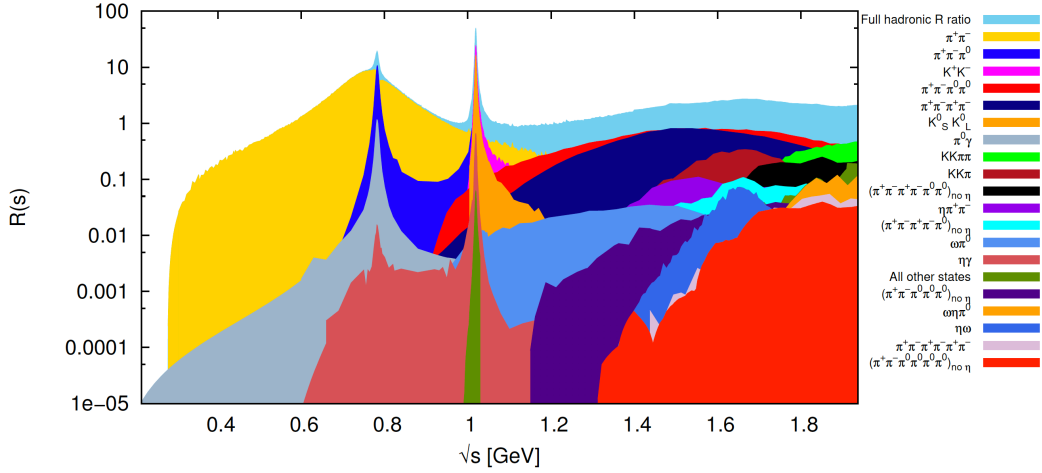


Figure 6.5: Contributions to the total hadronic cross section (expressed as the hadronic R-ratio,  $R(s) = \sigma_{\text{had}}(s)/(4\pi\alpha^2/(3s))$ ) from different final states below  $\sqrt{s} \sim 2$  GeV. The total hadronic cross section is depicted in light blue and each final state is included as a new layer on top in decreasing order of the size of its contribution to  $a_\mu^{\text{HVP LO}}$ . Reprinted from Ref. [33].

The dominant channel corresponds to the two pion channel, that contributes more than 70% of the total HVP. Fortunately, final states, thresholds contributions, or resonances for which there are no data are safely estimated. The estimation of the missing channels amounts to less than 0.5% of  $a_\mu^{\text{HVP}}$  [6, 48, 81].

There are some data-driven evaluations of  $a_\mu^{\text{HVP}}$  that differ in the treatment of the data as well as the assumptions made on the functional form of the form factors. The DHMZ [48, 81] and KNT [33, 47] groups use directly the bare cross section. The CHHK group reach an alternative approach, where they applied additional constraints from analyticity and unitarity to evaluate the  $\pi^0\gamma$ ,  $2\pi$  and  $3\pi$  channels [237, 584, 585]<sup>2</sup>. The outcomes from these three groups have been combined in a conservative procedure to account for differences between groups and tensions between data sets. The combination yields  $a_\mu^{\text{HVP LO}} = 6.931(40) \cdot 10^{-11}$  [6], with the corresponding results for the  $a_\mu^{\text{HVP NLO}} = -98.3(7) \cdot 10^{-11}$  [47] and  $a_\mu^{\text{HVP NNLO}} = 12.4(1) \cdot 10^{-11}$  [586] amounting the total HVP contribution of [6]

$$a_\mu^{\text{HVP}} = 6.845(40) \cdot 10^{-11}. \quad (6.4)$$

<sup>2</sup>DHMZ also applied similar constraints for the two-pion channel [48].

Further details about all data-driven determinations of  $a_\mu^{\text{HVP}}$ , which include those from other groups not used in the merged result, can be found in Ref. [6]. Prospects to improve the data-driven estimation of  $a_\mu^{\text{HVP}}$  lie in new  $e^+e^- \rightarrow$  hadrons cross section measurements, specially those of the  $\pi^+\pi^-$  channel. New  $\pi^+\pi^-$  data sets are expected from CMD-3, BABAR, BESIII [587] and Belle-II. The CMD-3 result is projected to be the most statistically precise of all the current measurements in the  $2\pi$  channel, with systematic uncertainties ranging from  $0.6 - 1\%$ .

Similarly, the  $e^+e^-$  data is used to evaluate the five-flavor hadronic contribution to the running QED coupling at the  $Z$ -pole,  $\Delta\alpha_{\text{had}}^{(5)}(M_Z^2)$ . This quantity is an essential input to global EW fits and, then, predictions of the EW fit parameters (for instance, the Higgs mass). This connection has been exploited in various works [588–592]. In order to bridge  $\Delta a_\mu$ , shifts in  $\sigma_{\text{had}}$  were studied in Ref. [590], they found that these shifts are excluded above  $\sqrt{s} \sim 0.7 \text{ GeV}$  at 95% C.L. Nonetheless, prospects for  $\Delta a_\mu$  originating below that energy were deemed improbable given the required increases in the hadronic cross section.

Further opportunities to study the HVP contributions are expected from the MUonE experiment [593,594], which is a proposed approach to evaluate the leading hadronic corrections to the muon  $g - 2$  purely from experiment (spacelike data instead of timelike measurements, which avoids the difficulties intrinsic to resonances).

## HVP from Lattice QCD

Determining the HVP contribution from lattice QCD is achieved by applying Euclidean spacetime discretization of the vacuum polarization tensor  $\Pi_{\mu\nu}(Q^2)$  for space-like  $Q^2$  in finite volumes and with finite lattice spacing, which is thus taken to continuum and infinite-volume limits. It is possible to perform comparison between different lattice groups thanks to the ability to split the calculation of  $a_\mu^{\text{HVP LO}}$  at  $\mathcal{O}(\alpha^2)$  according to quark-connected (conn) and quark-disconnected (dis) contributions as

$$a_\mu^{\text{HVP LO}}(\alpha^2) = a_{\mu,\text{conn}}^{\text{HVP LO}} + a_{\mu,\text{dis}}^{\text{HVP LO}}. \quad (6.5)$$

Since the different quark flavor-connections result in different statistical and systematic uncertainties, it is suitable to separate them as

$$a_{\mu,\text{conn}}^{\text{HVP LO}} = a_{\mu}^{\text{HVP LO}}(ud) + a_{\mu}^{\text{HVP LO}}(s) + a_{\mu}^{\text{HVP LO}}(c) + a_{\mu}^{\text{HVP LO}}(b), \quad (6.6)$$

where  $ud$  represents the contributions of the light  $u$  and  $d$  quarks ( $m_u = m_d$ ) and  $s$ ,  $c$  and  $b$  are the strange, charm and bottom quark contributions, respectively. Current lattice calculations include strong and electromagnetic isospin-breaking corrections  $\delta a_{\mu}^{\text{HVP LO}}$  as  $a_{\mu}^{\text{HVP LO}} = a_{\mu}^{\text{HVP LO}}(\alpha^2) + \delta a_{\mu}^{\text{HVP LO}}$ . The determination of the isosymmetric flavor terms in Eq. (6.6) and the corrections  $\delta a_{\mu}^{\text{HVP LO}}$  are prescription and scheme dependent, giving rise to different and comparable results between lattice calculations. A complete discussion of the different methods and analysis choices is given in Ref. [6]. Fortunately, all lattice prescriptions have common features. Thus, all results are extrapolated to the continuum and infinite-volume limits and interpolated or extrapolated to the physical point. The errors contain both statistical and systematic uncertainties, where the systematics appear from common issues faced by all analyses: long-distance effects, finite-volume effects, discretization effects, scale setting, chiral extrapolation/interpolation and quark mass tuning.

Outcomes from several lattice groups of the different flavor contributions and the total estimate of  $a_{\mu}^{\text{HVP LO}}$  are shown in Fig. 6.6. A combination using a conservative procedure from the ETM18/19 [34, 35], Mainz/CLS-19 [36], FHM-19 [37, 38], PACS-19 [39], RBC/UKQCD [40] and BMW-17 [41] leads to [6]

$$a_{\mu}^{\text{HVP LO}} = 711.6(18.4) \cdot 10^{-10}. \quad (6.7)$$

This value is also shown by a blue band in Fig. 6.6. These results are in the range between the data-driven approaches and a no-new physics (green band), but generally with errors too large to make a definitive statement. In consequence, the error on the average is consistent with both the data-driven approaches and the no-new physics scenario. After the publication of the WP, there have been two new results from the LM-20 and BMW-20 analyses,  $a_{\mu}^{\text{HVP LO}}[LM - 20] = 714(30) \cdot 10^{-10}$  [42] and  $a_{\mu}^{\text{HVP LO}}[BMW - 20] = 707.5(5.5) \cdot$

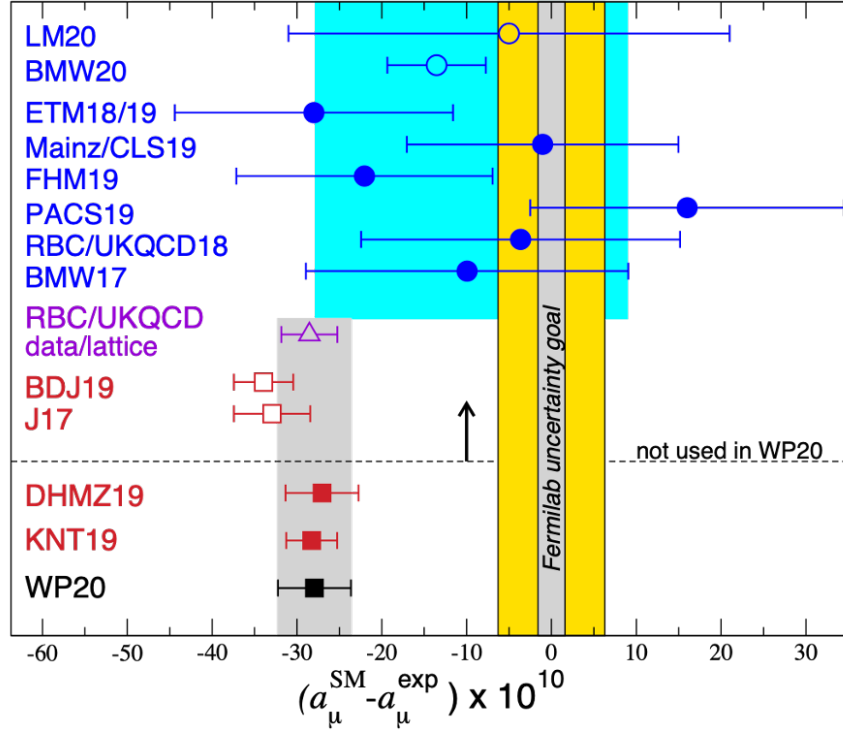


Figure 6.6: Results for  $(a_\mu^{\text{SM}} - a_\mu^{\text{EXP}}) \cdot 10^{10}$  when  $a_\mu^{\text{HVP LO}}$  is taken from several lattice [34–46] and data-driven [47–50] estimates. The filled dark blue circles are lattice results [34–41] that are included in the lattice average in Ref. [6], which is indicated by the light-blue band. The unfilled dark blue circles are those results not included in the averages [42–46, 51]. The red squares show results from data-driven estimation of  $a_\mu^{\text{HVP LO}}$ , where filled squares are those included in the merged data-driven result [47, 48] and unfilled are not [49, 50]. The purple triangle shows a hybrid result where noisy lattice data at very short and long distances are replaced by  $e^+e^- \rightarrow$  hadrons data [40]. The yellow band indicates the “no New Physics” scenario, where  $a_\mu^{\text{HVP LO}}$  results are large enough to bring  $a_\mu^{\text{SM}}$  into agreement with experiment. The grey band in the center of the yellow one indicates the projected experimental uncertainty from the Fermilab Muon  $g - 2$  experiment. Reprinted from Ref. [31].

$10^{-10}$  [43], respectively. The BMW-20 value is the first lattice result for  $a_\mu^{\text{HVP LO}}$  with sub-percent precision. This is  $1.3\sigma$  below the no-new physics scenario and  $2.1\sigma$  higher than the recommended data-driven result.

Recently, a new lattice analysis [595] found  $a_\mu^{\text{win}} = 237.30(1.46) \cdot 10^{-10}$  at the physical point that agrees with the BMW-20 results in the so-called “intermediate” window observables [40]<sup>3</sup>, for which both the short-distance and long-distance contributions in the integral representation of  $a_\mu^{\text{HVP}}$  are reduced. However, this result is at odds ( $\sim 3.8\sigma$  above) with the recent data-drive estimation in Ref. [596], which is  $a_\mu^{\text{win}} = 229.4(1.4) \cdot 10^{-10}$ . In fact, this result shows further evidence for a strong tension between lattice calculations and the data-driven approach.

Improvements in the precision of several lattice evaluations of  $a_\mu^{\text{HVP LO}}$  are also expected [6]. The main difficulties in reducing the uncertainties come from finite-volume effects, exponentially growing signal-to-noise problems at large Euclidean times, disconnected contributions, and strong isospin breaking and QED corrections.

## 6.2.4 HLbL contribution

Contributions from HLbL scattering (Fig. 6.7) represent the process in which an external soft and on-shell photon interacts through a hadronic blob with three off-shell photons that are coupled to the muon. These contributions are classified by a four-point function and thus require calculations that are more difficult than those of the two-point HVP function. Since the HLbL contributions enter at  $\mathcal{O}(\alpha^3)$ , they are suppressed by an additional order  $\alpha$  making them two orders of magnitude smaller than the HVP ones. The hadronic contributions to LbL scattering emerge from single mesons (e.g.  $\pi^0$ ,  $\eta$ ,  $\eta'$ ,  $f_0(980)$ ,  $a_0(980)$ ), axial-vector mesons (e.g.  $a_1$ ,  $f_1$ ), tensor mesons (e.g.  $f_2$ ,  $a_2$ ) and charged pion and kaon loops. Formerly, these contributions have been determined through model-dependent estimates from meson exchanges, the large  $N_c$  limit, chiral perturbation theory estimates and short distance con-

---

<sup>3</sup>The observable  $a_\mu^{\text{win}}$  accounts for about one third of the total  $a_\mu^{\text{HVP}}$ . When the data-driven evaluation of  $a_\mu^{\text{win}}$  is subtracted from the WP estimate [6] and replaced by this number, the tension between the SM prediction for  $a_\mu$  and experiment is reduced to  $2.9\sigma$ .

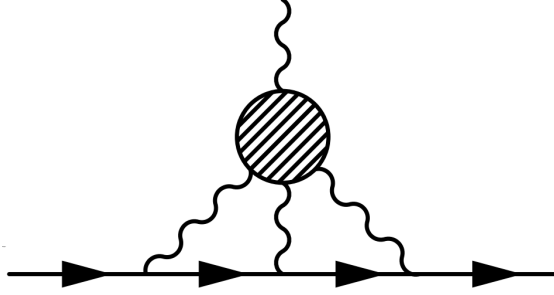


Figure 6.7: HLbL Feynman diagram at LO. The shaded blob represents all possible intermediate hadronic states. Reprinted from Ref. [46].

straints from the operator product expansion and pQCD [49, 597–600]. Luckily, motivated by the muon  $g-2$  theory initiative [6], the status of the estimations of  $a_\mu^{\text{HLbL}}$  is now improved because of newer calculations from data-driven dispersive approaches and from lattice QCD.

### Data-driven and dispersive HLbL

Current data-driven and dispersive methods to calculate  $a_\mu^{\text{HLbL}}$  supply a model-independent evaluation, where possible experimental data are used as input for several hadronic insertions and, when data are not available, theoretical calculations of the amplitudes can be employed. Additionally, there are being some improvements in the model-dependent estimates for the sub-leading contributions [601–607]. The HLbL tensor can be splitted into the sum of all intermediate states in direct and crossed channels as  $\Pi_{\mu\nu\lambda\sigma} = \Pi_{\mu\nu\lambda\sigma}^{\pi^0\text{-pole}} + \Pi_{\mu\nu\lambda\sigma}^{\pi\text{-box}} + \Pi_{\mu\nu\lambda\sigma}^{\pi\pi} + \dots$ . It turns out that

$$a_\mu^{\text{HLbL}} = a_\mu^{\pi^0\text{-pole}} + a_\mu^{\pi\text{-box}} + a_\mu^{\pi\pi} + \dots, \quad (6.8)$$

$a_\mu^{\text{HLbL}}$  is realized to be dominated by contributions arising below 1.5 GeV, with the  $\pi^0$ -pole being the most dominant contribution. Other single-particle states ( $\eta$  and  $\eta'$ ) are suppressed, and even more two-pion and two-kaon effects. The expressions for  $\eta^{(\prime)}$  and two-kaon effects are straightforward. The main experimental inputs to determine these contributions come in the form of  $\pi$ ,  $\eta$  and  $\eta'$  transition form factors (TFFs). These data are obtained as either single-virtual TFFs in the space-like regime from  $\gamma^*\gamma$  collisions or in the time-like region



from radiative production in  $e^+e^-$  collisions, single or double Dalitz decays of pseudoscalars, double-virtual TFFs, or from Dalitz decays of vector mesons.

Detailed descriptions of the dispersive calculations and experimental inputs of each of the contributions to  $a_\mu^{\text{HLbL}}$  are given in Refs. [608–618]. The values obtained from dispersive approaches are consistent with those from older estimates, with improved uncertainties. Summing all the values from the different contributions, the overall dispersive estimate for  $a_\mu^{\text{HLbL}}$  is then

$$a_\mu^{\text{HLbL}} = 92(19) \cdot 10^{-11}, \quad (6.9)$$

where the final uncertainty is a sum of data-driven errors added in quadrature and model-dependent errors added linearly [6, 608–618]. The NLO contribution is  $a_\mu^{\text{HLbL NLO}} = 2(1) \cdot 10^{-11}$ .

## HLbL from Lattice QCD

Thanks to the efforts of the Muon  $g - 2$  Theory Initiative [6], the total  $a_\mu^{\text{HLbL}}$  has been calculated by two lattice groups [619, 620]. In discretized Euclidean spacetime, it has been determined treating QED both perturbatively and non-perturbatively, in both finite ( $\text{QED}_L$ ) and infinite volumes ( $\text{QED}_\infty$ ). Large uncertainties arise from volume errors and non-zero lattice spacings. In  $\text{QED}_L$ ,  $a_\mu^{\text{HLbL}}$  is recovered by extrapolating to infinite-volume and continuum limits. Further details about derivations and the methodologies can be found in Refs. [6, 619, 620]. These two approaches have been tested by replacing quark loops with lepton loops and have been shown to perform well. Moreover, cross checks have been carried out between the results of both groups, which exhibit compatibility when checking effects from lattice spacings and finite/infinite volumes.

After the infinite volume and continuum extrapolations, the outcome from the RBC computation, with both QED and QCD gauge fields on the finite-volume  $\text{QED}_L$  is [619]

$$a_\mu^{\text{HLbL}} = 78.7(30.6)_{\text{stat}}(17.7)_{\text{sys}} \cdot 10^{-11}. \quad (6.10)$$

Contribution	Value $\times 10^{11}$	References
Experiment (BNL)	116 592 089(63)	Ref. [95]
Experiment (FNAL)	116 592 040(54)	Ref. [96]
Experiment (Average)	116 592 061(41)	Refs. [95, 96]
HVP LO ( $e^+e^-$ )	6 931(40)	Refs. [33, 47, 48, 81, 237, 585]
HVP NLO ( $e^+e^-$ )	-98.3(7)	Ref. [47]
HVP NNLO ( $e^+e^-$ )	12.4(1)	Ref. [586]
HVP LO (lattice, $udsc$ )	7 116(184)	Refs. [35, 36, 38-41, 46, 621]
HLbL (phenomenology)	92(19)	Refs. [49, 597, 608-618]
HLbL NLO (phenomenology)	2(1)	Ref. [622]
HLbL (lattice, $uds$ )	79(35)	Ref. [619]
HLbL (phenomenology + lattice)	90(17)	Refs. [49, 597, 608-619]
QED	116 584 718.931(104)	Refs. [32, 576]
Electroweak	153.6(1.0)	Refs. [582, 583]
HVP ( $e^+e^-$ , LO + NLO + NNLO)	6 845(40)	Refs. [33, 47, 48, 81, 237, 585, 586]
HLbL (phenomenology + lattice + NLO)	92(19)	Refs. [49, 597, 608-619, 622]
Total SM Value	116 591 810(43)	Refs. [32, 33, 47, 48, 81, 237, 576, 582, 583, 585, 586, 597, 608-613, 619, 622]
Difference: $\Delta a_\mu = a_\mu^{\text{exp}} - a_\mu^{\text{SM}}$	251(59)	

Table 6.1: Summary of the contributions to  $a_\mu^{\text{SM}}$ . Adapted from Ref. [6].

This number was obtained using several lattice ensembles, with different lattice spacing and volume, with all particles at their physical masses and including contributions from connected and disconnected diagrams. Although this result is not as precise as the dispersive HLbL computation, some improvements in precision are expected in the future. In  $\text{QED}_\infty$ , the RBC group has performed preliminary calculations of both connected and leading disconnected diagrams with physical masses. A recent estimate from the Mainz group found  $a_\mu^{\text{HLbL}} = 107(15) \cdot 10^{-11}$  [620], which is consistent with the result in Ref. [619], but with a smaller uncertainty.

### 6.2.5 The SM prediction for $a_\mu$

The recommended value for the SM prediction of the anomalous magnetic moment of the muon is [6]

$$a_\mu^{\text{SM}} = 116\,591\,810(43) \cdot 10^{-11} \text{ (0.37 ppm)}. \quad (6.11)$$

The several contributions that enter into  $a_\mu^{\text{SM}}$  are summarized in Table 6.1.

### 6.3 Data-driven calculations of HVP

Due to the properties of analyticity and unitarity, the loop integrals containing insertions of HVP in photon propagators can be expressed in the form of dispersion integrals over the cross section of a virtual photon decaying into hadrons (optical theorem). This cross section can be determined in  $e^+e^-$  annihilation, either in direct scan mode, where the energy of the beam is adjusted to measurements at different center-of-mass (CM) energies, or by relying on the method of radiative return, where a collider is operating at a fixed CM energy. The high statistics on the second one provides with an effective scan over different masses of the hadronic system through the emission of initial-state photons, whose spectrum can be calculated and, even in some cases, measured directly. Besides, it is possible to use hadronic  $\tau$  decays to determine hadronic spectral functions, which can be related to the required cross section by means of an isospin rotation.

At leading-order (LO), i.e.,  $\mathcal{O}(\alpha^2)$ , the dispersion integral is given by [623, 624]

$$a_\mu^{HVP,LO} = \frac{\alpha^2}{3\pi^2} \int_{M_\pi^2}^{\infty} \frac{K(s)}{s} R(s) ds, \quad (6.12)$$

with the kernel function

$$K(s) = \frac{x^2}{2}(2-x^2) + \frac{(1+x^2)(1+x)^2}{x^2} \left( \log(1+x) - x + \frac{x^2}{2} \right) + \frac{1+x}{1-x} x^2 \log x, \quad (6.13)$$

where  $x = \frac{1-\beta_\mu}{1+\beta_\mu}$ ,  $\beta_\mu = \sqrt{1-4m_\mu^2/s}$ . The kernel is a slowly varying monotonic function, which goes from the two pion threshold up to large  $s$ .  $R(s)$  is the so-called (hadronic) R-ratio defined by

$$R(s) = \frac{\sigma^0(e^+e^- \rightarrow \text{hadronic}(+\gamma))}{\sigma_{pt}}, \quad \sigma_{pt} = \frac{4\pi\alpha^2}{3s}. \quad (6.14)$$

The factor  $K(s)/s$  in Eq. (6.12) enhances the contributions at lowest energies. The superscript in  $\sigma^0$  indicates that the total hadronic cross sections in the dispersion integral must

be the bare cross section, excluding effects from vacuum polarization (VP) that lead to the running of the QED coupling. If these effects are included as part of the measured hadronic cross section, this data has to be “undressed”, i.e., VP effects must be subtracted. Otherwise, there would be a double counting and, therefore, iterated VP insertions are taken into account as part of the higher-order HVP contributions.

Contrarily, the hadronic cross section used in the dispersion integral is normally taken to be inclusive with respect to final-state radiation of additional photons. While this is in contradiction to the formal power counting in  $\alpha$ , it is impossible to subtract the real and virtual photonic FSR effects in hadron production, especially for higher-multiplicity states for which these QED effects are difficult to model. Since these FSR effects are not included explicitly in the higher-order VP contributions, this procedure is fully consistent. The threshold for hadron production is provided by the  $\pi^0\gamma$  cross section and thus the lower limit of the dispersion integral is  $M_{\pi^0}^2$ .

There are similar expressions to Eq. (6.12) for the HVP contributions at next-to-leading order (NLO) [625] and next-to-next-to-leading order (NNLO) [586]. They are more difficult and require double and triple integrations. The NLO contributions are numerically of the order of the HLbL contributions, but negative in sign. The NNLO contributions turn out to be somewhat larger than naively expected and, therefore, should be evaluated as a nonnegligible component of  $a_\mu^{HVP,LO}$ .

### 6.3.1 Hadronic cross sections at low energies

At low energies, the total cross section is obtained by summing all possible different final states. Measurements for more than 35 exclusive channels from different experiments have been published over many years. At low energies the most important channel is the two-pion channel, that contributes more than 70% of  $a_\mu^{HVP,LO}$ . This channel comes mainly from decays of the  $\rho$  meson, with an admixture with the  $\omega$ . Sub-leading contributions arise from decays

of the  $\omega$  and  $\phi$  in the three-pion and two-kaon channels, and from four-pion final states with more complicated production mechanism. The interferences between different production mechanisms are taken into account since we are taking the incoherent sum over distinct final states. In order to achieve an accurate description of the total cross section it is necessary to include higher-multiplicity final states (up to six pions) and final states containing pions and kaons or the  $\eta$ . Contributions for which no reliable data exists, but which are expected to be non-negligible, have to be estimated, e.g., the case for multi-pion channels consisting mainly of neutral pions. Such final states can be approximated by assuming isospin symmetry, which can be used to model relations between measured and unknown channels. The reliability of such relations is difficult to quantify and is usually mitigated by assigning a large fractional error to these final states. Nonetheless, with more channels having been measured in recent years, the role of these isospin-based estimates has been largely reduced. For leading contributions very close to the threshold, where data is limited, the hadronic cross section can be estimated based on additional constraints, e.g., from chiral perturbation theory ( $\chi PT$ ).

## Input data

### Exclusive measurements

- **$\pi^+\pi^-$  channel**

Since the contribution from this channel is very important, there has been a large experimental effort to obtain reliable and precise data. Most old measurements are now essentially obsolete. The most recent evaluations only use the results obtained in the last decade or so.

Precise measurements in the  $\rho$  region came from Novosibirsk with CMD-2 [626] and SND [54], revising older results <sup>4</sup>. Also, CMD-2 has obtained results above the  $\rho$  region [628], as well as a second set of data across the  $\rho$  resonance [629]. Neither

---

<sup>4</sup>There were problems with large radiative corrections in previous analyses of CMD-2 [627] and SND [396].

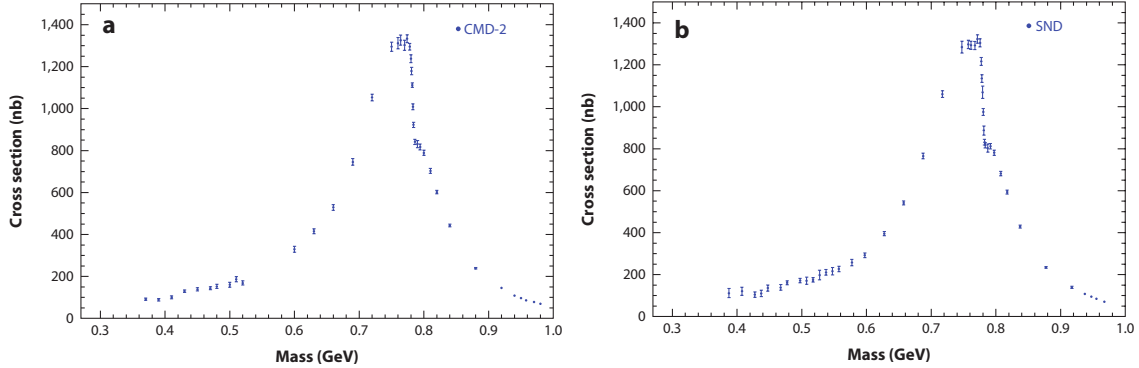


Figure 6.8: CMD-2 [52, 53] (left) and SND [54] (right) data for  $e^+e^- \rightarrow \pi^+\pi^-$  in the  $\rho$  region. Reprinted from Ref. [55].

experiment can separate pions and muons, except for near threshold using momentum measurement and kinematics for CMD-2, with the purpose that the measured quantity is the ratio  $(N_{\pi\pi} + N_{\mu\mu})/N_{ee}$ . The pion-pair cross section is obtained after subtracting the muon-pair contribution and normalizing to the Bhabha events, using computed QED cross section for both, including their respective radiative corrections. In Fig. 6.8, these results are corrected for leptonic and hadronic VP, and for photon radiation by the pions, in such a way that the deduced cross section corresponds to  $\pi^+\pi^-$  including pion-radiated photons and virtual final-state QED effects.

The KLOE [56] and BABAR [20,21] ISR analyses are initially very different. First, the CM energy is close to the studied energy in the case of KLOE (soft ISR photons), while it is very far in the BABAR case (hard ISR photons). In KLOE-2008 and KLOE-2012 the ISR photon is not detected and reconstructed kinematically, assuming no extra photons. Since the cross section strongly peaks along the beams, a large statistics of ISR events is get. Pion pairs are separated from muon pair with kinematical constraints. In BABAR, the ISR photon is detected at large angle (about 10% efficiency) with the intent that the full event is observed, and an additional photon can be included in the kinematical fit (undetected forward additional ISR or detected ISR/FSR photon). Another big difference concerns the ISR luminosity: in the KLOE-2008 and KLOE-2010 analyses it is computed using the NLO PHOKHARA generator [402], while in

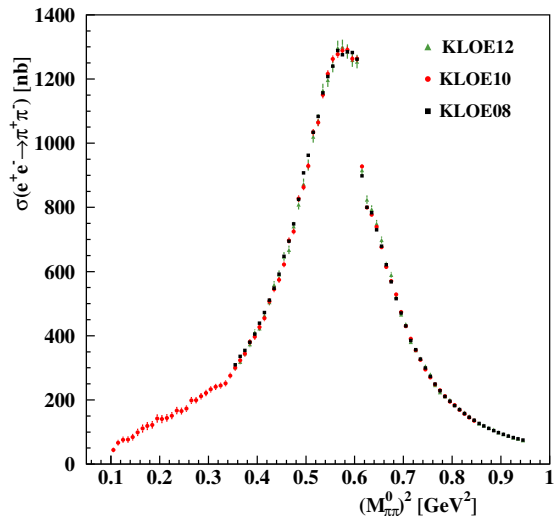


Figure 6.9: The KLOE  $e^+e^- \rightarrow \pi^+\pi^-$  measurement in the  $\rho$  region obtained in three experimental configurations [56–58]. Adapted from Ref. [58].

BABAR both pion and muon pairs are measured and the ratio  $\pi\pi(\gamma)/\mu\mu(\gamma)$  directly gives the  $\pi\pi(\gamma)$  cross section. The small-angle ISR photon provides a suppression of the sizeable LO  $|\text{FSR}|^2$  contribution in KLOE, and the remaining part is computed from PHOKHARA. In BABAR, the  $|\text{FSR}|^2$  contribution is negligible because of the large value of  $s$ . The KLOE method with small-angle undetected ISR photons also reduces the range of  $\pi\pi$  masses on the low side because of the limited angular acceptance of the detector. To solve this problem, the analyses of KLOE-2010 were performed with large-angle ISR [57]. Finally, the KLOE-2012 measurement [58] was obtained using the same ratio method as BABAR (Fig. 6.9), but with undetected small-angle ISR photons. This ratio is taken in small mass bin (6 MeV) for KLOE, while for BABAR larger intervals (50 MeV) are used in order to reduce statistical fluctuations on the individual cross sections values, using the expected variation of the  $\mu\mu(\gamma)$  cross section within each interval and the bin-to-bin correlations in the covariance matrix.

The three KLOE measurements have been recently combined utilizing the correlations between the different data sets [88]. The combination method was intended at providing a coherent KLOE data set with a fully consistent treatment of uncertainties

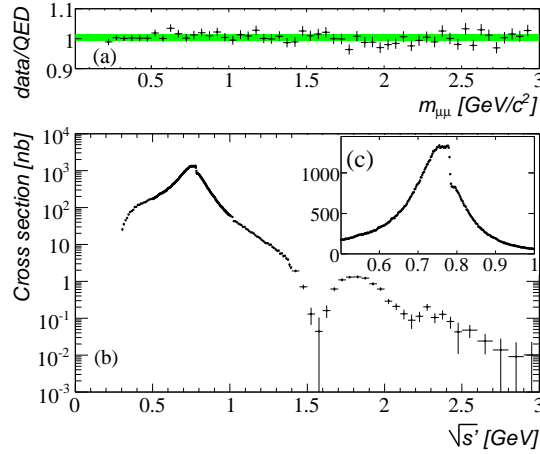


Figure 6.10: BABAR results [20, 21] using the large-angle ISR method:  $e^+e^- \rightarrow \mu^+\mu^-$  compared to NLO QED (top) and  $e^+e^- \rightarrow \pi^+\pi^-$  from threshold to 3 GeV utilizing the  $\pi\pi/\mu\mu$  ratio (bottom). Reprinted from Ref. [21].

between the three analyses.

To reduce systematic uncertainties, the BABAR method includes the simultaneous measurement of the process  $e^+e^- \rightarrow \mu^+\mu^-$ , which by itself can be inspected against the QED prediction taking into account the  $e^+e^-$  luminosity. The comparison of the BABAR data with NLO QED displays a good agreement from threshold to 3 GeV within a total uncertainty of 1.1%, governed by the luminosity uncertainty (Fig. 6.10).

Recent results with the ISR method in the charm region and large-angle ISR tagging have been obtained by BESIII [59] and a group utilizing the data from CLEO-c [60]. Both have a larger statistical uncertainty. This is shown in Fig. 6.11.

Although lots of data for the  $\pi^+\pi^-$  channel with an improved precision over time have been recorded, the consistency among them is far from excellent.

- **Other two-body channels**

The  $\pi^0\gamma$  final state is the first open hadronic channel and defines the lower limit of integration of the dispersion integral. Moreover, recent measurements with better precision from SND over the full spectrum up to 2 GeV are now available [630, 631].

Cross section for the final states with  $K^+K^-$  and  $K_S K_L$  are depicted in Fig. 6.12 for



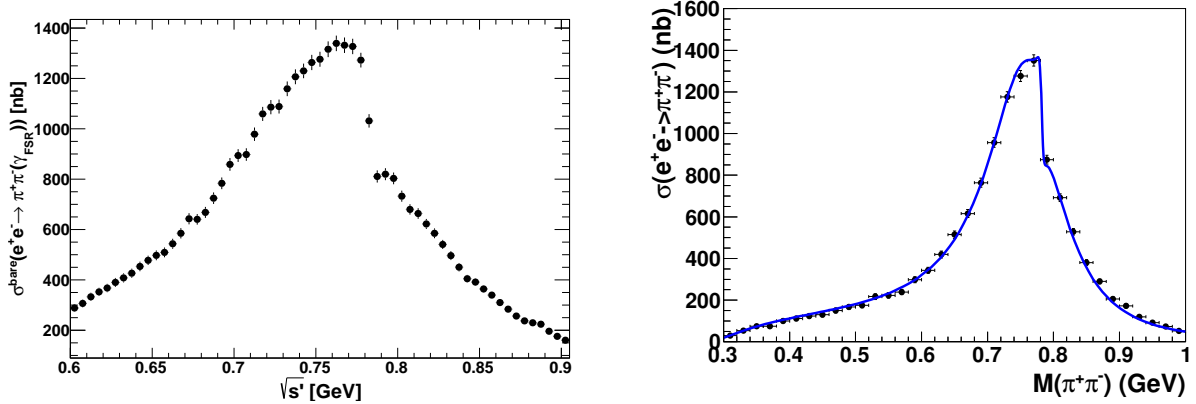


Figure 6.11: Results from BESIII (left, reprinted from Ref. [59]) and CLEO-c (right, reprinted from Ref. [60]) on  $e^+e^- \rightarrow \pi^+\pi^-$  in the  $\rho$  region using large-angle detected ISR photons.

CMD-2 [62, 632], SND [61, 633], and BABAR [63]. They are governed by the  $\phi$  resonance. Here, the broad mass range available through the ISR approach is impressive. Recent results were obtained at VEPP-2000 by CMD-3 [90] and SND [634], which differ substantially from the earlier CMD-2 and SND measurements at VEPP-2M. Although experiments are in good agreement for  $K_S K_L$ , the situation is more problematic for  $K^+ K^-$ .

BABAR [635–637] and CMD-3 [638] have achieved precise measurements of the  $p\bar{p}$  final state. The cross section for  $e^+e^- \rightarrow p\bar{p}$  displays little energy dependence from threshold to 2 GeV. Here the ISR method also allows the measurements to be performed over a large energy range up to 6 GeV. A cross section compatible to that of  $p\bar{p}$  from threshold to 2 GeV is observed in the measurement of  $e^+e^- \rightarrow n\bar{n}$  from SND [639]. The nuclear-pair production at 2 GeV accounts for about 4% of the total hadronic cross section.

- **Multi-hadronic channels**

The cross section for different exclusive channels has been measured with the scan method up to 1.4 GeV by CMD-2 and SND and extended more recently up to 2 GeV using the VEPP-2000 collider and the upgraded CMD-3 and SND detectors. BABAR has used extensively the ISR approach, covering the range from threshold to typically

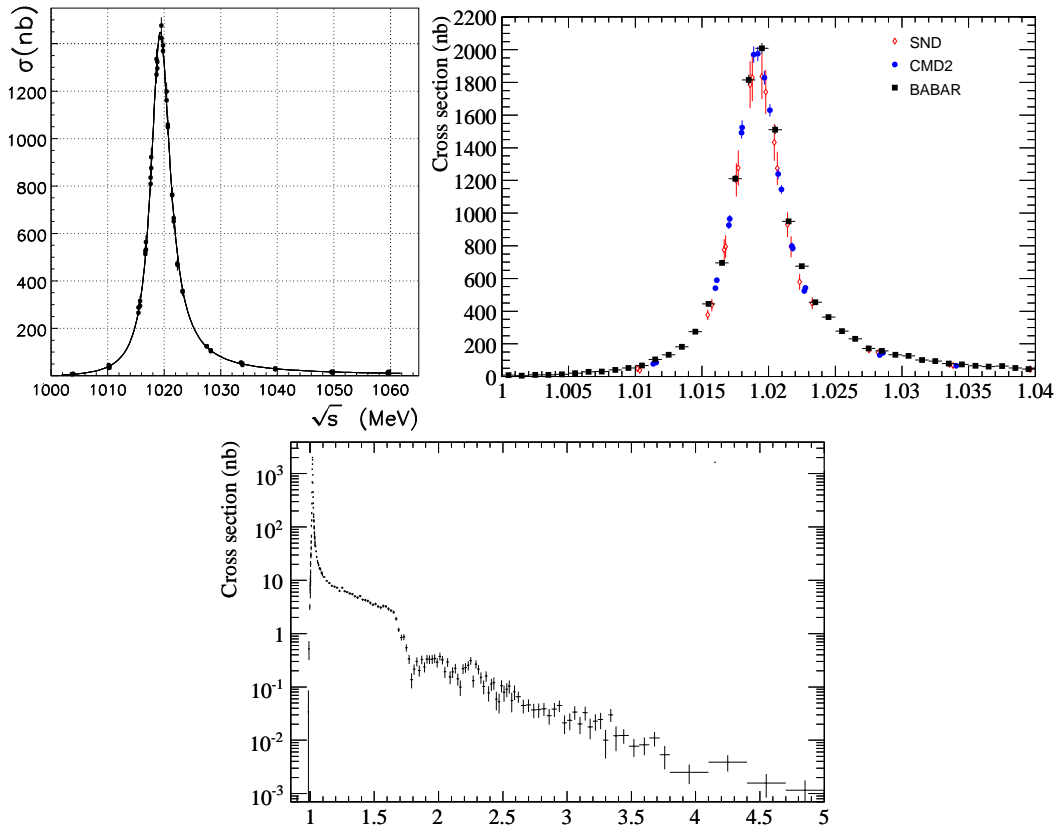


Figure 6.12: Cross sections for  $e^+e^- \rightarrow K_S K_L$  measured by SND [61] (upper left), and  $e^+e^- \rightarrow K^+K^-$  by CMD-2 [62], SND [61], and BABAR [63] (upper right), and BABAR over a wider energy range (bottom). Reprinted from Refs. [61, 63].

3 – 5 GeV. An almost complete set of exclusive measurements up to about 2 GeV is represented by the BABAR results. Above 2 GeV, many channels with higher multiplicity open up that in practice cannot be studied independently, in such a way that the method that uses the sum of exclusive cross sections is no longer applicable. There is an excellent agreement between BABAR and the final state measurements by the scan method at VEPP-2000, which provides a nice consistency check.

The largest multi-hadronic cross sections below 2 GeV are for the 3-pion and 4-pion final states. The 3-pion cross section is dominated at low energies by the  $\omega$  (see Fig. 6.13) and  $\phi$  resonances as measured by the CMD-2 [64,640] and SND [66] experiments. Above the  $\phi$  region, results are at hand from BABAR [65] and SND [641], which agree with each other as in Fig. 6.14, albeit both disagree strongly with the earlier results from DM2 [642]. For the final states of  $2\pi^+2\pi^-$  [68,69] and  $\pi^+\pi^-2\pi^0$  [70], the development provided by the ISR BABAR results is striking both in terms of precision and mass coverage, see Fig. 6.14. Previous results from VEPP-2M [643–645] and VEPP-2000 [646] only extended to 1.4 GeV. Results on exclusive final states containing up to 6 quasi-stable hadrons are available [647,648]. The limitation on hadron multiplicity, set to a great extent by the difficulty to select and identify multi- $\pi^0$  final states, does not allow a reliable reconstruction of the full hadronic rate above 2 GeV as a sum over individually measured exclusive cross sections.

Several processes with smaller cross sections have to be considered to saturate the total hadronic rate. Some results on final states including  $\eta$  mesons are shown in Fig. 6.15, specifically  $\eta\pi^+\pi^-$  from BABAR [71,72], CMD-2 [73], and SND [74], and  $\eta\pi^+\pi^-\pi^0$  from CMD-3 [75]. Besides, recent data sets for  $\eta\pi^+\pi^-$  are at hand from SND [649] and CMD-3 [650]. For the final states of  $\eta4\pi$  only results from BABAR are available, both for  $\eta2\pi^+\pi^-$  [71] and  $\eta\pi^+\pi^-2\pi^0$  [651]. A lot of progress was recently achieved by BABAR on  $K\bar{K}n$  pions final states with the complete set of measurements for all charge configurations  $n = 1, 2$  [76–80] owing to the detection of  $K_S$ ,  $K_L$ , charged pions and kaons, and multiple  $\pi^0$  (Fig. 6.16).

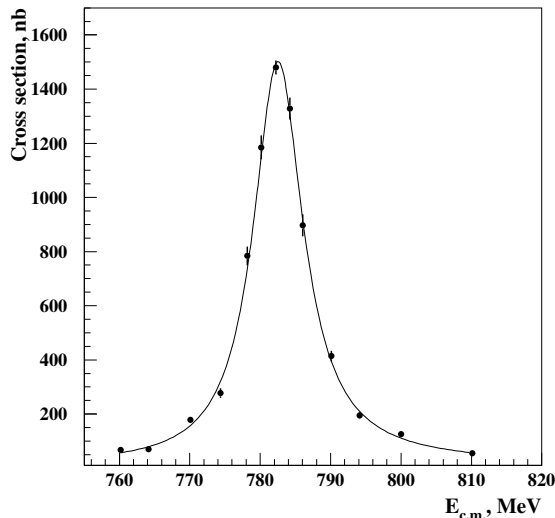


Figure 6.13: The  $\omega$  resonance in the  $\pi^+\pi^-\pi^0$  mode from CMD-2. Reprinted from Ref. [64].

There are additional measurements for some specific channels,  $K^+K^-\pi^+\pi^-$  [652] and  $K_S K_L \pi^0$  [653]. Finally, cross sections for  $K^+K^-\eta$  [77] and  $K_S K_L \eta$  [79] are also available from BABAR.

#### Narrow resonances

The contributions of the very narrow resonances  $J/\psi$  and  $\psi(2S)$  are obtained by numerically integrating their undressed Breit-Wigner line shapes. The uncertainties in the integrals are dominated by the knowledge of their bare electronic widths available from experiment [3,654].

#### Inclusive R measurements

Above 2 GeV the annihilation cross section needs to be measured inclusively due to the large number of open exclusive channels. Precise results from BESII [82–84] are in the 2 – 4.5 GeV range. The KEDR collaboration has recently published results from an inclusive  $R$  scan from  $\sqrt{s} = 1.84$  to 3.05 GeV [85,86], complementing their preceding measurements obtained between 3.12 and 3.72 GeV [85]. This data is the most precise and complete in this energy range with a typical systematic uncertainty of 3%. It constitutes a very valuable input to test the validity of the pQCD estimate (Fig. 6.17). Between 2 GeV and the charm threshold,

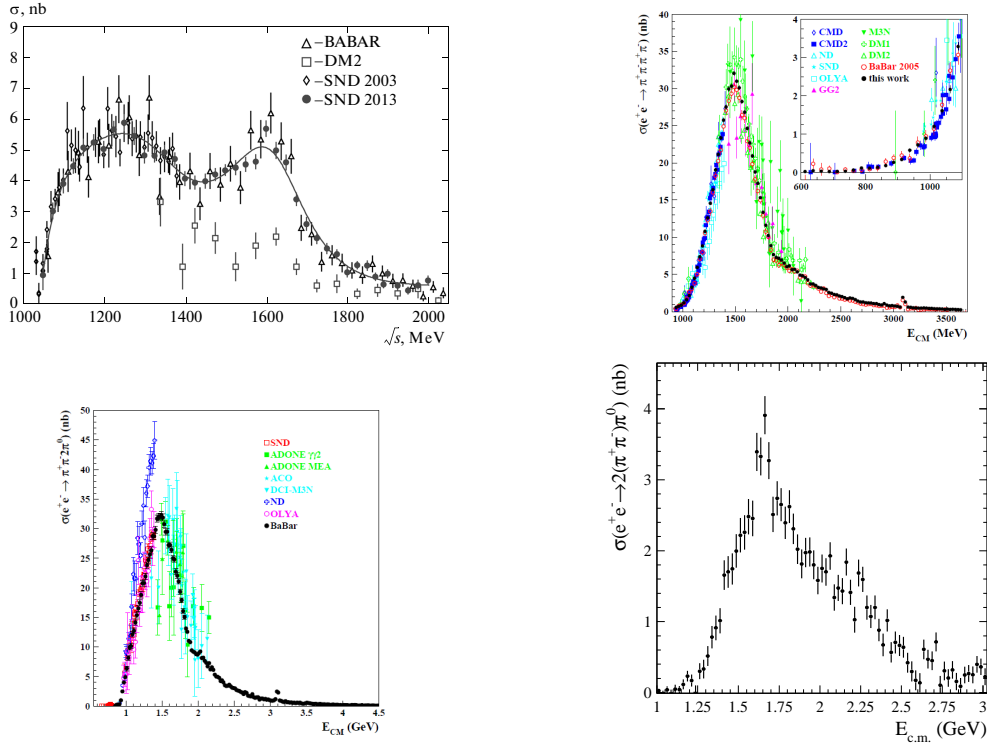


Figure 6.14: Multi-pion cross sections results. Top left:  $\pi^+\pi^-\pi^0$  from BABAR [65], SND [66,67], and previous experiments. Top right:  $2\pi^+2\pi^-$  BABAR [68,69] and elderly experiments. Bottom:  $\pi^+\pi^-2\pi^0$  from BABAR [70] and older experiments (left), and  $2\pi^+2\pi^-\pi^0$  from BABAR [71] (right). Reprinted from Refs. [67,69–71].

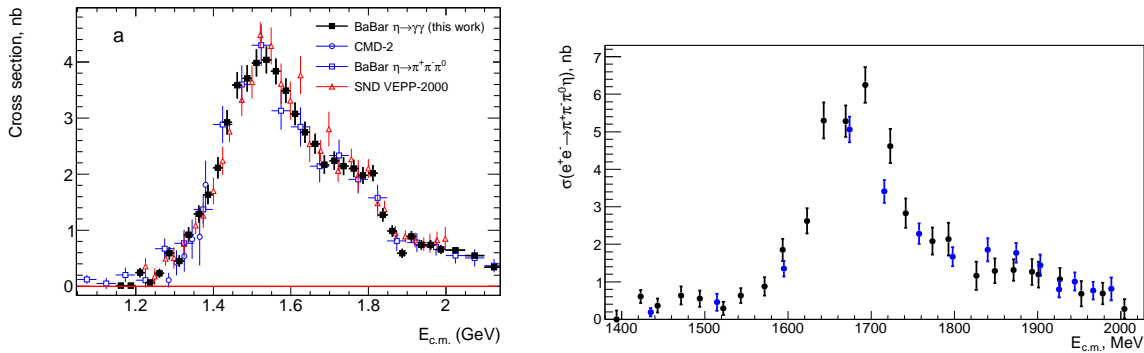


Figure 6.15: Results from BABAR [71, 72], CMD-2 [73], and SND [74] on the cross sections for  $e^+e^- \rightarrow \eta\pi^+\pi^-$  (left), and from CMD-3 [75] for  $e^+e^- \rightarrow \eta\pi^+\pi^-\pi^0$  (right). Reprinted from Refs. [72, 75].

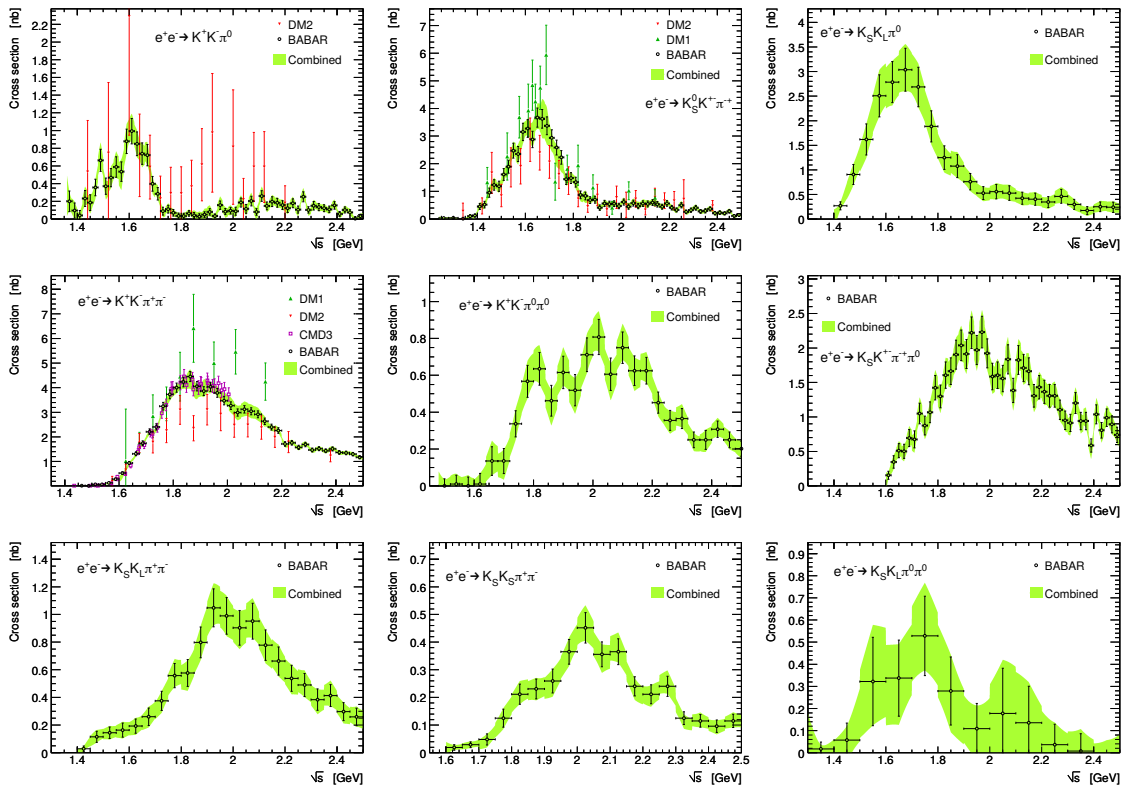


Figure 6.16: BABAR results [76–80] on the cross sections for  $e^+e^- \rightarrow K\bar{K}\pi$  (top row) and  $e^+e^- \rightarrow K\bar{K}\pi\pi$  (second and third rows). Reprinted from Ref. [81].

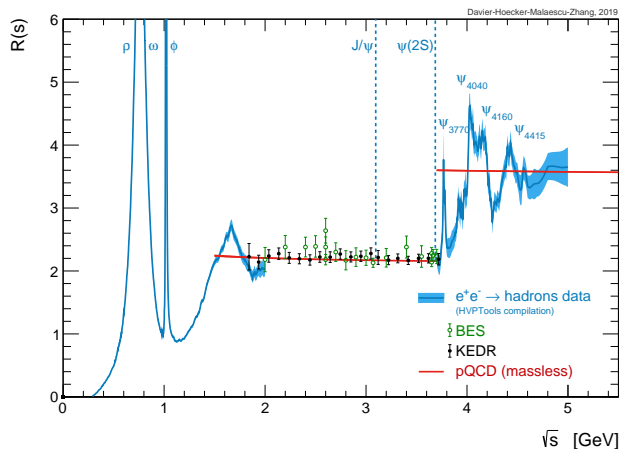


Figure 6.17: The total hadronic  $e^+e^-$  annihilation cross section ratio  $R$  as a function of  $\sqrt{s}$  [81]. Inclusive measurements from BES [82–84] and KEDR [85–87] are depicted as data points, while the sum of exclusive channels from this analysis is given by the narrow blue bands. The prediction from massless pQCD is also shown (solid red line). Reprinted from Ref. [48].

the  $R$  value (hadronic cross section scaled to the  $s$ -channel point-like fermion-pair lowest-order cross section) behaves smoothly with a weak energy dependence, and it agrees with the pQCD prediction within experimental uncertainties. Fig. 6.17 depicts the results on  $R$ , which are based on the sum of exclusive channels below 2 GeV [81] and the inclusive measurements above. The coincidence between the measurements in the two regions is good enough and consistent with the quoted uncertainties.

### 6.3.2 Tensions in hadronic data

The precision of the data-driven approach is affected by some discrepancies among the different data sets.

#### Tensions in the $\pi^+\pi^-$ channel

Approximately 3/4 of the full hadronic contribution to the muon  $g - 2$  is accounted by the  $\pi^+\pi^-$  channel. Hence, there is a need for the highest precision. Many experimental measurements have been performed in the last four decades, however it is only in the last fifteen years that sufficient statistics and small systematic uncertainties have been reached.

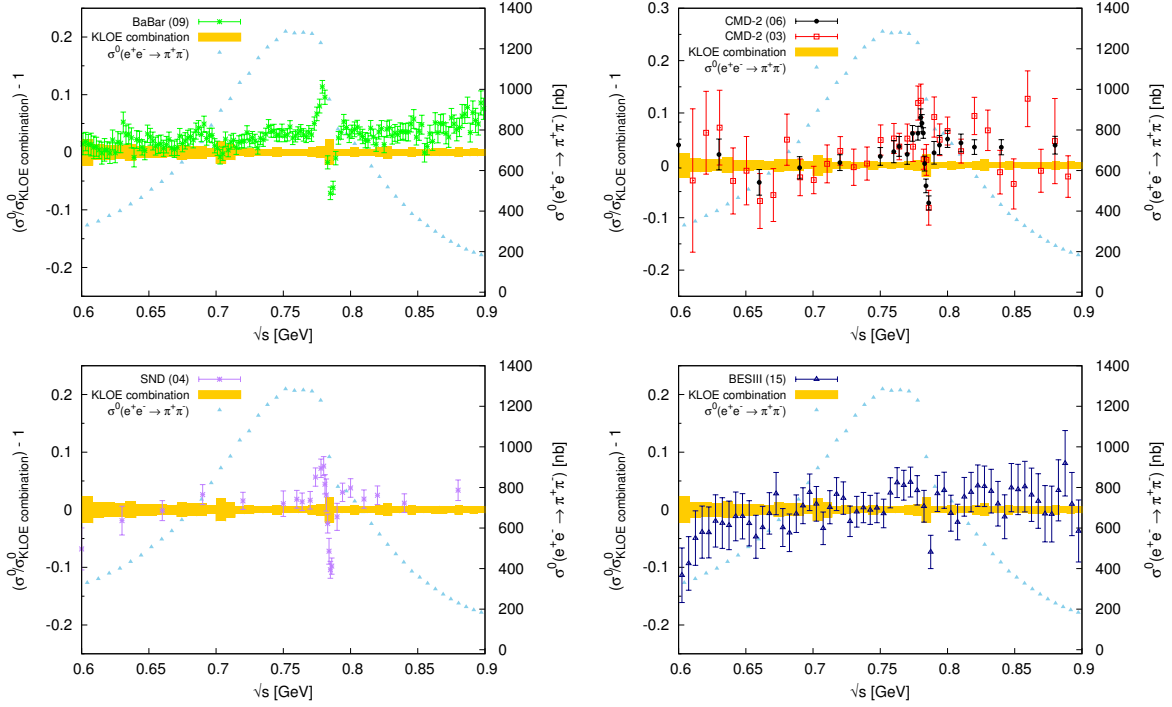


Figure 6.18: The  $\pi^+\pi^-$  cross section from the KLOE combination compared to the BABAR, CMD-2, SND, and BESIII data points in the 0.6 – 0.9 GeV range [88]. The KLOE combination is represented by the yellow band. The uncertainties shown are the diagonal and systematic uncertainties added in quadrature. Reprinted from Ref. [88].

Nevertheless, the situation is not very good since the two most precise measurements by KLOE and BABAR do not agree well within their quoted uncertainties. The state worsens after combining [88] the three KLOE measurements based on different ISR methods since the uncertainty is reduced. Fig. 6.18 displays the ratios of the recent measurements by CMD-2, SND, BABAR, and BESIII to the combined KLOE cross section in the 0.6 – 0.9 GeV mass region, where the KLOE band and the data points involve the full diagonal error. Some features are evident: (1) the normalization at the peak is generally higher than KLOE, (2) there exists a trend for a linear increase on the ratio with mass, and (3) a clear disagreement is seen in the narrow  $\rho$ – $\omega$  interference region. Because of the higher precision of the BABAR data, these characteristics are most clearly visible there, but they are also present for the other experiments. Although there is a fair agreement below 0.70 – 0.75 GeV, the KLOE data seems noticeably lower on the  $\rho$  peak and above by a factor rising to a few percent.



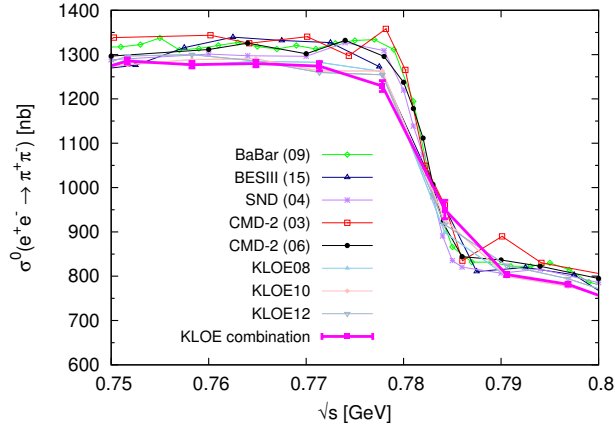


Figure 6.19: The  $\pi^+\pi^-$  cross section from KLOE combination, BABAR, CMD-2, SND, and BESIII in the  $\rho - \omega$  interference region [88]. Reprinted from Ref. [88].

A common oscillatory pattern is shown by the ratios in the  $\rho - \omega$  interference region. In Ref. [88] the ratio of a particular experiment was computed with respect to the linearly interpolated value between adjoining KLOE points, some bias is expected especially in the interference region with its fast-changing cross section. This oscillation is not present for the ratio KLOE to BABAR [20], where the fit to the BABAR data is used as reference to avoid these effects. The interference pattern is more eradicated in KLOE (Fig. 6.19), most likely because of the choice of wide mass bins. A vertical offset is evident in the plot on the  $\rho$  peak. However, the effect of the  $\rho - \omega$  interference pattern is mostly cancelled when integrating over the mass spectrum. Therefore, differences in this region among experiments are not expected to produce large biases for the integral values.

The most salient discrepancy between the KLOE and BABAR data aims to one or various systematic effects not properly covered by the estimated systematic uncertainties. At this moment, other experiments are barely precise to resolve this discrepancy, lying between those of KLOE and BABAR, and overlapping with both. The contributions to the dispersion integral from the region between 0.6 and 0.9 GeV for each experiment is shown in Fig. 6.20. One-parameter fits give  $\chi^2/d.o.f$  values of 4.5/4 and 3.6/4 when all experimental data sets are included except BABAR and all experimental data sets are included except KLOE. Hence, BESIII/CLEO/CMD-2/SND are compatible with either KLOE and BABAR.

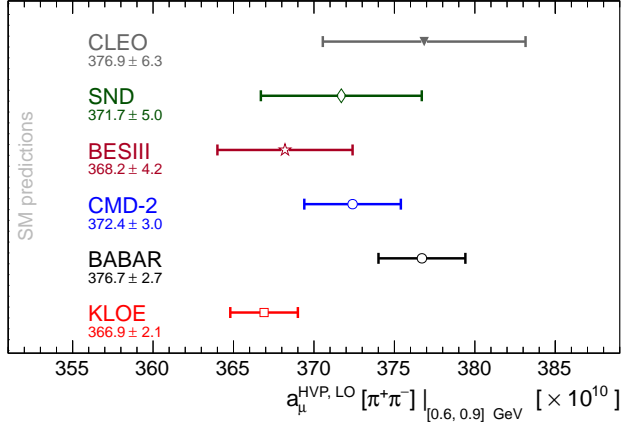


Figure 6.20: Comparison of results for  $a_\mu^{\text{HVP}}[\pi\pi]$  evaluated between 0.6 GeV and 0.9 GeV for the different experiments. Reprinted from Ref. [6].

In the combination procedure performed by both DHMZ and KNT, local tensions were treated by introducing scaling factors for the uncertainties. Global tension was also accounted for in the DHMZ analysis. Further details can be found in the WP [6].

There is also some tension when the three KLOE measurements [88] are combined. The ratios of the cross section values between KLOE-2012 and KLOE-2008, along with KLOE-2010 and KLOE-2008, were computed using all the correlations between the measurements, for both the statistical and systematic uncertainties. Some systematic deviations from unity, which are statistically significant and not completely taken into account by the local scaling procedure, are depicted in Fig. 6.21. This effect is probably an underestimated systematic uncertainty in the combined result. Given the fact that these deviations are canceled out when integrating the spectrum, the integral values are consistent [88]. These discrepancies are not present in the ratio between the KLOE-2012 and KLOE-2010 measurements, see Fig. 6.21.

Recently the SND collaboration has presented their results at VEPP-2000 on the  $\pi^+\pi^-$  mode [89] with increased statistics and reduced systematic errors (0.8%) compared to their analysis at VEPP-2M. A fit of the pion form factor taking into account a vector-meson dominance (VMD) ansatz for the  $\rho$  resonance along with  $\omega$  and  $\rho'$  contributions was performed. This description of their data is used to compare with existence data. The resulting com-

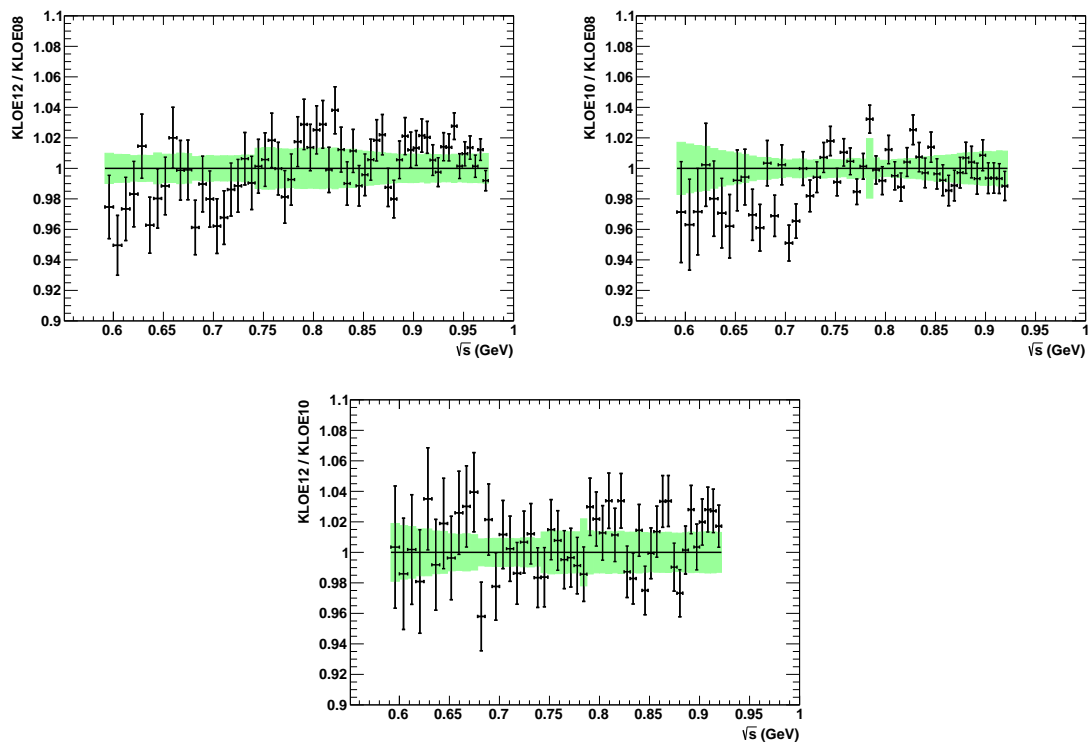


Figure 6.21: Ratios of cross sections [88] from KLOE-2012 to KLOE-2008 (top left), KLOE-2010 to KLOE-2008 (top right), and KLOE-2012 to KLOE-2010 (bottom). The uncommon systematic uncertainties in the respective ratios are indicated by the green bands. Reprinted from Ref. [6].

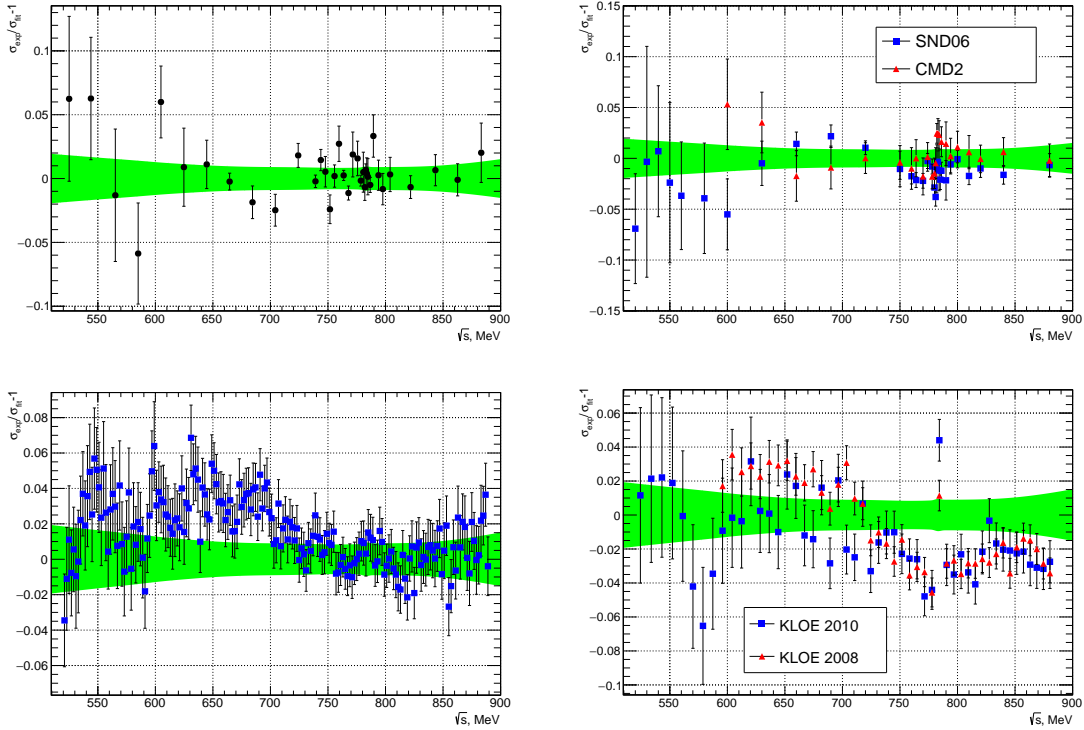


Figure 6.22: Top left: ratio of SND-2020  $\pi^+\pi^-$  cross section values to form factor fit. Top right: ratio of older SND and CMD-2 cross sections to new SND fit. Bottom: akin ratios for BABAR (left) and KLOE-2008 and KLOE-2010 (right). Reprinted from Ref. [89].

comparison ratios are illustrated in Fig. 6.22 for BABAR, KLOE-2008 and KLOE-2012, and VEPP-2M results from SND and CMD-2. Here, the most severe discrepancies were found with the KLOE and BABAR data. At first instance, below 0.7 GeV both KLOE-2008 and BABAR are higher than SND by 2–4%, while KLOE-2010 is more in agreement. Conversely, above 0.7 GeV SND agrees well with BABAR, while both KLOE measurements are below by 2 – 3%. More experimental studies with high precision are needed to understand the KLOE-BABAR discrepancy. These new results from SND are not included in the current version of the WP [6].

### Tensions in the $K^+K^-$ channel

Tensions among data sets are also present in the  $K^+K^-$  channel (Fig. 6.23, top panel). A discrepancy up to 20% between BABAR [63] and SND [633] was observed for masses between

1.05 and 1.4 GeV. However, this problem has been resolved with the most recent SND result [6], despite the fact that the origin of the previous systematic shift is not discussed.

There are also some concerns regarding data on the  $\phi(1020)$  resonance. Formerly, a 5.1% difference between CMD-2 [62] at VEPP-2M and BABAR [63], with the CMD-2 data being lower, was observed. SND [61] results are also low compared to BABAR, but the difference is not significant in view of the larger SND systematic uncertainty (6.8%). New results from CMD-3 at VEPP-2000 [90] display the opposite effect: they are 5.5% higher than the BABAR (Fig. 6.23, middle). The quoted systematic uncertainty of 2.2%, of which only 1.2% is assigned to the detection efficiency, is greatly exceeded by the discrepancy of almost 11% between the two CMD-2/3 data sets. The upward cross section shift is claimed to originate from a better understanding of the detection efficiency of kaons with very low energy in the CMD-3 data, given the fact that the  $\phi(1020)$  is very close to the  $K^+K^-$  threshold. In comparison with the CMD-2/3 data and SND data sets, the ISR method of BABAR benefits from higher-momentum kaons with better detection efficiency thanks to the final state boost.

Since the situation is unresolved, both CMD-2/3 data sets should be kept, which, owing to the uncertainty of the rescaling procedure, gives a deterioration of the precision (by a factor of  $\sim 2$ ) of the combined data (Fig. 6.23, bottom). A better understanding of the data from CMD-2/3 and SND is necessary to improve this situation.

### 6.3.3 Use of hadronic tau decay data

In 1997 precise  $\tau$ -spectral functions became available [11, 12, 18, 397, 455, 527, 655] which, to the extent that flavor  $SU(2)$  in the light hadron sector is a good symmetry, allows one to obtain the isovector part of the  $e^+e^-$  cross-section [249]. The idea to use the  $\tau$  spectral data to improve the evaluation of the hadronic contributions  $a_\mu^{\text{had}}$  was realized by Alemany, Davier and Höcker [656]. It is based on the fact that in the limit of isospin invariance, the spectral function of the vector current decay  $\tau^- \rightarrow X^- \nu_\tau$  is related to the  $e^+e^- \rightarrow X^0$  cross section of the corresponding isovector final state  $X^0$  (the so-called conserved vector current (CVC) relation),

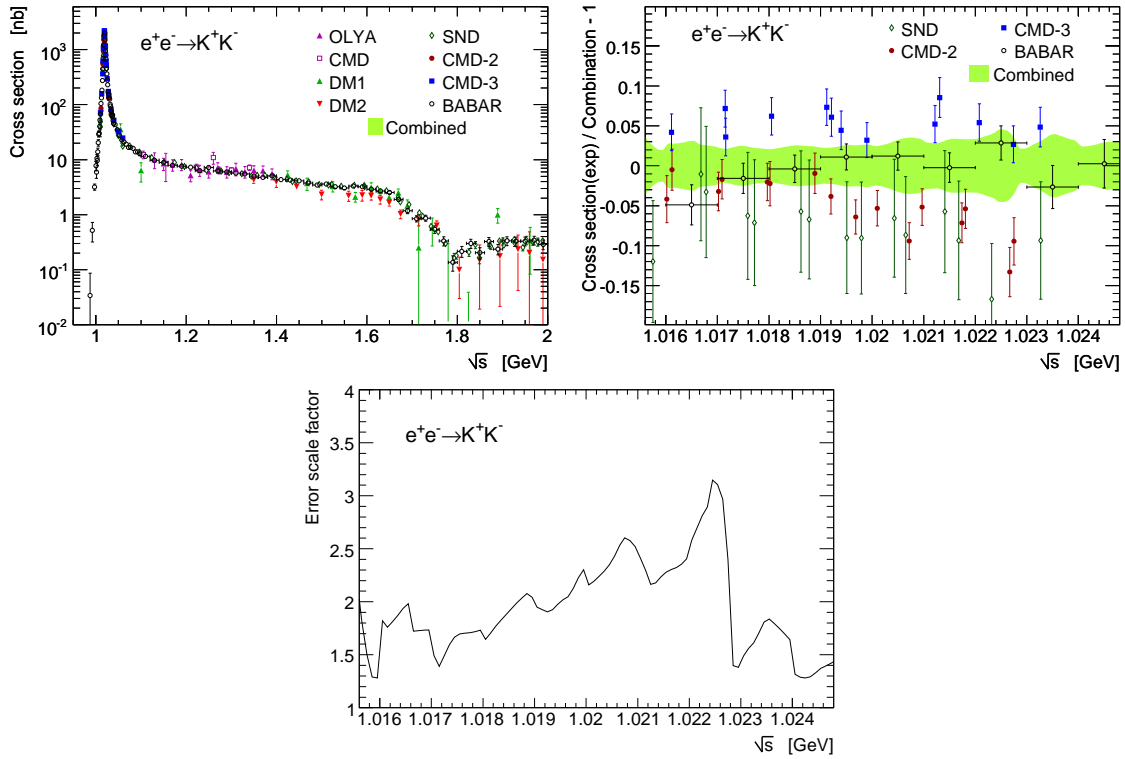


Figure 6.23: Top left: bare cross sections for  $e^+e^- \rightarrow K^+K^-$ . Top right: comparison between individual  $e^+e^- \rightarrow K^+K^-$  cross sections measurements from BABAR [63], CMD-2 [62], CMD-3 [90], SND [61], and the HVPTools combination. Bottom: local scale factor vs. CM energy applied to the combined  $K^+K^-$  cross section uncertainty to account for inconsistency in the individual measurements. Reprinted from Ref. [48].

$$\sigma_{X^0}^{J=1}(s) = \frac{4\pi\alpha^2}{s} v_{1,X^-}(s), \quad (6.15)$$

where  $s$  is the CM energy-squared or equivalently the invariant mass-squared of the  $\tau$  final state  $X$ ,  $\alpha$  is the fine-structure constant, and  $v_{1,X^-}$  is the non-strange, isospin-one vector spectral function given by

$$v_{1,X^-} = \frac{m_\tau^2}{6|V_{ud}|^2} \frac{\mathcal{B}_{X^-}}{\mathcal{B}_e} \frac{1}{N_X} \frac{dN_X}{ds} \times \left[ \left(1 - \frac{s}{m_\tau^2}\right)^2 \left(1 + \frac{2s}{m_\tau^2}\right) \right]^{-1} \frac{R_{\text{IB}}(s)}{S_{\text{EW}}}. \quad (6.16)$$

Here,  $m_\tau$  is the  $\tau$  mass,  $|V_{ud}|$  the CKM matrix element,  $\mathcal{B}_{X^-}$  and  $\mathcal{B}_e$  are the branching ratios of  $\tau^- \rightarrow X^-(\gamma)\nu_\tau$  (final-state photon radiation is implied for  $\tau$  branching ratios) and of  $\tau^- \rightarrow e^-\bar{\nu}_e\nu_\tau$ ,  $(1/N_X)dN_X/ds$  is the normalized  $\tau$  spectral function (invariant mass spectrum) of the hadronic final state,  $R_{\text{IB}}$  represents  $s$ -dependent isospin-breaking (IB) corrections, and  $S_{\text{EW}}$  is the short-distance electroweak radiative corrections [7].

Both spectral functions and branching ratios for the tau have been precisely measured at LEP and at the  $B$  factories under independent conditions. Despite the fact that  $B$  factories have much larger statistics, the immense QCD backgrounds must be reduced at the cost of small efficiencies with corresponding irreducible systematic uncertainty. The opposite happened at LEP with  $Z$  decays into two boosted  $\tau$ 's and small well-understood backgrounds inducing small systematic uncertainties, however with moderately high statistics. Thus, branching ratios are well measured at LEP, while the determination of normalized spectral functions exploit the high statistics at  $B$  factories. For the dominant  $2\pi$  channel the branching ratio has been measured by ALEPH [397] in agreement the other experiments [12, 18, 487, 527, 657] and the most precise spectral function has been achieved by Belle [18]. A combined spectral function from all experiments is available in Ref. [7].

Focusing on the dominant  $2\pi$  channel, the IB correction term  $R_{\text{IB}}(s)$  is given by

$$R_{\text{IB}}(s) = \frac{\text{FSR}(s)}{G_{\text{EM}}(s)} \frac{\beta_0^3(s)}{\beta_-^3(s)} \left| \frac{F_0(s)}{F_-(s)} \right|^2, \quad (6.17)$$

where  $\text{FSR}(s)$  corresponds to the final-state radiative corrections [658, 659],  $G_{\text{EM}}(s)$  denotes the long-distance radiative corrections of order  $\alpha$  to the photon-inclusive  $\tau^- \rightarrow$

$\pi^- \pi^0 \nu_\tau(\gamma)$  spectrum [7],  $\beta_0^3(s)/\beta_-^3(s)$  considers the impact on the ratio of phase space factors of the  $\pi^\pm - \pi^0$  mass splitting and is important only close to threshold (Fig. 6.24), and  $F_0(s)$  and  $F_-(s)$  are the time-like electromagnetic and weak pion form factors, respectively.

The ratio  $|F_0(s)/F_-(s)|^2$  is the most difficult to estimate reliably, because of some IB effect that need to be taken into account. Among them, the ratio from the IB part of the  $\rho - \omega$  interference and the impact of IB differences in the masses and widths of the charged and neutral  $\rho$  mesons can be estimated from data, although with some residual dependence. On the other hand, contributions produced by an IB difference in the charge and neutral  $\rho$  isovector current decay constants and/or a purely IB  $\rho^0$  isoscalar current decay constant, both of which are expected to exist, would manifest themselves as small IB differences in the broad  $\rho$  distributions for which there is no clear phenomenological method of estimating their impact. A possibility is to assume that those contributions are numerically negligible, estimate the contributions one is able to constrain phenomenologically, and then check if the sum of the partial set of corrections, when applied to the  $\tau \rightarrow \pi \pi \nu_\tau$  distribution, brings the result into agreement with  $e^+ e^- \rightarrow \pi^+ \pi^-$  distribution results. If that was the case, this would provide post facto evidence for the smallness of the IB contributions that are difficult to estimate phenomenologically. A huge effort has been spent on investigating this possibility. At present we are unable to take advantage of the  $\tau$  data, since the sum of the partial set of IB corrections that result does not yet provide an understanding of the IB difference between the  $\tau$  and  $e^+ e^- \rightarrow \pi^+ \pi^-$  distributions. An alternative possibility consists in using lattice simulations to include all sources of IB simultaneously and evaluate the IB inclusive  $\tau$ - $e^+ e^-$   $a_\mu^{\text{HVP,LO}}$  difference.

Below 1 GeV, the pion form factors are governed by the  $\rho$  meson resonance. Important IB effects are then expected from the mass and width differences between the  $\rho^\pm$  and  $\rho^0$  mesons, and  $\rho - \omega$  mixing. The difference between the corrections used in Ref. [7] and those from Refs. [91] is mostly because of different width differences considered. The width difference  $\delta\Gamma_\rho(s) = \Gamma_{\rho^0} - \Gamma_{\rho^-}$  used in Ref. [7] was based on [660]

$$\delta\Gamma_\rho(s) = \frac{g_{\rho\pi\pi}^2 \sqrt{s}}{48\pi} \left[ \beta_0^3(s)(1 + \delta_0) - \beta_-^3(s)(1 + \delta_-) \right], \quad (6.18)$$



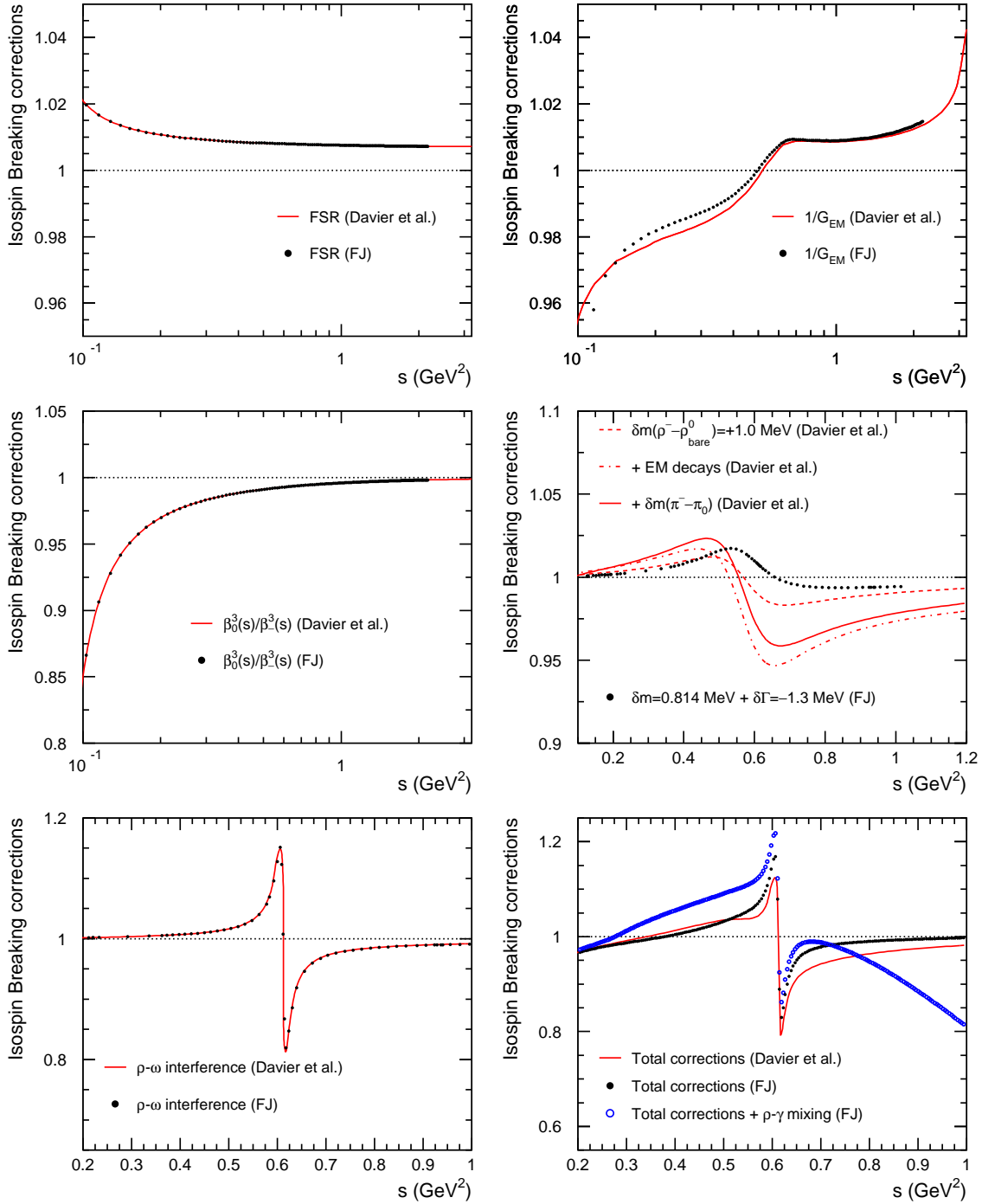


Figure 6.24: Comparison of IB corrections used by Davier et al. [7] and by F. Jegerlehner [91]. The different plots correspond to FSR (top left),  $1/G_{EM}$  (top right),  $\beta_0^3(s)/\beta_3^3(s)$  ratio term (middle left), the effect of the  $\rho$  mass and width difference in the  $|F_0/F_-|$  term (middle right), the effect of the  $\rho - \omega$  interference in the  $|F_0/F_-|$  term (bottom left), and the total corrections (bottom right). The difference between the open blue points and the solid black one in the last plot come from the  $\rho - \gamma$  mixing corrections proposed in Ref. [91]. Reprinted from Ref. [92].

where  $g_{\rho\pi\pi}$  is the strong coupling of the isospin invariant  $\rho\pi\pi$  vertex and  $\delta_{0,-}$  represents the radiative corrections for photon inclusive  $\rho \rightarrow \pi\pi$  decays and other electromagnetic decays, in contrast to

$$\delta\Gamma_\rho = \frac{g_{\rho\pi\pi}^2}{48\pi} \left( \beta_0^3(s)M_{\rho^0} - \beta_-^3(s)M_{\rho^-} \right), \quad (6.19)$$

used in Ref [91]. The numerical values of Eqs. (6.18) and (6.19) at  $M_\rho = 775$  MeV are  $+0.76$  MeV and  $-1.3$  MeV, respectively. Another small difference that contributes to the IB difference originates from the mass difference  $\delta M_\rho = M_{\rho^-} - M_{\rho^0}$  of  $1.0(9)$  MeV [7] and  $0.814$  MeV [91]. This explains the systematic uncertainties when estimating the IB corrections related to phenomenological form factor parameterizations. To avoid a circularity problem, the  $\rho$  parameters need to be determined from other reactions than  $e^+e^- \rightarrow \pi^+\pi^-$  and  $\tau^- \rightarrow \pi^-\pi^0\nu_\tau$ , but since, for instance, the Breit-Wigner parameters are reaction dependent, this induces a systematic uncertainty that is difficult to control, one aspect of which is the need to define a  $\rho^0$  in the presence of electromagnetic interactions and therefore a convention for  $\rho^0 - \gamma$  mixing.

The impact of the IB corrections applied to  $a_\mu^{\text{HVP,LO}}$  are depicted in Table 6.2 [7] using  $\tau$ -data in the dominant  $\pi\pi$  channel for the energy range between the threshold and  $1.8$  GeV. The short-distance correction,  $S_{\text{EW}} = 1.0235(3)$  [7] is dominant. The uncertainty of the FSR and  $\pi\pi\gamma$  electromagnetic corrections is an estimate of the structure-dependent effects (pion form factor) in virtual corrections and of intermediate resonance contributions to real photon emission [7]. The uncertainty of  $G_{\text{EM}}(s)$  is evaluated using the two models depicted in Fig. 6.24. The systematic uncertainty assigned to the  $\rho - \omega$  interference contribution accounts for the difference in  $a_\mu^{\text{HVP,LO}}$  between two phenomenological fits, where the mass and width of the  $\omega$  resonance are either left free to vary or fixed according to the world-average values. The IB corrections were also tested using two different parameterizations of the form factor, the total uncertainty takes into account the full difference between the Gounaris-Sakurai (GS) [661] and the Kühn-Santamaria (KS) parameterizations [7].

An important independent cross-check is provided by the  $\tau^- \rightarrow \pi^-\pi^0\nu_\tau$  branching frac-

Source	$\Delta a_\mu^{\text{HVP,LO}}[\pi\pi, \tau]$	$\Delta \mathcal{B}_{\pi^-\pi^0}^{\text{CVC}}$
$S_{\text{EW}}$	-12.21(5)	+0.57(1)
$G_{\text{EM}}$	-1.92(90)	-0.07(17)
FSR	+4.67(47)	-0.19(2)
$\rho - \omega$ interference	+2.80(19)	-0.01(1)
$M_{\pi^\pm} - M_{\pi^0}$ effect on $\sigma$	-7.88	+0.19
$M_{\pi^\pm} - M_{\pi^0}$ effect on $\Gamma_\rho$	+4.09	-0.22
$M_{\rho^\pm} - M_{\rho_{\text{bare}}^0}$	+0.20 <sup>+0.27</sup> <sub>-0.19</sub>	+0.08(8)
$\pi\pi\gamma$ , electromagnetic decays	-5.91(59)	+0.34(3)
$\delta(\text{GS} - \text{KS})$	-0.67	-0.03
Total	-16.07(1.85)	+0.69(22)

Table 6.2: Contributions to  $10^{10} \cdot a_\mu^{\text{HVP,LO}}[\pi\pi](\tau)$  and  $10^2 \cdot \mathcal{B}_{\pi^-\pi^0}^{\text{CVC}}$  from the IB corrections [6]. Corrections shown correspond to the Gounaris-Sakurai (GS) parameterization [7]. The total uncertainty includes the difference with Kühn-Santamaria (KS) parameterization quoted as  $\delta(\text{GS} - \text{KS})$ .

tion  $\mathcal{B}_{\pi^-\pi^0} = \Gamma(\tau^- \rightarrow \pi^-\pi^0\nu_\tau)/\Gamma_\tau$ , another key quantity that can be directly measured [49]. This "τ-observable", which is a genuine charged channel quantity, can be evaluated in terms of the  $I = 1$  part of the  $e^+e^- \rightarrow \pi^+\pi^-$  cross section after taking into account the IB corrections. The effects of these to the branching fraction are also shown in Table 6.2. Using CVC, the branching fraction of  $\tau$  decaying into a  $G$ -parity even hadronic final state  $X^-$  is given by

$$\mathcal{B}_X^{\text{CVC}} = \frac{3}{2} \frac{\mathcal{B}_e |V_{ud}|^2}{\pi \alpha^2 m_\tau^2} \int_{s_{\text{th}}}^{m_\tau^2} ds s \sigma_{X^0}^I(s) \times \left(1 - \frac{s}{m_\tau^2}\right)^2 \left(1 + \frac{2s}{m_\tau^2}\right) \frac{S_{\text{EW}}}{R_{\text{IB}}(s)}, \quad (6.20)$$

where  $s_{\text{th}}$  is the threshold of the invariant mass-squared of the final state  $X^0$  in  $e^+e^-$  annihilation. CVC comparisons of  $\tau$  branching fractions are of special interest because they are particularly insensitive to the shape of the  $\tau$  spectral function, so avoiding biases in the unfolding of the raw mass distributions from acceptance and resolution effects.

Regardless of the improved IB corrections, there still exists a sizable discrepancy between the  $e^+e^-$  based prediction of  $692.3(4.2) \cdot 10^{-10}$  and the  $\tau$  based one of  $703.0(4.4) \cdot 10^{-10}$  [655]. This difference amounts to  $10.7(4.9) \cdot 10^{-10}$ , corresponding to a deviation of  $2.2\sigma$ . After the IB correction, the shape of the combined  $\tau$  spectral function is also different from the one

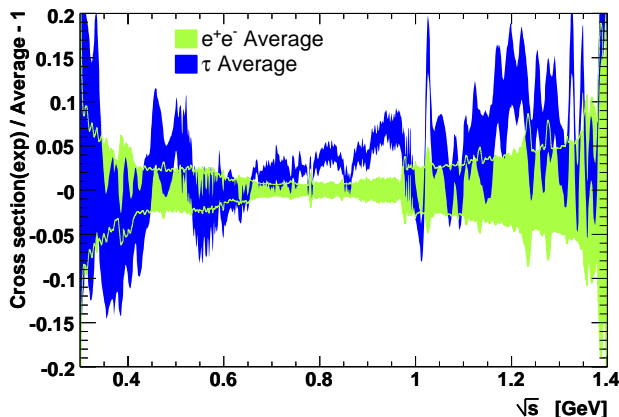


Figure 6.25: Relative comparison between the combined  $\tau$  after the IB corrections and  $e^+e^- \rightarrow \pi^+\pi^-$  spectral function contributions. Reprinted from Ref. [93].

from  $e^+e^-$  data, see Fig. 6.25. The discrepancy reflected in the  $\tau$  branching ratios is shown in Fig. 6.26.

A model-dependent  $\rho - \gamma$  mixing, which appears only in the  $e^+e^-$  data, was proposed in Ref. [91] to explain the  $e^+e^- - \tau$  discrepancy. This correction corresponds to the difference between the open blue points and the solid black points in Fig. 6.24 (bottom right), showing an uncomfortably increasing effect above the  $\rho$  peak. Contrary to  $\gamma - Z$  mixing on the  $Z$  resonance, well established theoretically and experimentally, the description of photon mixing with strongly interacting  $\rho$  may be affected by some uncertainties that are difficult to estimate. The correction [91], shown in Fig. 6.27, seems to overestimate the observed difference.

At present, our understanding of the IB corrections to  $\tau$  data is sadly not yet at the level of precision to match the  $e^+e^-$  data, which does not allow their use for the HVP dispersion integral. Since it remains a possibility, in Chapter 6, we revisit the tau-based data-driven approach by extending previous work by Cirigliano *et al.* [94,379], using ChPT with resonances.

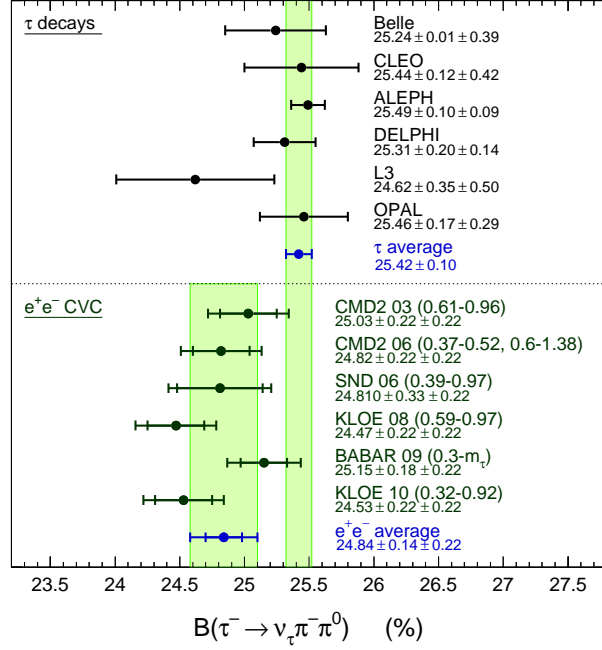


Figure 6.26: The measured branching ratios for  $\tau^- \rightarrow \pi^- \pi^0 \nu_\tau$  decays compared to the predictions from the  $e^+e^- \rightarrow \pi^+\pi^-$  spectral functions, after applying the IB corrections. The long and short vertical error bands represent the  $\tau$  and  $e^+e^-$  averages, respectively. Reprinted from Ref. [7].

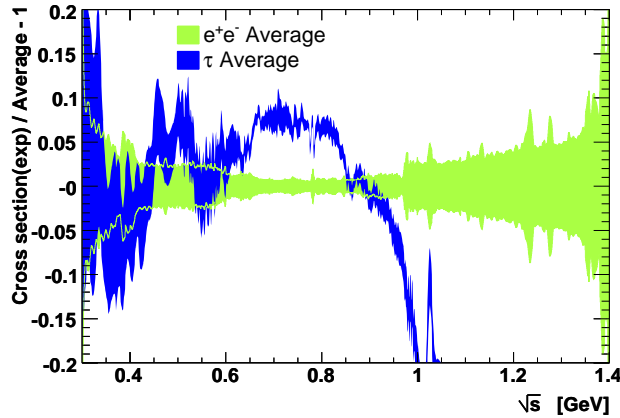


Figure 6.27: Same as Fig. 6.25, apart from the  $\rho - \gamma$  mixing correction proposed in Ref. [91] has been applied to the  $\tau$  data.

# Chapter 7

## Isospin-breaking corrections to

$\tau^- \rightarrow \pi^- \pi^0 \nu_\tau$  decays and the muon

$g - 2$

### 7.1 Introduction

The anomalous magnetic moment of the (first electron, and then) muon ( $a_\mu \equiv (g_\mu - 2)/2$ ) has been crucial for the development of quantum field theory and the understanding of radiative corrections within it. Over the years, it has validated those computed in QED at increasing precision and (in the muon case) started probing the other Standard Model sectors, electroweak and QCD, setting also -and more interestingly- stringent constraints on new physics contributions. In the absence of any direct hint for heavy new particles or interactions at the LHC, clean observables both from experiment and theory -among which  $a_\mu$  stands out- are reinforced as a promising gate for the eagerly awaited further (indirect) discoveries in high-energy physics.

With the forthcoming measurement of  $a_\mu$  at FNAL [662] we will finally have an experimental update on the long-standing discrepancy (at 3 to 4 sigmas) between the SM prediction

of this observable (recently refined in [6])<sup>1</sup> and its most accurate measurement, at BNL [95]. On the theory side, a tremendous effort driven by the Muon g-2 Theory Initiative<sup>2</sup> has been reducing (and making more robust) the SM errors during the last few years, in order to profit maximally from the new data. In the near future, both the FNAL [662] and the J-PARC [676] experiments will shrink the current experimental uncertainty ( $63 \cdot 10^{-11}$ ) by a factor four. A commensurate improvement on the theory error is essential in maximizing the reach on new physics of these measurements.

The SM uncertainty on  $a_\mu$  ( $43 \cdot 10^{-11}$ ) is saturated by that of the hadronic contributions, where the error of the dominant hadronic vacuum polarization (HVP,LO) part has been reduced to  $40 \cdot 10^{-11}$ , versus  $17 \cdot 10^{-11}$  of the light-by-light piece [6]. In turn, the HVP,LO contribution is dominated by the  $\pi\pi$  cut (yielding  $\sim 73\%$  of the overall value), where good-quality data of the corresponding  $e^+e^-$  hadronic cross-sections [20,21,52,54,56,57,59,88,628,629] enables its computation by dispersive methods [623,624]. Alternatively, one can also use isospin-rotated  $\tau \rightarrow \pi\pi\nu_\tau$  measurements with that purpose, as was put forward in LEP times [656], despite the required IB corrections cannot be computed in a model-independent way presently. Still, while a lattice QCD computation of these is achieved, the authors find convenient testing the consistency of both extractions of  $a_\mu^{HVP,LO\pi\pi}$ , in light of the tensions between different sets of  $e^+e^- \rightarrow \pi^+\pi^-$  data that has not been resolved so far [6].

In addition to the previous data-based determinations of  $a_\mu^{HVP,LO}$ , lattice QCD is also achieving computations with reduced errors, although not yet competitive with the  $e^+e^-$  evaluations [6]. One notable exception to this being the recent very accurate result ( $53 \cdot 10^{-11}$  error) of the BMW Coll. [43], according to which the difference with respect to the SM prediction is at the one sigma level.

Concerning the tau based determination, Refs. [94,379] computed the required isospin violating and electromagnetic corrections using Resonance Chiral Theory ( $R\chi T$ ) [224,225] and Refs. [677,678] using Vector Meson Dominance (VMD). These series of articles were

---

<sup>1</sup>The SM prediction [6] is based on [32,33,35–41,46–49,81,237,576,582,583,585,586,597,608–619,621,622] (see also the last developments in Refs. [43,584,596,603–605,607,620,663–675]).

<sup>2</sup>Its website is <https://muon-gm2-theory.illinois.edu/>.

employed by Ref. [7] (updated in Refs. [406, 655]) which, remarkably, found that the discrepancy of the SM prediction with the measurement is reduced substantially when tau data is employed <sup>3</sup>. Notwithstanding, as precise measurements of  $\sigma(e^+e^- \rightarrow \text{hadrons})$  became available in the last fifteen years, the  $e^+e^-$  based evaluation gained preference over using tau data. Indeed, Ref. [6] concludes that ‘at the required precision to match the  $e^+e^-$  data, the present understanding of the IB (isospin breaking) corrections to  $\tau$  data is unfortunately not yet at a level allowing their use for the HVP dispersion integrals’, despite Ref. [91] claiming that (the model-dependent)  $\rho - \gamma$  mixing in the neutral channel makes it agree with the results in the charged current. It is the purpose of this work <sup>4</sup> to extend previous  $R\chi T$  analyses [94, 379] of the required IB corrections to di-pion tau decays so that they can again be useful, when combined with  $\sigma(e^+e^- \rightarrow \pi^+\pi^-(\gamma))$ , to increase the accuracy of the SM prediction of  $a_\mu^{HVP,LO}$ . In this spirit, we note that F. Jegerlehener [681] indeed combines both sets of data (using the IB corrections of Ref. [91]), which reduces the error of  $a_\mu^{HVP,LO}$  by  $\sim 17\%$  [681].

Within the global effort of the Muon g-2 theory initiative, we revisit in this work the  $R\chi T$  computations including operators that -in the chiral limit- start to contribute at  $\mathcal{O}(p^6)$ . This is possible by the knowledge acquired after the analyses of Cirigliano *et al.* [94, 379] (where operators contributing at  $\mathcal{O}(p^4)$  were considered), through a series of works studying operator product expansion (OPE) restrictions on  $R\chi T$  couplings on several relevant 3–point Green functions (and related form factors) [385–387, 453, 459, 461, 465, 471, 472, 517, 548, 618, 682–692] <sup>5 6</sup>. This procedure will also allow us to evaluate an uncertainty for the results by Cirigliano *et al.* [94], which is one of the main outcomes of this work, together with the new results, including operators that start contributing to the  $\mathcal{O}(p^6)$  chiral low-energy constants

---

<sup>3</sup>The difference between the SM prediction of  $a_\mu$  and the BNL measurement is  $3.7\sigma$  [6]. If isospin-rotated tau data is employed for  $a_\mu^{HVP,LO}$ , it amounts to  $2.4\sigma$  [655], instead. This difference could in principle be due to new physics effects, hinting at a lepton universality violation in the corresponding non-standard vector and/or tensor couplings at low-energies [512, 519, 679]. See the most updated discussions of its connection with  $\alpha_{QED}$  in the electroweak fit in Refs. [589–592].

<sup>4</sup>Currently, a lattice evaluation of IB for using tau data in  $a_\mu^{HVP,LO\pi\pi}$  is in progress [680].

<sup>5</sup>See also e.g. Refs. [693–699].

<sup>6</sup>Similar radiative corrections were computed for the  $\tau \rightarrow \eta\pi\nu_\tau\gamma$  decays in  $R\chi T$  [700], even though part of our contributions here were suppressed (and thus neglected) there because of G-parity.



(LECs).

The chapter is organized as follows. In section 7.2 we review the main features of the  $\tau^- \rightarrow \pi^- \pi^0 \nu_\tau \gamma$  decays and split the model-independent part from the hadron form factors, computed in  $R\chi T$  including new terms, subleading in the chiral expansion. We then recall the short-distance (SD) QCD constraints on the Lagrangian couplings, their phenomenological determinations and explain our estimation of the remaining free couplings, based on chiral counting. After that, in section 7.3 we recap the radiative corrections needed for the tau-based calculation of  $a_\mu^{HVP,LO}$  and predict several observables for the processes where the real photon is detected together with the pion pair. Then, in section 7.4 we evaluate  $a_\mu^{HVP,LO|\pi\pi}$  using tau data, which is the main result of this investigation. Finally, our conclusions are presented in section 7.5. Several appendices complement the main material, explaining how the coefficients dominating uncertainties were fitted, giving a full account of the kinematics, and providing with the complete expressions for the structure-dependent (axial-)vector form factors of the  $\tau^- \rightarrow \pi^- \pi^0 \nu_\tau \gamma$  decays.

## 7.2 $\tau^- \rightarrow \pi^- \pi^0 \gamma \nu_\tau$ decays

### 7.2.1 Amplitude

For the radiative decay  $\tau^-(P) \rightarrow \pi^-(p_-) \pi^0(p_0) \nu_\tau(q) \gamma(k)$ , we can split the contribution due to the bremsstrahlung off the initial tau lepton from the one coming from the hadronic part.

We write down the general structure for these processes [94, 701]

$$T = e G_F V_{ud}^* \epsilon^\mu(k)^* \left\{ F_\nu \bar{u}(q) \gamma^\nu (1 - \gamma_5) (m_\tau + \not{P} - \not{k}) \gamma_\mu u(P) \right. \\ \left. + (V_{\mu\nu} - A_{\mu\nu}) \bar{u}(q) \gamma^\nu (1 - \gamma_5) u(P) \right\}, \quad (7.1)$$

where  $F_\nu = (p_0 - p_-)_\nu f_+(s) / 2P \cdot k$ , with the charged pion vector form factor  $f_+(s)$  defined through  $\langle \pi^0 \pi^- | \bar{d} \gamma^\mu u | 0 \rangle = \sqrt{2} f_+(s) (p_- - p_0)^\mu$  and  $s = (p_- + p_0)^2$ . Gauge invariance ( $\epsilon_\mu \rightarrow$

$\epsilon_\mu + k_\mu$ ) implies the Ward identities

$$k_\mu V^{\mu\nu} = (p_- - p_0)^\nu f_+(s), \quad k_\mu A^{\mu\nu} = 0. \quad (7.2)$$

Imposing Eq. (7.2) and Lorentz invariance, we have the following expression for the vector structure-dependent tensor

$$\begin{aligned} V^{\mu\nu} &= f_+ \left[ (P - q)^2 \right] \frac{p_-^\mu (p_- + k - p_0)^\nu}{p_- \cdot k} - f_+ \left[ (P - q)^2 \right] g^{\mu\nu} \\ &+ \frac{f_+ \left[ (P - q)^2 \right] - f_+(s)}{(p_0 + p_-) \cdot k} (p_0 + p_-)^\mu (p_0 - p_-)^\nu \\ &+ v_1 (g^{\mu\nu} p_- \cdot k - p_-^\mu k^\nu) + v_2 (g^{\mu\nu} p_0 \cdot k - p_0^\mu k^\nu) \\ &+ v_3 (p_0 \cdot k p_-^\mu - p_- \cdot k p_0^\mu) p_-^\nu + v_4 (p_0 \cdot k p_-^\mu - p_- \cdot k p_0^\mu) (p_0 + p_- + k)^\nu, \end{aligned} \quad (7.3)$$

and for the axial one

$$\begin{aligned} A^{\mu\nu} &= ia_1 \epsilon^{\mu\nu\rho\sigma} (p_0 - p_-)_\rho k_\sigma + ia_2 W^\nu \epsilon^{\mu\lambda\rho\sigma} k_\lambda p_{-\rho} p_{0\sigma} \\ &+ ia_3 \epsilon^{\mu\nu\rho\sigma} k_\rho W_\sigma + ia_4 (p_0 + k)^\nu \epsilon^{\mu\lambda\rho\sigma} k_\lambda p_{-\rho} p_{0\sigma}, \end{aligned} \quad (7.4)$$

where  $W \equiv P - q = p_- + p_0 + k$ . We could use the basis given in Ref. [700] but instead we prefer a modified one that resembles the decomposition in Ref. [94] (see also Ref. [701]). These tensor structures depend on four vector ( $v_i$ ) and four axial-vector ( $a_i$ ) form factors. For the axial structure, the Schouten's identity has been used.

Taking into account that  $(P - q)^2 = s + 2(p_0 + p_-) \cdot k$ , the Low's theorem [702] is manifestly satisfied

$$\begin{aligned} V^{\mu\nu} &= f_+(s) \frac{p_-^\mu}{p_- \cdot k} (p_- - p_0)^\nu + f_+(s) \left( \frac{p_-^\mu k^\nu}{p_- \cdot k} - g^{\mu\nu} \right) \\ &+ 2 \frac{df_+(s)}{ds} \left( \frac{p_0 \cdot k}{p_- \cdot k} p_-^\mu - p_0^\mu \right) (p_- - p_0)^\nu + \mathcal{O}(k). \end{aligned} \quad (7.5)$$

## 7.2.2 Theoretical framework

We will present in the following the model-dependent contributions to the  $V_{\mu\nu}$  and  $A_{\mu\nu}$  tensors. We will closely follow Ref. [94]<sup>7</sup>, extending it to include subleading terms in the chiral expansion. In this reference, a large- $N_C$  [388–390] inspired computation was carried out. Specifically, it was restricted to the dominant (for  $N_C \rightarrow \infty$ ) tree level diagrams, although the relevant loop corrections for the  $\tau^- \rightarrow \pi^- \pi^0 \nu_\tau \gamma$  decays –giving the  $\rho$  (and  $a_1$ , for completeness) off-shell width<sup>8</sup>– were taken into account<sup>9</sup>. Also, given the limited phase space of tau decays and the fact that the region  $E \lesssim M_\rho + \Gamma_\rho$  is the most important one for the IB corrections needed for  $a_\mu^{HVP, LO|\pi\pi}$  [94], the contribution of the  $\rho(1450)$  and other heavier resonances was neglected in this reference (despite the fact that, in the large- $N_C$  limit, there is an infinite tower of resonances per channel), as we will also do<sup>10</sup>. Within this setting, our computation will include all  $R\chi T$  operators contributing to the  $\mathcal{O}(p^6)$  chiral low-energy constants. Our results agree with those in Ref. [94], providing the new contributions with resonance operators that are suppressed by one chiral order in the low-energy limit (where possible, our computations have been checked against the results in Ref. [700]).

As explained in Ref. [94], this procedure warrants the correct low-energy limit (as given by Chiral Perturbation Theory [169, 193, 194, 215, 531]) and includes consistently the most general pion and photon interactions with the lightest resonances. Demanding the known QCD SD constraints results in relations among the Lagrangian couplings, and chiral counting can be employed to estimate those still unconstrained after using phenomenological information. It should then provide an accurate description of the  $\tau^- \rightarrow \pi^- \pi^0 \nu_\tau \gamma$  decays for  $s \lesssim 1 \text{ GeV}^2$ , which gives  $\sim 99.8\%$  of the whole  $a_\mu^{HVP, LO|\pi\pi}$  contribution.

<sup>7</sup>Using this approach a first prediction of the  $\tau^- \rightarrow \pi^- \pi^0 \ell^+ \ell^- \nu_\tau$  decays ( $\ell = e, \mu$ ) was given in Ref. [703].

<sup>8</sup>We will introduce them following Ref. [383] for the  $\rho(770)$  and Refs. [453, 467] for the  $a_1(1260)$  resonances.

<sup>9</sup>See Refs. [218, 382, 704–708] for next-to-leading order (NLO) computations in  $1/N_C$ , allowing to include the scale dependence of the Chiral Perturbation Theory LECs in the low-energy limit of  $R\chi T$ .

<sup>10</sup>Nevertheless, we will include the dominant effect of the  $\rho(1450)$  and  $\rho(1700)$  resonances in our dispersive pion form factor [19, 28] and check the negligible impact of heavier resonances in the  $v_i$  and  $a_i$  form factors in our analysis.

### 7.2.3 Vector Form Factors

Within  $R\chi T$  [224, 225, 385, 684], the diagrams contributing to the vector form factors of the  $\tau^- \rightarrow \pi^- \pi^0 \gamma \nu_\tau$  decays including operators that start contributing to the  $\mathcal{O}(p^6)$  LECs are shown in Figs. 7.1, 7.2 and 7.3<sup>11</sup>. The first three diagrams in fig. 7.1 and the first diagram in fig. 7.2 contribute to the pion vector form factor entering the structure-independent (SI) piece<sup>12</sup>

$$\begin{aligned}
f_+(s) = & 1 + \frac{G_V F_V}{F^2} \frac{s}{m_\rho^2 - s} + \frac{\sqrt{2} F_V s}{F^2 (m_\rho^2 - s)} \left[ 2 \left( 2\lambda_8^V + \lambda_9^V + 2\lambda_{10}^V \right) m_\pi^2 - s\lambda_{21}^V \right] \\
& + \frac{2\sqrt{2} G_V s}{F^2 (m_\rho^2 - s)} \left[ 4\lambda_6^V m_\pi^2 - s\lambda_{22}^V \right] \\
& + \frac{4s}{F^2 (m_\rho^2 - s)} \left[ 4\lambda_6^V m_\pi^2 - s\lambda_{22}^V \right] \left[ 2 \left( 2\lambda_8^V + \lambda_9^V + 2\lambda_{10}^V \right) m_\pi^2 - s\lambda_{21}^V \right].
\end{aligned} \tag{7.6}$$

The contribution of both the last diagram in fig. 7.1 and the last diagram in fig. 7.2 vanishes for a real photon, as the corresponding ( $f_+(0) = 1$  part) contribution is already in the SI piece. We note we are using  $F \sim 92$  MeV for the pion decay constant and that QCD OPE constraints  $\lambda_{21}^V = \lambda_{22}^V = 0$  [385]. In fact, we will see in sec. 7.2.5 that all modifications induced by the  $\lambda_i^V$  couplings to  $f_+(s)$  (7.6) vanish once SD QCD constraints are accounted for.

For the vector form factors, we get

$$v_1 = v_1^0 + v_1^R + v_1^{RR} + v_1^{RRR} + v_{GI1}^{R+RR}, \tag{7.7a}$$

$$v_2 = v_2^0 + v_2^R + v_2^{RR} + v_2^{RRR} + v_{GI2}^{R+RR}, \tag{7.7b}$$

$$v_3 = v_3^0 + v_3^R + v_3^{RR} + v_3^{RRR} + v_{GI3}^{R+RR}, \tag{7.7c}$$

$$v_4 = v_4^0 + v_4^R + v_4^{RR} + v_4^{RRR} + v_{GI4}^{R+RR}, \tag{7.7d}$$

<sup>11</sup>The contributions involving scalar and pseudoscalar resonances are discussed at the end of section 7.2.3.

<sup>12</sup>Relevant  $R\chi T$  couplings are introduced after Eq. (7.7) and in sec. 7.2.5 below.

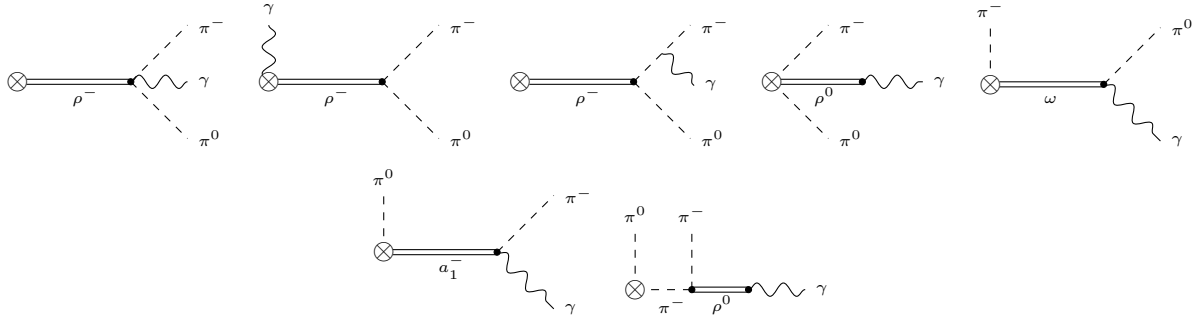


Figure 7.1: One-resonance exchange contributions from the  $R\chi T$  to the vector form factors of the  $\tau^- \rightarrow \pi^- \pi^0 \gamma \nu_\tau$  decays.

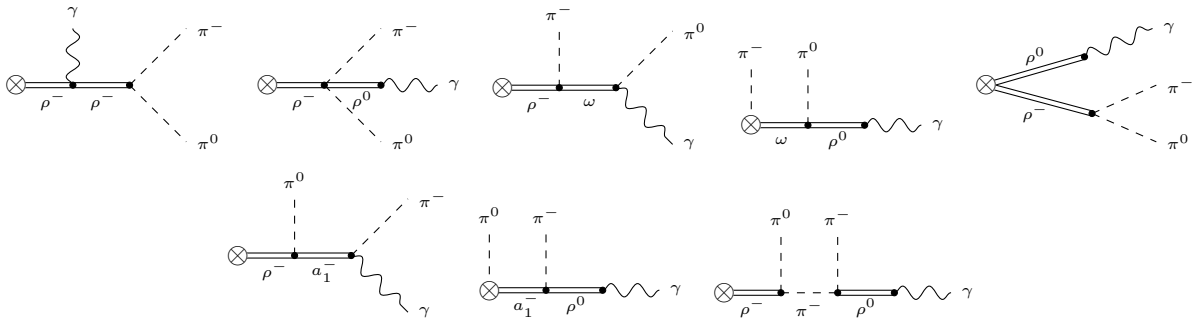


Figure 7.2: Two-resonance exchange contributions from the  $R\chi T$  to the vector form factors of the  $\tau^- \rightarrow \pi^- \pi^0 \gamma \nu_\tau$  decays.

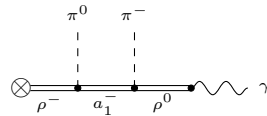


Figure 7.3: Three-resonance exchange contributions from the  $R\chi T$  to the vector form factors of the  $\tau^- \rightarrow \pi^- \pi^0 \gamma \nu_\tau$  decays.

where  $v_i^0$  is the contribution in Ref. [94] ( $D_R^{-1}$  stands for the inverse resonance propagator)<sup>13</sup>

$$\begin{aligned}
v_1^0 &\equiv \frac{F_V G_V}{F^2 M_\rho^2} \left( 2 + 2M_\rho^2 D_\rho^{-1} [(P - q)^2] + s D_\rho^{-1}(s) + s M_\rho^2 D_\rho^{-1}(s) D_\rho^{-1} [(P - q)^2] \right) \\
&\quad + \frac{F_V^2}{2F^2 M_\rho^2} \left( -1 - M_\rho^2 D_\rho^{-1} [(P - q)^2] + (P - q)^2 D_\rho^{-1} [(P - q)^2] \right) \\
&\quad + \frac{F_A^2}{F^2 M_{a_1}^2} \left( M_{a_1}^2 - m_\pi^2 + \frac{1}{2}s \right) D_{a_1}^{-1} [(p_- + k)^2], \\
v_2^0 &\equiv \frac{F_V G_V s}{F^2 M_\rho^2} \left( -D_\rho^{-1}(s) - M_\rho^2 D_\rho^{-1}(s) D_\rho^{-1} [(P - q)^2] \right) \\
&\quad + \frac{F_V^2}{2F^2 M_\rho^2} \left( -1 - M_\rho^2 D_\rho^{-1} [(P - q)^2] - (P - q)^2 D_\rho^{-1} [(P - q)^2] \right) \\
&\quad + \frac{F_A^2}{F^2 M_{a_1}^2} \left( M_{a_1}^2 - m_\pi^2 - k \cdot p_- \right) D_{a_1}^{-1} [(p_- + k)^2], \\
v_3^0 &\equiv \frac{F_A^2}{F^2 M_{a_1}^2} D_{a_1}^{-1} [(p_- + k)^2], \\
v_4^0 &\equiv -\frac{2F_V G_V}{F^2} D_\rho^{-1}(s) D_\rho^{-1} [(P - q)^2] + \frac{F_V^2}{F^2 M_\rho^2} D_\rho^{-1} [(P - q)^2],
\end{aligned}$$

and  $v_i^R$ ,  $v_i^{RR}$ ,  $v_i^{RRR}$  and  $v_{GIi}^{R+RR}$ <sup>14</sup> correspond to contributions including operators which do not contribute to the NLO chiral LECs. Due to their length, the expressions for these form factors are in App. I. In writing the new contributions to  $v_i$ , the basis given in Ref. [385] has been used for the even-intrinsic parity operators (with couplings  $\lambda_i^X$ ) and the basis given in Ref. [684] has been employed for the odd-intrinsic parity operators ( $\kappa_i^X$  couplings). Both sets of  $\lambda_i^X$  and  $\kappa_i^X$  couplings have dimensions of inverse energy.

Including operators with at most one resonance, only the contribution from the exchange of  $\rho$  and  $a_1$  resonances on the vector form factor appeared [94]. Allowing for multi-resonance operators we also have contributions with  $\omega$  exchange, coming from the odd-intrinsic parity sector, for both vector and axial-vector form factors (as well as resonance contributions on the axial form factor, absent in Ref. [94]). Apparently, such  $\omega$  contributions were responsible for the larger effect of the IB corrections obtained in Refs. [677,678] with respect to Refs. [94,379].

<sup>13</sup>We recall that  $F_R$  gives the coupling of the  $R = V, A$  resonance to the  $r = v, a$  external current and the  $\rho\pi\pi$  vertex receives contributions both from  $F_V$  and  $G_V$ .

<sup>14</sup>In general, diagrams are gauge-invariant by themselves. Those giving the contribution  $v_{GIi}^{R+RR}$  need to be summed to achieve gauge invariance. These are the first three diagrams in fig. 7.1 and the first diagram in fig. 7.2.

As a result, Ref. [7] (and later evaluations by this group) ascribed an error to these corrections covering both contradictory evaluations. As we include (among others) contributions with an  $\omega - \rho - \pi$  vertex in this work, closer agreement with the VMD evaluation should, in principle, be expected.

We have verified that all diagrams including scalar mesons vanish in the isospin symmetry limit. We point out that all contributions involving pseudoscalar mesons can be obtained from those with an axial-vector resonance by replacing it by a pseudoscalar resonance. Then, at leading chiral order, the saturation of the LECs by spin-one mesons [224] shows that diagrams including pseudoscalar resonances are suppressed. If we assume that this feature also holds at the next chiral order, then pseudoscalar resonance exchanges could be safely neglected<sup>15</sup>.

#### 7.2.4 Axial-Vector Form Factors

The axial form factors at chiral  $\mathcal{O}(p^4)$  get contributions from the Wess-Zumino-Witten functional [212, 213]:

$$a_1^0 \equiv \frac{1}{8\pi^2 F^2}, \quad a_2^0 \equiv \frac{-1}{4\pi^2 F^2 [(P - q)^2 - m_\pi^2]}. \quad (7.8)$$

The diagrams that receive contributions due to the anomaly are shown in fig. 7.4<sup>16</sup>.

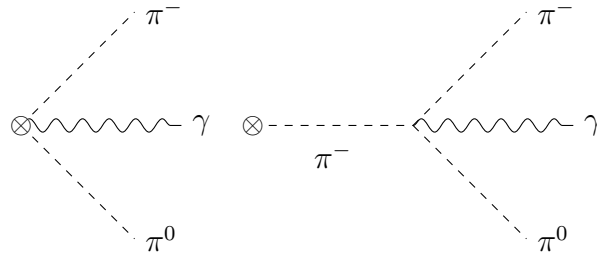


Figure 7.4: Anomalous diagrams contributing to the axial tensor amplitude  $A^{\mu\nu}$  at  $\mathcal{O}(p^4)$ .

<sup>15</sup>Since contributions from scalar and pseudoscalar resonances are suppressed, we will neglect them for the axial form factors in the next section.

<sup>16</sup>The first diagram, when coupled to a vector current, contributes to the SI piece in  $V^{\mu\nu}$ .

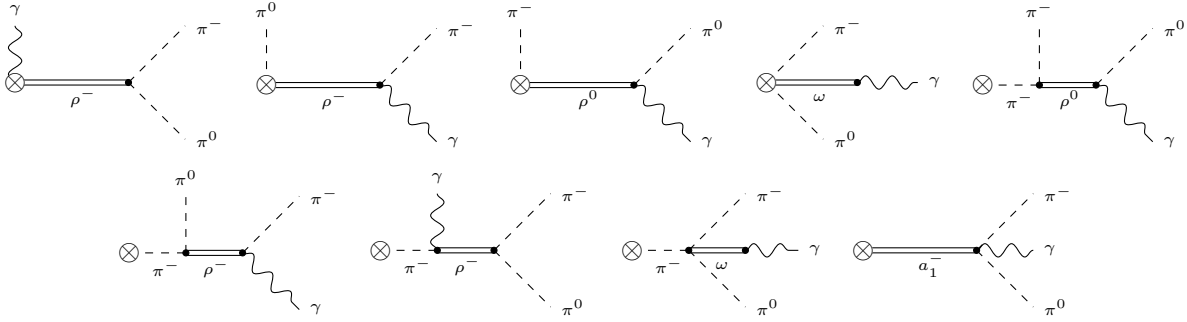


Figure 7.5: One-resonance exchange contributions from the  $R\chi T$  to the axial-vector form factors of the  $\tau^- \rightarrow \pi^- \pi^0 \gamma \nu_\tau$  decays.

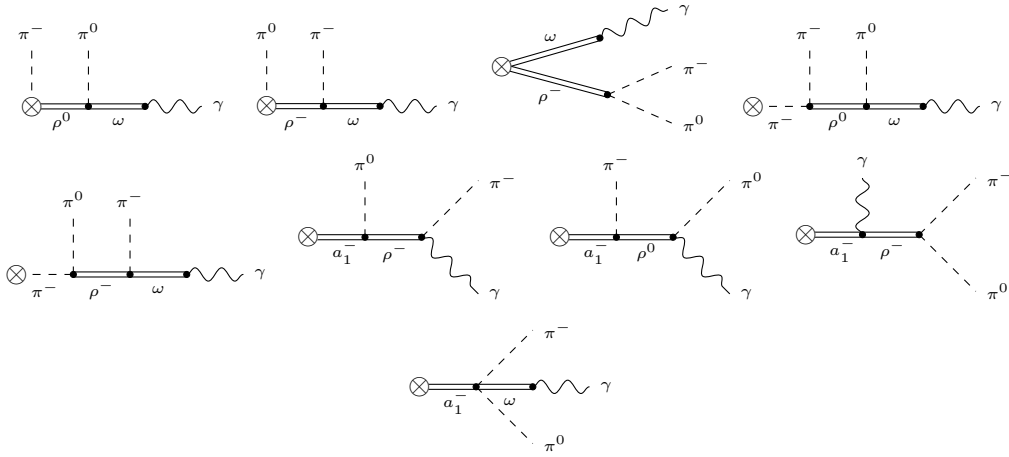


Figure 7.6: Two-resonance exchange contributions from the  $R\chi T$  to the axial-vector form factors of the  $\tau^- \rightarrow \pi^- \pi^0 \gamma \nu_\tau$  decays.

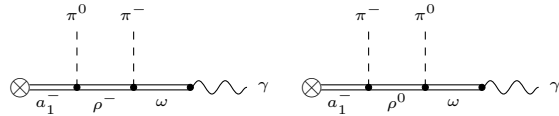


Figure 7.7: Three-resonance exchange contributions from the  $R\chi T$  to the axial-vector form factors of the  $\tau^- \rightarrow \pi^- \pi^0 \gamma \nu_\tau$  decays.



For the axial form factors, we get

$$a_1 = a_1^0 + a_1^R + a_1^{RR} + a_1^{RRR}, \quad (7.9a)$$

$$a_2 = a_2^0 + a_2^R + a_2^{RR} + a_2^{RRR}, \quad (7.9b)$$

$$a_3 = a_3^R + a_3^{RR} + a_3^{RRR}, \quad (7.9c)$$

$$a_4 = a_4^R + a_4^{RR} + a_4^{RRR}, \quad (7.9d)$$

where  $a_i^R$ ,  $a_i^{RR}$  and  $a_i^{RRR}$  include  $\mathcal{O}(p^6)$  vertices. Due to their length, the expressions for these form factors appear in App. J.

### 7.2.5 SD constraints

Including operators which start contributing to the  $\mathcal{O}(p^6)$  LECs, we have now so many parameters (see Table 7.1) allowed by the discrete symmetries of QCD and chiral symmetry that, in practice, prevent making phenomenological predictions. It is possible to find relations between these couplings by means of SD properties of QCD and its OPE. We summarize these results in this section.

For the parameters contributing to 2-point Green Functions (and related form factors), the constraints [224–226, 412, 413, 709, 710]:

$$\begin{aligned} F_V G_V &= F^2, & F_V^2 - F_A^2 &= F^2, \\ F_V^2 M_V^2 &= F_A^2 M_A^2, & 4c_d c_m &= F^2, \\ 8(c_m^2 - d_m^2) &= F^2, & c_m = c_d = \sqrt{2}d_m &= F/2 \end{aligned} \quad (7.10)$$

are set, respectively, by the known asymptotic behaviour of: the pion vector form factor, the  $V - A$  correlator (yielding the Weinberg sum rules), the scalar form factor and the  $S - P$  correlator.

We note that the vanishing of the axial pion form factor (giving the  $\pi$ -to- $\gamma$  matrix element) at infinite momentum transfer demands -if only the original  $R\chi T$  Lagrangian [225] is used-

$2F_V G_V = F_V^2$ . This, together with the two first Eqs. in (7.10), determine

$$F_V = \sqrt{2}F, \quad G_V = \frac{F}{\sqrt{2}}, \quad F_A = F, \quad (7.11)$$

all in terms of the pion decay constant. These relations were employed in Ref. [94]. We emphasize that -once operators contributing to the NLO chiral LECs are considered [385, 684]-, the relations (7.11) no longer hold true (see Ref. [687]). Seen from another perspective, consistent sets of SD relations on  $n$ -point Green functions vary with  $n$ . For  $n = 2$  one has the set (7.11) [224]. We shall also consider the set obtained for  $n = 3$  [385, 684, 687] (where operators with more than one resonance field start to appear) in the following. We will come back to discussing the actual values of the  $F_V$ ,  $G_V$  and  $F_A$  couplings before closing this section, as they are essential to assess the error associated to the IB corrections computed in Ref. [94].

Now, we consider  $R\chi T$  operators which do not contribute to the NLO chiral LECs. For the even intrinsic parity sector [385, 548]<sup>17</sup>:

$$\begin{aligned} \lambda_{13}^P &= 0, & \lambda_{17}^S &= \lambda_{18}^S = 0, \\ \lambda_{17}^A &= 0, & \lambda_6^V &= \lambda_{21}^V = \lambda_{22}^V = 0, \end{aligned} \quad (7.12)$$

using these SD constraints in Eq. (7.6) and the Brodsky-Lepage behaviour [515, 516] of  $f_+(s)$ , we get:

$$2\lambda_8^V + \lambda_9^V + 2\lambda_{10}^V = 0. \quad (7.13)$$

The study of the  $\langle VAP \rangle$  and  $\langle SPP \rangle$  Green functions yield the following restrictions on the

---

<sup>17</sup>The corresponding coefficients are denoted  $\lambda_i^R$ , with the upper index showing the resonance fields involved.

resonance couplings [385–387] (the Weinberg sum rules in Eq. (7.10) were used below):

$$\begin{aligned}
\sqrt{2}\lambda_0 &= -4\lambda_1^{VA} - \lambda_2^{VA} - \frac{\lambda_4^{VA}}{2} - \lambda_5^{VA} = \frac{1}{2\sqrt{2}}(\lambda' + \lambda''), \\
\sqrt{2}\lambda' &= \lambda_2^{VA} - \lambda_3^{VA} + \frac{\lambda_4^{VA}}{2} + \lambda_5^{VA} = \frac{F_V}{2\sqrt{F_V^2 - F^2}}, \\
\sqrt{2}\lambda'' &= \lambda_2^{VA} - \frac{\lambda_4^{VA}}{2} - \lambda_5^{VA} = \frac{2F^2 - F_V^2}{2F_V\sqrt{F_V^2 - F^2}}, \\
\lambda_1^{PV} &= -4\lambda_2^{PV} = -\frac{F^2}{4\sqrt{2}d_m F_V}, \quad \lambda_1^{PA} = \frac{F^2}{16\sqrt{2}d_m\sqrt{F_V^2 - F^2}}.
\end{aligned} \tag{7.14}$$

For the odd-intrinsic parity sector [684]<sup>18</sup>:

$$\begin{aligned}
\kappa_{14}^V &= \frac{N_C}{256\sqrt{2}\pi^2 F_V}, \quad 2\kappa_{12}^V + \kappa_{16}^V = -\frac{N_C}{32\sqrt{2}\pi^2 F_V}, \quad \kappa_{17}^V = -\frac{N_C}{64\sqrt{2}\pi^2 F_V}, \quad \kappa_5^P = 0, \\
\kappa_{2}^{VV} &= \frac{F^2 + 16\sqrt{2}d_m F_V \kappa_3^{PV}}{32F_V^2} - \frac{N_C M_V^2}{512\pi^2 F_V^2}, \quad 8\kappa_2^{VV} - \kappa_3^{VV} = \frac{F^2}{8F_V^2}.
\end{aligned} \tag{7.15}$$

The analysis of the  $\langle VAS \rangle$  Green's function yields [684]:

$$\begin{aligned}
\kappa_2^S = \kappa_{14}^A &= 0, \quad \kappa_4^V = 2\kappa_{15}^V, \quad \kappa_6^{VA} = \frac{F^2}{32F_A F_V}, \\
F_V (2\kappa_1^{SV} + \kappa_2^{SV}) &= 2F_A \kappa_1^{SA} = \frac{F^2}{16\sqrt{2}c_m},
\end{aligned} \tag{7.16}$$

and through the study of the  $\langle VVA \rangle$  Green's function in Ref. [618]:

$$F_V \kappa_5^{VA} = -\frac{N_C M_V^2}{64\pi^2 F_A}. \tag{7.17}$$

A comparison between two basis for the odd-intrinsic operators [682, 684] was given in Ref.

---

<sup>18</sup>The corresponding coefficients are denoted  $\kappa_i^R$ , with the upper index showing the resonance fields involved.

[687], which is consistent with those in Eq. (7.15) <sup>19</sup>

$$\begin{aligned}
M_V \left( 2\kappa_{12}^V + 4\kappa_{14}^V + \kappa_{16}^V - \kappa_{17}^V \right) &= 4c_3 + c_1 &= 0, \\
M_V \left( 2\kappa_{12}^V + \kappa_{16}^V - 2\kappa_{17}^V \right) &= c_1 - c_2 + c_5 &= 0, \\
-M_V \kappa_{17}^V &= c_5 - c_6 &= \frac{N_C M_V}{64\sqrt{2}\pi^2 F_V}, \\
M_V \kappa_{15}^V &= c_4 &, \\
8\kappa_2^{VV} &= d_1 + 8d_2 &= \frac{F^2}{8F_V^2} - \frac{N_C M_V^2}{64\pi^2 F_V^2}, \\
\kappa_3^{VV} &= d_3 &= -\frac{N_C}{64\pi^2} \frac{M_V^2}{F_V^2}, \\
1 + \frac{32\sqrt{2}F_V d_m \kappa_3^{PV}}{F^2} &= 0, \\
F_V^2 &= 3F^2,
\end{aligned} \tag{7.18}$$

For the even- and odd-intrinsic parity sectors, there are 115 (EIP)+67 (OIP)=182 operators saturating the  $\mathcal{O}(p^6)$  LECs but only a few of them contribute to a given process. The form factors of the  $\tau^- \rightarrow \pi^- \pi^0 \gamma \nu_\tau$  decays at  $\mathcal{O}(p^6)$  are given by 32 (EIP)+23(OIP)=55 operators (Table 7.1). Taking into account the relations in Eqs. (7.12)-(7.18) we get 24 (EIP)+17 (OIP)=41 undetermined couplings.

In order to estimate the unknown parameters, we basically followed (but for the results

Even-intrinsic parity (EIP) [385]	
$\hat{O}_i^V$	6,7,8,9,10,12,13,14,15,16,17,18,19,20,21,22
$\hat{O}_i^A$	4,12,13,15,16,17
$\hat{O}_i^{VV}$	2,3,4,5,7
$\hat{O}_i^{VA}$	1,2,3,4,5
Odd-intrinsic parity (OIP) [684]	
$\hat{O}_{i\mu\nu\alpha\beta}^V$	1,2,3,6,7,8,9,10,11,12,14,16,17
$\hat{O}_{i\mu\nu\alpha\beta}^A$	5,6,7
$\hat{O}_{i\mu\nu\alpha\beta}^{VV}$	2,3,4
$\hat{O}_{i\mu\nu\alpha\beta}^{VA}$	2,3,4,5

Table 7.1: Operators contributing at  $\mathcal{O}(p^6)$  to the vector and axial-vector form factors.

in appendix G) the strategy devised in Ref. [700]. We will restore to the available phenomenological information on these couplings and estimate -based on chiral counting- those for which we lack it.

<sup>19</sup>We note, particularly, the last of these Eqs., which is at odds with (7.11).

Eq. (7.14) leaves two  $\lambda_i^{VA}$  couplings undetermined, the numerical values of the restricted combinations (see their definitions in terms of the  $\lambda_i^{VA}$  in [387]) are:

$$\lambda' \sim 0.4, \quad \lambda'' \sim -0.14, \quad \lambda_0 \sim 0.07. \quad (7.19)$$

Since the same linear combination of  $\lambda_4^{VA}$  and  $\lambda_5^{VA}$  is in all couplings in Eq. (7.19), we choose  $\lambda_4^{VA}$  as independent. By similar reasons we take  $\lambda_2^{VA}$  as the other independent coupling. Based on Eq. (7.19), we conservatively estimate  $|\lambda_2^{VA}| \sim |\lambda_4^{VA}| \leq 0.4$ .

According to Ref. [385] the  $\lambda_i^X$  couplings can be estimated from low energy couplings  $C_i^R$  of the  $\mathcal{O}(p^6)$   $\chi PT$  Lagrangian as <sup>20</sup>

$$\begin{aligned} |\lambda_i^V| &\sim \frac{3M_V^2}{2F} C_i^R \sim 0.025 \text{ GeV}^{-1}, \\ |\lambda_i^{VV}| &\sim \frac{M_V^4}{2F^2} C_i^R \sim 0.1, \end{aligned} \quad (7.20)$$

where we take the relation  $|C_i^R| \sim \frac{1}{F^2(4\pi)^4}$  linked to  $|L_i^R| \sim \frac{1}{(4\pi)^2} \sim 5 \cdot 10^{-3}$  which corresponds to the typical size of the  $\mathcal{O}(p^4)$  LECs. This sets a reasonable upper bound on  $|\lambda_i^V| \sim |\lambda_i^A| \lesssim 0.025 \text{ GeV}^{-1}$  and  $|\lambda_i^{VV}| \sim |\lambda_i^{VA}| \lesssim 0.1$ .

For the anomalous sector, we have the following predictions from the Eq. (7.18):  $-M_V \kappa_{17}^V = c_5 - c_6 \sim 0.016$ ,  $8\kappa_2^{VV} = d_1 + 8d_2 \sim -0.070$  and  $\kappa_3^{VV} = d_3 \sim -0.112$ . There is a sign ambiguity on the determination of  $c_3$  from  $\tau^- \rightarrow \eta\pi^- \pi^0 \nu_\tau$  decays [461]. We will take  $c_3 = 0.007_{-0.012}^{+0.020}$  according to the determinations by Y. H. Chen *et al.* in Refs. [685, 688, 711] (which is also in agreement with the most elaborated  $e^+e^- \rightarrow (\eta/\pi^0)\pi^+\pi^-$  fit [465]). Although  $c_4$  was first evaluated by studying  $\sigma(e^+e^- \rightarrow KK\pi)$  in Ref. [453], this yielded an inconsistent result for  $\tau^- \rightarrow K^- \gamma \nu_\tau$  branching ratio [471], so we will use  $c_4 = -0.0024 \pm 0.0006$  [688] as the most reliable estimation. In view of all these results, we will take  $|c_i| \lesssim 0.015$  as a reasonable estimate, which is translated to  $|\kappa_i^V| \lesssim 0.025 \text{ GeV}^{-1}$ . Since there is not enough information on  $\kappa_i^A$ , we will take  $|\kappa_i^A| \sim |\kappa_i^V| \lesssim 0.025 \text{ GeV}^{-1}$ . We will see in the following sections that the observables that we consider and the IB corrections for  $a_\mu^{HVP, LO|\pi\pi}$  depend mostly on the  $\kappa_i^V$  couplings (besides  $F_V$ ,  $G_V$  and  $F_A$ ) for this reason we perform a global fit to better bind

<sup>20</sup>Couplings of operators with two resonance fields are dimensionless [385, 684].

these couplings (see App. G) <sup>21</sup>.

We turn now to the remaining couplings. We will employ  $d_2 = 0.08 \pm 0.08$ , which has been determined simultaneously with  $c_3$  [465, 685, 688, 711]. For  $d_4$  we will assume  $|d_4| < 0.15$ , or in terms of  $\kappa_i^{VV}$ , we get  $|\kappa_i^{VV}| \lesssim 0.1$ . Again we will adopt  $|\kappa_i^{VA}| \sim |\kappa_i^{VV}| \lesssim 0.1$ , which agrees with the prediction  $\kappa_5^{VA} \sim -0.14$  in Eq. (7.17).

Using only operators contributing to the  $\mathcal{O}(p^4)$  LECs we have the consistent set for 2-point Green functions (7.11). However, including operators which start contributing at  $\mathcal{O}(p^6)$ , we shall use the relations for 2 and 3-point Green functions (Eq. (7.10) and Eqs. (7.12) to (7.18)). In particular,  $F_V = \sqrt{3}F$ , which implies (via (7.10))  $G_V = F/\sqrt{3}$  and  $F_A = \sqrt{2}F$ . Therefore, we will also be showing the Cirigliano *et al.* results [94] with the latter set of constraints (inconsistent for 2-point Green functions) so that the impact of the change of  $F_V$ ,  $F_A$  and  $G_V$  between these two cases is appreciated.

We will refer to the original [94] constraints (7.11) as ‘ $F_V = \sqrt{2}F$ ’ and by ‘ $F_V = \sqrt{3}F$ ’ to their consistent set of values ( $F_V = \sqrt{3}F$ ,  $G_V = F/\sqrt{3}$ ,  $F_A = \sqrt{2}F$ ) up to 3-point Green functions. In this last way, we stress that the consistent set of SD constraints in both parity sectors [385, 387, 684, 687] determines the  $F_V = \sqrt{3}F$  relations (among many others, reviewed in this section).

### 7.3 Radiative corrections for hadronic vacuum polarization

The four-body differential decay width is given by [94] <sup>22</sup>

$$d\Gamma = \frac{(2\pi)^4}{2m_\tau} |\mathcal{M}|^2 \delta^4(P - p_- - p_0 - k - q) \frac{d^3p_-}{(2\pi)^3 2E_-} \frac{d^3p_0}{(2\pi)^3 2E_0} \frac{d^3q}{(2\pi)^3 2E_\nu} \frac{d^3k}{(2\pi)^3 2E_\gamma}, \quad (7.21)$$

<sup>21</sup>The results obtained assuming  $|\kappa_i^V| \lesssim 0.025 \text{ GeV}^{-1}$  can be found in <https://arxiv.org/abs/2007.11019v1>. While both results agree remarkably, the errors are reduced in the current procedure.

<sup>22</sup>Although the analytical results in this section were presented in the quoted reference, we include them here given their importance in the evaluation of the relevant IB corrections, and take advantage to add a few explanations to previous discussions of this subject [94, 678].

using the relation  $\frac{d^3 p_-}{2E_-} \frac{d^3 p_0}{2E_0} = \frac{\pi^2}{4m_\tau^2} ds du dx$  and integrating over the three-momentum of the photon and neutrino <sup>23</sup>, we get

$$d\Gamma = \frac{1}{32(2\pi)^6 m_\tau^2} \left[ \int \frac{d^3 q}{2E_\nu} \frac{d^3 k}{2E_\gamma} \overline{|\mathcal{M}|^2} \delta^4(P - p_- - p_0 - k - q) \right] ds du dx, \quad (7.22)$$

working at leading order in the Low expansion and in the isospin limit  $m_u = m_d$ , we have

$$\mathcal{M} = e \epsilon^{*\mu}(k) \mathcal{M}_{\pi\pi}^{(0)} \left( \frac{p_{-\mu}}{p_- \cdot k} - \frac{P_\mu}{P \cdot k} \right) + \mathcal{O}(k^0), \quad (7.23)$$

where  $\mathcal{M}_{\pi\pi}^{(0)} = G_F V_{ud}^* \sqrt{S_{EW}} f_+(s) (p_- - p_0)_\nu \bar{u}(q) \gamma^\nu (1 - \gamma_5) u(P)$  is the amplitude at leading order for the non-radiative decay that includes the SD electroweak radiative corrections ( $S_{EW}$ ). At  $\mathcal{O}(k^{-1})$ , the amplitude for the radiative decay is proportional to the amplitude of the non-radiative decay according to the Low's theorem [702].

The unpolarized spin-averaged squared amplitude is given by

$$\begin{aligned} \overline{|\mathcal{M}|^2} &= 4\pi\alpha \overline{|\mathcal{M}_{\pi\pi}^{(0)}|^2} \sum_\gamma \epsilon^{*\mu}(k) \epsilon^\nu(k) \left( \frac{p_{-\mu}}{p_- \cdot k + \frac{1}{2}M_\gamma^2} - \frac{P_\mu}{P \cdot k - \frac{1}{2}M_\gamma^2} \right) \\ &\times \left( \frac{p_{-\nu}}{p_- \cdot k + \frac{1}{2}M_\gamma^2} - \frac{P_\nu}{P \cdot k - \frac{1}{2}M_\gamma^2} \right) + \mathcal{O}(k^{-1}), \end{aligned} \quad (7.24)$$

using the relation  $\sum_\gamma \epsilon^{*\mu}(k) \epsilon^\nu(k) = -g^{\mu\nu}$  and massive photons ( $k^\mu k_\mu = M_\gamma^2$ ). The sum over photon polarizations should include the longitudinal part, since our photon has mass and the amplitude is no longer gauge invariant. We do not take into account this contribution because it will vanish in the limit  $M_\gamma \rightarrow 0$ .

Thus, Eq. (7.24) becomes

$$\begin{aligned} \overline{|\mathcal{M}|^2} &= 4\pi\alpha \overline{|\mathcal{M}_{\pi\pi}^{(0)}|^2} \left( \frac{2P \cdot p_-}{(p_- \cdot k + \frac{1}{2}M_\gamma^2)(P \cdot k - \frac{1}{2}M_\gamma^2)} - \frac{m_\pi^2}{(p_- \cdot k + \frac{1}{2}M_\gamma^2)^2} \right. \\ &\left. - \frac{m_\tau^2}{(P \cdot k - \frac{1}{2}M_\gamma^2)^2} \right) + \mathcal{O}(k^{-1}), \end{aligned} \quad (7.25)$$

<sup>23</sup>The kinematics for these decays are in App. H.

where

$$\overline{|\mathcal{M}_{\pi\pi}^{(0)}|^2} = 4G_F^2 |V_{ud}|^2 S_{EW} |f_+(s)|^2 (D(s, u) + \mathcal{O}(k)), \quad (7.26)$$

with  $D(s, u) = \frac{1}{2}m_\tau^2(m_\tau^2 - s) + 2m_\pi^4 - 2u(m_\tau^2 - s + 2m_\pi^2) + 2u^2$ . Eq. (7.25) does not contribute at  $\mathcal{O}(k^{-1})$ , these terms are canceled out by those in Eq. (7.26) according to the Burnett-Kroll theorem [712].

Replacing Eqs. (7.25) and (7.26) in Eq. (7.22), we get

$$d\Gamma = \frac{\alpha G_F^2 |V_{ud}|^2 S_{EW}}{4(2\pi)^4 m_\tau^3} |f_+(s)|^2 D(s, u) \left( 2P \cdot p_- I_{11}(s, u, x) - m_\pi^2 I_{02}(s, u, x) - m_\tau^2 I_{20}(s, u, x) \right) ds du dx + \mathcal{O}(k^0), \quad (7.27)$$

the  $I_{mn}(s, u, x)$  is defined as

$$I_{mn}(s, u, x) = \frac{1}{2\pi} \int \frac{d^3q}{2E_\nu} \frac{d^3k}{2E_\gamma} \frac{\delta^4(P - p_- - p_0 - k - q)}{\left(P \cdot k - \frac{1}{2}M_\gamma^2\right)^m \left(p_- \cdot k + \frac{1}{2}M_\gamma^2\right)^n}, \quad (7.28)$$

performing an integration over  $x$ , we can split the decay width according to the integration region

$$\frac{d^2\Gamma}{ds du} = \frac{d^2\Gamma}{ds du} \Big|_{\mathcal{D}_{III}} + \frac{d^2\Gamma}{ds du} \Big|_{\mathcal{D}_{IV/III}} + \mathcal{O}(k^0), \quad (7.29)$$

where

$$\begin{aligned} \frac{d^2\Gamma}{ds du} \Big|_{\mathcal{D}_{III}} &= \frac{\alpha G_F^2 |V_{ud}|^2 S_{EW}}{4(2\pi)^4 m_\tau^3} |f_+(s)|^2 D(s, u) \times \\ &\quad (J_{11}(s, u, M_\gamma) + J_{02}(s, u, M_\gamma) + J_{20}(s, u, M_\gamma)), \end{aligned} \quad (7.30)$$

and

$$\begin{aligned} \frac{d^2\Gamma}{ds du} \Big|_{\mathcal{D}_{IV/III}} &= \frac{\alpha G_F^2 |V_{ud}|^2 S_{EW}}{4(2\pi)^4 m_\tau^3} |f_+(s)|^2 D(s, u) \times \\ &\quad (K_{11}(s, u) + K_{02}(s, u) + K_{20}(s, u)), \end{aligned} \quad (7.31)$$



with

$$J_{mn}(s, u, M_\gamma) = c_{mn} \int_{M_\gamma^2}^{x_+(s, u)} dx I_{mn}(s, u, x), \quad (7.32)$$

$$K_{mn}(s, u) = c_{mn} \int_{x_-(s, u)}^{x_+(s, u)} dx I_{mn}(s, u, x), \quad (7.33)$$

and

$$c_{mn} = \begin{cases} 2P \cdot p_- & m = n = 1, \\ -m_\tau^2 & m = 2, n = 0, \\ -m_{\pi^-}^2 & m = 0, n = 2. \end{cases} \quad (7.34)$$

Eq. (7.28) is an invariant, so we can evaluate it in any reference frame in order to simplify the integration, working in the  $\gamma - \nu_\tau$  center of mass, we have

$$I_{mn}(s, u) = \frac{1}{2^3(2\pi)} \int \frac{x - M_\gamma^2}{x \left(P \cdot k - \frac{1}{2}M_\gamma^2\right)^m \left(p_- \cdot k + \frac{1}{2}M_\gamma^2\right)^n} d \cos \theta_\nu d\phi_-. \quad (7.35)$$

Integrating this equation over  $x$  in  $\mathcal{D}_{IV/III}$  and  $\mathcal{D}_{III}$ , as in Refs. [94, 713] we get ( $\text{Li}_2(x) = -\int_0^1 \frac{dt}{t} \log(1 - xt)$ )

$$J_{11}(s, u) = \log \left( \frac{2x_+(s, u)\bar{\gamma}}{M_\gamma} \right) \frac{1}{\bar{\beta}} \log \left( \frac{1 + \bar{\beta}}{1 - \bar{\beta}} \right) + \frac{1}{\bar{\beta}} \left( \text{Li}_2(1/Y_2) - \text{Li}_2(Y_1) + \log^2(-1/Y_2)/4 - \log^2(-1/Y_1)/4 \right), \quad (7.36)$$

$$J_{20}(s, u) = \log \left( \frac{M_\gamma(m_\tau^2 - s)}{m_\tau x_+(s, u)} \right), \quad (7.37)$$

$$J_{02}(s, u) = \log \left( \frac{M_\gamma(m_\tau^2 + m_{\pi^0}^2 - s - u)}{m_{\pi^-} x_+(s, u)} \right), \quad (7.38)$$

$$K_{20}(s, u) = K_{0,2}(s, u) = \log \left( \frac{x_-(s, u)}{x_+(s, u)} \right), \quad (7.39)$$

where the expressions in Eq. (7.36) are given by

$$Y_{1,2} = \frac{1 - 2\bar{\alpha} \pm \sqrt{(1 - 2\bar{\alpha})^2 - (1 - \bar{\beta}^2)}}{1 + \bar{\beta}}, \quad (7.40)$$

with

$$\begin{aligned}
\bar{\alpha} &= \frac{(m_\tau^2 - s)(m_\tau^2 + m_{\pi^0}^2 - s - u)}{(m_{\pi^-}^2 + m_\tau^2 - u)} \cdot \frac{\lambda(u, m_{\pi^-}^2, m_\tau^2)}{2\bar{\delta}}, \\
\bar{\beta} &= -\frac{\sqrt{\lambda(u, m_{\pi^-}^2, m_\tau^2)}}{m_{\pi^-}^2 + m_\tau^2 - u}, \\
\bar{\gamma} &= \frac{\sqrt{\lambda(u, m_{\pi^-}^2, m_\tau^2)}}{2\sqrt{\bar{\delta}}}, \\
\bar{\delta} &= -m_{\pi^0}^4 m_\tau^2 + m_{\pi^-}^2 (m_\tau^2 - s)(m_{\pi^0}^2 - u) - su(-m_\tau^2 + s + u) \\
&\quad + m_{\pi^0}^2 (-m_\tau^4 + su + m_\tau^2 s + m_\tau^2 u).
\end{aligned}$$

Experimentally, it is impossible to measure the full photon spectrum because of acceptances, efficiencies and cuts. For this reason, we need to calculate the inclusive decay width, since we can not distinguish the radiative decay from the non-radiative decay for low-energy (or collinear) photons.

For the non-radiative decay, we have

$$\frac{d^2\Gamma}{ds du} = \frac{G_F^2 |V_{ud}|^2 S_{EW}}{64\pi^3 m_\tau^3} |f_+(s)|^2 \left(1 + f_{loop}^{elm}(u, M_\gamma)\right)^2 D(s, u), \quad (7.42)$$

that includes isospin violation and photonic corrections according to Ref. [379], where  $f_{loop}^{elm}(u, M_\gamma)$  is given by

$$\begin{aligned}
f_{loop}^{elm}(u, M_\gamma) &= \frac{\alpha}{4\pi} \left( (u - m_\pi^2) \mathcal{A}(u) + (u - m_\pi^2 - m_\tau^2) \mathcal{B}(u) \right. \\
&\quad \left. + 2(m_\pi^2 + m_\tau^2 - u) \mathcal{C}(u, M_\gamma) + 2 \log \frac{m_\pi m_\tau}{M_\gamma^2} \right), \quad (7.43)
\end{aligned}$$

with

$$\begin{aligned}
\mathcal{A}(u) &= \frac{1}{u} \left( -\frac{1}{2} \log r_\tau + \frac{2-y_\tau}{\sqrt{r_\tau}} \frac{x_\tau}{1-x_\tau^2} \log x_\tau \right), \\
\mathcal{B}(u) &= \frac{1}{u} \left( \frac{1}{2} \log r_\tau + \frac{2r_\tau-y_\tau}{\sqrt{r_\tau}} \frac{x_\tau}{1-x_\tau^2} \log x_\tau \right), \\
\mathcal{C}(u, M_\gamma) &= \frac{1}{m_\tau m_\pi} \frac{x_\tau}{1-x_\tau^2} \left( -\frac{1}{2} \log^2 x_\tau + 2 \log x_\tau \log(1-x_\tau^2) - \frac{\pi^2}{6} + \frac{1}{8} \log^2 r_\tau \right. \\
&\quad \left. + Li_2(x_\tau^2) + Li_2\left(1 - \frac{x_\tau}{\sqrt{r_\tau}}\right) + Li_2(1 - x_\tau \sqrt{r_\tau}) - \log x_\tau \log \frac{M_\gamma^2}{m_\tau m_\pi} \right),
\end{aligned}$$

in terms of the variables

$$r_\tau = \frac{m_\tau^2}{m_\pi^2}, \quad y_\tau = 1 + r_\tau - \frac{u}{m_\tau^2}, \quad x_\tau = \frac{1}{2\sqrt{r_\tau}} \left( y_\tau - \sqrt{y_\tau^2 - 4r_\tau} \right),$$

Thus, the inclusive decay width is

$$\left. \frac{d^2\Gamma}{ds du} \right|_{\pi\pi(\gamma)} = \frac{G_F^2 |V_{ud}|^2 S_{EW}}{64\pi^3 m_\tau^3} |f_+(s)|^2 D(s, u) \Delta(s, u), \quad (7.45)$$

where

$$\Delta(s, u) = 1 + 2f_{loop}^{elm}(u, M_\gamma) + g_{rad}(s, u, M_\gamma). \quad (7.46)$$

In the previous expression we neglected the quadratic term for  $f_{loop}^{elm}(u, M_\gamma)$ , and

$$g_{rad}(s, u, M_\gamma) = g_{brems}(s, u, M_\gamma) + g_{rest}(s, u), \quad (7.47)$$

with

$$g_{brems}(s, u, M_\gamma) = \frac{\alpha}{\pi} (J_{11}(s, u, M_\gamma) + J_{20}(s, u, M_\gamma) + J_{02}(s, u, M_\gamma)), \quad (7.48a)$$

$$g_{rest}(s, u) = \frac{\alpha}{\pi} (K_{11}(s, u) + K_{20}(s, u) + K_{02}(s, u)). \quad (7.48b)$$

Integrating Eq. (7.45) over  $u$ , and using

$$\int_{u_-(s)}^{u_+(s)} D(s, u) du = \frac{m_\tau^6}{6} \left(1 - \frac{s}{m_\tau^2}\right)^2 \left(1 - \frac{4m_\pi^2}{s}\right)^{3/2} \left(1 + \frac{2s}{m_\tau^2}\right),$$

we have

$$\begin{aligned} \left. \frac{d\Gamma}{ds} \right|_{\pi\pi(\gamma)} &= \frac{G_F^2 |V_{ud}|^2 m_\tau^3 S_{EW}}{384\pi^3} |f_+(s)|^2 \left(1 - \frac{s}{m_\tau^2}\right)^2 \left(1 - \frac{4m_\pi^2}{s}\right)^{3/2} \times \\ &\quad \left(1 + \frac{2s}{m_\tau^2}\right) G_{EM}(s), \end{aligned} \quad (7.49)$$

for this we follow the same notation as in Ref. [94],

$$G_{EM}(s) = \frac{\int_{\mathcal{R}^{IV}} D(s, u) \Delta(s, u) du}{\int_{u_-(s)}^{u_+(s)} D(s, u) du}. \quad (7.50)$$

We can split the electromagnetic correction factor ( $G_{EM}(s)$ ) in two parts,  $G_{EM}^{(0)}(s)$  and  $G_{EM}^{rest}(s)$ , the first one corresponds to taking  $g_{rest}(s, u) \rightarrow 0$  and the second one is the remainder of  $G_{EM}(s)$ ,

$$G_{EM}^{(0)}(s) = \frac{\int_{\mathcal{R}^{III}} D(s, u) \left(1 + 2f_{loop}^{elm}(u, M_\gamma) + g_{brem_s}(s, u, M_\gamma)\right) du}{\int_{u_-(s)}^{u_+(s)} D(s, u) du}, \quad (7.51a)$$

$$G_{EM}^{rest}(s) = \frac{\int_{\mathcal{R}^{IV/III}} D(s, u) g^{rest}(s, u) du}{\int_{u_-(s)}^{u_+(s)} D(s, u) du}. \quad (7.51b)$$

In Eq. (7.51a), the term  $2f_{loop}^{elm}(u, M_\gamma) + g_{brem_s}(s, u, M_\gamma)$  is finite when  $M_\gamma \rightarrow 0$ ,

$$\begin{aligned} 2f_{loop}^{elm}(u, M_\gamma) + g_{brem_s}(s, u, M_\gamma) &= \frac{\alpha}{4\pi} \left( (u - m_\pi^2) \mathcal{A}(u) + (u - m_\pi^2 - m_\tau^2) \mathcal{B}(u) \right. \\ &\quad \left. + 2(m_\pi^2 + m_\tau^2 - u) \mathcal{C}(u) \right) \\ &\quad + \frac{\alpha}{\pi} (J_{11}(s, u) + J_{20}(s, u) + J_{02}(s, u)). \end{aligned} \quad (7.52)$$

In this limit, we have

$$\begin{aligned} \mathcal{C}(u) = & \frac{1}{m_\tau m_\pi} \frac{x_\tau}{1-x_\tau^2} \left( -\frac{1}{2} \log^2 x_\tau + 2 \log x_\tau \log(1-x_\tau^2) - \frac{\pi^2}{6} + \frac{1}{8} \log^2 r_\tau \right. \\ & \left. + Li_2(x_\tau^2) + Li_2\left(1 - \frac{x_\tau}{\sqrt{r_\tau}}\right) + Li_2(1 - x_\tau \sqrt{r_\tau}) \right), \end{aligned} \quad (7.53)$$

$$\begin{aligned} J_{11}(s, u) = & \frac{1}{2} \log\left(\frac{4x_+^2(s, u)\bar{\gamma}^2}{m_\pi m_\tau}\right) \frac{1}{\bar{\beta}} \log\left(\frac{1+\bar{\beta}}{1-\bar{\beta}}\right) \\ & + \frac{1}{\bar{\beta}} \left( Li_2(1/Y_2) - Li_2(Y_1) + \log^2(-1/Y_2)/4 - \log^2(-1/Y_1)/4 \right), \end{aligned} \quad (7.54)$$

$$J_{20}(s, u) = \log\left(\frac{m_\tau^2 - s}{x_+(s, u)}\right), \quad (7.55)$$

$$J_{02}(s, u) = \log\left(\frac{m_\tau^2 + m_\pi^2 - s - u}{x_+(s, u)}\right), \quad (7.56)$$

where  $x_+(s, u)$  is defined in Eq. (H.19).

The leading Low approximation for  $G_{EM}^{(0)}(s)$  is plotted in fig. 7.8. This function has two poles, one at  $s = 4m_\pi^2$  and the other at  $s = m_\tau^2$ .

We will use the same conventions as Ref. [94], so we denote as ‘complete Bremsstrahlung’ the amplitude where the structure-dependent (‘SD’) part vanishes, i.e.  $v_1 = v_2 = v_3 = v_4 = a_1 = a_2 = a_3 = a_4 = 0$ . For convenience, we will refer in the following simply as  $\mathcal{O}(p^4)$  and  $\mathcal{O}(p^6)$  to the contributions from  $R\chi T$  including operators that contribute up to  $\mathcal{O}(p^4)$  and up to  $\mathcal{O}(p^6)$  chiral LECs, respectively <sup>24</sup>.

In  $G_{EM}(s)$ , the difference between using the  $F_V = \sqrt{2}F$  or  $F_V = \sqrt{3}F$  constraints at  $\mathcal{O}(p^4)$  is only appreciated for  $s \lesssim 0.35 \text{ GeV}^2$ , with the latter set producing the largest deviation with respect to the SI result (fig. 7.8). It is important to note that -as put forward in Ref. [94]- with  $F_V = \sqrt{2}F$  constraints (those consistent for 2-point Green functions) the impact of the ‘SD’ corrections on  $G_{EM}(s)$  is negligible and the evaluation with SI gives already an excellent approximation. On the contrary, we find that using the  $F_V = \sqrt{3}F$  set this is no longer true, which will increase the  $G_{EM}(s)$  correction in  $\alpha_\mu^{HVP, LO|\pi\pi}$  using  $\tau$  data

---

<sup>24</sup>The different SD constraints applying in each case were discussed at length in section 7.2.5.

(even before adding the  $\mathcal{O}(p^6)$  contributions).

In fig. 7.8 several contributions to the  $G_{EM}(s)$  function are shown: the  $G_{EM}^{(0)}$  part by a dashed blue line and the complete Bremsstrahlung (SI) contribution with a solid black line. The full amplitude including all  $R\chi T$  operators which contribute at  $\mathcal{O}(p^4)$  ( $\mathcal{O}(p^6)$ ) are represented by black dashed/dotted (red dashed-dotted) lines in fig. 7.8. For the  $\mathcal{O}(p^4)$  contribution we distinguish between using  $F_V = \sqrt{2}F$  ( $F_V = \sqrt{3}F$ ), represented by dashed (dotted) lines. Compared to previous results [94, 379, 677, 678], we note the appearance of a bump near the end of the phase space on  $G_{EM}(s)$  due to the inclusion of the  $\rho(1450)$  and the  $\rho(1700)$  resonances in the dispersive representation of the vector form factor [19, 28]. The blue band in fig. 7.8 shows the uncertainty of the  $\mathcal{O}(p^6)$  contribution, evaluated according to that on the couplings which were determined phenomenologically or estimated from chiral counting in section 7.2.5 (see also appendix G) <sup>25</sup>. While the central values of the  $\mathcal{O}(p^6)$  corrections change mildly the results obtained at  $\mathcal{O}(p^4)$  <sup>26</sup>, their huge uncertainty band suggests that our estimate of the  $R\chi T$  couplings which start contributing at  $\mathcal{O}(p^6)$  was very conservative (one naively expects a  $\sim 1/N_C$  uncertainty for a large- $N_C$  expansion <sup>27</sup>). Lacking a better way for this estimation, we consider this uncertainty band as a conservative upper limit on the corresponding uncertainties. Therefore, our error bands at  $\mathcal{O}(p^6)$  should be regarded accordingly in the following. On the contrary, the small modification induced by those  $\mathcal{O}(p^6)$  couplings fixed by SD constraints (with all remaining ones vanishing) with respect to the  $\mathcal{O}(p^4)$  [94] results, suggests that the difference between those is a realistic estimate of the missing subdominant terms in Ref. [94] <sup>28</sup> and will be given as such in the remainder of the chapter.

---

<sup>25</sup>These were varied assuming Gaussian errors, and the band was generated so as to cover all data points obtained in 100 spectrum simulations. Results were stable upon increasing statistics. The corresponding blue bands were obtained similarly in Figs. 7.12 to 7.14.

<sup>26</sup>This is reasonable, since  $SI$  is basically unchanged by the  $\mathcal{O}(p^4)$  contributions.

<sup>27</sup>This rough estimate of the parametric uncertainty is supported by the computation of  $\chi PT$  LECs including such corrections (see e. g. Refs. [218, 705, 707]). We note that in this work resonance widths (dominant next-to-leading order effect in the large- $N_C$  expansion for the considered decays) are included. Also the uncertainty corresponding to including excited resonances (an infinite number of them appears for  $N_C \rightarrow \infty$ ) was checked to be negligible.

<sup>28</sup>These were not estimated in Ref. [94] as SI was already an excellent approximation to the result up to  $\mathcal{O}(p^4)$  (using the  $F_V = \sqrt{2}F$  set).

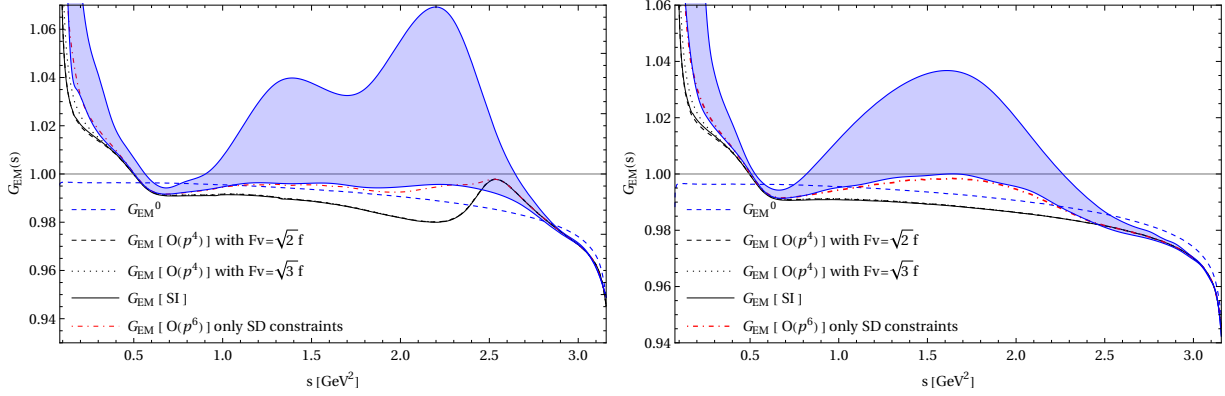


Figure 7.8: Correction function  $G_{EM}^{(0)}(s)$  in Eq. (7.51a) (blue dashed line). The solid line shows the  $G_{EM}(s)$  function neglecting the structure-dependent part (SI), i.e. by taking  $v_1 = v_2 = v_3 = v_4 = a_1 = a_2 = a_3 = a_4 = 0$ , the dashed and dotted lines are the  $\mathcal{O}(p^4)$   $G_{EM}(s)$  function (with either  $F_V = \sqrt{2}F$  or  $F_V = \sqrt{3}F$  constraints). The blue shaded region is the full  $\mathcal{O}(p^6)$  contribution, including (overestimated) uncertainties. The left-hand side plot corresponds to the dispersive parametrization [19] while the right-hand side corresponds to the Guerrero-Pich parametrization [15] of the form factor (the latter was used in Ref. [94]).

### 7.3.1 Radiative decay

The differential decay width [713] is given by

$$d\Gamma = \frac{\lambda^{1/2}(s, m_{\pi^0}^2, m_{\pi^-}^2)}{2(4\pi)^6 m_\tau^2 s} \overline{|\mathcal{M}|^2} dE_\gamma dx ds d\cos\theta_- d\phi_-, \quad (7.57)$$

where  $\overline{|\mathcal{M}|^2}$  is the unpolarized spin-averaged squared amplitude that corresponds to the  $\tau^- \rightarrow \pi^- \pi^0 \gamma \nu_\tau$  decays, and  $E_\gamma$  is the photon energy in the  $\tau$  rest frame. It is not worth to quote here the full analytical expression for  $\overline{|\mathcal{M}|^2}$ .

For these decays, we have the following integration region

$$\mathcal{D} = \left\{ E_\gamma^{min} \leq E_\gamma \leq E_\gamma^{max}, x_{min} \leq x \leq x_{max}, s_{min} \leq s \leq s_{max}, \right. \\ \left. -1 \leq \cos\theta_- \leq +1, 0 \leq \phi_- \leq 2\pi \right\}, \quad (7.58)$$

with boundaries

$$\begin{aligned}
\frac{(m_\tau^2 - s + x)}{4m_\tau^2} - \frac{\lambda^{1/2}(s, x, m_\tau^2)}{4m_\tau} &\leq E_\gamma(s, x) \leq \frac{(m_\tau^2 - s + x)}{4m_\tau} + \frac{\lambda^{1/2}(s, x, m_\tau^2)}{4m_\tau}, \\
4m_\pi^2 &\leq s(x) \leq (m_\tau - \sqrt{x})^2, \\
0 &\leq x \leq (m_\tau - 2m_\pi)^2,
\end{aligned} \tag{7.59}$$

or interchanging the last two limits,

$$\begin{aligned}
0 &\leq x(s) \leq (m_\tau - \sqrt{s})^2, \\
4m_\pi^2 &\leq s \leq m_\tau^2.
\end{aligned} \tag{7.60}$$

There are other ways to write these,

$$\begin{aligned}
4m_\pi^2 &\leq s(x, E_\gamma) \leq \frac{(m_\tau - 2E_\gamma)(2m_\tau E_\gamma - x)}{2E_\gamma} \\
0 &\leq x(E_\gamma) \leq \frac{2E_\gamma(m_\tau^2 - 4m_\pi^2 - 2m_\tau E_\gamma)}{m_\tau - 2E_\gamma}, \\
E_\gamma^{cut} &\leq E_\gamma \leq \frac{m_\tau^2 - 4m_\pi^2}{2m_\tau},
\end{aligned} \tag{7.61}$$

or exchanging  $x \leftrightarrow E_\gamma$ ,

$$\begin{aligned}
\frac{(m_\tau^2 + x - 4m_\pi^2)}{4m_\tau} - \frac{\lambda^{1/2}(x, m_\tau^2, 4m_\pi^2)}{4m_\tau} &\leq E_\gamma(s) \leq \frac{(m_\tau^2 + x - 4m_\pi^2)}{4m_\tau} + \frac{\lambda^{1/2}(x, m_\tau^2, 4m_\pi^2)}{4m_\tau}, \\
0 &\leq x \leq (m_\tau - 2m_\pi)^2,
\end{aligned} \tag{7.62}$$

and

$$\begin{aligned}
0 &\leq x(s, E_\gamma) \leq \frac{2E_\gamma(m_\tau^2 - s - 2E_\gamma m_\tau)}{m_\tau - 2E_\gamma} \\
4m_\pi^2 &\leq s(E_\gamma) \leq m_\tau(m_\tau - 2E_\gamma), \\
E_\gamma^{cut} &\leq E_\gamma \leq \frac{m_\tau^2 - 4m_\pi^2}{2m_\tau}.
\end{aligned} \tag{7.63}$$

Further, interchanging  $s \leftrightarrow E_\gamma$ , we get

$$\begin{aligned}
E_\gamma^{cut} &\leq E_\gamma(s) \leq \frac{m_\tau^2 - s}{2m_\tau}, \\
4m_\pi^2 &\leq s \leq m_\tau(m_\tau - 2E_\gamma^{cut}).
\end{aligned} \tag{7.64}$$

We recall that this amplitude has IR divergences due to soft photons, i.e.  $E_\gamma \rightarrow 0$ , which



is the same problem with  $M_\gamma \rightarrow 0$  outlined in the previous section. Correspondingly, the experiment is not able to measure photons with energies smaller than some  $E_\gamma^{cut}$  (which is related with the experimental resolution).

Concerning the  $\mathcal{O}(p^6)$  contributions, once we employ the relations obtained from the SD behaviour of QCD and its OPE, it is seen that observables are basically insensitive (at the percent level of precision) to  $\mathcal{O}(1)$  changes of all the couplings but  $\kappa_i^V$  (the  $\rho - \omega - \pi$  vertex is described by these couplings), which will saturate the (overestimated) uncertainty of our predictions at this order.

If we integrate Eq. (7.57) using the limits in Eq. (7.64) and the dispersive vector form factor [19, 28], we get the  $\pi^- \pi^0$  invariant mass distribution, the photon energy distribution and the branching ratios as a function of  $E_\gamma^{cut}$ , shown in Figs. 7.10, 7.11, 7.12, 7.13 and 7.14 and summarized in Table 7.2. In these figures, the dotdashed red line corresponds to taking the limit where all the couplings at  $\mathcal{O}(p^6)$  vanish except for those constrained by SD and the band overestimates the corresponding uncertainties.

$E_\gamma^{cut}$	BR(Brems)	BR( $F_V = \sqrt{2}F$ ) [ $\mathcal{O}(p^4)$ ]	BR( $F_V = \sqrt{3}F$ ) [ $\mathcal{O}(p^4)$ ]
100 MeV	$8.6 \times 10^{-4}$	$9.0 \times 10^{-4}$	$9.5 \times 10^{-4}$
300 MeV	$1.7 \times 10^{-4}$	$1.9 \times 10^{-4}$	$2.3 \times 10^{-4}$
500 MeV	$2.8 \times 10^{-5}$	$3.9 \times 10^{-5}$	$5.4 \times 10^{-5}$

Table 7.2: Branching ratios  $\text{Br}(\tau^- \rightarrow \pi^- \pi^0 \gamma \nu_\tau)$  for different values of  $E_\gamma^{cut}$ . The second column corresponds to the complete Bremsstrahlung and the third and fourth to the  $\mathcal{O}(p^4)$  contributions.

$E_\gamma^{cut}$	BR(SD) [ $\mathcal{O}(p^6)$ ]	BR [ $\mathcal{O}(p^6)$ ]
100 MeV	$1.3 \times 10^{-3}$	$(1.9 \pm 0.3) \times 10^{-3}$
300 MeV	$5.1 \times 10^{-4}$	$(1.1 \pm 0.3) \times 10^{-3}$
500 MeV	$2.4 \times 10^{-4}$	$(0.6 \pm 0.2) \times 10^{-3}$

Table 7.3: Branching ratios  $\text{Br}(\tau^- \rightarrow \pi^- \pi^0 \gamma \nu_\tau)$  for different  $E_\gamma^{cut}$  values at  $\mathcal{O}(p^6)$ .

As it can be observed from Table 7.2 and fig. 7.14, the main contribution at  $\mathcal{O}(p^4)$  cor-

responds to the complete Bremsstrahlung (SI) amplitude (in agreement with Ref. [94]), and the value for the branching ratio becomes smaller with larger values of  $E_\gamma^{cut}$ . The values in Table 7.2 are slightly different from those reported in Ref. [94], this effect is mainly due to the parametrization of the pion vector form factor (see fig. 7.9). The form factor obtained from the dispersion relation [19] is above the one obtained using the Guerrero-Pich parametrization [15] at  $s \simeq M_\rho^2$ , and also the former includes the  $\rho(1450)$  and  $\rho(1700)$  resonances.

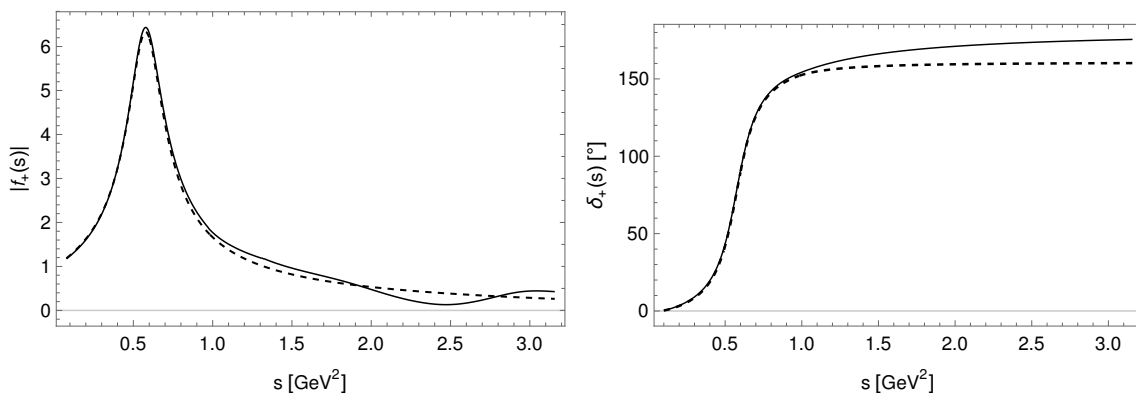


Figure 7.9: Modulus and phase of the pion vector form factor,  $f_+(s)$ . The solid line corresponds to the dispersive representation used in Ref. [19] while the dashed line corresponds to the Guerrero-Pich parametrization [15] employed by Ref. [94].

According to our discussion on error estimation of the  $\mathcal{O}(p^4)$  result (including the uncertainty coming from missing higher-order terms from the result at  $\mathcal{O}(p^6)$  when only SD constraints are used), we have -for  $E_\gamma^{cut} = 300$  MeV-  $BR(\tau^- \rightarrow \pi^- \pi^0 \nu_\tau) = (1.9_{-0.0}^{+3.2}) \cdot 10^{-4}$ .

The spectrum for these decays with  $v_i = a_i = 0$  is plotted in fig. 7.10, the dominant peak corresponds to bremsstrahlung off the  $\pi^-$ , and the secondary receives two contributions: one from bremsstrahlung off the  $\tau$  lepton and another from a resonance exchange in  $V_{\mu\nu}$  (for  $E_\gamma^{cut} \leq 100$  MeV, these two are merged into one single peak). The rate and spectrum are dominated by the complete bremsstrahlung (SI) contribution.

In fig. 7.11, we show the distribution for  $E_\gamma^{cut} = 300$  MeV taking into account the SI contribution (dotted line) and the  $\mathcal{O}(p^4)$  amplitude obtained using  $F_V = \sqrt{2}F$  (dashed line)

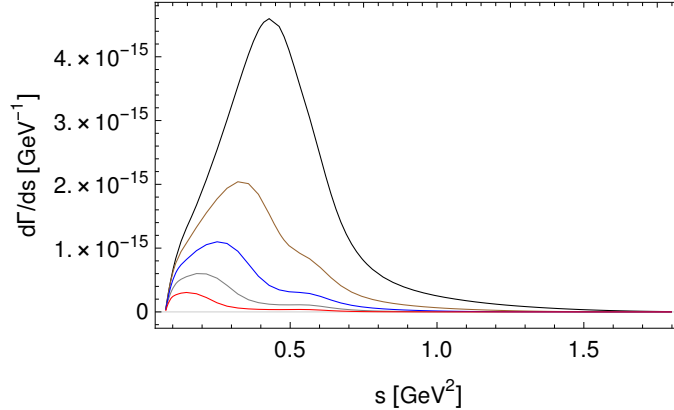


Figure 7.10: The  $\pi^-\pi^0$  hadronic invariant mass distribution for the  $\tau^- \rightarrow \pi^-\pi^0\gamma\nu_\tau$  decays for  $E_\gamma^{cut} = 100$  MeV (black),  $E_\gamma^{cut} = 200$  MeV (brown),  $E_\gamma^{cut} = 300$  MeV (blue),  $E_\gamma^{cut} = 400$  MeV (gray) and  $E_\gamma^{cut} = 500$  MeV (red) using only the Bremsstrahlung (SI) contribution.

and  $F_V = \sqrt{3}F$  (solid line), the most important contribution corresponds to the  $\rho$  resonance exchange at  $s \sim 0.6$  GeV<sup>2</sup>. The main difference between these two approaches is seen in fig. 7.11, where up to  $s \sim 0.4$  GeV<sup>2</sup> the dashed line is below and the solid line is above the bremsstrahlung (SI) contribution (dotted line). The dashed line is quite similar to the distribution in fig. 2 of Ref. [94] while the solid line resembles closely the distribution in fig. 4.6 of Ref. [713] obtained from the vector meson dominance (VMD) model [714] neglecting the  $\omega$ -resonance contribution.

In fig. 7.12 we show a comparison between the di-pion distribution at different orders. As we can see, the inclusion of the corrections at  $\mathcal{O}(p^6)$  gives a noticeable enhancement at low  $s$ .

For the photon energy distribution, fig. 7.13, we can differentiate between the full amplitude (solid, dashed lines up to  $\mathcal{O}(p^4)$  and dotdashed red line up to  $\mathcal{O}(p^6)$ ) and the bremsstrahlung contribution (dotted line) but, as in the case of the branching fraction, the distribution decreases for high-energies. In the case of the  $\mathcal{O}(p^6)$  distribution there is an enhancement at middle and high photon energies.

According to Figs. 7.11 to 7.14, measurements of the  $\pi\pi$  invariant mass, of the photon

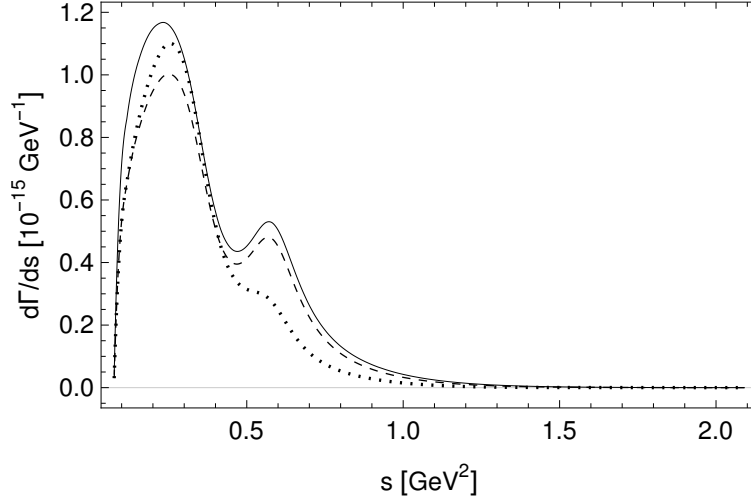


Figure 7.11: The  $\pi^-\pi^0$  hadronic invariant mass distributions for  $E_\gamma^{cut} = 300$  MeV. The solid and dashed lines represent the  $\mathcal{O}(p^4)$  corrections using  $F_V = \sqrt{3}F$  and  $F_V = \sqrt{2}F$ , respectively. The dotted line stands for the Bremstrahlung contribution (SI).

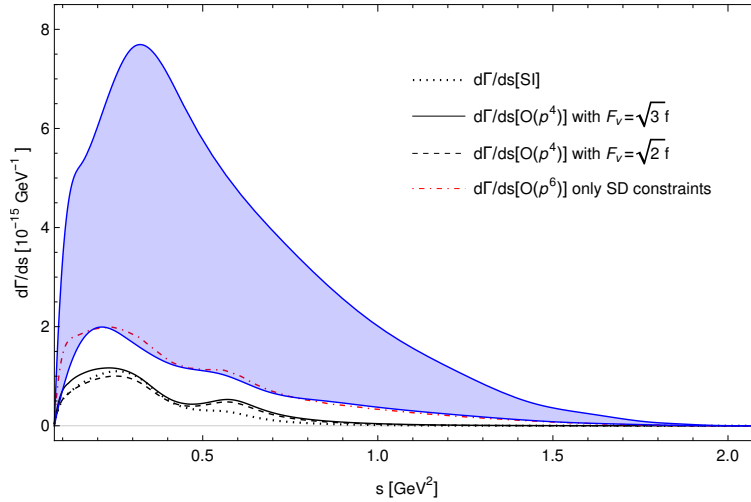


Figure 7.12: The  $\pi^-\pi^0$  hadronic invariant mass distributions for  $E_\gamma^{cut} = 300$  MeV. The solid and dashed line represent the  $\mathcal{O}(p^4)$  corrections using  $F_V = \sqrt{3}F$  and  $F_V = \sqrt{2}F$ , respectively. The dotted line represents the Bremstrahlung contribution (SI). The dot-dashed red line corresponds to using only SD constraints at  $\mathcal{O}(p^6)$  and the blue shaded region overestimates the corresponding uncertainties.

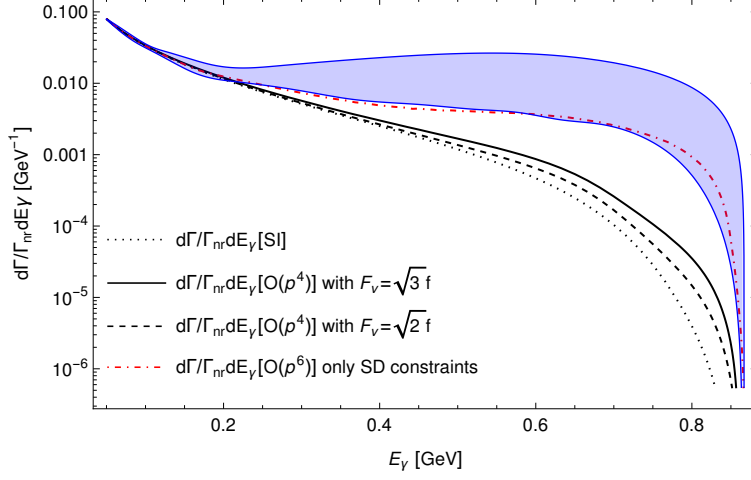


Figure 7.13: Photon energy distribution for the  $\tau^- \rightarrow \pi^- \pi^0 \gamma \nu_\tau$  decays normalized with the non-radiative decay width. The dotted line represents the Bremsstrahlung contribution. The solid and dashed lines represent the  $\mathcal{O}(p^4)$  corrections using  $F_V = \sqrt{3}f$  and  $F_V = \sqrt{2}f$ , respectively. The dotdashed red line corresponds to using only SD constraints at  $\mathcal{O}(p^6)$  (with overestimated uncertainties in the blue shaded area).

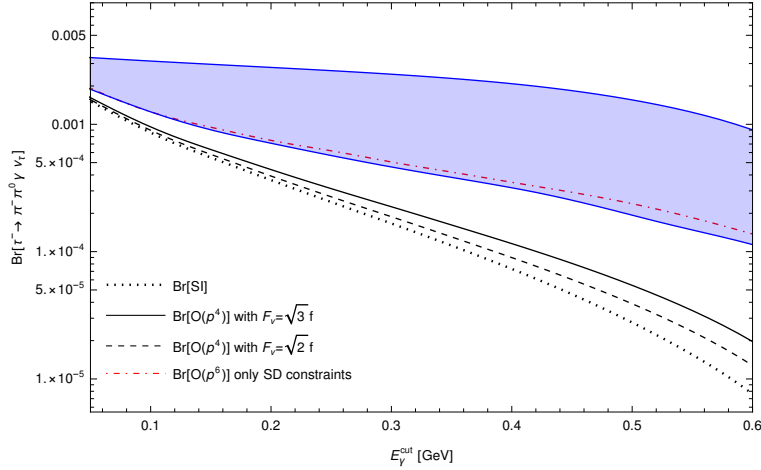


Figure 7.14: Branching ratio for the  $\tau^- \rightarrow \pi^- \pi^0 \gamma \nu_\tau$  decays as a function of  $E_\gamma^{cut}$ . The dotted line represents the Bremsstrahlung contribution, the solid line and dashed line represent the  $\mathcal{O}(p^4)$  corrections using  $F_V = \sqrt{3}f$  and  $F_V = \sqrt{2}f$ , respectively. The dotdashed red line is the  $\mathcal{O}(p^6)$  contribution using only SD constraints and neglecting all other couplings. The blue shaded region overestimates the  $\mathcal{O}(p^6)$  uncertainties.

spectrum and the partial decay width, for a reasonable cut on  $E_\gamma$  (at low enough energies the inner bremsstrahlung contribution hides completely any structure-dependent effect), could decrease substantially the uncertainty of the  $\mathcal{O}(p^6)$  computation. This was already emphasized in Ref. [94] but remained unmeasured at BaBar and Belle. We hope these data can finally be acquired and analyzed at Belle-II.

In fig. 7.15, we show the branching ratio for  $E_\gamma^{cut} = 100, 300, \text{ and } 500 \text{ MeV}$  from top to bottom. The outcomes were summarized in Table 7.3.

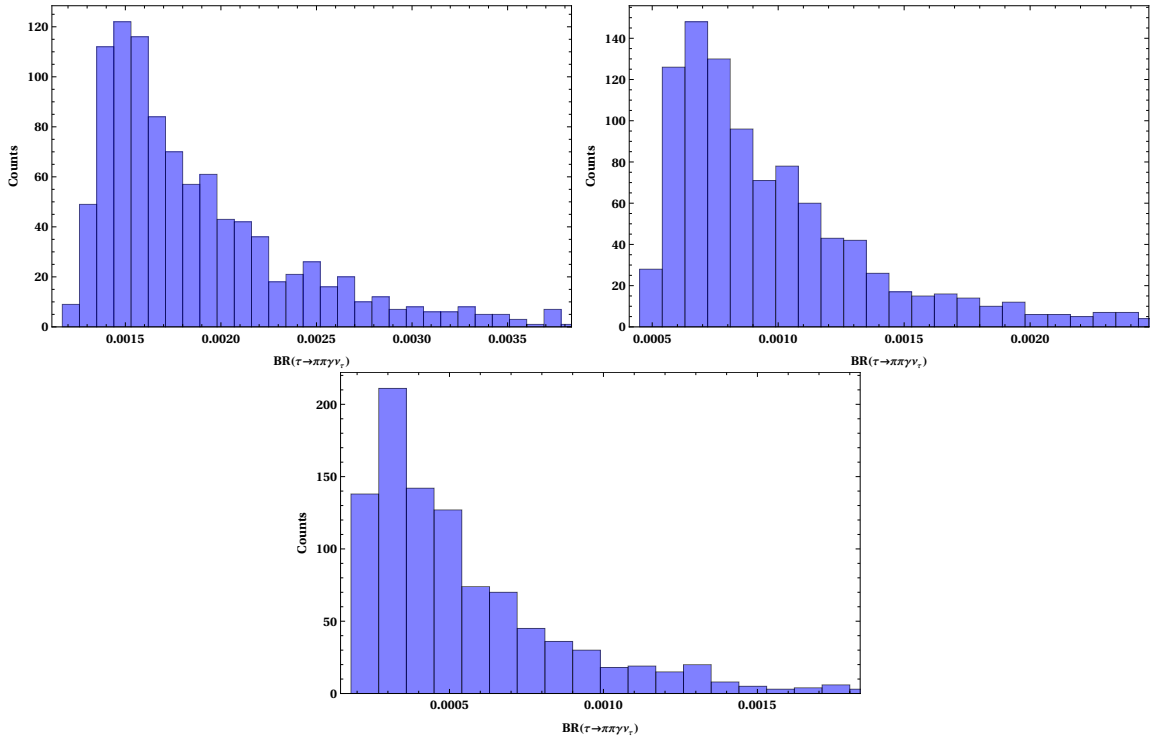


Figure 7.15: Predictions for the branching ratio at  $\mathcal{O}(p^6)$  for a sample of 1000 points, with  $E_{cut} = 100, 300, \text{ and } 500 \text{ MeV}$  from top to bottom.

## 7.4 IB corrections to $a_\mu^{HVP,LO} \pi\pi$

We can evaluate the leading contributions to the hadronic vacuum polarization (HVP) by means of the dispersion relation [715],

$$a_\mu^{HVP,LO} = \frac{1}{4\pi^3} \int_{s_{thr}}^{\infty} ds K(s) \sigma_{e^-e^+ \rightarrow hadrons}^0(s), \quad (7.65)$$

where  $K(s)$  is a smooth QED kernel concentrated at low energies, which increases the  $E \lesssim M_\rho$  contribution,

$$K(s) = \frac{x^2}{2}(2-x^2) + \frac{(1+x^2)(1+x)^2}{x^2} \left( \ln(1+x) - x + \frac{x^2}{2} \right) + \frac{(1+x)}{(1-x)} x^2 \ln(x), \quad (7.66)$$

with

$$x = \frac{1 - \beta_\mu}{1 + \beta_\mu}, \quad \beta_\mu = \sqrt{1 - 4m_\mu^2/s},$$

and  $\sigma_{e^-e^+ \rightarrow hadrons}^0(s)$  is the bare hadronic cross section<sup>29</sup>. We can relate the hadronic spectral function from  $\tau$  decays to the  $e^+e^-$  hadronic cross section by including the radiative corrections and the IB effects. For the  $\pi\pi$  final state, we have [94, 379]:

$$\sigma_{\pi\pi}^0 = \left[ \frac{K_\sigma(s)}{K_\Gamma(s)} \frac{d\Gamma_{\pi\pi[\gamma]}}{ds} \right] \frac{R_{IB}(s)}{S_{EW}}, \quad (7.67)$$

where

$$K_\Gamma(s) = \frac{G_F^2 |V_{ud}|^2 m_\tau^3}{384\pi^3} \left( 1 - \frac{s}{m_\tau^2} \right)^2 \left( 1 + \frac{2s}{m_\tau^2} \right), \quad (7.68)$$

$$K_\sigma(s) = \frac{\pi\alpha^2}{3s},$$

and the IB corrections

$$R_{IB}(s) = \frac{FSR(s)}{G_{EM}(s)} \frac{\beta_{\pi^+\pi^-}^3}{\beta_{\pi^+\pi^0}^3} \left| \frac{F_V(s)}{f_+(s)} \right|^2. \quad (7.69)$$

---

<sup>29</sup>Although final state radiation would belong to HVP,NLO it is always included in HVP,LO (and not in HVP,NLO) as eliminating this radiation from the measured data is unfeasible. Thus, a final state radiation (FSR) factor is also needed in the radiative corrections discussed below.

The  $S_{EW}$  term encodes the SD electroweak corrections [256, 274, 364, 365, 520–523] and  $FSR(s)$  accounts for the radiation from the final-state pions [658, 659]. The  $G_{EM}(s)$  term was already discussed at length in section 7.3, the  $\beta_{\pi^+\pi^-}^3/\beta_{\pi^+\pi^0}^3$  term is a phase space factor and the last term in  $R_{IB}(s)$  is a ratio between the neutral ( $F_V(s)$ ) and the charged ( $f_+(s)$ ) pion form factor.

In order to study the effect of the radiative correction  $G_{EM}(s)$  on  $a_\mu^{HVP,LO}[\pi\pi]$ , we have evaluated the following expression [94]

$$\Delta a_\mu^{HVP,LO} = \frac{1}{4\pi^3} \int_{s_1}^{s_2} ds K(s) \left[ \frac{K_\sigma(s)}{K_\Gamma(s)} \frac{d\Gamma_{\pi\pi[\gamma]}}{ds} \right] \left( \frac{R_{IB}(s)}{S_{EW}} - 1 \right), \quad (7.70)$$

taking  $S_{EW} = 1$ ,  $\frac{\beta_{\pi^+\pi^-}^3}{\beta_{\pi^+\pi^0}^3} = 1$  and  $\left| \frac{F_V(s)}{f_+(s)} \right|^2 = 1$ . The results are summarized in Table 7.4 using DR form factor. The results obtained for the  $G_{EM}^{(0)}(s)$  and the complete  $\mathcal{O}(p^4)$  contribution (with  $F_V = \sqrt{2}F$ ) agree with those in [94], which are  $+16 \cdot 10^{-11}$  and  $-10 \cdot 10^{-11}$ , respectively (for the whole integral). In Table 7.5, we summarized the results obtained using the Guerrero-Pich [15] parametrization of the form factor (which only accounts for the completely dominant  $\rho$  exchange), which are in nice agreement with those found with the dispersive form factor (that also includes the  $\rho(1450)$  and  $\rho(1700)$  effects). This checks, a posteriori, that excited resonance contributions make a negligible effect in the  $G_{EM}(s)$  corrections to  $a_\mu^{HVP,LO}$  30.

The values in the last column of Tables 7.4 and 7.5 were obtained evaluating the Eq. (7.70) according to the couplings discussed in section 7.2.5 for a sample of 200 points for each interval of integration (results were stable under increasing this number).

The other contributions are summarized in Table 7.6.

- The  $S_{EW}$  contribution  $S_{EW} = 1.0201$  gives  $\Delta a_\mu^{HVP,LO} = -103.1 \times 10^{-11}$ , consistent with earlier determinations (using slightly different values of  $S_{EW}$ ) and with a negligible error.

---

<sup>30</sup>By replacing  $D_\rho^{-1}(x)$  by  $(1 + \beta_{\rho'})^{-1}(D_\rho^{-1}(x) + \beta_{\rho'} D_{\rho'}^{-1}(x))$ , with  $\beta_{\rho'} \in [0.12, 0.15]$  [28] throughout the  $v_i$  and  $a_i$  form factors, we have verified that the impact of the  $\rho'$  on the  $G_{EM}(s)$  correction to  $a_\mu^{HVP,LO}[\pi\pi,\tau]$  is negligible. Similarly, the error induced by other excited resonances shall also be irrelevant.



$[s_1, s_2]$	$\Delta a_{\mu, G_{EM}^{(0)}}^{\text{HVP,LO}}$	$\Delta a_{\mu, \text{SI}}^{\text{HVP,LO}}$	$\Delta a_{\mu, [\mathcal{O}(p^4)]}^{\text{HVP,LO}}$	$\Delta a_{\mu, [\mathcal{O}(p^4)]}^{\text{HVP,LO}}$	$\Delta a_{\mu, [SD]}^{\text{HVP,LO}}$	$\Delta a_{\mu, [\mathcal{O}(p^6)]}^{\text{HVP,LO}}$
$[4m_\pi^2, 1 \text{ GeV}^2]$	+17.8	-11.0	-11.3	-17.0	-32.4	$-74.8 \pm 44.0$
$[4m_\pi^2, 2 \text{ GeV}^2]$	+18.3	-10.1	-10.3	-16.0	-31.9	$-75.9 \pm 45.5$
$[4m_\pi^2, 3 \text{ GeV}^2]$	+18.4	-10.0	-10.2	-15.9	-31.9	$-75.9 \pm 45.6$
$[4m_\pi^2, m_\tau^2]$	+18.4	-10.0	-10.2	-15.9	-31.9	$-75.9 \pm 45.6$

Table 7.4: Contributions to  $\Delta a_\mu^{\text{HVP,LO}}$  in units of  $10^{-11}$  using the dispersive representation of the form factor. From the two evaluations labelled  $\mathcal{O}(p^4)$ , the left(right) one corresponds to  $F_V = \sqrt{2}F$  ( $F_V = \sqrt{3}F$ ).

$[s_1, s_2]$	$\Delta a_{\mu, G_{EM}^{(0)}}^{\text{HVP,LO}}$	$\Delta a_{\mu, \text{SI}}^{\text{HVP,LO}}$	$\Delta a_{\mu, [\mathcal{O}(p^4)]}^{\text{HVP,LO}}$	$\Delta a_{\mu, [\mathcal{O}(p^4)]}^{\text{HVP,LO}}$	$\Delta a_{\mu, [SD]}^{\text{HVP,LO}}$	$\Delta a_{\mu, [\mathcal{O}(p^6)]}^{\text{HVP,LO}}$
$[4m_\pi^2, 1 \text{ GeV}^2]$	+17.3	-10.2	-10.4	-15.9	-28.3	$-63.2 \pm 16.5$
$[4m_\pi^2, 2 \text{ GeV}^2]$	+17.7	-9.4	-9.6	-15.2	-28.1	$-58.1 \pm 12.2$
$[4m_\pi^2, 3 \text{ GeV}^2]$	+17.8	-9.3	-9.5	-15.1	-28.0	$-67.8 \pm 17.5$
$[4m_\pi^2, m_\tau^2]$	+17.8	-9.3	-9.5	-15.1	-28.0	$-64.9 \pm 13.4$

Table 7.5: Contributions to  $\Delta a_\mu^{\text{HVP,LO}}$  in units of  $10^{-11}$  using the GP parametrization of the form factor. From the two evaluations labelled  $\mathcal{O}(p^4)$ , the left(right) one corresponds to  $F_V = \sqrt{2}F$  ( $F_V = \sqrt{3}F$ ).

- The phase space (PS) correction induces  $\Delta a_\mu^{HVP,LO} = -74.5 \times 10^{-11}$  (trivially in agreement with previous computations), again with tiny uncertainties.
- The final state radiation (FSR, which is formally *NLO*) yields  $\Delta a_\mu^{HVP,LO} = +45.5(4.6) \times 10^{-11}$ , in accord with Ref. [7] (its value was not quoted in Ref. [94]).
- The correction due to the ratio of the form factors (fig. 7.16) is harder to evaluate. We have considered two alternatives, labelled FF1 and FF2, that we explain next. We use the following numerical inputs for the  $\rho - \omega$  mixing parameter  $\theta_{\rho\omega} = (-3.5 \pm 0.7) \times 10^{-3} \text{ GeV}^2$  [94] and  $\Gamma_{\rho^0} - \Gamma_{\rho^+} = 0.3 \pm 1.3 \text{ MeV}$ ,  $m_{\rho^\pm} - m_{\rho^0} = 0.7 \pm 0.8 \text{ MeV}$  and  $m_{\rho^0} = 775.26 \pm 0.25 \text{ MeV}$  from PDG [541].

In FF1, as in Ref. [94], we include the measurement of the  $\pi\pi\gamma$  channel of the  $\rho^0$   $\Gamma_{\rho^0 \rightarrow \pi^+\pi^-\gamma} = 1.5 \pm 0.2 \text{ MeV}$ , and the measurement of  $\Gamma_{\rho^0 \rightarrow \pi^0\gamma}$  and  $\Gamma_{\rho^+ \rightarrow \pi^+\gamma}$  which are approximately 0.1 MeV [3]. Thus, we estimate  $\Gamma_{\rho^0 \rightarrow \pi^+\pi^-\gamma} - \Gamma_{\rho^\pm \rightarrow \pi^\pm\pi^0\gamma} = 1.5 \pm 1.3 \text{ MeV}$ . In this way, we get a positive correction of  $\Delta a_\mu^{HVP,LO} = +40.9(48.9) \times 10^{-11}$ . The uncertainty on the third column of Table 7.6 (FF1) corresponds to sum the errors due to uncertainties of  $\rho - \omega$  mixing (8.5), the  $\rho^+ - \rho^0$  mass difference (15.9), and the  $\rho^+ - \rho^0$  width difference (45.5) in quadrature (in units of  $10^{-11}$ ).

On the other hand, in FF2 we use the same numerical inputs for  $\Gamma_{\rho^0 \rightarrow \pi^+\pi^-\gamma} - \Gamma_{\rho^\pm \rightarrow \pi^\pm\pi^0\gamma} = 0.45 \pm 0.45 \text{ MeV}$  as in Ref. [94] (and all the others as we did before), we obtain a positive correction of  $\Delta a_\mu^{HVP,LO} = +77.6(24.0) \times 10^{-11}$ . The uncertainty on the fourth column Table 7.6 (FF2) corresponds to sum the errors due to uncertainties of  $\rho - \omega$  mixing (8.6), the  $\rho^+ - \rho^0$  mass difference (15.9), and the  $\rho^+ - \rho^0$  width difference (15.8) in quadrature (in units of  $10^{-11}$ ).

This correction was  $+(61 \pm 26 \pm 3) \cdot 10^{-11}$  in [94] and  $+(86 \pm 32 \pm 7) \cdot 10^{-11}$  in [7], in agreement (despite the big errors) with our FF2 and FF1 determinations, respectively.

- Finally, we get  $(-15.9_{-16.0}^{+5.7}) \cdot 10^{-11}$  ( $(-76 \pm 46) \cdot 10^{-11}$ ) for the  $G_{EM}(s)$  correction at  $\mathcal{O}(p^4)$  ( $\mathcal{O}(p^6)$ ), versus  $-10 \cdot 10^{-11}$  in [94] and  $-37 \cdot 10^{-11}$  in [677] (from the last two results,

$(-19.2 \pm 9.0) \cdot 10^{-11}$  was used in [7]). As explained before, the previous uncertainty on the  $\mathcal{O}(p^6)$  can only be taken as an upper bound on it. Also interesting is the  $G_{EM}(s)$  correction when only the couplings restricted by SD are used (with all others at this order set to zero), which allows us to estimate the effect of missing higher-order terms on the  $\mathcal{O}(p^4)$  result quoted above. This  $\mathcal{O}(p^4)$  result, which is our reference value, is consistent with both the earlier  $R\chi T$  [94] and the VMD [7] evaluations, albeit with a larger (asymmetric) error.

$[s_1, s_2]$	SEW	PS	FSR	FF1	FF2	EM
$[4m_\pi^2, 1 \text{ GeV}^2]$	-101.1	-74.1	+44.7	$+41.8 \pm 49.0$	$+78.4 \pm 24.5$	$-17.0^{+5.7}_{-15.4}$
$[4m_\pi^2, 2 \text{ GeV}^2]$	-103.1	-74.4	+45.5	$+40.9 \pm 48.9$	$+77.6 \pm 24.0$	$-16.0^{+5.7}_{-15.9}$
$[4m_\pi^2, 3 \text{ GeV}^2]$	-103.1	-74.5	+45.5	$+40.9 \pm 48.9$	$+77.6 \pm 24.0$	$-15.9^{+5.7}_{-16.0}$
$[4m_\pi^2, m_\tau^2]$	-103.1	-74.5	+45.5	$+40.9 \pm 48.9$	$+77.6 \pm 24.0$	$-15.9^{+5.7}_{-16.0}$

$[s_1, s_2]$	$\Delta a_\mu(\text{FF1})$	$\Delta a_\mu(\text{FF2})$
$[4m_\pi^2, 1 \text{ GeV}^2]$	$-105.7^{+49.5}_{-51.6}$	$-69.1^{+25.6}_{-29.3}$
$[4m_\pi^2, 2 \text{ GeV}^2]$	$-107.1^{+49.4}_{-51.6}$	$-70.4^{+25.1}_{-29.2}$
$[4m_\pi^2, 3 \text{ GeV}^2]$	$-107.1^{+49.4}_{-51.7}$	$-70.4^{+25.1}_{-29.2}$
$[4m_\pi^2, m_\tau^2]$	$-107.1^{+49.4}_{-51.7}$	$-70.4^{+25.1}_{-29.2}$

Table 7.6: Contributions to  $\Delta a_\mu^{HVP,LO}$  in units of  $10^{-11}$  using the DR form factor as the reference one.

In fig. 7.17, we show the full IB correction factor  $R_{IB}(s)$  for the different orders of approximation in the  $G_{EM}(s)$  factor using the DR parametrization of the form factor. As we can see, there is a difference between the contributions at  $\mathcal{O}(p^4)$  and those at  $\mathcal{O}(p^6)$  for energies below  $\sim 0.5\text{GeV}^2$  and above  $\sim 0.7\text{GeV}^2$ .

An important cross-check is the branching fraction  $B_{\pi\pi^0} = \Gamma(\tau \rightarrow \pi\pi^0\nu_\tau)/\Gamma_\tau$  which is a directly measured quantity. It can also be evaluated from the  $I = 1$  component of the  $e^+e^- \rightarrow \pi^+\pi^-(\gamma)$  cross section after taking into account the IB corrections. The branching fraction is given by

$$B_{\pi\pi^0}^{CVC} = B_e \int_{4m_\pi^2}^{m_\tau^2} ds \sigma_{\pi^+\pi^-(\gamma)}(s) \mathcal{N}(s) \frac{S_{EW}}{R_{IB}(s)}, \quad (7.71)$$

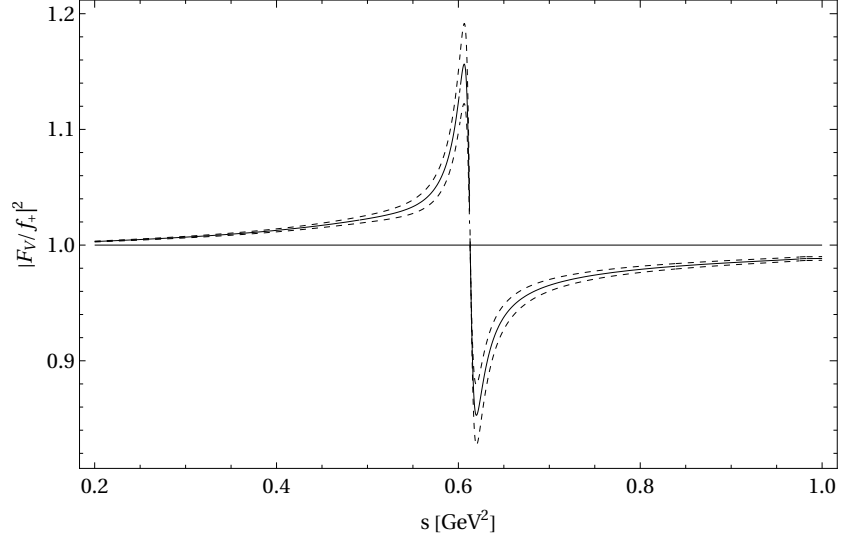


Figure 7.16: Ratio of the form factors (FF1) for  $\theta_{\rho\omega} = (-3.5 \pm 0.7) \times 10^{-3} \text{ GeV}^2$ . The solid line represents the mean value.

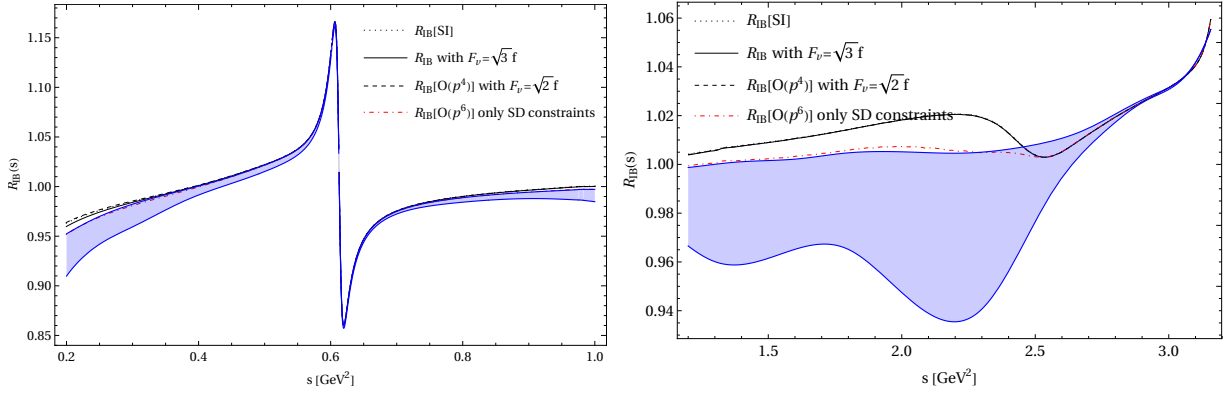


Figure 7.17: Full IB correction factor  $R_{IB}(s)$  for the different orders of approximation in  $G_{EM}(s)$  using the central values given in (FF1). The blue region corresponds to the (over-estimated) corrections at  $\mathcal{O}(p^6)$  in  $G_{EM}(s)$ .

where

$$\mathcal{N}(s) = \frac{3|V_{ud}|^2}{2\pi\alpha_0^2 m_\tau^2} s \left(1 - \frac{s}{m_\tau^2}\right)^2 \left(1 + \frac{2s}{m_\tau^2}\right). \quad (7.72)$$

Using the most recent data obtained from BaBar [20]<sup>31</sup> for the  $e^+e^- \rightarrow \pi^+\pi^-(\gamma)$  cross section and taking the same numerical inputs as we did for FF1, we get

$$B_{\pi\pi^0}^{CVC} = \begin{cases} (24.76 \pm 0.11 \pm 0.25 \pm 0.01 \pm 0.01 \pm 0.02)\%, & \text{SI,} \\ (24.77 \pm 0.11 \pm 0.25 \pm 0.01 \pm 0.01 \pm 0.02)\%, & F_V = \sqrt{2}F, \\ (24.77 \pm 0.11 \pm 0.25 \pm 0.01 \pm 0.01 \pm 0.02)\%, & F_V = \sqrt{3}F, \\ (24.80 \pm 0.11 \pm 0.25 \pm 0.01 \pm 0.01 \pm 0.02)\%, & \text{SD,} \end{cases} \quad (7.73)$$

where ‘SI’, ‘ $F_V = \sqrt{2}F$ ’, ‘ $F_V = \sqrt{3}F$ ’ and ‘SD’ correspond to the different approximations of the  $G_{EM}(s)$  factor. The result for  $F_V = \sqrt{2}F$  is our reference one, with a negligible uncertainty from the missing higher-order terms starting at  $\mathcal{O}(p^6)$ .

On the other hand, when we use the same numerical inputs as in the case of FF2, we get (again our reference result is the  $F_V = \sqrt{2}F$  one, with the uncertainties quoted below)

$$B_{\pi\pi^0}^{CVC} = \begin{cases} (24.57 \pm 0.11 \pm 0.08 \pm 0.01 \pm 0.01 \pm 0.02)\%, & \text{SI,} \\ (24.57 \pm 0.11 \pm 0.08 \pm 0.01 \pm 0.01 \pm 0.02)\%, & F_V = \sqrt{2}F, \\ (24.58 \pm 0.11 \pm 0.08 \pm 0.01 \pm 0.01 \pm 0.02)\%, & F_V = \sqrt{3}F, \\ (24.61 \pm 0.11 \pm 0.08 \pm 0.01 \pm 0.01 \pm 0.02)\%, & \text{SD.} \end{cases} \quad (7.74)$$

In both cases, the first error corresponds to the statistical experimental uncertainty on  $\sigma_{\pi\pi(\gamma)}$ , the second is related to uncertainty on the  $\rho^+ - \rho^0$  width difference, the third to the uncertainty in the  $\rho^+ - \rho^0$  mass difference and the fourth to the uncertainty of the  $\rho - \omega$  mixing. The last error corresponds to the corrections induced by FSR on  $B_{\pi\pi^0}^{CVC}$ , which reduces  $\sim -0.20(2)\%$  the  $\pi\pi$  branching fraction.

If we include all the couplings contributing to  $G_{EM}(s)$  at  $\mathcal{O}(p^6)$  according to section 7.2.5

---

<sup>31</sup>We thank to Alex Keshavarzi and Bogdan Malaescu for providing us tables with the measurement of the  $e^+e^- \rightarrow \pi^+\pi^-(\gamma)$  cross section.

we have an additional error associated to the EM contributions. Thus, we get

$$B_{\pi\pi^0}^{CVC} = (24.80 \pm 0.11 \pm 0.25 \pm 0.01 \pm 0.01 \pm 0.02_{-0.01}^{+0.21})\%, \quad (7.75)$$

for FF1, and

$$B_{\pi\pi^0}^{CVC} = (24.61 \pm 0.11 \pm 0.08 \pm 0.01 \pm 0.01 \pm 0.02_{-0.01}^{+0.21})\%. \quad (7.76)$$

for FF2. Both previous results match perfectly our reference determinations obtained with  $F_V = \sqrt{2}F$ .

These results are in good agreement (though better for FF1) with the value reported by the Belle [18] collaboration,

$$B_{\pi\pi^0}^\tau = (25.24 \pm 0.01 \pm 0.39)\%, \quad (7.77)$$

where the first uncertainty is statistical and the second is systematic. Nonetheless, they are in some tension with the very precise ALEPH measurement  $(25.471 \pm 0.097 \pm 0.085)\%$  [397].

We show in fig. 7.18 the prediction for the  $e^+e^- \rightarrow \pi^+\pi^-$  cross section using the data reported by Belle [18] (as it is the most precise measurement of this spectrum) for the normalized spectrum  $(1/N_{\pi\pi})(dN_{\pi\pi}/ds)$  compared to the last measurements from BaBar [20] and KLOE [58]<sup>32</sup>.

We recall that the  $e^+e^- \rightarrow \pi^+\pi^-$  cross section obtained using  $\tau$  data is given by [18]

$$\sigma_{\pi\pi}^0 = \frac{1}{\mathcal{N}(s)} \times \left(\frac{B_{\pi\pi}}{B_e}\right) \times \left(\frac{1}{N_{\pi\pi}} \frac{dN_{\pi\pi}}{ds}\right) \left(\frac{R_{IB}(s)}{S_{EW}}\right). \quad (7.78)$$

In fig. 7.18 the  $\tau$ -based prediction is obtained using the  $\mathcal{O}(p^4)$  result for  $G_{EM}(s)$ , with the estimated uncertainty from missing higher-order corrections given by the result at  $\mathcal{O}(p^6)$  (employing only the SD constraints). The blue dotted line shown overestimates the error

---

<sup>32</sup>We have chosen to show in the comparison these two  $e^+e^-$  data sets as the results from both Colls. are those deviating the most, and thus mainly responsible from the tension in  $\sigma(e^+e^- \rightarrow \pi^+\pi^-)$ .

at  $\mathcal{O}(p^6)$ .

From fig. 7.18, we observe good agreement between the BaBar data and the  $\tau$  decays prediction (slightly better for FF1) <sup>33</sup>. The previous comparisons make us consider our evaluation with FF1 the reference one (so that its difference with FF2 will assess the size of the error induced by IB among the  $\rho \rightarrow \pi\pi\gamma$  decay channels) <sup>34</sup>.

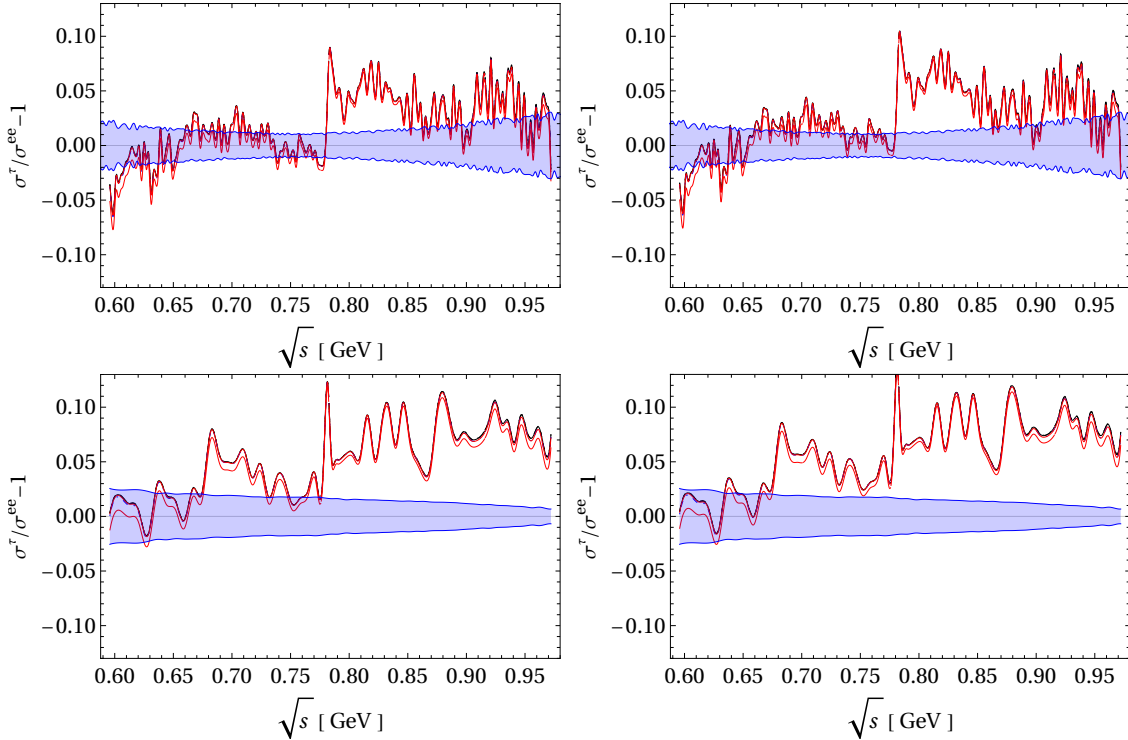


Figure 7.18: Comparison between the different data sets from BaBar (above) and KLOE (below) with  $\Delta\Gamma_{\pi\pi\gamma} = 1.5$  MeV (left-hand) and  $\Delta\Gamma_{\pi\pi\gamma} = 0.45$  MeV (right-hand) for FF1 and FF2, respectively. The blue region corresponds to the experimental error on  $\sigma_{\pi\pi(\gamma)}$ . The solid and dashed lines represent the contributions with  $F_V = \sqrt{3}F$  and  $F_V = \sqrt{2}F$  at  $\mathcal{O}(p^4)$ , respectively. The dotted line is the SI contribution. The red line depicts the envelope of  $G_{EM}(s)$  at  $\mathcal{O}(p^6)$ , that overestimates the uncertainty at this order. The blue dotdashed line is the  $\mathcal{O}(p^6)$  contribution using only SD constraints.

Using Eq. (7.78) we evaluate the IB-corrected  $a_\mu^{HVP,LO}[\pi\pi, \tau]$  from the Belle mass spectrum. We use the PDG values [541] for  $m_\tau$ ,  $V_{ud}$  and  $B_e$ .

<sup>33</sup>One can also check how important the  $\rho^+ - \rho^0$  width difference is around  $s \simeq M_\rho^2$ .

<sup>34</sup>We, nevertheless, recall that recent BESIII data [59] and evaluations within the Hidden Local Symmetry model [50, 716–718] agree better with the KLOE data than with BaBar's.

In tables 7.7 (7.8) we show IB-corrected  $a_\mu^{HVP,LO}[\pi\pi, \tau]$  in units of  $10^{-10}$  using the measured mass spectrum by Belle (ALEPH). For each dataset, results for the different approximations to  $G_{EM}(s)$  are shown. We choose showing first the results with both Belle and ALEPH datasets as the first (second) one yields the most accurate spectral function (branching ratio) measurement. As in Ref. [7] (and later works by the Orsay group), the contributions are split in two intervals. In the first one,  $\sqrt{s} \in [2m_{\pi^\pm}, 0.36 \text{ GeV}]$ , (the very scarce) data is not used, as this affects the precision of the integral. Instead, we use the results of the dispersive fits in Ref. [28]. We proceed analogously in tables 7.9 and 7.10 with the CLEO [12] and OPAL [527]<sup>35</sup> measurements.

FF1							
$[s_1, s_2]$	SI	$F_V = \sqrt{2}F$	$F_V = \sqrt{3}F$	SD	min	max	mean
$[0.1296 \text{ GeV}^2, 1 \text{ GeV}^2]$	499.43	499.42	499.05	498.16	492.18	498.41	495.30
$[0.1296 \text{ GeV}^2, 2 \text{ GeV}^2]$	509.47	509.46	509.09	508.14	501.87	508.40	505.13
$[0.1296 \text{ GeV}^2, 3 \text{ GeV}^2]$	509.68	509.67	509.30	508.35	502.08	508.61	505.34
$[0.1296 \text{ GeV}^2, 3.125 \text{ GeV}^2]$	509.72	509.71	509.34	508.40	502.12	508.65	505.39
FF2							
$[s_1, s_2]$	SI	$F_V = \sqrt{2}F$	$F_V = \sqrt{3}F$	SD	min	max	mean
$[0.1296 \text{ GeV}^2, 1 \text{ GeV}^2]$	503.03	503.02	502.65	501.75	495.76	502.01	498.88
$[0.1296 \text{ GeV}^2, 2 \text{ GeV}^2]$	513.08	513.06	512.70	511.75	505.46	512.00	508.73
$[0.1296 \text{ GeV}^2, 3 \text{ GeV}^2]$	513.29	513.28	512.91	511.96	505.66	512.21	508.94
$[0.1296 \text{ GeV}^2, 3.125 \text{ GeV}^2]$	513.33	513.32	512.95	512.01	505.71	512.26	508.98

Table 7.7: IB-corrected  $a_\mu^{HVP,LO}[\pi\pi, \tau]$  in units of  $10^{-10}$  using the measured mass spectrum by Belle with  $B_{\pi\pi} = (25.24 \pm 0.01 \pm 0.39)\%$ . Different approximation to  $G_{EM}(s)$  are displayed in the various columns. The last three of them show the results at  $\mathcal{O}(p^6)$  and their differences overestimate the error at this order. The error of the  $\mathcal{O}(p^4)$  prediction (obtained with  $F_V = \sqrt{2}F$ ) can be quantified from its difference with the SD value (corresponding to the  $\mathcal{O}(p^6)$  contribution using only SD constraints).

Taking into account all di-pion tau decay data from the ALEPH [397], Belle [18], CLEO [12] and OPAL [527] Colls. (the latter yielding the largest contribution to  $a_\mu^{HVP,LO}[\pi\pi]$  ex-

<sup>35</sup>We thank to Jorge Portolés for providing us with the OPAL data set.



FF1							
$[s_1, s_2]$	SI	$F_V = \sqrt{2}F$	$F_V = \sqrt{3}F$	SD	min	max	mean
$[0.1296 \text{ GeV}^2, 1 \text{ GeV}^2]$	495.28	495.27	494.92	494.05	488.25	494.30	491.27
$[0.1296 \text{ GeV}^2, 2 \text{ GeV}^2]$	506.57	506.56	506.21	505.29	499.15	505.53	502.34
$[0.1296 \text{ GeV}^2, 3 \text{ GeV}^2]$	506.82	506.81	506.45	505.53	499.38	505.77	502.58
$[0.1296 \text{ GeV}^2, 3.125 \text{ GeV}^2]$	506.82	506.81	506.46	505.53	499.39	505.78	502.58
FF2							
$[s_1, s_2]$	SI	$F_V = \sqrt{2}F$	$F_V = \sqrt{3}F$	SD	min	max	mean
$[0.1296 \text{ GeV}^2, 1 \text{ GeV}^2]$	498.86	498.85	498.50	497.63	491.81	497.87	494.84
$[0.1296 \text{ GeV}^2, 2 \text{ GeV}^2]$	510.16	510.15	509.80	508.87	502.72	509.12	505.92
$[0.1296 \text{ GeV}^2, 3 \text{ GeV}^2]$	510.41	510.40	510.04	509.12	502.95	509.36	506.16
$[0.1296 \text{ GeV}^2, 3.125 \text{ GeV}^2]$	510.41	510.40	510.05	509.12	502.96	509.36	506.16

Table 7.8: IB-corrected  $a_\mu^{HVP,LO}[\pi\pi, \tau]$  in units of  $10^{-10}$  using the measured mass spectrum by ALEPH with  $B_{\pi\pi} = (25.471 \pm 0.097 \pm 0.085)\%$ . The rest is as in Table 7.7.

FF1							
$[s_1, s_2]$	SI	$F_V = \sqrt{2}F$	$F_V = \sqrt{3}F$	SD	min	max	mean
$[0.1296 \text{ GeV}^2, 1 \text{ GeV}^2]$	498.51	498.50	498.14	497.27	491.43	497.52	494.47
$[0.1296 \text{ GeV}^2, 2 \text{ GeV}^2]$	508.98	508.97	508.61	507.69	501.54	507.93	504.74
$[0.1296 \text{ GeV}^2, 3 \text{ GeV}^2]$	509.15	509.14	508.79	507.86	501.70	508.11	504.91
$[0.1296 \text{ GeV}^2, 3.125 \text{ GeV}^2]$	509.20	509.18	508.83	507.91	501.75	508.15	504.95
FF2							
$[s_1, s_2]$	SI	$F_V = \sqrt{2}F$	$F_V = \sqrt{3}F$	SD	min	max	mean
$[0.1296 \text{ GeV}^2, 1 \text{ GeV}^2]$	502.10	502.09	501.74	500.86	495.00	501.11	498.06
$[0.1296 \text{ GeV}^2, 2 \text{ GeV}^2]$	512.58	512.57	512.22	511.29	505.12	511.58	508.33
$[0.1296 \text{ GeV}^2, 3 \text{ GeV}^2]$	512.76	512.75	512.39	511.47	505.29	511.71	508.50
$[0.1296 \text{ GeV}^2, 3.125 \text{ GeV}^2]$	512.80	512.79	512.43	511.51	505.33	511.75	508.54

Table 7.9: IB-corrected  $a_\mu^{HVP,LO}[\pi\pi, \tau]$  in units of  $10^{-10}$  using the measured mass spectrum by CLEO with  $B_{\pi\pi} = (25.36 \pm 0.44)\%$ . The rest is as in Table 7.7.

FF1							
$[s_1, s_2]$	SI	$F_V = \sqrt{2}F$	$F_V = \sqrt{3}F$	SD	min	max	mean
$[0.1296 \text{ GeV}^2, 1 \text{ GeV}^2]$	509.50	509.51	509.07	508.04	501.31	508.34	504.82
$[0.1296 \text{ GeV}^2, 2 \text{ GeV}^2]$	521.29	521.29	520.86	519.77	512.69	520.06	516.34
$[0.1296 \text{ GeV}^2, 3 \text{ GeV}^2]$	521.49	521.49	521.06	519.96	512.88	520.25	516.56
$[0.1296 \text{ GeV}^2, 3.125 \text{ GeV}^2]$	521.49	521.49	521.06	519.97	512.88	520.26	516.57
FF2							
$[s_1, s_2]$	SI	$F_V = \sqrt{2}F$	$F_V = \sqrt{3}F$	SD	min	max	mean
$[0.1296 \text{ GeV}^2, 1 \text{ GeV}^2]$	512.99	512.99	512.56	511.53	504.78	511.82	508.30
$[0.1296 \text{ GeV}^2, 2 \text{ GeV}^2]$	524.79	524.79	524.36	523.27	516.17	523.56	519.86
$[0.1296 \text{ GeV}^2, 3 \text{ GeV}^2]$	524.99	524.99	524.56	523.46	516.36	523.76	520.06
$[0.1296 \text{ GeV}^2, 3.125 \text{ GeV}^2]$	524.99	524.99	524.56	523.46	516.36	523.76	520.06

Table 7.10: IB-corrected  $a_\mu^{HVP,LO}[\pi\pi, \tau]$  in units of  $10^{-10}$  using the measured mass spectrum by OPAL with  $B_{\pi\pi} = (25.46 \pm 0.17 \pm 0.29)\%$ . The rest is as in Table 7.7.

$a_\mu^{HVP,LO}[\pi\pi, \tau]$			
Experiment	$2m_{\pi^\pm} - 0.36 \text{ GeV}$	$0.36 - 1.8 \text{ GeV}$	TOTAL
Belle	$8.81 \pm 0.00 \pm 0.14_{-0.34}^{+0.16}$	$511.14 \pm 1.94 \pm 7.99_{-2.09}^{+1.91}$	$519.95 \pm 1.94 \pm 7.99_{-2.12}^{+1.91}$
ALEPH	$8.89 \pm 0.00 \pm 0.05_{-0.34}^{+0.16}$	$508.26 \pm 4.48 \pm 2.82_{-2.09}^{+1.91}$	$517.15 \pm 4.48 \pm 2.82_{-2.12}^{+1.91}$
CLEO	$8.85 \pm 0.00 \pm 0.15_{-0.34}^{+0.16}$	$510.63 \pm 3.40 \pm 8.93_{-2.08}^{+1.90}$	$519.48 \pm 3.40 \pm 8.93_{-2.11}^{+1.90}$
OPAL	$8.89 \pm 0.00 \pm 0.12_{-0.34}^{+0.15}$	$522.81 \pm 10.04 \pm 7.00_{-2.12}^{+1.87}$	$531.70 \pm 10.04 \pm 7.00_{-2.15}^{+1.87}$

Table 7.11: IB-corrected  $a_\mu^{HVP,LO}[\pi\pi, \tau]$  in units of  $10^{-10}$  at  $\mathcal{O}(p^4)$ . The first error is related to the systematic uncertainties on the mass spectrum, and also include contributions from the  $\tau$ -mass and  $V_{ud}$  uncertainties. The second error arises from  $B_{\pi\pi^0}$  and  $B_e$ , and the third error from the isospin-breaking corrections.

$a_\mu^{HVP,LO}[\pi\pi, \tau]$			
Experiment	$2m_{\pi^\pm} - 0.36 \text{ GeV}$	$0.36 - 1.8 \text{ GeV}$	TOTAL
Belle	$7.77 \pm 0.00 \pm 0.12_{-0.59}^{+1.20}$	$507.18 \pm 1.91 \pm 7.88_{-3.76}^{+4.72}$	$514.95 \pm 1.91 \pm 7.88_{-3.81}^{+4.87}$
ALEPH	$7.84 \pm 0.00 \pm 0.04_{-0.60}^{+1.21}$	$504.37 \pm 4.35 \pm 2.79_{-3.70}^{+4.63}$	$512.21 \pm 4.35 \pm 2.79_{-3.75}^{+4.78}$
CLEO	$7.80 \pm 0.00 \pm 0.14_{-0.59}^{+1.21}$	$506.74 \pm 3.28 \pm 8.84_{-3.71}^{+4.63}$	$514.54 \pm 3.28 \pm 8.84_{-3.76}^{+4.78}$
OPAL	$7.84 \pm 0.00 \pm 0.10_{-0.60}^{+1.20}$	$518.32 \pm 9.69 \pm 6.92_{-4.12}^{+5.25}$	$526.16 \pm 9.69 \pm 6.92_{-4.16}^{+5.39}$

Table 7.12: IB-corrected  $a_\mu^{HVP,LO}[\pi\pi, \tau]$  in units of  $10^{-10}$  at  $\mathcal{O}(p^6)$ . The rest is as in Table 7.11.

ceeding  $\sim 10.7 \cdot 10^{-10}$  the mean, although with the largest errors as well) in Tables 7.11 and 7.12 at  $\mathcal{O}(p^4)$  and  $\mathcal{O}(p^6)$ , respectively, we get the combined tau-data contribution

$$10^{10} \cdot a_{\mu}^{HVP,LO|\pi\pi,\tau \text{ data}} = 519.6 \pm 2.8_{\text{spectra+BRs}}^{+1.9}_{-2.1IB}, \quad (7.79)$$

at  $\mathcal{O}(p^4)$  and

$$10^{10} \cdot a_{\mu}^{HVP,LO|\pi\pi,\tau \text{ data}} = 514.6 \pm 2.8_{\text{spectra+BRs}}^{+5.0}_{-3.9IB}, \quad (7.80)$$

at  $\mathcal{O}(p^6)$ .

The *IB* errors come from the uncertainty on  $\Gamma(\rho \rightarrow \pi\pi\gamma)$  (FF1 vs FF2) and either from the difference between the  $F_V = \sqrt{2}F$  and *SD* results (in Eq. (7.79)) or from the difference between the 'mean' and 'min'/'max' results (in Eq. (7.80)).

Contrary to previous estimates [7, 91, 94, 406, 655], the errors in  $a_{\mu}^{HVP,LO|\pi\pi,\tau \text{ data}}$  happen to be dominated by the uncertainty on the *IB* contributions (but for the lower error on Eq. (7.79)).

When Eqs. (7.79) and (7.80) are supplemented with the four-pion tau decays measurements (up to 1.5 GeV) and with  $e^+e^-$  data at larger energies in these modes (and with  $e^+e^-$  data in all other channels making up the hadronic cross section), we get [48, 655]

$$10^{10} \cdot a_{\mu}^{HVP,LO|\tau \text{ data}} = 705.7 \pm 2.8_{\text{spectra+BRs}}^{+1.9}_{-2.1IB} \pm 2.0_{e^+e^-} \pm 0.1_{\text{narrowres}} \pm 0.7_{QCD}, \quad (7.81)$$

at  $\mathcal{O}(p^4)$ , and

$$10^{10} \cdot a_{\mu}^{HVP,LO|\tau \text{ data}} = 700.7 \pm 2.8_{\text{spectra+BRs}}^{+5.0}_{-3.9IB} \pm 2.0_{e^+e^-} \pm 0.1_{\text{narrowres}} \pm 0.7_{QCD}, \quad (7.82)$$

at  $\mathcal{O}(p^6)$  and we have also included the uncertainties corresponding to using  $e^+e^-$  data for those contributions not covered by tau decay measurements and to the inclusion of narrow resonances and the perturbative QCD part.

Adding errors in quadrature, an uncertainty of  ${}_{-4.1}^{+4.0}$  ( ${}_{-5.2}^{+6.1}$ ) is obtained at  $\mathcal{O}(p^4)$  ( $\mathcal{O}(p^6)$ ). These numbers (all in units of  $10^{-10}$ ) have to be compared with the error of 4.0 in Ref. [6].

When all other (QED, EW and subleading hadronic) contributions are added to eqs.

(7.81) and (7.82) according to Ref. [6], the  $4.2\sigma$  [6] deficit of the SM prediction with respect to the experimental average (FNAL+BNL) [95,96] is reduced to

$$\Delta a_\mu \equiv a_\mu^{exp} - a_\mu^{SM} = (12.5 \pm 6.0) \cdot 10^{-10}, \quad (7.83)$$

at  $\mathcal{O}(p^4)$ , and

$$\Delta a_\mu \equiv a_\mu^{exp} - a_\mu^{SM} = (17.5_{-7.5}^{+6.8}) \cdot 10^{-10}, \quad (7.84)$$

at  $\mathcal{O}(p^6)$ , which are  $2.1$  and  $2.3\sigma$ , respectively.

In figure 7.19 we show a comparison between our  $\mathcal{O}(p^4)$  and  $\mathcal{O}(p^6)$  calculation with respect to the estimation based in the  $e^+e^-$  data driven [6] and the lattice results from the BMW collaboration [43].

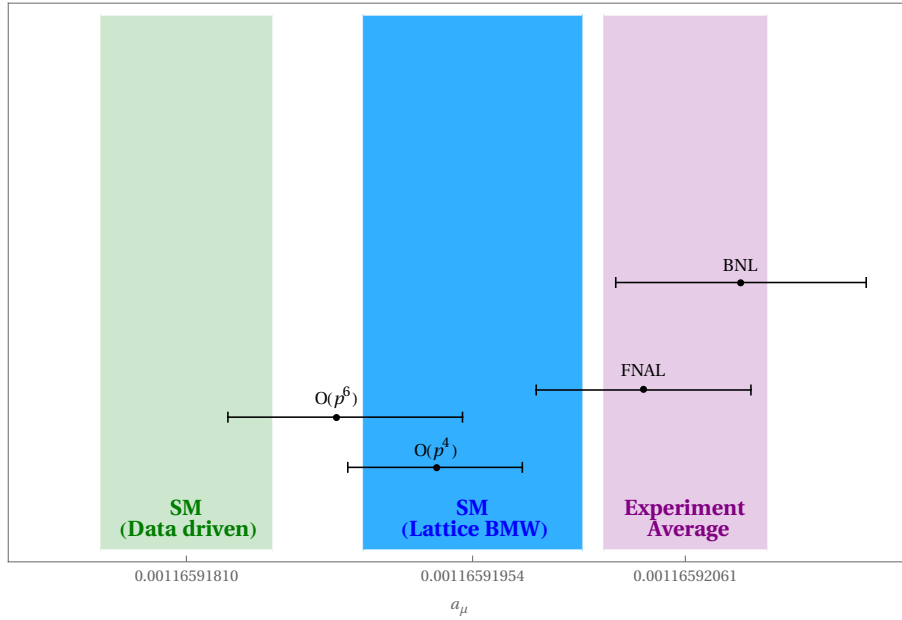


Figure 7.19: Comparison between the experimental values of  $a_\mu$  from BNL [95] and FNAL [96] with respect to the Muon  $g - 2$  Theory Initiative recommended value [6], the lattice QCD calculation from the BMW collaboration [43] and our results [97].

## 7.5 Conclusions

In this work we have revisited the resonance chiral Lagrangian computation of the isospin-breaking and radiative corrections to the  $\tau^- \rightarrow \pi^- \pi^0 \nu_\tau \gamma$  decays in Ref. [94], by including the terms that start to contribute to the  $\mathcal{O}(p^6)$  chiral LECs. Our main motivation for that was to revisit the determination of  $a_\mu^{HVP,LO}$  using tau decay data, so that it could -when combined with the  $e^+e^-$  measurements- reduce the Standard Model error on  $a_\mu$ , thus enhancing the sensitivity to new physics of the current BNL and future FNAL and J-PARC measurements.

Our isospin breaking corrections improve the agreement between  $\tau$  and  $e^+e^-$  di-pion data (both in the spectrum and its integral), which endorses our evaluation of  $a_\mu^{HVP,LO|\tau \text{ data}}$ . Our main results are  $a_\mu^{HVP,LO|\tau \text{ data}} = (705.7^{+4.0}_{-4.1}) \cdot 10^{-10}$  (including the same contributions as in Ref. [94]), and  $a_\mu^{HVP,LO|\tau \text{ data}} = (700.7^{+6.1}_{-5.2}) \cdot 10^{-10}$  (when the operators starting to contribute to the  $\mathcal{O}(p^6)$  LECs are also considered). These reduce the anomaly  $\Delta a_\mu \equiv a_\mu^{exp} - a_\mu^{SM}$  to 2.0 and 2.3  $\sigma$ , respectively.

We also provide with a detailed study of the  $\pi\pi$  spectrum,  $E_\gamma$  distribution and branching ratio, for different cuts on the photon energy. These  $\tau^- \rightarrow \pi^- \pi^0 \nu_\tau \gamma$  decays observables have the potential to reduce drastically the error of our predictions, so we eagerly await their measurement at Belle-II.

# Chapter 8

## Lamb shift and hyperfine splitting in muonic hydrogen

### 8.1 Introduction

The energy levels of muonic atoms are very sensitive to effects of quantum electrodynamics (QED), nuclear structure, and recoil, thanks to the muon mass, which is about 206 times heavier than the electron [719]. The enhancement factor, as compared to H, is of order  $(m_\mu/m_e)^3 \sim 10^7$ , making muonic hydrogen ( $\mu H$ ) a neat laboratory for studies of the proton structure.

The measurement of the Lamb shift in muonic hydrogen [103] has encouraged great renewed interest in the energy levels of muonic atoms. Precise research of the Lamb shift (LS) and hyperfine structure (HFS) of light muonic atoms is an elemental issue for testing the Standard model, particularly the QED calculations, establishing the exact values of SM parameters, like the Rydberg constant, detailed study of the proton structure, and searching for effects of new physics [720]. A number of theoretical analyses of the Lamb shift (the  $2p-2s$  transition) in light muonic atoms have been published [721–730] before the measurement was performed.

The last decade has witnessed a remarkable breakthrough in the laser spectroscopy of

muonic atoms, starting from the long-awaited observation of the  $2S - 2P$  transition in  $\mu H$  by the CREMA Collaboration [102, 103]. This measurement appears to be quite far from the predicted value, which made it very hard to find, and very fascinating when observed. It presumed a proton charge radius,  $r_P$ , which was  $7\sigma$  smaller than the state-of-the-art value at that time (see CODATA '10 [100] in Fig. 8.1). The CODATA value encompasses decades of  $r_P$  determinations using the traditional techniques:  $ep$  scattering and  $H$  spectroscopy. This huge discrepancy, known as the proton-radius puzzle, motivated a wealth of activity at the intersection of nuclear, particle, and atomic physics, reaching out to physics beyond the Standard Model [731–734]. The subsequent measurements of the  $\mu D$  Lamb shift [121] showed a similar discrepancy for the deuteron charge radius,  $r_d$ , see Fig. 8.2. These two measurements are related by the  $H - D$  isotopic shift measurement of the  $1S - 2S$  transitions [735], which restraint the difference,  $r_d^2 - r_p^2$ . They are sometimes commonly referred to as the “ $Z = 1$  radius puzzle”, highlighting that no such discrepancy has been found in muonic helium [736]. When the theory updates in Refs. [101, 120] are used, the  $r_p$  value obtained from  $\mu D$  via the isotopic shift is in agreement with the value extracted from  $\mu H$  at the permille level.

At present, more than a decade after the radius-puzzle installment, there is some consensus, adopted also by the CODATA group [98], that the  $\mu H$  value is an order-of-magnitude more precise, and also, more accurate. The discrepancy with the previous extractions may simply lie in unaccounted systematic uncertainties. This view is supported by some of the recent measurements using  $H$ . Aside from the  $H(1S - 3S)$  transition measurement by the Paris group [107], the other four new measurements in  $H$  gave smaller radii than the CODATA '10: three of them agree with the muonic results [105, 106, 108], while a very recent measurement of the  $H(2S - 8D)$  [104] shows a slightly tension.

On the side of  $ep$  scattering, the recent PRad experiment [109] has found a smaller value of  $r_p$ , in agreement with  $\mu H$ , confirming different analysis of scattering data that agree with the muonic result [110, 111, 115–118]. The initial-state radiation experiment at MAMI does not allow to discriminate between the small and large scenarios at this time [737] since it

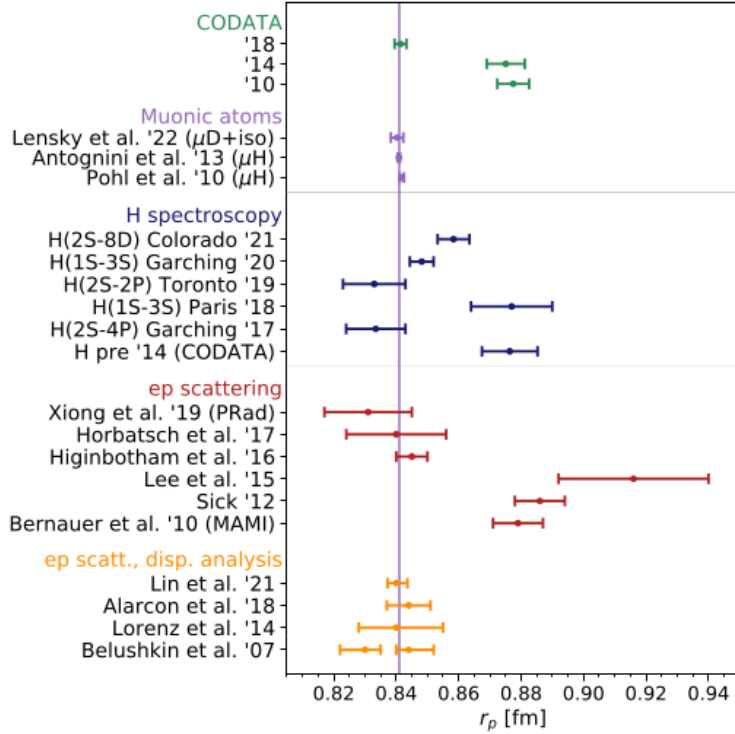


Figure 8.1: Selection of recent proton charge radius determinations [8]. The band corresponds to the  $\mu H$ '13 value. The references are (from top to bottom): CODATA [98–100], muonic atoms [101–103],  $H$  spectroscopy [99,104–108],  $ep$  scattering [109–114], dispersive analysis of  $ep$  scattering [115–118].

has a larger uncertainty.

In Fig. 8.1, the discrepancy is diffused quite considerably by the latest results. However, this problem has not become clear and a new round of experiments is underway, which include the first measurements from  $\mu p$  scattering by MUSE [738] and AMBER collaborations [739], improved  $ep$  scattering measurements from PRAD-II [740] and the PRES Collaboration at MAMI, as well as spectroscopy measurements of  $H$  in Rydberg states [741],  $He^+(1S - 2S)$  [742,743] and simple molecules such as  $HD^+$ ,  $H_2^+$  and  $H_2$ .

Even if the proton-radius puzzle vanishes, several aspects of the underlying theory can be studied just by performing more precise measurements. For instance, the proton radius from  $\mu H$ , in combination with the  $1S - 2S$  transition in  $H$ , leads to the most precise determination of the Rydberg constant  $R_\infty$ . When it is combined with the  $H - D$  isotopic shift, the most



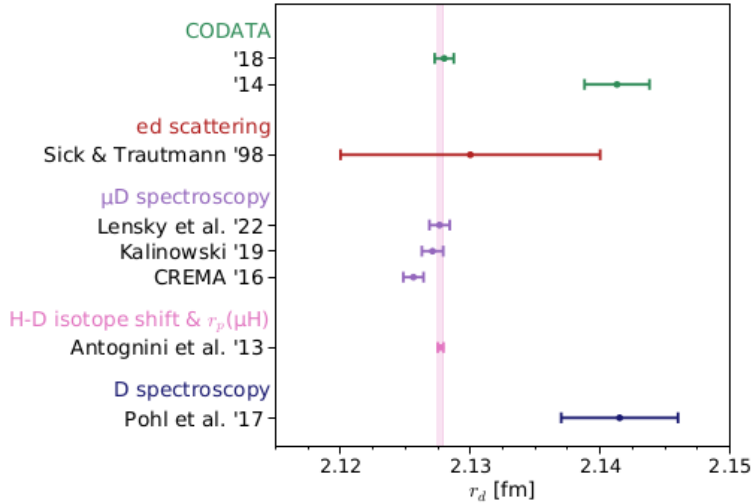


Figure 8.2: Deuteron charge radius determinations [8]. The results here correspond to: CODATA [98, 99], *ed* scattering [119],  $\mu D$  spectroscopy [101, 120, 121],  $H - D$  isotopic shift and  $\mu H$  Lamb shift [102],  $D$  spectroscopy [122].

precise determination of the deuteron radius can be obtained. Subsequently, in combination with the measured Lamb shift in  $\mu D$ , it provides a stringent test for the theory of the deuteron structure, viz., the nucleon-nucleon interaction. The proton radius in combination with the spectroscopy of  $H$ ,  $D$ ,  $HD^+$  and other simple systems, can be used to achieve precision tests of bound-state QED for few-body systems, which impacts the precision of several fundamental quantities. Although the current  $HD^+$  results barely favor the muonic ones [744], its potential is huge. On the scattering side, the precise value of  $r_p$  permits a better determination of the proton electric form factor  $G_{E_p}(Q^2)$ . Thanks to the increased precision, one becomes sensitive to some scenarios of physics beyond the Standard Model, in addition to those proposed as explanation of the puzzle in the first place [745–748].

Another important topic concerns the ongoing efforts to measure the ground-state hfs in  $\mu H$ . The CREMA Collaboration aims to measure with a precision of 1 ppm by means of pulsed laser spectroscopy. Besides, two other collaborations, at J-PARC [749] and RIKEN-RAL [126, 750–753], are planning measurements of these transitions using different techniques. The hfs resonance is two orders of magnitude narrower than the  $2S - 2P$  line width,

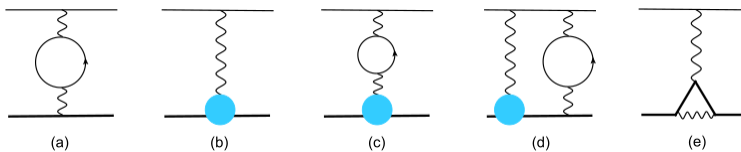


Figure 8.3: Main corrections in  $\mu H$ . Here, the cyan blobs represent the finite-size effects, thin and thick lines the muon and proton, respectively.

and therefore, difficult to find. Further details can be found in Ref. [8].

## 8.2 Nuclear effects in hydrogen-like atoms

Muonic atoms have a small Bohr radius, and thus, a larger sensitivity to nuclear structure, and short-range effects in general. Whilst the finite-size contribution is improved by a factor of  $10^7$ , relative to normal atoms, the QED effects contributing to the  $2S - 2P$  splitting is increased only by a factor of 50, promoting the finite-size contribution to be the second largest contribution, surpassed only by the one-loop eVP, shown in Fig. 8.3(a). There are plenty of Refs. [721, 722, 754–756] accounting for these effects. However, a more precise calculation will always be welcome, as soon as a more precise measurement emerges. Important for this program is the progress on the nuclear side, since many of the corrections require the input of nuclear and nucleon form factor and structure functions.

The first contribution comes from solving the Coulomb problem by using either the Dirac or Schrödinger equation [757]. It assumes a point-like nucleus with the electric charge  $Ze$ , thus the effects beyond this approximation arise as perturbative corrections to the Lamb shift, fine and hyperfine structure; organized in powers of the fine-structure constant  $\alpha = e^2/4\pi$ , and mass ratios. Among the nuclear-structure effects, (i) the *finite-size* effects come from the fact that the nucleus is not a point but it has a smeared electromagnetic distribution, Fig. 8.3(b-d), and (ii) the *polarizability* effects in Fig. 8.3(a) is caused by deformations of this distribution within the atom. The finite-size effects can be entirely described by the elastic form factors, like  $G_E(Q^2)$  and  $G_M(Q^2)$  in case of a spin-1/2 nucleus, while the polarizability ones require a more complicated input, viz., structure functions.

## 8.3 Theory updates and future $\mu H$

Perturbation theory is used to calculate the various corrections to the energy levels, involving an expansion of both operators and wave functions. The radiative (QED) corrections are obtained in an expansion in  $\alpha$ , binding effects and relativistic effects in  $(Z\alpha)$ , and recoil corrections in the ratio of the masses of the two-body system ( $m/M$ ), where  $Z = 1$  is the atomic charge number and  $\alpha$  is the fine structure constant [758]. The contributions related to the proton structure are in part described by an expansion in powers of  $r_E$  and  $r_Z$ .

### 8.3.1 Lamb shift in $\mu H$

Two transition frequencies in muonic hydrogen have been measured. One starts from the  $2S$ -triplet state  $\nu_t = 2P_{3/2}^{F=2} - 2S_{1/2}^{F=1}$  [102] and the other from the  $2S$ -singlet state  $\nu_s = 2P_{3/2}^{F=1} - 2S_{1/2}^{F=0}$  [102, 103], Fig. 8.4C. The principle of the muonic hydrogen Lamb shift experiment [102] is to form muonic hydrogen in the  $2S$  state (Fig. 8.4A) and measure the  $2S - 2P$  energy splitting (Fig. 8.4C) by means of laser spectroscopy (Fig. 8.4B).

From these two transition measurements, the Lamb shift ( $\Delta E_L = \Delta E_{2P_{1/2} - 2S_{1/2}}$ ) and the  $2S$ -HFS splitting ( $\Delta E_{HFS}$ ) can be deduced independently by the linear combination [758]

$$\begin{aligned} \frac{1}{4}h\nu_s + \frac{3}{4}h\nu_t &= \Delta E_L + 8.8123(2)\text{meV} \\ h\nu_s - h\nu_t &= \Delta E_{HFS} - 3.2480(2)\text{meV}. \end{aligned}$$

Finite size effects are included in  $\Delta_L$  and  $\Delta E_{HFS}$ . This terms include the calculated values of the  $2P$  fine structure, the  $2P_{3/2}$  hyperfine splitting, and the mixing of the  $2P$  states [722, 754, 759, 760]. The finite proton size effects on the  $2P$  fine and hyperfine structure are smaller than  $1 \cdot 10^{-4}$  meV because of the small overlap between the  $2P$  wave functions and the nucleus. Their uncertainties arising from the proton structure are then negligible. Using the measured transition frequencies  $\nu_s$  and  $\nu_t$  and Eq. (8.1), they found [102]

$$\begin{aligned} \Delta E_L^{\text{exp}} &= 202.3706(23)\text{meV}, \\ \Delta E_L^{\text{exp}} &= 22.8089(51)\text{meV}, \end{aligned} \tag{8.1}$$

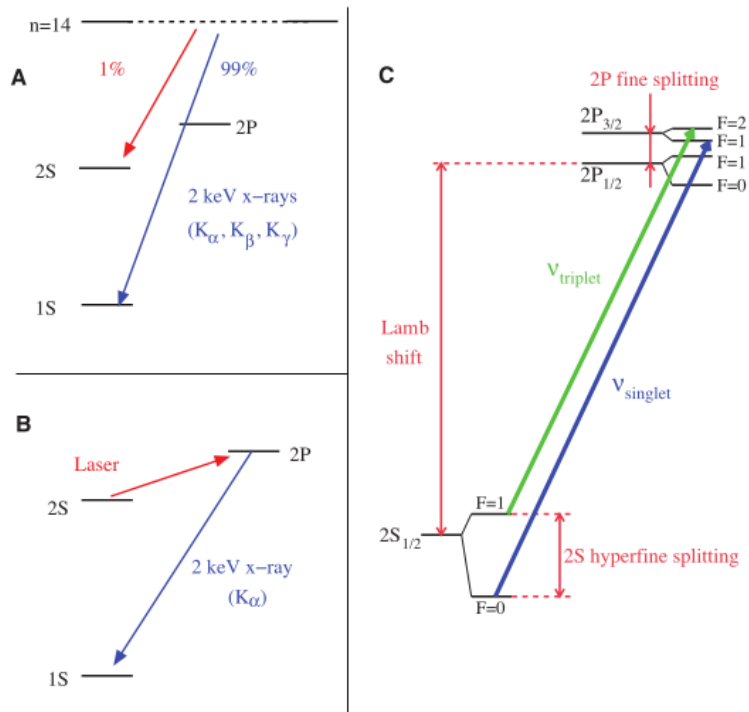


Figure 8.4: (A) Formation of  $\mu H$  in highly excited states and subsequent cascade with emission of “prompt”  $K_{\alpha,\beta,\gamma^*}$ . (B) Laser excitation of the 2S - 2P transition with subsequent decay to the ground state with  $K_\alpha$  emission. (C) 2S and 2P energy levels. The measured transitions  $\nu_s$  and  $\nu_t$  are indicated along with the Lamb shift, 2S-HFS, and 2P-Pine and hyperfine splitting. Reprinted from Ref. [102].

The statistical and systematic uncertainties of  $\nu_s$  and  $\nu_t$  have been added quadratically to get the final result.

On the theory side, the updated summary for the  $\mu H$  Lamb shift is given in Eq. (8.2). Its accuracy is limited by the  $2\gamma$  exchange, finite-size effects and the hVP.

$$E_{1P-2S}(\mu H) = \left[ \underbrace{205.0074}_{\text{Uehling}} + \underbrace{1.0153}_{r_p \text{ indep.}} + \underbrace{0.0114(3)}_{\text{hVP}} + \underbrace{0.0006(1) - 5.2275(10) \left(\frac{r_p}{\text{fm}}\right)^2}_{\text{f.s. corr.}} - \underbrace{E_{2S}^{(2\gamma)}}_{2\gamma \text{ exchange}} \right] \text{meV}, \quad (8.2)$$

Utilizing the data-driven evaluation of the  $2\gamma$ -exchange in Ref. [761],  $\Delta E_{2S}^{(2\gamma)} = -33(2) \mu\text{eV}$ , one gets [8]

$$r_p(\mu H) = 0.84099(12)_{\text{sys}}(23)_{\text{stat}}(3)_{\text{hVP}}(8)_{\text{f.s.}}(23)_{2\gamma} \text{ fm} = 0.84099(36) \text{ fm}, \quad (8.3)$$

where  $r_p$  is the root mean square (RMS) charge radius given in fm and defined as  $r_p^2 = \int d^3r r^2 \rho_E(r)$  with  $\rho_E$  being the normalized proton charge distribution.

The uncertainty of the radius is restricted by the precision of the  $2S - 2P$  measurements and the prediction of the  $2\gamma$ -exchange contribution, with the measurement accuracy limited by statistics. The frequency uncertainty of the laser pulses delivered by the Raman cell (the last stage of the laser system used to generate the pulses at  $6 \mu\text{m}$ ) gives the systematic uncertainty of 300 MHz. The typical atomic physics systematics like Stark, collisional and Zeeman shifts are strongly suppressed in the tightly-bound  $\mu H$  atom.

The CREMA setup can be upgraded to improve the  $2S - 2P$  measurements by a factor 5, accessible by increasing the statistics by 25 and reducing the systematics by 3. On the one hand, by having a longer data-taking time (from 1 week to 5 weeks) and by increasing the laser pulse energy (from 0.2 mJ to 1 mJ), in addition to a slight improvement of the setup, the statistics could be improved. On the other hand, the systematics could be reduced by using novel optical parametric down-conversion technologies under progress for the measurements of the HFS in  $\mu H$ . Developments in this technology enable increasing both the laser pulse

energy and the frequency control.

### 8.3.2 Hyperfine splitting in $\mu H$

The interaction between the bound particle and the magnetic field induced by the magnetic moment of the nucleus give rise to shifts and splittings of the energy levels dubbed hyperfine effects. In classical electrodynamics, the interaction between the magnetic moments  $\boldsymbol{\mu}_p$  and  $\boldsymbol{\mu}_\mu$  of proton and muon, respectively, is described by [762]

$$H_{HFS}^{\text{classical}} = -\frac{2}{3}\boldsymbol{\mu}_p \cdot \boldsymbol{\mu}_\mu \delta(\mathbf{r}), \quad (8.4)$$

where  $\delta(\mathbf{r})$  is the delta-function in coordinate space. A similar Hamiltonian can be derived in quantum field theory from the one-photon exchange diagram. Using coulomb wave function, this gives rise in the first-order perturbation theory to an energy shift for muonic hydrogen  $nS$ -states of [754]

$$\begin{aligned} E_{\text{HFS}}(F) &= \frac{4(Z\alpha)^4 m_\tau^3}{3n^3 m_\mu m_p} (1 + \kappa)(1 + a_\mu) \frac{1}{2} \left[ F(F+1) - \frac{3}{2} \right] \\ &= \Delta E_{\text{Fermi}} \frac{1}{2} \left[ F(F+1) - \frac{3}{2} \right], \end{aligned} \quad (8.5)$$

where  $\Delta E_{\text{Fermi}} = 22.8320 \text{ meV}$  [754] is the Fermi energy,  $m_p$  is the proton mass,  $F$  is the total angular momentum,  $\kappa$  and  $a_\mu$  are the proton and muon anomalous magnetic moments, respectively. The  $F = 1$  state is shifted by  $1/4 \times 22.8320 \text{ meV}$  while the  $F = 0$  state by  $-3/4 \times 22.8320 \text{ meV}$ , see Fig. 8.4c. A summary of the corrections arising from QED, recoil, nuclear structure, hadronic and weak interactions effects can be found in Table 3 in Ref. [758].

The structure-dependent corrections, scaling as the reduced mass of the system, become large in  $\mu H$  compared to hydrogen. The largest correction is given by finite-size effect which, in the non-relativistic limit, is given by the well-known Zemach term [763, 764]

$$\Delta E_{\text{Zemach}} = -\Delta E_{\text{Fermi}} \cdot 2(Z\alpha)m_\tau r_Z, \quad (8.6)$$

where  $r_Z$  is the Zemach radius defined as

$$r_Z = \int d^3r \int d^3r' r' \rho_E(\mathbf{r}) \rho_M(\mathbf{r} - \mathbf{r}'), \quad (8.7)$$

with  $\rho_M$  and  $\rho_E$  being the normalized proton magnetization and charge distributions, respectively. The convolution between charge and magnetization distribution in  $r_Z$  is a consequence of the interaction of the proton spin distributed spatially (given by the magnetic form factor) with the spatial distribution of the muon spin which is described by the atomic muon wave function. The latter is slightly affected, particularly at the origin, by the charge-finite-size effect and consequently by  $\rho_E$ . In a quantum field framework, this contribution arises from two-photon exchange processes. The intermediate virtual proton may be either “on-shell” or “off-shell”, as in the case of the Lamb shift. Therefore, proton polarizability contributions need to be accounted for [765]. This term has the largest uncertainty. It emerges from the uncertainty of the polarized structure functions  $g_1$  [766, 767] and  $g_2$  [768] (measured in inelastic polarized electron-proton scattering) needed as an input to evaluate this contribution. For the HFS (contrary to the Lamb shift), no subtraction term is required for the calculation of the two-photon exchange diagram via Compton scattering and dispersion analysis [769].

The Zemach-radius contribution can be evaluated based on empirically known form factors [8]

$$r_Z = -\frac{4}{\pi} \int_0^\infty \frac{dQ}{Q^2} \left[ \frac{G_E(Q^2)G_M(Q^2)}{1 + \kappa_N} - 1 \right]. \quad (8.8)$$

A recent dispersive analysis of the nucleon electromagnetic form factors from the Bonn group [115] yields:

$$r_{Z_p} = 1.054^{(+0.003)}_{(-0.002)} \text{stat} \text{ } ^{(+0.000)}_{(-0.001)} \text{sys} \text{ fm}, \quad \Delta_Z(\mu H) = -7403^{+21}_{-16} \text{ppm}. \quad (8.9)$$

On the other hand, one can determine this contribution from the experimental HFS, given predictions for the remaining theory contributions. At the moment, only the 1S-HFS in  $H$  and the 2S-HFS in  $\mu H$  have been measured. The corresponding extractions of the Zemach radius are depicted in Table 8.1 and compared with the form-factor determinations. Given

$ep$ scattering		$\mu H$ 2S HFS		$H$ 1S HFS	
Lin et al. [115]	Borah et al. [770]	Antognini et al. [102]	$B\chi PT$ [771]	Volotka et al. [125]	$B\chi PT$ [771]
$1.054^{+0.003}_{-0.002}$	1.0227(107)	1.082(37)	1.041(31)	1.045(16)	1.012(14)

Table 8.1: Determinations of the proton Zemach radius  $r_{Z_p}$ , in units of fm [8].

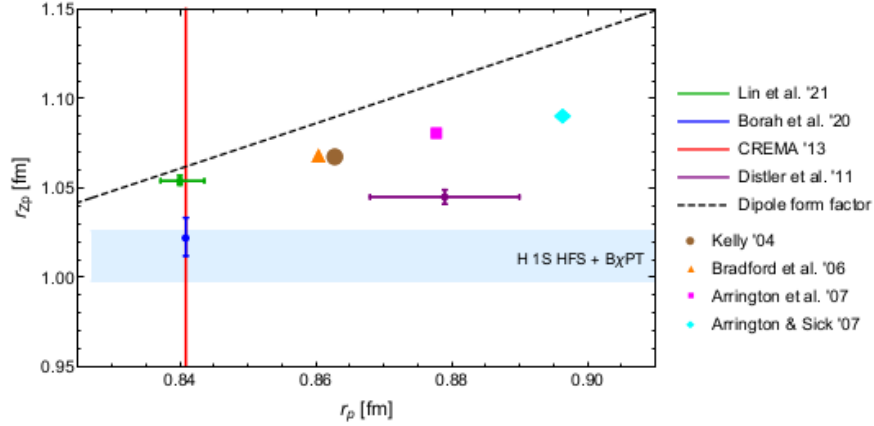


Figure 8.5: Correlation between the Zemach and charge radius of the proton.

that baryon  $\chi PT$  ( $B\chi PT$ ) gives a smaller prediction for the polarizability contribution than data-driven evaluations, it also gives a smaller Zemach radius.

There is a considerable linear correlation between the Zemach and charge radius, see Fig. 8.5. The black dashed line represents the usual dipole approximation,  $1/(1 + Q^2/\Lambda^2)^2$ , for the form factors  $G_E$  and  $G_M$ . This correlation is more general since the proton size is set predominantly by one QCD scale,  $\Lambda_{QCD}$ . In Fig. 8.5, the current determination of  $r_{Z_p}$  from  $H$  is represented by the blue band, while  $r_p$  from  $\mu H$  corresponds to the solid red line. The upcoming 1S-HFS measurement in  $\mu H$  is expected to have a big impact on the precise determination of  $r_{Z_p}$ .

The leading recoil correction to the HFS is caused by the same two-photon exchange diagram and is of order  $(Z\alpha)(n/M)\tilde{E}_{\text{Fermi}}$ , where  $\tilde{E}_{\text{Fermi}}$  is the Fermi energy without contribution of the muon anomalous magnetic moment [721].

The main HFS contributions have been confirmed and refined by Indelicato [755] by numerical integration of the hyperfine Hamiltonian with Bohr-Weisskopf (magnetization distri-



bution) correction using Dirac wave functions. The latter has been computed for Coulomb finite-size and Uehling potentials. All-order finite size, relativistic, and eVP effects are then included in the wave function. This calculation is performed for various  $r_E$  and  $r_Z$ , assuming exponential charge and magnetization distributions.

The improved  $2S - 2P$  measurements considered above will improve the precision of the  $2S$  HFS measurement. Nonetheless, a new level of precision will be reached in the upcoming CREMA measurements of  $1S$  HFS [772]. On the theory side, a comprehensive account of the different contributions to these HFS transitions has been made in Ref. [8]:

$$E_{1S-\text{HFS}} = \left[ \underbrace{182.443}_{E_F} + \underbrace{1.350(7)}_{\text{QED+weak}} + \underbrace{0.004}_{\text{hVP}} - \underbrace{1.30653(17) \left( \frac{r_{Zp}}{\text{fm}} \right) + E_F (1.01656(4) \Delta_{\text{recoil}} + 1.00402 \Delta_{\text{pol}})}_{2\gamma \text{ incl. radiative corr.}} \right] \text{meV}, \quad (8.10a)$$

$$E_{2S-\text{HFS}} = \left[ \underbrace{22.8054}_{\frac{1}{8}E_F} + \underbrace{0.1524(8)}_{\text{QED+weak}} + \underbrace{0.0006(1)}_{\text{hVP}} - \underbrace{0.16319(2) \left( \frac{r_{Zp}}{\text{fm}} \right) + \frac{1}{8}E_F (1.01580(4) \Delta_{\text{recoil}} + 1.00326 \Delta_{\text{pol}})}_{2\gamma \text{ incl. radiative corr.}} \right] \text{meV}. \quad (8.10b)$$

When a high-precision measurement of the  $1S$  HFS in  $\mu H$  is at hand, it can be used together with  $H$  to accurately disentangle the Zemach and polarizability contributions,  $\Delta_Z$  and  $\Delta_{\text{pol}}$ , with extraordinary precision. This can be achieved thanks to the difference between  $H$  and  $\mu H$  for the eVP corrections to the  $2\gamma$  exchange, see Eqs. (8.10a) and (8.12). With an anticipated uncertainty of 1 ppm for the  $\mu H$   $1S$  HFS experiment, the Zemach radius will be determined with a relative uncertainty of  $5 \cdot 10^{-3}$  and  $\Delta_{\text{pol}}(\mu H)$  with an absolute uncertainty of 40 ppm. Thus, it will lead to the best empirical determination of the proton Zemach radius from spectroscopy, without the uncertainty related to the polarizability.

The  $1S$  HFS in  $H$  has already been measured with  $\delta = 7 \cdot 10^{-13}$  accuracy [773, 774]:

$$E_{1S-\text{HFS}}^{\text{exp}}(H) = 1\,420.405\,751\,768(1) \text{ MHz}. \quad (8.11)$$

The corresponding theory prediction is given in Eq. (8.12). Compared to a previous compilation by Volotka [125], the eVP correction has been recalculated in Ref. [8] which agrees with those in Ref. [775],

$$E_{1S\text{-HFS}}(H) = \left[ \underbrace{1418840.082(9)}_{E_F} + \underbrace{1\,612.673(3)}_{\text{QED+weak}} + \underbrace{0.274}_{\mu\text{VP}} + \underbrace{0.077}_{\text{hVP}} - 54.430(7) \left( \frac{r_{Z_p}}{\text{fm}} \right) + E_F (0.99807(13) \Delta_{\text{recoil}} + 1.00002 \Delta_{\text{pol}}) \right] \text{kHz}. \quad (8.12)$$

$\underbrace{\hspace{15em}}_{2\gamma \text{ incl. radiative corr.}}$

The high-precision in HFS measurements was already used to constrain the  $2\gamma$ -exchange contribution and its effect in the HFS of  $\mu H$  in Refs. [776, 777]. In Ref. [8], an update of the  $\mu\text{VP}$  and  $\text{hVP}$  contributions was obtained from a rescaling of the recent results from muonium [778], giving rise to considerably larger results (by a factor of 3 and 5, respectively) compared to those in Ref. [125].

Through a rescaling from  $H$  to  $\mu H$ , a complete prediction of the HFS in  $\mu H$  is found [8]:

$$E_{1S\text{-HFS}}(\mu H) = 182.634(8) \text{ meV}, \quad E_{2S\text{-HFS}}(\mu H) = 22.8130(9) \text{ meV}, \quad (8.13)$$

where an uncertainty due to possible scaling violation of  $\Delta_{\text{pol}}$  at the level of 2% (assuming  $\Delta_{\text{pol}} = 400 \text{ ppm}$ ) has also been included. This result is shown in Fig. 8.6, together with other existing  $\mu H$   $2S$  HFS measurements. All theory predictions agree, even though the data-driven dispersive evaluations and the  $B\chi\text{PT}$  prediction disagree in the polarizability contribution (see Ref. [8] for a summary). This is because most works use the experimental  $H$  HFS to refine their prediction for the total  $2\gamma$ -exchange effect. The discrepancy in polarizability is then compensated by slightly different Zemach radii.

Eventually, a prediction of the hadronic contributions to the  $1S$  HFS in  $H$  from the measurement of the  $1S$  HFS in  $\mu H$  might allow for a test of the  $H$  HFS theory. Nevertheless, this would need further improvements for the recoil corrections from  $2\gamma$ -exchange and for the uncertainty from missing contributions in the  $\mu H$  theory.

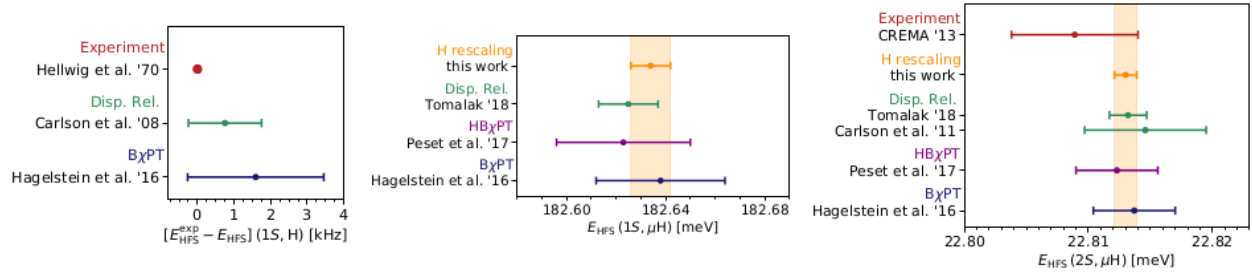


Figure 8.6: Experimental values and theoretical predictions for the  $1S$  and  $2S$  HFS in  $H$  and  $\mu H$  [8].

## 8.4 New Physics searches

Precision spectroscopy of atoms and molecules could sense energy shifts caused by physics beyond the standard model (BSM) involving a low-mass and weakly coupled sector that escapes detection in high-energy colliders [746, 747, 779]. These searches typically involve a contrast between theoretical predictions and experiments that eventually will be limited by hadronic effects. Thus, the search for BSM physics consists in looking for deviations between  $r_p$  values extracted from the various systems:  $ep$  scattering,  $H$ ,  $\mu H$  and molecules. Any deviation might reveal an inconsistency of the theoretical framework pointing to the existence of BSM physics [8]. Currently, these searches are limited by the uncertainty of the  $r_p$  as determined from measurements other than  $\mu H$ .

In Ref. [104], the authors highlighted that  $R_\infty$  extracted from  $H$  tends to decrease as the  $n$  of either the upper or lower state increases. This trend could be explained by a fifth-force expressed as a Yukawa-like potential with a large scale [780] which mitigates the tension between  $\mu H$  and recent  $H$  measurements [104].

A peculiar sensitivity of  $\mu H$ ,  $\mu D$  and  $H(1S - 2S)$  to a dark sector with masses in the keV to GeV was highlighted in Ref. [781]. The sensitivity showed in this study is greatly enhanced when accounting for the upcoming measurements of the  $1S$  HFS in  $\mu H$ , and improved determinations of  $r_p$ .

In order to exploit  $r_p$  for BSM searches, one needs to use its accuracy to improve other fundamental constants which increases the predictive power of our theories. For that purpose,

boosting the  $2\gamma$ - and  $3\gamma$ -exchange contributions is crucial.

# Chapter 9

## Axial-vector contributions to the HFS of muonic hydrogen

### 9.1 Introduction

The electromagnetic interactions of axial-vector mesons have attracted much attention recently. In particular, in the context of the hadronic light-by-light (HLbL) contribution to the anomalous magnetic moment of the muon [6, 49, 601–603, 614, 618, 671, 673, 782, 783], but also concerning their contribution to the hyperfine structure (HFS) of muonic hydrogen [784, 785].

In the present study [786], we revise different aspects of their role in the HFS, briefly discussing axial-vector mesons decays into  $\ell^+\ell^-$  that enter the HFS calculation. On the one hand, we analyze the role of the high-energy behavior. This was missing in previous pioneering studies of the HFS [784, 785], but has been found to play an important role in the context of the HLbL [601–603]. We find that the impact is by no means negligible, representing a 50% effect. On the other hand, we use short-distance constraints connecting the Compton scattering tensor and the axial form factor of the nucleon. This allows to unambiguously fix the sign of the HFS contribution and to better understand potential off-shell effects [784, 785]. Overall, we obtain a value with opposite sign with respect to previous estimates that, together with the non-negligible impact of the high-energy behavior,

represents the main result of this work. Besides, a discussion concerning the uncertainties on the relevant coupling constants and off-shell effects complements this study.

This chapter is organized as follows: in Sect. 9.2, we discuss the amplitude for  $A \rightarrow \ell^+ \ell^-$  decays, a necessary ingredient in our calculation. Building on the former, section 9.3 outlines the contribution to the HFS on a general basis. The particular models are outlined in section 9.4 based on resonance saturation. The final results and conclusions, including the impact on the Zemach radius are given in section 9.5. Further information, including the form factor description, is relegated to the appendices.

## 9.2 $A \rightarrow \ell^+ \ell^-$ decays

The axial-vector meson decays to a lepton pair play a central role in computing their contribution to the HFS, to be discussed in the section below. Furthermore, they can provide important information regarding  $A \rightarrow \gamma^* \gamma^*$  transitions [783, 787] (see also the comments at the end of this section). We outline next the evaluation of the relevant matrix element appearing in these decays, which comparison to existing results will provide an additional (intermediate) cross-check of our evaluation.

The aforementioned process occurs through the electromagnetic interactions and involves the  $A \rightarrow \gamma^* \gamma^*$  transition, which can be expressed on the basis of Lorentz invariance and  $CP$  symmetry as [618]<sup>1</sup>

$$i \mathcal{M}_{A \rightarrow \gamma^* \gamma^*} = ie^2 \left\{ B_2(q_1^2, q_2^2) i \epsilon_{\mu\alpha\rho\beta} q_1^\beta [q_2^\alpha q_{2\nu} - g_\nu^\alpha q_2^2] + B_2(q_2^2, q_1^2) i \epsilon_{\nu\alpha\rho\beta} q_2^\beta [q_1^\alpha q_{1\mu} - g_\mu^\alpha q_1^2] \right. \\ \left. + i \epsilon_{\mu\nu\alpha\beta} q_1^\alpha q_2^\beta [\bar{q}_{12\rho} C_A(q_1^2, q_2^2) + q_{12\rho} C_S(q_1^2, q_2^2)] \right\} \epsilon^{*\mu}(q_1) \epsilon^{*\nu}(q_2) \epsilon^\rho(q_{12}) \equiv ie^2 \mathcal{M}_{A\mu\nu\rho} \epsilon^{*\mu}(q_1) \epsilon^{*\nu}(q_2) \epsilon^\rho(q_{12}), \quad (9.1)$$

---

<sup>1</sup>We use  $\epsilon^{0123} = +1$ . The interested reader is referred to Ref. [618] for relations to other bases. Comparing to the basis in [784],  $A_4 - \bar{A}_3 = B_2$ ,  $\bar{A}_4 - A_3 = \bar{B}_2$ ,  $2C_S = A_3 + \bar{A}_3$ ,  $2C_A = A_3 - \bar{A}_3$ , as well as  $F_{AV\gamma^*\gamma^*}^{(0)}(q_1^2, q_2^2) = -B_{2S}(q_1^2, q_2^2)$ . Also, comparing to the basis in [783, 788],  $m_A^2 B_2 = -\mathcal{F}_3$ ,  $m_A^2 \bar{B}_2 = \mathcal{F}_2$ ,  $m_A^2 C_A = \mathcal{F}_1$ . In addition, the form factors with well-defined symmetry are related by  $2m_A^2 B_{2S} = \mathcal{F}_s$ ,  $-2m_A^2 B_{2a} = \mathcal{F}_{a_2}$ ,  $m_A^2 C_A = \mathcal{F}_{a_1}$ .



Figure 9.1: The leading contribution to  $A \rightarrow \ell^+ \ell^-$  decays (left). The axial-vector meson contribution to the  $\ell^- p \rightarrow \ell^- p$  amplitude relevant to the HFS (right). The grey blob includes structure-dependent axial-photon-photon interactions.

where  $q_{12} = q_1 + q_2 = q$  and  $\bar{q}_{12} = q_1 - q_2$ . Here,  $\epsilon^{*\mu}(q_1)$  and  $\epsilon^{*\nu}(q_2)$  are the polarization vectors of the photons, while  $\epsilon^\rho(q)$  is the polarization vector of the axial-vector meson with  $A = a_1, f_1^{(\prime)}$ . Importantly, the basis in eq. (9.1) is free of kinematic singularities, see also [788]. The form factors,  $B_2(q_1^2, q_2^2)$ ,  $C_A(q_1^2, q_2^2)$  and  $C_S(q_1^2, q_2^2)$ , encode the strong interaction dynamics. To guarantee Bose symmetry,  $C_A(q_1^2, q_2^2)$  must be antisymmetric and  $C_S(q_1^2, q_2^2)$  must be symmetric under  $q_1 \leftrightarrow q_2$ . The contribution from  $C_S$  vanishes when the axial-vector meson is on-shell and, in this basis, can be omitted when considering high-energy constraints [603], which is not necessarily the case in other bases (see also Refs. [783, 788]). In the last expression,  $C_A$  corresponds to transverse photons ( $TT$ ) and  $B_2$  is a combination of  $TT$  and  $LT$  polarization states ( $L$  standing for longitudinal).

The leading order contribution to  $A \rightarrow \ell^+ \ell^-$  decays is given by the diagram shown in fig. 9.1a, which corresponding amplitude can be expressed by means of Eq. (9.1) as

$$i\mathcal{M} = -e^4 \epsilon_\rho \int \frac{d^4 k}{(2\pi)^4} \frac{\bar{u} \gamma_\nu [(k - \not{p}) + m_\ell] \gamma_\mu v}{q_1^2 q_2^2 [(k - p)^2 - m_\ell^2]} \mathcal{M}_A^{\mu\nu\rho}(q_1, q_2), \quad (9.2)$$

with  $q_1 = k$  and  $q_2 = q - k$ . In the following, it will be useful to express the most general amplitude for these decays, that based on Lorentz invariance and  $CP$  symmetry can be written as

$$i\mathcal{M} = i \bar{u}(q - p) \left[ A_1(q^2) \gamma^\rho + A_2(q^2) q^\rho \right] \gamma^5 v(p) \epsilon_\rho(q) \equiv i\mathcal{M}_{A \rightarrow \bar{\ell}\ell}^\rho \epsilon_\rho(q). \quad (9.3)$$

Note that the  $A_2$  amplitude is a pure off-shell effect and, as such, it does not contribute to the decay width, while we keep it here as it will generally contribute to the Compton-scattering tensor that appears in the HFS.

The scalar functions  $A_{1,2}(q^2)$  given in Eq. 9.3 can be obtained by means of the following projection operators ( $p_{1(2)}$  corresponds to the  $\ell^-(\ell^+)$  momentum)

$$A_1(q^2) = \frac{-1}{4(q^2 - 4m_\ell^2)} \text{Tr} \left[ (\not{p}_2 - m_\ell) \left( \gamma_\rho + \frac{2m_\ell}{q^2} q_\rho \right) \gamma^5 (\not{p}_1 + m_\ell) \mathcal{M}_{A \rightarrow \bar{\ell}\ell}^\rho \right], \quad (9.4)$$

$$\begin{aligned} A_2(q^2) &= \frac{m_\ell}{2q^2(q^2 - 4m_\ell^2)} \text{Tr} \left[ (\not{p}_2 - m_\ell) \left( \gamma_\rho - \frac{q^2 - 6m_\ell^2}{m_\ell q^2} q_\rho \right) \gamma^5 (\not{p}_1 + m_\ell) \mathcal{M}_{A \rightarrow \bar{\ell}\ell}^\rho \right] \\ &= -\frac{2m_\ell}{q^2} A_1(q^2) - \frac{1}{2q^4} \text{Tr} \left[ (\not{p}_2 - m_\ell) q_\rho \gamma^5 (\not{p}_1 + m_\ell) \mathcal{M}_{A \rightarrow \bar{\ell}\ell}^\rho \right]. \end{aligned} \quad (9.5)$$

Thus, the  $A_i(q^2)$  amplitudes are given by

$$\begin{aligned} A_1(q^2) &= \frac{\alpha^2}{i\pi^2} \frac{1}{l^2 q^2} \int d^4k \frac{C_A(q_1^2, q_2^2) \omega_A + B_{2S}(q_1^2, q_2^2) \omega_{2S} + B_{2A}(q_1^2, q_2^2) \omega_{2A}}{q_1^2 q_2^2 [(k-p)^2 - m_\ell^2]}, \quad (9.6) \\ \omega_{2S} &= \pm(q_1^2 \pm q_2^2) \{ l^2 (q \cdot q_1)(q \cdot q_2) - q^2 (k \cdot l) [q_1 \cdot q_2 - q^2] \} - l^2 q^2 \left\{ \begin{matrix} 2q_1^2 q_2^2 \\ 0 \end{matrix} \right\}, \\ \omega_A &= (q_1^2 - q_2^2) \{ -q^2 (k \cdot l) (q_1 \cdot q_2) + l^2 [k^2 q^2 - (k \cdot q)^2] \}, \end{aligned}$$

and

$$\begin{aligned} A_2(q^2) &= -\frac{2m_\ell}{q^2} A_1(q^2) + \frac{\alpha^2}{i\pi^2} \frac{4m_\ell}{q^4} \int d^4k \frac{k^2 q^2 - (k \cdot q)^2}{k^2 (q-k)^2 [(k-p)^2 - m_\ell^2]} \left\{ -q^2 C_S(q_1^2, q_2^2) \right. \\ &\quad \left. - (q_1^2 - q_2^2) [C_A(q_1^2, q_2^2) - B_{2A}(q_1^2, q_2^2)] - (q_1^2 + q_2^2) B_{2S}(q_1^2, q_2^2) \right\}, \quad (9.7) \end{aligned}$$

where we have defined  $l \equiv p_{\ell^-} - p_{\ell^+}$ .

In the previous equations, we have used form factors with well-defined symmetry following Refs. [603, 618]:  $B_2(q_1^2, q_2^2) = B_{2S}(q_1^2, q_2^2) + B_{2A}(q_1^2, q_2^2)$  and  $B_2(q_2^2, q_1^2) = B_{2S}(q_1^2, q_2^2) - B_{2A}(q_1^2, q_2^2)$ .

Noteworthy, the current evaluation allows to cross-check our results for  $A_1(m_A^2)$  against those in Refs. [783, 787], finding a nice agreement and reinforcing our results, to be used



	VMD	eVMD	heVMD	DIP	heDIP	OPE
$\mathcal{B}_{e^+e^-}$	1.90 $^{(92)}_{(74)}$	1.55 $^{(50)}_{(38)}$	1.66 $^{(45)}_{(42)}$	2.87 $^{(3.69)}_{(1.73)}$	2.73 $^{(3.86)}_{(1.69)}$	2.67 $^{(3.99)}_{(1.75)}$

Table 9.1: Branching fraction for  $f_1 \rightarrow e^+e^-$  decays in units of  $10^{-9}$  with the different form factors outlined in appendix L (ideal mixing case). In particular the first three columns correspond to models incorporating a vector meson mass  $m_V = 0.77$  GeV, whereas the last three columns have effective masses around 1 GeV, illustrating the relevance of the intermediate  $V\gamma$  state. For reference, this branching ratio is  $< 9.4 \times 10^{-9}$  at 90% confidence level [9].

below in the  $q^2 \rightarrow 0$  limit for the HFS.

Finally, we would like to comment on an important aspect. Namely, that  $A \rightarrow e^+e^-$  decays are particularly sensitive to the intermediate  $V\gamma$  contributions (and thereby to the timelike region), showing less sensitivity to high-energies or the spacelike regime. This is a consequence of the Landau-Yang theorem [789, 790] and is opposite to  $\pi(\eta) \rightarrow \ell^+\ell^-$  decays [791], where the imaginary part is dominated by the intermediate  $2\gamma$  state. Due to this reason, and the fact that several form factors appear (in contrast to the HFS where the knowledge of  $B_{2S}$  suffices), we refrain from discussing this further. Still, we use different models for the  $B_{2S}$  form factor (see appendix L) to illustrate our claim for the  $f_1(1285)$  case. In particular, taking the unpolarized spin-averaged squared matrix element  $\overline{\mathcal{M}}^2$  and the corresponding partial decay width

$$\overline{\mathcal{M}}^2 = \frac{4}{3}q^2\beta_\ell^2|A_1(q^2)|^2, \quad \Gamma_{A \rightarrow \ell\ell} = \frac{1}{12\pi}M_A\beta_\ell^3|A_1(M_A^2)|^2, \quad (\beta_\ell^2 = 1 - 4m_\ell^2/s), \quad (9.8)$$

we find the results in table 9.1 using the form factors discussed in appendix L. From the results therein, we find that the form factors including an explicit vector meson mass of  $m_V = 0.77$  GeV (VMD, eVMDm, heVMD) display similar results, with mild corrections from their different high-energy behavior. On the contrary, they differ substantially from those employing an effective mass that successfully describes the L3 data [792, 793] in the (singly-virtual) spacelike region, regardless of their high-energy behavior. As we will show, this is the opposite for the HFS that, as such, might not benefit substantially from a precise knowledge of  $A \rightarrow e^+e^-$  decays.

### 9.3 The contribution to the HFS

Having computed the  $\mathcal{M}_{A \rightarrow \bar{\ell}\ell}^\rho(q^2)$  amplitude in eq. (9.3), the contribution of axial-vector mesons to the HFS is straightforward. In particular, the relevant amplitude of the  $\ell^- p \rightarrow \ell^- p$  process driven by axial-vector mesons, fig. 9.1b, can be expressed as

$$i\mathcal{M}_{\ell p} = ig_{ANN}[\bar{u}(A_1\gamma^\mu + A_2q^\mu)\gamma^5 u]_\ell \frac{-g_{\mu\nu} + \frac{q_\mu q_\nu}{m_A^2}}{q^2 - m_A^2} [\bar{u}\gamma^\nu\gamma^5 u]_N, \quad (9.9)$$

where we have introduced the coupling of the axial-vector mesons to the nucleons,  $g_{ANN}$ , via

$$\mathcal{L}_{a_1NN} = -g_{a_1NN}(\bar{N}\gamma_\mu\gamma^5\vec{\sigma}N)\vec{a}_1^\mu, \quad \mathcal{L}_{f_1NN} = -g_{f_1NN}(\bar{N}\gamma_\mu\gamma^5 N)f_1^\mu. \quad (9.10)$$

Determining the couplings above will be an important part of our study, that we postpone to section 9.4. Pursuing further the nonrelativistic potential for the HFS, and making use of the relation  $\mathcal{M}_{\ell p} = -2m_\ell 2m_N \tilde{V}_{NR}(\mathbf{q}^2)$ , we obtain<sup>2</sup>

$$\tilde{V}_{NR}(\mathbf{q}^2) = g_{ANN} \left[ \frac{A_1(-\mathbf{q}^2)}{m_A^2 + \mathbf{q}^2} \left\{ (\hat{\boldsymbol{\sigma}}_\ell \cdot \hat{\boldsymbol{\sigma}}_N) + \frac{(\mathbf{q} \cdot \hat{\boldsymbol{\sigma}}_\ell)(\mathbf{q} \cdot \hat{\boldsymbol{\sigma}}_N)}{m_A^2} \right\} - \frac{\tilde{A}_2(-\mathbf{q}^2)}{m_A^2} (\mathbf{q} \cdot \hat{\boldsymbol{\sigma}}_\ell)(\mathbf{q} \cdot \hat{\boldsymbol{\sigma}}_N) \right], \quad (9.11)$$

where  $\hat{\boldsymbol{\sigma}}_{\ell(N)}$  are Pauli matrices acting on the lepton(nucleon) spinors and  $2m_\ell \tilde{A}_2 = A_2$ . In the following, we restrict ourselves to the leading-order contribution in  $\alpha$ . This justifies, in analogy with [784], to neglect the terms proportional to  $(\mathbf{q} \cdot \hat{\boldsymbol{\sigma}}_\ell)(\mathbf{q} \cdot \hat{\boldsymbol{\sigma}}_N)$ , as well as to take  $A_1(-\mathbf{q}^2) \rightarrow A_1(0)$ , both effects being suppressed by  $m_\ell\alpha/\Lambda$  (see appendix M). Furthermore, this justifies to keep with the leading term in the spinors' nonrelativistic expansion [781]. Neglecting those terms, the expression above corresponds to a nonrelativistic potential

$$\tilde{V}_{NR}(\mathbf{q}^2) \simeq g_{ANN} \frac{A_1(0)}{m_A^2 + \mathbf{q}^2} (\hat{\boldsymbol{\sigma}}_\ell \cdot \hat{\boldsymbol{\sigma}}_N), \quad V_{NR}(r) = \frac{g_{ANN} A_1(0)}{4\pi r} e^{-m_A r} (\hat{\boldsymbol{\sigma}}_\ell \cdot \hat{\boldsymbol{\sigma}}_N). \quad (9.12)$$

---

<sup>2</sup>We use  $\bar{u}(p_2, s_2)\gamma^5 u(p_1, s_1) \xrightarrow{\text{NR}} \langle \mathbf{p}_1 - \mathbf{p}_2 | [\xi_{s_2}^\dagger \boldsymbol{\sigma} \xi_{s_1}] | \mathbf{p}_1 - \mathbf{p}_2 \rangle$  and  $\bar{u}(p_2, s_2)\gamma^\mu\gamma^5 u(p_1, s_1) \xrightarrow{\text{NR}} 2m[\xi_{s_2}^\dagger(0, \boldsymbol{\sigma})\xi_{s_1}]$ , where  $\mathbf{p}_1 - \mathbf{p}_2 \rightarrow \pm\mathbf{q}$  for nucleons(leptons).

This agrees with the recent study in Ref. [781] upon identifying their coupling constants  $g_A^{(1)} \rightarrow A_1(0)$ ,  $g_A^{(2)} \rightarrow -g_{ANN}$ . The corresponding shifts for each level can be obtained through  $\Delta E = \langle \Psi_{n,l,m} | V_{\text{NR}}(r) | \Psi_{n,l,m} \rangle$ , with  $\Psi_{n,l,m}$  the hydrogen atom wavefunctions. In particular, for the HFS we are interested in, corresponding to the energy difference  $E(nS_{1/2}^{F=1}) - E(nS_{1/2}^{F=0})$  [781], it leads to:

$$\Delta E_1^{\text{HFS}} = \frac{g_{ANN} A_1(0)}{\pi} \frac{(\mu\alpha)^3}{m_A^2} \frac{1}{(1 + \frac{2\mu\alpha}{m_A})^2} \langle \hat{\sigma}_\ell \cdot \hat{\sigma}_N \rangle_{(\Delta F)} = \frac{g_{ANN} A_1(0)}{\pi} \frac{(\mu\alpha)^3}{m_A^2} \frac{4}{(1 + \frac{2\mu\alpha}{m_A})^2}, \quad (9.13)$$

$$\Delta E_2^{\text{HFS}} = \frac{g_{ANN} A_1(0)}{16\pi} \frac{(\mu\alpha)^3}{m_A^2} \frac{2 + (\frac{\mu\alpha}{m_A})^2}{(1 + \frac{\mu\alpha}{m_A})^4} \langle \hat{\sigma}_\ell \cdot \hat{\sigma}_N \rangle_{(\Delta F)} = \frac{g_{ANN} A_1(0)}{4\pi} \frac{(\mu\alpha)^3}{m_A^2} \frac{2 + (\frac{\mu\alpha}{m_A})^2}{(1 + \frac{\mu\alpha}{m_A})^4}, \quad (9.14)$$

for  $n = 1, 2$ , where  $\mu$  is the reduced mass, and the factor of 4 in the right-hand side arises from the spin expectation value. We note that  $A_1(0)$  can be expressed following the notation in Ref. [784] as

$$A_1(0) = \frac{4}{3} \left( \frac{\alpha}{\pi} \right)^2 \int_0^\infty dk^2 L_\ell(k^2) B_{2S}(-k^2, -k^2), \quad (9.15)$$

with  $L_\ell(k^2)$  defined in Ref. [784] (see Eq. (14) therein).<sup>3</sup> The previous results show that only the  $B_{2S}$  form factor contributes to the HFS to leading order in  $\alpha$ , simplifying the calculation as compared to  $A \rightarrow e^+e^-$  decays. Likewise, it is straightforward to check that the general results in Ref. [784] amount to our eqs. (9.13) and (9.14) times a factor of  $(-2)$ . While we could not trace the factor of 2, the relative sign appears comparing to their Eqs. (5),(20). Still, the sign depends on their photon momentum flow and  $\epsilon^{0123}$  convention, that are unclear. More importantly, the final sign arising from eqs. (9.13) to (9.15) will depend on the relative sign for  $B_{2S}(0,0)$  and  $g_{ANN}$ , that was fixed in Ref. [784] on the basis of quark-loop models. In the following section, we introduce our setting to compute the HFS, that unambiguously fixes the sign in a transparent manner, finally confirming our

---

<sup>3</sup>We further note that, for the dipole (DIP) parametrization employed in Ref. [784],  $A_1(0) = \frac{4}{3} \left( \frac{\alpha}{\pi} \right)^2 B_{2S}(0,0) I(m_\ell)$ , with  $I(m_\ell)$  defined in the Eq. (27) from Ref. [784].

opposite sign for the numerical results. In any case, our agreement with Refs. [783, 787] regarding  $A_1(m_A^2)$ , and Ref. [781] in deriving the nonrelativistic potential, further reinforces our findings, eqs. (9.13) and (9.14).

## 9.4 Model results

In order to obtain a numerical estimate for the HFS, determining the  $g_{ANN}$  couplings is almost as important as fixing the sign of  $B_{2S}(0, 0)g_{ANN}$ . In the following, we use short-distance constraints, that allow to relate the nucleon Compton scattering tensor to the nucleon axial form factors in a transparent manner. This allows to fix the sign and, eventually, obtain the desired couplings within a resonance saturation scheme. In particular, the relevant short-distance constraint follows from the operator product expansion (OPE) of two vector currents in the limit where  $q_1^2 \sim q_2^2 \sim \hat{q}^2 \gg \{q_{12}^2, \Lambda_{\text{QCD}}^2\}$ , where we have introduced  $\hat{q} \equiv (q_1 - q_2)/2$  and  $q_{12} = q_1 + q_2$ . This reads [597, 603]:

$$\int d^4x d^4y e^{i(q_1 \cdot x + q_2 \cdot y)} T\{j^\mu(x) j^\nu(y)\} = \frac{-2}{\hat{q}^2} \epsilon^{\mu\nu\alpha\hat{q}} \int d^4z e^{iq_{12} \cdot z} j_{5\alpha}(z) + \mathcal{O}\left(\frac{\Lambda_{\text{QCD}}^2}{\hat{q}^2}\right), \quad (9.16)$$

with  $j_5^\mu = \bar{q}\gamma^\mu\gamma^5\mathcal{Q}^2q$ ,  $\epsilon^{\mu\nu\rho q_i} \equiv \epsilon^{\mu\nu\rho\alpha}q_{i\alpha}$ , and  $\epsilon^{0123} = 1$ . Note actually that, since the typical momentum in the atomic system is of  $\mathcal{O}(m_\ell\alpha)$ , this is indeed the relevant limit in this calculation when the loop momentum in fig. 9.1b is large. Regarding the axial-vector meson form factor, this implies [603, 618, 783, 788]

$$\lim_{\hat{q}^2 \rightarrow \infty} \hat{q}^4 B_{2S}(\hat{q}^2, \hat{q}^2) = \sum_a \text{tr}(\mathcal{Q}^2 \lambda^a) m_A F_A^a, \quad (9.17)$$

where we have introduced the axial decay constant  $\langle 0 | \bar{q}\gamma^\mu\gamma^5\frac{\lambda^a}{2}q | A \rangle = F_A^a m_A$ . This fixes  $\text{sgn} B_{2S}(0, 0) = \text{sgn} F_A m_A$  provided the form factor does not change sign in the spacelike region (which is the case here and in Ref. [784]), thus reducing the problem to determine the sign for  $F_A^a m_A g_{ANN}$ . The latter combination appears indeed in the axial form factors of the

proton ( $a = 3, 8, 0$ ),

$$\langle p(k') | \bar{q} \gamma_\mu \gamma^5 \lambda^a q | p(k) \rangle = \bar{u}(k') \left[ \gamma_\mu G_{\mathcal{A}}^a(q^2) + \frac{q_\mu}{2m_N} G_{\mathcal{P}}^a(q^2) \right] \gamma^5 u(k), \quad (9.18)$$

when adopting a resonance saturation scheme. In particular, one finds [794]

$$G_{\mathcal{A}}^a(q^2) = \sum_A \frac{2F_A^a m_A g_{ANN}}{m_A^2 - q^2}, \quad (9.19)$$

where the sum goes over the (infinite number of) axial-vector meson resonances. As we shall show, this ultimately allows to fix  $\text{sgn } g_{ANN} m_A F_A^a$  in terms of  $G_{\mathcal{A}}^a(0)$ , which sign is well-known. Ultimately, the previous modelling guarantees to fulfill the corresponding OPE constraint for the Compton scattering tensor

$$\lim_{q^2 \gg \{q_{12}^2, \Lambda_{\text{QCD}}^2\}} \int d^4x e^{iq_1 \cdot x} \langle p(k') | T \{ j^\mu(x) j^\nu(0) \} | p(k) \rangle = \frac{-2}{\hat{q}^2} \epsilon^{\mu\nu\alpha\hat{q}} \langle p(k') | j_{5\alpha}(0) | p(k) \rangle \quad (9.20)$$

provided eq. (9.17) is satisfied. In the following, we discuss the results obtained when truncating the sum in eq. (9.19) with either one or two resonances.

### 9.4.1 One-resonance saturation

First, we start truncating the sum in eq. (9.19) with the lightest resonance. Then, the value of the coupling constants can be determined in terms of  $G_{\mathcal{A}}^a(0)$  as follows

$$G_A^3(0) = g_A^3 = 2g_{a_1 NN} \frac{F_A}{m_{a_1}}, \quad (9.21)$$

$$G_A^8(0) = \frac{g_A^8}{\sqrt{3}} = 2F_A \left[ \frac{g_{f_1 NN}}{m_{f_1}} \cos(\phi - \phi_0) + \frac{g_{f_1' NN}}{m_{f_1'}} \sin(\phi - \phi_0) \right], \quad (9.22)$$

$$G_A^0(0) = \sqrt{\frac{2}{3}} g_A^0 = 2F_A \left[ -\frac{g_{f_1 NN}}{m_{f_1}} \sin(\phi - \phi_0) + \frac{g_{f_1' NN}}{m_{f_1'}} \cos(\phi - \phi_0) \right], \quad (9.23)$$

	VMD	eVMD	DIP	heVMD	heDIP	OPE
$f_1(1285)$	1.68( $\frac{27}{25}$ )	1.21( $\frac{47}{31}$ )	0.99( $\frac{17}{15}$ )	1.34( $\frac{34}{14}$ )	1.33( $\frac{48}{33}$ )	1.53( $\frac{25}{24}$ )
$a_1(1260)$	1.68( $\frac{27}{25}$ )	1.03( $\frac{65}{28}$ )	0.91( $\frac{20}{18}$ )	1.17( $\frac{51}{16}$ )	1.14( $\frac{53}{31}$ )	1.41( $\frac{31}{28}$ )
$f_1(1420)$	2.99( $\frac{35}{33}$ )	0.78( $\frac{14}{13}$ )	0.78( $\frac{15}{13}$ )	0.96( $\frac{12}{11}$ )	0.96( $\frac{33}{23}$ )	1.20( $\frac{22}{21}$ )

Table 9.2: The results for  $A_1(0)/[\alpha^2 B_{2S}(0,0)]$  for  $\ell = \mu$ . For simplicity, we take ideal mixing in VMD models, implying that  $m_V = 0.77$  GeV  $\simeq m_{\rho,\omega}$  for  $a_1, f_1$  and  $m_V = m_\phi$  for the  $f'_1$ .

with  $\phi$  the  $f_1 - f'_1$  mixing angle in the flavor basis and  $\phi_0 = \arctan \sqrt{2}$  (cf. appendix L).<sup>4</sup> This implies (we adopt a positive  $F_A$ ),

$$g_{a_1 NN} = 5.6(1.1), \quad g_{f_1 NN} = 2.01(0.17), \quad g_{f'_1 NN} = -0.33(0.08), \quad (\phi = 0), \quad (9.24)$$

$$g_{a_1 NN} = 5.6(1.1), \quad g_{f_1 NN} = 1.93(0.16), \quad g_{f'_1 NN} = 0.71(21), \quad (\phi_{L3} = 26.7(5.0)^\circ), \quad (9.25)$$

where we used  $g_A^3 = 1.2730(13)$  [796],  $g_A^8 = 0.530(18)$ ,  $g_A^0 = 0.392(24)$  [797],  $F_A = 140(10)$  MeV [453, 467, 603] and the PDG [798] masses with an additional uncertainty accounting for the half-width rule [799]. The errors obtained for  $g_{a_1 NN}$ ,  $g_{f_1 NN}$ ,  $g_{f'_1 NN}$  are dominated by  $m_{a_1}$ ,  $F_A$ , and  $g_A^{8,0}$ , respectively. Our results are similar to [784], with a slight departure in the  $f_1^{(\prime)}$  cases —partly related to their use of the OZI rule (that in our scheme would require  $g_A^8 = g_A^0$ ). At this point, it is worth emphasizing that the ad hoc  $1/e$  off-shell factor introduced in Ref. [784] spoils the appropriate normalization for the axial form factors precisely at the  $q^2 \rightarrow 0$  point and should be avoided. Further discussions on this point are included in the following section.

Having estimated the axial couplings, we move on to our results for  $A_1(0)$ . Taking the models from appendix L, we obtain the values in table 9.2. There, we find that models failing to incorporate the doubly-virtual high-energy  $Q^2$  scaling (eVMD, DIP) underestimate the value for  $A_1(0)$  —even if correctly reproducing the singly-virtual L3 data. This is the case for the form factor in Ref. [784], that corresponds to our DIP column. This implies that

<sup>4</sup>In the basis from Refs. [792, 793], the relation is  $\phi = \theta_A + \phi_0 - \pi/2$  which, for the mixing angle given there using  $\gamma\gamma^* \rightarrow f_1^{(\prime)}$  reaction, results in  $\phi = 26.7(2)^\circ$ . Recent studies [795] suggest a range for the mixing angle  $\phi \in (-7, 23)^\circ$ .

A	$\frac{A_1(0)}{\alpha^2 B_{2S}^A}$	$B_{2S}^A(0,0)$ [GeV <sup>-2</sup> ]	$\Delta E_A^{HFS}(1S)$ [meV]	$\Delta E_A^{HFS}(2S)$ [meV]
$f_1(1285)$	1.53(25) $^{(+00)}_{(-20)}$	0.269(30)	0.011(2)(1)(1)(0)[0]	0.0014 $^{(+2)}_{(-3)}(1)(2)(0)[0]$
$a_1(1260)$	1.41(30) $^{(+00)}_{(-27)}$	0.245(63)	0.029 $^{(+6)}_{(-8)}(6)(7)(2)[0]$	0.0036 $^{(+8)}_{(-10)}(7)(9)(2)[0]$
$f_1(1420)$	1.20(22) $^{(+00)}_{(-24)}$	0.197(30)	-0.001(0)(0)(0)(0) $^{(+3)}_{(-0)}$	-0.0001(0)(0)(0)(0) $^{(+3)}_{(-0)}$
TOTAL			0.039 $^{(+12)}_{(-13)}^{(+3)}_{(-0)}$	0.0049 $^{(+14)}_{(-16)}^{(+3)}_{(-0)}$

Table 9.3: Results for the HFS of muonic hydrogen. The central values for the  $g_{ANN}$  couplings are those from ideal mixing, eq. (9.24). The second column displays results from OPE column in table 9.2, including as an additional uncertainty the difference with other models therein (see details in the text). The final two columns include uncertainties from  $A_1(0)$ ,  $g_{ANN}$ ,  $B_{2S}$ ,  $m_A$  and an additional uncertainty from the mixing within brackets (see details in the text).

in the present calculation one should employ only those form factors describing L3 data and incorporating the high-energy behavior (heVMD, heDIP, OPE). Among them, the OPE model represents our preferred choice since: (i) it reproduces L3 data [792, 793]; (ii) it is the only one that fulfills the pQCD scaling for a large virtual photon regardless the second photon virtuality; (iii) for two virtual photons, it fulfills the OPE, eq. (9.17) (find further details in appendix L). As such, we take it as the central value, incorporating the difference with respect to heVMD and heDIP models as an additional uncertainty. Having determined the value for  $A_1(0)$ , we estimate the contribution of the lowest-lying axial-vector mesons to the HFS, that are collected in table 9.3. In the following section, we extend the model including an additional multiplet of axial-vector mesons. While this induces further model dependence concerning the transition form factors, it is known that at least two resonances are required to have a satisfactory description of the axial form factors of the nucleon. As such, it will serve as an estimate of our systematic uncertainties and to discuss off-shell effects.

## 9.4.2 Two-resonance saturation

The one-resonance saturation employed in the previous section to describe the axial form factors of the nucleon and to estimate the  $g_{ANN}$  couplings does not provide a satisfac-

tory description of the axial form factor of the nucleon, that is better parametrized by a dipole form either in electroproduction [800] or lattice QCD data [801–806]. This can be partly understood on the basis of the high-energy behavior of the axial form factor,  $\lim_{Q^2 \rightarrow \infty} G_A^a(-Q^2) \sim \alpha_s^2(-Q^2)Q^{-4}$  [807–809], that requires the presence of at least two resonances to recover a  $Q^{-4}$  behavior [794]. This suggests the necessity to go beyond the one resonance saturation scheme, while this comes at the cost of non-negligible modeling of the poorly known heavy axial-vector meson resonances, including their masses and form factors. In order to estimate the masses of the heavier multiplets, we use the Regge trajectory from Ref. [799]:  $m_{a_1(n)}^2 = m_{a_1}^2 + n\mu_3^2$ ,  $m_{f_1^{(\prime)}(n)}^2 = m_{f_1^{(\prime)}}^2 + n\mu_0^2$ , with  $\mu_{3/0}^2 = 1.36/1.19 \text{ GeV}^2$ . Imposing the normalization and the  $Q^{-4}$  behavior of the axial form factors, we obtain the following coupling constants using ideal mixing

$$g_{a_1 NN} = 11.8, \quad g_{f_1 NN} = 4.78, \quad g_{f_1' NN} = -0.90, \quad (9.26)$$

$$g_{a_1(1) NN} = -8.6, \quad g_{f_1(1) NN} = -3.64, \quad g_{f_1'(1) NN} = 0.71. \quad (9.27)$$

The next part concerns the description of the  $B_{2S}$  form factor of the heavy resonances. Lacking any experimental data, we resort to a Regge-like model from Ref. [603]

$$B_{2S}^{A_n}(q_1^2, q_2^2) = \frac{B_{2S}^{A_n}(0, 0)(M_a^2 + n\Lambda^2)^2}{[q_1^2 + q_2^2 - (M_a^2 + n\Lambda^2)]^2}, \quad B_{2S}^{A_0}(0, 0) = \frac{B_{2S}^{A_0}(0, 0)M_a^4 m_{A_n}}{(M_a^2 + n\Lambda^2)^2 m_{A_0}}, \quad (9.28)$$

that was created to describe some features of the  $\langle VVA \rangle$  Green's function. As this induces further model dependence for the second multiplet ( $n = 1$ ), for which no data is available, we will use our results in this section to estimate systematic uncertainties in the one resonance saturation approach. Our results are given in table 9.4.

We find that the enhanced couplings for the lowest-lying multiplet essentially double the HFS contribution with respect to the previous section. Such enhancement is partially cancelled by the contribution of the second multiplet, that reduces the final shift to a 60% effect. Such variation could be taken as an off-shell effect, as it induces additional  $q^2$  dependence besides the lowest-lying multiplet. However, its complexity goes beyond the  $1/e$  factor in



A	$\frac{A_1(0)}{\alpha^2 B_{2S}^A}$	$g_{ANN}$	$B_{2S}^A(0,0)$ [GeV <sup>-2</sup> ]	$\Delta E_A^{HFS}(1S)$ [meV]	$\Delta E_A^{HFS}(2S)$ [meV]
$f_1(1285)$	1.53	4.78	0.269	0.0269	0.0034
$f_1(1^{\text{st}} \text{ excitation})$	3.05	-3.64	0.093	-0.0082	-0.0010
Subtotal				0.0187	0.0024
$a_1(1260)$	1.41	11.8	0.245	0.0605	0.0076
$a_1(1^{\text{st}} \text{ excitation})$	2.93	-8.6	0.082	-0.0162	-0.0020
Subtotal				0.0443	0.0056
$f_1(1420)$	1.20	-0.90	0.197	-0.0024	-0.0003
$f_1'(1^{\text{st}} \text{ excitation})$	2.72	0.71	0.051	0.0007	0.0001
Subtotal				-0.0017	-0.0002
Total				0.0613	0.0078

Table 9.4: The contributions from the ground and first excited states contribution to the HFS (errors not included, see details in the text). The results compare to those in table 9.3. The first resonance contribution is enhanced with respect to table 9.3 as a result of the  $g_{ANN}$  coupling, whereas the first excited states partially damp this effect.

Ref. [784] and a precise estimate would demand a better knowledge of the properties of the heavy axial-vector mesons, including their  $g_{ANN}$  couplings and form factors.

Given the large theoretical uncertainties in the results derived, especially owing to the masses and form factors of the second multiplet, we stick to our results in the previous section and will assign the difference between the results in this and the previous subsection as an additional systematic uncertainty of our results. Overall, this points to a substantially larger contribution from the first multiplet and a partial reduction from heavier states.

## 9.5 Results and conclusions

As our final result for the HFS, we take as our central value the result obtained with the one resonance saturation, incorporating as an additional systematic uncertainty the difference with respect to the two-resonance saturation approach. This gives

$$\Delta E_A^{HFS}(1S) = 0.039^{(+12)}_{(-13)}^{(+3)}_{(-0)}^{(+22)}_{(-00)} \text{ meV}, \quad \Delta E_A^{HFS}(2S) = 0.0049^{(+14)}_{(-16)}^{(+3)}_{(-0)}^{(+29)}_{(-00)} \text{ meV}. \quad (9.29)$$

Compared to Ref. [784], we find an opposite sign (and a factor of 2 difference) in the calculation. Our results for the  $A \rightarrow \ell^+ \ell^-$  amplitude and the nonrelativistic expansion are in good agreement with existing studies, that further reinforces our findings. Besides, we find an important role (a 50% effect roughly) of the doubly-virtual high-energy behavior of the transition form factor, that was one of our main goals in this study —such effects should be included in future calculations of  $\Delta E_A^{HFS}$ .

In addition, to fix the relevant signs of the form factors and coupling constants, we made use of the OPE. This provides a connection among the Compton scattering tensor and the axial form factors of the nucleon, that unambiguously defines the relevant signs when using a resonance saturation scheme. For the simplest scenario, that incorporates the lowest-lying resonance, we find similar couplings to those in Ref. [784], while substantial effects are found when two resonances are included. These are required to achieve a reasonable description of the axial form factors of the nucleon and points to a larger contribution of the lowest-lying multiplet together with a mild effect from the next one. The latter could be considered as an off-shell effect and discourages the use of ad hoc suppression factors as in Ref. [784]. The difference between the two scenarios is accounted for as an additional systematic uncertainty and points to the necessity of a better understanding of the nucleon to axial-vector meson couplings in order to improve in precision.

Finally, we address the impact of this effect on the Zemach radius extraction by the CREMA Collaboration [102,103], that measured the HFS of the  $2S$  state, obtaining  $\Delta E_{HFS}^{\text{exp}} = 22.8089(51)$  meV. Comparing to the theoretical results for the HFS,  $\Delta E_{HFS}^{\text{th}} = 22.9843(30) - 0.1621(10) r_Z$  meV, see [754, 765, 810, 811] and Table 3 from Ref. [758], they obtained  $r_Z = 1.082(37)$  fm [102]. Incorporating the missing contributions from the axial vector mesons to the theoretical estimate in eq. (9.29) together with the pseudoscalar contribution [812],  $\Delta E_{HFS}^{\pi} = -(0.09 \pm 0.06) \mu\text{eV}$ , we obtain

$$r_Z = 1.112(31)_{\text{exp}}(19)_{\text{th}} \left( \begin{smallmatrix} +20 \\ -10 \end{smallmatrix} \right)_{\text{axials}}. \quad (9.30)$$

The value is in mild tension with other estimates,  $r_Z = 1.086(12)$  fm [123] and  $r_Z =$

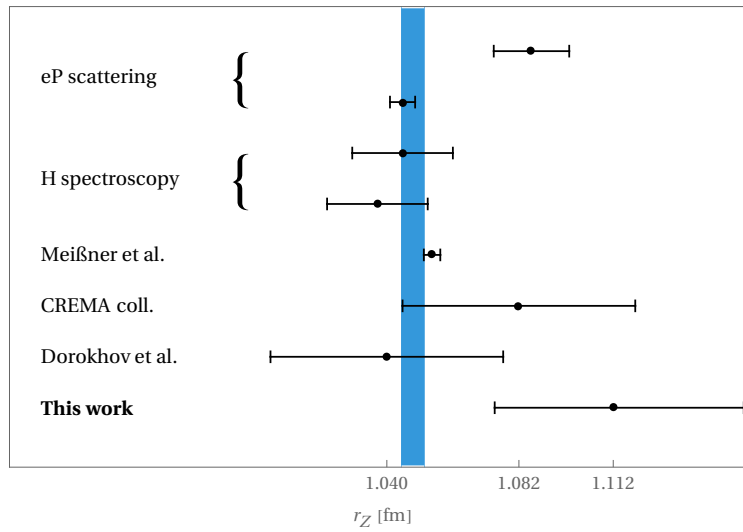


Figure 9.2: The Zemach radius ( $r_Z$ ) from the references in the text and this work. The blue band represents the average from Refs. [123–126].

1.045(4) fm [124], from electron-proton scattering,  $r_Z = 1.045(16)$  fm [125] and  $r_Z = 1.037(16)$  fm [126] from Hydrogen spectroscopy, and  $r_Z = 1.054(3)$  fm [115] from electron-proton scattering and  $e^+e^-$  annihilation. We summarize these results in Fig. 9.2 where the blue band corresponds to the average for electron-proton (eP) scattering and hydrogen (H) spectroscopy.

# Appendix A

## $F_T(s)$ including resonances as explicit degrees of freedom

We show in this appendix that it is not convenient to build  $F_T(s)/F_T(0)$  including resonances as explicit degrees of freedom.

As we will see, the tensor current couples to the  $J^{PC} = 1^{--}$  and  $J^{PC} = 1^{+-}$  resonances, but the contribution of the second tower of resonances is suppressed in the processes under consideration. This can be seen phenomenologically, since the  $b_1(1235)$  resonance (which shares all quantum numbers with the  $\rho(770)$  meson but has opposed parity) is not known to couple to the two-pion system (precisely because of parity  $b_1$  cannot decay into two pseudoscalars, though it could be exchanged in meson-meson scattering, but  $\pi\pi$  scattering data do not show any hint for exchange of the  $b_1$  meson). Therefore, the  $\rho(770)$  is the lightest resonance whose exchange provides an energy-dependence to  $F_T$ , increasing its effect and allowing us to set more restrictive bounds on  $\hat{e}_T$  (we neglect the contributions from  $\rho$  excitations in this study).

We shall now discuss the chiral couplings of meson resonances to the pseudoscalar Goldstone fields in the presence of tensor currents. We use the antisymmetric tensor representation [224, 225] in order to describe the relevant spin-one degrees of freedom. To determine the resonance exchange contributions to the  $\tau^- \rightarrow \pi^- \pi^0 \nu_\tau$  decays (or to the effective chiral

Lagrangian) we need the lowest order operators in the chiral expansion which are linear in the resonance fields. Using the  $P$  and  $C$  transformation properties of given  $J^{PC}$  resonance fields:  $V(1^{--})$ ,  $A(1^{++})$ ,  $S(0^{++})$ ,  $P(0^{-+})$  (see Table 2 in ref. [224]), and  $H(1^{+-})$  and  $T(2^{++})$  (see ref. [813]), we can, for the first time, construct the  $R\chi T$  Lagrangian linear in resonance fields and coupled to the tensor source of lowest chiral order, which has the following two pieces:

$$\mathcal{L}[V(1^{--})] = F_V^T M_V \langle V_{\mu\nu} t_+^{\mu\nu} \rangle, \quad (\text{A.1a})$$

$$\mathcal{L}[H(1^{+-})] = iF_H^T M_H \langle H_{\mu\nu} t_-^{\mu\nu} \rangle. \quad (\text{A.1b})$$

In the following, we neglect the effect of the latter operator (assuming  $F_H^T$  negligible) because of the seemingly small  $b_1\pi\pi$  coupling commented above. A straightforward computation of the contribution of the former operator to the relevant hadronic matrix element yields

$$\langle \pi^0 \pi^- | \bar{d} \sigma^{\mu\nu} u | 0 \rangle = iF_T(s) (p_{\pi^0}^\mu p_{\pi^-}^\nu - p_{\pi^-}^\mu p_{\pi^0}^\nu), \quad (\text{A.2})$$

where

$$F_T(s) = \frac{\sqrt{2}\Lambda_2}{F^2} \left[ 1 + \frac{G_V F_V^T}{\Lambda_2} \frac{M_\rho}{M_\rho^2 - s} \right], \quad (\text{A.3})$$

in which the operator  $\frac{iG_V}{\sqrt{2}} \langle V_{\mu\nu} u^\mu u^\nu \rangle$  [224] was used in order to obtain the  $\rho\pi\pi$  coupling.

Eq. (A.3) depends on three *a priori* unknown couplings. Fortunately, short-distance QCD properties can shed light on their values, as we explain next. First, it is known from the analysis of two-point correlators within  $R\chi T$  that  $G_V = F/\sqrt{2}$  [224] (also  $F_V = \sqrt{2}F$ , which is used next). The large- $N_C$  asymptotic analysis of  $\langle VV \rangle$ ,  $\langle TT \rangle$  and  $\langle VT \rangle$  correlators determines  $F_V^T/F_V = 1/\sqrt{2}$  [814], in such a way that only  $\Lambda_2$  remains unrestricted and eq. (A.3) simplifies to

$$F_T(s) = \frac{\sqrt{2}\Lambda_2}{F^2} + \frac{M_\rho}{M_\rho^2 - s}. \quad (\text{A.4})$$

The  $\rho$  meson contribution shifts the value of  $F_T(0)$  by  $\sim 65\%$ , which is unphysical.

As in the case of the vector form factor, the  $\rho$ -propagator in eq. (A.3) is modified by the

inclusion of the width  $\Gamma_\rho(s)$  (proportional to the imaginary part of the corresponding loop contributions) and also by shifting the pole mass value (according to the real part of the loop contribution), as required by analyticity. Specifically,

$$(M_\rho^2 - x)^{-1} \rightarrow \left\{ M_\rho^2 \left( 1 + \frac{x}{96\pi^2 F^2} \text{Re} \left[ A_\pi(x) + \frac{A_K(x)}{2} \right] \right) - x - iM_\rho \Gamma_\rho(x) \right\}^{-1}, \quad (\text{A.5})$$

with

$$\begin{aligned} \Gamma_\rho(x) &= \frac{M_\rho x}{96\pi F^2} \left[ \theta(x - 4m_\pi^2) \sigma_\pi^3(x) + \theta(x - 4m_K^2) \frac{\sigma_K^3(x)}{2} \right] \\ &= -\frac{M_\rho x}{96\pi^2 F^2} \text{Im} \left[ A \left( \frac{m_\pi^2}{x}, \frac{m_\pi^2}{M_\rho^2} \right) + \frac{1}{2} A \left( \frac{m_K^2}{x}, \frac{m_K^2}{M_\rho^2} \right) \right] \end{aligned}$$

and  $(A_P(x))$  is short for  $A \left( \frac{m_P^2}{x}, \frac{m_P^2}{M_\rho^2} \right)$

$$\text{Re}A_P(x) = \text{Log} \frac{m_P^2}{M_\rho^2} + 8 \frac{m_P^2}{x} - \frac{5}{3} + \sigma_P^3(x) \text{Log} \left| \frac{\sigma_P(x) + 1}{\sigma_P(x) - 1} \right|, \quad (\text{A.6})$$

being  $\sigma_P(x) = \sqrt{1 - \frac{4m_P^2}{x}}$ .

The tensor form factor,  $F_T(s)$ , given by eq. (A.4), and using the substitution eq. (A.5), is plotted in figure A.1 for  $\Lambda_2 = 12$  MeV [514]. There, it is seen how the  $\rho(770)$  meson contribution modifies the constant  $\chi PT$  lowest-order result for  $|F_T(s)|$ . The form factor phase,  $\delta_T(s)$ , grows from zero to  $\sim 110^\circ$  for  $0.85 \leq \sqrt{s} \leq 0.90$  GeV and decreases softly to zero for larger energies. Both  $|F_T(s)|$  and  $\delta_T(s)$  are influenced by the on-shell  $\rho(770)$  meson width as expected, according to its value of  $\sim 145$  MeV.

At this point unitarity arguments may convince us that this description of  $F_T(s)$  cannot be complete <sup>1</sup>. As explained in ref. [427], the phase of  $F_T(s)$  must coincide with the phase of  $F_+(s)$  in the elastic region (in this paper this was shown for the tau decays into the  $K\pi$  system, but it is completely analogous to the  $\pi\pi$  one considered here). We briefly review the

---

<sup>1</sup>We thank Bastian Kubis for pointing this to us.

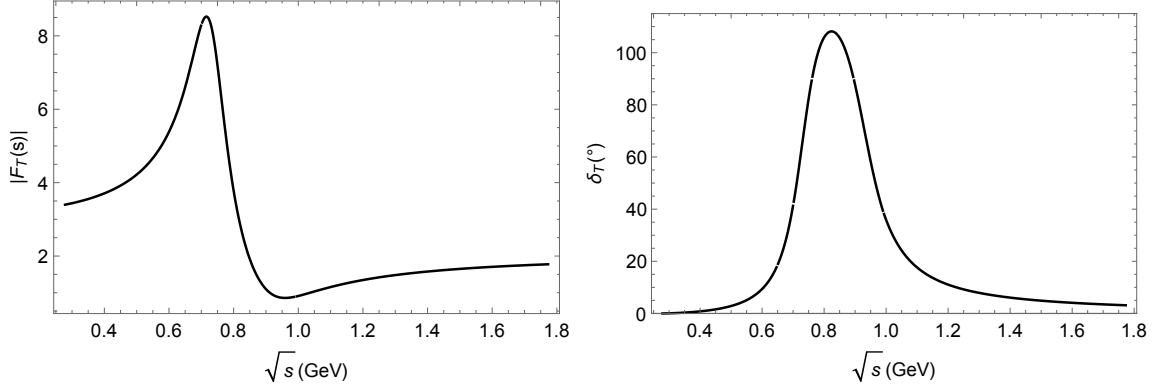


Figure A.1: Modulus and phase,  $|F_T(s)|$  (left) and  $\delta_T(s)$  (right), of the tensor form factor,  $F_T(s)$ , corresponding to the description explained in this appendix.

argument in what follows.

The unitarity relation for  $F_+(s)$  can be written

$$\text{Im } mF_+(s) = \sigma_\pi(s)F_+(s)(f_1^1(s))^*\theta(s - 4m_\pi^2), \quad (\text{A.7})$$

where  $f_1^1(s)$  is the the corresponding partial wave in  $\pi\pi$  scattering. The previous equation implies that, in the elastic region,  $\delta_1^1(s) = \delta_+(s)$ , which is again Watson's theorem. The crucial point is that an analogous unitarity relation holds for  $F_T(s)$ :

$$\text{Im } mF_T(s) = \sigma_\pi(s)F_T(s)(f_1^1(s))^*\theta(s - 4m_\pi^2), \quad (\text{A.8})$$

from which one can immediately derive that, in the elastic region,  $\delta_T(s) = \delta_+(s)$ , a feature that is not satisfied by our expression for  $F_T(s)$  considered up to now (and it will not be satisfied for any value of  $\Lambda_2$ ). This should not be understood as a failure of eq. (A.4) (together with eq. (A.5)), but rather as a manifestation of its incompleteness. Indeed, the contributions from the next-to-leading order  $\chi PT$  Lagrangian with tensor sources ( $\mathcal{O}(p^6)$  in the chiral counting [518]) should provide with the needed energy-dependence to satisfy eq. (A.8). However, since the number of such operators is 75 (plus 3 contact terms) even in the  $SU(2)$  case [518], we refrain from proceeding this way as any predictability would be lost.

# Appendix B

## Chiral ward Identities among four- and five-point Green functions

In  $\chi PT$ , the Green functions are obtained through functional derivatives of the generating functional  $Z(v, a, s, p)$ . This functional is constructed in order that it is invariant under transformations generated by the vector currents

$$Z(v, a, s, p) = Z(v', a', s', p'), \quad (\text{B.1})$$

where

$$v'_\mu \pm a'_\mu = g(v_\mu \pm a_\mu) g^\dagger + i\partial_\mu g^\dagger, \quad (\text{B.2a})$$

$$s' + ip' = g(s + ip) g^\dagger, \quad g(x) \in SU(3). \quad (\text{B.2b})$$

In particular, seagulls and Schwinger terms are automatically taken into account for an infinitesimal transformation  $g = 1 + i\alpha + \mathcal{O}(\alpha^2)$ ,

$$\delta v_\mu = i[\alpha, v_\mu] + \partial_\mu \alpha \equiv D_\mu \alpha, \quad (\text{B.3a})$$

$$\delta I = i[\alpha, I], \quad I = a_\mu, s, p. \quad (\text{B.3b})$$



One obtains from Eq. B.1

$$\left\langle \alpha D_\mu \frac{\delta Z}{\delta v_\mu(x)} \right\rangle = i \sum_i \left\langle [\alpha, I(x)] \frac{\delta Z}{\delta I(x)} \right\rangle, \quad (\text{B.4})$$

differentiating Eq. B.4 with respect to  $v_\nu^{1-i2}(y)$ ,  $v_\rho^3(z)$ ,  $v_\sigma^{1+i2}(w)$  and  $v_\lambda^3(t)$  we get an expression that relates the divergence of the Green function of five points with that of four points.

# Appendix C

## Amplitude for the $\tau^- \rightarrow \pi^- \pi^- \gamma \nu_\tau$ decays

For the radiative decay  $\tau^-(P) \rightarrow \pi^-(p_-) \pi^0(p_0) \nu_\tau(q) \gamma(k)$ , we can split the contribution due to the bremsstrahlung off the initial tau lepton and the other coming from the hadronic part, this is shown in the figure C.1. We write down the general structure for these processes

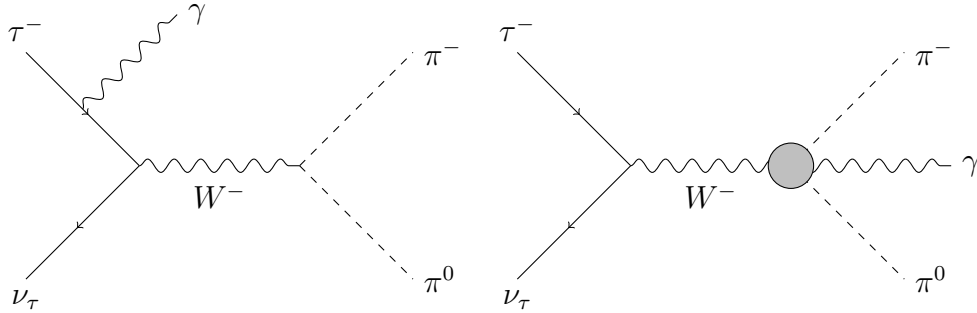


Figure C.1: Feynman diagrams for the  $\tau^- \rightarrow \pi^- \pi^0 \nu_\tau \gamma$  decays.

$$\begin{aligned}
 T = eG_F V_{ud}^* \epsilon^\mu(k)^* \{ & F_\nu \bar{u}(q) \gamma^\nu (1 - \gamma_5) (m_\tau + \not{P} - \not{k}) \gamma_\mu u(P) \\
 & + (V_{\mu\nu} - A_{\mu\nu}) \bar{u}(q) \gamma^\nu (1 - \gamma_5) u(P) \}, \tag{C.1}
 \end{aligned}$$

where  $F_\nu = (p_0 - p_-)_\nu f_+(s) / 2P \cdot k$ . Gauge invariance ( $\epsilon_\mu \rightarrow \epsilon_\mu + k_\mu$ ) implies the ward identities

$$k_\mu V^{\mu\nu} = (p_- - p_0)^\nu f_+(s), \quad \text{with } s = (p_- + p_0)^2 \quad (\text{C.2a})$$

$$k_\mu A^{\mu\nu} = 0. \quad (\text{C.2b})$$

In order to determine the general structure for  $V_{\mu\nu}$  and  $A_{\mu\nu}$ , we followed the same technique as in Ref. [701], first we isolate the photon off the final  $\pi^-$ , this process  $W^-(P - q) \rightarrow \pi^-(p_-) \pi^0(p_0) \gamma(k)$  is shown in the diagram C.2, the effective coupling is:

$$\Gamma^\mu = -ie(p' + p)^\mu, \quad (\text{C.3})$$

this contribution is proportional to the form factor  $f_+[(P - q)^2]$ .

We can write  $V^{\mu\nu}$  as  $V^{\mu\nu} = \bar{V}^{\mu\nu} + V_1^{\mu\nu}$ , where  $V_1^{\mu\nu}$  is the contribution that we have found

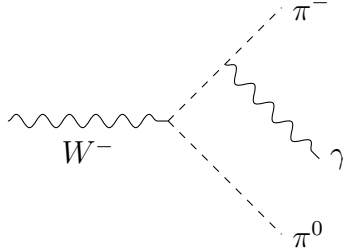


Figure C.2: Bremsstrahlung off the charged-pion.

before.

$$V_1^{\mu\nu} = \frac{p_-^\mu (p_- - p_0 + k)^\nu}{p_- \cdot k} f_+[(P - q)^2], \quad (\text{C.4a})$$

$$k_\mu V_1^{\mu\nu} = (p_- - p_0 + k)^\nu f_+[(P - q)^2], \quad (\text{C.4b})$$

and finally

$$k_\mu \bar{V}^{\mu\nu} = (p_- - p_0)^\nu f_+(s) - (p_- - p_0 + k)^\nu f_+[(P - q)^2]. \quad (\text{C.5})$$

We propose an structure for  $\bar{V}^{\mu\nu}$  using the four momentum  $(P - q)$ ,  $p_-$ ,  $p_0$  and  $k$  but only three of them are l. i., so we have

$$\bar{V}^{\mu\nu} = b_1 g^{\mu\nu} + b_2 p_-^\mu k^\nu + b_3 p_0^\mu k^\nu + b_4 p_-^\mu p_0^\nu + b_5 p_0^\mu p_-^\nu + b_6 p_-^\mu p_-^\nu + b_7 p_0^\mu p_0^\nu \quad (\text{C.6})$$

or through a change of basis,

$$\begin{aligned} \bar{V}^{\mu\nu} = & b_1 g^{\mu\nu} + b_2 p_-^\mu k^\nu + b_3 p_0^\mu k^\nu + b'_4 (p_0 + p_-)^\mu p_0^\nu + b'_5 (p_0 + p_-)^\mu p_-^\nu \\ & + b'_6 (p_0 - p_-)^\mu p_-^\nu + b'_7 (p_0 - p_-)^\mu p_0^\nu, \end{aligned} \quad (\text{C.7})$$

imposing the ward identity and making the change  $b_2 \rightarrow -v_1 + (p_0 \cdot k) v_4$ ,  $b_3 \rightarrow -v_2 - (p_- \cdot k) v_4$ ,  $b_7 \rightarrow -(p_- \cdot k) v_4$ ,  $b_5 \rightarrow -(p_- \cdot k) (v_3 + v_4)$  (or  $b'_7 \rightarrow -(p_0 + p_-) \cdot k v_4/2$ ,  $b'_6 \rightarrow -(p_0 + p_-) \cdot k (v_3 + v_4)/2$ ), we obtained these two equivalent expressions for  $V^{\mu\nu}$

$$\begin{aligned} V^{\mu\nu} = & f_+(s) \frac{p_-^\mu (p_- - p_0)^\nu}{p_- \cdot k} + f_+ [(P - q)^2] \left( \frac{p_-^\mu k^\nu}{p_- \cdot k} - g^{\mu\nu} \right) \\ & + v_1 (g^{\mu\nu} p_- \cdot k - p_-^\mu k^\nu) + v_2 (g^{\mu\nu} p_0 \cdot k - p_0^\mu k^\nu) \\ & + v_3 (p_0 \cdot k p_-^\mu - p_- \cdot k p_0^\mu) p_-^\nu + v_4 (p_0 \cdot k p_-^\mu - p_- \cdot k p_0^\mu) (p_0 + p_- + k)^\nu \end{aligned} \quad (\text{C.8})$$

and

$$\begin{aligned} V^{\mu\nu} = & f_+ [(P - q)^2] \frac{p_-^\mu (p_- + k - p_0)^\nu}{p_- \cdot k} - f_+ [(P - q)^2] g^{\mu\nu} \\ & + \frac{f_+ [(P - q)^2] - f_+(s)}{(p_0 + p_-) \cdot k} (p_0 + p_-)^\mu (p_0 - p_-)^\nu \\ & + v_1 (g^{\mu\nu} p_- \cdot k - p_-^\mu k^\nu) + v_2 (g^{\mu\nu} p_0 \cdot k - p_0^\mu k^\nu) \\ & + v_3 (p_0 \cdot k p_-^\mu - p_- \cdot k p_0^\mu) p_-^\nu + v_4 (p_0 \cdot k p_-^\mu - p_- \cdot k p_0^\mu) (p_0 + p_- + k)^\nu. \end{aligned} \quad (\text{C.9})$$

The second is the more useful than the first one because if we take into account that  $(P - q)^2 = s + 2(p_0 + p_-) \cdot k$ , the Low's theorem [702] is manifestly satisfied

$$\begin{aligned}
V^{\mu\nu} = & f_+(s) \frac{p_-^\mu}{p_- \cdot k} (p_- - p_0)^\nu + f_+(s) \left( \frac{p_-^\mu k^\nu}{p_- \cdot k} - g^{\mu\nu} \right) \\
& + 2 \frac{df_+(s)}{ds} \left( \frac{p_0 \cdot k}{p_- \cdot k} p_-^\mu - p_0^\mu \right) (p_- - p_0)^\nu + \mathcal{O}(k)
\end{aligned} \tag{C.10}$$

For the axial structure, we followed the same method

$$\begin{aligned}
A^{\mu\nu} = & c_1 \epsilon^{\mu\nu\rho\sigma} p_{-\rho} p_{0\sigma} + c_2 \epsilon^{\mu\nu\rho\sigma} p_{-\rho} k_\sigma + c_3 \epsilon^{\mu\nu\rho\sigma} p_{0\rho} k_\sigma + c_4 p_-^\nu \epsilon^{\mu\lambda\rho\sigma} p_{-\lambda} p_{0\rho} k_\sigma \\
& + c_5 p_0^\nu \epsilon^{\mu\lambda\rho\sigma} p_{-\lambda} p_{0\rho} k_\sigma + c_6 k^\nu \epsilon^{\mu\lambda\rho\sigma} p_{-\lambda} p_{0\rho} k_\sigma + c_7 p_-^\mu \epsilon^{\nu\lambda\rho\sigma} p_{-\lambda} p_{0\rho} k_\sigma \\
& + c_8 p_0^\mu \epsilon^{\nu\lambda\rho\sigma} p_{-\lambda} p_{0\rho} k_\sigma
\end{aligned} \tag{C.11}$$

imposing the ward identity for  $A^{\mu\nu}$ , we found one equation that satisfied  $k_\mu A^{\mu\nu} = 0$

$$c_1 - c_7 (k \cdot p_-) - c_8 (k \cdot p_0) = 0 \tag{C.12a}$$

with this equation and using the Schouten's identity we get

$$\begin{aligned}
A^{\mu\nu} = & A_1 \epsilon^{\mu\nu\rho\sigma} p_{-\rho} k_\sigma + A_2 \epsilon^{\mu\nu\rho\sigma} p_{0\rho} k_\sigma \\
& + A_3 p_-^\nu \epsilon^{\mu\lambda\rho\sigma} p_{-\lambda} p_{0\rho} k_\sigma + A_4 p_0^\nu \epsilon^{\mu\lambda\rho\sigma} p_{-\lambda} p_{0\rho} k_\sigma,
\end{aligned} \tag{C.13}$$

where  $A_1 = c_2 + c_7 p_- \cdot p_0 + c_8 m_\pi^2 - c_6 k \cdot p_0$ ,  $A_2 = c_3 - c_7 m_\pi^2 - c_8 p_- \cdot p_0 + c_6 k \cdot p_0$ ,  $A_3 = c_4 + c_7$  and  $A_4 = c_5 + c_8$ . For this case, there are only four Lorentz structures contributing to  $A^{\mu\nu}$ . We can chose the basis given in Ref. [700]

$$A^{\mu\nu} = i\epsilon^{\mu\nu\rho\sigma} (a'_1 p_{0\rho} k_\sigma + a'_2 k_\rho W_\sigma) + i\epsilon^{\mu\lambda\rho\sigma} k_\lambda p_{-\rho} p_{0\sigma} (a'_3 W^\nu + a'_4 (p_0 + k)^\nu), \tag{C.14}$$

which is a linear combination of the basis in eq. C.13, where  $W \equiv P - q = p_- + p_0 + k$ , but instead we're going to use a modified one that resembles the decomposition given by

Ref. [94]

$$\begin{aligned}
A^{\mu\nu} = & ia_1 \epsilon^{\mu\nu\rho\sigma} (p_0 - p_-)_\rho k_\sigma + ia_2 (P - q)^\nu \epsilon^{\mu\lambda\rho\sigma} k_\lambda p_{-\rho} p_{0\sigma} \\
& + ia_3 \epsilon^{\mu\nu\rho\sigma} k_\rho W_\sigma + ia_4 (p_0 + k)^\nu \epsilon^{\mu\lambda\rho\sigma} k_\lambda p_{-\rho} p_{0\sigma}.
\end{aligned} \tag{C.15}$$

## C.1 Anomaly

We have a contribution to these two diagrams (Fig. C.3) due to the chiral anomaly. The

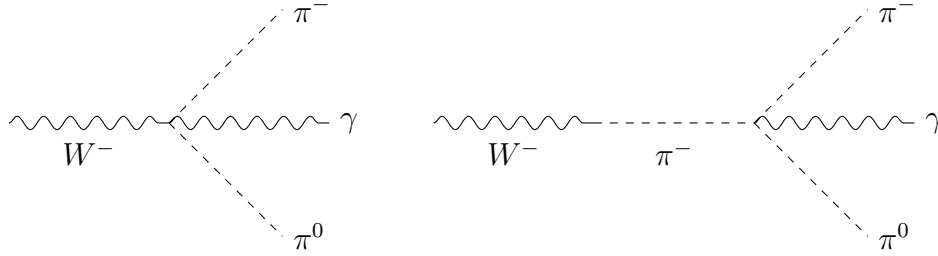


Figure C.3: Anomalous diagrams for the transition  $W^- (P - q) \rightarrow \pi^- (p_-) \pi^0 (p_0) \gamma (k)$  contributing to the axial tensor amplitude  $A^{\mu\nu}$

Wess-Zumino-Witten functional  $\mathcal{O}(p^4)$  [212, 213] can be expressed in two terms which are

$$\begin{aligned}
\mathcal{L}_{anom}(W\gamma) &= -\frac{i\alpha}{4\sqrt{2}\pi \sin\theta_W} \epsilon^{\mu\nu\alpha\beta} W_\mu^+ F_{\nu\alpha} \left\langle T_+ \left\{ U^\dagger D_\beta U, Q + \frac{1}{2} U^\dagger Q U \right\} \right\rangle + h.c., \\
&= -\frac{i\alpha V_{ud}^*}{8\pi \sin\theta_W f^2} \epsilon^{\mu\nu\alpha\beta} W_\mu F_{\nu\alpha} \left( \pi^0 \partial_\beta \pi^+ - \pi^+ \partial_\beta \pi^0 \right) + \dots,
\end{aligned} \tag{C.16}$$

where  $D_\mu U = \partial_\mu U + ieA_\mu [Q, U]$  is the covariant derivative with respect to electromagnetism only, and

$$\begin{aligned}
\mathcal{L}_{anom}(\phi^3\gamma) &= -\frac{e}{16\pi^2} \epsilon^{\mu\nu\rho\sigma} A_\sigma \left\langle Q \left[ \partial_\mu U \partial_\nu U^\dagger \partial_\rho U U^\dagger - \partial_\mu U^\dagger \partial_\nu U \partial_\rho U^\dagger U \right] \right\rangle \\
&= -i \frac{e}{4\pi^2 f^3} \epsilon^{\mu\nu\rho\sigma} A_\sigma \partial_\mu \pi^+ \partial_\nu \pi^- \partial_\rho \pi^0 + \dots,
\end{aligned} \tag{C.17}$$

where  $F_{\mu\nu} = \partial_\mu A_\nu - \partial_\nu A_\mu$ . Eq. C.16 give us the coupling between  $W\pi^-\pi^0\gamma$ ,

$$\Gamma^{\mu\nu} = -\frac{g_W e V_{ud}^*}{16\pi^2 f^2} \epsilon^{\mu\nu\alpha\beta} (p_0 - p_-)_\alpha k_\beta, \quad (\text{C.18})$$

while Eq. C.17 give us the coupling between  $\pi^-\pi^-\pi^0\gamma$

$$\Gamma^\mu = -\frac{ie}{4\pi^2 f^3} \epsilon^{\mu\alpha\beta\rho} (P - q)_\alpha p_{-\beta} p_{0\rho}, \quad (\text{C.19})$$

then we get

$$a_1 = \frac{1}{8\pi^2 f^2}, \quad a_2 = \frac{-1}{4\pi^2 f^2 [(P - q)^2 - m_\pi^2]}, \quad (\text{C.20})$$

or

$$a'_1 = \frac{1}{4\pi^2 f^2}, \quad a'_2 = \frac{1}{8\pi^2 f^2}, \quad a'_3 = \frac{-1}{4\pi^2 f^2 [(P - q)^2 - m_\pi^2]}. \quad (\text{C.21})$$

## C.2 $R\chi T$ contributions

Using the antisymmetric formalism for spin-one fields, we write the  $R\chi T$  Lagrangian as [224, 225, 813]

$$\mathcal{L}_{res}(R) = \sum_{R=T,V,A,H,S,P} [\mathcal{L}_{kin}(R) + \mathcal{L}_2(R)], \quad (\text{C.22})$$

with

$$\begin{aligned} \mathcal{L}_{kin}(R) &= -\frac{1}{2} \langle T_{\mu\nu} D_T^{\mu\nu,\rho\sigma} T_{\rho\sigma} \rangle, \quad R = T \\ \mathcal{L}_{kin}(R) &= -\frac{1}{2} \left\langle \nabla^\lambda R_{\lambda\mu} \nabla_\nu R^{\nu\mu} - \frac{1}{2} M_R^2 R_{\mu\nu} R^{\mu\nu} \right\rangle - \frac{1}{2} \partial^\lambda R_{1,\lambda\mu} \partial_\nu R_1^{\nu\mu} \\ &\quad + \frac{1}{4} M_{R_1}^2 R_{1,\mu\nu} R_1^{\mu\nu}, \quad R = V, A, H \\ \mathcal{L}_{kin}(R) &= \frac{1}{2} \langle \nabla^\mu R \nabla_\mu R - M_R^2 R^2 \rangle + \frac{1}{2} \left\{ \partial^\mu R_1 \partial_\mu R_1 - M_{R_1}^2 \right\}, \quad R = S, P \end{aligned} \quad (\text{C.23})$$

where

$$\nabla_\mu R = \partial_\mu R + [\Gamma_\mu, R],$$

$$\Gamma_\mu = \frac{1}{2} \left\{ u^\dagger [\partial_\mu - i(v_\mu + a_\mu)] u + u [\partial_\mu - i(v_\mu - a_\mu)] u^\dagger \right\},$$

and

$$\begin{aligned} D_T^{\mu\nu,\rho\sigma} &= \left( \partial^\mu \partial_\mu + M_T^2 \right) \left[ \frac{1}{2} (g^{\mu\rho} g^{\nu\sigma} + g^{\mu\sigma} g^{\nu\rho}) - g^{\mu\nu} g^{\rho\sigma} \right] \\ &+ g^{\rho\sigma} \partial^\mu \partial^\nu + g^{\mu\nu} \partial^\rho \partial^\sigma - \frac{1}{2} (g^{\nu\sigma} \partial^\mu \partial^\rho + g^{\rho\nu} \partial^\mu \partial^\sigma + g^{\mu\sigma} \partial^\rho \partial^\nu + g^{\rho\mu} \partial^\sigma \partial^\nu), \end{aligned}$$

$M_R$  and  $M_{R_1}$  are the masses in the chiral limit. Interactions with the  $V$ ,  $A$ ,  $S$  and  $P$  fields start to order  $p^2$  and are given by

$$\mathcal{L}_2 [V(1^{--})] = \frac{F_V}{2\sqrt{2}} \langle V_{\mu\nu} f_+^{\mu\nu} \rangle + \frac{iG_V}{\sqrt{2}} \langle V_{\mu\nu} u^\mu u^\nu \rangle, \quad (\text{C.24a})$$

$$\mathcal{L}_2 [A(1^{++})] = \frac{F_A}{2\sqrt{2}} \langle A_{\mu\nu} f_-^{\mu\nu} \rangle, \quad (\text{C.24b})$$

$$\mathcal{L}_2 [S(0^{++})] = c_d \langle S u_\mu u^\mu \rangle + c_m \langle S \chi_+ \rangle, \quad (\text{C.24c})$$

$$\mathcal{L}_2 [P(0^{-+})] = i d_m \langle P \chi_- \rangle. \quad (\text{C.24d})$$

Thus, we get

$$J_{W^- \rightarrow \rho^-}^\nu = -i\sqrt{2} F_V (P - q)_\mu \langle \rho^- (P - q) | \rho^{+\mu\nu} | 0 \rangle \quad (\text{C.25})$$

$$J_{W^- \rightarrow \rho^- \gamma}^\nu = ie\sqrt{2} F_V \epsilon_\mu^*(k) \langle \rho^- (p_- + p_0) | \rho^{+\mu\nu} | 0 \rangle \quad (\text{C.26})$$

$$J_{W^- \rightarrow \rho^- \pi^0}^\nu = \frac{\sqrt{2}}{f} (2G_V p_{0\mu} - F_V (P - q)_\mu) \langle \rho^- (p_- + k) | \rho^{+\mu\nu} | 0 \rangle \quad (\text{C.27})$$

$$J_{W^- \rightarrow \rho^0 \pi^-}^\nu = -\frac{\sqrt{2}}{f} (2G_V p_{-\mu} - F_V (P - q)_\mu) \langle \rho^0 (p_0 + k) | \rho^{0\mu\nu} | 0 \rangle \quad (\text{C.28})$$

$$J_{W^- \rightarrow \pi^- \pi^0 \rho^0}^\nu = \frac{i}{\sqrt{2} f^2} (4G_V p_{-\mu} - F_V (P - q)_\mu) \langle \rho^0(k) | \rho^{0\mu\nu} | 0 \rangle \quad (\text{C.29})$$

$$\begin{aligned} J_{W^- \rightarrow \rho^- \rho^0}^\nu &= \sqrt{2} \left\{ k^\lambda \langle \rho^- (p_0 + p_-) \rho^0(k) | \rho_{\lambda\kappa}^0 \rho^{+\nu\kappa} | 0 \rangle \right. \\ &\quad \left. - (p_- + p_0)^\lambda \langle \rho^- (p_0 + p_-) \rho^0(k) | \rho^{0\nu\kappa} \rho_{\lambda\kappa}^+ | 0 \rangle \right\} \end{aligned} \quad (\text{C.30})$$



$$J_{W^- \rightarrow a_1^-}^\nu = -i\sqrt{2}F_A (P - q)_\mu \langle a_1^- (P - q) | a_1^{+\mu\nu} | 0 \rangle \quad (\text{C.31})$$

$$J_{W^- \rightarrow a_1^- \gamma}^\nu = ie\sqrt{2}F_A \epsilon_\mu^*(k) \langle a_1^- (p_- + p_0) | a_1^{+\mu\nu} | 0 \rangle \quad (\text{C.32})$$

$$J_{W^- \rightarrow a_1^- \pi^0}^\nu = -\frac{\sqrt{2}F_A}{f} (P - q)_\mu \langle a_1^- (p_- + k) | a_1^{+\mu\nu} | 0 \rangle \quad (\text{C.33})$$

$$J_{W^- \rightarrow a_1^0 \pi^-}^\nu = \frac{\sqrt{2}F_A}{f} (P - q)_\mu \langle a_1^0 (p_0 + k) | a_1^{0\mu\nu} | 0 \rangle \quad (\text{C.34})$$

$$G_{\rho^- \rightarrow \pi^- \pi^0} = \frac{2G_V}{f^2} p_{-\mu} p_{0\nu} \langle 0 | \rho^{-\mu\nu} | \rho^- (p_- + p_0) \rangle \quad (\text{C.35})$$

$$G_{\pi^- \rightarrow \pi^- \rho^0} = -\frac{2G_V}{f^2} (\mathcal{P} + p_-)_\mu p_{-\nu} \langle \rho^0 (\mathcal{P}) | \rho^{0\mu\nu} | 0 \rangle \quad (\text{C.36})$$

$$G_{\pi^- \rightarrow \pi^0 \rho^-} = \frac{2G_V}{f^2} (P - q)_\mu p_{0\nu} \langle \rho^- (p_- + k) | \rho^{-\mu\nu} | 0 \rangle \quad (\text{C.37})$$

$$G_{\rho^0 \rightarrow \gamma} = e F_V k^\mu \epsilon^{*\nu}(k) \langle 0 | \rho_{\mu\nu}^0 | \rho^0(k) \rangle \quad (\text{C.38})$$

$$G_{\omega \rightarrow \gamma} = \frac{1}{3} e F_V k^\mu \epsilon^{*\nu}(k) \langle 0 | \omega_{\mu\nu} | \omega(k) \rangle \quad (\text{C.39})$$

$$G_{\rho^- \rightarrow \pi^- \pi^0 \gamma} = \frac{e}{2f^2} (4G_V p_0^\mu + F_V k^\mu) \epsilon^{*\nu}(k) \langle 0 | \rho_{\mu\nu}^- | \rho^- (P - q) \rangle \quad (\text{C.40})$$

$$G_{\rho^- \rightarrow \rho^- \gamma} = -ie \epsilon_\nu^*(k) \left\{ (p_- + p_0)^\lambda \langle \rho^- (p_- + p_0) | \rho_{\lambda\rho}^+ \rho^{-\nu\rho} | \rho^- (P - q) \rangle \right. \\ \left. + (P - q)^\lambda \langle \rho^- (p_- + p_0) | \rho^{+\nu\rho} \rho_{\lambda\rho}^- | \rho^- (P - q) \rangle \right\} \quad (\text{C.41})$$

$$G_{\rho^- \rightarrow \rho^0 \pi^- \pi^0} = \frac{i}{2f^2} \left\{ k^\lambda (p_0 - p_-)_\nu \langle \rho^0(k) | \rho_{\lambda\rho}^0 \rho^{-\nu\rho} | \rho^- (P - q) \rangle \right. \\ \left. + (P - q)^\lambda (p_0 - p_-)_\nu \langle \rho^0(k) | \rho^{0\nu\rho} \rho_{\lambda\rho}^- | \rho^- (P - q) \rangle \right\} \quad (\text{C.42})$$

$$G_{a_1^- \rightarrow \pi^- \gamma} = -ie \frac{F_A}{f} k^\mu \epsilon^{*\nu}(k) \langle 0 | a_{1\mu\nu}^- | a_1^- (p_- + k) \rangle \quad (\text{C.43})$$

For the first diagram, we have

$$= \frac{\sqrt{2}F_V G_V (P - q)^2}{f^2 k \cdot p_-} e \epsilon_\mu^*(k) D_\rho^{-1} [(P - q)^2] p_-^\mu (k - p_0 + p_-)^\nu \\ - \frac{2\sqrt{2}F_V G_V}{f^2} e \epsilon_\mu^*(k) D_\rho^{-1} [(P - q)^2] p_-^\mu (k + p_0 + p_-)^\nu, \quad (\text{C.44})$$

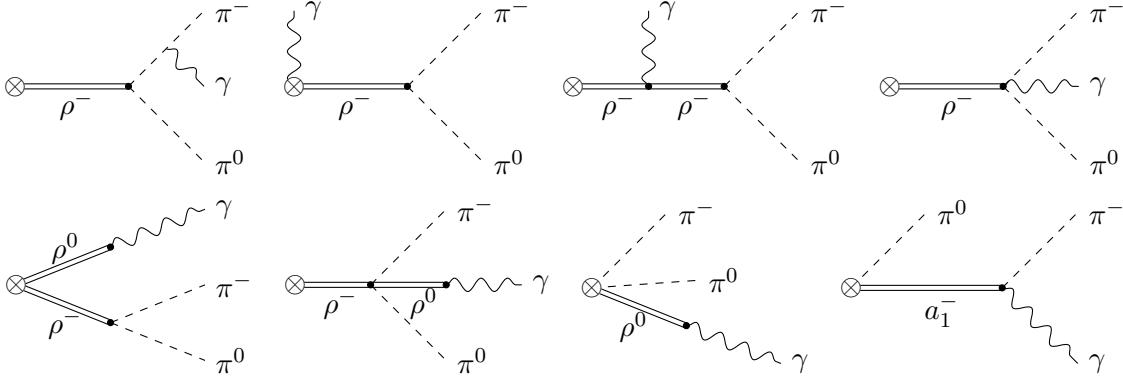


Figure C.4:  $\rho$  and  $a_1$  exchange diagrams for the model at  $\mathcal{O}(p^4)$

for the second diagram, we get

$$= \frac{2\sqrt{2}F_V G_V}{f^2 M_\rho^2} e \epsilon_\mu^*(k) D_\rho^{-1}(s) M_\rho^2 (p_-^\mu p_0^\nu - p_-^\nu p_0^\mu), \quad (\text{C.45})$$

for the third diagram

$$\begin{aligned} &= \frac{2\sqrt{2}F_V G_V}{f^2 M_\rho^2} e \epsilon_\mu^*(k) D_\rho^{-1}(s) D_\rho^{-1}[(P-q)^2] M_\rho^2 \left\{ \frac{1}{2} s (k \cdot p_- g^{\mu\nu} - p_-^\mu k^\nu) \right. \\ &\quad - \frac{1}{2} s (k \cdot p_0 g^{\mu\nu} - p_0^\mu k^\nu) - (k \cdot p_0 p_-^\mu - k \cdot p_- p_0^\mu) (p_- + p_0 + k)^\nu \\ &\quad \left. - s p_-^\mu p_-^\nu - (P-q)^2 p_0^\mu p_-^\nu + (P-q)^2 p_-^\mu p_0^\nu + s p_0^\mu p_0^\nu \right\}, \end{aligned} \quad (\text{C.46})$$

for the fourth diagram

$$\begin{aligned} &= -\frac{\sqrt{2}F_V^2}{2f^2 M_\rho^2} e \epsilon_\mu^*(k) D_\rho^{-1}[(P-q)^2] M_\rho^2 \{ (k \cdot p_- g^{\mu\nu} - p_-^\mu k^\nu) + (k \cdot p_0 g^{\mu\nu} - p_0^\mu k^\nu) \} \\ &\quad + \frac{2\sqrt{2}F_V G_V}{f^2 M_\rho^2} e \epsilon_\mu^*(k) D_\rho^{-1}[(P-q)^2] M_\rho^2 \{ (k \cdot p_- g^{\mu\nu} - p_-^\mu k^\nu) \\ &\quad + p_-^\mu p_0^\nu + p_0^\mu p_-^\nu + p_-^\mu k^\nu - \frac{1}{2} (P-q)^2 g^{\mu\nu} \}, \end{aligned} \quad (\text{C.47})$$

for the fifth diagram

$$= \frac{\sqrt{2}F_V G_V}{f^2 M_\rho^2} e \epsilon_\mu^*(k) D_\rho^{-1}(s) \{s(k \cdot p_- g^{\mu\nu} - p_-^\mu k^\nu) - s(k \cdot p_0 g^{\mu\nu} - p_0^\mu k^\nu)\}, \quad (\text{C.48})$$

for the sixth diagram

$$= \frac{\sqrt{2}F_V^2}{2f^2 M_\rho^2} e \epsilon_\mu^*(k) D_\rho^{-1}[(P-q)^2] \left\{ (P-q)^2 (k \cdot p_- g^{\mu\nu} - p_-^\mu k^\nu) \right. \\ \left. - (P-q)^2 (k \cdot p_0 g^{\mu\nu} - p_0^\mu k^\nu) + 2(k \cdot p_0 p_-^\mu - k \cdot p_- p_0^\mu) (p_- + p_0 + k)^\nu \right\}, \quad (\text{C.49})$$

for the seventh diagram

$$= -\frac{\sqrt{2}F_V^2}{2f^2 M_\rho^2} e \epsilon_\mu^*(k) \{(k \cdot p_- g^{\mu\nu} - p_-^\mu k^\nu) + (k \cdot p_0 g^{\mu\nu} - p_0^\mu k^\nu)\} \\ + \frac{2\sqrt{2}F_V G_V}{f^2 M_\rho^2} e \epsilon_\mu^*(k) (k \cdot p_- g^{\mu\nu} - p_-^\mu k^\nu), \quad (\text{C.50})$$

and finally, for the  $a_1^-$  exchange diagram

$$= \frac{\sqrt{2}F_A^2}{f^2 M_{a_1}^2} e \epsilon_\mu^*(k) D_{a_1}^{-1}[(p_- + k)^2] \left\{ \left( M_{a_1}^2 - m_\pi^2 + \frac{1}{2}s \right) (k \cdot p_- g^{\mu\nu} - p_-^\mu k^\nu) \right. \\ \left. + \left( M_{a_1}^2 - m_\pi^2 - k \cdot p_- \right) (k \cdot p_0 g^{\mu\nu} - p_0^\mu k^\nu) + (k \cdot p_0 p_-^\mu - k \cdot p_- p_0^\mu) p_-^\nu \right\}, \quad (\text{C.51})$$

with  $D_a(s) = M_a^2 - s$  the resonance propagators.

The overall contribution for these diagrams is

$$= \sqrt{2}e \epsilon_\mu^*(k) [v_1 (g^{\mu\nu} p_- \cdot k - p_-^\mu k^\nu) + v_2 (g^{\mu\nu} p_0 \cdot k - p_0^\mu k^\nu) \\ + v_3 (p_0 \cdot k p_-^\mu - p_- \cdot k p_0^\mu) p_-^\nu \\ + v_4 (p_0 \cdot k p_-^\mu - p_- \cdot k p_0^\mu) (p_0 + p_- + k)^\nu + X^{\mu\nu}], \quad (\text{C.52})$$

where

$$\begin{aligned}
v_1 &= \frac{F_V G_V}{f^2 M_\rho^2} \left( 2 + 2M_\rho^2 D_\rho^{-1} [(P - q)^2] + s D_\rho^{-1}(s) + s M_\rho^2 D_\rho^{-1}(s) D_\rho^{-1} [(P - q)^2] \right) \\
&\quad + \frac{F_V^2}{2f^2 M_\rho^2} \left( -1 - M_\rho^2 D_\rho^{-1} [(P - q)^2] + (P - q)^2 D_\rho^{-1} [(P - q)^2] \right) \\
&\quad + \frac{F_A^2}{f^2 M_{a_1}^2} \left( M_{a_1}^2 - m_\pi^2 + \frac{1}{2}s \right) D_{a_1}^{-1} [(p_- + k)^2], \\
v_2 &= \frac{F_V G_V s}{f^2 M_\rho^2} \left( -D_\rho^{-1}(s) - M_\rho^2 D_\rho^{-1}(s) D_\rho^{-1} [(P - q)^2] \right) \\
&\quad + \frac{F_V^2}{2f^2 M_\rho^2} \left( -1 - M_\rho^2 D_\rho^{-1} [(P - q)^2] - (P - q)^2 D_\rho^{-1} [(P - q)^2] \right) \\
&\quad + \frac{F_A^2}{f^2 M_{a_1}^2} \left( M_{a_1}^2 - m_\pi^2 - k \cdot p_- \right) D_{a_1}^{-1} [(p_- + k)^2], \\
v_3 &= \frac{F_A^2}{f^2 M_{a_1}^2} D_{a_1}^{-1} [(p_- + k)^2], \\
v_4 &= -\frac{2F_V G_V}{f^2} D_\rho^{-1}(s) D_\rho^{-1} [(P - q)^2] + \frac{F_V^2}{f^2 M_\rho^2} D_\rho^{-1} [(P - q)^2], \\
X^{\mu\nu} &= \frac{2F_V G_V}{f^2} D_\rho^{-1}(s) D_\rho^{-1} [(P - q)^2] \left[ (2M_\rho^2 - s) p_-^\mu p_0^\nu - M_\rho^2 p_0^\mu p_-^\nu - s p_-^\mu p_-^\nu \right. \\
&\quad \left. + M_\rho^2 p_0^\mu p_0^\nu + (M_\rho^2 - s) p_-^\mu k^\nu - \frac{1}{2} (P - q)^2 (M_\rho^2 - s) g^{\mu\nu} \right].
\end{aligned}$$

The term proportional to  $g^{\mu\nu}$  in  $X^{\mu\nu}$  is a contribution to the diagram shown in Fig. C.5, and the others are contributions to  $[f_+ [(P - q)^2] - f_+(s)]$  in eq. C.9. Thus,

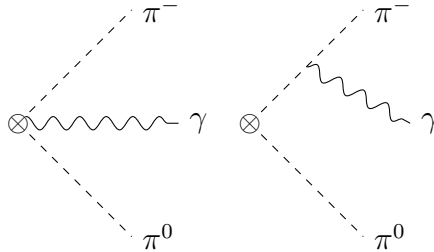


Figure C.5: Diagrams that receives contribution from  $X^{\mu\nu}$

$$X^{\mu\nu} = \frac{2F_V G_V}{f^2} D_\rho^{-1} [(P - q)^2] p_-^\mu (p_- + p_0 + k)^\nu, \quad (\text{C.54})$$

is not gauge invariant and receives contributions from diagram 3 and 4 which is canceled out by the contribution of the first diagram.

There is no contribution coming from the transverse part,  $\Omega_{\mu\nu,\rho\sigma}^T$ , for the  $\rho$ -exchange diagrams.

Using the contributions to  $\mathcal{O}(p^6)$  for the even- and the odd-intrinsic parity sectors [385,684], we get

$\hat{\mathcal{O}}_i^V$

$$G_{\rho^0 \rightarrow \gamma} = 8\sqrt{2}\lambda_6 m_\pi^2 e k^\mu \epsilon^{*\nu}(k) \langle 0 | \rho_{\mu\nu}^0 | \rho^0(k) \rangle \quad (\text{C.55})$$

$$G_{\omega \rightarrow \gamma} = \frac{8\sqrt{2}}{3} \lambda_6 m_\pi^2 e k^\mu \epsilon^{*\nu}(k) \langle 0 | \omega_{\mu\nu} | \omega(k) \rangle \quad (\text{C.56})$$

$$G_{\rho^- \rightarrow \pi^- \pi^0} = \frac{2\sqrt{2}}{f^2} (4m_\pi^2 \lambda_8 + 2m_\pi^2 \lambda_9 + 4m_\pi^2 \lambda_{10} - s\lambda_{21}) p_-^\mu p_0^\nu \langle 0 | \rho_{\mu\nu}^- | \rho^-(p_- + p_0) \rangle \quad (\text{C.57})$$

$$G_{\pi^- \rightarrow \pi^- \rho^0} = -\frac{2\sqrt{2}}{f^2} (4m_\pi^2 \lambda_8 + 2m_\pi^2 \lambda_9 + 4m_\pi^2 \lambda_{10} - \mathcal{P}^2 \lambda_{21}) (\mathcal{P} + p_-)^\mu p_-^\nu \times \langle \rho^0(\mathcal{P}) | \rho_{\mu\nu}^0 | 0 \rangle \quad (\text{C.58})$$

$$G_{\pi^- \rightarrow \pi^0 \rho^-} = \frac{2\sqrt{2}}{f^2} (4m_\pi^2 \lambda_8 + 2m_\pi^2 \lambda_9 + 4m_\pi^2 \lambda_{10} - (p_- + k)^2 \lambda_{21}) (P - q)^\mu p_0^\nu \times \langle \rho^-(p_- + k) | \rho_{\mu\nu}^+ | 0 \rangle \quad (\text{C.59})$$

$$\begin{aligned}
G_{\rho^- \rightarrow \pi^- \pi^0 \gamma} &= \frac{2\sqrt{2}}{f^2} e \left\{ 2\lambda_6 m_\pi^2 k^\mu \epsilon^{*\nu}(k) + 4\lambda_8 m_\pi^2 p_0^\mu \epsilon^{*\nu}(k) + 2\lambda_9 m_\pi^2 p_0^\mu \epsilon^{*\nu}(k) \right. \\
&\quad + 4\lambda_{10} m_\pi^2 p_0^\mu \epsilon^{*\nu}(k) - 2\lambda_{12} (p_- \cdot p_0) k^\mu \epsilon^{*\nu}(k) + 4\lambda_{20} m_\pi^2 k^\mu \epsilon^{*\nu}(k) \\
&\quad + \lambda_{13} \left[ p_-^\mu (p_0 \cdot k g^{\alpha\nu} - k^\nu p_0^\alpha) + p_0^\mu (p_- \cdot k g^{\alpha\nu} - k^\nu p_-^\alpha) \right] \epsilon_\alpha^*(k) \\
&\quad - \lambda_{14} \left[ p_-^\mu (p_0 \cdot k g^{\alpha\nu} - k^\nu p_0^\alpha) - p_0^\mu (p_- \cdot k g^{\alpha\nu} - k^\nu p_-^\alpha) \right] \epsilon_\alpha^*(k) \\
&\quad + \lambda_{15} \left[ p_-^\mu (p_0 \cdot k g^{\alpha\nu} - k^\nu p_0^\alpha) - p_0^\mu (p_- \cdot k g^{\alpha\nu} - k^\nu p_-^\alpha) \right] \epsilon_\alpha^*(k) \\
&\quad + \lambda_{16} (p_- + k)^\mu (p_0 \cdot k g^{\alpha\nu} - k^\nu p_0^\alpha) \epsilon_\alpha^*(k) \\
&\quad - \lambda_{17} (s - 2m_\pi^2 + 2k \cdot p_0) k^\mu \epsilon^{*\nu}(k) \\
&\quad - \lambda_{18} (p_- \cdot k g^{\alpha\mu} - k^\mu p_-^\alpha) p_0^\nu \epsilon_\alpha^*(k) + \lambda_{19} (p_0 \cdot k g^{\alpha\mu} - k^\mu p_0^\alpha) p_0^\nu \epsilon_\alpha^*(k) \\
&\quad - \lambda_{21} \left[ (P - q)^2 p_0^\mu \epsilon^{*\nu}(k) - 2(p_- + p_0)_\alpha \epsilon^{*\alpha}(k) p_-^\mu p_0^\nu \right] \\
&\quad \left. - \lambda_{22} \left( \frac{1}{2}s + 2k \cdot p_0 \right) k^\mu \epsilon^{*\nu}(k) \right\} \langle 0 | \rho_{\mu\nu}^- | \rho^-(p_- + p_0 + k) \rangle
\end{aligned} \tag{C.60}$$

$$J_{W^- \rightarrow \rho^-}^\rho = 4i \left( -4\lambda_6 m_\pi^2 + \lambda_{22} (P - q)^2 \right) (P - q)_\mu \langle \rho^-(P - q) | \rho^{+\mu\rho} | 0 \rangle \tag{C.61}$$

$$\begin{aligned}
J_{W^- \rightarrow \rho^- \gamma}^\rho &= 4ie \left\{ \left( 4\lambda_6 m_\pi^2 \epsilon_\mu^*(k) - \lambda_7 [(k \cdot p_- g_{\mu\alpha} - k_\mu p_{-\alpha}) + (k \cdot p_0 g_{\mu\alpha} - k_\mu p_{0\alpha})] \right) \epsilon^{*\alpha}(k) \right. \\
&\quad - \lambda_{22} \left[ s \epsilon_\mu^*(k) + 2(P - q)^\alpha \epsilon_\alpha^*(k) (P - q)_\mu \right] \langle \rho^-(p_- + p_0) | \rho^{+\mu\rho} | 0 \rangle \\
&\quad + (\lambda_7 (P - q)^\mu (k^\nu \epsilon^{*\rho}(k) - k^\rho \epsilon^{*\nu}(k)) - \lambda_{22} k^\mu \epsilon^{*\nu}(k) (p_- + p_0 - k)^\rho) \\
&\quad \left. \times \langle \rho^-(p_- + p_0) | \rho_{\mu\nu}^+ | 0 \rangle \right\}
\end{aligned} \tag{C.62}$$

$$\begin{aligned}
J_{W^- \rightarrow \rho^0 \pi^- \pi^0}^\rho = & i \frac{4}{f^2} \left\{ \left( -2\lambda_6 m_\pi^2 (P - q)_\mu + 2(2\lambda_8 + \lambda_9) m_\pi^2 p_{-\mu} + \lambda_{12} (s - 2m_\pi^2) (P - q)_\mu \right. \right. \\
& - \lambda_{13} \left[ \frac{1}{2} s (p_0 + p_-)_\mu + (k \cdot p_- p_{0\mu} + k \cdot p_0 p_{-\mu}) \right] \\
& + (\lambda_{14} - \lambda_{15}) \left[ \frac{1}{2} s (p_0 - p_-)_\mu + (k \cdot p_- p_{0\mu} - k \cdot p_0 p_{-\mu}) \right] \\
& + \lambda_{16} \left( \frac{1}{2} s + k \cdot p_- \right) (k + p_-)_\mu - 2\lambda_{17} (m_\pi^2 + k \cdot p_-) (P - q)_\mu \\
& + \lambda_{18} \left( \frac{1}{2} s + 2k \cdot p_- + k \cdot p_0 \right) p_{-\mu} + \lambda_{19} (s + 2k \cdot p_-) p_{-\mu} \\
& - 4\lambda_{20} m_\pi^2 (P - q)_\mu + \lambda_{22} (k \cdot p_0 - k \cdot p_-) (P - q)_\mu \left\langle \rho^0(k) \left| \rho^{0\mu\rho} \right| 0 \right\rangle \\
& + (\lambda_{13} (P - q)^\nu (p_0^\mu p_-^\rho + p_-^\mu p_0^\rho) - (\lambda_{14} - \lambda_{15}) (P - q)^\nu (p_0^\mu p_-^\rho - p_-^\mu p_0^\rho) \\
& + \lambda_{16} (P - q)^\mu (k + p_-)^\nu p_-^\rho + \lambda_{18} (P - q)^\mu (k + p_-)^\rho p_-^\nu \\
& \left. + 2\lambda_{19} (P - q)^\mu p_-^\nu p_-^\rho - \lambda_{21} p_-^\mu p_0^\nu (p_- + p_0 - k)^\rho \right\} \left\langle \rho^0(k) \left| \rho_{\mu\nu}^0 \right| 0 \right\rangle \}
\end{aligned} \tag{C.63}$$

$$\begin{aligned}
J_{W^- \rightarrow \rho^0 \pi^-}^\rho = & \frac{4}{f} \left\{ \left( 4\lambda_6 m_\pi^2 (P - q)_\mu - 2(2\lambda_8 + \lambda_9 + \lambda_{10}) m_\pi^2 p_{-\mu} \right. \right. \\
& - (\lambda_{16} - 2\lambda_{17}) p_- \cdot (P - q) (P - q)_\mu \\
& - \lambda_{18} (P - q)^2 p_{-\mu} - 2\lambda_{19} p_- \cdot (P - q) p_{-\mu} + 4\lambda_{20} m_\pi^2 (P - q)_\mu \\
& \left. + \lambda_{21} (p_0 + k)^2 p_{-\mu} - \lambda_{22} (p_0 + k)^2 (P - q)_\mu \right\} \left\langle \rho^0(p_0 + k) \left| \rho^{0\mu\rho} \right| 0 \right\rangle \\
& - \left( \lambda_{18} (P - q)^\mu p_-^\nu (P - q)^\rho + 2\lambda_{19} (P - q)^\mu p_-^\nu p_-^\rho \right) \left\langle \rho^0(p_0 + k) \left| \rho_{\mu\nu}^0 \right| 0 \right\rangle \}
\end{aligned} \tag{C.64}$$

$$\begin{aligned}
J_{W^- \rightarrow \rho^- \pi^0}^\rho = & \frac{4}{f} \left\{ \left( -4\lambda_6 m_\pi^2 (P - q)_\mu + 2(2\lambda_8 + \lambda_9 + \lambda_{10}) m_\pi^2 p_{0\mu} \right. \right. \\
& + (\lambda_{16} - 2\lambda_{17}) p_0 \cdot (P - q) (P - q)_\mu \\
& + \lambda_{18} (P - q)^2 p_{0\mu} + 2\lambda_{19} p_0 \cdot (P - q) p_{0\mu} - 4\lambda_{20} m_\pi^2 (P - q)_\mu \\
& \left. - \lambda_{21} (p_- + k)^2 p_{0\mu} + \lambda_{22} (p_- + k)^2 (P - q)_\mu \right\} \left\langle \rho^-(p_- + k) \left| \rho^{+\mu\rho} \right| 0 \right\rangle \\
& + (\lambda_{18} (P - q)^\mu p_0^\nu (P - q)^\rho + 2\lambda_{19} (P - q)^\mu p_0^\nu p_0^\rho) \left\langle \rho^-(p_- + k) \left| \rho_{\mu\nu}^+ \right| 0 \right\rangle \}
\end{aligned} \tag{C.65}$$

$\hat{\mathcal{O}}_i^{VV}$

$$G_{\rho^- \rightarrow \rho^0 \pi^- \pi^0} = i \frac{2}{f^2} \left\{ 2\lambda_2^{VV} (p_- \cdot p_0) \delta_\beta^\alpha - (\lambda_3^{VV} - \lambda_4^{VV}) (p_-^\alpha p_{0\beta} - p_0^\alpha p_{-\beta}) \right. \\ \left. + 2\lambda_5^{VV} (p_-^\alpha p_{0\beta} + p_0^\alpha p_{-\beta}) \right\} \langle \rho^0(k) | \rho_{\mu\alpha}^- \rho^{0\mu\beta} | \rho^-(P-q) \rangle \quad (\text{C.66})$$

$$G_{\rho^- \rightarrow \rho^- \gamma} = -i2e\lambda_7^{VV} (k^\mu \epsilon_\nu^*(k) - k_\nu \epsilon^{*\mu}(k)) \langle \rho^-(p_- + p_0) | \rho_{\mu\alpha}^- \rho^{+\alpha\nu} | \rho^-(P-q) \rangle \quad (\text{C.67})$$

$$G_{a_1^- \rightarrow a_1^- \gamma} = -i2e\lambda_7^{VV} (k^\mu \epsilon_\nu^*(k) - k_\nu \epsilon^{*\mu}(k)) \langle a_1^-(p_- + p_0) | a_{1\mu\alpha}^- a_1^{+\alpha\nu} | a_1^-(P-q) \rangle \quad (\text{C.68})$$

$$G_{\rho^- \rightarrow \rho^-} = -4i\lambda_6^{VV} m_\pi^2 \langle \rho^-(P-q) | \rho_{\mu\alpha}^- \rho^{+\alpha\nu} | \rho^-(P-q) \rangle \quad (\text{C.69})$$

$$J_{W^- \rightarrow \rho^- \rho^0}^\rho = 2\sqrt{2}\lambda_7^{VV} (P-q)^\mu \left\{ \langle \rho^0(k) \rho^-(p_- + p_0) | \rho^{+\alpha\rho} \rho_{\mu\alpha}^0 | 0 \rangle \right. \\ \left. - \langle \rho^0(k) \rho^-(p_- + p_0) | \rho^{0\alpha\rho} \rho_{\mu\alpha}^+ | 0 \rangle \right\} \quad (\text{C.70})$$

$\hat{\mathcal{O}}_i^{VA}$

$$G_{\rho^- \rightarrow a_1^- \pi^0} = \frac{2}{f} \left\{ (2\lambda_1^{VA} m_\pi^2 + \lambda_5^{VA} p_0 \cdot (P-q)) \langle a_1^-(p_- + k) | \rho_{\mu\nu}^- a_1^{+\mu\nu} | \rho^-(P-q) \rangle \right. \\ \left. + (-2\lambda_2^{VA} p_0^\mu p_{0\alpha} + \lambda_3^{VA} (P-q)^\mu p_{0\alpha} - \lambda_4^{VA} p_0^\mu (P-q)_\alpha) \right. \\ \left. \times \langle a_1^-(p_- + k) | \rho_{\mu\nu}^- a_1^{+\nu\alpha} | \rho^-(P-q) \rangle \right\} \quad (\text{C.71})$$

$$G_{\rho^- \rightarrow a_1^0 \pi^-} = \frac{2}{f} \left\{ (-2\lambda_1^{VA} m_\pi^2 - \lambda_5^{VA} p_- \cdot (P-q)) \langle a_1^0(p_0 + k) | \rho_{\mu\nu}^- a_1^{0\mu\nu} | \rho^-(P-q) \rangle \right. \\ \left. + (2\lambda_2^{VA} p_-^\mu p_{-\alpha} - \lambda_3^{VA} (P-q)^\mu p_{-\alpha} + \lambda_4^{VA} p_-^\mu (P-q)_\alpha) \right. \\ \left. \times \langle a_1^0(p_0 + k) | \rho_{\mu\nu}^- a_1^{0\nu\alpha} | \rho^-(P-q) \rangle \right\} \quad (\text{C.72})$$

$$G_{a_1^- \rightarrow \rho^- \pi^0} = \frac{2}{f} \left\{ (-2\lambda_1^{VA} m_\pi^2 + \lambda_5^{VA} p_0 \cdot (p_- + k)) \langle \rho^-(p_- + k) | \rho_{\mu\nu}^+ a_1^{-\mu\nu} | a_1^-(P-q) \rangle \right. \\ \left. + (2\lambda_2^{VA} p_0^\mu p_{0\alpha} + \lambda_3^{VA} (p_- + k)^\mu p_{0\alpha} - \lambda_4^{VA} p_0^\mu (p_- + k)_\alpha) \right. \\ \left. \times \langle \rho^-(p_- + k) | \rho_{\mu\nu}^+ a_1^{-\nu\alpha} | a_1^-(P-q) \rangle \right\} \quad (\text{C.73})$$

$$G_{a_1^- \rightarrow \rho^0 \pi^-} = \frac{2}{f} \left\{ (2\lambda_1^{VA} m_\pi^2 - \lambda_5^{VA} p_- \cdot \mathcal{P}) \langle \rho^0(\mathcal{P}) | \rho_{\mu\nu}^0 a_1^{-\mu\nu} | a_1^-(\mathcal{P} + p_-) \rangle \right. \\ \left. + (-2\lambda_2^{VA} p_-^\mu p_{-\alpha} - \lambda_3^{VA} \mathcal{P}^\mu p_{-\alpha} + \lambda_4^{VA} p_-^\mu \mathcal{P}_\alpha) \right. \\ \left. \times \langle \rho^0(\mathcal{P}) | \rho_{\mu\nu}^0 a_1^{-\nu\alpha} | a_1^-(\mathcal{P} + p_-) \rangle \right\} \quad (\text{C.74})$$



$$\begin{aligned}
J_{W^- \rightarrow \rho^0 a_1^-}^\rho = & 2\sqrt{2} \left\{ \left( -\lambda_2^{VA} \left[ g^{\rho\alpha} (P-q)_\mu + \delta_\mu^\rho (P-q)^\alpha \right] + \lambda_3^{VA} k_\mu g^{\rho\alpha} - \lambda_4^{VA} k^\alpha \delta_\mu^\rho \right. \right. \\
& + \lambda_6^{VA} \left[ g^{\rho\alpha} (P-q)_\mu - \delta_\mu^\rho (P-q)^\alpha \right] \left. \right\} \times \left\langle \rho^0(k) a_1^-(p_- + p_0) \left| \rho^{0\mu\nu} a_{1\nu\alpha}^+ \right| 0 \right\rangle \\
& + \lambda_5^{VA} k^\rho \left\langle \rho^0(k) a_1^-(p_- + p_0) \left| \rho^{0\mu\nu} a_{1\mu\nu}^+ \right| 0 \right\rangle \left. \right\}
\end{aligned} \tag{C.75}$$

$$\begin{aligned}
J_{W^- \rightarrow \rho^- a_1^0}^\rho = & 2\sqrt{2} \left\{ \left( \lambda_2^{VA} \left[ g^{\rho\alpha} (P-q)_\mu + \delta_\mu^\rho (P-q)^\alpha \right] - \lambda_3^{VA} (p_- + p_0)_\mu g^{\rho\alpha} + \lambda_4^{VA} (p_- + p_0)^\alpha \delta_\mu^\rho \right. \right. \\
& - \lambda_6^{VA} \left[ g^{\rho\alpha} (P-q)_\mu - \delta_\mu^\rho (P-q)^\alpha \right] \left. \right\} \times \left\langle \rho^-(p_- + p_0) a_1^0(k) \left| \rho^{+\mu\nu} a_{1\nu\alpha}^0 \right| 0 \right\rangle \\
& - \lambda_5^{VA} (p_- + p_0)^\rho \left\langle \rho^-(p_- + p_0) a_1^0(k) \left| \rho^{-\mu\nu} a_{1\mu\nu}^0 \right| 0 \right\rangle \left. \right\}
\end{aligned} \tag{C.76}$$

$\hat{O}_i^A$

$$J_{W^- \rightarrow a_1^-}^\rho = -i4 \left[ 4\lambda_{16}^A m_\pi^2 - \lambda_{17}^A (P-q)^2 \right] (P-q)_\mu \left\langle a_1^-(P-q) \left| a_1^{+\mu\rho} \right| 0 \right\rangle \tag{C.77}$$

$$\begin{aligned}
J_{W^- \rightarrow a_1^- \pi^0}^\rho = & \frac{4}{f} \left\{ \left( -4\lambda_4^A m_\pi^2 (P-q)_\mu + 2\lambda_{12}^A p_0 \cdot (P-q) p_{0\mu} - 2\lambda_{13}^A p_0 \cdot (P-q) (P-q)_\mu \right. \right. \\
& + \lambda_{15}^A (P-q)^2 p_{0\mu} - 4\lambda_{16}^A m_\pi^2 (P-q)_\mu + \lambda_{17}^A (p_- + k)^2 (P-q)_\mu \left. \right\} \\
& \times \left\langle a_1^-(p_- + k) \left| a_1^{+\mu\rho} \right| 0 \right\rangle \\
& + \left( 2\lambda_{12}^A (P-q)^\mu p_0^\nu p_0^\rho + \lambda_{15}^A (P-q)^\mu p_0^\nu (P-q)^\rho \right) \left\langle a_1^-(p_- + k) \left| a_{1\mu\nu}^+ \right| 0 \right\rangle
\end{aligned} \tag{C.78}$$

$$\begin{aligned}
J_{W^- \rightarrow a_1^0 \pi^-}^\rho = & \frac{4}{f} \left\{ \left( 4\lambda_4^A m_\pi^2 (P-q)_\mu - 2\lambda_{12}^A p_- \cdot (P-q) p_{-\mu} + 2\lambda_{13}^A p_- \cdot (P-q) (P-q)_\mu \right. \right. \\
& - \lambda_{15}^A (P-q)^2 p_{-\mu} + 4\lambda_{16}^A m_\pi^2 (P-q)_\mu + \lambda_{17}^A (p_0 + k)^2 (P-q)_\mu \left. \right\} \\
& \times \left\langle a_1^0(p_0 + k) \left| a_1^{0\mu\rho} \right| 0 \right\rangle \\
& - \left( 2\lambda_{12}^A (P-q)^\mu p_-^\nu p_-^\rho + \lambda_{15}^A (P-q)^\mu p_-^\nu (P-q)^\rho \right) \left\langle a_1^0(p_0 + k) \left| a_{1\mu\nu}^0 \right| 0 \right\rangle
\end{aligned} \tag{C.79}$$

$$\begin{aligned}
J_{W^- \rightarrow a_1^- \gamma}^\rho &= i4e \left\{ \left( - \left( \lambda_{12}^A + \lambda_{14}^A \right) [k \cdot (P - q) g_{\mu\alpha} - (P - q)_\alpha k_\mu] \epsilon^{*\alpha}(k) \right. \right. \\
&\quad \left. \left. + 4\lambda_{16}^A m_\pi^2 \epsilon_\mu^*(k) - \lambda_{17}^A \left[ s \epsilon_\mu^*(k) + 2(p_- + p_0)_\alpha \epsilon^{*\alpha}(k) (P - q)_\mu \right] \right) \right. \\
&\quad \left. \times \langle a_1^-(p_- + p_0) | a_1^{+\mu\rho} | 0 \rangle \right. \\
&\quad \left. + \left[ \left( \lambda_{12}^A - \lambda_{14}^A \right) (P - q)^\nu (k^\mu \epsilon^{*\rho}(k) - k^\rho \epsilon^{*\mu}(k)) - 2\lambda_{13}^A k^\rho k^\mu \epsilon^{*\nu}(k) \right] \right. \\
&\quad \left. \times \langle a_1^-(p_- + p_0) | a_{1\mu\nu}^+ | 0 \rangle \right\} \tag{C.80}
\end{aligned}$$

$$\begin{aligned}
G_{a_1^- \rightarrow \pi^- \gamma} &= -i \frac{2\sqrt{2}}{f} e \left[ 4\lambda_4^A m_\pi^2 k^\mu \epsilon^{*\nu}(k) + 2\lambda_{12}^A (k \cdot p_- g^{\mu\alpha} - p_-^\alpha k^\mu) \epsilon_\alpha^* p_-^\nu \right. \\
&\quad \left. - 2\lambda_{13}^A (k \cdot p_-) k^\mu \epsilon^{*\nu}(k) + 4\lambda_{16}^A m_\pi^2 k^\mu \epsilon^{*\nu}(k) - \lambda_{17}^A (p_- + k)^2 k^\mu \epsilon^{*\nu} \right] \\
&\quad \times \langle 0 | a_{1\mu\nu}^- | a_1^-(p_- + k) \rangle \tag{C.81}
\end{aligned}$$

$\hat{\mathcal{O}}_i^S$

$$J_{W^- \rightarrow a_0^- \gamma}^\rho = \frac{8}{3} \lambda_{15}^S e [k \cdot (P - q) g^{\mu\rho} - (P - q)^\mu k^\rho] \epsilon_\mu^* \langle a_0^-(p_0 + p_-) | a_0^+ | 0 \rangle \tag{C.82}$$

$$\begin{aligned}
J_{W^- \rightarrow f_0 \pi^-}^\rho &= i \frac{4}{f} \left[ 4\lambda_6^S m_\pi^2 p_-^\rho + 2\lambda_7^S m_\pi^2 p_-^\rho - 2\lambda_8^S m_\pi^2 p_-^\rho - \lambda_{17}^S (p_0 + k)^2 p_-^\rho \right. \\
&\quad \left. - \lambda_{12}^S \left( (P - q)^2 p_-^\rho - p_- \cdot (P - q) (P - q)^\rho \right) \right] \langle f_0(p_0 + k) | f_0 | 0 \rangle \tag{C.83}
\end{aligned}$$

$\hat{O}_{i\mu\nu\alpha\beta}^V$

$$\begin{aligned}
J_{W^- \rightarrow \omega\pi^- \pi^0}^\rho &= \frac{4}{f^2} \left\{ 2 \left( \kappa_1^V - \kappa_2^V + \kappa_3^V \right) p_0^\alpha p_-^\beta (p_0 + p_-)^\rho \right. \\
&\quad + 2 \left[ \left( \kappa_1^V - \kappa_2^V + \kappa_3^V \right) p_- \cdot p_0 + \left( 2\kappa_9^V - \kappa_{10}^V \right) m_\pi^2 \right] g^{\rho\alpha} (p_0 - p_-)^\beta \\
&\quad - \left( \kappa_1^V - \kappa_2^V + \kappa_3^V + \kappa_6^V + \kappa_7^V - \kappa_8^V \right) (P - q)^\alpha \left( p_0^\beta p_-^\rho - p_-^\beta p_0^\rho \right) \\
&\quad - \left( \kappa_1^V - \kappa_2^V + \kappa_3^V - \kappa_6^V - \kappa_7^V + \kappa_8^V \right) g^{\rho\alpha} \left[ (P - q) \cdot p_- p_0^\beta - (P - q) \cdot p_0 p_-^\beta \right] \\
&\quad + 2\kappa_{12}^V \left[ (P - q)^\alpha \left( p_0^\beta p_0^\rho - p_-^\beta p_-^\rho \right) - g^{\rho\alpha} \left( (P - q) \cdot p_0 p_0^\beta - (P - q) \cdot p_- p_-^\beta \right) \right] \\
&\quad + \kappa_{16}^V (P - q)^\alpha \left[ (p_0 + k)^\beta p_0^\rho - (p_- + k)^\beta p_-^\rho \right] \\
&\quad - \kappa_{17}^V (P - q)^\alpha \left[ (p_0 + k)^\rho p_0^\beta - (p_- + k)^\rho p_-^\beta \right] \\
&\quad - \kappa_{16}^V g^{\rho\alpha} \left[ (P - q) \cdot p_0 (p_0 + k)^\beta - (P - q) \cdot p_- (p_- + k)^\beta \right] \\
&\quad \left. + \kappa_{17}^V g^{\rho\alpha} \left[ (P - q) \cdot (p_0 + k) p_0^\beta - (P - q) \cdot (p_- + k) p_-^\beta \right] \right\} \\
&\quad \times \epsilon_{\mu\nu\alpha\beta} \langle \omega(k) | \omega^{\mu\nu} | 0 \rangle
\end{aligned} \tag{C.84}$$

$$\begin{aligned}
J_{W^- \rightarrow \rho^- \gamma}^\rho &= \frac{4e}{3} \left\{ \left( -\kappa_{11}^V + \kappa_{12}^V \right) (P - q)^\alpha \left[ k^\beta \epsilon^{*\rho}(k) - k^\rho \epsilon^{*\beta}(k) \right] \right. \\
&\quad - \left( \kappa_{11}^V + \kappa_{12}^V \right) g^{\rho\alpha} \left[ k \cdot (P - q) g^{\sigma\beta} - (P - q)^\sigma k^\beta \right] \epsilon_\sigma^*(k) \\
&\quad \left. - \kappa_{16}^V k^\alpha \epsilon^{*\beta}(k) k^\rho \right\} \epsilon_{\mu\nu\alpha\beta} \langle \rho^-(p_- + p_0) | \rho^{+\mu\nu} | 0 \rangle
\end{aligned} \tag{C.85}$$

$$\begin{aligned}
J_{W^- \rightarrow \omega\pi^-}^\rho &= i \frac{4}{f} \left\{ -2\kappa_{12}^V (P - q)^\alpha p_-^\beta p_-^\rho + \left[ 2\kappa_{12}^V (P - q) \cdot p_- - \kappa_{17}^V (P - q)^2 \right] g^{\rho\alpha} p_-^\beta \right. \\
&\quad \left. + \left[ 4\kappa_{14}^V m_\pi^2 + \kappa_{16}^V p_- \cdot (P - q) \right] g^{\rho\alpha} (P - q)^\beta + \kappa_{17}^V (P - q)^\alpha p_-^\beta (P - q)^\rho \right\} \\
&\quad \times \epsilon_{\mu\nu\alpha\beta} \langle \omega(p_0 + k) | \omega^{\mu\nu} | 0 \rangle
\end{aligned} \tag{C.86}$$

$$\begin{aligned}
G_{\pi^- \rightarrow \omega\pi^- \pi^0} &= \frac{4\sqrt{2}}{f^3} \left\{ \left( \kappa_1^V - \kappa_2^V + \kappa_3^V \right) \left[ (P - q + p_-)^\alpha p_0^\beta (P - q) \cdot p_- \right. \right. \\
&\quad \left. - (P - q + p_0)^\alpha p_-^\beta (P - q) \cdot p_0 \right] + \left( 2\kappa_9^V - \kappa_{10}^V \right) m_\pi^2 p_0^\alpha p_-^\beta \\
&\quad \left. + \left[ - \left( \kappa_1^V - \kappa_2^V + \kappa_3^V \right) p_- \cdot p_0 - \left( 2\kappa_9^V - \kappa_{10}^V \right) m_\pi^2 \right] (P - q)^\alpha (p_0 - p_-)^\beta \right\} \\
&\quad \times \epsilon_{\mu\nu\alpha\beta} \langle \omega(k) | \omega^{\mu\nu} | 0 \rangle
\end{aligned} \tag{C.87}$$

$$G_{\rho^0 \rightarrow \pi^0 \gamma} = \frac{2\sqrt{2}}{3f} e \left\{ -2\kappa_{12}^V [k \cdot p_0 g^{\rho\alpha} - p_0^\rho k^\alpha] \epsilon_\rho^*(k) p_0^\beta + \left( 4\kappa_{14}^V m_\pi^2 - \kappa_{16}^V k \cdot p_0 \right) k^\alpha \epsilon^{*\beta}(k) \right\} \\ \times \epsilon_{\mu\nu\alpha\beta} \langle 0 | \rho^{0\mu\nu} | \rho^0(p_0 + k) \rangle \quad (\text{C.88})$$

$$G_{\omega \rightarrow \pi^0 \gamma} = \frac{2\sqrt{2}}{f} e \left\{ -2\kappa_{12}^V [k \cdot p_0 g^{\rho\alpha} - p_0^\rho k^\alpha] \epsilon_\rho^*(k) p_0^\beta + \left( 4\kappa_{14}^V m_\pi^2 - \kappa_{16}^V k \cdot p_0 \right) k^\alpha \epsilon^{*\beta}(k) \right\} \\ \times \epsilon_{\mu\nu\alpha\beta} \langle 0 | \omega^{\mu\nu} | \omega(p_0 + k) \rangle \quad (\text{C.89})$$

$$G_{\rho^- \rightarrow \pi^- \gamma} = \frac{2\sqrt{2}}{3f} e \left\{ -2\kappa_{12}^V [k \cdot p_- g^{\rho\alpha} - p_-^\rho k^\alpha] \epsilon_\rho^*(k) p_-^\beta + \left( 4\kappa_{14}^V m_\pi^2 - \kappa_{16}^V k \cdot p_- \right) k^\alpha \epsilon^{*\beta}(k) \right\} \\ \times \epsilon_{\mu\nu\alpha\beta} \langle 0 | \rho^{-\mu\nu} | \rho^-(p_- + k) \rangle \quad (\text{C.90})$$

$$G_{\pi^- \rightarrow \rho^- \gamma} = \frac{2\sqrt{2}}{3f} e \left\{ -2\kappa_{12}^V [k \cdot (P - q) g^{\rho\alpha} - (P - q)^\rho k^\alpha] \epsilon_\rho^*(k) (P - q)^\beta \right. \\ \left. + \left( 4\kappa_{14}^V m_\pi^2 + \kappa_{16}^V k \cdot (P - q) \right) k^\alpha \epsilon^{*\beta}(k) \right\} \epsilon_{\mu\nu\alpha\beta} \langle \rho^-(p_- + p_0) | \rho^{+\mu\nu} | 0 \rangle \quad (\text{C.91})$$

$$G_{\gamma \rightarrow \pi^0 \rho^0} = \frac{2\sqrt{2}}{3f} e \left\{ 2\kappa_{12}^V [p_0 \cdot (p_0 + k) g^{\rho\alpha} - p_0^\rho (p_0 + k)^\alpha] p_0^\beta \right. \\ \left. + \left( 4\kappa_{14}^V m_\pi^2 + \kappa_{16}^V p_0 \cdot (p_0 + k) \right) g^{\rho\alpha} (p_0 + k)^\beta \right. \\ \left. - \kappa_{17}^V \left[ (p_0 + k)^2 g^{\rho\alpha} - (p_0 + k)^\alpha (p_0 + k)^\rho \right] p_0^\beta \right\} \epsilon_{\mu\nu\alpha\beta} \langle \rho^0(k) | \rho^{0\mu\nu} A_\rho | \gamma(P - q) \rangle \quad (\text{C.92})$$

$$G_{\gamma \rightarrow \pi^0 \omega} = \frac{2\sqrt{2}}{f} e \left\{ 2\kappa_{12}^V [p_0 \cdot (p_0 + k) g^{\rho\alpha} - p_0^\rho (p_0 + k)^\alpha] p_0^\beta \right. \\ \left. + \left( 4\kappa_{14}^V m_\pi^2 + \kappa_{16}^V p_0 \cdot (p_0 + k) \right) g^{\rho\alpha} (p_0 + k)^\beta \right. \\ \left. - \kappa_{17}^V \left[ (p_0 + k)^2 g^{\rho\alpha} - (p_0 + k)^\alpha (p_0 + k)^\rho \right] p_0^\beta \right\} \epsilon_{\mu\nu\alpha\beta} \langle \omega(k) | \omega^{\mu\nu} A_\rho | \gamma(P - q) \rangle \quad (\text{C.93})$$

$\hat{\mathcal{O}}_{i\mu\nu\alpha\beta}^A$

$$\begin{aligned}
J_{W^- \rightarrow f_1 \pi^-}^\rho &= i \frac{4}{f} \left\{ \left[ (\kappa_3^A + \kappa_{15}^A) p_- \cdot (P - q) + 4\kappa_{11}^A m_\pi^2 \right] g^{\rho\alpha} (P - q)^\beta \right. \\
&\quad + \left[ 2\kappa_8^A p_- \cdot (P - q) - \kappa_{16}^A (P - q)^2 + 2\kappa_{12}^A m_\pi^2 \right] g^{\rho\alpha} p_-^\beta \\
&\quad \left. - \left[ 2\kappa_8^A p_-^\rho - \kappa_{16}^A (P - q)^\rho \right] (P - q)^\alpha p_-^\beta \right\} \epsilon_{\mu\nu\alpha\beta} \langle f_1(p_0 + k) | f_1^{\mu\nu} | 0 \rangle
\end{aligned} \tag{C.94}$$

$$\begin{aligned}
G_{a_1^- \rightarrow \pi^- \pi^0 \gamma} &= i \frac{2\sqrt{2}}{3f^2} \left( \kappa_5^A - \kappa_6^A + \kappa_7^A \right) e \epsilon_\sigma^*(k) \left[ (k \cdot p_0 g^{\alpha\sigma} - p_0^\sigma k^\alpha) p_-^\beta - (k \cdot p_- g^{\alpha\sigma} - p_-^\sigma k^\alpha) p_0^\beta \right] \\
&\quad \times \epsilon_{\mu\nu\alpha\beta} \langle 0 | a_1^{-\mu\nu} | a_1^-(P - q) \rangle
\end{aligned} \tag{C.95}$$

$\hat{\mathcal{O}}_{i\mu\nu\alpha\beta}^{RR}$

$$\begin{aligned}
J_{W^- \rightarrow \rho^- \omega}^\rho &= i 2\sqrt{2} \epsilon_{\mu\nu\alpha\beta} \left\{ \left( \kappa_3^{VV} g^{\rho\alpha} k_\sigma + \kappa_4^{VV} \delta_\sigma^\rho k^\alpha \right) \langle \rho^-(p_- + p_0) \omega(k) | \rho^{+\beta\sigma} \omega^{\mu\nu} | 0 \rangle \right. \\
&\quad \left. + \left( \kappa_3^{VV} g^{\rho\alpha} (p_0 + p_-)_\sigma + \kappa_4^{VV} \delta_\sigma^\rho (p_0 + p_-)^\alpha \right) \langle \rho^-(p_- + p_0) \omega(k) | \rho^{+\mu\nu} \omega^{\beta\sigma} | 0 \rangle \right\}
\end{aligned} \tag{C.96}$$

$$\begin{aligned}
G_{\rho^- \rightarrow \omega \pi^-} &= i \frac{2}{f} \epsilon_{\mu\nu\alpha\beta} \left\{ -4\kappa_2^{VV} m_\pi^2 \langle \omega(\mathcal{P}) | \rho^{-\mu\nu} \omega^{\alpha\beta} | \rho^-(\mathcal{P} + p_-) \rangle \right. \\
&\quad + \left( \kappa_3^{VV} p_-^\alpha \mathcal{P}_\sigma + \kappa_4^{VV} p_{-\sigma} \mathcal{P}^\alpha \right) \langle \omega(\mathcal{P}) | \rho^{-\beta\sigma} \omega^{\mu\nu} | \rho^-(\mathcal{P} + p_-) \rangle \\
&\quad \left. - \left( \kappa_3^{VV} p_-^\alpha (\mathcal{P} + p_-)_\sigma + \kappa_4^{VV} p_{-\sigma} (\mathcal{P} + p_-)^\alpha \right) \langle \omega(\mathcal{P}) | \rho^{-\mu\nu} \omega^{\beta\sigma} | \rho^-(\mathcal{P} + p_-) \rangle \right\}
\end{aligned} \tag{C.97}$$

$$\begin{aligned}
G_{\rho^0 \rightarrow \omega \pi^0} &= i \frac{2}{f} \epsilon_{\mu\nu\alpha\beta} \left\{ -4\kappa_2^{VV} m_\pi^2 \langle \omega(k) | \rho^{0\mu\nu} \omega^{\alpha\beta} | \rho^0(p_0 + k) \rangle \right. \\
&\quad + \left( \kappa_3^{VV} p_0^\alpha k_\sigma + \kappa_4^{VV} p_{0\sigma} k^\alpha \right) \langle \omega(k) | \rho^{0\beta\sigma} \omega^{\mu\nu} | \rho^0(p_0 + k) \rangle \\
&\quad \left. - \left( \kappa_3^{VV} p_0^\alpha (p_0 + k)_\sigma + \kappa_4^{VV} p_{0\sigma} (p_0 + k)^\alpha \right) \langle \omega(k) | \rho^{0\mu\nu} \omega^{\beta\sigma} | \rho^0(p_0 + k) \rangle \right\}
\end{aligned} \tag{C.98}$$

$$\begin{aligned}
G_{\omega \rightarrow \rho^0 \pi^0} &= i \frac{2}{f} \epsilon_{\mu\nu\alpha\beta} \left\{ -4\kappa_2^{VV} m_\pi^2 \langle \rho^0(k) | \rho^{0\mu\nu} \omega^{\alpha\beta} | \omega(p_0 + k) \rangle \right. \\
&\quad + \left( \kappa_3^{VV} p_0^\alpha k_\sigma + \kappa_4^{VV} p_{0\sigma} k^\alpha \right) \langle \rho^0(k) | \rho^{0\mu\nu} \omega^{\beta\sigma} | \omega(p_0 + k) \rangle \\
&\quad \left. - \left( \kappa_3^{VV} p_0^\alpha (p_0 + k)_\sigma + \kappa_4^{VV} p_{0\sigma} (p_0 + k)^\alpha \right) \langle \rho^0(k) | \rho^{0\beta\sigma} \omega^{\mu\nu} | \omega(p_0 + k) \rangle \right\}
\end{aligned} \tag{C.99}$$

$\hat{O}_{i\mu\nu\alpha\beta}^{VA}$

$$G_{a_1^- \rightarrow \omega \pi^- \pi^0} = \frac{2}{f^2} [\kappa_2^{VA} - \kappa_3^{VA} - \kappa_4^{VA}] (p_{0\sigma} p_-^\alpha - p_{-\sigma} p_0^\alpha) \epsilon_{\mu\nu\alpha\beta} \langle \omega(k) | \omega^{\mu\nu} a_1^{-\beta\sigma} | a_1^- (P - q) \rangle \quad (\text{C.100})$$

$$G_{a_1^- \rightarrow \rho^- \gamma} = -\frac{2}{3} \kappa_5^{VA} (k^\alpha \epsilon_\sigma^*(k) - k_\sigma \epsilon^{*\alpha}(k)) \epsilon_{\mu\nu\alpha\beta} \langle \rho^-(p_- + p_0) | \rho^{+\mu\nu} a_1^{-\beta\sigma} | a_1^- (P - q) \rangle \quad (\text{C.101})$$

# Appendix D

## Magnetic dipole moment of the $\rho$ meson

Measurement of the magnetic dipole moment of vector mesons is not an easy task because they have a very short lifetime about  $10^{-24}$  s, but it is possible to infer it indirectly through its impact on some low energy processes.

The electromagnetic vertex for a vector particle ( $V$ ) is defined by [815]

$$\langle V(q_2, \eta) | J_{EM}^\mu(0) | V(q_1, \epsilon) \rangle \equiv \eta_\nu^\dagger \epsilon_\lambda \Gamma^{\mu\nu\lambda}, \quad (\text{D.1})$$

where  $q_i$ 's are the momenta,  $\eta$  and  $\epsilon$  are the polarization vectors. The most general Lorentz structure that preserves  $C$ ,  $P$  and  $CP$  is the following

$$\begin{aligned} \Gamma^{\mu\nu\lambda} = & \alpha(q^2) g^{\nu\lambda} (q_1 + q_2)^\mu + \beta(q^2) (g^{\mu\nu} q^\lambda - g^{\mu\lambda} q^\nu) - \frac{\gamma(q^2)}{M_V^2} (q_1 + q_2)^\mu q^\nu q^\lambda \\ & - q_1^\lambda g^{\mu\nu} - q_2^\nu g^{\mu\lambda}, \end{aligned} \quad (\text{D.2})$$

where  $\alpha(q^2)$ ,  $\beta(q^2)$  and  $\gamma(q^2)$  are the electromagnetic form factors [816, 817]. The magnetic dipole moment of the  $\rho$  meson can be obtained from the  $V(q_1, \epsilon) \rightarrow V(q_2, \mu) \gamma(q)$  electromagnetic vertex using the Eqs. (C.41) and (C.67), and for a spin 1 particle in the formalism

of antisymmetric tensor fields [224, 225]

$$\langle 0 | W_{\mu\nu} | W, p \rangle = iM^{-1} [p_\mu \epsilon_\nu(p) - p_\nu \epsilon_\mu(p)], \quad (\text{D.3})$$

with the usual polarization vector  $\epsilon_\mu(p)$ .

Thus, we get

$$\begin{aligned} \left\langle V(q_2, \eta) \left| \frac{\delta \mathcal{L}_{R\chi T}}{\delta v_\mu} \right| V(q_1, \epsilon) \right\rangle = & \eta_\nu^\dagger \epsilon_\lambda \left\{ g^{\nu\lambda} (q_1 + q_2)^\mu + (1 - 2\lambda_7^{VV}) [g^{\mu\nu} k^\lambda - g^{\mu\lambda} k^\nu] \right. \\ & \left. + \frac{2\lambda_7^{VV}}{M_V^2} (q_1 + q_2)^\mu q^\nu q^\lambda \right\}, \end{aligned} \quad (\text{D.4})$$

comparing with eq. (D.2), we have  $Q_V = \alpha(0) = 1$  (in units of  $e$ ),  $\mu_V = \beta(0) = 1 - 2\lambda_7^{VV}$  (in units of  $e/2M_V$ ) and  $X_{E_V} = 1 - \beta(0) + 2\gamma(0) = -2\lambda_7^{VV}$  (in units of  $e/M_V^2$ ) where  $\gamma(0) = -2\lambda_7^{VV}$ . At tree level, the prediction for the  $W$  gauge boson is  $\alpha(0) = 1$ ,  $\beta(0) \equiv 1 + \kappa + \lambda = 2$  and  $\gamma(0) \equiv \lambda = 0$  ( $\kappa = 1$  and  $\lambda = 0$ ) [816, 817], which correspond to  $Q_W = 1$ ,  $\mu_W = 2$  and  $X_{E_W} = -1$ .



# Appendix E

## Pseudoscalar resonances in radiative di-pion tau decay

Taking into account the pseudoscalar resonances, we have the following contributions:

$\mathcal{O}_i^P$

$$J_{W^- \rightarrow \pi'^- \pi^0}^\rho = -\frac{4}{f} \lambda_9^P [(P-q)^2 p_0^\rho - p_0 \cdot (P-q) (P-q)^\rho] \langle \pi'^- (p_- + k) | \pi'^+ | 0 \rangle \quad (\text{E.1})$$

$$J_{W^- \rightarrow \pi'^0 \pi^-}^\rho = \frac{4}{f} \lambda_9^P [(P-q)^2 p_-^\rho - p_- \cdot (P-q) (P-q)^\rho] \langle \pi'^0 (p_0 + k) | \pi'^0 | 0 \rangle \quad (\text{E.2})$$

$$J_{W^- \rightarrow \pi'^- \gamma}^\rho = -8ie \lambda_{11}^P (P-q)_\mu [k^\mu \epsilon^{*\rho}(k) - k^\rho \epsilon^{*\mu}(k)] \langle \pi'^- (p_- + p_0) | \pi'^+ | 0 \rangle \quad (\text{E.3})$$

$$G_{\pi'^- \rightarrow \pi^- \gamma} = -i \frac{4\sqrt{2}}{f} e \lambda_{13}^P m_\pi^2 p_{-\mu} \epsilon^{*\mu}(k) \langle 0 | \pi'^- | \pi'^- (p_- + k) \rangle \quad (\text{E.4})$$

$\mathcal{O}_i^{PV}$

$$G_{\pi'^- \rightarrow \rho^0 \pi^-} = -\frac{2}{f} \lambda_1^{PV} \mathcal{P}^\mu p_-^\nu \langle \rho^0(\mathcal{P}) | \rho_{\mu\nu}^0 \pi'^- | \pi'^- (\mathcal{P} + p_-) \rangle \quad (\text{E.5})$$

$$G_{\pi'^- \rightarrow \rho^- \pi^0} = \frac{2}{f} \lambda_1^{PV} (p_- + k)^\mu p_0^\nu \langle \rho^-(p_- + k) | \rho_{\mu\nu}^+ \pi'^- | \pi'^- (P - q) \rangle \quad (\text{E.6})$$

$$G_{\rho^- \rightarrow \pi'^- \pi^0} = \frac{2}{f} \lambda_1^{PV} (p_- + k)^\mu p_0^\nu \langle \pi'^- (p_- + k) | \rho_{\mu\nu}^- \pi'^+ | \rho^- (P - q) \rangle \quad (\text{E.7})$$

$\mathcal{O}_{i\mu\nu\alpha\beta}^P$

$$J_{W^- \rightarrow \pi'^- \gamma}^\rho = -\frac{32}{3} e \kappa_5^P \epsilon_{\mu\nu\alpha\beta} g^{\rho\mu} (P - q)^\nu k^\alpha \epsilon^{*\beta}(k) \langle \pi'^- (p_- + p_0) | \pi'^+ | 0 \rangle \quad (\text{E.8})$$

$$G_{\pi'^- \rightarrow \pi^- \pi^0 \gamma} = i \frac{4\sqrt{2}}{3f^2} (\kappa_2^P + 2\kappa_3^P) e k^\mu \epsilon^{*\nu}(k) p_-^\alpha p_0^\beta \epsilon_{\mu\nu\alpha\beta} \langle 0 | \pi'^- | \pi'^- (P - q) \rangle \quad (\text{E.9})$$

$\mathcal{O}_{i\mu\nu\alpha\beta}^{PV}$

$$G_{\pi'^- \rightarrow \omega \pi^- \pi^0} = \frac{2}{f^2} (2\kappa_1^{PV} - \kappa_2^{PV}) \epsilon_{\mu\nu\alpha\beta} p_-^\alpha p_0^\beta \langle \omega(k) | \omega^{\mu\nu} \pi'^- | \pi'^- (P - q) \rangle \quad (\text{E.10})$$

$$G_{\pi'^- \rightarrow \rho^- \gamma} = \frac{4}{3} e \kappa_3^{PV} \epsilon_{\mu\nu\alpha\beta} k^\alpha \epsilon^{*\beta}(k) \langle \rho^- (p_- + p_0) | \rho^{+\mu\nu} \pi'^- | \pi'^- (P - q) \rangle \quad (\text{E.11})$$

## E.1 Mixing

We have a mixing between the P resonance and the  $\pi$  meson

$$\begin{aligned} \mathcal{L} = & \dots - \frac{1}{2} m_\pi^2 [\pi^0 \pi^0 + 2\pi^- \pi^+] - \frac{1}{2} (m_{\pi'}^2 - 4\lambda_3^{PP} m_\pi^2) [\pi'^0 \pi'^0 + 2\pi'^- \pi'^+] \\ & + \frac{2\sqrt{2}}{f} m_\pi^2 (d_m + 4\lambda_{10}^P m_\pi^2 - \lambda_{13}^P m_\pi^2) [\pi'^0 \pi^0 + \pi'^+ \pi^- + \pi'^- \pi^+] + \dots, \end{aligned} \quad (\text{E.12})$$

this equation can be rewritten in a similar way

$$\mathcal{L} = \dots - \frac{1}{2} \Pi^\dagger M_1 \Pi - \frac{1}{2} \Pi_0^\dagger M_0 \Pi_0 + \dots, \quad (\text{E.13})$$

where  $\Pi = (\pi^+, \pi^-, \pi'^+, \pi'^-)^t$ ,  $\Pi_0 = (\pi^0, \pi'^0)^t$ ,

$$\mathbb{M}_1 = \begin{pmatrix} m_\pi^2 & 0 & -\frac{2\sqrt{2}}{f}m_\pi^2 d'_m & 0 \\ 0 & m_\pi^2 & 0 & -\frac{2\sqrt{2}}{f}m_\pi^2 d'_m \\ -\frac{2\sqrt{2}}{f}m_\pi^2 d'_m & 0 & m_1^2 & 0 \\ 0 & -\frac{2\sqrt{2}}{f}m_\pi^2 d'_m & 0 & m_1^2 \end{pmatrix}, \quad (\text{E.14})$$

and

$$\mathbb{M}_0 = \begin{pmatrix} m_\pi^2 & -\frac{2\sqrt{2}}{f}m_\pi^2 d'_m \\ -\frac{2\sqrt{2}}{f}m_\pi^2 d'_m & m_1^2 \end{pmatrix}, \quad (\text{E.15})$$

with  $m_1^2 = m_{\pi'}^2 - 4\lambda_3^{PP}m_\pi^2$ , and  $d'_m = d_m + 4\lambda_{10}^P m_\pi^2 - \lambda_{13}^P m_\pi^2$ .

The flavor eigenstates  $(\Pi, \Pi_0)$  are related to the mass eigenstates  $(\tilde{\Pi}, \tilde{\Pi}_0)$  via their mixing angle  $\theta'$

$$\begin{pmatrix} \tilde{\pi}^+ \\ \tilde{\pi}^- \\ \tilde{\pi}'^+ \\ \tilde{\pi}'^- \end{pmatrix} = \begin{pmatrix} \cos \theta' & 0 & \sin \theta' & 0 \\ 0 & \cos \theta' & 0 & \sin \theta' \\ -\sin \theta' & 0 & \cos \theta' & 0 \\ 0 & -\sin \theta' & 0 & \cos \theta' \end{pmatrix} \begin{pmatrix} \pi^+ \\ \pi^- \\ \pi'^+ \\ \pi'^- \end{pmatrix}, \quad (\text{E.16})$$

$$\begin{pmatrix} \tilde{\pi}^0 \\ \tilde{\pi}'^0 \end{pmatrix} = \begin{pmatrix} \cos \theta' & \sin \theta' \\ -\sin \theta' & \cos \theta' \end{pmatrix} \begin{pmatrix} \pi^0 \\ \pi'^0 \end{pmatrix}, \quad (\text{E.17})$$

with

$$\tan \theta' = \frac{\sqrt{(m_1^2 - m_\pi^2)^2 + \frac{32}{f^2}m_\pi^4 d_m'^2} - (m_1^2 - m_\pi^2)}{\frac{4\sqrt{2}}{f}m_\pi^2 d'_m} \simeq \frac{2\sqrt{2}}{f} \frac{m_\pi^2 d'_m}{m_1^2 - m_\pi^2}. \quad (\text{E.18})$$

The masses are  $\mathbb{M}_1^D = \text{diag}(m_-, m_-, m_+, m_+)$  and  $\mathbb{M}_0^D = \text{diag}(m_-, m_+)$ , where

$$m_\pm = \frac{1}{2} \left( m_1^2 + m_\pi^2 \pm \sqrt{(m_1^2 - m_\pi^2)^2 + \frac{32}{f^2}m_\pi^4 d_m'^2} \right) \simeq \left\{ \frac{m_1^2}{m_\pi^2} \right\} \pm \frac{8m_\pi^4 d_m'^2}{f^2(m_1^2 - m_\pi^2)}. \quad (\text{E.19})$$

After this change of basis, we have the following contributions

$$J_{W \rightarrow \pi^+ \pi^-}^\rho = -i\sqrt{2}f \sin \theta' (P - q)^\rho \langle \pi^- (P - q) | \tilde{\pi}'^+ | 0 \rangle \quad (\text{E.20})$$

$$\begin{aligned}
J_{W^- \rightarrow \pi'^- \pi^0}^\rho &= \left\{ -\frac{4}{f} \lambda_9^P \cos^2 \theta' [(P-q)^2 p_0^\rho - p_0 \cdot (P-q) (P-q)^\rho] \right. \\
&\quad + \frac{4}{f} \lambda_9^P \sin^2 \theta' [(P-q)^2 (p_- + k)^\rho - (p_- + k) \cdot (P-q) (P-q)^\rho] \\
&\quad \left. - \sqrt{2} \sin \theta' \cos \theta' (p_- + k - p_0)^\rho \right\} \langle \pi'^- (p_- + k) | \tilde{\pi}'^+ | 0 \rangle
\end{aligned} \tag{E.21}$$

$$\begin{aligned}
G_{\pi'^- \rightarrow \pi^- \pi^0 \gamma} &= \left\{ i \frac{4\sqrt{2}}{3f^2} (\kappa_2^P + 2\kappa_3^P) \cos^3 \theta' e k^\mu \epsilon^{*\nu} (k) p_-^\alpha p_0^\beta \right. \\
&\quad \left. - i \frac{e}{4\pi^2 f^3} \cos^2 \theta' \sin \theta' (P-q)^\mu \epsilon^{*\nu} (k) p_-^\alpha p_0^\beta \right\} \epsilon_{\mu\nu\alpha\beta} \langle 0 | \tilde{\pi}'^- | \pi'^- (P-q) \rangle
\end{aligned} \tag{E.22}$$

$$\begin{aligned}
G_{\pi'^- \rightarrow \pi^- \gamma} &= -i \left\{ \frac{4\sqrt{2}}{f} \cos^2 \theta' \lambda_{13}^P m_\pi^2 p_{-\mu} \epsilon^{*\mu} (k) + 2 \sin \theta' \cos \theta' p_{-\mu} \epsilon^{*\mu} (k) \right\} \\
&\quad \times \langle 0 | \tilde{\pi}'^- | \pi'^- (p_- + k) \rangle
\end{aligned} \tag{E.23}$$

$$\begin{aligned}
G_{\pi'^- \rightarrow \rho^0 \pi^-} &= -\frac{2}{f} \lambda_1^{PV} \cos^2 \theta' \mathcal{P}^\mu p_-^\nu \langle \rho^0 (\mathcal{P}) | \rho_{\mu\nu}^0 \tilde{\pi}'^- | \pi'^- (\mathcal{P} + p_-) \rangle \\
&\quad - \sin \theta' \cos \theta' G_{\pi^- \rightarrow \rho^0 \pi^-}
\end{aligned} \tag{E.24}$$

$$\begin{aligned}
G_{\pi'^- \rightarrow \rho^- \pi^0} &= \frac{2}{f} \lambda_1^{PV} \cos^2 \theta' (p_- + k)^\mu p_0^\nu \langle \rho^- (p_- + k) | \rho_{\mu\nu}^+ \tilde{\pi}'^- | \pi'^- (P-q) \rangle \\
&\quad - \sin \theta' \cos \theta' G_{\pi^- \rightarrow \rho^- \pi^0}
\end{aligned} \tag{E.25}$$

$$\begin{aligned}
G_{\rho^- \rightarrow \pi'^- \pi^0} &= \frac{2}{f} \lambda_1^{PV} \cos^2 \theta' (p_- + k)^\mu p_0^\nu \langle \pi'^- (p_- + k) | \rho_{\mu\nu}^- \tilde{\pi}'^+ | \rho^- (P-q) \rangle \\
&\quad - \sin \theta' \cos \theta' G_{\rho^- \rightarrow \pi^- \pi^0}
\end{aligned} \tag{E.26}$$

$$\begin{aligned}
G_{\pi'^- \rightarrow \rho^- \gamma} &= \frac{4}{3} e \kappa_3^{PV} \cos \theta' \epsilon_{\mu\nu\alpha\beta} k^\alpha \epsilon^{*\beta} (k) \langle \rho^- (p_- + p_0) | \rho^{+\mu\nu} \tilde{\pi}'^- | \pi'^- (P-q) \rangle \\
&\quad - \sin \theta' G_{\pi^- \rightarrow \rho^- \gamma}
\end{aligned} \tag{E.27}$$

$$\begin{aligned}
G_{\pi'^- \rightarrow \omega \pi^- \pi^0} &= \frac{2}{f^2} (2\kappa_1^{PV} - \kappa_2^{PV}) \cos^3 \theta' \epsilon_{\mu\nu\alpha\beta} p_-^\alpha p_0^\beta \langle \omega (k) | \omega^{\mu\nu} \tilde{\pi}'^- | \pi'^- (P-q) \rangle \\
&\quad - \sin \theta' \cos^2 \theta' G_{\pi^- \rightarrow \omega \pi^- \pi^0}
\end{aligned} \tag{E.28}$$

# Appendix F

## Virtual corrections to di-meson tau decays

The radiative corrections to the  $\tau^- \rightarrow P^- P^0 \nu_\tau$  decays at  $\mathcal{O}(p^2)$  in ChPT are shown along with Eqs. (F.7-F.9). The Feynman rules needed for this calculation are:

$$\left\langle \pi^- \pi^0 \left| \frac{\delta \mathcal{L}_2}{\delta v_\mu} \right| 0 \right\rangle = \sqrt{2}(p_- - p_0)^\mu, \quad \left\langle \pi^- \pi^0 \gamma \left| \frac{\delta \mathcal{L}_2}{\delta v_\mu} \right| 0 \right\rangle = -\sqrt{2}e \epsilon^\mu(k), \quad (\text{F.1})$$

$$\left\langle K^- K^0 \left| \frac{\delta \mathcal{L}_2}{\delta v_\mu} \right| 0 \right\rangle = -(p_- - p_0)^\mu, \quad \left\langle K^- K^0 \gamma \left| \frac{\delta \mathcal{L}_2}{\delta v_\mu} \right| 0 \right\rangle = e \epsilon^\mu(k), \quad (\text{F.2})$$

$$\left\langle K^- \pi^0 \left| \frac{\delta \mathcal{L}_2}{\delta v_\mu} \right| 0 \right\rangle = \frac{1}{\sqrt{2}}(p_K - p_\pi)^\mu, \quad \left\langle K^- \pi^0 \gamma \left| \frac{\delta \mathcal{L}_2}{\delta v_\mu} \right| 0 \right\rangle = -\frac{1}{\sqrt{2}}e \epsilon^\mu(k), \quad (\text{F.3})$$

$$\left\langle \pi^- \bar{K}^0 \left| \frac{\delta \mathcal{L}_2}{\delta v_\mu} \right| 0 \right\rangle = -(p_\pi - p_K)^\mu, \quad \left\langle \pi^- \bar{K}^0 \gamma \left| \frac{\delta \mathcal{L}_2}{\delta v_\mu} \right| 0 \right\rangle = e \epsilon^\mu(k), \quad (\text{F.4})$$

$$\langle \pi^-(p) \gamma(k) | i\mathcal{L}_2 | \pi^-(p') \rangle = -ie(p + p')_\mu \epsilon^{*\mu}(k), \quad (\text{F.5})$$

$$\langle K^-(p) \gamma(k) | i\mathcal{L}_2 | K^-(p') \rangle = -ie(p + p')_\mu \epsilon^{*\mu}(k). \quad (\text{F.6})$$

The results in Eqs. (F.5) and (F.6) are in perfect agreement with the prediction from sQED.

$$\begin{aligned}
&= -i \frac{G_F}{\sqrt{2}} V_{uD}^* \int \frac{d^4 k}{(2\pi)^4} \bar{u}(q) \gamma_\mu (1 - \gamma^5) \left[ \frac{i(\not{P} - \not{k} + m_\tau)}{(P - k)^2 - m_\tau^2} \right] [-ie\gamma_\alpha] u(P) \\
&\quad \times [C_V(p_- - k - p_0)^\mu] [-ie(2p_- - k)_\beta] \left[ \frac{-ig^{\alpha\beta}}{k^2 - M_\gamma^2} \right] \left[ \frac{i}{(p_- - k)^2 - m_-^2} \right] \\
&= -i \frac{G_F}{\sqrt{2}} V_{uD}^* \bar{u}(q) \gamma^\mu (1 - \gamma^5) u(P) \delta H_{1\mu}(s, u),
\end{aligned} \tag{F.7}$$

$$\begin{aligned}
&= -i \frac{G_F}{\sqrt{2}} V_{uD}^* \int \frac{d^4 k}{(2\pi)^4} \bar{u}(q) \gamma^\mu (1 - \gamma^5) \left[ \frac{i(\not{P} - \not{k} + m_\tau)}{(P - k)^2 - m_\tau^2} \right] [-ie\gamma_\alpha] u(P) \\
&\quad \times [-e C_V g_{\mu\beta}] \left[ \frac{-ig^{\alpha\beta}}{k^2 - M_\gamma^2} \right] \\
&= -i \frac{G_F}{\sqrt{2}} V_{uD}^* \bar{u}(q) \gamma^\mu (1 - \gamma^5) u(P) \delta H_{2\mu}(s, u),
\end{aligned} \tag{F.8}$$

$$\begin{aligned}
&= -i \frac{G_F}{\sqrt{2}} V_{uD}^* \bar{u}(q) \gamma^\mu (1 - \gamma^5) u(P) \int \frac{d^4 k}{(2\pi)^4} [-e C_V g_{\mu\alpha}] \left[ \frac{i}{(p_- - k)^2 - m_-^2} \right] \\
&\quad \times \left[ \frac{-ig^{\alpha\beta}}{k^2 - M_\gamma^2} \right] [-ie(2p_- - k)_\beta] \\
&= -i \frac{G_F}{\sqrt{2}} V_{uD}^* \bar{u}(q) \gamma^\mu (1 - \gamma^5) u(P) \delta H_{3\mu}(s, u),
\end{aligned} \tag{F.9}$$

where

$$\delta H_2^\mu(t, u) = ie^2 C_V \int \frac{d^4 k}{(2\pi)^4} \frac{2(P + k)^\mu}{[k^2 - M_\gamma^2][(P - k)^2 - m_\tau^2]} \tag{F.10}$$

$$\delta H_3^\mu(t, u) = ie^2 C_V \int \frac{d^4 k}{(2\pi)^4} \frac{(2p_- - k)^\mu}{[k^2 - M_\gamma^2][(p_- - k)^2 - m_-^2]}, \tag{F.11}$$

and  $C_V^{\pi\pi, KK, K^-\pi^0, K^0\pi^-} = \{\sqrt{2}, -1, \frac{1}{\sqrt{2}}, -1\}$ . We have omitted the analytic expression for  $\delta H_2^\mu(t, u)$  due to its length. The overall contribution is given by

$$\begin{aligned}
\delta H^\mu(t, u) &= \delta H_1^\mu(t, u) + \delta H_2^\mu(t, u) + \delta H_3^\mu(t, u) \\
&= C_V \delta f_+(u) (p_1 - p_0)^\mu + C_V \delta f_-(u) (p_1 + p_0)^\mu,
\end{aligned} \tag{F.12}$$

where

$$\delta f_+(u) = \frac{\alpha}{4\pi} \left\{ 2 + \frac{1}{\epsilon} - \gamma_E + \log 4\pi - \log \frac{m_\tau^2}{\mu^2} + (u - m_-^2) \mathcal{A}(u) + (u - m_-^2 - m_\tau^2) \mathcal{B}(u) \right. \\ \left. + 2(m_-^2 + m_\tau^2 - u) \mathcal{C}(u, M_\gamma) + 2 \log \frac{m_- m_\tau}{M_\gamma^2} \right\}, \quad (\text{F.13})$$

$$\delta f_-(u) = \frac{\alpha}{4\pi} \left\{ -5 - 3 \left( \frac{1}{\epsilon} - \gamma_E + \log 4\pi \right) + \log \frac{m_-^2}{\mu^2} + 2 \log \frac{m_\tau^2}{\mu^2} + (3u + m_-^2 - 2m_\tau^2) \mathcal{A}(u) \right. \\ \left. + (u + m_-^2 - m_\tau^2) \mathcal{B}(u) \right\}, \quad (\text{F.14})$$

$$\mathcal{A}(u) = \frac{1}{u} \left[ -\frac{1}{2} \log r_\tau + \frac{2-y}{\sqrt{r_\tau}} \frac{x}{1-x^2} \log x \right], \quad (\text{F.15})$$

$$\mathcal{B}(u) = \frac{1}{u} \left[ \frac{1}{2} \log r_\tau + \frac{2r_\tau - y}{\sqrt{r_\tau}} \frac{x}{1-x^2} \log x \right], \quad (\text{F.16})$$

$$\mathcal{C}(u, M_\gamma) = \frac{1}{m_\tau m_-} \frac{x}{1-x^2} \left[ -\frac{1}{2} \log^2 x + 2 \log x \log(1-x^2) - \frac{\pi^2}{6} + \frac{1}{8} \log^2 r_\tau \right. \\ \left. + \text{Li}_2(x^2) + \text{Li}_2 \left( 1 - \frac{x}{\sqrt{r_\tau}} \right) + \text{Li}_2(1 - x\sqrt{r_\tau}) - \log x \log \frac{M_\gamma^2}{m_\tau m_-} \right]. \quad (\text{F.17})$$

Here,  $\mathcal{A}(u)$ ,  $\mathcal{B}(u)$  and  $\mathcal{C}(u, M_\gamma)$  are written in terms of the variables

$$r_\tau = \frac{m_\tau^2}{m_-^2}, \quad y = 1 + r_\tau - \frac{u}{m_-^2}, \quad x = \frac{1}{2\sqrt{r_\tau}} \left( y - \sqrt{y^2 - 4r_\tau} \right), \quad (\text{F.18})$$

and the dilogarithm

$$\text{Li}_2(x) = - \int_0^1 \frac{dt}{t} \log(1 - xt). \quad (\text{F.19})$$

The radiative corrections to these decays induce dependence in the  $u$ -variable. From a comparison with the results in Ref. [380], we get the following relation

$$\delta \bar{f}_+(u) = \frac{\alpha}{4\pi} \frac{1}{f_+(0)} \left[ \Gamma_1(u, m_\tau^2, m_-^2) + \Gamma_2(u, m_\tau^2, m_-^2) \right] + \dots \\ = \frac{\alpha}{4\pi} \frac{1}{f_+(0)} \left[ (u - m_-^2) \mathcal{A}(u) + (u - m_-^2 - m_\tau^2) \mathcal{B}(u) \right] + \dots, \quad (\text{F.20})$$

and

$$\delta \bar{f}_-(u) = \frac{\alpha}{4\pi} \frac{1}{f_+(0)} \left[ \Gamma_1(u, m_\tau^2, m_-^2) - \Gamma_2(u, m_\tau^2, m_-^2) \right] + \dots \\ = \frac{\alpha}{4\pi} \frac{1}{f_+(0)} \left[ (3u + m_-^2 - 2m_\tau^2) \mathcal{A}(u) + (u + m_-^2 - m_\tau^2) \mathcal{B}(u) \right] + \dots. \quad (\text{F.21})$$

$R\chi T$  contributions will be shown elsewhere and the phenomenological application of these results (apart from the  $\pi\pi$  mode) is work in progress.

# Appendix G

## Fit of leading odd-intrinsic parity resonance couplings to the $\mathcal{O}(p^6)$ LECs

Since the  $\kappa_i^V$  couplings are related with the  $\omega$  exchange which is known to give an important contribution to the  $\tau \rightarrow \pi\pi\gamma\nu_\tau$  decays, we perform a global fit using the relations for the resonance saturation of the anomalous sector LECs at NLO [684], the eqs. (7.10)-(7.18) in section 7.2.5 and the estimation of the LECs in [818].



Neglecting all the other contributions, we get

$$\kappa_1^V = (-2.1 \pm 0.7) \cdot 10^{-2} \text{ GeV}^{-1}, \quad (\text{G.1a})$$

$$\kappa_2^V = (-8.8 \pm 9.1) \cdot 10^{-3} \text{ GeV}^{-1}, \quad (\text{G.1b})$$

$$\kappa_3^V = (2.2 \pm 5.8) \cdot 10^{-3} \text{ GeV}^{-1}, \quad (\text{G.1c})$$

$$\kappa_6^V = (-2.1 \pm 0.3) \cdot 10^{-2} \text{ GeV}^{-1}, \quad (\text{G.1d})$$

$$\kappa_7^V = (1.2 \pm 0.5) \cdot 10^{-2} \text{ GeV}^{-1}, \quad (\text{G.1e})$$

$$\kappa_8^V = (3.1 \pm 0.9) \cdot 10^{-2} \text{ GeV}^{-1}, \quad (\text{G.1f})$$

$$\kappa_9^V = (-0.1 \pm 5.9) \cdot 10^{-3} \text{ GeV}^{-1}, \quad (\text{G.1g})$$

$$\kappa_{10}^V = (-5.9 \pm 9.6) \cdot 10^{-3} \text{ GeV}^{-1}, \quad (\text{G.1h})$$

$$\kappa_{11}^V = (-3.0 \pm 0.6) \cdot 10^{-2} \text{ GeV}^{-1}, \quad (\text{G.1i})$$

$$\kappa_{12}^V = (1.0 \pm 0.8) \cdot 10^{-2} \text{ GeV}^{-1}, \quad (\text{G.1j})$$

$$\kappa_{13}^V = (-5.3 \pm 1.1) \cdot 10^{-3} \text{ GeV}^{-1}, \quad (\text{G.1k})$$

$$\kappa_{18}^V = (4.7 \pm 0.8) \cdot 10^{-3} \text{ GeV}^{-1}. \quad (\text{G.1l})$$

These values are in good agreement with our earlier estimation in section 7.2.5,  $|\kappa_i^V| \lesssim 0.025 \text{ GeV}^{-1}$ .

# Appendix H

## Kinematics of four body tau decays

### H.1 $\tau^-(P) \rightarrow \pi^-(p_-)\pi^0(p_0)\gamma(k)\nu_\tau(q)$ kinematics

In order to describe this type of decays we need five independent variables. We choose  $s = (p_- + p_0)^2$ ,  $u = (P - p_-)^2$ ,  $x = (k + q)^2$ ,  $\theta_\nu$  which is the angle between the direction of the  $\pi^-\pi^0$  CM frame in the  $\tau$  lepton rest frame and the direction of  $\vec{q}$  in the  $\pi^-\pi^0$  CM frame (see fig. H.1) and  $\phi_-$ , which is angle between the plane of the  $\pi^-\pi^0$  CM frame and the plane of the  $\gamma\nu_\tau$  CM frame.

We can write the invariants in terms of these variables

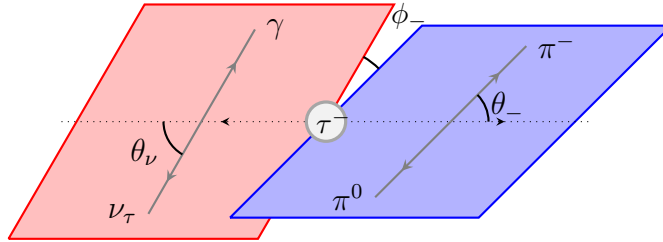


Figure H.1: The  $\tau^- \rightarrow \pi^-\pi^0\gamma\nu_\tau$  decay in the  $\tau$ -lepton rest frame.

$$P \cdot p_0 = \frac{s + u - x - m_{\pi^-}^2}{2}, \quad (\text{H.1a})$$

$$q \cdot k = \frac{x - M_\gamma^2}{2}, \quad (\text{H.1b})$$

$$p_- \cdot p_0 = \frac{s - m_{\pi^-}^2 - m_{\pi^0}^2}{2}, \quad (\text{H.1c})$$

$$p_0 \cdot (q + k) = \frac{u - x - m_{\pi^0}^2}{2}, \quad (\text{H.1d})$$

$$P \cdot (q + k) = \frac{x - s + m_\tau^2}{2}, \quad (\text{H.1e})$$

$$\begin{aligned} P \cdot p_- &= \frac{(m_{\pi^-}^2 - m_{\pi^0}^2 + s)(m_\tau^2 + s - x)}{4s} + \frac{\lambda^{1/2}(s, x, m_\tau^2)\lambda^{1/2}(m_\tau^2, m_{\pi^-}^2, m_{\pi^0}^2)}{4s} \cos \theta_- \\ &= \frac{m_\tau^2 + m_{\pi^-}^2 - u}{2}, \end{aligned} \quad (\text{H.2})$$

$$P \cdot k = \frac{(m_\tau^2 - s + x)(x + M_\gamma^2)}{4x} - \frac{(x - M_\gamma^2)\lambda^{1/2}(s, x, m_\tau^2)}{4x} \cos \theta_\nu, \quad (\text{H.3})$$

$$\begin{aligned} p_- \cdot k &= \frac{(x + M_\gamma^2)(m_\tau^2 - s - u + m_{\pi^0}^2)}{4x} - \frac{(x - M_\gamma^2) \cos \theta_\nu}{4x \lambda^{1/2}(s, x, m_\tau^2)} A(s, u, x) \\ &\quad - \frac{(x - M_\gamma^2) \lambda^{1/2}(s, m_{\pi^-}^2, m_{\pi^0}^2)}{4\sqrt{x}\sqrt{s}} \sin \theta_\nu \sin \theta_- \cos \phi_-, \end{aligned} \quad (\text{H.4})$$

$$\begin{aligned} \epsilon^{\mu\nu\alpha\beta} k_\mu P_\nu p_{-\alpha} q_\beta &= \frac{(x - M_\gamma^2)\lambda^{1/2}(s, m_{\pi^-}^2, m_{\pi^0}^2) \lambda^{1/2}(s, x, m_\tau^2)}{8\sqrt{s}\sqrt{x}} \times \\ &\quad \sin \theta_\nu \sin \theta_- \sin \phi_-, \end{aligned} \quad (\text{H.5})$$

$$\begin{aligned} \epsilon^{\mu\nu\alpha\beta} k_\mu P_\nu p_{-\alpha} p_{0\beta} &= \epsilon^{\mu\nu\alpha\beta} k_\mu P_\nu p_{0\alpha} q_\beta = \epsilon^{\mu\nu\alpha\beta} k_\mu p_{-\nu} p_{0\alpha} q_\beta = \epsilon^{\mu\nu\alpha\beta} P_\mu p_{-\nu} p_{0\alpha} q_\beta \\ &= -\epsilon^{\mu\nu\alpha\beta} k_\mu P_\nu p_{-\alpha} q_\beta, \end{aligned} \quad (\text{H.6})$$

where

$$A(s, u, x) = m_\tau^4 + s(s + u) + x(u - s - 2m_{\pi^-}^2) + m_{\pi^0}^2(m_\tau^2 - s + x) - m_\tau^2(2s + u + x). \quad (\text{H.7})$$

Working in the  $\tau$ -lepton rest frame, we have

$$E_\gamma = \frac{(m_\tau^2 - s + x)(x + M_\gamma^2)}{4m_\tau x} - \frac{(x - M_\gamma^2)\lambda^{1/2}(s, x, m_\tau^2)}{4m_\tau x} \cos \theta_\nu, \quad (\text{H.8})$$

$$E_\nu = |\vec{q}| = \frac{(m_\tau^2 - s + x)(x - M_\gamma^2)}{4m_\tau x} + \frac{(x - M_\gamma^2)\lambda^{1/2}(s, x, m_\tau^2)}{4m_\tau x} \cos \theta_\nu, \quad (\text{H.9})$$

$$\begin{aligned} \vec{k} = & \left( -\frac{(x + M_\gamma^2)\lambda^{1/2}(s, x, m_\tau^2)}{4m_\tau x} + \frac{(m_\tau^2 - s + x)(x - M_\gamma^2)}{4m_\tau x} \cos \theta_\nu \right) \hat{e}_z \\ & + \frac{x - M_\gamma^2}{2\sqrt{x}} \sin \theta_\nu \hat{e}_x, \end{aligned} \quad (\text{H.10})$$

$$\begin{aligned} \vec{q} = & \left( -\frac{(x - M_\gamma^2)\lambda^{1/2}(s, x, m_\tau^2)}{4m_\tau x} - \frac{(m_\tau^2 - s + x)(x - M_\gamma^2)}{4m_\tau x} \cos \theta_\nu \right) \hat{e}_z \\ & - \frac{x - M_\gamma^2}{2\sqrt{x}} \sin \theta_\nu \hat{e}_x, \end{aligned} \quad (\text{H.11})$$

$$\begin{aligned} E_- = & \frac{(m_\tau^2 + s - x)(s + m_{\pi^-}^2 - m_{\pi^0}^2)}{4m_\tau s} + \frac{\lambda^{1/2}(s, x, m_\tau^2) \lambda^{1/2}(s, m_{\pi^-}^2, m_{\pi^0}^2)}{4m_\tau s} \cos \theta_- \\ = & \frac{m_\tau^2 + m_{\pi^-}^2 - u}{2m_\tau}, \end{aligned} \quad (\text{H.12})$$

$$\begin{aligned} E_0 = & \frac{(m_\tau^2 + s - x)(s - m_{\pi^-}^2 + m_{\pi^0}^2)}{4m_\tau s} - \frac{\lambda^{1/2}(s, x, m_\tau^2) \lambda^{1/2}(s, m_{\pi^-}^2, m_{\pi^0}^2)}{4m_\tau s} \cos \theta_- \\ = & \frac{s + u - x - m_{\pi^-}^2}{2m_\tau}, \end{aligned} \quad (\text{H.13})$$

$$|\vec{p}_-| = \frac{\lambda^{1/2}(u, m_\tau^2, m_{\pi^-}^2)}{2m_\tau}, \quad (\text{H.14})$$

$$\begin{aligned} \vec{p}_- = & \left( \frac{(s + m_{\pi^-}^2 - m_{\pi^0}^2)\lambda^{1/2}(s, x, m_\tau^2)}{4m_\tau s} + \frac{(m_\tau^2 + s - x)\lambda^{1/2}(s, m_{\pi^-}^2, m_{\pi^0}^2)}{4m_\tau s} \cos \theta_- \right) \hat{e}_z \\ & + \frac{\lambda^{1/2}(s, m_{\pi^-}^2, m_{\pi^0}^2)}{2\sqrt{s}} \sin \theta_- \hat{e}_\rho, \end{aligned} \quad (\text{H.15})$$

$$\begin{aligned} \vec{p}_0 = & \left( \frac{(s - m_{\pi^-}^2 + m_{\pi^0}^2)\lambda^{1/2}(s, x, m_\tau^2)}{4m_\tau s} - \frac{(m_\tau^2 + s - x)\lambda^{1/2}(s, m_{\pi^-}^2, m_{\pi^0}^2)}{4m_\tau s} \cos \theta_- \right) \hat{e}_z \\ & - \frac{\lambda^{1/2}(s, m_{\pi^-}^2, m_{\pi^0}^2)}{2\sqrt{s}} \sin \theta_- \hat{e}_\rho, \end{aligned} \quad (\text{H.16})$$

$$\cos \theta_- = \frac{2s(m_\tau^2 + m_{\pi^-}^2 - u) - (m_\tau^2 + s - x)(s + m_{\pi^-}^2 - m_{\pi^0}^2)}{\lambda^{1/2}(s, x, m_\tau^2) \lambda^{1/2}(s, m_{\pi^-}^2, m_{\pi^0}^2)}, \quad (\text{H.17})$$

$$\cos \theta_\nu = \frac{(m_\tau^2 - s + x)(x + M_\gamma^2) - 4m_\tau E_\gamma x}{(x - M_\gamma^2)\lambda^{1/2}(s, x, m_\tau^2)}, \quad (\text{H.18})$$

where  $\lambda(x, y, z) = x^2 + y^2 + z^2 - 2xy - 2xz - 2yz$  is the Kallen function, and  $\hat{e}_\rho = \cos \phi_- \hat{e}_x +$

$\sin \phi_- \hat{e}_y$ .

From eq. (H.17), we get

$$x_{\pm}(s, u) = \frac{-m_{\pi^-}^4 + (m_{\pi^0}^2 - s)(m_{\tau}^2 - u) + m_{\pi^-}^2(m_{\tau}^2 + m_{\pi^0}^2 + s + u)}{2m_{\pi^-}^2} \pm \frac{\lambda^{1/2}(u, m_{\tau}^2, m_{\pi^-}^2) \lambda^{1/2}(s, m_{\pi^-}^2, m_{\pi^0}^2)}{2m_{\pi^-}^2}, \quad (\text{H.19})$$

and

$$u_{\pm}(s, x) = m_{\tau}^2 + m_{\pi^-}^2 - \frac{(m_{\tau}^2 + s - x)(s + m_{\pi^-}^2 - m_{\pi^0}^2)}{2s} \pm \frac{\lambda^{1/2}(s, x, m_{\tau}^2) \lambda^{1/2}(s, m_{\pi^-}^2, m_{\pi^0}^2)}{2s}, \quad (\text{H.20})$$

these bounds on  $u$  and  $x$  correspond to the forward and backward direction, i.e. by taking  $\theta_- = 0, \pi$ .

For the non-radiative decay, we have

$$\mathcal{D}^{III} = \left\{ u_-(s, 0) \leq u \leq u_+(s, 0), (m_{\pi^-} + m_{\pi^0})^2 \leq s \leq m_{\tau}^2 \right\}, \quad (\text{H.21})$$

this region is plotted in fig. H.2 which corresponds to the projection  $\mathcal{R}^{III}$  onto the  $su$ -plane.

In the case of the radiative decay, we have

$$\mathcal{D}^{IV} = \left\{ x_{min}(s, u) \leq x \leq x_{max}(s, u), u_{min}(s) \leq u \leq u_{max}(s), (m_{\pi^-} + m_{\pi^0})^2 \leq s \leq (m_{\tau} - M_{\gamma})^2 \right\}, \quad (\text{H.22})$$

with

$$x_{min}(s, u) = \begin{cases} x_-(s, u) & u_+(s, M_{\gamma}^2) \leq u \leq (m_{\tau} - m_{\pi^-})^2, \quad (m_{\pi^-} + m_{\pi^0})^2 \leq s \leq s^* \\ M_{\gamma}^2 & u_-(s, M_{\gamma}^2) \leq u \leq u_+(s, M_{\gamma}^2), \quad s^* \leq s \leq (m_{\tau} - M_{\gamma})^2, \end{cases} \quad (\text{H.23})$$

$$x_{max}(s, u) = x_+(s, u), \quad (\text{H.24})$$

$$u_{min}(s) = u_-(s, M_\gamma^2), \quad (\text{H.25})$$

$$u_{max}(s) = \begin{cases} (m_\tau - m_{\pi^-})^2 & (m_{\pi^-} + m_{\pi^0})^2 \leq s \leq s^*, \\ u_+(s, M_\gamma^2) & s^* \leq s \leq (m_\tau - M_\gamma)^2, \end{cases} \quad (\text{H.26})$$

where  $s^* = \frac{m_\tau(m_\tau m_{\pi^-} + m_{\pi^0}^2 - m_{\pi^-}^2) - M_\gamma^2 m_{\pi^-}}{m_\tau - m_{\pi^-}}$  is the value that maximizes  $u_+(s, M_\gamma^2)$ . We will be working in the isospin-limit ( $m_u = m_d$ ), i.e.  $m_{\pi^-}^2 = m_{\pi^0}^2$  and thus many of the last expressions will be simplified.

We use a non-vanishing  $M_\gamma$  in order to deal with the IR divergences, at the end these divergences are canceled out by those divergences of the non-radiative decay so we can take the limit  $M_\gamma \rightarrow 0$ . The projection  $\mathcal{R}^{IV} = \mathcal{R}^{IV/III} \cup \mathcal{R}^{III}$  of the  $\mathcal{D}^{IV}$  is plotted in fig. H.2 for  $M_\gamma \rightarrow 0$ .

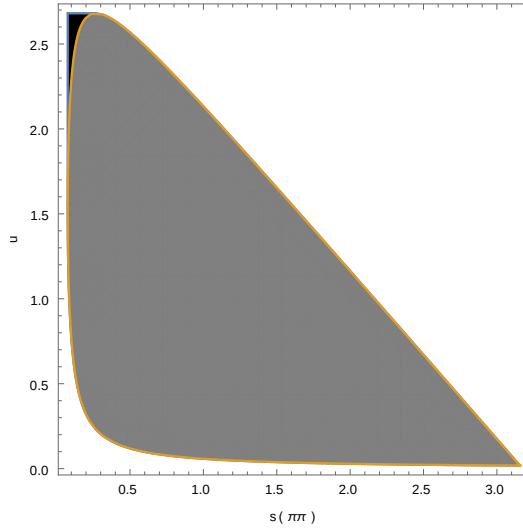


Figure H.2: Projection of the kinematic region for the non-radiative decay  $\mathcal{R}^{III}$  (gray) and the radiative decay  $\mathcal{R}^{IV} = \mathcal{R}^{IV/III} \cup \mathcal{R}^{III}$  (black and gray) onto the  $su$ -plane.  $\mathcal{R}^{IV/III}$  (black) is the kinematic region which is only accessible to the radiative decay.



# Appendix I

## Vector Form Factors in radiative di-pion tau decays

We present here the vector form factors in  $\tau^- \rightarrow \pi^- \pi^0 \nu_\tau \gamma$  decays.

$$\begin{aligned}
v_1^R = & \frac{1}{F^2} \left( \frac{16k \cdot p_0 (2\kappa_{12}^V + \kappa_{16}^V) (-2k \cdot p_- + s) (2\kappa_{12}^V + \kappa_{16}^V) + 2(P - q)^2 \kappa_{17}^V}{D_\omega [(k + p_0)^2]} \right. \\
& + \frac{\sqrt{2}F_V}{M_\rho^2} \left( 2s\lambda_{12}^V - (4k \cdot p_0 + s) (\lambda_{13}^V + \lambda_{14}^V - \lambda_{15}^V) + (2k \cdot p_- + s)\lambda_{16}^V - 4k \cdot p_- \lambda_{17}^V \right. \\
& + 4k \cdot p_- \lambda_{18}^V + s\lambda_{18}^V + 4k \cdot p_- \lambda_{19}^V + 2s\lambda_{19}^V + 4k \cdot p_0 \lambda_{21}^V + 2k \cdot p_0 \lambda_{22}^V - 2k \cdot p_- \lambda_{22}^V \Big) \\
& + \frac{1}{M_{a_1}^2 D_{a_1} [(k + p_-)^2]} \left( -8(-2k \cdot p_0 M_{a_1}^2 s + (k \cdot p_- - M_{a_1}^2) s^2 + 2(k \cdot p_0)(k \cdot p_-) \right. \\
& (2M_{a_1}^2 + s)(\lambda_{12}^A)^2 - 8k \cdot p_- (2k \cdot p_0 + s)(2M_{a_1}^2 + s)(\lambda_{13}^A)^2 - 2\sqrt{2}F_A (k \cdot p_0) s \lambda_{15}^A \\
& - 2\sqrt{2}F_A (k \cdot p_-) s \lambda_{15}^A - \sqrt{2}F_A s^2 \lambda_{15}^A - 8\sqrt{2}F_A k \cdot p_- M_{a_1}^2 \lambda_{17}^A - 4\sqrt{2}F_A (k \cdot p_-) s \lambda_{17}^A \\
& + 16(k \cdot p_0)(k \cdot p_-) s \lambda_{15}^A \lambda_{17}^A + 16(k \cdot p_-)^2 s \lambda_{15}^A \lambda_{17}^A + 8(k \cdot p_-) s^2 \lambda_{15}^A \lambda_{17}^A \\
& + 32(k \cdot p_-)^2 M_{a_1}^2 (\lambda_{17}^A)^2 + 16(k \cdot p_-)^2 s (\lambda_{17}^A)^2 + \lambda_{13}^A (8(k \cdot p_-) s (P - q)^2 \lambda_{15}^A \\
& + (2k \cdot p_0 - 2k \cdot p_- + s)(2M_{a_1}^2 + s)(\sqrt{2}F_A - 8k \cdot p_- \lambda_{17}^A)) + \lambda_{12}^A (-8(s(2k \cdot p_- (M_{a_1}^2 - s) \\
& + M_{a_1}^2 s) + 2k \cdot p_0 (4k \cdot p_- M_{a_1}^2 - 2(k \cdot p_-) s + M_{a_1}^2 s)) \lambda_{13}^A - 8(k \cdot p_- - M_{a_1}^2) s (P - q)^2 \lambda_{15}^A \\
& \left. \left. + (k \cdot p_0 (4M_{a_1}^2 - 2s) - s(2M_{a_1}^2 + s) + k \cdot p_- (-4M_{a_1}^2 + 2s)) (\sqrt{2}F_A - 8k \cdot p_- \lambda_{17}^A) \right) \right) \Big)
\end{aligned}
\tag{I.1}$$



$$\begin{aligned}
v_1^{RR} = & \frac{1}{2\sqrt{2}F^2} \left( \frac{64k \cdot p_0 F_V (-2k \cdot p_- + s)(2\kappa_{12}^V + \kappa_{16}^V) + 2(P-q)^2 \kappa_{17}^V \kappa_3^{VV}}{M_\rho^2 D_\omega [(k+p_0)^2]} \right. \\
& - \frac{64k \cdot p_0 (4k \cdot p_0 + 2k \cdot p_- + s)(2\kappa_{12}^V + \kappa_{16}^V) \kappa_3^{VV} (-F_V + 2\sqrt{2}(P-q)^2 \lambda_{22}^V)}{D_\rho [(P-q)^2] D_\omega [(k+p_0)^2]} \\
& + \frac{2F_V}{M_{a_1}^2 M_\rho^2 D_{a_1} [(k+p_-)^2]} \left( 2(2\sqrt{2}F_A k \cdot p_- M_{a_1}^2 - \sqrt{2}F_A (k \cdot p_-) s + \sqrt{2}F_A M_{a_1}^2 s \right. \\
& + 4(-2k \cdot p_0 M_{a_1}^2 s + (k \cdot p_- - M_{a_1}^2) s^2 + 2(k \cdot p_0)(k \cdot p_-)(2M_{a_1}^2 + s)) \lambda_{12}^A \\
& + 4(2k \cdot p_0 + s)(2k \cdot p_- M_{a_1}^2 - (k \cdot p_-) s + M_{a_1}^2 s) \lambda_{13}^A + 8(k \cdot p_0)(k \cdot p_-) s \lambda_{15}^A \\
& + 8(k \cdot p_-)^2 s \lambda_{15}^A - 8k \cdot p_0 M_{a_1}^2 s \lambda_{15}^A - 8k \cdot p_- M_{a_1}^2 s \lambda_{15}^A + 4(k \cdot p_-) s^2 \lambda_{15}^A \\
& - 4M_{a_1}^2 s^2 \lambda_{15}^A - 16(k \cdot p_-)^2 M_{a_1}^2 \lambda_{17}^A + 8(k \cdot p_-)^2 s \lambda_{17}^A - 8k \cdot p_- M_{a_1}^2 s \lambda_{17}^A \lambda_2^{VA} \\
& - k \cdot p_- (2\sqrt{2}F_A M_{a_1}^2 + \sqrt{2}F_A s + 4(4k \cdot p_0 M_{a_1}^2 - 2(k \cdot p_0) s - s^2)) \lambda_{12}^A \\
& + 4(2k \cdot p_0 + s)(2M_{a_1}^2 + s) \lambda_{13}^A - 8(k \cdot p_0) s \lambda_{15}^A - 8(k \cdot p_-) s \lambda_{15}^A - 4s^2 \lambda_{15}^A \\
& \left. - 16k \cdot p_- M_{a_1}^2 \lambda_{17}^A - 8(k \cdot p_-) s \lambda_{17}^A (\lambda_4^{VA} + 2\lambda_5^{VA}) \right) \\
& + \frac{(\sqrt{2}F_V - 4(P-q)^2 \lambda_{22}^V)}{M_{a_1}^2 D_{a_1} [(k+p_-)^2] D_\rho [(P-q)^2]} \left( -2(-4\sqrt{2}(-2k \cdot p_0 M_{a_1}^2 s + (k \cdot p_- - M_{a_1}^2) s^2) \right. \\
& + 2(k \cdot p_0)(k \cdot p_-)(2M_{a_1}^2 + s)) \lambda_{12}^A + (4k \cdot p_0 M_{a_1}^2 - 2(k \cdot p_0) s - s^2) \\
& (F_A - 4\sqrt{2}k \cdot p_- \lambda_{13}^A - 4\sqrt{2}k \cdot p_- \lambda_{17}^A) \lambda_2^{VA} - 2s(P-q)^2 (F_A + 4\sqrt{2}(k \cdot p_- - M_{a_1}^2)) \lambda_{12}^A \\
& - 4\sqrt{2}k \cdot p_- \lambda_{13}^A - 4\sqrt{2}k \cdot p_- \lambda_{17}^A \lambda_3^{VA} + (2k \cdot p_0 + s)(-4\sqrt{2}(2k \cdot p_- M_{a_1}^2 - (k \cdot p_-) s \\
& + M_{a_1}^2 s) \lambda_{12}^A + (2M_{a_1}^2 + s)(F_A - 4\sqrt{2}k \cdot p_- \lambda_{13}^A - 4\sqrt{2}k \cdot p_- \lambda_{17}^A) (\lambda_4^{VA} + 2\lambda_5^{VA})) \\
& \left. + \frac{2F_V}{M_\rho^2 D_\rho [(P-q)^2]} \left( -2(P-q)^2 \lambda_{22}^V ((P-q)^2 - 8s \lambda_2^{VV}) \right. \right. \\
& - 2(4k \cdot p_0 + s) \lambda_3^{VV} + 8k \cdot p_0 \lambda_4^{VV} + 2s \lambda_4^{VV} - 16k \cdot p_0 \lambda_5^{VV} - 4s \lambda_5^{VV} \\
& \left. + \sqrt{2}F_V (-4s \lambda_2^{VV} - (4k \cdot p_0 + s)(\lambda_3^{VV} - \lambda_4^{VV} + 2\lambda_5^{VV})) \right) \\
& \left. - \frac{4F_V (\sqrt{2}(4k \cdot p_0 + s) G_V \lambda_7^{VV} + s \lambda_{21}^V (s - 2(4k \cdot p_0 + s) \lambda_7^{VV}))}{M_\rho^2 D_\rho [s]} \right)
\end{aligned} \tag{I.2}$$

$$\begin{aligned}
v_1^{RRR} = & - \frac{F_V(-\sqrt{2}F_V + 4(P-q)^2\lambda_{22}^V)}{\sqrt{2}F^2M_{a_1}^2M_\rho^2D_{a_1}[(k+p_-)^2]D_\rho[(P-q)^2]}(-4(-2k \cdot p_0M_{a_1}^2s \\
& + (k \cdot p_- - M_{a_1}^2)s^2 + 2(k \cdot p_0)(k \cdot p_-)(2M_{a_1}^2 + s))(\lambda_2^{VA})^2 \\
& - k \cdot p_-(\lambda_4^{VA} + 2\lambda_5^{VA})(-2s(P-q)^2\lambda_3^{VA} + (2k \cdot p_0 + s)(2M_{a_1}^2 + s)(\lambda_4^{VA} + 2\lambda_5^{VA})) \\
& + 2\lambda_2^{VA}(2(k \cdot p_- - M_{a_1}^2)s(P-q)^2\lambda_3^{VA} + (s(2k \cdot p_-(M_{a_1}^2 - s) + M_{a_1}^2s) \\
& + 2k \cdot p_0(4k \cdot p_-M_{a_1}^2 - 2(k \cdot p_-)s + M_{a_1}^2s))(\lambda_4^{VA} + 2\lambda_5^{VA})))
\end{aligned} \tag{I.3}$$

$$\begin{aligned}
v_{GI1}^{R+RR} = & \frac{1}{F^2D_\rho[(P-q)^2]D_\rho[s]} \left( \sqrt{2}F_V(2(M_\rho^2 - s)s\lambda_{12}^V - (M_\rho^2 - s)(4k \cdot p_0 + s)\lambda_{13}^V \right. \\
& - 4k \cdot p_0M_\rho^2\lambda_{14}^V + 4(k \cdot p_0)s\lambda_{14}^V - M_\rho^2s\lambda_{14}^V + s^2\lambda_{14}^V + 4k \cdot p_0M_\rho^2\lambda_{15}^V - 4(k \cdot p_0)s\lambda_{15}^V \\
& + M_\rho^2s\lambda_{15}^V - s^2\lambda_{15}^V - 2k \cdot p_0M_\rho^2\lambda_{16}^V + 2(k \cdot p_0)s\lambda_{16}^V + 4k \cdot p_0M_\rho^2\lambda_{17}^V - 4(k \cdot p_0)s\lambda_{17}^V \\
& + 2M_\rho^2s\lambda_{17}^V - 2s^2\lambda_{17}^V - 4k \cdot p_0M_\rho^2\lambda_{18}^V + 4(k \cdot p_0)s\lambda_{18}^V - M_\rho^2s\lambda_{18}^V + s^2\lambda_{18}^V \\
& - 2k \cdot p_0M_\rho^2\lambda_{19}^V + 2(k \cdot p_0)s\lambda_{19}^V - 4k \cdot p_-M_\rho^2\lambda_{21}^V + 4(k \cdot p_-)s\lambda_{21}^V - 2M_\rho^2s\lambda_{21}^V \\
& + s^2\lambda_{21}^V + 6k \cdot p_0M_\rho^2\lambda_{22}^V + 2k \cdot p_-M_\rho^2\lambda_{22}^V - 6(k \cdot p_0)s\lambda_{22}^V - 2(k \cdot p_-)s\lambda_{22}^V \\
& + 2M_\rho^2s\lambda_{22}^V - 2s^2\lambda_{22}^V + 8(k \cdot p_0)s\lambda_{21}^V\lambda_7^{VV} + 2s^2\lambda_{21}^V\lambda_7^{VV}) + 2G_V(\sqrt{2}(4k \cdot p_0 + s) \\
& ((P-q)^2 - M_\rho^2)\lambda_7^V - (4k \cdot p_0 + s)F_V\lambda_7^{VV} + \sqrt{2}\lambda_{22}^V(-16(k \cdot p_0)^2 - (2M_\rho^2 - s) \\
& (2k \cdot p_- + s) - 2k \cdot p_0(8k \cdot p_- - 2M_\rho^2 + 3s) + 2(4k \cdot p_0 + s)(P-q)^2\lambda_7^{VV})) \\
& - 4(s(4k \cdot p_0 + s)((P-q)^2 - M_\rho^2)\lambda_7^V\lambda_{21}^V + \lambda_{22}^V(2(M_\rho^2 - s)s(P-q)^2\lambda_{12}^V \\
& - (M_\rho^2 - s)(4k \cdot p_0 + s)(P-q)^2\lambda_{13}^V - 8(k \cdot p_0)^2M_\rho^2\lambda_{14}^V - 8(k \cdot p_0)(k \cdot p_-)M_\rho^2\lambda_{14}^V \\
& + 8(k \cdot p_0)^2s\lambda_{14}^V + 8(k \cdot p_0)(k \cdot p_-)s\lambda_{14}^V - 6k \cdot p_0M_\rho^2s\lambda_{14}^V - 2k \cdot p_-M_\rho^2s\lambda_{14}^V \\
& + 6(k \cdot p_0)s^2\lambda_{14}^V + 2(k \cdot p_-)s^2\lambda_{14}^V - M_\rho^2s^2\lambda_{14}^V + s^3\lambda_{14}^V + 8(k \cdot p_0)^2M_\rho^2\lambda_{15}^V \\
& + 8(k \cdot p_0)(k \cdot p_-)M_\rho^2\lambda_{15}^V - 8(k \cdot p_0)^2s\lambda_{15}^V - 8(k \cdot p_0)(k \cdot p_-)s\lambda_{15}^V \\
& + 6k \cdot p_0M_\rho^2s\lambda_{15}^V + 2k \cdot p_-M_\rho^2s\lambda_{15}^V - 6(k \cdot p_0)s^2\lambda_{15}^V - 2(k \cdot p_-)s^2\lambda_{15}^V + M_\rho^2s^2\lambda_{15}^V \\
& - s^3\lambda_{15}^V - 4(k \cdot p_0)^2M_\rho^2\lambda_{16}^V - 4(k \cdot p_0)(k \cdot p_-)M_\rho^2\lambda_{16}^V + 4(k \cdot p_0)^2s\lambda_{16}^V
\end{aligned}$$

$$\begin{aligned}
& + 4(k \cdot p_0)(k \cdot p_-)s\lambda_{16}^V - 2k \cdot p_0 M_\rho^2 s\lambda_{16}^V + 2(k \cdot p_0)s^2\lambda_{16}^V + 8(k \cdot p_0)^2 M_\rho^2 \lambda_{17}^V \\
& + 8(k \cdot p_0)(k \cdot p_-)M_\rho^2 \lambda_{17}^V - 8(k \cdot p_0)^2 s\lambda_{17}^V - 8(k \cdot p_0)(k \cdot p_-)s\lambda_{17}^V \\
& + 8k \cdot p_0 M_\rho^2 s\lambda_{17}^V + 4k \cdot p_- M_\rho^2 s\lambda_{17}^V - 8(k \cdot p_0)s^2\lambda_{17}^V - 4(k \cdot p_-)s^2\lambda_{17}^V \\
& + 2M_\rho^2 s^2\lambda_{17}^V - 2s^3\lambda_{17}^V - 8(k \cdot p_0)^2 M_\rho^2 \lambda_{18}^V - 8(k \cdot p_0)(k \cdot p_-)M_\rho^2 \lambda_{18}^V \\
& + 8(k \cdot p_0)^2 s\lambda_{18}^V + 8(k \cdot p_0)(k \cdot p_-)s\lambda_{18}^V - 6k \cdot p_0 M_\rho^2 s\lambda_{18}^V - 2k \cdot p_- M_\rho^2 s\lambda_{18}^V \\
& + 6(k \cdot p_0)s^2\lambda_{18}^V + 2(k \cdot p_-)s^2\lambda_{18}^V - M_\rho^2 s^2\lambda_{18}^V + s^3\lambda_{18}^V - 4(k \cdot p_0)^2 M_\rho^2 \lambda_{19}^V \\
& - 4(k \cdot p_0)(k \cdot p_-)M_\rho^2 \lambda_{19}^V + 4(k \cdot p_0)^2 s\lambda_{19}^V + 4(k \cdot p_0)(k \cdot p_-)s\lambda_{19}^V \\
& - 2k \cdot p_0 M_\rho^2 s\lambda_{19}^V + 2(k \cdot p_0)s^2\lambda_{19}^V - 8(k \cdot p_0)(k \cdot p_-)M_\rho^2 \lambda_{21}^V - 8(k \cdot p_-)^2 M_\rho^2 \lambda_{21}^V \\
& - 16(k \cdot p_0)^2 s\lambda_{21}^V - 8(k \cdot p_0)(k \cdot p_-)s\lambda_{21}^V + 8(k \cdot p_-)^2 s\lambda_{21}^V + 4k \cdot p_0 M_\rho^2 s\lambda_{21}^V \\
& - 8k \cdot p_- M_\rho^2 s\lambda_{21}^V - 6(k \cdot p_0)s^2\lambda_{21}^V + 6(k \cdot p_-)s^2\lambda_{21}^V - 2M_\rho^2 s^2\lambda_{21}^V + s^3\lambda_{21}^V \\
& + 8(k \cdot p_0)^2 M_\rho^2 \lambda_{22}^V + 8(k \cdot p_0)(k \cdot p_-)M_\rho^2 \lambda_{22}^V - 8(k \cdot p_0)^2 s\lambda_{22}^V \\
& - 8(k \cdot p_0)(k \cdot p_-)s\lambda_{22}^V + 6k \cdot p_0 M_\rho^2 s\lambda_{22}^V + 2k \cdot p_- M_\rho^2 s\lambda_{22}^V - 6(k \cdot p_0)s^2\lambda_{22}^V \\
& - 2(k \cdot p_-)s^2\lambda_{22}^V + M_\rho^2 s^2\lambda_{22}^V - s^3\lambda_{22}^V + 16(k \cdot p_0)^2 s\lambda_{21}^V \lambda_7^{VV} \\
& + 16(k \cdot p_0)(k \cdot p_-)s\lambda_{21}^V \lambda_7^{VV} + 12(k \cdot p_0)s^2\lambda_{21}^V \lambda_7^{VV} + 4(k \cdot p_-)s^2\lambda_{21}^V \lambda_7^{VV} \\
& + 2s^3\lambda_{21}^V \lambda_7^{VV})))
\end{aligned} \tag{I.4}$$

$$\begin{aligned}
v_2^R = & \frac{1}{F^2} \left( \frac{8(2k \cdot p_- + s)}{M_\omega^2 D_\omega [(k + p_0)^2]} \left( -4(k \cdot p_0 - M_\omega^2)(2k \cdot p_- + s)(\kappa_{12}^V)^2 + k \cdot p_0 \kappa_{16}^V \right. \right. \\
& \left. \left( (4k \cdot p_0 + 2k \cdot p_- - 2M_\omega^2 + s)\kappa_{16}^V - 2(P - q)^2 \kappa_{17}^V + \kappa_{12}^V((-8(k \cdot p_0)^2 + 4k \cdot p_0 M_\omega^2 \right. \right. \\
& \left. \left. + 2M_\omega^2(2k \cdot p_- + s))\kappa_{16}^V + 4(k \cdot p_0 - M_\omega^2)(P - q)^2 \kappa_{17}^V \right) + \frac{\sqrt{2}F_V}{M_\rho^2} \left( 2s\lambda_{12}^V - s\lambda_{13}^V \right. \right. \\
& \left. \left. + 4k \cdot p_- \lambda_{14}^V + s\lambda_{14}^V - 4k \cdot p_- \lambda_{15}^V - s\lambda_{15}^V - 4k \cdot p_- \lambda_{17}^V + 2k \cdot p_- \lambda_{18}^V - 4k \cdot p_- \lambda_{21}^V \right. \right. \\
& \left. \left. + 2k \cdot p_0 \lambda_{22}^V - 2k \cdot p_- \lambda_{22}^V \right) + \frac{2\sqrt{2}}{M_{a_1}^2 D_{a_1} [(k + p_-)^2]} \left( 4\sqrt{2}(k \cdot p_-)^2 (2k \cdot p_0 + 2M_{a_1}^2 + s) \right. \right. \\
& \left. \left( \lambda_{12}^A \right)^2 + \lambda_{12}^A (4\sqrt{2}k \cdot p_- (-4(k \cdot p_0)(k \cdot p_-) + 2k \cdot p_0 M_{a_1}^2 + 2k \cdot p_- M_{a_1}^2 - 2(k \cdot p_-)s \right. \\
& \left. + M_{a_1}^2 s)\lambda_{13}^A + 4\sqrt{2}(k \cdot p_-)^2 (P - q)^2 \lambda_{15}^A + (-2(k \cdot p_0)(k \cdot p_-) + 2(k \cdot p_-)^2 \right. \\
& \left. + 2k \cdot p_0 M_{a_1}^2 + 2k \cdot p_- M_{a_1}^2 - (k \cdot p_-)s + M_{a_1}^2 s)(-F_A + 4\sqrt{2}k \cdot p_- \lambda_{17}^A) \right. \\
& \left. - (k \cdot p_- - M_{a_1}^2)(-4\sqrt{2}k \cdot p_- (2k \cdot p_0 + s)(\lambda_{13}^A)^2 - 4k \cdot p_- \lambda_{17}^A (F_A - 2\sqrt{2}k \cdot p_- \lambda_{17}^A) \right. \\
& \left. + (P - q)^2 \lambda_{15}^A (-F_A + 4\sqrt{2}k \cdot p_- \lambda_{17}^A) + \lambda_{13}^A (4\sqrt{2}k \cdot p_- (P - q)^2 \lambda_{15}^A \right. \\
& \left. \left. + (2k \cdot p_0 - 2k \cdot p_- + s)(F_A - 4\sqrt{2}k \cdot p_- \lambda_{17}^A) \right) \right) \left. \right) \left. \right)
\end{aligned} \tag{I.5}$$

$$\begin{aligned}
v_2^{RR} = & \frac{1}{\sqrt{2}F^2} \left( \frac{8F_V(2k \cdot p_- + s)}{M_\rho^2 M_\omega^2 D_\omega [(k+p_0)^2]} \left( 2(P-q)^2 \kappa_{17}^V (-M_\omega^2 \kappa_3^{VV} + (2k \cdot p_0 - M_\omega^2) \kappa_4^{VV}) \right. \right. \\
& + \kappa_{16}^V (M_\omega^2 (2k \cdot p_- + s) \kappa_3^{VV} - (2k \cdot p_0 - M_\omega^2) (4k \cdot p_0 + 2k \cdot p_- + s) \kappa_4^{VV}) \\
& + 2(2k \cdot p_- + s) \kappa_{12}^V (M_\omega^2 \kappa_3^{VV} + D_\omega [(k+p_0)^2] \kappa_4^{VV}) \left. \right) \\
& + \frac{16(2k \cdot p_- + s)(-F_V + 2\sqrt{2}(P-q)^2 \lambda_{22}^V)}{M_\omega^2 D_\rho [(P-q)^2] D_\omega [(k+p_0)^2]} \left( k \cdot p_0 \kappa_{16}^V (((P-q)^2 + M_\omega^2) \kappa_3^{VV} \right. \\
& + (2k \cdot p_0 - M_\omega^2) \kappa_4^{VV}) + \kappa_{12}^V ((-4(k \cdot p_0)^2 + 2M_\omega^2(2k \cdot p_- + s) \\
& - 2k \cdot p_0(2k \cdot p_- - 3M_\omega^2 + s)) \kappa_3^{VV} + 2k \cdot p_0(-2k \cdot p_0 + M_\omega^2) \kappa_4^{VV}) \left. \right) \\
& - \frac{2k \cdot p_- F_V}{M_{a_1}^2 M_\rho^2 D_{a_1} [(k+p_-)^2]} \left( 2k \cdot p_- (-\sqrt{2}F_A + 4(2k \cdot p_0 + 2M_{a_1}^2 + s) \lambda_{12}^A \right. \\
& - 4(2k \cdot p_0 + s) \lambda_{13}^A + 8k \cdot p_0 \lambda_{15}^A + 8k \cdot p_- \lambda_{15}^A + 4s \lambda_{15}^A + 8k \cdot p_- \lambda_{17}^A) \lambda_2^{VA} \\
& - (-4(2k \cdot p_0(k \cdot p_- - M_{a_1}^2) - M_{a_1}^2 s + k \cdot p_- (-2M_{a_1}^2 + s)) \lambda_{12}^A + (k \cdot p_- - M_{a_1}^2) \\
& (\sqrt{2}F_A + 4(2k \cdot p_0 + s) \lambda_{13}^A - 4(P-q)^2 \lambda_{15}^A - 8k \cdot p_- \lambda_{17}^A)) (\lambda_4^{VA} + 2\lambda_5^{VA}) \left. \right) \\
& - \frac{(\sqrt{2}F_V - 4(P-q)^2 \lambda_{22}^V)}{M_{a_1}^2 D_{a_1} [(k+p_-)^2] D_\rho [(P-q)^2]} \left( 2(4\sqrt{2}(k \cdot p_-)^2 (2k \cdot p_0 + 2M_{a_1}^2 + s) \lambda_{12}^A \right. \\
& + (2k \cdot p_0(k \cdot p_- - M_{a_1}^2) - M_{a_1}^2 s + k \cdot p_- (-2M_{a_1}^2 + s)) (F_A - 4\sqrt{2}k \cdot p_- \lambda_{13}^A \\
& - 4\sqrt{2}k \cdot p_- \lambda_{17}^A)) \lambda_2^{VA} - (4\sqrt{2}(k \cdot p_-)^2 \lambda_{12}^A + (k \cdot p_- - M_{a_1}^2) (F_A - 4\sqrt{2}k \cdot p_- \lambda_{13}^A \\
& - 4\sqrt{2}k \cdot p_- \lambda_{17}^A)) (2(P-q)^2 \lambda_3^{VA} - (2k \cdot p_0 + s) (\lambda_4^{VA} + 2\lambda_5^{VA})) \left. \right) \\
& + \frac{F_V}{M_\rho^2 D_\rho [(P-q)^2]} \left( \sqrt{2}F_V (-4s \lambda_2^{VV} + (4k \cdot p_- + s) (\lambda_3^{VV} - \lambda_4^{VV}) - 2s \lambda_5^{VV}) \right. \\
& + 2(P-q)^2 \lambda_{22}^V ((P-q)^2 + 8s \lambda_2^{VV} - 2(4k \cdot p_- + s) (\lambda_3^{VV} - \lambda_4^{VV}) + 4s \lambda_5^{VV}) \left. \right) \\
& + \frac{2F_V(\sqrt{2}(4k \cdot p_- + s) G_V \lambda_7^{VV} + s \lambda_{21}^V (s - 2(4k \cdot p_- + s) \lambda_7^{VV}))}{M_\rho^2 D_\rho [s]} \left. \right)
\end{aligned} \tag{I.6}$$

$$\begin{aligned}
v_2^{RRR} = & -\frac{\sqrt{2}k \cdot p_- F_V (-\sqrt{2}F_V + 4(P-q)^2 \lambda_{22})}{F^2 M_{a_1}^2 M_\rho^2 D_{a_1} [(k+p_-)^2] D_\rho [(P-q)^2]} \left( 4k \cdot p_- (2k \cdot p_0 + 2M_{a_1}^2 + s) (\lambda_2^{VA})^2 \right. \\
& - (k \cdot p_- - M_{a_1}^2) (\lambda_4^{VA} + 2\lambda_5^{VA}) (2(P-q)^2 \lambda_3^{VA} - (2k \cdot p_0 + s) (\lambda_4^{VA} + 2\lambda_5^{VA})) \\
& - 2\lambda_2^{VA} (2k \cdot p_- (P-q)^2 \lambda_3^{VA} + (-4(k \cdot p_0) (k \cdot p_-) + 2k \cdot p_0 M_{a_1}^2 \\
& \left. + 2k \cdot p_- M_{a_1}^2 - 2(k \cdot p_-) s + M_{a_1}^2 s) (\lambda_4^{VA} + 2\lambda_5^{VA})) \right) \quad (I.7)
\end{aligned}$$

$$\begin{aligned}
v_{GI2}^{R+RR} = & \frac{\sqrt{2}F_V}{F^2 D_\rho [(P-q)^2] D_\rho [s]} \left( 2(M_\rho^2 - s) s \lambda_{12}^V + s(-M_\rho^2 + s) \lambda_{13}^V + 4k \cdot p_- M_\rho^2 \lambda_{14}^V \right. \\
& - 4(k \cdot p_-) s \lambda_{14}^V + M_\rho^2 s \lambda_{14}^V - s^2 \lambda_{14}^V - 4k \cdot p_- M_\rho^2 \lambda_{15}^V + 4(k \cdot p_-) s \lambda_{15}^V - M_\rho^2 s \lambda_{15}^V \\
& + s^2 \lambda_{15}^V - 2k \cdot p_0 M_\rho^2 \lambda_{16}^V - 2k \cdot p_- M_\rho^2 \lambda_{16}^V + 2(k \cdot p_0) s \lambda_{16}^V + 2(k \cdot p_-) s \lambda_{16}^V \\
& - M_\rho^2 s \lambda_{16}^V + s^2 \lambda_{16}^V + 4k \cdot p_0 M_\rho^2 \lambda_{17}^V - 4(k \cdot p_0) s \lambda_{17}^V + 2M_\rho^2 s \lambda_{17}^V - 2s^2 \lambda_{17}^V \\
& + 2k \cdot p_- M_\rho^2 \lambda_{18}^V - 2(k \cdot p_-) s \lambda_{18}^V + 2k \cdot p_0 M_\rho^2 \lambda_{19}^V + 2k \cdot p_- M_\rho^2 \lambda_{19}^V - 2(k \cdot p_0) s \lambda_{19}^V \\
& - 2(k \cdot p_-) s \lambda_{19}^V + M_\rho^2 s \lambda_{19}^V - s^2 \lambda_{19}^V - 4k \cdot p_- M_\rho^2 \lambda_{21}^V + 4(k \cdot p_-) s \lambda_{21}^V + s^2 \lambda_{21}^V \\
& + 6k \cdot p_0 M_\rho^2 \lambda_{22}^V + 2k \cdot p_- M_\rho^2 \lambda_{22}^V - 6(k \cdot p_0) s \lambda_{22}^V - 2(k \cdot p_-) s \lambda_{22}^V + 2M_\rho^2 s \lambda_{22}^V \\
& - 2s^2 \lambda_{22}^V - 8(k \cdot p_-) s \lambda_{21}^V \lambda_7^{VV} - 2s^2 \lambda_{21}^V \lambda_7^{VV} - 2G_V (\sqrt{2}(4k \cdot p_- + s) \\
& ((P-q)^2 - M_\rho^2) \lambda_7^V - (4k \cdot p_- + s) F_V \lambda_7^{VV} + \sqrt{2} \lambda_{22}^V (-16(k \cdot p_-)^2 + 8k \cdot p_- M_\rho^2 \\
& - 10(k \cdot p_-) s - s^2 - 2k \cdot p_0 (8k \cdot p_- + s) + 2(P-q)^2 (4k \cdot p_- + s) \lambda_7^{VV})) \\
& + 4(s(4k \cdot p_- + s) ((P-q)^2 - M_\rho^2) \lambda_7^V \lambda_{21}^V + \lambda_{22}^V (-2(M_\rho^2 - s) s (P-q)^2 \lambda_{12}^V \\
& + (M_\rho^2 - s) s (P-q)^2 \lambda_{13}^V - 8(k \cdot p_0) (k \cdot p_-) M_\rho^2 \lambda_{14}^V - 8(k \cdot p_-)^2 M_\rho^2 \lambda_{14}^V \\
& + 8(k \cdot p_0) (k \cdot p_-) s \lambda_{14}^V + 8(k \cdot p_-)^2 s \lambda_{14}^V - 2k \cdot p_0 M_\rho^2 s \lambda_{14}^V - 6k \cdot p_- M_\rho^2 s \lambda_{14}^V \\
& \left. + 2(k \cdot p_0) s^2 \lambda_{14}^V + 6(k \cdot p_-) s^2 \lambda_{14}^V - M_\rho^2 s^2 \lambda_{14}^V + s^3 \lambda_{14}^V + 8(k \cdot p_0) (k \cdot p_-) M_\rho^2 \lambda_{15}^V \right)
\end{aligned}$$

$$\begin{aligned}
& + 8(k \cdot p_-)^2 M_\rho^2 \lambda_{15}^V - 8(k \cdot p_0)(k \cdot p_-) s \lambda_{15}^V - 8(k \cdot p_-)^2 s \lambda_{15}^V + 2k \cdot p_0 M_\rho^2 s \lambda_{15}^V \\
& + 6k \cdot p_- M_\rho^2 s \lambda_{15}^V - 2(k \cdot p_0) s^2 \lambda_{15}^V - 6(k \cdot p_-) s^2 \lambda_{15}^V + M_\rho^2 s^2 \lambda_{15}^V - s^3 \lambda_{15}^V \\
& + 4(k \cdot p_0)^2 M_\rho^2 \lambda_{16}^V + 8(k \cdot p_0)(k \cdot p_-) M_\rho^2 \lambda_{16}^V + 4(k \cdot p_-)^2 M_\rho^2 \lambda_{16}^V - 4(k \cdot p_0)^2 s \lambda_{16}^V \\
& - 8(k \cdot p_0)(k \cdot p_-) s \lambda_{16}^V - 4(k \cdot p_-)^2 s \lambda_{16}^V + 4k \cdot p_0 M_\rho^2 s \lambda_{16}^V + 4k \cdot p_- M_\rho^2 s \lambda_{16}^V \\
& - 4(k \cdot p_0) s^2 \lambda_{16}^V - 4(k \cdot p_-) s^2 \lambda_{16}^V + M_\rho^2 s^2 \lambda_{16}^V - s^3 \lambda_{16}^V - 8(k \cdot p_0)^2 M_\rho^2 \lambda_{17}^V \\
& - 8(k \cdot p_0)(k \cdot p_-) M_\rho^2 \lambda_{17}^V + 8(k \cdot p_0)^2 s \lambda_{17}^V + 8(k \cdot p_0)(k \cdot p_-) s \lambda_{17}^V \\
& - 8k \cdot p_0 M_\rho^2 s \lambda_{17}^V - 4k \cdot p_- M_\rho^2 s \lambda_{17}^V + 8(k \cdot p_0) s^2 \lambda_{17}^V + 4(k \cdot p_-) s^2 \lambda_{17}^V \\
& - 2M_\rho^2 s^2 \lambda_{17}^V + 2s^3 \lambda_{17}^V - 4(k \cdot p_0)(k \cdot p_-) M_\rho^2 \lambda_{18}^V - 4(k \cdot p_-)^2 M_\rho^2 \lambda_{18}^V \\
& + 4(k \cdot p_0)(k \cdot p_-) s \lambda_{18}^V + 4(k \cdot p_-)^2 s \lambda_{18}^V - 2k \cdot p_- M_\rho^2 s \lambda_{18}^V + 2(k \cdot p_-) s^2 \lambda_{18}^V \\
& - 4(k \cdot p_0)^2 M_\rho^2 \lambda_{19}^V - 8(k \cdot p_0)(k \cdot p_-) M_\rho^2 \lambda_{19}^V - 4(k \cdot p_-)^2 M_\rho^2 \lambda_{19}^V + 4(k \cdot p_0)^2 s \lambda_{19}^V \quad (\text{I.8}) \\
& + 8(k \cdot p_0)(k \cdot p_-) s \lambda_{19}^V + 4(k \cdot p_-)^2 s \lambda_{19}^V - 4k \cdot p_0 M_\rho^2 s \lambda_{19}^V - 4k \cdot p_- M_\rho^2 s \lambda_{19}^V \\
& + 4(k \cdot p_0) s^2 \lambda_{19}^V + 4(k \cdot p_-) s^2 \lambda_{19}^V - M_\rho^2 s^2 \lambda_{19}^V + s^3 \lambda_{19}^V + 8(k \cdot p_0)(k \cdot p_-) M_\rho^2 \lambda_{21}^V \\
& + 8(k \cdot p_-)^2 M_\rho^2 \lambda_{21}^V - 24(k \cdot p_0)(k \cdot p_-) s \lambda_{21}^V - 24(k \cdot p_-)^2 s \lambda_{21}^V + 12k \cdot p_- M_\rho^2 s \lambda_{21}^V \\
& - 2(k \cdot p_0) s^2 \lambda_{21}^V - 14(k \cdot p_-) s^2 \lambda_{21}^V - s^3 \lambda_{21}^V - 8(k \cdot p_0)^2 M_\rho^2 \lambda_{22}^V \\
& - 8(k \cdot p_0)(k \cdot p_-) M_\rho^2 \lambda_{22}^V + 8(k \cdot p_0)^2 s \lambda_{22}^V + 8(k \cdot p_0)(k \cdot p_-) s \lambda_{22}^V \\
& - 6k \cdot p_0 M_\rho^2 s \lambda_{22}^V - 2k \cdot p_- M_\rho^2 s \lambda_{22}^V + 6(k \cdot p_0) s^2 \lambda_{22}^V + 2(k \cdot p_-) s^2 \lambda_{22}^V - M_\rho^2 s^2 \lambda_{22}^V \\
& + s^3 \lambda_{22}^V + 16(k \cdot p_0)(k \cdot p_-) s \lambda_{21}^V \lambda_7^{VV} + 16(k \cdot p_-)^2 s \lambda_{21}^V \lambda_7^{VV} + 4(k \cdot p_0) s^2 \lambda_{21}^V \lambda_7^{VV} \\
& + 12(k \cdot p_-) s^2 \lambda_{21}^V \lambda_7^{VV} + 2s^3 \lambda_{21}^V \lambda_7^{VV} \Big)
\end{aligned}$$

$$\begin{aligned}
v_3^R = & \frac{2}{F^2} \left( \frac{8}{M_\omega^2 D_\omega [(k+p_0)^2]} \left( -4(4(k \cdot p_0)^2 - M_\omega^2(2k \cdot p_- + s) + k \cdot p_0 \right. \right. \\
& (2k \cdot p_- - 2M_\omega^2 + s)(\kappa_{12}^V)^2 + k \cdot p_0 \kappa_{16}^V ((2k \cdot p_- + s)\kappa_{16}^V - 2(P-q)^2 \kappa_{17}^V) \\
& + 2\kappa_{12}^V ((4(k \cdot p_0)^2 - 2k \cdot p_0 M_\omega^2 + M_\omega^2(2k \cdot p_- + s))\kappa_{16}^V + 2(k \cdot p_0 - M_\omega^2) \\
& (P-q)^2 \kappa_{17}^V) \left. \right) + \frac{\sqrt{2}F_V(2\lambda_{13}^V + \lambda_{16}^V + \lambda_{18}^V + 2\lambda_{19}^V)}{M_\rho^2} \\
& + \frac{8}{M_{a_1}^2 D_{a_1} [(k+p_-)^2]} \left( (-2(k \cdot p_0)(k \cdot p_-) + 2k \cdot p_0 M_{a_1}^2 + 2k \cdot p_- M_{a_1}^2 - (k \cdot p_-) s \right. \\
& + M_{a_1}^2 s)(\lambda_{12}^A)^2 - 8k \cdot p_- (2k \cdot p_0 + s)(\lambda_{13}^A)^2 - 2\sqrt{2}F_A k \cdot p_0 \lambda_{15}^A - 2\sqrt{2}F_A k \cdot p_- \lambda_{15}^A \\
& - \sqrt{2}F_A s \lambda_{15}^A - 4\sqrt{2}F_A k \cdot p_- \lambda_{17}^A + 16(k \cdot p_0)(k \cdot p_-) \lambda_{15}^A \lambda_{17}^A + 16(k \cdot p_-)^2 \lambda_{15}^A \lambda_{17}^A \\
& + 8(k \cdot p_-) s \lambda_{15}^A \lambda_{17}^A + 16(k \cdot p_-)^2 (\lambda_{17}^A)^2 + \lambda_{13}^A (8k \cdot p_- (P-q)^2 \lambda_{15}^A + (2k \cdot p_0 \\
& - 2k \cdot p_- + s)(\sqrt{2}F_A - 8k \cdot p_- \lambda_{17}^A)) + \lambda_{12}^A (8(k \cdot p_0 (4k \cdot p_- - 2M_{a_1}^2) - M_{a_1}^2 s \\
& + 2k \cdot p_- (M_{a_1}^2 + s))\lambda_{13}^A - 8(k \cdot p_- - M_{a_1}^2)(P-q)^2 \lambda_{15}^A + (2k \cdot p_0 - 2k \cdot p_- + 4M_{a_1}^2 \\
& \left. \left. + s)(-\sqrt{2}F_A + 8k \cdot p_- \lambda_{17}^A) \right) \right) \Big)
\end{aligned} \tag{I.9}$$



$$\begin{aligned}
v_3^{RR} = & \frac{1}{\sqrt{2}F^2} \left( -\frac{16F_V}{M_\rho^2 M_\omega^2 D_\omega [(k+p_0)^2]} \left( 2\kappa_{12}^V (-M_\omega^2 (2k \cdot p_- + s) \kappa_3^{VV} + (2k \cdot p_0 - M_\omega^2) \right. \right. \\
& (4k \cdot p_0 + 2k \cdot p_- + s) \kappa_4^{VV}) - ((2k \cdot p_- + s) \kappa_{16}^V - 2(P-q)^2 \kappa_{17}^V) (M_\omega^2 \kappa_3^{VV} \\
& \left. \left. + D_\omega [(k+p_0)^2] \kappa_4^{VV} \right) + \frac{32(-F_V + 2\sqrt{2}(P-q)^2 \lambda_{22}^V)}{M_\omega^2 D_\rho [(P-q)^2] D_\omega [(k+p_0)^2]} \left( -2\kappa_{12}^V ((k \cdot p_0)^2 \right. \right. \\
& - M_\omega^2 (2k \cdot p_- + s) + k \cdot p_0 (2k \cdot p_- - 3M_\omega^2 + s) \kappa_3^{VV} + k \cdot p_0 (-2k \cdot p_0 + M_\omega^2) \kappa_4^{VV} \\
& \left. \left. + k \cdot p_0 \kappa_{16}^V (((P-q)^2 + M_\omega^2) \kappa_3^{VV} + D_\omega [(k+p_0)^2] \kappa_4^{VV}) \right) \right) \\
& + \frac{2F_V}{M_{a_1}^2 M_\rho^2 D_{a_1} [(k+p_-)^2]} \left( -2(-4(2k \cdot p_0 (k \cdot p_- - M_{a_1}^2) - M_{a_1}^2 s + k \cdot p_- \right. \\
& (-2M_{a_1}^2 + s)) \lambda_{12}^A + (k \cdot p_- - M_{a_1}^2) (\sqrt{2}F_A + 4(2k \cdot p_0 + s) \lambda_{13}^A - 4(P-q)^2 \lambda_{15}^A \\
& - 8k \cdot p_- \lambda_{17}^A) \lambda_2^{VA} + k \cdot p_- (-\sqrt{2}F_A + 4(2k \cdot p_0 + 2M_{a_1}^2 + s) \lambda_{12}^A - 4(2k \cdot p_0 + s) \lambda_{13}^A \\
& \left. \left. + 8k \cdot p_0 \lambda_{15}^A + 8k \cdot p_- \lambda_{15}^A + 4s \lambda_{15}^A + 8k \cdot p_- \lambda_{17}^A) (\lambda_4^{VA} + 2\lambda_5^{VA}) \right) \right) \\
& + \frac{(-\sqrt{2}F_V + 4(P-q)^2 \lambda_{22}^V)}{M_{a_1}^2 D_{a_1} [(k+p_-)^2] D_\rho [(P-q)^2]} \left( -2(4\sqrt{2}(2k \cdot p_0 (k \cdot p_- - M_{a_1}^2) - M_{a_1}^2 s \right. \\
& + k \cdot p_- (-2M_{a_1}^2 + s)) \lambda_{12}^A + (2k \cdot p_0 + 2M_{a_1}^2 + s) (F_A - 4\sqrt{2}k \cdot p_- \lambda_{13}^A \\
& - 4\sqrt{2}k \cdot p_- \lambda_{17}^A) \lambda_2^{VA} + (F_A + 4\sqrt{2}(k \cdot p_- - M_{a_1}^2) \lambda_{12}^A - 4\sqrt{2}k \cdot p_- \lambda_{13}^A \\
& \left. \left. - 4\sqrt{2}k \cdot p_- \lambda_{17}^A) (2(P-q)^2 \lambda_3^{VA} - (2k \cdot p_0 + s) (\lambda_4^{VA} + 2\lambda_5^{VA})) \right) \right) \\
& \left. + \frac{8F_V (\sqrt{2}F_V - 4(P-q)^2 \lambda_{22}^V) \lambda_5^{VV}}{M_\rho^2 D_\rho [(P-q)^2]} \right)
\end{aligned} \tag{I.10}$$

$$\begin{aligned}
v_3^{RRR} = & -\frac{\sqrt{2}F_V (-\sqrt{2}F_V + 4(P-q)^2 \lambda_{22}^V)}{F^2 M_{a_1}^2 M_\rho^2 D_{a_1} [(k+p_-)^2] D_\rho [(P-q)^2]} \left( -4(2k \cdot p_0 (k \cdot p_- - M_{a_1}^2) \right. \\
& - M_{a_1}^2 s + k \cdot p_- (-2M_{a_1}^2 + s)) (\lambda_2^{VA})^2 + k \cdot p_- (\lambda_4^{VA} + 2\lambda_5^{VA}) (2(P-q)^2 \lambda_3^{VA} \\
& - (2k \cdot p_0 + s) (\lambda_4^{VA} + 2\lambda_5^{VA})) + 2\lambda_2^{VA} (2(k \cdot p_- - M_{a_1}^2) (P-q)^2 \lambda_3^{VA} \\
& \left. \left. - (k \cdot p_0 (4k \cdot p_- - 2M_{a_1}^2) - M_{a_1}^2 s + 2k \cdot p_- (M_{a_1}^2 + s)) (\lambda_4^{VA} + 2\lambda_5^{VA})) \right) \right)
\end{aligned} \tag{I.11}$$

$$v_{GI3}^{R+RR} = \frac{2\sqrt{2}}{F^2 D_\rho [(P-q)^2]} (F_V - 2\sqrt{2}(P-q)^2 \lambda_{22}^V) (2\lambda_{13}^V + \lambda_{16}^V + \lambda_{18}^V + \lambda_{19}^V) \quad (\text{I.12})$$

$$\begin{aligned} v_4^R = & \frac{2}{F^2} \left( \frac{8}{M_\omega^2 D_\omega [(k+p_0)^2]} \left( 4(k \cdot p_0 - M_\omega^2)(2k \cdot p_- + s)(\kappa_{12}^V)^2 + k \cdot p_0 \kappa_{16}^V \right. \right. \\ & \left. \left. - (2k \cdot p_- + s)\kappa_{16}^V + 2(2k \cdot p_- + M_\omega^2 + s)\kappa_{17}^V - 2\kappa_{12}^V (M_\omega^2(2k \cdot p_- + s)\kappa_{16}^V \right. \right. \\ & \left. \left. + 2(-M_\omega^2(2k \cdot p_- + s) + k \cdot p_0(2k \cdot p_- - M_\omega^2 + s))\kappa_{17}^V \right) \right. \\ & - \frac{\sqrt{2}F_V(\lambda_{13}^V + \lambda_{14}^V - \lambda_{15}^V - \lambda_{21}^V)}{M_\rho^2} \\ & \left. - \frac{\sqrt{2}(2\lambda_{12}^A + \lambda_{15}^A)(-F_A + 4\sqrt{2}k \cdot p_- (\lambda_{12}^A + \lambda_{13}^A + \lambda_{17}^A))}{D_{a_1} [(k+p_-)^2]} \right) \quad (\text{I.13}) \end{aligned}$$

$$\begin{aligned} v_4^{RR} = & \frac{\sqrt{2}}{F^2} \left( - \frac{8F_V}{M_\rho^2 M_\omega^2 D_\omega [(k+p_0)^2]} \left( (2k \cdot p_- + s)\kappa_{16}^V (M_\omega^2 \kappa_3^{VV} + (-2k \cdot p_0 + M_\omega^2)\kappa_4^{VV}) \right. \right. \\ & \left. \left. - 2\kappa_{17}^V (M_\omega^2 (P-q)^2 \kappa_3^{VV} - (2k \cdot p_0 - M_\omega^2)(2k \cdot p_- + s)\kappa_4^{VV}) + 2(2k \cdot p_- + s)\kappa_{12}^V \right. \right. \\ & \left. \left. (M_\omega^2 \kappa_3^{VV} + D_\omega [(k+p_0)^2] \kappa_4^{VV}) \right) - \frac{16\kappa_3^{VV}(-F_V + 2\sqrt{2}(P-q)^2 \lambda_{22}^V)}{M_\omega^2 D_\rho [(P-q)^2] D_\omega [(k+p_0)^2]} \right. \\ & \left. \left( (2M_\omega^2(2k \cdot p_- + s) - 2k \cdot p_0(2k \cdot p_- - 2M_\omega^2 + s))\kappa_{12}^V + k \cdot p_0(2k \cdot p_- + 2M_\omega^2 + s)\kappa_{16}^V \right) \right. \\ & + \frac{(\sqrt{2}F_V - 4(P-q)^2 \lambda_{22}^V)(-F_A + 4\sqrt{2}k \cdot p_- (\lambda_{12}^A + \lambda_{13}^A + \lambda_{17}^A))(2\lambda_2^{VA} - \lambda_3^{VA})}{D_{a_1} [(k+p_-)^2] D_\rho [(P-q)^2]} \\ & + \frac{4k \cdot p_- F_V (2\lambda_{12}^A + \lambda_{15}^A)(2\lambda_2^{VA} - \lambda_4^{VA} - 2\lambda_5^{VA})}{M_\rho^2 D_{a_1} [(k+p_-)^2]} - \frac{2F_V(\sqrt{2}G_V - 2s\lambda_{21}^V)\lambda_7^{VV}}{M_\rho^2 D_\rho [s]} \\ & \left. - \frac{F_V(\sqrt{2}F_V(\lambda_3^{VV} - \lambda_4^{VV} + 2\lambda_5^{VV}) - 2(P-q)^2 \lambda_{22}^V(-1 + 2\lambda_3^{VV} - 2\lambda_4^{VV} + 4\lambda_5^{VV}))}{M_\rho^2 D_\rho [(P-q)^2]} \right) \quad (\text{I.14}) \end{aligned}$$

$$v_4^{RRR} = - \frac{2\sqrt{2}F_V k \cdot p_- (\sqrt{2}F_V - 4(P-q)^2 \lambda_{22}^V)(2\lambda_2^{VA} - \lambda_3^{VA})(2\lambda_2^{VA} - \lambda_4^{VA} - 2\lambda_5^{VA})}{F^2 M_\rho^2 D_{a_1} [(k+p_-)^2] D_\rho [(P-q)^2]} \quad (\text{I.15})$$

$$\begin{aligned}
v_{GI4}^{R+RR} = & \frac{2\sqrt{2}F_V}{F^2 D_\rho [(P-q)^2] D_\rho [s]} \left( (-M_\rho^2 + s) (\lambda_{13}^V + \lambda_{14}^V - \lambda_{15}^V + \lambda_{18}^V + \lambda_{19}^V) + 2M_\rho^2 \lambda_{21}^V - s \lambda_{21}^V \right. \\
& + 2s \lambda_{21}^V \lambda_7^{VV} + 4G_V (\sqrt{2}((P-q)^2 - M_\rho^2) \lambda_7^V - F_V \lambda_7^{VV} + \sqrt{2} \lambda_{22}^V (-4k \cdot p_0 - 4k \cdot p_- \\
& + 3M_\rho^2 - 2s + 2(P-q)^2 \lambda_7^{VV})) - 8(s((P-q)^2 - M_\rho^2) \lambda_7^V \lambda_{21}^V + \lambda_{22}^V (-M_\rho^2 - s) \\
& (P-q)^2 \lambda_{13}^V - (M_\rho^2 - s)(P-q)^2 \lambda_{14}^V + 2k \cdot p_0 M_\rho^2 \lambda_{15}^V + 2k \cdot p_- M_\rho^2 \lambda_{15}^V - 2(k \cdot p_0) s \lambda_{15}^V \\
& - 2(k \cdot p_-) s \lambda_{15}^V + M_\rho^2 s \lambda_{15}^V - s^2 \lambda_{15}^V - 2k \cdot p_0 M_\rho^2 \lambda_{18}^V - 2k \cdot p_- M_\rho^2 \lambda_{18}^V + 2(k \cdot p_0) s \lambda_{18}^V \\
& + 2(k \cdot p_-) s \lambda_{18}^V - M_\rho^2 s \lambda_{18}^V + s^2 \lambda_{18}^V - 2k \cdot p_0 M_\rho^2 \lambda_{19}^V - 2k \cdot p_- M_\rho^2 \lambda_{19}^V + 2(k \cdot p_0) s \lambda_{19}^V \\
& + 2(k \cdot p_-) s \lambda_{19}^V - M_\rho^2 s \lambda_{19}^V + s^2 \lambda_{19}^V + 4k \cdot p_0 M_\rho^2 \lambda_{21}^V + 4k \cdot p_- M_\rho^2 \lambda_{21}^V - 8(k \cdot p_0) s \lambda_{21}^V \\
& - 8(k \cdot p_-) s \lambda_{21}^V + 5M_\rho^2 s \lambda_{21}^V - 4s^2 \lambda_{21}^V + 4(k \cdot p_0) s \lambda_{21}^V \lambda_7^{VV} + 4(k \cdot p_-) s \lambda_{21}^V \lambda_7^{VV} \\
& \left. + 2s^2 \lambda_{21}^V \lambda_7^{VV} \right)
\end{aligned} \tag{I.16}$$

# Appendix J

## Axial Form Factors in radiative di-pion tau decays

We copy here the axial-vector form factors in  $\tau^- \rightarrow \pi^- \pi^0 \nu_\tau \gamma$  decays.

$$\begin{aligned}
a_1^R = & \frac{\sqrt{2}}{3F^2} \left( - \frac{2(P-q)^2 F_V (\kappa_1^V - \kappa_2^V + \kappa_3^V + \kappa_6^V + \kappa_7^V - \kappa_8^V - 2\kappa_{12}^V - \kappa_{16}^V + \kappa_{17}^V)}{M_\omega^2} \right. \\
& + \frac{4((P-q)^2 \kappa_{11}^V + s \kappa_{12}^V - (k \cdot p_0 + k \cdot p_-) \kappa_{16}^V) (-G_V + \sqrt{2} s \lambda_{21}^V)}{D_\rho[s]} \\
& + \frac{1}{M_\rho^2 D_\rho [(k+p_-)^2]} \left( F_V (2k \cdot p_- + s) (2(k \cdot p_- - M_\rho^2) \kappa_{12}^V - k \cdot p_- \kappa_{16}^V) \right. \\
& + G_V (-4(2(k \cdot p_-)^2 + (k \cdot p_-) s - M_\rho^2 s) \kappa_{12}^V + 2k \cdot p_- (2k \cdot p_- - 2M_\rho^2 + s) \kappa_{16}^V) \\
& + \sqrt{2} (-2\kappa_{12}^V ((k \cdot p_- - M_\rho^2) (2k \cdot p_0 + s) (2k \cdot p_- + s) \lambda_{16}^V - 2(k \cdot p_- - M_\rho^2) \\
& (2k \cdot p_0 + s) (2k \cdot p_- + s) \lambda_{17}^V + 8(k \cdot p_0) (k \cdot p_-)^2 \lambda_{18}^V + 8(k \cdot p_-)^3 \lambda_{18}^V \\
& + 4(k \cdot p_0) (k \cdot p_-) s \lambda_{18}^V + 8(k \cdot p_-)^2 s \lambda_{18}^V - 4k \cdot p_0 M_\rho^2 s \lambda_{18}^V - 4k \cdot p_- M_\rho^2 s \lambda_{18}^V \\
& + 2(k \cdot p_-) s^2 \lambda_{18}^V - 2M_\rho^2 s^2 \lambda_{18}^V + 8(k \cdot p_0) (k \cdot p_-)^2 \lambda_{19}^V + 8(k \cdot p_0) (k \cdot p_-) M_\rho^2 s \lambda_{19}^V \\
& + 8(k \cdot p_-)^2 M_\rho^2 \lambda_{19}^V + 4(k \cdot p_0) (k \cdot p_-) s \lambda_{19}^V + 4(k \cdot p_-)^2 s \lambda_{19}^V - 4k \cdot p_0 M_\rho^2 s \lambda_{19}^V \\
& + 2(k \cdot p_-) s^2 \lambda_{19}^V - 2M_\rho^2 s^2 \lambda_{19}^V - 8(k \cdot p_-)^3 \lambda_{21}^V - 4(k \cdot p_-)^2 s \lambda_{21}^V + 4k \cdot p_- M_\rho^2 s \lambda_{21}^V \\
& \left. + 8(k \cdot p_-)^3 \lambda_{22}^V - 8(k \cdot p_-)^2 M_\rho^2 \lambda_{22}^V + 4(k \cdot p_-)^2 s \lambda_{22}^V - 4k \cdot p_- M_\rho^2 s \lambda_{22}^V \right)
\end{aligned}$$

$$\begin{aligned}
& + k \cdot p_- \kappa_{16}^V ((2k \cdot p_0 + s)(2k \cdot p_- + s) \lambda_{16}^V + 2(-(2k \cdot p_0 + s)(2k \cdot p_- + s) \lambda_{17}^V \\
& + (P - q)^2(2k \cdot p_- - 2M_\rho^2 + s) \lambda_{18}^V + 4(k \cdot p_0)(k \cdot p_-) \lambda_{19}^V - 8k \cdot p_0 M_\rho^2 \lambda_{19}^V \\
& - 4k \cdot p_- M_\rho^2 \lambda_{19}^V + 2(k \cdot p_0) s \lambda_{19}^V + 2(k \cdot p_-) s \lambda_{19}^V - 2M_\rho^2 s \lambda_{19}^V + s^2 \lambda_{19}^V - 4(k \cdot p_-)^2 \\
& \lambda_{21}^V + 4k \cdot p_- M_\rho^2 \lambda_{21}^V - 2(k \cdot p_-) s \lambda_{21}^V + 4(k \cdot p_-)^2 \lambda_{22}^V + 2(k \cdot p_-) s \lambda_{22}^V)) \\
& + \frac{1}{M_\rho^2 D_\rho [(k + p_0)^2]} \left( F_V (4k \cdot p_0 + 2k \cdot p_- + s) (2(k \cdot p_0 - M_\rho^2) \kappa_{12}^V - k \cdot p_0 \kappa_{16}^V) \right. \\
& + G_V (-4(4(k \cdot p_0)^2 - M_\rho^2(2k \cdot p_- + s) + k \cdot p_0(2k \cdot p_- - 2M_\rho^2 + s)) \kappa_{12}^V + 2k \cdot p_0 \\
& (4k \cdot p_0 + 2k \cdot p_- - 2M_\rho^2 + s) \kappa_{16}^V) + \sqrt{2}(k \cdot p_0 \kappa_{16}^V ((2k \cdot p_- + s)(4k \cdot p_0 + 2k \cdot p_- + s) \\
& \lambda_{16}^V + 2(-(2k \cdot p_- + s)(4k \cdot p_0 + 2k \cdot p_- + s) \lambda_{17}^V + (8(k \cdot p_0)^2 + 12(k \cdot p_0)(k \cdot p_-) \\
& + 4(k \cdot p_-)^2 - 4k \cdot p_0 M_\rho^2 - 4k \cdot p_- M_\rho^2 + 6(k \cdot p_0) s + 4(k \cdot p_-) s - 2M_\rho^2 s + s^2) \lambda_{18}^V \\
& + 8(k \cdot p_0)(k \cdot p_-) \lambda_{19}^V + 4(k \cdot p_-)^2 \lambda_{19}^V - 4k \cdot p_- M_\rho^2 \lambda_{19}^V + 4(k \cdot p_0) s \lambda_{19}^V \\
& + 4(k \cdot p_-) s \lambda_{19}^V - 2M_\rho^2 s \lambda_{19}^V + s^2 \lambda_{19}^V - 8(k \cdot p_0)^2 \lambda_{21}^V - 4(k \cdot p_0)(k \cdot p_-) \lambda_{21}^V \\
& + 4k \cdot p_0 M_\rho^2 \lambda_{21}^V - 2(k \cdot p_0) s \lambda_{21}^V + 8(k \cdot p_0)^2 \lambda_{22}^V + 4(k \cdot p_0)(k \cdot p_-) \lambda_{22}^V + 2(k \cdot p_0) s \lambda_{22}^V) \\
& - 2\kappa_{12}^V ((k \cdot p_0 - M_\rho^2)(2k \cdot p_- + s)(4k \cdot p_0 + 2k \cdot p_- + s) \lambda_{16}^V + 2(-(k \cdot p_0 - M_\rho^2) \\
& (2k \cdot p_- + s)(4k \cdot p_0 + 2k \cdot p_- + s) \lambda_{17}^V + (P - q)^2(4(k \cdot p_0)^2 - M_\rho^2(2k \cdot p_- + s) \\
& + k \cdot p_0(2k \cdot p_- - 2M_\rho^2 + s)) \lambda_{18}^V + 8(k \cdot p_0)^2(k \cdot p_-) \lambda_{19}^V + 4(k \cdot p_0)(k \cdot p_-)^2 \lambda_{19}^V \\
& - 4(k \cdot p_0)(k \cdot p_-) M_\rho^2 \lambda_{19}^V - 4(k \cdot p_-)^2 M_\rho^2 \lambda_{19}^V + 4(k \cdot p_0)^2 s \lambda_{19}^V + 4(k \cdot p_0)(k \cdot p_-) s \lambda_{19}^V \\
& - 2k \cdot p_0 M_\rho^2 s \lambda_{19}^V - 4k \cdot p_- M_\rho^2 s \lambda_{19}^V + (k \cdot p_0) s^2 \lambda_{19}^V - M_\rho^2 s^2 \lambda_{19}^V - 8(k \cdot p_0)^3 \lambda_{21}^V \\
& - 4(k \cdot p_0)^2(k \cdot p_-) \lambda_{21}^V + 4(k \cdot p_0)^2 M_\rho^2 \lambda_{21}^V + 4(k \cdot p_0)(k \cdot p_-) M_\rho^2 \lambda_{21}^V - 2(k \cdot p_0)^2 s \lambda_{21}^V \\
& + 2k \cdot p_0 M_\rho^2 s \lambda_{21}^V + 8(k \cdot p_0)^3 \lambda_{22}^V + 4(k \cdot p_0)^2(k \cdot p_-) \lambda_{22}^V - 8(k \cdot p_0)^2 M_\rho^2 \lambda_{22}^V \\
& \left. - 4(k \cdot p_0)(k \cdot p_-) M_\rho^2 \lambda_{22}^V + 2(k \cdot p_0)^2 s \lambda_{22}^V - 2k \cdot p_0 M_\rho^2 s \lambda_{22}^V) \right) \\
& + \frac{2(P - q)^2(\kappa_5^A - \kappa_6^A + \kappa_7^A)(-F_A + 2\sqrt{2}(P - q)^2 \lambda_{17}^A)}{D_{a_1} [(P - q)^2]}
\end{aligned}$$

(J.1)

$$\begin{aligned}
a_1^{RR} = & \frac{1}{3\sqrt{2}F^2} \left( \frac{4sF_V\kappa_3^{VV}(-\sqrt{2}G_V + 2s\lambda_{21}^V)}{M_\omega^2 D_\rho[s]} \right. \\
& - \frac{1}{M_\rho^2 M_\omega^2 D_\rho [(k+p_-)^2]} \left( F_V(\sqrt{2}(2k \cdot p_- + s)F_V(M_\rho^2\kappa_3^{VV} + D_\rho [(k+p_-)^2] \kappa_4^{VV}) \right. \\
& + 2\sqrt{2}G_V(M_\rho^2(2k \cdot p_- - s)\kappa_3^{VV} - (2k \cdot p_- + s)D_\rho [(k+p_-)^2] \kappa_4^{VV}) \\
& + 2(2k \cdot p_- - M_\rho^2)(2k \cdot p_- + s)\kappa_4^{VV}((2k \cdot p_0 + s)\lambda_{16}^V - 2(2k \cdot p_0 + s)\lambda_{17}^V + 4k \cdot p_0\lambda_{18}^V \\
& + 4k \cdot p_- \lambda_{18}^V + 2s\lambda_{18}^V + 4k \cdot p_0\lambda_{19}^V + 2s\lambda_{19}^V - 4k \cdot p_- \lambda_{21}^V + 4k \cdot p_- \lambda_{22}^V) - 2M_\rho^2\kappa_3^{VV} \\
& ((2k \cdot p_0 + s)(2k \cdot p_- + s)\lambda_{16}^V - 2(2k \cdot p_0 + s)(2k \cdot p_- + s)\lambda_{17}^V - 2(2k \cdot p_- - s) \\
& (P - q)^2\lambda_{18}^V - 24(k \cdot p_0)(k \cdot p_-)\lambda_{19}^V - 16(k \cdot p_-)^2\lambda_{19}^V + 4(k \cdot p_0)s\lambda_{19}^V - 4(k \cdot p_-)s\lambda_{19}^V \\
& + 2s^2\lambda_{19}^V + 8(k \cdot p_-)^2\lambda_{21}^V - 4(k \cdot p_-)s\lambda_{21}^V + 8(k \cdot p_-)^2\lambda_{22}^V + 4(k \cdot p_-)s\lambda_{22}^V)) \left. \right) \\
& + \frac{1}{M_\rho^2 M_\omega^2 D_\rho [(k+p_0)^2]} \left( F_V(-\sqrt{2}F_V(4k \cdot p_0 + 2k \cdot p_- + s)(M_\rho^2\kappa_3^{VV} + D_\rho [(k+p_0)^2] \right. \\
& \kappa_4^{VV}) + 2\sqrt{2}G_V(M_\rho^2(2k \cdot p_- + s)\kappa_3^{VV} + (4k \cdot p_0 + 2k \cdot p_- + s)D_\rho [(k+p_0)^2] \kappa_4^{VV}) \\
& - 2(2k \cdot p_0 - M_\rho^2)(4k \cdot p_0 + 2k \cdot p_- + s)\kappa_4^{VV}((2k \cdot p_- + s)\lambda_{16}^V - 2(2k \cdot p_- + s)\lambda_{17}^V \\
& + 4k \cdot p_0\lambda_{18}^V + 4k \cdot p_- \lambda_{18}^V + 2s\lambda_{18}^V + 4k \cdot p_- \lambda_{19}^V + 2s\lambda_{19}^V - 4k \cdot p_0\lambda_{21}^V + 4k \cdot p_0\lambda_{22}^V) \\
& + 2M_\rho^2\kappa_3^{VV}((2k \cdot p_- + s)(4k \cdot p_0 + 2k \cdot p_- + s)\lambda_{16}^V + 2(-(2k \cdot p_- + s) \\
& (4k \cdot p_0 + 2k \cdot p_- + s)\lambda_{17}^V + (2k \cdot p_- + s)(P - q)^2\lambda_{18}^V + 4(k \cdot p_-)^2\lambda_{19}^V \\
& + 4(k \cdot p_-)s\lambda_{19}^V + s^2\lambda_{19}^V - 4(k \cdot p_0)(k \cdot p_-)\lambda_{21}^V - 2(k \cdot p_0)s\lambda_{21}^V + 8(k \cdot p_0)^2\lambda_{22}^V \\
& + 4(k \cdot p_0)(k \cdot p_-)\lambda_{22}^V + 2(k \cdot p_0)s\lambda_{22}^V)) \left. \right) \\
& + \frac{2(P - q)^2 F_V(\kappa_2^{VA} - \kappa_3^{VA} - \kappa_4^{VA})(-\sqrt{2}F_A + 4(P - q)^2\lambda_{17}^A)}{M_\omega^2 D_{a_1} [(P - q)^2]} \\
& - \frac{4(P - q)^2 \kappa_5^{VA}(-\sqrt{2}G_V + 2s\lambda_{21}^V)(-F_A + 2\sqrt{2}(P - q)^2\lambda_{17}^A)}{D_{a_1} [(P - q)^2] D_\rho[s]} \\
& - \frac{2(F_A - 2\sqrt{2}(P - q)^2\lambda_{17}^A)}{M_\rho^2 D_{a_1} [(P - q)^2] D_\rho [(k+p_-)^2]} \left( k \cdot p_- \kappa_{16}^V(-2(-(2M_\rho^2 - s)(2k \cdot p_- + s) \right. \\
& + 2k \cdot p_0(2k \cdot p_- - 4M_\rho^2 + s))\lambda_2^{VA} - 2M_\rho^2(4k \cdot p_0 + 2k \cdot p_- + s)\lambda_3^{VA} \\
& + (2k \cdot p_- + s)((2k \cdot p_0 + 4k \cdot p_- - 2M_\rho^2 + s)\lambda_4^{VA} + 2(2k \cdot p_0 + s)\lambda_5^{VA}) \\
& \left. + 2\kappa_{12}^V(2((k \cdot p_-)s^2 - M_\rho^2 s^2 + 2(k \cdot p_-)^2(2M_\rho^2 + s) + 2k \cdot p_0(2(k \cdot p_-)^2) \right.
\end{aligned}$$

$$\begin{aligned}
& - M_\rho^2 s + k \cdot p_- (2M_\rho^2 + s)) \lambda_2^{VA} - 2k \cdot p_- M_\rho^2 (4k \cdot p_0 + 2k \cdot p_- + s) \lambda_3^{VA} \\
& - (2k \cdot p_- + s) ((4(k \cdot p_-)^2 - 2k \cdot p_- M_\rho^2 + 2k \cdot p_0 (k \cdot p_- - M_\rho^2) + (k \cdot p_-) s \\
& - M_\rho^2 s) \lambda_4^{VA} + 2(k \cdot p_- - M_\rho^2) (2k \cdot p_0 + s) \lambda_5^{VA})) \\
& + \frac{2(F_A - 2\sqrt{2}(P - q)^2 \lambda_{17}^A)}{M_\rho^2 D_{a_1} [(P - q)^2] D_\rho [(k + p_0)^2]} \left( - k \cdot p_0 \kappa_{16}^V (-2(2k \cdot p_- + s) (4k \cdot p_0 + 2k \cdot p_- \right. \\
& - 2M_\rho^2 + s) \lambda_2^{VA} - 2M_\rho^2 (2k \cdot p_- + s) \lambda_3^{VA} + (4k \cdot p_0 + 2k \cdot p_- + s) ((4k \cdot p_0 + 2k \cdot p_- \quad (J.2) \\
& - 2M_\rho^2 + s) \lambda_4^{VA} + 2(2k \cdot p_- + s) \lambda_5^{VA})) + 2\kappa_{12}^V (-2(2k \cdot p_- + s) (4(k \cdot p_0)^2 \\
& - M_\rho^2 (2k \cdot p_- + s) + k \cdot p_0 (2k \cdot p_- - 2M_\rho^2 + s)) \lambda_2^{VA} + 2k \cdot p_0 M_\rho^2 (2k \cdot p_- + s) \lambda_3^{VA} \\
& + (4k \cdot p_0 + 2k \cdot p_- + s) ((4(k \cdot p_0)^2 - M_\rho^2 (2k \cdot p_- + s) + k \cdot p_0 (2k \cdot p_- - 2M_\rho^2 + s)) \\
& \left. \lambda_4^{VA} + 2(k \cdot p_0 - M_\rho^2) (2k \cdot p_- + s) \lambda_5^{VA})) \right)
\end{aligned}$$

$$\begin{aligned}
a_1^{RRR} = & - \frac{F_V (\sqrt{2} F_A - 4(P - q)^2 \lambda_{17}^A)}{3\sqrt{2} F^2 M_\rho^2 M_\omega^2 D_{a_1} [(P - q)^2] D_\rho [(k + p_0)^2] D_\rho [(k + p_-)^2]} \left( - M_\rho^2 (2k \cdot p_- + s) \right. \\
& D_\rho [(k + p_-)^2] \kappa_3^{VV} (2(2k \cdot p_- + s) \lambda_2^{VA} + 4k \cdot p_0 \lambda_3^{VA} - (4k \cdot p_0 + 2k \cdot p_- + s) \\
& (\lambda_4^{VA} + 2\lambda_5^{VA})) + D_\rho [(k + p_0)^2] (2D_\rho [(k + p_-)^2] \kappa_4^{VV} (-2(3k \cdot p_0 + k \cdot p_- + s) \\
& (2k \cdot p_- + s) \lambda_2^{VA} + (8(k \cdot p_0)^2 + 6(k \cdot p_-)^2 + 5(k \cdot p_-) s + s^2 + 5k \cdot p_0 \\
& (2k \cdot p_- + s)) \lambda_4^{VA} + 2(3k \cdot p_0 + k \cdot p_- + s) (2k \cdot p_- + s) \lambda_5^{VA}) + M_\rho^2 \kappa_3^{VV} \\
& (2(12(k \cdot p_0)(k \cdot p_-) + 8(k \cdot p_-)^2 - 2(k \cdot p_0) s + 2(k \cdot p_-) s - s^2) \lambda_2^{VA} \\
& \left. - 4k \cdot p_- (4k \cdot p_0 + 2k \cdot p_- + s) \lambda_3^{VA} + (2k \cdot p_0 + s) (2k \cdot p_- + s) (\lambda_4^{VA} + 2\lambda_5^{VA})) \right) \quad (J.3)
\end{aligned}$$

$$\begin{aligned}
a_2^R = & \frac{4\sqrt{2}}{3F^2} \left( -\frac{2(P-q)^2 F_V(\kappa_1^V - \kappa_2^V + \kappa_3^V)}{M_\omega^2 D_\pi [(P-q)^2]} \right. \\
& + \frac{F_V(3\kappa_1^V - 3\kappa_2^V + 3\kappa_3^V + \kappa_6^V + \kappa_7^V - \kappa_8^V - 2\kappa_{12}^V - \kappa_{16}^V + \kappa_{17}^V)}{M_\omega^2} \\
& + \frac{2\sqrt{2}k \cdot p_0(2\kappa_{12}^V + \kappa_{16}^V)(\lambda_{18}^V + 2\lambda_{19}^V)}{D_\rho [(k+p_0)^2]} - \frac{2k \cdot p_0(2\kappa_{12}^V + \kappa_{16}^V)(-G_V + 2\sqrt{2}k \cdot p_0\lambda_{21}^V)}{D_\pi [(P-q)^2] D_\rho [(k+p_0)^2]} \\
& - \frac{2k \cdot p_-(2\kappa_{12}^V + \kappa_{16}^V)(-G_V + 2\sqrt{2}k \cdot p_-\lambda_{21}^V)}{D_\pi [(P-q)^2] D_\rho [(k+p_-)^2]} + \frac{2(\kappa_{11}^V + \kappa_{12}^V)(G_V - \sqrt{2}s\lambda_{21}^V)}{D_\rho [s]} \\
& - \frac{2(k \cdot p_0 + k \cdot p_-)(2\kappa_{12}^V + \kappa_{16}^V)(G_V - \sqrt{2}s\lambda_{21}^V)}{D_\pi [(P-q)^2] D_\rho [s]} + \frac{1}{M_\rho^2 D_\rho [(k+p_-)^2]} \\
& \left( G_V(4(k \cdot p_- - M_\rho^2)\kappa_{12}^V - 2k \cdot p_-\kappa_{16}^V) + F_V(-2(k \cdot p_- - M_\rho^2)\kappa_{12}^V + k \cdot p_-\kappa_{16}^V) \right. \\
& + \sqrt{2}(-k \cdot p_-\kappa_{16}^V((2k \cdot p_0 + s)\lambda_{16}^V - 2(2k \cdot p_0 + s)\lambda_{17}^V + 4k \cdot p_0\lambda_{18}^V + 4k \cdot p_-\lambda_{18}^V \\
& - 2M_\rho^2\lambda_{18}^V + 2s\lambda_{18}^V + 4k \cdot p_0\lambda_{19}^V + 2s\lambda_{19}^V - 4k \cdot p_-\lambda_{21}^V + 4k \cdot p_-\lambda_{22}^V) + 2\kappa_{12}^V \\
& ((k \cdot p_- - M_\rho^2)(2k \cdot p_0 + s)\lambda_{16}^V - 2(k \cdot p_- - M_\rho^2)(2k \cdot p_0 + s)\lambda_{17}^V + 2(2(k \cdot p_-)^2 \\
& + 2k \cdot p_0(k \cdot p_- - M_\rho^2) - M_\rho^2s + k \cdot p_-(-M_\rho^2 + s))\lambda_{18}^V + 2(k \cdot p_- - M_\rho^2) \\
& \left. \left. ((2k \cdot p_0 + s)\lambda_{19}^V + 2k \cdot p_-(-\lambda_{21}^V + \lambda_{22}^V)) \right) \right) + \frac{(\kappa_5^A - \kappa_6^A + \kappa_7^A)(F_A - 2\sqrt{2}(P-q)^2\lambda_{17}^A)}{D_{a_1} [(P-q)^2]} \Bigg)
\end{aligned} \tag{J.4}$$



$$\begin{aligned}
a_2^{RR} = & \frac{2\sqrt{2}}{3F^2} \left( \frac{8k \cdot p_0 F_V \kappa_3^{VV} (\lambda_{18}^V + 2\lambda_{19}^V)}{M_\omega^2 D_\rho [(k + p_0)^2]} + \frac{4k \cdot p_0 F_V \kappa_3^{VV} (\sqrt{2}G_V - 4k \cdot p_0 \lambda_{21}^V)}{M_\omega^2 D_\pi [(P - q)^2] D_\rho [(k + p_0)^2]} \right. \\
& + \frac{4k \cdot p_- F_V \kappa_3^{VV} (\sqrt{2}G_V - 4k \cdot p_- \lambda_{21}^V)}{M_\omega^2 D_\pi [(P - q)^2] D_\rho [(k + p_-)^2]} + \frac{2F_V \kappa_3^{VV} (\sqrt{2}G_V - 2s\lambda_{21}^V)}{M_\omega^2 D_\rho [s]} \\
& + \frac{F_V}{M_\rho^2 M_\omega^2 D_\rho [(k + p_-)^2]} \left( \sqrt{2}F_V (M_\rho^2 \kappa_3^{VV} + D_\rho [(k + p_-)^2] \kappa_4^{VV}) \right. \\
& - 2\sqrt{2}G_V (M_\rho^2 \kappa_3^{VV} + D_\rho [(k + p_-)^2] \kappa_4^{VV}) - 2M_\rho^2 \kappa_3^{VV} ((2k \cdot p_0 + s)\lambda_{16}^V \\
& - 2(2k \cdot p_0 + s)\lambda_{17}^V + 4k \cdot p_0 \lambda_{18}^V + 2s\lambda_{18}^V + 4k \cdot p_0 \lambda_{19}^V + 2s\lambda_{19}^V - 4k \cdot p_- \lambda_{21}^V \\
& + 4k \cdot p_- \lambda_{22}^V) + 2(2k \cdot p_- - M_\rho^2) \kappa_4^{VV} ((2k \cdot p_0 + s)\lambda_{16}^V - 2(2k \cdot p_0 + s)\lambda_{17}^V \\
& + 4k \cdot p_0 \lambda_{18}^V + 4k \cdot p_- \lambda_{18}^V + 2s\lambda_{18}^V + 4k \cdot p_0 \lambda_{19}^V + 2s\lambda_{19}^V - 4k \cdot p_- \lambda_{21}^V \\
& \left. + 4k \cdot p_- \lambda_{22}^V) \right) + \frac{F_V (\kappa_2^{VA} - \kappa_3^{VA} - \kappa_4^{VA}) (\sqrt{2}F_A - 4(P - q)^2 \lambda_{17}^A)}{M_\omega^2 D_{a_1} [(P - q)^2]} \\
& + \frac{2\kappa_5^{VA} (\sqrt{2}G_V - 2s\lambda_{21}^V) (F_A - 2\sqrt{2}(P - q)^2 \lambda_{17}^A)}{D_{a_1} [(P - q)^2] D_\rho [s]} \\
& + \frac{4k \cdot p_0 (2\kappa_{12}^V + \kappa_{16}^V) (F_A - 2\sqrt{2}(P - q)^2 \lambda_{17}^A) (2\lambda_2^{VA} - \lambda_3^{VA})}{D_{a_1} [(P - q)^2] D_\rho [(k + p_0)^2]} \\
& + \frac{2(F_A - 2\sqrt{2}(P - q)^2 \lambda_{17}^A)}{M_\rho^2 D_{a_1} [(P - q)^2] D_\rho [(k + p_-)^2]} \left( k \cdot p_- \kappa_{16}^V (-2(2k \cdot p_0 + s)\lambda_2^{VA} \right. \\
& + (2k \cdot p_0 + 4k \cdot p_- - 2M_\rho^2 + s)\lambda_4^{VA} + 2(2k \cdot p_0 + s)\lambda_5^{VA}) + 2\kappa_{12}^V \\
& (2(k \cdot p_- - M_\rho^2)(2k \cdot p_0 + s)\lambda_2^{VA} + (-2(k \cdot p_0)(k \cdot p_-) - 4(k \cdot p_-)^2 \\
& + 2k \cdot p_0 M_\rho^2 + 2k \cdot p_- M_\rho^2 - (k \cdot p_-)s + M_\rho^2 s)\lambda_4^{VA} - 2(k \cdot p_- - M_\rho^2) \\
& \left. (2k \cdot p_0 + s)\lambda_5^{VA} \right) \Big)
\end{aligned} \tag{J.5}$$

$$\begin{aligned}
a_2^{RRR} = & - \frac{2\sqrt{2}F_V (\sqrt{2}F_A - 4(P - q)^2 \lambda_{17}^A)}{3F^2 M_\rho^2 M_\omega^2 D_{a_1} [(P - q)^2] D_\rho [(k + p_0)^2] D_\rho [(k + p_-)^2]} \left( 4k \cdot p_0 M_\rho^2 \right. \\
& D_\rho [(k + p_-)^2] \kappa_3^{VV} (-2\lambda_2^{VA} + \lambda_3^{VA}) + D_\rho [(k + p_0)^2] (M_\rho^2 (2k \cdot p_0 + s)\kappa_3^{VV} \\
& (2\lambda_2^{VA} - \lambda_4^{VA} - 2\lambda_5^{VA}) + D_\rho [(k + p_-)^2] \kappa_4^{VV} (2(2k \cdot p_0 + s)\lambda_2^{VA} \\
& \left. - (2k \cdot p_0 + 4k \cdot p_- + s)\lambda_4^{VA} - 2(2k \cdot p_0 + s)\lambda_5^{VA}) \right)
\end{aligned} \tag{J.6}$$

$$\begin{aligned}
a_3^R = & \frac{\sqrt{2}}{3F^2} \left( - \frac{4F_V(k \cdot p_0 - k \cdot p_-)(\kappa_1^V - \kappa_2^V + \kappa_3^V + \kappa_6^V + \kappa_7^V - \kappa_8^V - \kappa_{17}^V)}{M_\omega^2} \right. \\
& - \frac{4(k \cdot p_0 - k \cdot p_-)(2\kappa_{11}^V - \kappa_{16}^V)(G_V - \sqrt{2}s\lambda_{21}^V)}{D_\rho[s]} \\
& + \frac{1}{M_\rho^2 D_\rho [(k + p_0)^2]} \left( - 2G_V(2(4(k \cdot p_0)^2 + M_\rho^2(2k \cdot p_- + s) - k \cdot p_0 \right. \\
& (2k \cdot p_- + 2M_\rho^2 + s))\kappa_{12}^V + k \cdot p_0(-4k \cdot p_0 + 2k \cdot p_- + 2M_\rho^2 + s)\kappa_{16}^V) \\
& + F_V(2(4(k \cdot p_0)^2 - k \cdot p_0(2k \cdot p_- + s) + M_\rho^2(2k \cdot p_- + s))\kappa_{12}^V + k \cdot p_0 \\
& (-4k \cdot p_0 + 2k \cdot p_- + 4M_\rho^2 + s)\kappa_{16}^V) - \sqrt{2}(k \cdot p_0\kappa_{16}^V(-4k \cdot p_0 - 2k \cdot p_- \\
& - 4M_\rho^2 - s)(2k \cdot p_- + s)\lambda_{16}^V + 2((4k \cdot p_0 - 2k \cdot p_- - 4M_\rho^2 - s)(2k \cdot p_- + s)\lambda_{17}^V \\
& + (-8(k \cdot p_0)^2 + 4(k \cdot p_-)^2 - 2k \cdot p_0(2k \cdot p_- - 2M_\rho^2 + s) + 4k \cdot p_-(M_\rho^2 + s) \\
& + s(2M_\rho^2 + s))\lambda_{18}^V - 8(k \cdot p_0)(k \cdot p_-)\lambda_{19}^V + 4(k \cdot p_-)^2\lambda_{19}^V + 4k \cdot p_-M_\rho^2\lambda_{19}^V \\
& - 4(k \cdot p_0)s\lambda_{19}^V + 4(k \cdot p_-)s\lambda_{19}^V + 2M_\rho^2s\lambda_{19}^V + s^2\lambda_{19}^V + 8(k \cdot p_0)^2\lambda_{21}^V \\
& - 4(k \cdot p_0)(k \cdot p_-)\lambda_{21}^V - 4k \cdot p_0M_\rho^2\lambda_{21}^V - 2(k \cdot p_0)s\lambda_{21}^V - 8(k \cdot p_0)^2\lambda_{22}^V \\
& + 4(k \cdot p_0)(k \cdot p_-)\lambda_{22}^V + 8k \cdot p_0M_\rho^2\lambda_{22}^V + 2(k \cdot p_0)s\lambda_{22}^V) + 2\kappa_{12}^V((2k \cdot p_- + s) \\
& (4(k \cdot p_0)^2 - k \cdot p_0(2k \cdot p_- + s) + M_\rho^2(2k \cdot p_- + s))\lambda_{16}^V + 2(-(2k \cdot p_- + s) \\
& (4(k \cdot p_0)^2 - k \cdot p_0(2k \cdot p_- + s) + M_\rho^2(2k \cdot p_- + s))\lambda_{17}^V + (8(k \cdot p_0)^3 - k \cdot p_0 \\
& (2k \cdot p_- + s)^2 + M_\rho^2(2k \cdot p_- + s)^2 + 2(k \cdot p_0)^2(2k \cdot p_- - 2M_\rho^2 + s))\lambda_{18}^V \\
& + 8(k \cdot p_0)^2(k \cdot p_-)\lambda_{19}^V - 4(k \cdot p_0)(k \cdot p_-)^2\lambda_{19}^V - 4(k \cdot p_0)(k \cdot p_-)M_\rho^2\lambda_{19}^V \\
& + 4(k \cdot p_-)^2M_\rho^2\lambda_{19}^V + 4(k \cdot p_0)^2s\lambda_{19}^V - 4(k \cdot p_0)(k \cdot p_-)s\lambda_{19}^V - 2k \cdot p_0M_\rho^2s\lambda_{19}^V \\
& + 4k \cdot p_-M_\rho^2s\lambda_{19}^V - (k \cdot p_0)s^2\lambda_{19}^V + M_\rho^2s^2\lambda_{19}^V - 8(k \cdot p_0)^3\lambda_{21}^V + 4(k \cdot p_0)^2(k \cdot p_-)\lambda_{21}^V \\
& + 4(k \cdot p_0)^2M_\rho^2\lambda_{21}^V - 4(k \cdot p_0)(k \cdot p_-)M_\rho^2\lambda_{21}^V + 2(k \cdot p_0)^2s\lambda_{21}^V - 2k \cdot p_0M_\rho^2s\lambda_{21}^V \\
& + 8(k \cdot p_0)^3\lambda_{22}^V - 4(k \cdot p_0)^2(k \cdot p_-)\lambda_{22}^V + 4(k \cdot p_0)(k \cdot p_-)M_\rho^2\lambda_{22}^V - 2(k \cdot p_0)^2s\lambda_{22}^V \\
& \left. \left. + 2k \cdot p_0M_\rho^2s\lambda_{22}^V) \right) \right) + \frac{1}{M_\rho^2 D_\rho [(k + p_-)^2]} \left( 2G_V(2(2(k \cdot p_-)^2 - (k \cdot p_-)s + M_\rho^2s)\kappa_{12}^V \right. \\
& \left. + k \cdot p_-(-2k \cdot p_- + 2M_\rho^2 + s)\kappa_{16}^V) - F_V(2(2(k \cdot p_-)^2 + 2k \cdot p_-M_\rho^2 - (k \cdot p_-)s \right.
\end{aligned}$$

$$\begin{aligned}
& + M_\rho^2 s) \kappa_{12}^V + k \cdot p_- (-2k \cdot p_- + 4M_\rho^2 + s) \kappa_{16}^V + \sqrt{2}(k \cdot p_- \kappa_{16}^V (-2k \cdot p_- - 4M_\rho^2 - s) \\
& (2k \cdot p_0 + s) \lambda_{16}^V + 2((2k \cdot p_- - 4M_\rho^2 - s)(2k \cdot p_0 + s) \lambda_{17}^V - (2k \cdot p_- - 2M_\rho^2 - s) \\
& (P - q)^2 \lambda_{18}^V - 4(k \cdot p_0)(k \cdot p_-) \lambda_{19}^V + 4k \cdot p_- M_\rho^2 \lambda_{19}^V + 2(k \cdot p_0) s \lambda_{19}^V - 2(k \cdot p_-) s \lambda_{19}^V \\
& + 2M_\rho^2 s \lambda_{19}^V + s^2 \lambda_{19}^V + 4(k \cdot p_-)^2 \lambda_{21}^V - 4k \cdot p_- M_\rho^2 \lambda_{21}^V - 2(k \cdot p_-) s \lambda_{21}^V - 4(k \cdot p_-)^2 \lambda_{22}^V \\
& + 8k \cdot p_- M_\rho^2 \lambda_{22}^V + 2(k \cdot p_-) s \lambda_{22}^V)) + 2\kappa_{12}^V ((2k \cdot p_0 + s)(2(k \cdot p_-)^2 + 2k \cdot p_- M_\rho^2 \\
& - (k \cdot p_-) s + M_\rho^2 s) \lambda_{16}^V + 2((2k \cdot p_0 + s)(-2(k \cdot p_-)^2 - M_\rho^2 s + k \cdot p_- (-2M_\rho^2 + s)) \lambda_{17}^V \\
& + (P - q)^2 (2(k \cdot p_-)^2 - (k \cdot p_-) s + M_\rho^2 s) \lambda_{18}^V + 4(k \cdot p_0)(k \cdot p_-)^2 \lambda_{19}^V - 4(k \cdot p_0) \\
& (k \cdot p_-) M_\rho^2 \lambda_{19}^V + 4(k \cdot p_-)^2 M_\rho^2 \lambda_{19}^V - 2(k \cdot p_0)(k \cdot p_-) s \lambda_{19}^V + 2(k \cdot p_-)^2 s \lambda_{19}^V \\
& + 2k \cdot p_0 M_\rho^2 s \lambda_{19}^V - (k \cdot p_-) s^2 \lambda_{19}^V + M_\rho^2 s^2 \lambda_{19}^V - 4(k \cdot p_-)^3 \lambda_{21}^V + 2(k \cdot p_-)^2 s \lambda_{21}^V \\
& - 2k \cdot p_- M_\rho^2 s \lambda_{21}^V + 4(k \cdot p_-)^3 \lambda_{22}^V + 4(k \cdot p_-)^2 M_\rho^2 \lambda_{22}^V - 2(k \cdot p_-)^2 s \lambda_{22}^V \\
& + 2k \cdot p_- M_\rho^2 s \lambda_{22}^V)) + \frac{4(-k \cdot p_0 + k \cdot p_-)(\kappa_5^A - \kappa_6^A + \kappa_7^A)(F_A - 2\sqrt{2}(P - q)^2 \lambda_{17}^A)}{D_{a_1} [(P - q)^2]} \Big)
\end{aligned} \tag{J.7}$$

$$\begin{aligned}
a_3^{RR} = & \frac{1}{3\sqrt{2}F^2} \left( \frac{F_V}{M_\rho^2 M_\omega^2 D_\rho [(k+p_0)^2]} \left( \sqrt{2}F_V (M_\rho^2 (4k \cdot p_0 + 2k \cdot p_- + s) \kappa_3^{VV} \right. \right. \\
& + (-4k \cdot p_0 + 2k \cdot p_- + s) D_\rho [(k+p_0)^2] \kappa_4^{VV}) - 2(\sqrt{2}G_V (M_\rho^2 (2k \cdot p_- + s) \kappa_3^{VV} \\
& + (-4k \cdot p_0 + 2k \cdot p_- + s) D_\rho [(k+p_0)^2] \kappa_4^{VV}) + (2k \cdot p_0 - M_\rho^2) (4k \cdot p_0 \\
& - 2k \cdot p_- - s) \kappa_4^{VV} ((2k \cdot p_- + s) \lambda_{16}^V - 2(2k \cdot p_- + s) \lambda_{17}^V + 4k \cdot p_0 \lambda_{18}^V \\
& + 4k \cdot p_- \lambda_{18}^V + 2s \lambda_{18}^V + 4k \cdot p_- \lambda_{19}^V + 2s \lambda_{19}^V - 4k \cdot p_0 \lambda_{21}^V + 4k \cdot p_0 \lambda_{22}^V) \\
& + M_\rho^2 \kappa_3^{VV} ((2k \cdot p_- + s) (4k \cdot p_0 + 2k \cdot p_- + s) \lambda_{16}^V + 2(-(2k \cdot p_- + s) \\
& (4k \cdot p_0 + 2k \cdot p_- + s) \lambda_{17}^V + (2k \cdot p_- + s) (P-q)^2 \lambda_{18}^V + 4(k \cdot p_-)^2 \lambda_{19}^V \\
& + 4(k \cdot p_-) s \lambda_{19}^V + s^2 \lambda_{19}^V - 4(k \cdot p_0) (k \cdot p_-) \lambda_{21}^V - 2(k \cdot p_0) s \lambda_{21}^V + 8(k \cdot p_0)^2 \lambda_{22}^V \\
& + 4(k \cdot p_0) (k \cdot p_-) \lambda_{22}^V + 2(k \cdot p_0) s \lambda_{22}^V)) \left. \right) + \frac{F_V}{M_\rho^2 M_\omega^2 D_\rho [(k+p_-)^2]} \\
& \left( -\sqrt{2}F_V (M_\rho^2 (6k \cdot p_- + s) \kappa_3^{VV} + (-2k \cdot p_- + s) D_\rho [(k+p_-)^2] \kappa_4^{VV}) \right. \\
& + 2(\sqrt{2}G_V (M_\rho^2 (2k \cdot p_- + s) \kappa_3^{VV} + (-2k \cdot p_- + s) D_\rho [(k+p_-)^2] \kappa_4^{VV}) \\
& + (2k \cdot p_- - M_\rho^2) (2k \cdot p_- - s) \kappa_4^{VV} ((2k \cdot p_0 + s) \lambda_{16}^V - 2(2k \cdot p_0 + s) \lambda_{17}^V \\
& + 4k \cdot p_0 \lambda_{18}^V + 4k \cdot p_- \lambda_{18}^V + 2s \lambda_{18}^V + 4k \cdot p_0 \lambda_{19}^V + 2s \lambda_{19}^V - 4k \cdot p_- \lambda_{21}^V \\
& + 4k \cdot p_- \lambda_{22}^V) + M_\rho^2 \kappa_3^{VV} ((2k \cdot p_0 + s) (6k \cdot p_- + s) \lambda_{16}^V + 2(-(2k \cdot p_0 + s) \\
& (6k \cdot p_- + s) \lambda_{17}^V + (2k \cdot p_- + s) (P-q)^2 \lambda_{18}^V - 4(k \cdot p_0) (k \cdot p_-) \lambda_{19}^V \\
& + 8(k \cdot p_-)^2 \lambda_{19}^V + 2(k \cdot p_0) s \lambda_{19}^V + 2(k \cdot p_-) s \lambda_{19}^V + s^2 \lambda_{19}^V - 4(k \cdot p_-)^2 \lambda_{21}^V \\
& - 2(k \cdot p_-) s \lambda_{21}^V + 12(k \cdot p_-)^2 \lambda_{22}^V + 2(k \cdot p_-) s \lambda_{22}^V)) \left. \right) + \frac{4F_V}{M_\omega^2 D_{a_1} [(P-q)^2]} \\
& \left( (-k \cdot p_0 + k \cdot p_-) (\kappa_2^{VA} - \kappa_3^{VA} - \kappa_4^{VA}) (\sqrt{2}F_A - 4(P-q)^2 \lambda_{17}^A) \right) \\
& + \frac{8(-k \cdot p_0 + k \cdot p_-) \kappa_5^{VA} (\sqrt{2}G_V - 2s \lambda_{21}^V) (F_A - 2\sqrt{2}(P-q)^2 \lambda_{17}^A)}{D_{a_1} [(P-q)^2] D_\rho [s]} \\
& + \frac{2(F_A - 2\sqrt{2}(P-q)^2 \lambda_{17}^A)}{M_\rho^2 D_{a_1} [(P-q)^2] D_\rho [(k+p_-)^2]} \left( k \cdot p_- \kappa_{16}^V ((-8(k \cdot p_0) (k \cdot p_-) + 8k \cdot p_- M_\rho^2 \right. \\
& + 4(k \cdot p_0) s - 4(k \cdot p_-) s + 4M_\rho^2 s + 2s^2) \lambda_2^{VA} + 2M_\rho^2 (4k \cdot p_0 - 2k \cdot p_- + s) \lambda_3^{VA}
\end{aligned}$$

$$\begin{aligned}
& + 4(k \cdot p_0)(k \cdot p_-) \lambda_4^{VA} + 8(k \cdot p_-)^2 \lambda_4^{VA} - 8k \cdot p_0 M_\rho^2 \lambda_4^{VA} - 4k \cdot p_- M_\rho^2 \lambda_4^{VA} \\
& - 2(k \cdot p_0) s \lambda_4^{VA} - 2(k \cdot p_-) s \lambda_4^{VA} - 2M_\rho^2 s \lambda_4^{VA} - s^2 \lambda_4^{VA} + 8(k \cdot p_0)(k \cdot p_-) \lambda_5^{VA} \\
& - 16k \cdot p_0 M_\rho^2 \lambda_5^{VA} - 4(k \cdot p_0) s \lambda_5^{VA} + 4(k \cdot p_-) s \lambda_5^{VA} - 8M_\rho^2 s \lambda_5^{VA} - 2s^2 \lambda_5^{VA} \\
& + 2\kappa_{12}^V (2(2k \cdot p_0)(k \cdot p_- - M_\rho^2)(2k \cdot p_- - s) - (k \cdot p_-) s^2 + M_\rho^2 s^2 \\
& + 2(k \cdot p_-)^2 (2M_\rho^2 + s)) \lambda_2^{VA} + 2k \cdot p_- M_\rho^2 (4k \cdot p_0 - 2k \cdot p_- + s) \lambda_3^{VA} \\
& - 4(k \cdot p_0)(k \cdot p_-)^2 \lambda_4^{VA} - 8(k \cdot p_-)^3 \lambda_4^{VA} - 4(k \cdot p_0)(k \cdot p_-) M_\rho^2 \lambda_4^{VA} \\
& + 4(k \cdot p_-)^2 M_\rho^2 \lambda_4^{VA} + 2(k \cdot p_0)(k \cdot p_-) s \lambda_4^{VA} + 2(k \cdot p_-)^2 s \lambda_4^{VA} \\
& - 2k \cdot p_0 M_\rho^2 s \lambda_4^{VA} - 4k \cdot p_- M_\rho^2 s \lambda_4^{VA} + (k \cdot p_-) s^2 \lambda_4^{VA} - M_\rho^2 s^2 \lambda_4^{VA} \\
& - 8(k \cdot p_0)(k \cdot p_-)^2 \lambda_5^{VA} - 8(k \cdot p_0)(k \cdot p_-) M_\rho^2 \lambda_5^{VA} + 4(k \cdot p_0)(k \cdot p_-) s \lambda_5^{VA} \\
& - 4(k \cdot p_-)^2 s \lambda_5^{VA} - 4k \cdot p_0 M_\rho^2 s \lambda_5^{VA} - 4k \cdot p_- M_\rho^2 s \lambda_5^{VA} + 2(k \cdot p_-) s^2 \lambda_5^{VA} \\
& - 2M_\rho^2 s^2 \lambda_5^{VA} \Big) + \frac{2(F_A - 2\sqrt{2}(P - q)^2 \lambda_{17}^A)}{M_\rho^2 D_{a_1} [(P - q)^2] D_\rho [(k + p_0)^2]} \left( k \cdot p_0 \kappa_{16}^V (2(4k \cdot p_0 - 2k \cdot p_- \right. \\
& - 2M_\rho^2 - s)(2k \cdot p_- + s) \lambda_2^{VA} - 2M_\rho^2 (2k \cdot p_- + s) \lambda_3^{VA} - 16(k \cdot p_0)^2 \lambda_4^{VA} \\
& + 4(k \cdot p_-)^2 \lambda_4^{VA} + 8k \cdot p_0 M_\rho^2 \lambda_4^{VA} + 4k \cdot p_- M_\rho^2 \lambda_4^{VA} + 4(k \cdot p_-) s \lambda_4^{VA} \\
& + 2M_\rho^2 s \lambda_4^{VA} + s^2 \lambda_4^{VA} - 16(k \cdot p_0)(k \cdot p_-) \lambda_5^{VA} + 8(k \cdot p_-)^2 \lambda_5^{VA} \\
& + 16k \cdot p_- M_\rho^2 \lambda_5^{VA} - 8(k \cdot p_0) s \lambda_5^{VA} + 8(k \cdot p_-) s \lambda_5^{VA} + 8M_\rho^2 s \lambda_5^{VA} + 2s^2 \lambda_5^{VA} \\
& + 2\kappa_{12}^V (-2(2k \cdot p_- + s)(4(k \cdot p_0)^2 + M_\rho^2 (2k \cdot p_- + s) - k \cdot p_0 \\
& (2k \cdot p_- + 2M_\rho^2 + s)) \lambda_2^{VA} - 2k \cdot p_0 M_\rho^2 (2k \cdot p_- + s) \lambda_3^{VA} + 16(k \cdot p_0)^3 \lambda_4^{VA} \\
& - 4(k \cdot p_0)(k \cdot p_-)^2 \lambda_4^{VA} - 8(k \cdot p_0)^2 M_\rho^2 \lambda_4^{VA} + 4(k \cdot p_0)(k \cdot p_-) M_\rho^2 \lambda_4^{VA} \\
& + 4(k \cdot p_-)^2 M_\rho^2 \lambda_4^{VA} - 4(k \cdot p_0)(k \cdot p_-) s \lambda_4^{VA} + 2k \cdot p_0 M_\rho^2 s \lambda_4^{VA} \\
& + 4k \cdot p_- M_\rho^2 s \lambda_4^{VA} - (k \cdot p_0) s^2 \lambda_4^{VA} + M_\rho^2 s^2 \lambda_4^{VA} + 16(k \cdot p_0)^2 (k \cdot p_-) \lambda_5^{VA} \\
& - 8(k \cdot p_0)(k \cdot p_-)^2 \lambda_5^{VA} + 8(k \cdot p_-)^2 M_\rho^2 \lambda_5^{VA} + 8(k \cdot p_0)^2 s \lambda_5^{VA} \\
& \left. - 8(k \cdot p_0)(k \cdot p_-) s \lambda_5^{VA} + 8k \cdot p_- M_\rho^2 s \lambda_5^{VA} - 2(k \cdot p_0) s^2 \lambda_5^{VA} + 2M_\rho^2 s^2 \lambda_5^{VA} \right) \Big) \Big) \tag{J.8}
\end{aligned}$$

$$\begin{aligned}
a_3^{RRR} = & \frac{F_V(\sqrt{2}F_A - 4(P - q)^2\lambda_{17}^A)}{3\sqrt{2}F^2M_\rho^2M_\omega^2D_{a_1}[(P - q)^2]D_\rho[(k + p_0)^2]D_\rho[(k + p_-)^2]} \left( -M_\rho^2(2k \cdot p_- + s) \right. \\
& D_\rho[(k + p_-)^2] \kappa_3^{VV}(2(2k \cdot p_- + s)\lambda_2^{VA} + 4k \cdot p_0\lambda_3^{VA} - (4k \cdot p_0 + 2k \cdot p_- + s) \\
& (\lambda_4^{VA} + 2\lambda_5^{VA})) - D_\rho[(k + p_0)^2](2(k \cdot p_0 - k \cdot p_-)D_\rho[(k + p_-)^2] \kappa_4^{VV} \\
& (-2(2k \cdot p_- + 3s)\lambda_2^{VA} + (8k \cdot p_0 + 6k \cdot p_- + s)\lambda_4^{VA} + 2(2k \cdot p_- + 3s)\lambda_5^{VA}) \\
& + M_\rho^2\kappa_3^{VV}(2(4(k \cdot p_0)(k \cdot p_-) - 8(k \cdot p_-)^2 - 2(k \cdot p_0)s - 2(k \cdot p_-)s - s^2)\lambda_2^{VA} \\
& \left. - 4k \cdot p_-(4k \cdot p_0 - 2k \cdot p_- + s)\lambda_3^{VA} + (2k \cdot p_0 + s)(6k \cdot p_- + s)(\lambda_4^{VA} + 2\lambda_5^{VA})) \right)
\end{aligned} \tag{J.9}$$

$$\begin{aligned}
a_4^R = & \frac{4\sqrt{2}}{3F^2M_\rho^2} \left( \frac{1}{D_\rho [(k+p_0)^2]} \left( G_V(4(k \cdot p_0 - M_\rho^2)\kappa_{12}^V - 2k \cdot p_0\kappa_{16}^V) \right. \right. \\
& + F_V(-2(k \cdot p_0 - M_\rho^2)\kappa_{12}^V + k \cdot p_0\kappa_{16}^V) + \sqrt{2}(-k \cdot p_0\kappa_{16}^V((2k \cdot p_- + s)\lambda_{16}^V \\
& - 2(2k \cdot p_- + s)\lambda_{17}^V + 4k \cdot p_0\lambda_{18}^V + 4k \cdot p_-\lambda_{18}^V + 2s\lambda_{18}^V + 4k \cdot p_-\lambda_{19}^V + 4M_\rho^2\lambda_{19}^V \\
& + 2s\lambda_{19}^V - 4k \cdot p_0\lambda_{21}^V + 4k \cdot p_0\lambda_{22}^V) + 2\kappa_{12}^V((k \cdot p_0 - M_\rho^2)(2k \cdot p_- + s)\lambda_{16}^V \\
& - 2(k \cdot p_0 - M_\rho^2)(2k \cdot p_- + s)\lambda_{17}^V + 4(k \cdot p_0)^2\lambda_{18}^V + 4(k \cdot p_0)(k \cdot p_-)\lambda_{18}^V \\
& - 4k \cdot p_0M_\rho^2\lambda_{18}^V - 4k \cdot p_-\lambda_{18}^V + 2(k \cdot p_0)s\lambda_{18}^V - 2M_\rho^2s\lambda_{18}^V + 4(k \cdot p_0)(k \cdot p_-)\lambda_{19}^V \\
& - 4k \cdot p_0M_\rho^2\lambda_{19}^V - 4k \cdot p_-\lambda_{19}^V + 2(k \cdot p_0)s\lambda_{19}^V - 2M_\rho^2s\lambda_{19}^V - 4(k \cdot p_0)^2\lambda_{21}^V \\
& + 4k \cdot p_0M_\rho^2\lambda_{21}^V + 4(k \cdot p_0)^2\lambda_{22}^V - 4k \cdot p_0M_\rho^2\lambda_{22}^V)) \left. + \frac{1}{D_\rho [(k+p_-)^2]} \right. \\
& \left( F_V(2(k \cdot p_- - M_\rho^2)\kappa_{12}^V - k \cdot p_-\kappa_{16}^V) + G_V(-4(k \cdot p_- - M_\rho^2)\kappa_{12}^V + 2k \cdot p_-\kappa_{16}^V) \right. \\
& + \sqrt{2}(k \cdot p_-\kappa_{16}^V((2k \cdot p_0 + s)\lambda_{16}^V - 2(2k \cdot p_0 + s)\lambda_{17}^V + 4k \cdot p_0\lambda_{18}^V + 4k \cdot p_-\lambda_{18}^V \\
& + 2s\lambda_{18}^V + 4k \cdot p_0\lambda_{19}^V + 4M_\rho^2\lambda_{19}^V + 2s\lambda_{19}^V - 4k \cdot p_-\lambda_{21}^V + 4k \cdot p_-\lambda_{22}^V) \\
& + \kappa_{12}^V(-2(k \cdot p_- - M_\rho^2)(2k \cdot p_0 + s)\lambda_{16}^V + 4(k \cdot p_- - M_\rho^2)(2k \cdot p_0 + s)\lambda_{17}^V \\
& - 4(k \cdot p_- - M_\rho^2)(P - q)^2\lambda_{18}^V - 8(k \cdot p_0)(k \cdot p_-)\lambda_{19}^V + 8k \cdot p_0M_\rho^2\lambda_{19}^V + 8k \cdot p_-\lambda_{19}^V \\
& - 4(k \cdot p_-)s\lambda_{19}^V + 4M_\rho^2s\lambda_{19}^V + 8(k \cdot p_-)^2\lambda_{21}^V - 8k \cdot p_-\lambda_{21}^V - 8(k \cdot p_-)^2\lambda_{22}^V \\
& \left. \left. + 8k \cdot p_-\lambda_{22}^V) \right) \right)
\end{aligned} \tag{J.10}$$

$$\begin{aligned}
a_4^{RR} = & \frac{2\sqrt{2}}{3F^2M_\rho^2} \left( \frac{F_V}{M_\omega^2 D_\rho [(k+p_0)^2]} \left( \sqrt{2}F_V(M_\rho^2\kappa_3^{VV} + D_\rho [(k+p_0)^2] \kappa_4^{VV}) \right. \right. \\
& - 2\sqrt{2}G_V(M_\rho^2\kappa_3^{VV} + D_\rho [(k+p_0)^2] \kappa_4^{VV}) + 2(2k \cdot p_0 - M_\rho^2)\kappa_4^{VV} \\
& ((2k \cdot p_- + s)\lambda_{16}^V - 2(2k \cdot p_- + s)\lambda_{17}^V + 4k \cdot p_0\lambda_{18}^V + 4k \cdot p_-\lambda_{18}^V + 2s\lambda_{18}^V \\
& + 4k \cdot p_-\lambda_{19}^V + 2s\lambda_{19}^V - 4k \cdot p_0\lambda_{21}^V + 4k \cdot p_0\lambda_{22}^V) - 2M_\rho^2\kappa_3^{VV}((2k \cdot p_- + s)\lambda_{16}^V \\
& - 2(2k \cdot p_- + s)\lambda_{17}^V + 4k \cdot p_0\lambda_{18}^V + 4k \cdot p_-\lambda_{18}^V + 2s\lambda_{18}^V + 8k \cdot p_0\lambda_{19}^V + 4k \cdot p_-\lambda_{19}^V \\
& \left. \left. + 2s\lambda_{19}^V - 4k \cdot p_0\lambda_{21}^V + 4k \cdot p_0\lambda_{22}^V) \right) + \frac{F_V}{M_\omega^2 D_\rho [(k+p_-)^2]} \left( -\sqrt{2}F_V(M_\rho^2\kappa_3^{VV} \right. \right. \\
& + D_\rho [(k+p_-)^2] \kappa_4^{VV}) + 2\sqrt{2}G_V(M_\rho^2\kappa_3^{VV} + D_\rho [(k+p_-)^2] \kappa_4^{VV}) \\
& - 2(2k \cdot p_- - M_\rho^2)\kappa_4^{VV}((2k \cdot p_0 + s)\lambda_{16}^V - 2(2k \cdot p_0 + s)\lambda_{17}^V + 4k \cdot p_0\lambda_{18}^V \\
& + 4k \cdot p_-\lambda_{18}^V + 2s\lambda_{18}^V + 4k \cdot p_0\lambda_{19}^V + 2s\lambda_{19}^V - 4k \cdot p_-\lambda_{21}^V + 4k \cdot p_-\lambda_{22}^V) \\
& \left. \left. + 2M_\rho^2\kappa_3^{VV}((2k \cdot p_0 + s)\lambda_{16}^V - 2(2k \cdot p_0 + s)\lambda_{17}^V + 4k \cdot p_0\lambda_{18}^V + 4k \cdot p_-\lambda_{18}^V \right) \right)
\end{aligned}$$



$$\begin{aligned}
& + 2s\lambda_{18}^V + 4k \cdot p_0\lambda_{19}^V + 8k \cdot p_-\lambda_{19}^V + 2s\lambda_{19}^V - 4k \cdot p_-\lambda_{21}^V + 4k \cdot p_-\lambda_{22}^V) \\
& - \frac{2(F_A - 2\sqrt{2}(P - q)^2\lambda_{17}^A)}{D_{a_1} [(P - q)^2] D_\rho [(k + p_-)^2]} \left( k \cdot p_-\kappa_{16}^V (-2(2k \cdot p_0 + 2M_\rho^2 + s)\lambda_2^{VA} \right. \\
& + 2M_\rho^2\lambda_3^{VA} + 2k \cdot p_0\lambda_4^{VA} + 4k \cdot p_-\lambda_4^{VA} - 2M_\rho^2\lambda_4^{VA} + s\lambda_4^{VA} + 4k \cdot p_0\lambda_5^{VA} + 2s\lambda_5^{VA}) \\
& + 2\kappa_{12}^V (2(2(k \cdot p_0)(k \cdot p_-) - 2k \cdot p_0M_\rho^2 - 2k \cdot p_-\lambda_2^{VA} + (k \cdot p_-)s - M_\rho^2s)\lambda_2^{VA} \\
& + 2k \cdot p_-\lambda_3^{VA} - 2(k \cdot p_0)(k \cdot p_-)\lambda_4^{VA} - 4(k \cdot p_-)^2\lambda_4^{VA} + 2k \cdot p_0M_\rho^2\lambda_4^{VA} \\
& + 2k \cdot p_-\lambda_4^{VA} - (k \cdot p_-)s\lambda_4^{VA} + M_\rho^2s\lambda_4^{VA} - 4(k \cdot p_0)(k \cdot p_-)\lambda_5^{VA} \\
& + 4k \cdot p_0M_\rho^2\lambda_5^{VA} - 2(k \cdot p_-)s\lambda_5^{VA} + 2M_\rho^2s\lambda_5^{VA}) \left. + \frac{2(F_A - 2\sqrt{2}(P - q)^2\lambda_{17}^A)}{D_{a_1} [(P - q)^2] D_\rho [(k + p_0)^2]} \right) \\
& \left( k \cdot p_0\kappa_{16}^V (-2(2k \cdot p_- + 2M_\rho^2 + s)\lambda_2^{VA} + 2M_\rho^2\lambda_3^{VA} + 4k \cdot p_0\lambda_4^{VA} + 2k \cdot p_-\lambda_4^{VA} \right. \\
& - 2M_\rho^2\lambda_4^{VA} + s\lambda_4^{VA} + 4k \cdot p_-\lambda_5^{VA} + 2s\lambda_5^{VA}) + \kappa_{12}^V (4(-M_\rho^2(2k \cdot p_- + s) \\
& + k \cdot p_0(2k \cdot p_- - 2M_\rho^2 + s))\lambda_2^{VA} + 4k \cdot p_0M_\rho^2\lambda_3^{VA} - 8(k \cdot p_0)^2\lambda_4^{VA} \\
& - 4(k \cdot p_0)(k \cdot p_-)\lambda_4^{VA} + 4k \cdot p_0M_\rho^2\lambda_4^{VA} + 4k \cdot p_-\lambda_4^{VA} - 2(k \cdot p_0)s\lambda_4^{VA} \\
& + 2M_\rho^2s\lambda_4^{VA} - 8(k \cdot p_0)(k \cdot p_-)\lambda_5^{VA} + 8k \cdot p_-\lambda_5^{VA} - 4(k \cdot p_0)s\lambda_5^{VA} \\
& \left. + 4M_\rho^2s\lambda_5^{VA}) \right) \Big)
\end{aligned} \tag{J.11}$$

$$\begin{aligned}
\alpha_4^{RRR} = & - \frac{4\sqrt{2}F_V(k \cdot p_0 - k \cdot p_-)(\sqrt{2}F_A - 4(P - q)^2\lambda_{17}^A)}{3F^2M_\rho^2M_\omega^2D_{a_1} [(P - q)^2] D_\rho [(k + p_0)^2] D_\rho [(k + p_-)^2]} \\
& \left( - D_\rho [(k + p_0)^2] D_\rho [(k + p_-)^2] \kappa_4^{VV} (2\lambda_2^{VA} + \lambda_4^{VA} - 2\lambda_5^{VA}) \right. \\
& \left. + M_\rho^2\kappa_3^{VV} (2(M_\rho^2 + (P - q)^2)\lambda_2^{VA} - 2M_\rho^2\lambda_3^{VA} + D_\rho [(P - q)^2] (\lambda_4^{VA} + 2\lambda_5^{VA})) \right)
\end{aligned} \tag{J.12}$$

# Appendix K

## Axial structure of the nucleon

The axial current expressed in terms of the light quarks fields

$$A_\mu^a \equiv \bar{q} \gamma_\mu \gamma^5 T^a q, \quad (\text{K.1})$$

where for the two and three flavor case  $T^a = \frac{\tau^a}{2}$  and  $T^a = \frac{\lambda^a}{2}$ , being  $\tau^a$  the Pauli matrices and  $\lambda^a$  the Gell-Mann matrices for  $SU(2)$  and  $SU(3)$ , respectively.

The matrix-element of the  $SU(2)$  isovector axial quark current between nucleon states is given by [800, 819, 820]

$$\langle N(p') | A_\mu^a | N(p) \rangle = \bar{u}(p') \left[ \gamma_\mu G_A(t) + \frac{(p' - p)_\mu}{2m} G_P(t) \right] \gamma^5 \frac{\tau^a}{2} u(p), \quad (\text{K.2})$$

with  $t \equiv (p' - p)^2$  the invariant momentum transfer squared and  $m = (m_p + m_n)/2$ . However, we will work in the isospin limit  $m_p = m_n$  ( $m_u = m_d$ ).

The eq. (K.2) follows from Lorentz invariance and  $C$ ,  $P$ ,  $T$  and isospin conservation and the absence of second class currents [436], which is consistent with the experimental observations [821].  $G_A(t)$  is the nucleon axial form factor and  $G_P(t)$  is the induced pseudoscalar form factor.

If we take the divergence of eq. (K.2), we obtain

$$\partial^\mu \langle N(p') | A_\mu^a | N(p) \rangle = i \bar{u}(p') \left[ 2m G_A(t) + \frac{t}{2m} G_P(t) \right] \gamma^5 \frac{\tau^a}{2} u(p) \quad (\text{K.3})$$

Furthermore, we can use the Ward identity, eq. (K.4), and the PCAC hypothesis

$$\partial^\mu \bar{q} \gamma_\mu \gamma^5 q = 2\bar{q} \mathbb{M} i \gamma^5 q + n_q \frac{g_s^2}{16\pi^2} G_i^{\mu\nu} \tilde{G}_{\mu\nu}^i - \left( \frac{N_c}{3} \right) \frac{e^2}{16\pi^2} F_{\mu\nu} \tilde{F}^{\mu\nu}, \quad (\text{K.4})$$

where  $\mathbb{M} = \text{diag}(m_u, \dots, m_q)$ ,  $n_q = 2, 3$  is the number of flavors being considered and  $N_c$  is the number of colours. Thus, in the chiral limit we have

$$\partial^\mu \langle N(p') | A_\mu^a | N(p) \rangle = 0. \quad (\text{K.5})$$

Therefore, from eqs. (K.3) and (K.5) we get

$$G_P(t) = -\frac{4m^2}{t} G_A(t) \quad \text{or} \quad G_P(t) = \frac{4m^2}{M_P^2 - t} G_A(t) + \mathcal{O}(M_P), \quad (\text{K.6})$$

which is the well-known pion pole term. This term arises from a direct coupling between a pseudoscalar and an axial current.

## K.1 The coupling of $P$ to the nucleon

According to Ref. [822], the coupling of a pseudoscalar meson to a nucleon is given by the  $\chi PT$  Lagrangian

$$\mathcal{L}_N^{(1)} = \bar{\Psi} \left( i \not{D} - m + \frac{g_0}{2} \not{\psi} \gamma^5 \right) \Psi, \quad (\text{K.7})$$

where  $D_\mu = \partial_\mu + \Gamma_\mu$ ,  $\Gamma_\mu = \frac{1}{2} [u^\dagger (\partial_\mu - ir_\mu) u + u (\partial_\mu - i\ell_\mu) u^\dagger]$  and  $\Psi = (p \ n)^T$ .

From this expression, we get

$$\begin{aligned} \mathcal{L}_N^{(1)} &= \dots - \frac{g_0}{2f_\pi} \bar{p} \gamma^\mu \gamma^5 p \partial_\mu \pi^0 + \frac{g_0}{2f_\pi} \bar{n} \gamma^\mu \gamma^5 n \partial_\mu \pi^0 + \dots \\ &= \dots + \frac{g_0 m_N}{f_\pi} \bar{p} i \gamma^5 p \pi^0 - \frac{g_0 m_N}{f_\pi} \bar{n} i \gamma^5 n \pi^0 + \dots \end{aligned} \quad (\text{K.8})$$

which corresponds to the  $SU(2)$  limit. In the case of  $SU(3)$ , we have [132, 133]

$$\mathcal{L}_1^{(B)} = \langle \bar{B} i \gamma^\mu \nabla_\mu B \rangle - m_B \langle \bar{B} B \rangle + \frac{D}{2} \langle \bar{B} \gamma^\mu \gamma^5 \{u_\mu, B\} \rangle + \frac{F}{2} \langle \bar{B} \gamma^\mu \gamma^5 [u_\mu, B] \rangle \quad (\text{K.9})$$

where

$$B = \begin{pmatrix} \frac{1}{\sqrt{2}} \Sigma^0 + \frac{1}{\sqrt{6}} \Lambda^0 & \Sigma^+ & p \\ \Sigma^- & -\frac{1}{\sqrt{2}} \Sigma^0 + \frac{1}{\sqrt{6}} \Lambda^0 & n \\ \Xi^- & \Xi^0 & -\frac{2}{\sqrt{6}} \Lambda^0 \end{pmatrix}, \quad \bar{B} \equiv B^\dagger \gamma^0, \quad (\text{K.10})$$

and  $\nabla_\mu B \equiv \partial_\mu B + [\Gamma_\mu, B]$  with  $\Gamma_\mu$  defined as before.

From this, we obtain

$$\begin{aligned} \mathcal{L}_1^{(B)} &= -\frac{g_0}{2f_\pi} \bar{p} \gamma^\mu \gamma^5 p \partial_\mu \pi^0 + \frac{g_0}{2f_\pi} \bar{n} \gamma^\mu \gamma^5 n \partial_\mu \pi^0 - \frac{g_\eta}{2f_\pi} \bar{p} \gamma^\mu \gamma^5 p \partial_\mu \eta - \frac{g_\eta}{2f_\pi} \bar{n} \gamma^\mu \gamma^5 n \partial_\mu \eta \\ &\quad - \frac{g_{\eta'}}{2f_\pi} \bar{p} \gamma^\mu \gamma^5 p \partial_\mu \eta' - \frac{g_{\eta'}}{2f_\pi} \bar{n} \gamma^\mu \gamma^5 n \partial_\mu \eta' \end{aligned} \quad (\text{K.11})$$

where

$$g_0 \equiv D + F, \quad (\text{K.12a})$$

$$g_\eta \equiv (C_q - \frac{1}{\sqrt{2}} C_s) D + (C_q + \frac{1}{\sqrt{2}} C_s) F, \quad (\text{K.12b})$$

$$g_{\eta'} \equiv (C_{q'} + \frac{1}{\sqrt{2}} C_{s'}) D + (C_{q'} - \frac{1}{\sqrt{2}} C_{s'}) F. \quad (\text{K.12c})$$

After an integration by parts and using the Dirac equation, we get

$$\begin{aligned}\mathcal{L}_1^{(B)} = & \frac{g_0 m_N}{f_\pi} \bar{p} i \gamma^5 p \pi^0 - \frac{g_0 m_N}{f_\pi} \bar{n} i \gamma^5 n \pi^0 + \frac{g_\eta m_N}{f_\pi} \bar{p} i \gamma^5 p \eta + \frac{g_\eta m_N}{f_\pi} \bar{n} i \gamma^5 n \eta \\ & + \frac{g_{\eta'} m_N}{f_\pi} \bar{p} i \gamma^5 p \eta' + \frac{g_{\eta'} m_N}{f_\pi} \bar{n} i \gamma^5 n \eta',\end{aligned}\tag{K.13}$$

which comply with the well-known Golberger-Treiman relation [823].

The coupling between a pseudoscalar meson to a nucleon is given by

$$\mathcal{L}_N = g_{PNN} \bar{q} i \gamma^5 \frac{\tau^a}{2} q \pi_a,\tag{K.14}$$

where  $\tau^a$  are the Pauli matrices.

From eq. (K.14), we get the pseudoscalar contribution to the axial current

$$\begin{aligned}\langle N(p') | A_\mu^a | N(p) \rangle &= -g_{PNN} \bar{u}(p') \gamma^5 \frac{\tau^a}{2} u(p) \frac{i}{(p' - p)^2 - m_P^2 + i\epsilon} [-i f_P^a (p' - p)_\mu] \\ &= -\sum_P \frac{g_{PNN} f_P^a}{(p' - p)^2 - m_P^2 + i\epsilon} \bar{u}(p') (p' - p)_\mu \gamma^5 u(p),\end{aligned}\tag{K.15}$$

where the following equation has been used,

$$\langle 0 | A_\mu^a | P(q) \rangle = i f_P^a q_\mu.\tag{K.16}$$

Finally, from the Lagrangian in eq. (K.7) we get

$$\langle N(p') | A_\mu^a | N(p) \rangle = g_0 \bar{u}(p') \gamma_\mu \gamma^5 \frac{\tau^a}{2} u(p),\tag{K.17}$$

putting all these together, we have

$$\langle N(p') | A_\mu^a | N(p) \rangle = \bar{u}(p') \left[ g_0 \gamma_\mu \gamma^5 - \frac{g_{PNN} f_P^a}{(p' - p)^2 - m_P^2 + i\epsilon} (p' - p)_\mu \gamma^5 \right] \frac{\tau^a}{2} u(p),\tag{K.18}$$

where the second term contains the pole contribution of  $G_P(t)$ .

## K.2 The coupling of $A$ to the nucleon

### K.2.1 Antisymmetric tensor field ( $A^{\mu\nu}$ )

If we use the antisymmetric tensor field representation for the axial vector meson instead of the more familiar vector one, we get the most general structure describing the coupling of the axial-vector resonance to the nucleon:

$$\begin{aligned} \langle N'(p') | A^{\mu\nu} | N(p) \rangle = & \bar{u}(p') \left[ \frac{1}{2} (q_1^\mu q_2^\nu - q_1^\nu q_2^\mu) \gamma^5 \tilde{G}_1 + \frac{1}{2} (\gamma^\mu q_1^\nu - \gamma^\nu q_1^\mu) \gamma^5 \tilde{G}_2 \right. \\ & + \frac{1}{2} (\gamma^\mu q_2^\nu - \gamma^\nu q_2^\mu) \gamma^5 \tilde{G}_3 + \epsilon^{\mu\nu\rho\sigma} q_{1\rho} q_{2\sigma} \tilde{G}_4 \\ & \left. + \frac{1}{2} (q_1^\mu q_2^\nu - q_1^\nu q_2^\mu) \tilde{F}_1 + \epsilon^{\mu\nu\rho\sigma} q_{1\rho} q_{2\sigma} \gamma^5 \tilde{F}_2 \right] u(p) \langle A(q_1) | A^{\mu\nu} | 0 \rangle, \end{aligned} \quad (\text{K.19})$$

where  $q_1 \equiv p - p'$  and  $q_2 \equiv p + p'$ , and  $\tilde{G}_1, \tilde{G}_2, \tilde{G}_3$  and  $\tilde{G}_4$  are C- and P-conserving form factors while  $\tilde{F}_1$  and  $\tilde{F}_2$  are form factors that break the intrinsic parity. Also,  $\tilde{G}_1$  and  $\tilde{F}_1$  are  $CP$ -odd. All the form factors, as expected, are G-conserving.

At  $\mathcal{O}(p^4)$  in  $\chi PT$ , we have

$$\mathcal{L}_2 = \frac{F_A}{2\sqrt{2}} \langle A_{\mu\nu} f_-^{\mu\nu} \rangle. \quad (\text{K.20})$$

Thus,

$$\left\langle 0 \left| \frac{\delta \mathcal{L}_2}{\delta a_\beta} \right| A(q) \right\rangle = -i\sqrt{2} F_A q_\alpha \langle 0 | A^{\alpha\beta} | A(q) \rangle. \quad (\text{K.21})$$

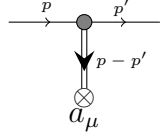
The longitudinal and transverse part of the propagator of  $A^{\mu\nu}$  are given by

$$\Omega_L^{\mu\nu,\rho\sigma}(k) = iD_A^{-1}(k^2) (g^{\mu\rho} g^{\nu\sigma} - g^{\mu\sigma} g^{\nu\rho}), \quad (\text{K.22a})$$

$$\Omega_T^{\mu\nu,\rho\sigma}(k) = iM_A^2 D_A^{-1}(k^2) (g^{\mu\rho} k^\nu k^\sigma - g^{\mu\sigma} k^\nu k^\rho - k^2 g^{\mu\rho} g^{\nu\sigma} - (\mu \leftrightarrow \nu)). \quad (\text{K.22b})$$

where  $D_A(k^2) = M_A^2 - k^2$ .

We are interested in the neutral current. The contribution from  $A^{\mu\nu}$  to the axial current is



$$\begin{aligned}
&= \bar{u}(p') \left[ \frac{\sqrt{2}F_A q_1^2}{D_A(q_1^2)} \tilde{F}_1 q_2^\mu + \frac{\sqrt{2}F_A q_1^2}{D_A(q_1^2)} \left( \tilde{G}_1 - \frac{2M_N}{q_1^2} \tilde{G}_3 \right) q_2^\mu \gamma^5 \right. \\
&\quad \left. - \frac{\sqrt{2}F_A q_1^2}{D_A(q_1^2)} \tilde{G}_2 \left( \gamma^\mu \gamma^5 + \frac{2M_N}{q_1^2} q_1^\mu \gamma^5 \right) \right] u(p),
\end{aligned} \tag{K.23}$$

where only the longitudinal part contributes to this diagram.

## K.2.2 Proca field ( $\hat{A}_\mu$ )

From  $R\chi T$ , the Lagrangian that describes the coupling between an axial-vector meson and an external source is given by [225]

$$\mathcal{L}^{II} = -\frac{f_A}{2\sqrt{2}} \langle \hat{A}_{\mu\nu} f_-^{\mu\nu} \rangle, \tag{K.24}$$

where  $\hat{A}_{\mu\nu} = \nabla_\mu \hat{A}_\nu - \nabla_\nu \hat{A}_\mu$ .

From eq. (K.24), we get

$$\left\langle 0 \left| \frac{\delta \mathcal{L}^{II}}{\delta a_\beta^b} \right| A(q) \right\rangle = \sqrt{2} f_A^b q^2 \left( g^{\alpha\beta} - \frac{q^\alpha q^\beta}{q^2} \right) \epsilon_\alpha(q). \tag{K.25}$$

If we use

$$\langle N(p') A(p-p') | N(p) \rangle \equiv -i H_A \bar{u}(p') \gamma^\mu \gamma^5 \frac{\tau^a}{2} u(p) \epsilon_\mu^*(q), \quad q \equiv p - p', \tag{K.26}$$

which is similar to the one employed in Ref. [824], we obtain

$$\langle N(p') | J_A^\rho | N(p) \rangle \equiv \frac{\sqrt{2} f_A^a H_A q_1^2}{D_A(q_1^2)} \bar{u}(p') \left[ \gamma^\rho \gamma^5 + \frac{2M_N}{q_1^2} q_1^\rho \gamma^5 \right] \frac{\tau^a}{2} u(p) \tag{K.27}$$

where  $D_A(s) \equiv M_A^2 - s$ .

It is possible to write the propagator in a subtracted term (s.t.) and contact term (c.t.) according to eq. (K.28) [603]

$$D^{\alpha\beta}(q^2) = -\frac{q^2 g^{\alpha\beta} - q^\alpha q^\beta}{M_A^2(q^2 - M_A^2)} + \frac{g^{\alpha\beta}}{M_A^2} \equiv \bar{D}^{\alpha\beta}(q^2) + \frac{g^{\alpha\beta}}{M_A^2}, \quad (\text{K.28})$$

also we can split the propagator as we did before in eq. (K.22),

$$D_T^{\alpha\beta}(q) = -\frac{g^{\alpha\beta} - \frac{q^\alpha q^\beta}{q^2}}{q^2 - M_A^2} = \bar{D}^{\alpha\beta}(q^2) + \frac{g^{\alpha\beta} - \frac{q^\alpha q^\beta}{q^2}}{M_A^2}, \quad (\text{K.29})$$

and

$$D_L^{\alpha\beta}(q) = \frac{q^\alpha q^\beta}{q^2 M_A^2}, \quad (\text{K.30})$$

with the projectors given by

$$P_T^{\mu\nu}(q) \equiv g^{\mu\nu} - \frac{q^\mu q^\nu}{q^2}, \quad (\text{K.31a})$$

$$P_L^{\mu\nu}(q) \equiv \frac{q^\mu q^\nu}{q^2}. \quad (\text{K.31b})$$

It is clear, from eq. (K.31), that eq. (K.25) only has the transverse contribution. Also, eq. (K.30) can be understood as the longitudinal part of the contact term.

If, instead of eq. (K.25), we use the relation in eq. (K.32)

$$\langle 0 | A_\beta^a | A(q) \rangle \equiv F_A^a m_A \epsilon_\beta(q), \quad (\text{K.32})$$



we get

$$\begin{aligned}
\langle N(p') | (J_A^a)^\rho | N(p) \rangle &\equiv \frac{F_A^a M_A H_A}{D_A(q_1^2)} \bar{u}(p') \left[ \gamma^\rho \gamma^5 + \frac{2M_N}{M_A^2} q_1^\rho \gamma^5 \right] \frac{\tau^a}{2} u(p) \\
&= \frac{F_A^a M_A H_A}{D_A(q_1^2)} \bar{u}(p') \left[ \gamma^\rho \gamma^5 + \frac{2M_N}{q_1^2} q_1^\rho \gamma^5 \right] \frac{\tau^a}{2} u(p) && \{\text{T}\} \text{ (s.t. + c.t.)} \\
&\quad - \frac{F_A^a H_A}{M_A} \bar{u}(p') \left[ \frac{2M_N}{q_1^2} q_1^\rho \gamma^5 \right] \frac{\tau^a}{2} u(p) && \{\text{L}\} \text{ (c.t.)},
\end{aligned} \tag{K.33}$$

where  $T$  and  $L$  refer to the contributions from eqs. (K.29) and (K.30), respectively.

Now, if we start from the Lagrangian

$$\mathcal{L} \equiv g_{ANN} \bar{\psi} \gamma_\nu \gamma^5 \partial_\mu \hat{A}^{\mu\nu} \psi, \tag{K.34}$$

we get the following contribution to the axial current

$$i\mathcal{M} = \frac{\sqrt{2} g_{ANN} f_A^a q_1^4}{D_A(q_1^2)} \bar{u}(p') \left[ \gamma^\rho \gamma^5 + \frac{2M_N}{q_1^2} q_1^\rho \gamma^5 \right] \frac{\tau^a}{2} u(p) \tag{K.35}$$

using eq. (K.25) and

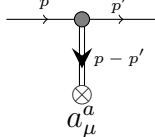
$$i\mathcal{M} = \frac{g_{ANN} F_A^a M_A q_1^2}{D_A(q_1^2)} \bar{u}(p') \left[ \gamma^\rho \gamma^5 + \frac{2M_N}{q_1^2} q_1^\rho \gamma^5 \right] \frac{\tau^a}{2} u(p) \tag{K.36}$$

using eq. (K.32).

Finally, we return to the eq. (K.19) and using the eq. (A.11) from Ref. [224]

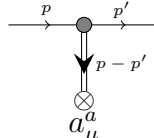
$$\langle A(q) | A^{\mu\nu} | 0 \rangle = -i M_A^{-1} [q^\mu g^{\nu\sigma} - q^\nu g^{\mu\sigma}] \epsilon_\sigma^*(q), \tag{K.37}$$

we get



$$\begin{aligned}
&= \bar{u}(p') \left[ \frac{\sqrt{2}f_A^a q_1^4}{M_A D_A(q_1^2)} \tilde{F}_1 q_2^\mu + \frac{\sqrt{2}f_A^a q_1^4}{M_A D_A(q_1^2)} \left( \tilde{G}_1 - \frac{2M_N}{q_1^2} \tilde{G}_3 \right) q_2^\mu \gamma^5 \right. \\
&\quad \left. - \frac{\sqrt{2}f_A^a q_1^4}{M_A D_A(q_1^2)} \tilde{G}_2 \left( \gamma^\mu \gamma^5 + \frac{2M_N}{q_1^2} q_1^\mu \gamma^5 \right) \right] \frac{\tau^a}{2} u(p)
\end{aligned} \tag{K.38}$$

using eq. (K.25) and



$$\begin{aligned}
&= \bar{u}(p') \left[ \frac{F_A^a q_1^2}{D_A(q_1^2)} \tilde{F}_1 q_2^\mu + \frac{F_A^a q_1^2}{D_A(q_1^2)} \left( \tilde{G}_1 - \frac{2M_N}{q_1^2} \tilde{G}_3 \right) q_2^\mu \gamma^5 \right. \\
&\quad \left. - \frac{F_A^a q_1^2}{D_A(q_1^2)} \tilde{G}_2 \left( \gamma^\mu \gamma^5 + \frac{2M_N}{q_1^2} q_1^\mu \gamma^5 \right) \right] \frac{\tau^a}{2} u(p)
\end{aligned} \tag{K.39}$$

using eq. (K.32).

### K.2.3 Effective coupling in $B\chi PT$

In a similar way to Dorokhov, where the effective coupling is given by the Hamiltonian of nucleon-axial-vector meson interaction

$$H_1(a_1 NN) = g_{a_1 NN} \bar{N} \tau \gamma_\mu \gamma^5 N a_1^\mu, \quad \text{for } a_1 \text{ exchange and} \tag{K.40a}$$

$$H_1(f_1 NN) = g_{f_1 NN} \bar{N} \tau \gamma_\mu \gamma^5 N f_1^\mu, \quad \text{for } f_1 \text{ exchange.} \tag{K.40b}$$

We find the lowest-order  $\chi PT$  Lagrangian that contributes to the ANN coupling using the antisymmetric tensor field representation of the axial-vector resonances, which is given by

$$\mathcal{L}_{ANN}^{\chi PT} = g_1 \langle \bar{B} \gamma^\mu \gamma^5 \{ \nabla^\nu A_{\mu\nu}, B \} \rangle + g_2 \langle \bar{B} \gamma^\mu \gamma^5 [ \nabla^\nu A_{\mu\nu}, B ] \rangle. \tag{K.41}$$

Other related terms, like

$$\langle \bar{B}\gamma^\mu(\gamma^5)\{A_{\mu\nu}, \nabla^\nu B\} \rangle, \quad \langle \bar{B}\gamma^\mu(\gamma^5)[A_{\mu\nu}, \nabla^\nu B] \rangle, \quad (\text{K.42a})$$

$$\langle \bar{B}\sigma^{\mu\nu}(\gamma^5)\{A_{\mu\nu}, B\} \rangle, \quad \langle \bar{B}\sigma^{\mu\nu}(\gamma^5)[A_{\mu\nu}, B] \rangle, \quad (\text{K.42b})$$

are not  $C$ -conserving. In order to build these operators, we have to recall that the  $A_{\mu\nu}$  field transforms under  $C$  and  $P$  as

$$\begin{aligned} A_{\mu\nu} &\rightarrow C A_{\mu\nu} C = (A_{\mu\nu})^T, \\ &\rightarrow P A_{\mu\nu} P = -A^{\mu\nu} \end{aligned} \quad (\text{K.43})$$

where

$$A_{\mu\nu} = \begin{pmatrix} \frac{a_1^0}{\sqrt{2}} + \frac{f_1}{\sqrt{2}} & a_1^+ & K_1^+ \\ a_1^- & -\frac{a_1^0}{\sqrt{2}} + \frac{f_1}{\sqrt{2}} & K_1^0 \\ K_1^- & \bar{K}_1^0 & -f_1' \end{pmatrix}_{\mu\nu}. \quad (\text{K.44})$$

Finally, we get from eq. (K.41)

$$\begin{aligned} \mathcal{L}_{ANN}^{\chi PT} &= g_{a_1 NN} \bar{p}\gamma^\mu\gamma^5 p \partial^\nu a_{1\mu\nu} - g_{a_1 NN} \bar{n}\gamma^\mu\gamma^5 n \partial^\nu a_{1\mu\nu} \\ &+ g_{f_1 NN} \bar{p}\gamma^\mu\gamma^5 p \partial^\nu f_{1\mu\nu} + g_{f_1 NN} \bar{n}\gamma^\mu\gamma^5 n \partial^\nu f_{1\mu\nu} \\ &- g_{f_1' NN} \bar{p}\gamma^\mu\gamma^5 p \partial^\nu f'_{1\mu\nu} - g_{f_1' NN} \bar{n}\gamma^\mu\gamma^5 n \partial^\nu f'_{1\mu\nu} \end{aligned} \quad (\text{K.45})$$

where

$$g_{a_1 NN} = g_{f_1 NN} = \frac{1}{\sqrt{2}}(g_1 + g_2), \quad \text{and} \quad g_{f_1' NN} = \frac{1}{\sqrt{2}}(g_1 - g_2). \quad (\text{K.46})$$

The Lagrangian in eq. (K.41) contributes to  $\tilde{G}_2$  in eq. (K.19).

## K.2.4 Coupling axial-vector to two photons

The most general structure that describes this coupling is given by

$$\begin{aligned}
\langle A(P) | J_{em}^\mu J_{em}^\nu | 0 \rangle = & \left\{ \left( k_1^\alpha k_2^\beta - k_1^\beta k_2^\alpha \right) \left[ G_1 \left( k_1^2 k_2^2 g^{\mu\nu} + k_1 \cdot k_2 k_1^\mu k_2^\nu - k_2^2 k_1^\mu k_1^\nu - k_1^2 k_2^\mu k_2^\nu \right) \right. \right. \\
& + G_2 \left( k_2^\mu k_1^\nu - k_1 \cdot k_2 g^{\mu\nu} \right) + \tilde{G}_1 \epsilon^{\mu\nu\rho\sigma} k_{1\rho} k_{2\sigma} \left. \right] \\
& + \tilde{G}_2 \left( g^{\mu\nu} \epsilon^{\alpha\beta\rho\sigma} k_{1\rho} k_{2\sigma} - k_1^\nu \epsilon^{\mu\alpha\beta\rho} k_{2\rho} + k_1 \cdot k_2 \epsilon^{\mu\nu\alpha\beta} + k_2^\mu \epsilon^{\nu\alpha\beta\rho} k_{1\rho} \right) \\
& + \tilde{G}_3 \left[ \left( k_1 \cdot k_2 k_1^\mu - k_1^2 k_2^\mu \right) \epsilon^{\nu\alpha\beta\rho} k_{2\rho} - \left( k_1 \cdot k_2 k_2^\nu - k_2^2 k_1^\nu \right) \epsilon^{\mu\alpha\beta\rho} k_{1\rho} \right] \\
& + \tilde{F}_1 \left[ \left( k_1 \cdot k_2 k_1^\mu - k_1^2 k_2^\mu \right) \epsilon^{\nu\alpha\beta\rho} k_{2\rho} + \left( k_1 \cdot k_2 k_2^\nu - k_2^2 k_1^\nu \right) \epsilon^{\mu\alpha\beta\rho} k_{1\rho} \right] \left. \right\} \\
& \times \langle A(P) | A_{\alpha\beta} | 0 \rangle,
\end{aligned} \tag{K.47}$$

where the Schouten identity has been used.

Here,  $G_i$  and  $\tilde{G}_i$  are antisymmetric and  $\tilde{F}_i$  is symmetric under  $k_1 \leftrightarrow k_2$ .  $\tilde{F}_i$  and  $\tilde{G}_i$  are  $C$ - and  $P$ -conserving.  $G_1$  and  $G_2$  are only  $C$ -conserving.

The eq. (K.47) complies with the Ward identity,

$$k_{1\mu} \langle N(p') | J_{em}^\mu J_{em}^\nu | N(p) \rangle = 0, \tag{K.48}$$

and

$$k_{2\nu} \langle N(p') | J_{em}^\mu J_{em}^\nu | N(p) \rangle = 0. \tag{K.49}$$

## K.2.5 $\langle N(p') | \mathbf{J}_{em}^\mu \mathbf{J}_{em}^\nu | N(p) \rangle$

Defining  $X \equiv k_1 + k_2$ ,  $W_1 \equiv p' + k_1$  and  $W_2 \equiv p' + k_2$ , we can write the most general structure that describes the coupling  $NN\gamma\gamma$  (see fig. K.1):

$$\begin{aligned}
\langle N(p') | J_{em}^\mu J_{em}^\nu | N(p) \rangle = & \bar{u}(p') \{ F_1 \mathcal{A}^{\mu\nu} + F_2 \mathcal{B}^{\mu\nu} + F_3 \mathcal{C}^{\mu\nu} + F_4 \mathcal{D}^{\mu\nu} + F_5 \mathcal{E}^{\mu\nu} \\
& + F_6 [D_B(W_2^2) \gamma^\mu (\not{W}_1 + m_B) \gamma^\nu + D_B(W_1^2) \gamma^\nu (\not{W}_2 + m_B) \gamma^\mu] \\
& + (F_7 \mathcal{F}^{\mu\nu} + F_8 \mathcal{G}^{\mu\nu} + G_1 \mathcal{H}^{\mu\nu} + G_2 \mathcal{I}^{\mu\nu}) \gamma^5 \\
& + (G_3 \mathcal{F}^{\mu\nu} + G_4 \mathcal{G}^{\mu\nu} + F_9 \mathcal{H}^{\mu\nu} + F_{10} \mathcal{I}^{\mu\nu}) (\not{k}_1 - \not{k}_2) \gamma^5 \\
& + (\tilde{F}_1 \mathcal{A}^{\mu\nu} + \tilde{F}_2 \mathcal{B}^{\mu\nu} + \tilde{F}_3 \mathcal{C}^{\mu\nu} + \tilde{F}_4 \mathcal{D}^{\mu\nu} + \tilde{F}_5 \mathcal{E}^{\mu\nu}) i\gamma^5 \\
& + \tilde{F}_6 \mathcal{F}^{\mu\nu} + \tilde{F}_7 \mathcal{G}^{\mu\nu} + \tilde{G}_1 \mathcal{H}^{\mu\nu} + \tilde{G}_2 \mathcal{I}^{\mu\nu} \\
& + (\tilde{G}_3 \mathcal{A}^{\mu\nu} + \tilde{G}_4 \mathcal{B}^{\mu\nu} + \tilde{G}_4 \mathcal{C}^{\mu\nu} + \tilde{G}_4 \mathcal{D}^{\mu\nu} + \tilde{G}_6 \mathcal{E}^{\mu\nu}) (\not{k}_1 - \not{k}_2) \gamma^5 \} u(p)
\end{aligned} \tag{K.50}$$

where  $F_i$  is symmetric and  $G_i$  is antisymmetric under the interchange  $k_1 \leftrightarrow k_2$ .  $F_i$  and  $G_i$  are C- and P-conserving while  $\tilde{F}_i$  and  $\tilde{G}_i$  are only C-conserving.

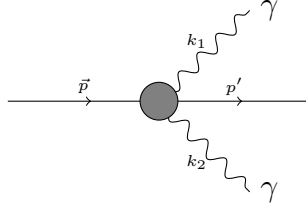


Figure K.1: Two photon exchange vertex.

With

$$\begin{aligned}
\mathcal{A}^{\mu\nu} = & (k_1^2 - k_2^2 - 2P \cdot (k_1 - k_2))(k_1^4 + k_2^4 + (P \cdot (k_1 - k_2))^2 + k_1^2(2k_2^2 - P \cdot (k_1 - k_2) - 2P \cdot (k_1 + k_2)) \\
& + k_2^2(P \cdot (k_1 - k_2) - 2P \cdot (k_1 + k_2)) + (P \cdot (k_1 + k_2))^2) g^{\mu\nu} + 2(k_1^2 - k_2^2 - P \cdot (k_1 - k_2)) \\
& (k_1^2 + k_2^2 - 2P \cdot (k_1 + k_2)) W_1^\mu W_2^\nu - 2P \cdot (k_1 - k_2)(k_1^2 + k_2^2 - 2P \cdot (k_1 + k_2)) W_2^\mu W_1^\nu \\
& + 2(k_1^2(-P \cdot (k_1 - k_2) + P \cdot (k_1 + k_2)) + (k_2^2 + P \cdot (k_1 - k_2) - P \cdot (k_1 + k_2))(P \cdot (k_1 - k_2) \\
& + P \cdot (k_1 + k_2))) (W_1^\mu W_1^\nu - W_2^\mu W_2^\nu) - (k_1^4 + k_2^4 + (P \cdot (k_1 - k_2))^2 + k_2^2(P \cdot (k_1 - k_2) - 2P \cdot (k_1 + k_2)) \\
& + (P \cdot (k_1 + k_2))^2 - k_1^2(-2k_2^2 + P \cdot (k_1 - k_2) + 2P \cdot (k_1 + k_2))) (X^\mu W_1^\nu - X^\nu W_2^\mu) \\
& + (-k_1^4 - k_2^4 - (P \cdot (k_1 - k_2))^2 - k_2^2(P \cdot (k_1 - k_2) - 2P \cdot (k_1 + k_2)) - (P \cdot (k_1 + k_2))^2 \\
& + k_1^2(-2k_2^2 + P \cdot (k_1 - k_2) + 2P \cdot (k_1 + k_2))) (X^\mu W_2^\nu - X^\nu W_1^\mu),
\end{aligned} \tag{K.51}$$

$$\begin{aligned}
\mathcal{B}^{\mu\nu} = & (k_1^2 - k_2^2 - 2P \cdot (k_1 - k_2))(k_1^2 + k_2^2 - P \cdot (k_1 + k_2))(k_1^4 + k_2^4 + (P \cdot (k_1 - k_2))^2 + k_1^2(2k_2^2 \\
& - P \cdot (k_1 - k_2) - 2P \cdot (k_1 + k_2)) + k_2^2(P \cdot (k_1 - k_2) - 2P \cdot (k_1 + k_2)) + (P \cdot (k_1 + k_2))^2) X^\mu X^\nu \\
& - (k_1^4 - k_2^4 - 3k_1^2 P \cdot (k_1 + k_2) + 3k_2^2 P \cdot (k_1 + k_2) + 2P \cdot (k_1 - k_2) P \cdot (k_1 + k_2))(k_1^4 + k_2^4 \\
& + k_2^2(P \cdot (k_1 - k_2) - 2P \cdot (k_1 + k_2)) + 2(P \cdot (k_1 + k_2))^2 - k_1^2(2k_2^2 + P \cdot (k_1 - k_2) \\
& + 2P \cdot (k_1 + k_2))) W_1^\mu W_2^\nu + (k_1^4 - k_2^4 - k_1^2 P \cdot (k_1 + k_2) + k_2^2 P \cdot (k_1 + k_2) - 2P \cdot (k_1 - k_2) \\
& P \cdot (k_1 + k_2))(k_1^2(P \cdot (k_1 - k_2) - 2P \cdot (k_1 + k_2)) + 2(P \cdot (k_1 + k_2))^2 - k_2^2(P \cdot (k_1 - k_2) \\
& + 2P \cdot (k_1 + k_2))) W_2^\mu W_1^\nu + (k_1^2(P \cdot (k_1 - k_2) - 2P \cdot (k_1 + k_2)) + 2(P \cdot (k_1 + k_2))^2 \\
& - k_2^2(P \cdot (k_1 - k_2) + 2P \cdot (k_1 + k_2)))(k_1^4 + k_2^4 + k_2^2(P \cdot (k_1 - k_2) - 2P \cdot (k_1 + k_2)) \\
& + 2(P \cdot (k_1 + k_2))^2 - k_1^2(2k_2^2 + P \cdot (k_1 - k_2) + 2P \cdot (k_1 + k_2))) (W_1^\mu W_1^\nu - W_2^\mu W_2^\nu) + (k_1^4 + k_2^4 \\
& + (P \cdot (k_1 - k_2))^2 + k_1^2(2k_2^2 - P \cdot (k_1 - k_2) - 2P \cdot (k_1 + k_2)) + k_2^2(P \cdot (k_1 - k_2) - 2P \cdot (k_1 + k_2)) \\
& + (P \cdot (k_1 + k_2))^2)(k_1^2(P \cdot (k_1 - k_2) - 2P \cdot (k_1 + k_2)) + 2(P \cdot (k_1 + k_2))^2 - k_2^2(P \cdot (k_1 - k_2) \\
& + 2P \cdot (k_1 + k_2))) (X^\mu W_1^\nu - X^\nu W_2^\mu) + (k_1^4 + k_2^4 + (P \cdot (k_1 - k_2))^2 + k_1^2(2k_2^2 - P \cdot (k_1 - k_2) \\
& - 2P \cdot (k_1 + k_2)) + k_2^2(P \cdot (k_1 - k_2) - 2P \cdot (k_1 + k_2)) + (P \cdot (k_1 + k_2))^2)(k_1^4 + k_2^4 \\
& + k_2^2(P \cdot (k_1 - k_2) - 2P \cdot (k_1 + k_2)) + 2(P \cdot (k_1 + k_2))^2 - k_1^2(2k_2^2 + P \cdot (k_1 - k_2) \\
& + 2P \cdot (k_1 + k_2))) (X^\mu W_2^\nu - X^\nu W_1^\mu),
\end{aligned} \tag{K.52}$$

$$\begin{aligned}
\mathcal{C}^{\mu\nu} = & (2k_1^2 - P \cdot (k_1 - k_2) - P \cdot (k_1 + k_2))(2k_2^2 + P \cdot (k_1 - k_2) - P \cdot (k_1 + k_2)) W_1^\mu W_2^\nu \\
& + (k_1^4 + k_2^4 + (P \cdot (k_1 - k_2))^2 + k_1^2(2k_2^2 - P \cdot (k_1 - k_2) - 2P \cdot (k_1 + k_2)) + k_2^2(P \cdot (k_1 - k_2) \\
& - 2P \cdot (k_1 + k_2)) + (P \cdot (k_1 + k_2))^2) (W_1^\mu W_1^\nu + W_2^\mu W_2^\nu) + (k_1^4 + k_2^4 - (P \cdot (k_1 - k_2))^2 \\
& + 2k_1^2(k_2^2 - P \cdot (k_1 + k_2)) - 2k_2^2 P \cdot (k_1 + k_2) + (P \cdot (k_1 + k_2))^2) W_2^\mu W_1^\nu \\
& + (k_1^2 - k_2^2 - 2P \cdot (k_1 - k_2))(k_1^2 + k_2^2 - P \cdot (k_1 + k_2)) (W_1^\mu W_1^\nu - W_2^\mu W_2^\nu),
\end{aligned} \tag{K.53}$$

$$\begin{aligned}
\mathcal{D}^{\mu\nu} = & - (2k_1^2 - P \cdot (k_1 - k_2) - P \cdot (k_1 + k_2))(2k_2^2 + P \cdot (k_1 - k_2) - P \cdot (k_1 + k_2))(k_1^4 - k_2^4 \\
& - 3k_1^2 P \cdot (k_1 + k_2) + 3k_2^2 P \cdot (k_1 + k_2) + 2P \cdot (k_1 - k_2) P \cdot (k_1 + k_2)) W_1^\mu W_2^\nu + (k_1^2 - k_2^2 \\
& - 2P \cdot (k_1 - k_2))(k_1^2 + k_2^2 - P \cdot (k_1 + k_2))(k_1^4 + k_2^4 + (P \cdot (k_1 - k_2))^2 + k_1^2(2k_2^2 - P \cdot (k_1 - k_2) \\
& - 2P \cdot (k_1 + k_2))) + k_2^2(P \cdot (k_1 - k_2) - 2P \cdot (k_1 + k_2)) + (P \cdot (k_1 + k_2))^2) (X^\mu W_1^\nu + X^\nu W_2^\mu) \\
& + ((k_1^4 - k_2^4)((k_1^2 + k_2^2)^2 - 2(k_1^2 - k_2^2) P \cdot (k_1 - k_2) + 3(P \cdot (k_1 - k_2))^2) - ((k_1^2 - k_2^2)(k_1^2 + k_2^2)^2 \\
& + 4(k_1^4 + 4k_1^2 k_2^2 + k_2^4) P \cdot (k_1 - k_2) + (k_1^2 - k_2^2) (P \cdot (k_1 - k_2))^2 + 2(P \cdot (k_1 - k_2))^3) P \cdot (k_1 + k_2) \\
& - (k_1^2 + k_2^2)(k_1^2 - k_2^2 - 12P \cdot (k_1 - k_2)) (P \cdot (k_1 + k_2))^2 + (k_1^2 - k_2^2 - 6P \cdot (k_1 - k_2)) \\
& (P \cdot (k_1 + k_2))^3) W_2^\mu W_1^\nu + (2k_1^2 - P \cdot (k_1 - k_2) - P \cdot (k_1 + k_2))(2k_2^2 + P \cdot (k_1 - k_2) \\
& - P \cdot (k_1 + k_2))(k_1^2(P \cdot (k_1 - k_2) - 2P \cdot (k_1 + k_2)) + 2(P \cdot (k_1 + k_2))^2 - k_2^2(P \cdot (k_1 - k_2) \\
& + 2P \cdot (k_1 + k_2))) (W_1^\mu W_1^\nu - W_2^\mu W_2^\nu) + (k_1^4 + k_2^4 + (P \cdot (k_1 - k_2))^2 + k_1^2(2k_2^2 - P \cdot (k_1 - k_2) \\
& - 2P \cdot (k_1 + k_2))) + k_2^2(P \cdot (k_1 - k_2) - 2P \cdot (k_1 + k_2)) + (P \cdot (k_1 + k_2))^2)^2 (X^\mu W_1^\nu - X^\nu W_2^\mu) \\
& - (2k_2^2 + P \cdot (k_1 - k_2) - P \cdot (k_1 + k_2))(-2k_1^2 + P \cdot (k_1 - k_2) + P \cdot (k_1 + k_2))(k_1^4 + k_2^4 \\
& + (P \cdot (k_1 - k_2))^2 + k_1^2(2k_2^2 - P \cdot (k_1 - k_2) - 2P \cdot (k_1 + k_2)) + k_2^2(P \cdot (k_1 - k_2) - 2P \cdot (k_1 + k_2)) \\
& + (P \cdot (k_1 + k_2))^2) (X^\mu W_2^\nu - X^\nu W_1^\mu),
\end{aligned}$$

(K.54)

$$\begin{aligned}
\mathcal{E}^{\mu\nu} = & (2k_1^8 - 2k_2^8 - 4k_2^6(P \cdot (k_1 - k_2) - 2P \cdot (k_1 + k_2)) + k_2^2(7P \cdot (k_1 - k_2) - 5P \cdot (k_1 + k_2))) \\
& (P \cdot (k_1 - k_2) - P \cdot (k_1 + k_2)) P \cdot (k_1 + k_2) - 4k_1^6(P \cdot (k_1 - k_2) + 2P \cdot (k_1 + k_2)) \\
& + k_2^4(-3(P \cdot (k_1 - k_2))^2 + 12P \cdot (k_1 - k_2) P \cdot (k_1 + k_2) - 11(P \cdot (k_1 + k_2))^2) \\
& + 2P \cdot (k_1 - k_2) P \cdot (k_1 + k_2)((P \cdot (k_1 - k_2))^2 + 3(P \cdot (k_1 + k_2))^2) + k_1^4(3(P \cdot (k_1 - k_2))^2 \\
& + 4k_2^2(P \cdot (k_1 - k_2) - P \cdot (k_1 + k_2)) + 12P \cdot (k_1 - k_2) P \cdot (k_1 + k_2) + 11(P \cdot (k_1 + k_2))^2) \\
& + k_1^2(P \cdot (k_1 - k_2) + P \cdot (k_1 + k_2))(4k_2^4 - P \cdot (k_1 + k_2)(7P \cdot (k_1 - k_2) + 5P \cdot (k_1 + k_2))) \\
W_1^\mu W_2^\nu + & (k_1^2 - k_2^2 - 2P \cdot (k_1 - k_2))(k_1^2 + k_2^2 - P \cdot (k_1 + k_2))(k_1^4 + k_2^4 + (P \cdot (k_1 - k_2))^2 \\
& + k_1^2(2k_2^2 - P \cdot (k_1 - k_2) - 2P \cdot (k_1 + k_2)) + k_2^2(P \cdot (k_1 - k_2) - 2P \cdot (k_1 + k_2)) \\
& + (P \cdot (k_1 + k_2))^2)(X^\mu W_2^\nu + X^\nu W_1^\mu) - (k_1^2 + k_2^2 - P \cdot (k_1 - k_2) - P \cdot (k_1 + k_2)) \\
& (k_1^2 + k_2^2 + P \cdot (k_1 - k_2) - P \cdot (k_1 + k_2))(k_1^4 - k_2^4 - k_1^2 P \cdot (k_1 + k_2) + k_2^2 P \cdot (k_1 + k_2) \\
& - 2P \cdot (k_1 - k_2) P \cdot (k_1 + k_2)) W_2^\mu W_1^\nu - (k_1^2 + k_2^2 - P \cdot (k_1 - k_2) - P \cdot (k_1 + k_2)) \\
& (k_1^2 + k_2^2 + P \cdot (k_1 - k_2) - P \cdot (k_1 + k_2))(k_1^4 + k_2^4 + k_2^2(P \cdot (k_1 - k_2) - 2P \cdot (k_1 + k_2)) \\
& + 2(P \cdot (k_1 + k_2))^2 - k_1^2(2k_2^2 + P \cdot (k_1 - k_2) + 2P \cdot (k_1 + k_2))) (W_1^\mu W_1^\nu - W_2^\mu W_2^\nu) \\
& - (k_1^2 + k_2^2 - P \cdot (k_1 - k_2) - P \cdot (k_1 + k_2))(k_1^2 + k_2^2 + P \cdot (k_1 - k_2) - P \cdot (k_1 + k_2)) \\
& (k_1^4 + k_2^4 + (P \cdot (k_1 - k_2))^2 + k_1^2(2k_2^2 - P \cdot (k_1 - k_2) - 2P \cdot (k_1 + k_2)) + k_2^2(P \cdot (k_1 - k_2) \\
& - 2P \cdot (k_1 + k_2)) + (P \cdot (k_1 + k_2))^2)(X^\mu W_1^\nu - X^\nu W_2^\mu) - (k_1^4 + k_2^4 + (P \cdot (k_1 - k_2))^2 \\
& + k_1^2(2k_2^2 - P \cdot (k_1 - k_2) - 2P \cdot (k_1 + k_2)) + k_2^2(P \cdot (k_1 - k_2) - 2P \cdot (k_1 + k_2)) \\
& + (P \cdot (k_1 + k_2))^2)^2 (X^\mu W_2^\nu - X^\nu W_1^\mu),
\end{aligned} \tag{K.55}$$

$$\mathcal{F}^{\mu\nu} = i \epsilon^{\mu\nu\rho\sigma} X_\rho (W_1 - W_2)_\sigma, \tag{K.56}$$

$$\begin{aligned}
\mathcal{G}^{\mu\nu} = & \left(k_1^2 + k_2^2 - P \cdot X\right) i \epsilon^{\mu\nu\rho\sigma} W_{1\rho} W_{2\sigma} - \frac{1}{2} P \cdot (W_1 - W_2) i \epsilon^{\mu\nu\rho\sigma} X_\rho (W_1 + W_2)_\sigma \\
& + W_1^\mu i \epsilon^{\nu\rho\sigma\omega} X_\rho W_{1\sigma} W_{2\omega} - W_2^\nu i \epsilon^{\mu\rho\sigma\omega} X_\rho W_{1\sigma} W_{2\omega},
\end{aligned} \tag{K.57}$$

$$\begin{aligned}
\mathcal{H}^{\mu\nu} = & \left(k_1^2 - k_2^2\right) i \epsilon^{\mu\nu\rho\sigma} W_{1\rho} W_{2\sigma} - P \cdot X i \epsilon^{\mu\nu\rho\sigma} X_\rho (W_1 + W_2)_\sigma \\
& + X^\mu i \epsilon^{\nu\rho\sigma\omega} X_\rho W_{1\sigma} W_{2\omega} + X^\nu i \epsilon^{\mu\rho\sigma\omega} X_\rho W_{1\sigma} W_{2\omega},
\end{aligned} \tag{K.58}$$



and

$$\begin{aligned} \mathcal{I}^{\mu\nu} = & P \cdot (W_1 - W_2) i \epsilon^{\mu\nu\rho\sigma} W_{1\rho} W_{2\sigma} - \frac{1}{2} (k_1^2 + k_2^2 - P \cdot X) i \epsilon^{\mu\nu\rho\sigma} X_\rho (W_1 + W_2)_\sigma \\ & + W_1^\mu i \epsilon^{\nu\rho\sigma\omega} X_\rho W_{1\sigma} W_{2\omega} + W_2^\nu i \epsilon^{\mu\rho\sigma\omega} X_\rho W_{1\sigma} W_{2\omega}, \end{aligned} \quad (\text{K.59})$$

The eq. (K.50) complies with the Ward identity,

$$k_{1\mu} \langle N(p') | J_{em}^\mu J_{em}^\nu | N(p) \rangle = 0, \quad (\text{K.60})$$

and

$$k_{2\nu} \langle N(p') | J_{em}^\mu J_{em}^\nu | N(p) \rangle = 0. \quad (\text{K.61})$$

In eq. (K.50),  $F_7$  and  $\tilde{F}_1$  to  $\tilde{F}_5$  receives contributions from the interchange of a pseudoscalar.

In the case of the proton,  $F_6$  receives contributions from QED at tree level

$$F_6 = D_B^{-1}(W_1^2) D_B^{-1}(W_2^2), \quad (\text{K.62})$$

where  $D_B(s) = m_B^2 - s$ .

Some useful relations that we get using the Schouten identity are:

$$\begin{aligned} & \bar{u}(p') i \epsilon^{\mu\nu\rho\sigma} X_\rho (W_1 - W_2)_\sigma \gamma^5 u(p) \\ & = \frac{1}{2m_B} \bar{u}(p') \left\{ \left( \gamma^\mu \gamma^5 i \epsilon^{\nu\rho\sigma\beta} - \gamma^\nu \gamma^5 i \epsilon^{\mu\rho\sigma\beta} \right) X_\rho (W_1 + W_2)_\sigma (W_1 - W_2)_\beta \right. \\ & \quad \left. + i \epsilon^{\mu\nu\rho\beta} X_\rho (W_1 + W_2)_\beta (k_1 - k_2) \gamma^5 \right\} u(p), \end{aligned} \quad (\text{K.63})$$

and

$$\begin{aligned} & i \epsilon^{\mu\nu\rho\sigma} X_\rho (W_1 - W_2)_\sigma (k_1 - k_2) \gamma^5 \\ & = (W_1 - W_2)^2 i \epsilon^{\mu\nu\rho\beta} \gamma_\beta \gamma^5 X_\rho - X \cdot (W_1 - W_2) i \epsilon^{\mu\nu\sigma\beta} \gamma_\beta \gamma^5 (W_1 - W_2)_\sigma \\ & \quad - \left[ (W_1 - W_2)^\mu i \epsilon^{\nu\rho\sigma\beta} - (W_1 - W_2)^\nu i \epsilon^{\mu\rho\sigma\beta} \right] \gamma_\beta \gamma^5 X_\rho (W_1 - W_2)_\sigma. \end{aligned} \quad (\text{K.64})$$

If we recall

$$\gamma^\mu \gamma^\nu \gamma^\rho = g^{\mu\nu} \gamma^\rho - g^{\mu\rho} \gamma^\nu + g^{\nu\rho} \gamma^\mu + i \epsilon^{\mu\nu\rho\sigma} \gamma_\sigma \gamma^5, \quad (\text{K.65})$$

using eq. (K.64) and eq. (K.65), we get

$$\begin{aligned} & \bar{u}(p') i \epsilon^{\mu\nu\rho\sigma} X_\rho (W_1 - W_2)_\sigma (\not{k}_1 - \not{k}_2) \gamma^5 u(p) \\ &= \bar{u}(p') \left\{ [(W_1 - W_2)^\mu (W_1 + W_2)^\nu - (W_1 - W_2)^\nu (W_1 + W_2)^\mu] (\not{k}_1 - \not{k}_2) \right. \\ & \quad + \frac{1}{2} X \cdot (W_1 - W_2) \mathbb{A}^{\mu\nu} - [(W_1 - W_2)^\mu \gamma^\nu - (W_1 - W_2)^\nu \gamma^\mu] (W_1^2 - W_2^2) \\ & \quad \left. + [(W_1 + W_2)^\mu \gamma^\nu - (W_1 + W_2)^\nu \gamma^\mu] (W_1 - W_2)^2 \right\} u(p), \end{aligned} \quad (\text{K.66})$$

and

$$\begin{aligned} & \bar{u}(p') i \epsilon^{\mu\nu\rho\sigma} X_\rho (W_1 - W_2)_\sigma \gamma^5 u(p) \\ &= -\frac{1}{2m_B} \bar{u}(p') \left\{ [X^\mu (W_1 + W_2)^\nu - X^\nu (W_1 + W_2)^\mu] (\not{k}_1 - \not{k}_2) \right. \\ & \quad + \frac{1}{2} X^2 \mathbb{A}^{\mu\nu} - [X^\mu \gamma^\nu - X^\nu \gamma^\mu] (W_1^2 - W_2^2) \\ & \quad \left. + [(W_1 + W_2)^\mu \gamma^\nu - (W_1 + W_2)^\nu \gamma^\mu] X \cdot (W_1 - W_2) \right\} u(p), \end{aligned} \quad (\text{K.67})$$

where

$$\mathbb{A}^{\mu\nu} \equiv \gamma^\mu (\not{W}_1 - \not{W}_2) \gamma^\nu - \gamma^\nu (\not{W}_1 - \not{W}_2) \gamma^\mu, \quad (\text{K.68})$$

with

$$k_{1\mu} \bar{u}(p') \mathbb{A}^{\mu\nu} u(p) = \bar{u}(p') \{ 2k_1 \cdot (W_1 + W_2) \gamma^\nu - 2\not{k}_1 (W_1 + W_2)^\nu \} u(p) \quad (\text{K.69a})$$

$$k_{2\nu} \bar{u}(p') \mathbb{A}^{\mu\nu} u(p) = \bar{u}(p') \{ 2k_2 \cdot (W_1 + W_2) \gamma^\mu - 2\not{k}_2 (W_1 + W_2)^\mu \} u(p). \quad (\text{K.69b})$$

The term proportional to  $F_6$  in eq. (K.50) can be written as

$$\begin{aligned}
& \bar{u}(p') \left[ D_B(W_2^2) \gamma^\mu (\not{W}_1 + m_B) \gamma^\nu + D_B(W_1^2) \gamma^\nu (\not{W}_2 + m_B) \gamma^\mu \right] u(p) \\
&= \bar{u}(p') \left\{ \frac{1}{4} (D_B(W_2^2) + D_B(W_1^2)) \mathbb{A}^{\mu\nu} - \frac{1}{2} (D_B(W_2^2) - D_B(W_1^2)) g^{\mu\nu} (\not{W}_1 - \not{W}_2) \right. \\
&\quad - \frac{1}{2} (D_B(W_2^2) - D_B(W_1^2)) [X^\mu \gamma^\nu - X^\nu \gamma^\mu] \\
&\quad + \frac{1}{2} (D_B(W_2^2) + D_B(W_1^2)) [(W_1 + W_2)^\mu \gamma^\nu + (W_1 + W_2)^\nu \gamma^\mu] \\
&\quad \left. + \frac{1}{2} (D_B(W_2^2) - D_B(W_1^2)) [(W_1 - W_2)^\mu \gamma^\nu + (W_1 - W_2)^\nu \gamma^\mu] \right\} u(p)
\end{aligned} \tag{K.70}$$

Hence  $F_6$  is already in  $F_i$  and  $G_j$  for  $i = 7, 8, 9, 10$  and  $j = 1, 2, 3, 4$ , respectively. Therefore it should be omitted in the decomposition eq. (K.50).

### K.3 Goldberger-Treiman (GT) relation

It is possible to split the contributions of the eq. (K.2) using the projectors in eq. (K.31),

$$\begin{aligned}
\langle N(p') | A_\mu^a | N(p) \rangle &= \bar{u}(p') \left[ \frac{2M_N}{t} G_A(t) + \frac{1}{2M_N} G_P(t) \right] (p' - p)_\mu \gamma^5 \frac{\tau^a}{2} u(p) \quad \{\mathbf{L}\} \\
&\quad + \bar{u}(p') \left[ \gamma_\mu - \frac{2M_N}{t} (p' - p)_\mu \right] G_A(t) \gamma^5 \frac{\tau^a}{2} u(p) \quad \{\mathbf{T}\},
\end{aligned} \tag{K.71}$$

if we take the divergence of eq. (K.71), we recover eq. (K.3). Including the results from eqs. (K.18) and (K.33) for  $t = 0$ ,

$$\partial^\mu \langle N(p') | A_\mu^a | N(p) \rangle = \left[ 2M_N g_0^a + \frac{2M_N F_A^a H_A}{M_A} \right] u(p') i \gamma^5 \frac{\tau^a}{2} u(p), \tag{K.72}$$

we get

$$g_A M_N = \sum_P g_{PNN} f_P^a + \sum_A \frac{M_N F_A^a H_A}{M_A} \tag{K.73}$$

where  $G_A(0) \equiv g_A = 1.2762(5)$  [798] is the axial-vector coupling constant which is measured in (polarized) neutron beta decays. The relation in eq. (K.73) reminds us the usual GT relation [823],  $g_0 M_N = g_{\pi NN} f_\pi$ .

## K.4 $P \rightarrow \ell\ell$ decays

We know that the most general structure for  $P \rightarrow \gamma^* \gamma^*$  transitions, which complies with gauge and Lorentz invariance, is given by [825]

$$\begin{aligned} \langle P | J_{em}^\mu J_{em}^\nu | 0 \rangle = & \left\{ F_{P\gamma^* \gamma^*}(k_1^2, k_2^2) \epsilon^{\mu\nu\rho\sigma} k_{1\rho} k_{2\sigma} + F_{P\gamma^* \gamma^*}^{CP1}(k_1^2, k_2^2) (k_1 \cdot k_2 g^{\mu\nu} - k_2^\mu k_1^\nu) \right. \\ & \left. + F_{P\gamma^* \gamma^*}^{CP2}(k_1^2, k_2^2) (k_1^2 k_2^2 g^{\mu\nu} + k_1 \cdot k_2 k_1^\mu k_2^\nu - k_2^2 k_1^\mu k_1^\nu - k_1^2 k_2^\mu k_2^\nu) \right\} \epsilon_\mu^*(k_1) \epsilon_\nu^*(k_2), \end{aligned} \quad (\text{K.74})$$

where  $F_{P\gamma^* \gamma^*}$  is C- and P-conserving,  $F_{P\gamma^* \gamma^*}^{CP1}$  and  $F_{P\gamma^* \gamma^*}^{CP2}$  are C-conserving. The last two are both  $CP$ -violating.  $F_{P\gamma^* \gamma^*}$ ,  $F_{P\gamma^* \gamma^*}^{CP1}$  and  $F_{P\gamma^* \gamma^*}^{CP2}$  are symmetric under  $k_1 \leftrightarrow k_2$ .

From the eq. (1.111), we can obtain the  $P\gamma\gamma$  Lagrangian (after interchanging  $\epsilon_{\mu\nu\rho\sigma}$  by  $-\epsilon^{\mu\nu\rho\sigma}$ ):

$$\begin{aligned} \mathcal{L}_{P\gamma\gamma} &= \frac{\sqrt{2}\alpha N_C}{8\pi F} \epsilon^{\mu\nu\alpha\beta} F_{\mu\nu} F_{\alpha\beta} \langle \phi Q^2 \rangle \\ &= \frac{\alpha N_C}{24\pi F} \epsilon^{\mu\nu\alpha\beta} F_{\mu\nu} F_{\alpha\beta} \left( \pi^0 + \frac{1}{3}(5C_q - \sqrt{2}C_s)\eta + \frac{1}{3}(5C_{q'} + \sqrt{2}C_{s'})\eta' \right). \end{aligned} \quad (\text{K.75})$$

Thus,

$$\langle P^0(k_1 + k_2) | j_{em}^\mu j_{em}^\nu | 0 \rangle = i r_P \frac{\alpha N_C}{3\pi F} \epsilon^{\mu\nu\rho\sigma} k_{1\rho} k_{2\sigma} \epsilon_\mu(k_1) \epsilon_\nu(k_2) \quad (\text{K.76})$$

where

$$r_P = \begin{cases} 1 & \text{if } P = \pi^0, \\ \frac{1}{3}(5C_q - \sqrt{2}C_s) & \text{if } P = \eta, \\ \frac{1}{3}(5C_{q'} + \sqrt{2}C_{s'}) & \text{if } P = \eta'. \end{cases} \quad (\text{K.77})$$

Therefore, the WZW action is responsible for the decays  $\pi^0 \rightarrow 2\gamma$  and  $\eta \rightarrow 2\gamma$ , and the interaction vertices  $\gamma 3\pi$  and  $\gamma\pi^+\pi^-\eta$ . The chiral anomaly makes a very stringent non-perturbative prediction for the  $\pi^0$  decay width,

$$\Gamma[\pi^0 \rightarrow \gamma\gamma] = \left(\frac{N_C}{3}\right)^2 \frac{\alpha^2 m_\pi^3}{64\pi^3 F^2} \simeq 7.7 \text{ eV}, \quad (\text{K.78})$$

which is in excellent agreement with the experimental measurement,  $\Gamma[\pi^0 \rightarrow \gamma\gamma] = (7.72 \pm 0.12) \text{ eV}$  [3].

Using the Eq. (K.74), we can calculate the amplitude for  $P \rightarrow \ell\ell$  decays (see fig. K.2).

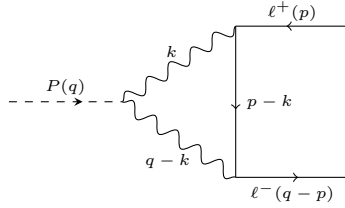


Figure K.2: Contributions to the  $P \rightarrow \ell\ell$  decays via a  $P$  coupling to  $\gamma\gamma$ .

Thus,

$$i\mathcal{M} = i \left[ g_P \bar{u}(q-p) i\gamma^5 v(p) + g_S \bar{u}(q-p) v(p) \right], \quad (\text{K.79})$$

with

$$g_P = -2\alpha^2 m_\ell \mathcal{A}(q^2) F_{P\gamma\gamma}(0) \quad (\text{K.80})$$

and

$$g_S = -i \frac{2\alpha^2 m_\ell}{\pi^2 q^2 \beta_\ell^2} \int d^4k \frac{F_{P\gamma^*\gamma^*}^{CP1}(k^2, (q-k)^2) w_1 + F_{P\gamma^*\gamma^*}^{CP2}(k^2, (q-k)^2) w_2}{k^2 (q-k)^2 [(p-k)^2 - m_\ell^2]}, \quad (\text{K.81})$$

where  $w_1 = k \cdot (q-k) l^2 + k \cdot l [k^2 + (k-q)^2]$ ,  $w_2 = k^2 (k-q)^2 l \cdot (l-2k)$ ,  $l \equiv p_{\ell^-} - p_{\ell^+} = q - 2p$ , and  $\beta_\ell = \sqrt{1 - 4m_\ell/q^2}$ . As we can see from Eqs. (K.80) and (K.81),  $g_P$  and  $g_S$  are  $CP$ -even and  $CP$ -odd, respectively.

$\mathcal{A}(q^2)$  is given by the loop integral

$$\mathcal{A}(q^2) = \frac{2i}{\pi^2 q^2} \int d^4k \frac{(q^2 k^2 - (q \cdot k)^2) \tilde{F}_{P\gamma^*\gamma^*}(k^2, (q-k)^2)}{k^2 (q-k)^2 [(p-k)^2 - m_\ell^2]} \quad (\text{K.82})$$

which is written in terms of the normalized TFF  $\tilde{F}_{P\gamma^*\gamma^*}(k^2, (q-k)^2)$ , where  $\tilde{F}_{P\gamma^*\gamma^*}(0, 0) = 1$ .

The expression for  $g_S$  in Eq. (K.81) is equal to that in Eq. (3.4) in Ref. [825] when  $p_{\ell^+}$  and  $p_{\ell^-}$  are interchanged.

The unpolarized spin-averaged squared matrix element  $\overline{\mathcal{M}^2}$  is given by

$$\overline{\mathcal{M}^2} = 2q^2 |g_P|^2 + 2q^2 \beta_\ell^2 |g_S|^2. \quad (\text{K.83})$$

Then, the decay width is

$$\Gamma_{P \rightarrow \ell\ell} = \frac{1}{8\pi} M_P \beta_\ell \left( |g_P|^2 + \beta_\ell^2 |g_S|^2 \right) \Big|_{q^2=M_P^2}. \quad (\text{K.84})$$

### K.4.1 Pseudoscalar meson exchange

The contribution to the HFS in muonic hydrogen due to the exchange of a pseudoscalar meson is shown in fig. K.3.

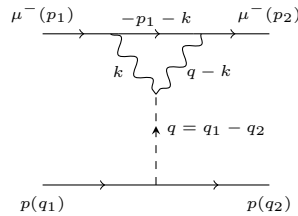


Figure K.3: Muon-proton interaction produced by a pseudoscalar exchange.

The amplitude of this interaction is given by

$$\begin{aligned}
i\mathcal{M}_P &= [\bar{N}(q_2)\Gamma^{(p)}N(q_1)][i\mathcal{D}_P(q^2)][\bar{\ell}(p_2)\Gamma^{(\mu)}\ell(p_1)] \\
&= \left[ ig_{PNN}\bar{u}(q_2)i\gamma^5u(q_1) \right] \frac{i}{q^2 - m_P^2} \left[ ig_P\bar{u}(p_2)i\gamma^5u(p_1) \right] \\
&= -i2m_\mu g_{PNN}\alpha^2 F_{P\gamma\gamma}(0) \frac{\mathcal{A}(q^2)}{q^2 - m_P^2} [\bar{u}(q_2)\gamma^5u(q_1)][\bar{u}(q_2)\gamma^5u(q_1)]
\end{aligned} \tag{K.85}$$

where we have neglected the contribution from the  $g_S$  coupling in Eq. (K.79). This is a good approximation since CP is conserved approximately.  $\mathcal{A}(q^2)$  is defined according to Eq. (K.82) with  $q \equiv p_2 - p_1 = q_1 - q_2$  and  $p = -p_1$ .

We can use the relations given in Eqs. (K.86) and (K.87),

$$u_r(p) = \begin{pmatrix} \sqrt{p \cdot \bar{\sigma}} \xi_r \\ \sqrt{p \cdot \sigma} \xi_r \end{pmatrix} = \sqrt{\frac{E+m}{2}} \begin{pmatrix} \left(1 - \frac{\vec{\sigma} \cdot \vec{p}}{E+m}\right) \xi_r \\ \left(1 + \frac{\vec{\sigma} \cdot \vec{p}}{E+m}\right) \xi_r \end{pmatrix}, \tag{K.86}$$

$$v_r(p) = \begin{pmatrix} \sqrt{p \cdot \sigma} \eta_r \\ -\sqrt{p \cdot \bar{\sigma}} \eta_r \end{pmatrix} = \sqrt{\frac{E+m}{2}} \begin{pmatrix} \left(1 - \frac{\vec{\sigma} \cdot \vec{p}}{E+m}\right) \eta_r \\ -\left(1 + \frac{\vec{\sigma} \cdot \vec{p}}{E+m}\right) \eta_r \end{pmatrix}, \tag{K.87}$$

where  $\sigma^\mu = (1, \vec{\sigma})$  and  $\bar{\sigma}^\mu = (1, -\vec{\sigma})$ , to write the amplitude in terms of the two-component spinor.

Therefore,

$$\begin{aligned}
\bar{u}_r(p_2)\gamma^5u_{r'}(p_1) &= \sqrt{(E_1+m_1)(E_2+m_2)}\xi_r^\dagger \left[ \frac{\vec{\sigma} \cdot \vec{p}_1}{E_1+m_1} - \frac{\vec{\sigma} \cdot \vec{p}_2}{E_2+m_2} \right] \xi_{r'} \\
&\simeq \xi_r^\dagger [\vec{\sigma} \cdot (\vec{p}_1 - \vec{p}_2)] \xi_{r'},
\end{aligned} \tag{K.88}$$

and

$$\begin{aligned}
\bar{u}(p_2)\gamma^\mu\gamma^5u(p_1) &= \frac{\sqrt{(E_1+m_1)(E_2+m_2)}}{2}\xi_r^\dagger \left[ (\sigma - \bar{\sigma})^\mu + (\sigma + \bar{\sigma})^\mu \frac{\vec{\sigma} \cdot \vec{p}_1}{E_1+m_1} + \frac{\vec{\sigma} \cdot \vec{p}_2}{E_2+m_2}(\sigma + \bar{\sigma})^\mu \right. \\
&\quad \left. + \frac{\vec{\sigma} \cdot \vec{p}_2}{E_2+m_2}(\sigma - \bar{\sigma})^\mu \frac{\vec{\sigma} \cdot \vec{p}_1}{E_1+m_1} \right] \xi_{r'}, \\
&\simeq \xi_r^\dagger \left[ m(\sigma - \bar{\sigma})^\mu + \frac{1}{2}(\sigma + \bar{\sigma})^\mu \vec{\sigma} \cdot (\vec{p}_1 + \vec{p}_2) \right] \xi_{r'},
\end{aligned} \tag{K.89}$$

when  $m = m_1 = m_2$  in the nonrelativistic limit.

Thus,

$$i\mathcal{M}_P = i2m_\mu g_{PNN} \alpha^2 F_{P\gamma\gamma}(0) \frac{\mathcal{A}(q^2)}{q^2 - m_P^2} [\xi_r^\dagger \vec{\sigma} \cdot \vec{q} \xi_{r'}] [\xi_s^\dagger \vec{\sigma} \cdot \vec{q} \xi_{s'}], \quad (\text{K.90})$$

where  $q^2 \equiv (q_1 - q_2)^2 = (p_2 - p_1)^2 \simeq -|\vec{q}|^2$  since  $E_1 \simeq E_2 \simeq m$ .

The pseudoscalar exchange contribution to the nonrelativistic Yukawa potential in momentum space is given by

$$\begin{aligned} \Delta V_P^{HFS}(\vec{q}) &= -\frac{\mathcal{M}_P}{4m_\mu m_N} = \lambda \mathcal{A}(-|\vec{q}|^2) \frac{\vec{\sigma}^{(p)} \cdot \vec{q} \vec{\sigma}^{(\mu)} \cdot \vec{q}}{|\vec{q}|^2 + m_P^2}, \\ \lambda &= \frac{g_{PNN} \alpha^2 F_{P\gamma\gamma}(0)}{2m_N} \end{aligned} \quad (\text{K.91})$$

where  $m_N$  is the proton mass. We can obtain the potential in the configuration space by performing a Fourier transform

$$\begin{aligned} \Delta V_P^{HFS}(\vec{r}) &= \lambda \int \frac{d^3\vec{q}}{(2\pi)^3} e^{i\vec{q}\cdot\vec{r}} \mathcal{A}(-|\vec{q}|^2) \frac{\vec{\sigma}^{(p)} \cdot \vec{q} \vec{\sigma}^{(\mu)} \cdot \vec{q}}{|\vec{q}|^2 + m_P^2}, \\ \vec{r} &= \vec{x} - \vec{y}. \end{aligned} \quad (\text{K.92})$$

We split the corrections induced by the  $q^2$ -dependence on  $\mathcal{A}$  by using the dispersion relation representation of  $\mathcal{A}(-|\vec{q}|^2)$ ,

$$\mathcal{A}(-|\vec{q}|^2) = \mathcal{A}(0) - \frac{|\vec{q}|^2}{\pi} \int_0^\infty ds' \frac{\text{Im} \mathcal{A}(s')}{s'(s' + |\vec{q}|^2 + i\epsilon)}, \quad (\text{K.93})$$

neglecting the second term in Eq. (K.93) ( $q^2 \rightarrow 0$ ), we get

$$\begin{aligned} \Delta V_P^{HFS}(\vec{r}) &\simeq \lambda \mathcal{A}(0) \int \frac{d^3\vec{q}}{(2\pi)^3} e^{i\vec{q}\cdot\vec{r}} \frac{\vec{\sigma}^{(p)} \cdot \vec{q} \vec{\sigma}^{(\mu)} \cdot \vec{q}}{|\vec{q}|^2 + m_P^2} \\ &\simeq \lambda \mathcal{A}(0) [\vec{\sigma}^{(p)} \cdot \vec{\nabla}_x] [\vec{\sigma}^{(\mu)} \cdot \vec{\nabla}_y] \int \frac{d^3\vec{q}}{(2\pi)^3} \frac{e^{i\vec{q}\cdot\vec{r}}}{|\vec{q}|^2 + m_P^2}, \end{aligned} \quad (\text{K.94})$$

the integral corresponds to the static Yukawa potential

$$\int \frac{d^3\vec{q}}{(2\pi)^3} \frac{e^{i\vec{q}\cdot\vec{r}}}{|\vec{q}|^2 + m_P^2} = \frac{1}{4\pi r} e^{-m_P r}. \quad (\text{K.95})$$



Performing the differentiation, we obtain

$$\Delta V_P^{HFS}(\vec{r}) \simeq -\frac{m_P^2}{12\pi} \lambda \mathcal{A}(0) \left[ \vec{\sigma}^{(\mu)} \cdot \vec{\sigma}^{(p)} V_{SS}^{(P)}(\vec{r}) + S_{12} V_T^{(P)}(\vec{r}) \right], \quad (\text{K.96})$$

where  $\vec{\sigma}^{(\mu)} \cdot \vec{\sigma}^{(p)}$  is called a spin exchange force and  $S_{12} = 3\vec{\sigma}^{(\mu)} \cdot \hat{r} \vec{\sigma}^{(p)} \cdot \hat{r} - \vec{\sigma}^{(\mu)} \cdot \vec{\sigma}^{(p)}$  a tensor force, and

$$V_{SS}^{(P)}(\vec{r}) = \frac{e^{-m_P r}}{r} - \frac{4\pi}{m_P^2} \delta^3(\vec{r}), \quad (\text{K.97a})$$

$$V_T^{(P)}(\vec{r}) = \left( 1 + \frac{3}{m_P r} + \frac{3}{m_P^2 r^2} \right) \frac{e^{-m_P r}}{r}. \quad (\text{K.97b})$$

$S_{12}$  is the so-called tensor operator and it vanishes for the  $S$  wave. Since  $\mu$  and  $p$  have spin 1/2, we find

$$\vec{\sigma}^{(\mu)} \cdot \vec{\sigma}^{(p)} = \begin{cases} 1 & S = 1 \\ -3 & S = 0 \end{cases} \quad (\text{K.98})$$

For the  $S$  wave, we have the following  $2S$  states:  $2S_{1/2}^{F=0}$  and  $2S_{1/2}^{F=1}$ . Now we can compute the expectation values for the Yukawa potential using the radial wave function for  $2S$  states,

$$\psi_{2S}(r) = \sqrt{\frac{(\mu\alpha)^3}{2}} e^{-\frac{\mu\alpha r}{2}} \left( 1 - \frac{\mu\alpha r}{2} \right), \quad (\text{K.99})$$

where  $\mu$  is the muon-proton reduced mass  $1/\mu = 1/m_\mu + 1/m_N$ .

Thus,

$$\begin{aligned} \langle 2S | V_{SS}^{(P)}(\vec{r}) | 2S \rangle &\equiv Y_S^{(P)}(m_P) = -\frac{(\mu\alpha)^4}{m_P^3} \frac{8 + 11\tilde{\alpha} + 8\tilde{\alpha}^2 + 2\tilde{\alpha}^3}{4(1 + \tilde{\alpha})^4}, \\ \tilde{\alpha} &= \frac{\mu\alpha}{m_P}. \end{aligned} \quad (\text{K.100})$$

Finally, we get the expressions for the shifts in the  $2S$  states of the muonic hydrogen,

$$\Delta E_P^{HFS}(2S) = \tilde{\lambda} Y_S^{(P)}(m_P) \quad \text{for } 2S_{1/2}^{F=1}, \quad (\text{K.101a})$$

$$\Delta E_P^{HFS}(2S) = -3\tilde{\lambda} Y_S^{(P)}(m_P) \quad \text{for } 2S_{1/2}^{F=0}, \quad (\text{K.101b})$$

where  $\tilde{\lambda} \equiv -\frac{m_P^2}{12\pi}\lambda\mathcal{A}(0)$ . We recover the same results as in Ref. [812].

The  $q^2$ -dependence on  $\mathcal{A}$  induces a correction to the potential in Eq. (K.94), which is given by

$$\delta V_P^{HFS}(\vec{r}) = \frac{\lambda}{12\pi^2} \int_0^\infty ds' \frac{\text{Im}\mathcal{A}(s')}{s'(s' - m_P^2 + i\epsilon)} \left[ \vec{\sigma}^{(p)} \cdot \vec{\sigma}^{(\mu)} h_1^{(P)}(r, s') + S_{12} h_2^{(P)}(r, s') \right] \quad (\text{K.102})$$

where

$$h_1^{(P)}(r, s') = \frac{s'^2 e^{-\sqrt{s'}r} - m_P^4 e^{-m_P r}}{r} - 4\pi(s' - m_P^2) \delta^3(\vec{r}) \quad (\text{K.103})$$

and

$$h_2^{(P)}(r, s') = s'^2 \left( 1 + \frac{3}{\sqrt{s'}r} + \frac{3}{s'r^2} \right) \frac{e^{-\sqrt{s'}r}}{r} - m_P^4 \left( 1 + \frac{3}{m_P r} + \frac{3}{m_P^2 r^2} \right) \frac{e^{-m_P r}}{r}. \quad (\text{K.104})$$

Using the Eqs. (K.96) and (K.102), which are compatible with the results in [812], we get

$$\begin{aligned} \Delta V_P^{HFS}(\vec{r}) &= 2S_{1/2}^{F=1} - 2S_{1/2}^{F=0} \\ &= \frac{2g_{PNN}\alpha^2 F_{P\gamma\gamma}(0)}{3m_N} \left\{ \mathcal{A}(0) \left[ \delta(\vec{r}) - \frac{m_P^2}{4\pi r} e^{-m_P r} \right] \right. \\ &\quad \left. - \frac{1}{\pi} \int_0^\infty ds' \frac{\text{Im}\mathcal{A}(s')}{s'} \left[ \delta(\vec{r}) + \frac{1}{4\pi r(s' - m_P^2)} \left( m_P^4 e^{-m_P r} - s'^2 e^{-\sqrt{s'}r} \right) \right] \right\} \end{aligned} \quad (\text{K.105})$$

with

$$F_{P\gamma\gamma}(0) = r_P \frac{N_C}{12\pi^2 F}, \quad r_P = \begin{cases} 1 & \text{if } P = \pi^0, \\ \frac{1}{3}(5C_q - \sqrt{2}C_s) & \text{if } P = \eta, \\ \frac{1}{3}(5C_{q'} + \sqrt{2}C_{s'}) & \text{if } P = \eta'. \end{cases} \quad (\text{K.106})$$

for  $P = \pi$ , we recover the expression in Eq. (17) for the potential in Ref. [785].

Therefore, the expectation value for a  $2S$  state is

$$\langle 2S | h_1^{(P)}(r, s') | 2S \rangle = s'^2 Y_S^{(P)}(\sqrt{s'}) - m_P^4 Y_S^{(P)}(m_P). \quad (\text{K.107})$$

So, the overall contribution to the shifts for a  $2S$  state is given by

$$\Delta E_P^{HFS} = \frac{m_P^2}{12\pi} \lambda \langle \vec{\sigma}^{(p)} \cdot \vec{\sigma}^{(\mu)} \rangle (-\mathcal{A}(0) + \delta\mathcal{A}) Y_S^{(P)}(m_P) \quad (\text{K.108})$$

where

$$\delta\mathcal{A} = \frac{2}{\pi} \int_0^\infty dx \frac{\text{Im} \mathcal{A}(m_P^2 x^2)}{x(x^2 - 1 + i\epsilon)} \left[ x^4 \frac{Y_S^{(P)}(m_P x)}{Y_S^{(P)}(m_P)} - 1 \right], \quad (\text{K.109})$$

which is the same result for  $\delta\mathcal{A}_2$  in Ref. [812] when  $\Lambda_\pi \rightarrow \infty$ .

# Appendix L

## Transition form factors

In this appendix, we describe the different models for the  $B_{2S}(q_1^2, q_2^2)$  form factor used in the main text. Specifically, we discuss different variants in order to study the relevance of the asymptotic behavior. In particular, for the doubly-virtual symmetric kinematics one has the result in eq. (9.17) (see also Ref. [788]), enforcing  $B_{2S}(-Q^2, -Q^2) \sim \mathcal{O}(Q^{-4})$  for large  $Q^2$  values. In addition, in the singly-virtual kinematic regime, it is also known from the light-cone expansion that, for large  $Q^2$  values,  $B_{2S}(-Q^2, -q^2) \sim \mathcal{O}(Q^{-4})$ , where  $q^2 \ll Q^2$  [783, 788], that is also suggested by L3 data [792, 793].

The most simple form factor corresponds to the standard VMD prescription

$$B_{2S}^{\text{VMD}}(q_1^2, q_2^2) = \frac{B_{2S}(0, 0)m_V^4}{(q_1^2 - m_V^2)(q_2^2 - m_V^2)}, \quad (\text{L.1})$$

that, however, fails to describe the singly- and doubly-virtual asymptotic behavior, but is relevant to our discussion regarding  $A \rightarrow e^+e^-$  decays. A variant that incorporates the appropriate high-energy behavior for singly-virtual kinematics is an extended VMD (eVMD) model with two resonances

$$B_{2S}^{\text{eVMD/DIP}}(q_1^2, q_2^2) = \frac{B_{2S}(0, 0)m_V^4 M^4}{(q_1^2 - m_V^2)(q_1^2 - M^2)(q_2^2 - m_V^2)(q_2^2 - M^2)}, \quad (\text{L.2})$$

that still fails reproducing the OPE. A simplified variant of this model is the common dipole

parametrization used in [784, 792, 793], where  $m_V = M$  and that we denote as DIP. We can amend this in a VMD incorporating the high-energy behavior (heVMD/heDIP) as follows

$$B_{2S}^{\text{he(VMD/DIP)}}(q_1^2, q_2^2) = \frac{B_{2S}(0, 0)m_V^4 M^4 [1 + q_1^2 q_2^2 \Lambda_{\text{OPE}}^{-4}]}{(q_1^2 - m_V^2)(q_1^2 - M^2)(q_2^2 - m_V^2)(q_2^2 - M^2)}. \quad (\text{L.3})$$

Still, we note that such a form factor does not fulfill the appropriate high-energy behavior for  $B_{2S}(-Q^2, -q^2)$  unless  $q^2 = 0$ . To better reproduce the high-energy behavior, we introduce the following form factor from Ref. [603] inspired in [608], that we label as OPE,

$$B_{2S}^{\text{OPE}}(q_1^2, q_2^2) = \frac{B_{2S}(0, 0)\Lambda_A^4}{(q_1^2 + q_2^2 - \Lambda_A^2)^2}. \quad (\text{L.4})$$

It describes L3 Collaboration results provided  $\Lambda_A$  is chosen according to the dipole parameters in L3 [792, 793] and its doubly-virtual space-like behavior is in good agreement with the holographic results in Ref. [601], representing our preferred choice.

For the normalization, we take the values for  $f_1, f'_1$  from L3 [792, 793] together with our estimate in [603, 618] for the  $a_1$ :  $B_{2S}(0, 0) = \{0.269(30), 0.197(30), 0.245(63)\}\text{GeV}^{-2}$  for  $\{f_1, f'_1, a_1\}$ . Regarding the mass parameter, we take both, for the OPE and (he)DIP variants,  $m_V = M = \Lambda_A = \{1.04(8), 0.926(79), 1.0(1)\} \text{ GeV}$ , see Refs. [603, 618, 792, 793]. Concerning the eVMD and heVD models, we fix the  $M$  parameter to reproduce the slope from the L3 Collaboration dipole in order to share the same low-energy behavior, which is accomplished adopting  $M^2 = \frac{\Lambda_A^2 m_V^2}{2m_V^2 - \Lambda_A^2} \sim 2 \text{ GeV}$  for  $m_V = 0.77 \text{ GeV}$ . Finally, to ensure the OPE behavior in eq. (9.17) in he(VMD/DIP) models, we find for ideal/L3 mixing

$$\Lambda_{\text{OPE}}^{f_1, f'_1, a_1} / m_V M = \{1.28(4)/1.37(5), 1.58(7)/1.26(6), 1.44(10)\} \text{ GeV}^{-1}, \quad (\text{L.5})$$

respectively. In the equation above, we have employed the following mixing scheme

$$\begin{pmatrix} f_1 \\ f'_1 \end{pmatrix} = \begin{pmatrix} \cos \theta & -\sin \theta \\ \sin \theta & \cos \theta \end{pmatrix} \begin{pmatrix} f^8 \\ f^0 \end{pmatrix}, \quad (\text{L.6})$$

where  $\theta$  is the mixing angle between the  $SU(3)$  singlet ( $f^0$ ) and octet ( $f^8$ ) states. Also, it is possible to write the last expression as

$$\begin{pmatrix} f_1 \\ f'_1 \end{pmatrix} = \begin{pmatrix} \cos \phi & -\sin \phi \\ \sin \phi & \cos \phi \end{pmatrix} \begin{pmatrix} f^{NS} \\ f^S \end{pmatrix}, \quad (\text{L.7})$$

where  $\phi$  is the mixing angle between the non-strange ( $f^{NS}$ ) and strange ( $f^S$ ) states.  $\theta$  and  $\phi$  are related through  $\theta = \phi - \phi_0$  with  $\phi_0 = \arctan \sqrt{2}$  and the ideal mixing angle corresponds to  $\phi = 0$ . The angles above relate to the one used in L3 Coll. [792, 793] ( $\theta_A = 62(5)^\circ$ ) as  $\theta = \theta_A - \frac{\pi}{2}$  ( $\phi = \theta_A + \phi_0 - \frac{\pi}{2}$ ). In this study, and following Ref. [618], we take as our preferred value  $\phi = 0$ , while we will take into consideration the L3 mixing angle as an additional uncertainty. Note also recent discussions concerning the mixing angle in Refs. [795, 826].

# Appendix M

## Higher-order effects in the non-relativistic potential

In this section we justify the suppression of the terms that have been neglected in evaluating the nonrelativistic potential in eq. (9.11). In particular, we start noticing the suppression corresponding to the potential of the kind  $\tilde{V}_{NR}(\mathbf{q}^2) = (\mathbf{q} \cdot \hat{\boldsymbol{\sigma}}_\ell)(\mathbf{q} \cdot \hat{\boldsymbol{\sigma}}_N)[m_A^2(m_A^2 + \mathbf{q}^2)]^{-1}$ , that in position space reads

$$\begin{aligned} V_{NR}(r) &= \frac{1}{3} \frac{\delta^{(3)}(r)}{m_A^2} \langle \hat{\boldsymbol{\sigma}}_\ell \cdot \hat{\boldsymbol{\sigma}}_N \rangle - \frac{1}{3} \frac{e^{-m_A r}}{4\pi r} \left[ S_{12} \left( 1 + \frac{3}{rm_A} + \frac{3}{(rm_A)^2} \right) + \langle \hat{\boldsymbol{\sigma}}_\ell \cdot \hat{\boldsymbol{\sigma}}_N \rangle \right], \\ &\Rightarrow \frac{1}{3} \left[ \frac{\delta^{(3)}(r)}{m_A^2} - \frac{e^{-m_A r}}{4\pi r} \right] \langle \hat{\boldsymbol{\sigma}}_\ell \cdot \hat{\boldsymbol{\sigma}}_N \rangle, \end{aligned} \quad (\text{M.1})$$

where in the last line we have omitted  $S_{12} = (3\hat{r}^i\hat{r}^j - \delta^{ij})\hat{\boldsymbol{\sigma}}_\ell^i\hat{\boldsymbol{\sigma}}_N^j$ , that is a rank-2 symmetric tensor and does not contribute to  $S$ -wave states. Accounting for this, the result reduces to the combination of the  $\delta^{(3)}(r)$  contribution and the Yukawa part in eqs. (9.13) and (9.14). Noting that  $|\Psi_{1(2),0,0}(0)|^2 = (\mu\alpha)^3/[(8)\pi]$ , the cancellation of the Yukawa and  $\delta$  terms in

eq. (M.1) to leading order in  $(\mu\alpha/m_A)$  is clear, with the final result reading

$$\Delta E_1^{\text{HFS}} = \left[ \frac{4(\mu\alpha)^4}{3\pi m_A^3} \frac{1+\epsilon}{(1+2\epsilon)^2} \right] \langle \hat{\boldsymbol{\sigma}}_\ell \cdot \hat{\boldsymbol{\sigma}}_N \rangle_{(F=1-F=0)}, \quad (\text{M.2})$$

$$\Delta E_2^{\text{HFS}} = \left[ \frac{(\mu\alpha)^4}{48\pi m_A^3} \frac{8+11\epsilon+8\epsilon^2+2\epsilon^3}{(1+\epsilon)^4} \right] \langle \hat{\boldsymbol{\sigma}}_\ell \cdot \hat{\boldsymbol{\sigma}}_N \rangle_{(F=1-F=0)}, \quad (\text{M.3})$$

where  $\epsilon = \mu\alpha/m_A$ . With these results at hand, it is straightforward to show the suppression from the  $A_1(\mathbf{q}^2)$  dependence. Noting  $A_1(q^2) = A_1(0) + \frac{q^2}{\pi} \int d\xi \frac{\text{Im} A(\xi)}{\xi - q^2}$ , the first term corresponds to our main result, whereas the second one leads to a potential of the kind  $V(r) = \frac{1}{\pi} \int d\xi \text{Im} A(\xi) \xi \left[ \frac{e^{-\sqrt{\xi}r}}{4\pi r} - \frac{\delta^{(3)}(r)}{\xi} \right]$  that, in parallel with eq. (M.1), is  $\alpha$  suppressed. Note in addition that the lower threshold in the previous integral corresponds to the intermediate  $V\gamma$  state, so one expects the relevant scale to be above  $m_V$ .



# Bibliography

- [1] B. Grzadkowski, M. Iskrzynski, M. Misiak, and J. Rosiek. Dimension-Six Terms in the Standard Model Lagrangian. *JHEP*, 10:085, 2010.
- [2] Antonio Pich. Effective Field Theory with Nambu-Goldstone Modes. 4 2018.
- [3] P. A. Zyla et al. Review of Particle Physics. *PTEP*, 2020(8):083C01, 2020.
- [4] Antonio Pich. Precision Tau Physics. *Prog. Part. Nucl. Phys.*, 75:41–85, 2014.
- [5] Yasmine Sara Amhis et al. Averages of  $b$ -hadron,  $c$ -hadron, and  $\tau$ -lepton properties as of 2018. *Eur. Phys. J.*, C81:226, 2021. updated results and plots available at <https://hflav.web.cern.ch/>.
- [6] T. Aoyama et al. The anomalous magnetic moment of the muon in the Standard Model. *Phys. Rept.*, 887:1–166, 2020.
- [7] M. Davier, A. Hoecker, G. Lopez Castro, B. Malaescu, X. H. Mo, G. Toledo Sanchez, P. Wang, C. Z. Yuan, and Z. Zhang. The Discrepancy Between tau and  $e^+e^-$  Spectral Functions Revisited and the Consequences for the Muon Magnetic Anomaly. *Eur. Phys. J. C*, 66:127–136, 2010.
- [8] Aldo Antognini, Franziska Hagelstein, and Vladimir Pascalutsa. The proton structure in and out of muonic hydrogen. 5 2022.
- [9] M. N. Achasov et al. Search for direct production of the  $f_1(1285)$  resonance in  $e^+e^-$  collisions. *Phys. Lett. B*, 800:135074, 2020.

- [10] Liping Gan, Bastian Kubis, Emilie Passemar, and Sean Tulin. Precision tests of fundamental physics with  $\eta$  and  $\eta'$  mesons. *Phys. Rept.*, 945:1–105, 2022.
- [11] R. Barate et al. Measurement of the spectral functions of vector current hadronic tau decays. *Z. Phys. C*, 76:15–33, 1997.
- [12] S. Anderson et al. Hadronic structure in the decay  $\tau \rightarrow \pi^- \pi^0 \nu_\tau$ . *Phys. Rev. D*, 61:112002, 2000.
- [13] L. M. Barkov et al. Electromagnetic Pion Form-Factor in the Timelike Region. *Nucl. Phys. B*, 256:365–384, 1985.
- [14] S. R. Amendolia et al. A Measurement of the Space - Like Pion Electromagnetic Form-Factor. *Nucl. Phys. B*, 277:168, 1986.
- [15] Francisco Guerrero and Antonio Pich. Effective field theory description of the pion form-factor. *Phys. Lett. B*, 412:382–388, 1997.
- [16] A. Pich and J. Portoles. The Vector form-factor of the pion from unitarity and analyticity: A Model independent approach. *Phys. Rev. D*, 63:093005, 2001.
- [17] A. Pich and J. Portoles. Vector form-factor of the pion: A Model independent approach. *Nucl. Phys. B Proc. Suppl.*, 121:179–182, 2003.
- [18] M. Fujikawa et al. High-Statistics Study of the  $\tau \rightarrow \pi^- \pi^0 \nu_\tau$  Decay. *Phys. Rev. D*, 78:072006, 2008.
- [19] D. Gómez Dumm and P. Roig. Dispersive representation of the pion vector form factor in  $\tau \rightarrow \pi \pi \nu_\tau$  decays. *Eur. Phys. J. C*, 73(8):2528, 2013.
- [20] J. P. Lees et al. Precise Measurement of the  $e^+e^- \rightarrow \pi^+\pi^-(\gamma)$  Cross Section with the Initial-State Radiation Method at BABAR. *Phys. Rev. D*, 86:032013, 2012.

- [21] Bernard Aubert et al. Precise measurement of the  $e^+ e^- \rightarrow \pi^+ \pi^- (\gamma)$  cross section with the Initial State Radiation method at BABAR. *Phys. Rev. Lett.*, 103:231801, 2009.
- [22] D. Epifanov et al. Study of  $\tau^- \rightarrow K(S) \pi^- \nu(\tau)$  decay at Belle. *Phys. Lett. B*, 654:65–73, 2007.
- [23] Matthias Jamin, Antonio Pich, and Jorge Portoles. What can be learned from the Belle spectrum for the decay  $\tau^- \rightarrow \nu(\tau) K(S) \pi^-$ . *Phys. Lett. B*, 664:78–83, 2008.
- [24] Matthias Jamin, Antonio Pich, and Jorge Portoles. Spectral distribution for the decay  $\tau^- \rightarrow \nu(\tau) K \pi$ . *Phys. Lett. B*, 640:176–181, 2006.
- [25] M. Jamin, J. A. Oller, and A. Pich. Scalar  $K \pi$  form factor and light quark masses. *Phys. Rev. D*, 74:074009, 2006.
- [26] Matthias Jamin, José Antonio Oller, and Antonio Pich. Order  $p^6$  chiral couplings from the scalar  $K\pi$  form-factor. *JHEP*, 02:047, 2004.
- [27] Matthias Jamin, Jose Antonio Oller, and Antonio Pich. Light quark masses from scalar sum rules. *Eur. Phys. J. C*, 24:237–243, 2002.
- [28] Sergi González-Solís and Pablo Roig. A dispersive analysis of the pion vector form factor and  $\tau^- \rightarrow K^- K_S \nu_\tau$  decay. *Eur. Phys. J. C*, 79(5):436, 2019.
- [29] K. Inami et al. Precise measurement of hadronic tau-decays with an eta meson. *Phys. Lett. B*, 672:209–218, 2009.
- [30] R. Escribano, S. González-Solís, M. Jamin, and P. Roig. Combined analysis of the decays  $\tau^- \rightarrow K_S \pi^- \nu_\tau$  and  $\tau^- \rightarrow K^- \eta \nu_\tau$ . *JHEP*, 09:042, 2014.
- [31] Alex Keshavarzi, Kim Siang Khaw, and Tamaki Yoshioka. Muon  $g-2$ : A review. *Nucl. Phys. B*, 975:115675, 2022.

- [32] Tatsumi Aoyama, Masashi Hayakawa, Toichiro Kinoshita, and Makiko Nio. Complete Tenth-Order QED Contribution to the Muon  $g-2$ . *Phys. Rev. Lett.*, 109:111808, 2012.
- [33] Alexander Keshavarzi, Daisuke Nomura, and Thomas Teubner. Muon  $g-2$  and  $\alpha(M_Z^2)$ : a new data-based analysis. *Phys. Rev. D*, 97(11):114025, 2018.
- [34] D. Giusti, F. Sanfilippo, and S. Simula. Light-quark contribution to the leading hadronic vacuum polarization term of the muon  $g-2$  from twisted-mass fermions. *Phys. Rev. D*, 98(11):114504, 2018.
- [35] D. Giusti, V. Lubicz, G. Martinelli, F. Sanfilippo, and S. Simula. Electromagnetic and strong isospin-breaking corrections to the muon  $g-2$  from Lattice QCD+QED. *Phys. Rev. D*, 99(11):114502, 2019.
- [36] Antoine Gérardin, Marco Cè, Georg von Hippel, Ben Hörz, Harvey B. Meyer, Daniel Mohler, Konstantin Ottnad, Jonas Wilhelm, and Hartmut Wittig. The leading hadronic contribution to  $(g-2)_\mu$  from lattice QCD with  $N_f = 2 + 1$  flavours of  $O(a)$  improved Wilson quarks. *Phys. Rev. D*, 100(1):014510, 2019.
- [37] C. T. H. Davies et al. Hadronic-vacuum-polarization contribution to the muon’s anomalous magnetic moment from four-flavor lattice QCD. *Phys. Rev. D*, 101(3):034512, 2020.
- [38] B. Chakraborty et al. Strong-Isospin-Breaking Correction to the Muon Anomalous Magnetic Moment from Lattice QCD at the Physical Point. *Phys. Rev. Lett.*, 120(15):152001, 2018.
- [39] Eigo Shintani and Yoshinobu Kuramashi. Hadronic vacuum polarization contribution to the muon  $g-2$  with 2+1 flavor lattice QCD on a larger than  $(10 \text{ fm})^4$  lattice at the physical point. *Phys. Rev. D*, 100(3):034517, 2019.
- [40] T. Blum, P. A. Boyle, V. Gülpers, T. Izubuchi, L. Jin, C. Jung, A. Jüttner, C. Lehner, A. Portelli, and J. T. Tsang. Calculation of the hadronic vacuum polarization con-

- tribution to the muon anomalous magnetic moment. *Phys. Rev. Lett.*, 121(2):022003, 2018.
- [41] Sz. Borsanyi et al. Hadronic vacuum polarization contribution to the anomalous magnetic moments of leptons from first principles. *Phys. Rev. Lett.*, 121(2):022002, 2018.
- [42] Christoph Lehner and Aaron S. Meyer. Consistency of hadronic vacuum polarization between lattice QCD and the R-ratio. *Phys. Rev. D*, 101:074515, 2020.
- [43] Sz. Borsanyi et al. Leading hadronic contribution to the muon magnetic moment from lattice QCD. *Nature*, 593(7857):51–55, 2021.
- [44] M. Della Morte, A. Francis, V. Gülpers, G. Herdoíza, G. von Hippel, H. Horch, B. Jäger, H. B. Meyer, A. Nyffeler, and H. Wittig. The hadronic vacuum polarization contribution to the muon  $g - 2$  from lattice QCD. *JHEP*, 10:020, 2017.
- [45] Bipasha Chakraborty, C. T. H. Davies, P. G. de Oliveira, J. Koponen, G. P. Lepage, and R. S. Van de Water. The hadronic vacuum polarization contribution to  $a_\mu$  from full lattice QCD. *Phys. Rev. D*, 96(3):034516, 2017.
- [46] Christopher Aubin, Thomas Blum, Cheng Tu, Maarten Golterman, Chulwoo Jung, and Santiago Peris. Light quark vacuum polarization at the physical point and contribution to the muon  $g - 2$ . *Phys. Rev. D*, 101(1):014503, 2020.
- [47] Alexander Keshavarzi, Daisuke Nomura, and Thomas Teubner.  $g-2$  of charged leptons,  $\alpha(M_Z^2)$ , and the hyperfine splitting of muonium. *Phys. Rev. D*, 101(1):014029, 2020.
- [48] M. Davier, A. Hoecker, B. Malaescu, and Z. Zhang. A new evaluation of the hadronic vacuum polarisation contributions to the muon anomalous magnetic moment and to  $\alpha(\mathbf{m}_Z^2)$ . *Eur. Phys. J. C*, 80(3):241, 2020. [Erratum: Eur.Phys.J.C 80, 410 (2020)].
- [49] Friedrich Jegerlehner. *The Anomalous Magnetic Moment of the Muon*, volume 274. Springer, Cham, 2017.

- [50] M. Benayoun, L. Delbuono, and F. Jegerlehner. BHLS<sub>2</sub>, a New Breaking of the HLS Model and its Phenomenology. *Eur. Phys. J. C*, 80(2):81, 2020. [Erratum: *Eur.Phys.J.C* 80, 244 (2020)].
- [51] Florian Burger, Xu Feng, Grit Hotzel, Karl Jansen, Marcus Petschlies, and Dru B. Renner. Four-Flavour Leading-Order Hadronic Contribution To The Muon Anomalous Magnetic Moment. *JHEP*, 02:099, 2014.
- [52] V. M. Aul'chenko et al. Measurement of the  $e^+ e^- \rightarrow \pi^+ \pi^-$  cross section with the CMD-2 detector in the 370 - 520-MeV c.m. energy range. *JETP Lett.*, 84:413–417, 2006.
- [53] R. R. Akhmetshin et al. High-statistics measurement of the pion form factor in the rho-meson energy range with the CMD-2 detector. *Phys. Lett. B*, 648:28–38, 2007.
- [54] M.N. Achasov et al. Update of the  $e^+ e^- \rightarrow \pi^+ \pi^-$  cross-section measured by SND detector in the energy region 400-MeV  $\leq s^{*1/2} \leq 1000$ -MeV. *J. Exp. Theor. Phys.*, 103:380–384, 2006.
- [55] Michel Davier. Low-Energy  $e^+e^-$  Hadronic Annihilation Cross Sections. *Ann. Rev. Nucl. Part. Sci.*, 63:407–434, 2013.
- [56] F. Ambrosino et al. Measurement of  $\sigma(e^+e^- \rightarrow \pi^+\pi^-\gamma(\gamma))$  and the dipion contribution to the muon anomaly with the KLOE detector. *Phys. Lett. B*, 670:285–291, 2009.
- [57] F. Ambrosino et al. Measurement of  $\sigma(e^+e^- \rightarrow \pi^+\pi^-)$  from threshold to 0.85 GeV<sup>2</sup> using Initial State Radiation with the KLOE detector. *Phys. Lett. B*, 700:102–110, 2011.
- [58] D. Babusci et al. Precision measurement of  $\sigma(e^+e^- \rightarrow \pi^+\pi^-\gamma)/\sigma(e^+e^- \rightarrow \mu^+\mu^-\gamma)$  and determination of the  $\pi^+\pi^-$  contribution to the muon anomaly with the KLOE detector. *Phys. Lett. B*, 720:336–343, 2013.

- [59] M. Ablikim et al. Measurement of the  $e^+e^- \rightarrow \pi^+\pi^-$  cross section between 600 and 900 MeV using initial state radiation. *Phys. Lett. B*, 753:629–638, 2016. [Erratum: *Phys.Lett.B* 812, 135982 (2021)].
- [60] T. Xiao, S. Dobbs, A. Tomaradze, Kamal K. Seth, and G. Bonvicini. Precision Measurement of the Hadronic Contribution to the Muon Anomalous Magnetic Moment. *Phys. Rev. D*, 97(3):032012, 2018.
- [61] M. N. Achasov et al. Measurements of the parameters of the  $\phi(1020)$  resonance through studies of the processes  $e^+e^- \rightarrow K^+K^-$ ,  $K_S K_L$ , and  $\pi^+\pi^-\pi^0$ . *Phys. Rev. D*, 63:072002, 2001.
- [62] R. R. Akhmetshin et al. Measurement of  $e^+e^- \rightarrow \phi \rightarrow K^+K^-$  cross section with the CMD-2 detector at VEPP-2M Collider. *Phys. Lett. B*, 669:217–222, 2008.
- [63] J. P. Lees et al. Precision measurement of the  $e^+e^- \rightarrow K^+K^-(\gamma)$  cross section with the initial-state radiation method at BABAR. *Phys. Rev. D*, 88(3):032013, 2013.
- [64] R. R. Akhmetshin et al. Measurement of omega meson parameters in  $\pi^+\pi^-\pi^0$  decay mode with CMD-2. *Phys. Lett. B*, 476:33–39, 2000.
- [65] Bernard Aubert et al. Study of  $e^+e^- \rightarrow \pi^+\pi^-\pi^0$  process using initial state radiation with BaBar. *Phys. Rev. D*, 70:072004, 2004.
- [66] M. N. Achasov et al. Study of the process  $e^+e^- \rightarrow \pi^+\pi^-\pi^0$  in the energy region  $s^{**}(1/2)$  from 0.98-GeV to 1.38-GeV. *Phys. Rev. D*, 66:032001, 2002.
- [67] V. M. Aul’chenko et al. Study of the  $e^+e^- \rightarrow \pi^+\pi^-\pi^0$  process in the energy range 1.05–2.00 GeV. *J. Exp. Theor. Phys.*, 121(1):27–34, 2015.
- [68] Bernard Aubert et al. The  $e^+e^- \rightarrow \pi^+\pi^-\pi^+\pi^-$ ,  $K^+K^-\pi^+\pi^-$ , and  $K^+K^-K^+K^-$  cross sections at center-of-mass energies 0.5-GeV - 4.5-GeV measured with initial-state radiation. *Phys. Rev. D*, 71:052001, 2005.

- [69] J. P. Lees et al. Initial-State Radiation Measurement of the  $e^+e^- \rightarrow \pi^+\pi^-\pi^+\pi^-$  Cross Section. *Phys. Rev. D*, 85:112009, 2012.
- [70] J. P. Lees et al. Measurement of the  $e^+e^- \rightarrow \pi^+\pi^-\pi^0\pi^0$  cross section using initial-state radiation at BABAR. *Phys. Rev. D*, 96(9):092009, 2017.
- [71] Bernard Aubert et al. The  $e^+e^- \rightarrow 2(\pi^+\pi^-)\pi^0$ ,  $2(\pi^+\pi^-)\eta$ ,  $K^+K^-\pi^+\pi^-\pi^0$  and  $K^+K^-\pi^+\pi^-\eta$  Cross Sections Measured with Initial-State Radiation. *Phys. Rev. D*, 76:092005, 2007. [Erratum: *Phys.Rev.D* 77, 119902 (2008)].
- [72] J. P. Lees et al. Study of the process  $e^+e^- \rightarrow \pi^+\pi^-\eta$  using initial state radiation. *Phys. Rev. D*, 97:052007, 2018.
- [73] R. R. Akhmetshin et al. Study of the process  $e^+e^- \rightarrow \pi^+\pi^-\pi^+\pi^-\pi^0$  with CMD-2 detector. *Phys. Lett. B*, 489:125–130, 2000.
- [74] V. M. Aulchenko et al. Measurement of the  $e^+e^- \rightarrow \eta\pi^+\pi^-$  cross section in the center-of-mass energy range 1.22-2.00 GeV with the SND detector at the VEPP-2000 collider. *Phys. Rev. D*, 91(5):052013, 2015.
- [75] R. R. Akhmetshin et al. Study of the process  $e^+e^- \rightarrow \pi^+\pi^-\pi^0\eta$  in the c.m. energy range 1394-2005 MeV with the CMD-3 detector. *Phys. Lett. B*, 773:150–158, 2017.
- [76] Bernard Aubert et al. The  $e^+e^- \rightarrow K^+K^-\pi^+\pi^-$ ,  $K^+K^-\pi^0\pi^0$  and  $K^+K^-\pi^+\pi^-$  cross-sections measured with initial-state radiation. *Phys. Rev. D*, 76:012008, 2007.
- [77] Bernard Aubert et al. Measurements of  $e^+e^- \rightarrow K^+K^-\eta$ ,  $K^+K^-\pi^0$  and  $K_s^0K^\pm\pi^\mp$  cross-sections using initial state radiation events. *Phys. Rev. D*, 77:092002, 2008.
- [78] J. P. Lees et al. Cross Sections for the Reactions  $e^+e^- \rightarrow K^+K^-\pi^+\pi^-$ ,  $K^+K^-\pi^0\pi^0$ , and  $K^+K^-\pi^+\pi^-$  Measured Using Initial-State Radiation Events. *Phys. Rev. D*, 86:012008, 2012.



- [79] J. P. Lees et al. Cross sections for the reactions  $e^+e^- \rightarrow K_S^0 K_L^0$ ,  $K_S^0 K_L^0 \pi^+ \pi^-$ ,  $K_S^0 K_S^0 \pi^+ \pi^-$ , and  $K_S^0 K_S^0 K^+ K^-$  from events with initial-state radiation. *Phys. Rev. D*, 89(9):092002, 2014.
- [80] J. P. Lees et al. Measurement of the  $e^+e^- \rightarrow K_S^0 K^\pm \pi^\mp \pi^0$  and  $K_S^0 K^\pm \pi^\mp \eta$  cross sections using initial-state radiation. *Phys. Rev. D*, 95(9):092005, 2017.
- [81] Michel Davier, Andreas Hoecker, Bogdan Malaescu, and Zhiqing Zhang. Reevaluation of the hadronic vacuum polarisation contributions to the Standard Model predictions of the muon  $g - 2$  and  $\alpha(m_Z^2)$  using newest hadronic cross-section data. *Eur. Phys. J. C*, 77(12):827, 2017.
- [82] J. Z. Bai et al. Measurement of the total cross-section for hadronic production by  $e^+e^-$  annihilation at energies between 2.6-GeV - 5-GeV. *Phys. Rev. Lett.*, 84:594–597, 2000.
- [83] J. Z. Bai et al. Measurements of the cross-section for  $e^+e^- \rightarrow$  hadrons at center-of-mass energies from 2-GeV to 5-GeV. *Phys. Rev. Lett.*, 88:101802, 2002.
- [84] M. Ablikim et al. R value measurements for  $e^+e^-$  annihilation at 2.60-GeV, 3.07-GeV and 3.65-GeV. *Phys. Lett. B*, 677:239–245, 2009.
- [85] V. V. Anashin et al. Measurement of  $R_{uds}$  and  $R$  between 3.12 and 3.72 GeV at the KEDR detector. *Phys. Lett. B*, 753:533–541, 2016.
- [86] V. V. Anashin et al. Precise measurement of  $R_{uds}$  and  $R$  between 1.84 and 3.72 GeV at the KEDR detector. *Phys. Lett. B*, 788:42–51, 2019.
- [87] V. V. Anashin et al. Measurement of  $R$  between 1.84 and 3.05 GeV at the KEDR detector. *Phys. Lett. B*, 770:174–181, 2017.
- [88] A. Anastasi et al. Combination of KLOE  $\sigma(e^+e^- \rightarrow \pi^+\pi^-\gamma(\gamma))$  measurements and determination of  $a_\mu^{\pi^+\pi^-}$  in the energy range  $0.10 < s < 0.95$  GeV<sup>2</sup>. *JHEP*, 03:173, 2018.

- [89] M. N. Achasov et al. Measurement of the  $e^+e^- \rightarrow \pi^+\pi^-$  process cross section with the SND detector at the VEPP-2000 collider in the energy region  $0.525 < \sqrt{s} < 0.883$  GeV. *JHEP*, 01:113, 2021.
- [90] E. A. Kozyrev et al. Study of the process  $e^+e^- \rightarrow K^+K^-$  in the center-of-mass energy range 1010–1060 MeV with the CMD-3 detector. *Phys. Lett. B*, 779:64–71, 2018.
- [91] Fred Jegerlehner and Robert Szafron.  $\rho^0 - \gamma$  mixing in the neutral channel pion form factor  $F_\pi^e$  and its role in comparing  $e^+e^-$  with  $\tau$  spectral functions. *Eur. Phys. J. C*, 71:1632, 2011.
- [92] Zhiqing Zhang. Review of Recent Calculations of the Hadronic Vacuum Polarisation Contribution. *EPJ Web Conf.*, 118:01036, 2016.
- [93] M. Davier, A. Hoecker, B. Malaescu, C. Z. Yuan, and Z. Zhang. Reevaluation of the hadronic contribution to the muon magnetic anomaly using new  $e^+e^- \rightarrow \pi^+\pi^-$  cross section data from BABAR. *Eur. Phys. J. C*, 66:1–9, 2010.
- [94] V. Cirigliano, G. Ecker, and H. Neufeld. Radiative tau decay and the magnetic moment of the muon. *JHEP*, 08:002, 2002.
- [95] G. W. Bennett et al. Final Report of the Muon E821 Anomalous Magnetic Moment Measurement at BNL. *Phys. Rev. D*, 73:072003, 2006.
- [96] B. Abi et al. Measurement of the Positive Muon Anomalous Magnetic Moment to 0.46 ppm. *Phys. Rev. Lett.*, 126(14):141801, 2021.
- [97] J. A. Miranda and P. Roig. New  $\tau$ -based evaluation of the hadronic contribution to the vacuum polarization piece of the muon anomalous magnetic moment. *Phys. Rev. D*, 102:114017, 2020.
- [98] Eite Tiesinga, Peter J. Mohr, David B. Newell, and Barry N. Taylor. CODATA recommended values of the fundamental physical constants: 2018\*. *Rev. Mod. Phys.*, 93(2):025010, 2021.

- [99] Peter J. Mohr, David B. Newell, and Barry N. Taylor. CODATA Recommended Values of the Fundamental Physical Constants: 2014. *Rev. Mod. Phys.*, 88(3):035009, 2016.
- [100] Peter J. Mohr, Barry N. Taylor, and David B. Newell. CODATA Recommended Values of the Fundamental Physical Constants: 2010. *Rev. Mod. Phys.*, 84:1527–1605, 2012.
- [101] Vadim Lensky, Franziska Hagelstein, Astrid Hiller Blin, and Vladimir Pascalutsa. Deuteron VVCS and nuclear structure effects in muonic deuterium at N<sup>3</sup>LO in pionless EFT. In *10th International workshop on Chiral Dynamics*, 3 2022.
- [102] Aldo Antognini et al. Proton Structure from the Measurement of  $2S - 2P$  Transition Frequencies of Muonic Hydrogen. *Science*, 339:417–420, 2013.
- [103] Randolph Pohl et al. The size of the proton. *Nature*, 466:213–216, 2010.
- [104] A. D. Brandt, S. F. Cooper, C. Rasoar, Z. Burkley, D. C. Yost, and A. Matveev. Measurement of the  $2S_{1/2} - 8D_{5/2}$  Transition in Hydrogen. *Phys. Rev. Lett.*, 128(2):023001, 2022.
- [105] Alexey Grinin, Arthur Matveev, Dylan C. Yost, Lothar Maisenbacher, Vitaly Wirthl, Randolph Pohl, Theodor W. Hänsch, and Thomas Udem. Two-photon frequency comb spectroscopy of atomic hydrogen. *Science*, 370(6520):1061–1066, 2020.
- [106] N. Bezginov, T. Valdez, M. Horbatsch, A. Marsman, A. C. Vutha, and E. A. Hessels. A measurement of the atomic hydrogen Lamb shift and the proton charge radius. *Science*, 365(6457):1007–1012, 2019.
- [107] Hélène Fleurbaey, Sandrine Galtier, Simon Thomas, Marie Bonnaud, Lucile Julien, François Biraben, François Nez, Michel Abgrall, and Jocelyne Guéna. New Measurement of the  $1S - 3S$  Transition Frequency of Hydrogen: Contribution to the Proton Charge Radius Puzzle. *Phys. Rev. Lett.*, 120(18):183001, 2018.
- [108] Axel Beyer et al. The Rydberg constant and proton size from atomic hydrogen. *Science*, 358(6359):79–85, 2017.

- [109] W. Xiong et al. A small proton charge radius from an electron–proton scattering experiment. *Nature*, 575(7781):147–150, 2019.
- [110] Marko Horbatsch, Eric A. Hessels, and Antonio Pineda. Proton radius from electron-proton scattering and chiral perturbation theory. *Phys. Rev. C*, 95(3):035203, 2017.
- [111] Douglas W. Higinbotham, Al Amin Kabir, Vincent Lin, David Meekins, Blaine Norum, and Brad Sawatzky. Proton radius from electron scattering data. *Phys. Rev. C*, 93(5):055207, 2016.
- [112] Gabriel Lee, John R. Arrington, and Richard J. Hill. Extraction of the proton radius from electron-proton scattering data. *Phys. Rev. D*, 92(1):013013, 2015.
- [113] Ingo Sick. Problems with proton radii. *Prog. Part. Nucl. Phys.*, 67:473–478, 2012.
- [114] J. C. Bernauer et al. High-precision determination of the electric and magnetic form factors of the proton. *Phys. Rev. Lett.*, 105:242001, 2010.
- [115] Yong-Hui Lin, Hans-Werner Hammer, and Ulf-G. Meißner. New Insights into the Nucleon’s Electromagnetic Structure. *Phys. Rev. Lett.*, 128(5):052002, 2022.
- [116] J. M. Alarcón, D. W. Higinbotham, C. Weiss, and Z. Ye. Proton charge radius extraction from electron scattering data using dispersively improved chiral effective field theory. *Phys. Rev. C*, 99(4):044303, 2019.
- [117] I. T. Lorenz, Ulf-G. Meißner, H. W. Hammer, and Y. B. Dong. Theoretical Constraints and Systematic Effects in the Determination of the Proton Form Factors. *Phys. Rev. D*, 91(1):014023, 2015.
- [118] M. A. Belushkin, H. W. Hammer, and U. G. Meissner. Dispersion analysis of the nucleon form-factors including meson continua. *Phys. Rev. C*, 75:035202, 2007.
- [119] Ingo Sick and Dirk Trautmann. On the rms radius of the deuteron. *Nucl. Phys. A*, 637:559–575, 1998.

- [120] Marcin Kalinowski. Deuteron charge radius from the Lamb-shift measurement in muonic deuterium. *Phys. Rev. A*, 99(3):030501, 2019.
- [121] Randolph Pohl et al. Laser spectroscopy of muonic deuterium. *Science*, 353(6300):669–673, 2016.
- [122] Randolph Pohl et al. Deuteron charge radius and Rydberg constant from spectroscopy data in atomic deuterium. *Metrologia*, 54(2):L1, 2017.
- [123] James Lewis Friar and Ingo Sick. Zemach moments for hydrogen and deuterium. *Phys. Lett. B*, 579:285–289, 2004.
- [124] Michael O. Distler, Jan C. Bernauer, and Thomas Walcher. The RMS Charge Radius of the Proton and Zemach Moments. *Phys. Lett. B*, 696:343–347, 2011.
- [125] A. V. Volotka, V. M. Shabaev, G. Plunien, and G. Soff. Zemach and magnetic radius of the proton from the hyperfine splitting in hydrogen. *Eur. Phys. J. D*, 33:23–27, 2005.
- [126] Arnaud Dupays, Alberto Beswick, Bruno Lepetit, Carlo Rizzo, and Dimitar Bakalov. Proton Zemach radius from measurements of the hyperfine splitting of hydrogen and muonic hydrogen. *Phys. Rev. A*, 68:052503, 2003.
- [127] S. L. Glashow. Partial Symmetries of Weak Interactions. *Nucl. Phys.*, 22:579–588, 1961.
- [128] Abdus Salam. Weak and Electromagnetic Interactions. *Conf. Proc. C*, 680519:367–377, 1968.
- [129] Steven Weinberg. A Model of Leptons. *Phys. Rev. Lett.*, 19:1264–1266, 1967.
- [130] W. Buchmuller and D. Wyler. Effective Lagrangian Analysis of New Interactions and Flavor Conservation. *Nucl. Phys. B*, 268:621–653, 1986.

- [131] Thomas Appelquist and J. Carazzone. Infrared Singularities and Massive Fields. *Phys. Rev. D*, 11:2856, 1975.
- [132] A. Pich. Chiral perturbation theory. *Rept. Prog. Phys.*, 58:563–610, 1995.
- [133] G. Ecker. Chiral perturbation theory. *Prog. Part. Nucl. Phys.*, 35:1–80, 1995.
- [134] Y. Aoki et al. FLAG Review 2021. 11 2021.
- [135] F. Englert and R. Brout. Broken Symmetry and the Mass of Gauge Vector Mesons. *Phys. Rev. Lett.*, 13:321–323, 1964.
- [136] Peter W. Higgs. Broken Symmetries and the Masses of Gauge Bosons. *Phys. Rev. Lett.*, 13:508–509, 1964.
- [137] G. S. Guralnik, C. R. Hagen, and T. W. B. Kibble. Global Conservation Laws and Massless Particles. *Phys. Rev. Lett.*, 13:585–587, 1964.
- [138] Nicola Cabibbo. Unitary Symmetry and Leptonic Decays. *Phys. Rev. Lett.*, 10:531–533, 1963.
- [139] Makoto Kobayashi and Toshihide Maskawa. CP Violation in the Renormalizable Theory of Weak Interaction. *Prog. Theor. Phys.*, 49:652–657, 1973.
- [140] S. L. Glashow, J. Iliopoulos, and L. Maiani. Weak Interactions with Lepton-Hadron Symmetry. *Phys. Rev. D*, 2:1285–1292, 1970.
- [141] R. Keith Ellis, W. James Stirling, and B. R. Webber. *QCD and collider physics*, volume 8. Cambridge University Press, 2 2011.
- [142] John Campbell, Joey Huston, and Frank Krauss. *The Black Book of Quantum Chromodynamics: A Primer for the LHC Era*. Oxford University Press, 12 2017.
- [143] Paul Langacker. *The Standard Model and Beyond*. Taylor & Francis, 2017.

- [144] Yorikiyo Nagashima. *Elementary particle physics: quantum field theory and particles, volume 1*. Wiley-VCH, Weinheim, 2010.
- [145] Yorikiyo Nagashima. *Elementary particle physics: Foundations of the standard model, volume 2*. Wiley-VCH, Weinheim, 2010.
- [146] C. A. Baker et al. An Improved experimental limit on the electric dipole moment of the neutron. *Phys. Rev. Lett.*, 97:131801, 2006.
- [147] J. M. Pendlebury et al. Revised experimental upper limit on the electric dipole moment of the neutron. *Phys. Rev. D*, 92(9):092003, 2015.
- [148] B. Graner, Y. Chen, E. G. Lindahl, and B. R. Heckel. Reduced Limit on the Permanent Electric Dipole Moment of Hg199. *Phys. Rev. Lett.*, 116(16):161601, 2016. [Erratum: *Phys.Rev.Lett.* 119, 119901 (2017)].
- [149] Jihn E. Kim and Gianpaolo Carosi. Axions and the Strong CP Problem. *Rev. Mod. Phys.*, 82:557–602, 2010. [Erratum: *Rev.Mod.Phys.* 91, 049902 (2019)].
- [150] T. van Ritbergen, J. A. M. Vermaseren, and S. A. Larin. The Four loop beta function in quantum chromodynamics. *Phys. Lett. B*, 400:379–384, 1997.
- [151] M. Czakon. The Four-loop QCD beta-function and anomalous dimensions. *Nucl. Phys. B*, 710:485–498, 2005.
- [152] P. A. Baikov, K. G. Chetyrkin, and J. H. Kühn. Five-Loop Running of the QCD coupling constant. *Phys. Rev. Lett.*, 118(8):082002, 2017.
- [153] Thomas Luthe, Andreas Maier, Peter Marquard, and York Schröder. Towards the five-loop Beta function for a general gauge group. *JHEP*, 07:127, 2016.
- [154] F. Herzog, B. Ruijl, T. Ueda, J. A. M. Vermaseren, and A. Vogt. The five-loop beta function of Yang-Mills theory with fermions. *JHEP*, 02:090, 2017.

- [155] Thomas Luthe, Andreas Maier, Peter Marquard, and York Schroder. The five-loop Beta function for a general gauge group and anomalous dimensions beyond Feynman gauge. *JHEP*, 10:166, 2017.
- [156] K. G. Chetyrkin, G. Falcioni, F. Herzog, and J. A. M. Vermaseren. Five-loop renormalisation of QCD in covariant gauges. *JHEP*, 10:179, 2017. [Addendum: *JHEP* 12, 006 (2017)].
- [157] William A. Bardeen, A. J. Buras, D. W. Duke, and T. Muta. Deep Inelastic Scattering Beyond the Leading Order in Asymptotically Free Gauge Theories. *Phys. Rev. D*, 18:3998, 1978.
- [158] David J. Gross and Frank Wilczek. Ultraviolet Behavior of Nonabelian Gauge Theories. *Phys. Rev. Lett.*, 30:1343–1346, 1973.
- [159] H. David Politzer. Reliable Perturbative Results for Strong Interactions? *Phys. Rev. Lett.*, 30:1346–1349, 1973.
- [160]  $\alpha_s(2019)$ : Precision measurements of the QCD coupling, 7 2019.
- [161] Gavin P. Salam. *The strong coupling: a theoretical perspective*, pages 101–121. 2019.
- [162] Antonio Pich, Juan Rojo, Rainer Sommer, and Antonio Vairo. Determining the strong coupling: status and challenges. *PoS, Confinement2018:035*, 2018.
- [163] Antonio Pich. Precision physics with inclusive QCD processes. *Prog. Part. Nucl. Phys.*, 117:103846, 2021.
- [164] M. Beneke. Renormalons. *Phys. Rept.*, 317:1–142, 1999.
- [165] M. Beneke, P. Marquard, P. Nason, and M. Steinhauser. On the ultimate uncertainty of the top quark pole mass. *Phys. Lett. B*, 775:63–70, 2017.



- [166] Andre H. Hoang, Christopher Lepenik, and Moritz Preisser. On the Light Massive Flavor Dependence of the Large Order Asymptotic Behavior and the Ambiguity of the Pole Mass. *JHEP*, 09:099, 2017.
- [167] Peter Marquard, Alexander V. Smirnov, Vladimir A. Smirnov, and Matthias Steinhauser. Quark Mass Relations to Four-Loop Order in Perturbative QCD. *Phys. Rev. Lett.*, 114(14):142002, 2015.
- [168] Antonio Pich. Effective field theory: Course. In *Les Houches Summer School in Theoretical Physics, Session 68: Probing the Standard Model of Particle Interactions*, pages 949–1049, 6 1998.
- [169] Steven Weinberg. Phenomenological Lagrangians. *Physica A*, 96(1-2):327–340, 1979.
- [170] H. Leutwyler. On the foundations of chiral perturbation theory. *Annals Phys.*, 235:165–203, 1994.
- [171] Matthias Neubert. Renormalization Theory and Effective Field Theories. 1 2019.
- [172] Aneesh V. Manohar. Introduction to Effective Field Theories. 4 2018.
- [173] Enrico Fermi. Tentativo di una teoria dell’emissione dei raggi beta. *Ric. Sci.*, 4:491–495, 1933.
- [174] B. Pontecorvo. Inverse beta processes and nonconservation of lepton charge. *Zh. Eksp. Teor. Fiz.*, 34:247, 1957.
- [175] Ziro Maki, Masami Nakagawa, and Shoichi Sakata. Remarks on the unified model of elementary particles. *Prog. Theor. Phys.*, 28:870–880, 1962.
- [176] Steven Weinberg. Baryon and Lepton Nonconserving Processes. *Phys. Rev. Lett.*, 43:1566–1570, 1979.
- [177] Frank Wilczek and A. Zee. Operator Analysis of Nucleon Decay. *Phys. Rev. Lett.*, 43:1571–1573, 1979.

- [178] Chung Ngoc Leung, S. T. Love, and S. Rao. Low-Energy Manifestations of a New Interaction Scale: Operator Analysis. *Z. Phys. C*, 31:433, 1986.
- [179] Elizabeth E. Jenkins, Aneesh V. Manohar, and Peter Stoffer. Low-Energy Effective Field Theory below the Electroweak Scale: Anomalous Dimensions. *JHEP*, 01:084, 2018.
- [180] Elizabeth E. Jenkins, Aneesh V. Manohar, and Peter Stoffer. Low-Energy Effective Field Theory below the Electroweak Scale: Operators and Matching. *JHEP*, 03:016, 2018.
- [181] Jason Aebischer, Andreas Crivellin, Matteo Fael, and Christoph Greub. Matching of gauge invariant dimension-six operators for  $b \rightarrow s$  and  $b \rightarrow c$  transitions. *JHEP*, 05:037, 2016.
- [182] Jason Aebischer, Matteo Fael, Christoph Greub, and Javier Virto. B physics Beyond the Standard Model at One Loop: Complete Renormalization Group Evolution below the Electroweak Scale. *JHEP*, 09:158, 2017.
- [183] Tanmoy Bhattacharya, Vincenzo Cirigliano, Rajan Gupta, Emanuele Mereghetti, and Boram Yoon. Dimension-5 CP-odd operators: QCD mixing and renormalization. *Phys. Rev. D*, 92(11):114026, 2015.
- [184] Gerhard Buchalla, Andrzej J. Buras, and Markus E. Lautenbacher. Weak decays beyond leading logarithms. *Rev. Mod. Phys.*, 68:1125–1144, 1996.
- [185] Alejandro Celis, Javier Fuentes-Martin, Avelino Vicente, and Javier Virto. DsixTools: The Standard Model Effective Field Theory Toolkit. *Eur. Phys. J. C*, 77(6):405, 2017.
- [186] Vincenzo Cirigliano, Sacha Davidson, and Yoshitaka Kuno. Spin-dependent  $\mu \rightarrow e$  conversion. *Phys. Lett. B*, 771:242–246, 2017.
- [187] Vincenzo Cirigliano, Martin Gonzalez-Alonso, and Michael L. Graesser. Non-standard Charged Current Interactions: beta decays versus the LHC. *JHEP*, 02:046, 2013.

- [188] Andreas Crivellin, Sacha Davidson, Giovanni Marco Pruna, and Adrian Signer. Renormalisation-group improved analysis of  $\mu \rightarrow e$  processes in a systematic effective-field-theory approach. *JHEP*, 05:117, 2017.
- [189] Sacha Davidson.  $\mu \rightarrow e\gamma$  and matching at  $m_W$ . *Eur. Phys. J. C*, 76(7):370, 2016.
- [190] W. Dekens and J. de Vries. Renormalization Group Running of Dimension-Six Sources of Parity and Time-Reversal Violation. *JHEP*, 05:149, 2013.
- [191] Adam Falkowski, Martín González-Alonso, and Kin Mimouni. Compilation of low-energy constraints on 4-fermion operators in the SMEFT. *JHEP*, 08:123, 2017.
- [192] Martín González-Alonso, Jorge Martin Camalich, and Kin Mimouni. Renormalization-group evolution of new physics contributions to (semi)leptonic meson decays. *Phys. Lett. B*, 772:777–785, 2017.
- [193] J. Gasser and H. Leutwyler. Chiral Perturbation Theory to One Loop. *Annals Phys.*, 158:142, 1984.
- [194] J. Gasser and H. Leutwyler. Chiral Perturbation Theory: Expansions in the Mass of the Strange Quark. *Nucl. Phys. B*, 250:465–516, 1985.
- [195] J. Bijnens, G. Ecker, and J. Gasser. Chiral perturbation theory. 11 1994.
- [196] Stefan Scherer. Introduction to chiral perturbation theory. *Adv. Nucl. Phys.*, 27:277, 2003.
- [197] J. Gasser. Light quark dynamics. *Lect. Notes Phys.*, 629:1–35, 2004.
- [198] Veronique Bernard and Ulf-G. Meissner. Chiral perturbation theory. *Ann. Rev. Nucl. Part. Sci.*, 57:33–60, 2007.
- [199] Stefan Scherer and Matthias R. Schindler. Quantum chromodynamics and chiral symmetry. *Lect. Notes Phys.*, 830:1–48, 2012.

- [200] Gerard 't Hooft. Symmetry Breaking Through Bell-Jackiw Anomalies. *Phys. Rev. Lett.*, 37:8–11, 1976.
- [201] Curtis G. Callan, Jr., R. F. Dashen, and David J. Gross. The Structure of the Gauge Theory Vacuum. *Phys. Lett. B*, 63:334–340, 1976.
- [202] R. J. Crewther. Chirality Selection Rules and the U(1) Problem. *Phys. Lett. B*, 70:349–354, 1977.
- [203] J. Goldstone. Field Theories with Superconductor Solutions. *Nuovo Cim.*, 19:154–164, 1961.
- [204] Murray Gell-Mann, R. J. Oakes, and B. Renner. Behavior of current divergences under SU(3) x SU(3). *Phys. Rev.*, 175:2195–2199, 1968.
- [205] Steven Weinberg. The Problem of Mass. *Trans. New York Acad. Sci.*, 38:185–201, 1977.
- [206] Murray Gell-Mann. Symmetries of baryons and mesons. *Phys. Rev.*, 125:1067–1084, 1962.
- [207] Susumu Okubo. Note on unitary symmetry in strong interactions. *Prog. Theor. Phys.*, 27:949–966, 1962.
- [208] Roger F. Dashen. Chiral SU(3) x SU(3) as a symmetry of the strong interactions. *Phys. Rev.*, 183:1245–1260, 1969.
- [209] L.R. Frontiers in physics. current algebras and applications to particle physics: Adler, s. l. and r. f. dashen, (w. a. benjamin, inc., new york, 1968. 394 pp.). *Nuclear Physics A*, 139(3):702, 1969.
- [210] V. de Alfaro, S. Fubini, G. Furlan, and C. Rossetti. Currents in Hadron Physics. 1973.
- [211] William A. Bardeen. Anomalous Ward identities in spinor field theories. *Phys. Rev.*, 184:1848–1857, 1969.

- [212] J. Wess and B. Zumino. Consequences of anomalous Ward identities. *Phys. Lett.*, 37B:95–97, 1971.
- [213] Edward Witten. Global Aspects of Current Algebra. *Nucl. Phys.*, B223:422–432, 1983.
- [214] J. Bijnens, G. Colangelo, and G. Ecker. Renormalization of chiral perturbation theory to order  $p^{*6}$ . *Annals Phys.*, 280:100–139, 2000.
- [215] J. Bijnens, L. Girlanda, and P. Talavera. The Anomalous chiral Lagrangian of order  $p^{*6}$ . *Eur. Phys. J. C*, 23:539–544, 2002.
- [216] T. Ebertshauser, H. W. Fearing, and S. Scherer. The Anomalous chiral perturbation theory meson Lagrangian to order  $p^{*6}$  revisited. *Phys. Rev. D*, 65:054033, 2002.
- [217] Aneesh Manohar and Howard Georgi. Chiral Quarks and the Nonrelativistic Quark Model. *Nucl. Phys.*, B234:189–212, 1984.
- [218] Antonio Pich, Ignasi Rosell, and Juan Jose Sanz-Cillero. The vector form factor at the next-to-leading order in  $1/N(C)$ : chiral couplings  $L9(\mu)$  and  $C88(\mu) - C90(\mu)$ . *JHEP*, 02:109, 2011.
- [219] Johan Bijnens and Gerhard Ecker. Mesonic low-energy constants. *Ann. Rev. Nucl. Part. Sci.*, 64:149–174, 2014.
- [220] Martin González-Alonso, Antonio Pich, and Antonio Rodríguez-Sánchez. Updated determination of chiral couplings and vacuum condensates from hadronic  $\tau$  decay data. *Phys. Rev. D*, 94(1):014017, 2016.
- [221] R. J. Dowdall, C. T. H. Davies, G. P. Lepage, and C. McNeile.  $V_{us}$  from  $\pi$  and  $K$  decay constants in full lattice QCD with physical  $u$ ,  $d$ ,  $s$  and  $c$  quarks. *Phys. Rev. D*, 88:074504, 2013.
- [222] A. Bazavov et al. Results for light pseudoscalar mesons. *PoS*, LATTICE2010:074, 2010.

- [223] S. Aoki et al. Review of lattice results concerning low-energy particle physics. *Eur. Phys. J. C*, 77(2):112, 2017.
- [224] G. Ecker, J. Gasser, A. Pich, and E. de Rafael. The Role of Resonances in Chiral Perturbation Theory. *Nucl. Phys.*, B321:311–342, 1989.
- [225] G. Ecker, J. Gasser, H. Leutwyler, A. Pich, and E. de Rafael. Chiral Lagrangians for Massive Spin 1 Fields. *Phys. Lett.*, B223:425–432, 1989.
- [226] A. Pich. Colorless mesons in a polychromatic world. In *Phenomenology of large  $N(c)$  QCD. Proceedings, Tempe, USA, January 9-11, 2002*, pages 239–258, 2002.
- [227] Kenneth M. Watson. Some general relations between the photoproduction and scattering of pi mesons. *Phys. Rev.*, 95:228–236, 1954.
- [228] R. Omnes. On the Solution of certain singular integral equations of quantum field theory. *Nuovo Cim.*, 8:316–326, 1958.
- [229] B. Ananthanarayan, G. Colangelo, J. Gasser, and H. Leutwyler. Roy equation analysis of pi pi scattering. *Phys. Rept.*, 353:207–279, 2001.
- [230] G. Colangelo, J. Gasser, and H. Leutwyler.  $\pi\pi$  scattering. *Nucl. Phys. B*, 603:125–179, 2001.
- [231] R. Garcia-Martin, R. Kaminski, J. R. Pelaez, J. Ruiz de Elvira, and F. J. Yndurain. The Pion-pion scattering amplitude. IV: Improved analysis with once subtracted Roy-like equations up to 1100 MeV. *Phys. Rev. D*, 83:074004, 2011.
- [232] I. Caprini, G. Colangelo, and H. Leutwyler. Regge analysis of the pi pi scattering amplitude. *Eur. Phys. J. C*, 72:1860, 2012.
- [233] C. Hanhart, A. Kupść, U. G. Meißner, F. Stollenwerk, and A. Wirzba. Dispersive analysis for  $\eta \rightarrow \gamma\gamma^*$ . *Eur. Phys. J. C*, 73(12):2668, 2013. [Erratum: *Eur.Phys.J.C* 75, 242 (2015)].

- [234] C. Hanhart, S. Holz, B. Kubis, A. Kupść, A. Wirzba, and C. W. Xiao. The branching ratio  $\omega \rightarrow \pi^+\pi^-$  revisited. *Eur. Phys. J. C*, 77(2):98, 2017. [Erratum: *Eur.Phys.J.C* 78, 450 (2018)].
- [235] H. Leutwyler. Electromagnetic form-factor of the pion. In *Continuous Advances in QCD 2002 / ARKADYFEST (honoring the 60th birthday of Prof. Arkady Vainshtein)*, pages 23–40, 12 2002.
- [236] Gilberto Colangelo. Hadronic contributions to  $a(\mu)$  below one-GeV. *Nucl. Phys. B Proc. Suppl.*, 131:185–191, 2004.
- [237] Gilberto Colangelo, Martin Hoferichter, and Peter Stoffer. Two-pion contribution to hadronic vacuum polarization. *JHEP*, 02:006, 2019.
- [238] John F. Donoghue, J. Gasser, and H. Leutwyler. The Decay of a Light Higgs Boson. *Nucl. Phys. B*, 343:341–368, 1990.
- [239] Bachir Moussallam.  $N(f)$  dependence of the quark condensate from a chiral sum rule. *Eur. Phys. J. C*, 14:111–122, 2000.
- [240] S. Descotes-Genon. Zweig rule violation in the scalar sector and values of low-energy constants. *JHEP*, 03:002, 2001.
- [241] J. T. Daub, H. K. Dreiner, C. Hanhart, B. Kubis, and U. G. Meissner. Improving the Hadron Physics of Non-Standard-Model Decays: Example Bounds on R-parity Violation. *JHEP*, 01:179, 2013.
- [242] Alejandro Celis, Vincenzo Cirigliano, and Emilie Passemar. Lepton flavor violation in the Higgs sector and the role of hadronic  $\tau$ -lepton decays. *Phys. Rev. D*, 89:013008, 2014.
- [243] J. T. Daub, C. Hanhart, and B. Kubis. A model-independent analysis of final-state interactions in  $\overline{B}_{d/s}^0 \rightarrow J/\psi\pi\pi$ . *JHEP*, 02:009, 2016.

- [244] Martin Wolfgang Winkler. Decay and detection of a light scalar boson mixing with the Higgs boson. *Phys. Rev. D*, 99(1):015018, 2019.
- [245] Stefan Ropertz, Christoph Hanhart, and Bastian Kubis. A new parametrization for the scalar pion form factors. *Eur. Phys. J. C*, 78(12):1000, 2018.
- [246] N. N. Khuri and S. B. Treiman. Pion-Pion Scattering and  $K + /- \rightarrow 3\pi$  Decay. *Phys. Rev.*, 119:1115–1121, 1960.
- [247] I. J. R. Aitchison and R. Pasquier. Three-Body Unitarity and Khuri-Treiman Amplitudes. *Phys. Rev.*, 152(4):1274, 1966.
- [248] Martin L. Perl et al. Evidence for Anomalous Lepton Production in  $e^+ - e^-$  Annihilation. *Phys. Rev. Lett.*, 35:1489–1492, 1975.
- [249] Yung-Su Tsai. Decay Correlations of Heavy Leptons in  $e^+ e^- \rightarrow \text{Lepton} + \text{Lepton}^-$ . *Phys. Rev. D*, 4:2821, 1971. [Erratum: *Phys.Rev.D* 13, 771 (1976)].
- [250] E. A. Garcés, M. Hernández Villanueva, G. López Castro, and P. Roig. Effective-field theory analysis of the  $\tau^- \rightarrow \eta^{(\prime)} \pi^- \nu_\tau$  decays. *JHEP*, 12:027, 2017.
- [251] Javier Rendón, Pablo Roig, and Genaro Toledo Sánchez. Effective-field theory analysis of the  $\tau^- \rightarrow (K\pi)^- \nu_\tau$  decays. *Phys. Rev. D*, 99(9):093005, 2019.
- [252] R. E. Behrends, R. J. Finkelstein, and A. Sirlin. Radiative corrections to decay processes. *Phys. Rev.*, 101:866–873, 1956.
- [253] S. M. Berman. Radiative corrections to muon and neutron decay. *Phys. Rev.*, 112:267–270, 1958.
- [254] Toichiro Kinoshita and Alberto Sirlin. Radiative corrections to Fermi interactions. *Phys. Rev.*, 113:1652–1660, 1959.
- [255] M. Roos and A. Sirlin. Remarks on the radiative corrections of order alpha-squared to muon decay and the determination of  $g(\mu)$ . *Nucl. Phys. B*, 29:296–304, 1971.



- [256] W. J. Marciano and A. Sirlin. Electroweak Radiative Corrections to tau Decay. *Phys. Rev. Lett.*, 61:1815–1818, 1988.
- [257] A. Ferroglia, G. Ossola, and A. Sirlin. Considerations concerning the radiative corrections to muon decay in the Fermi and standard theories. *Nucl. Phys. B*, 560:23–32, 1999.
- [258] Timo van Ritbergen and Robin G. Stuart. Complete two loop quantum electrodynamic contributions to the muon lifetime in the Fermi model. *Phys. Rev. Lett.*, 82:488–491, 1999.
- [259] Timo van Ritbergen and Robin G. Stuart. On the precise determination of the Fermi coupling constant from the muon lifetime. *Nucl. Phys. B*, 564:343–390, 2000.
- [260] Timo van Ritbergen and Robin G. Stuart. Hadronic contributions to the muon lifetime. *Phys. Lett. B*, 437:201–208, 1998.
- [261] M. Steinhauser and T. Seidensticker. Second order corrections to the muon lifetime and the semileptonic B decay. *Phys. Lett. B*, 467:271–278, 1999.
- [262] Alexey Pak and Andrzej Czarnecki. Mass effects in muon and semileptonic  $b \rightarrow c$  decays. *Phys. Rev. Lett.*, 100:241807, 2008.
- [263] Andrea Ferroglia, Christoph Greub, Alberto Sirlin, and Zhibai Zhang. Contributions of the W-boson propagator to  $\mu$  and  $\tau$  leptonic decay rates. *Phys. Rev. D*, 88(3):033012, 2013.
- [264] Matteo Fael, L. Mercolli, and M. Passera. W-propagator corrections to  $\mu$  and  $\tau$  leptonic decays. *Phys. Rev. D*, 88(9):093011, 2013.
- [265] A. Sirlin. Radiative Corrections in the SU(2)-L x U(1) Theory: A Simple Renormalization Framework. *Phys. Rev. D*, 22:971–981, 1980.

- [266] D. M. Webber et al. Measurement of the Positive Muon Lifetime and Determination of the Fermi Constant to Part-per-Million Precision. *Phys. Rev. Lett.*, 106:041803, 2011.
- [267] Bernard Aubert et al. Measurements of Charged Current Lepton Universality and  $|V_{us}|$  using Tau Lepton Decays to  $e^-\bar{\nu}_e\nu_\tau$ ,  $\mu^-\bar{\nu}_\mu\nu_\tau$ ,  $\pi^-\nu_\tau$ , and  $K^-\nu_\tau$ . *Phys. Rev. Lett.*, 105:051602, 2010.
- [268] K. Belous et al. Measurement of the  $\tau$ -lepton lifetime at Belle. *Phys. Rev. Lett.*, 112(3):031801, 2014.
- [269] M. B. Voloshin. The Onset of  $e^+e^- \rightarrow \tau^+\tau^-$  at threshold revisited. *Phys. Lett. B*, 556:153–162, 2003.
- [270] Brian H. Smith and M. B. Voloshin.  $e^+e^- \rightarrow \tau^+\tau^-$  at the threshold and beyond. *Phys. Lett. B*, 324:117–120, 1994. [Erratum: *Phys.Lett.B* 333, 564 (1994)].
- [271] P. Ruiz-Femenia and A. Pich. The NNLO  $\tau^+\tau^-$  production cross-section close to threshold. *Phys. Rev. D*, 64:053001, 2001.
- [272] M. Ablikim et al. Precision measurement of the mass of the  $\tau$  lepton. *Phys. Rev. D*, 90(1):012001, 2014.
- [273] F. Abudinén et al.  $\tau$  lepton mass measurement at Belle II. 8 2020.
- [274] William J. Marciano and A. Sirlin. Radiative corrections to  $\pi$ (lepton 2) decays. *Phys. Rev. Lett.*, 71:3629–3632, 1993.
- [275] Markus Finkemeier. Radiative corrections to  $\pi$ (12) and  $K$ (12) decays. *Phys. Lett. B*, 387:391–394, 1996.
- [276] Vincenzo Cirigliano and Ignasi Rosell. Two-loop effective theory analysis of  $\pi$  ( $K$ )  $\rightarrow e$  anti- $\nu$ /e [ $\gamma$ ] branching ratios. *Phys. Rev. Lett.*, 99:231801, 2007.
- [277] Vincenzo Cirigliano and Ignasi Rosell.  $\pi/K \rightarrow e$  anti- $\nu$ (e) branching ratios to  $O(e^{**2} p^{**4})$  in Chiral Perturbation Theory. *JHEP*, 10:005, 2007.

- [278] H. L. Anderson, T. Fujii, and R. H. Miller. Branching Ratio of the Electronic Mode of Positive Pion Decay. *Phys. Rev.*, 119:2050, 1960.
- [279] E. Di Capua, R. Garland, L. Pondrom, and A. Strelzoff. Study of the Decay  $\pi \rightarrow e \nu$ . *Phys. Rev.*, 133:B1333–B1340, 1964.
- [280] D. A. Bryman, M. S. Dixit, R. Dubois, J. A. Macdonald, T. Numao, B. Olaniyi, A. Olin, and J. M. Poutissou. Measurement of the  $\pi \rightarrow \nu_e$  Branching Ratio. *Phys. Rev. D*, 33:1211, 1986.
- [281] D. I. Britton et al. Measurement of the  $\pi^+ \rightarrow e^+$  neutrino branching ratio. *Phys. Rev. Lett.*, 68:3000–3003, 1992.
- [282] G. Czappek et al. Branching ratio for the rare pion decay into positron and neutrino. *Phys. Rev. Lett.*, 70:17–20, 1993.
- [283] A. Aguilar-Arevalo et al. Improved Measurement of the  $\pi \rightarrow e \nu$  Branching Ratio. *Phys. Rev. Lett.*, 115(7):071801, 2015.
- [284] A. R. Clark, B. Cork, T. Elioff, L. T. Kerth, J. F. Mcreynolds, D. Newton, and W. A. Wenzel. Measurement of branching ratio for  $k^+ \rightarrow e^+ \nu$ . *Phys. Rev. Lett.*, 29:1274–1277, 1972.
- [285] K. S. Heard et al. A Measurement of the  $K^+ \rightarrow e^+$  Neutrino /  $K^+ \rightarrow \mu^+$  Neutrino Branching Ratio. *Phys. Lett. B*, 55:327–330, 1975.
- [286] J. Heintze et al. A New Measurement of the ( $K^+ \rightarrow e^+$  Neutrino) ( $K^+ \rightarrow \text{Muon}^+$  Neutrino) Branching Ratio. *Phys. Lett. B*, 60:302–304, 1976.
- [287] F. Ambrosino et al. Precise measurement of  $\Gamma(K \rightarrow e \nu(\gamma))/\Gamma(K \rightarrow \mu \nu(\gamma))$  and study of  $K \rightarrow e \nu \gamma$ . *Eur. Phys. J. C*, 64:627–636, 2009. [Erratum: *Eur.Phys.J.* 65, 703 (2010)].

- [288] C. Lazzeroni et al. Test of lepton flavour universality in  $K^+ \rightarrow \ell^+ \nu$  decays. *Phys. Lett. B*, 698:105–114, 2011.
- [289] C. Lazzeroni et al. Precision Measurement of the Ratio of the Charged Kaon Leptonic Decay Rates. *Phys. Lett. B*, 719:326–336, 2013.
- [290] R. Decker and M. Finkemeier. Radiative corrections to the decay  $\tau \rightarrow \pi(K) \tau\text{-neutrino}$ . 2. *Phys. Lett. B*, 334:199–202, 1994.
- [291] Roger Decker and Markus Finkemeier. Short and long distance effects in the decay  $\tau \rightarrow \pi \tau\text{-neutrino}(\gamma)$ . *Nucl. Phys. B*, 438:17–53, 1995.
- [292] Roger Decker and Markus Finkemeier. Radiative corrections to the decay  $\tau \rightarrow \pi \tau\text{-neutrino}$ . *Nucl. Phys. B Proc. Suppl.*, 40:453–461, 1995.
- [293] M. A. Arroyo-Ureña, G. Hernández-Tomé, G. López-Castro, P. Roig, and I. Rosell. Radiative corrections to  $\tau \rightarrow \pi(K) \nu \tau[\gamma]$ : A reliable new physics test. *Phys. Rev. D*, 104(9):L091502, 2021.
- [294] M. A. Arroyo-Ureña, G. Hernández-Tomé, G. López-Castro, P. Roig, and I. Rosell. One-loop determination of  $\tau \rightarrow \pi(K) \nu \tau[\gamma]$  branching ratios and new physics tests. *JHEP*, 02:173, 2022.
- [295] L. Michel. Interaction between four half spin particles and the decay of the  $\mu$  meson. *Proc. Phys. Soc. A*, 63:514–531, 1950.
- [296] Claude Bouchiat and Louis Michel. Theory of  $\mu$ -Meson Decay with the Hypothesis of Nonconservation of Parity. *Phys. Rev.*, 106:170–172, 1957.
- [297] Toichiro Kinoshita and Alberto Sirlin. Muon Decay with Parity Nonconserving Interactions and Radiative Corrections in the Two-Component Theory. *Phys. Rev.*, 107:593–599, 1957.

- [298] Toichiro Kinoshita and Alberto Sirlin. Polarization of Electrons in Muon Decay with General Parity-Nonconserving Interactions. *Phys. Rev.*, 108:844–850, 1957.
- [299] Florian Scheck. Muon Physics. *Phys. Rept.*, 44:187, 1978.
- [300] W. Fetscher, H. J. Gerber, and K. F. Johnson. Muon Decay: Complete Determination of the Interaction and Comparison with the Standard Model. *Phys. Lett. B*, 173:102–106, 1986.
- [301] W. Fetscher and H.-J. Gerber. *PRECISION MEASUREMENTS IN MUON AND TAU DECAYS*, pages 657–705.
- [302] Antonio Pich and Joao P. Silva. Constraining new interactions with leptonic  $\tau$  decays. *Phys. Rev. D*, 52:4006–4018, 1995.
- [303] Andre Rouge. Tau lepton Michel parameters and new physics. *Eur. Phys. J. C*, 18:491–496, 2001.
- [304] Cecilia Jarlskog. Determination of the coupling constants in muon decay from experiments. *Nuclear Physics*, 75(3):659–668, 1966.
- [305] L. P. Roesch, V. L. Telegdi, P. Truttmann, A. Zehnder, L. Grenacs, and L. Palffy. MEASUREMENT OF THE AVERAGE AND LONGITUDINAL RECOIL POLARIZATIONS IN THE REACTION C-12 (MU-, NEUTRINO) B-12 (G.S.): PSEUDOSCALAR COUPLING AND NEUTRINO HELICITY. *Helv. Phys. Acta*, 55:74–99, 1982.
- [306] A. Jodidio et al. Search for Right-Handed Currents in Muon Decay. *Phys. Rev. D*, 34:1967, 1986. [Erratum: *Phys.Rev.D* 37, 237 (1988)].
- [307] W. Fetscher. HELICITY OF THE muon-neutrino IN  $\text{PI}^+$  DECAY: A COMMENT ON THE MEASUREMENT OF  $\text{P}(\text{MU}) \text{ XI DELTA} / \text{RHO}$  IN MUON DECAY. *Phys. Lett. B*, 140:117–118, 1984.

- [308] K. Mursula, M. Roos, and F. Scheck. The Lorentz Structure of Leptonic Charged Weak Interactions. 1. *Nucl. Phys. B*, 219:321–340, 1983.
- [309] A. Hillairet et al. Precision muon decay measurements and improved constraints on the weak interaction. *Phys. Rev. D*, 85:092013, 2012.
- [310] J. F. Bueno et al. Precise measurement of parity violation in polarized muon decay. *Phys. Rev. D*, 84:032005, 2011.
- [311] R. Bayes et al. Experimental Constraints on Left-Right Symmetric Models from Muon Decay. *Phys. Rev. Lett.*, 106:041804, 2011.
- [312] C. A. Gagliardi, R. E. Tribble, and N. J. Williams. Global analysis of muon decay measurements. *Phys. Rev. D*, 72:073002, 2005.
- [313] S. R. Mishra et al. Inverse Muon Decay,  $\nu_\mu e \rightarrow \mu^- \nu_e$ , at the Fermilab Tevatron. *Phys. Lett. B*, 252:170–176, 1990.
- [314] P. Vilain et al. A Precise measurement of the cross-section of the inverse muon decay muon-neutrino + e<sup>-</sup> → mu<sup>-</sup> + electron-neutrino. *Phys. Lett. B*, 364:121–126, 1995.
- [315] S. Kawasaki, T. Shirafuji, and S. Y. Tsai. Productions and decays of short-lived particles in e<sup>+</sup> e<sup>-</sup> colliding beam experiments. *Prog. Theor. Phys.*, 49:1656–1678, 1973.
- [316] So-Young Pi and A. I. Sanda. e<sup>+</sup> e<sup>-</sup> → u<sup>+</sup> u<sup>-</sup> → mu<sup>+</sup> e<sup>+</sup> Neutrinos: General Considerations. *Annals Phys.*, 106:171, 1977.
- [317] Johann Heinrich Kuhn and F. Wagner. Semileptonic Decays of the tau Lepton. *Nucl. Phys. B*, 236:16–34, 1984.
- [318] Charles A. Nelson. Test for 'maximal P - maximal C' violation in e<sup>-</sup> e<sup>+</sup> collisions from beam referenced spin correlation functions. *Phys. Rev. D*, 43:1465–1487, 1991.

- [319] Charles A. Nelson. Tests for 'New Physics' From Tau Spin Correlation Functions for  $Z^0 \rightarrow \tau^+\tau^- \rightarrow A^+ B^- X$ . *Phys. Rev. D*, 40:123, 1989. [Erratum: *Phys.Rev.D* 41, 2327 (1990)].
- [320] Charles A. Nelson. An Electroweak Test From the Harder Lepton's Energy Spectrum in  $Z^0 \rightarrow \tau^+\tau^- \rightarrow \mu^+e^- X$ . *Phys. Rev. Lett.*, 62:1347, 1989. [Erratum: *Phys.Rev.Lett.* 64, 496 (1990)].
- [321] Stephen Goozovat and Charles A. Nelson. Tests to completely measure the photon and Z0 boson couplings of the tau lepton. *Phys. Rev. D*, 44:2818–2835, 1991.
- [322] Wulf Fetscher. Leptonic tau decays: How to determine the Lorentz structure of the charged leptonic weak interaction by experiment. *Phys. Rev. D*, 42:1544–1567, 1990.
- [323] J. Bernabeu, N. Rius, and A. Pich. Tau spin correlations at the Z peak: Aplanarities of the decay products. *Phys. Lett. B*, 257:219–226, 1991.
- [324] R. Alemany, N. Rius, J. Bernabeu, J. J. Gomez-Cadenas, and A. Pich. Tau polarization at the Z peak from the acollinearity between both tau decay products. *Nucl. Phys. B*, 379:3–23, 1992.
- [325] M. Davier, L. Duflot, F. Le Diberder, and A. Rouge. The Optimal method for the measurement of tau polarization. *Phys. Lett. B*, 306:411–417, 1993.
- [326] K. Abe et al. Measurement of the tau-neutrino helicity and the Michel parameters in polarized e+ e- collisions. *Phys. Rev. Lett.*, 78:4691–4696, 1997.
- [327] A. Stahl and H. Voss. Testing the Lorentz structure of the charged weak current in tau decays. *Z. Phys. C*, 74:73–78, 1997.
- [328] A. Flores-Tlalpa, G. López Castro, and P. Roig. Five-body leptonic decays of muon and tau leptons. *JHEP*, 04:185, 2016.

- [329] A. Heister et al. Measurement of the Michel parameters and the  $\nu/\tau$  helicity in tau lepton decays. *Eur. Phys. J. C*, 22:217–230, 2001.
- [330] P. Abreu et al. A Study of the Lorentz structure in tau decays. *Eur. Phys. J. C*, 16:229–252, 2000.
- [331] K. Ackerstaff et al. Measurement of the Michel parameters in leptonic tau decays. *Eur. Phys. J. C*, 8:3–21, 1999.
- [332] M. Acciarri et al. Measurement of the Michel parameters and the average tau-neutrino helicity from tau decays at LEP. *Phys. Lett. B*, 438:405–416, 1998.
- [333] M. Acciarri et al. Measurement of the Michel parameters and the average tau-neutrino helicity from tau decays in  $e^+ e^- \rightarrow \tau^+ \tau^-$ . *Phys. Lett. B*, 377:313–324, 1996.
- [334] H. Albrecht et al. Determination of the Michel parameters  $\rho$ ,  $\xi$  and  $\delta$  in tau lepton decays with  $\tau \rightarrow \rho$  neutrino tags. *Phys. Lett. B*, 431:179–187, 1998.
- [335] H. Albrecht et al. Determination of the Michel parameters  $\xi$  and  $\delta$  in leptonic tau decays. *Phys. Lett. B*, 349:576–584, 1995.
- [336] H. Albrecht et al. The First measurement of the Michel parameter  $\eta$  in tau decays. *Phys. Lett. B*, 341:441–447, 1995.
- [337] H. Albrecht et al. A Determination of two Michel parameters in purely leptonic tau decays. *Phys. Lett. B*, 316:608–614, 1993.
- [338] H. Albrecht et al. Determination of the Michel parameter in tau decay. *Phys. Lett. B*, 246:278–284, 1990.
- [339] J. P. Alexander et al. Determination of the Michel parameters and the tau-neutrino helicity in tau decay. *Phys. Rev. D*, 56:5320–5329, 1997.
- [340] S. Behrends et al. NEW DETERMINATION OF THE MICHEL PARAMETER IN TAU DECAY. *Phys. Rev. D*, 32:2468–2470, 1985.



- [341] R. Ammar et al. A Measurement of the Michel parameters in leptonic decays of the tau. *Phys. Rev. Lett.*, 78:4686–4690, 1997.
- [342] H. Janssen et al. The Michel Parameter for the Decay  $\tau \rightarrow \nu_e$  Anti-neutrino. *Phys. Lett. B*, 228:273–280, 1989.
- [343] William T. Ford et al. Measurement of the Polarization of  $\tau$  Leptons Produced in  $e^+e^-$  Annihilation at  $\sqrt{s} = 29$ -GeV. *Phys. Rev. D*, 36:1971, 1987.
- [344] N. Danneberg et al. Muon decay: Measurement of the transverse polarization of the decay positrons and its implications for the Fermi coupling constant and time reversal invariance. *Phys. Rev. Lett.*, 94:021802, 2005.
- [345] B. Balke et al. Precise Measurement of the Asymmetry Parameter Delta in Muon Decay. *Phys. Rev. D*, 37:587–617, 1988.
- [346] I. Beltrami, H. Burkard, R. D. Von Dincklage, W. Fetscher, H. J. Gerber, K. F. Johnson, E. Pedroni, M. Salzmann, and F. Scheck. Muon Decay: Measurement of the Integral Asymmetry Parameter. *Phys. Lett. B*, 194:326–330, 1987.
- [347] H. Burkard, F. Corriveau, J. Egger, W. Fetscher, H. J. Gerber, K. F. Johnson, H. Kaspar, H. J. Mahler, M. Salzmann, and F. Scheck. Muon Decay: Measurement of the Transverse Positron Polarization and General Analysis. *Phys. Lett. B*, 160:343–348, 1985.
- [348] H. Burkard, F. Corriveau, J. Egger, W. Fetscher, H. J. Gerber, K. F. Johnson, H. Kaspar, H. J. Mahler, M. Salzmann, and F. Scheck. MUON DECAY: MEASUREMENT OF THE POSITRON POLARIZATION AND IMPLICATIONS FOR THE SPECTRUM SHAPE PARAMETER ETA, V-A AND T INVARIANCE. *Phys. Lett. B*, 150:242–246, 1985.

- [349] F. Corriveau, J. Egger, W. Fetscher, H. J. Gerber, K. F. Johnson, H. Kaspar, H. J. Mahler, M. Salzmann, and F. Scheck. DOES THE POSITRON FROM MUON DECAY HAVE TRANSVERSE POLARIZATION? *Phys. Lett. B*, 129:260–264, 1983.
- [350] S. E. Derenzo. Measurement of the low-energy end of the mu-plus decay spectrum. *Phys. Rev.*, 181:1854–1866, 1969.
- [351] Achim Stahl. The Michel parameter eta in tau decays. *Phys. Lett. B*, 324:121–124, 1994.
- [352] A. Stahl. Michel parameters: Averages and interpretation. *Nucl. Phys. B Proc. Suppl.*, 76:173–181, 1999.
- [353] Maria-Teresa Dova, John Swain, and Lucas Taylor. Anomalous charged current couplings of the  $\tau$  and implications for  $\tau$  compositeness and two Higgs doublet models. *Phys. Rev. D*, 58:015005, 1998.
- [354] Thomas Hebbeker and Wolfgang Lohmann. The Tau - W coupling. *Z. Phys. C*, 74:399–401, 1997.
- [355] H. Thurn and H. Kolanoski. A Test of the Lorentz structure of semihadronic tau decays. *Z. Phys. C*, 60:277–286, 1993.
- [356] D. M. Asner et al. Hadronic structure in the decay  $\tau^- \rightarrow \tau\text{-neutrino } \pi^- \pi^0 \pi^0$  and the sign of the tau-neutrino helicity. *Phys. Rev. D*, 61:012002, 2000.
- [357] T. E. Coan et al. Tau-neutrino helicity from  $h^+$  energy correlations. *Phys. Rev. D*, 55:7291–7295, 1997.
- [358] K. Ackerstaff et al. A Measurement of the hadronic decay current and the tau-neutrino helicity in  $\tau^- \rightarrow \pi^- \pi^- \pi^+ \tau\text{-neutrino}$ . *Z. Phys. C*, 75:593–605, 1997.
- [359] R. Akers et al. Measurement of the Hadronic Decay Current in  $\tau^- \rightarrow \pi^- \pi^- \pi^+ \tau\text{-neutrino}$ . *Z. Phys. C*, 67:45–56, 1995.

- [360] H. Albrecht et al. Analysis of the decay  $\tau^- \rightarrow \pi^- \pi^- \pi^+ \tau^- \nu_\tau$  and determination of the  $a_1(1260)$  resonance parameters. *Z. Phys. C*, 58:61–70, 1993.
- [361] H. Albrecht et al. Determination of the tau-neutrino helicity. *Phys. Lett. B*, 250:164–171, 1990.
- [362] A. Pich. Qcd tests from tau-decay data. *Proc. Tau-Charm Factory Workshop*, 343:416, 1989. L.V. Beers (Ed.).
- [363] H. B. Thacker and J. J. Sakurai. Lifetimes and branching ratios of heavy leptons. *Phys. Lett. B*, 36:103–105, 1971.
- [364] Eric Braaten and Chong-Sheng Li. Electroweak radiative corrections to the semi-hadronic decay rate of the tau lepton. *Phys. Rev. D*, 42:3888–3891, 1990.
- [365] Jens Erler. Electroweak radiative corrections to semileptonic tau decays. *Rev. Mex. Fis.*, 50:200–202, 2004.
- [366] Frederick J. Gilman and David Howard Miller. Decays of a Heavy Lepton Involving the Hadronic Vector Current. *Phys. Rev. D*, 17:1846, 1978.
- [367] Frederick J. Gilman and Sun Hong Rhie. Calculation of Exclusive Decay Modes of the tau. *Phys. Rev. D*, 31:1066, 1985.
- [368] Frederick J. Gilman. Tau Decays Involving the  $\eta$  Meson. *Phys. Rev. D*, 35:3541, 1987.
- [369] Johann H. Kuhn and A. Santamaria. Tau decays to pions. *Z. Phys. C*, 48:445–452, 1990.
- [370] S. I. Eidelman and V. N. Ivanchenko.  $e^+ e^-$  annihilation into hadrons and exclusive tau decays. *Phys. Lett. B*, 257:437–440, 1991.
- [371] Stephan Narison and A. Pich. Semiinclusive tau decays involving the vector or axial-vector hadronic currents. *Phys. Lett. B*, 304:359–365, 1993.

- [372] Johann H. Kuhn and E. Mirkes. Structure functions in tau decays. *Z. Phys. C*, 56:661–672, 1992. [Erratum: *Z.Phys.C* 67, 364 (1995)].
- [373] Johann H. Kuhn and E. Mirkes. Angular distributions in semileptonic tau decays. *Phys. Lett. B*, 286:381–386, 1992.
- [374] Vincenzo Cirigliano and Helmut Neufeld. A note on isospin violation in  $P_{12}(\gamma)$  decays. *Phys. Lett. B*, 700:7–10, 2011.
- [375] William J. Marciano. Precise determination of  $|V_{us}|$  from lattice calculations of pseudoscalar decay constants. *Phys. Rev. Lett.*, 93:231803, 2004.
- [376] Matthew Moulson. Experimental determination of  $V_{us}$  from kaon decays. *PoS*, CKM2016:033, 2017.
- [377] S. Aoki et al. FLAG Review 2019: Flavour Lattice Averaging Group (FLAG). *Eur. Phys. J. C*, 80(2):113, 2020.
- [378] John Hardy and I. S. Towner.  $|V_{ud}|$  from nuclear  $\beta$  decays. *PoS*, CKM2016:028, 2016.
- [379] V. Cirigliano, G. Ecker, and H. Neufeld. Isospin violation and the magnetic moment of the muon. *Phys. Lett.*, B513:361–370, 2001.
- [380] Mario Antonelli, Vincenzo Cirigliano, Alberto Lusiani, and Emilie Passemar. Predicting the  $\tau$  strange branching ratios and implications for  $V_{us}$ . *JHEP*, 10:070, 2013.
- [381] F. V. Flores-Baéz and J. R. Morones-Ibarra. Model Independent Electromagnetic corrections in hadronic  $\tau$  decays. *Phys. Rev. D*, 88(7):073009, 2013.
- [382] I. Rosell, J. J. Sanz-Cillero, and A. Pich. Quantum loops in the resonance chiral theory: The Vector form-factor. *JHEP*, 08:042, 2004.
- [383] D. Gomez Dumm, A. Pich, and J. Portoles. The Hadronic off-shell width of meson resonances. *Phys. Rev. D*, 62:054014, 2000.

- [384] J. J. Sanz-Cillero and A. Pich. Rho meson properties in the chiral theory framework. *Eur. Phys. J. C*, 27:587–599, 2003.
- [385] V. Cirigliano, G. Ecker, M. Eidemuller, Roland Kaiser, A. Pich, and J. Portoles. Towards a consistent estimate of the chiral low-energy constants. *Nucl. Phys.*, B753:139–177, 2006.
- [386] V. Cirigliano, G. Ecker, M. Eidemuller, Roland Kaiser, A. Pich, and J. Portoles. The  $\rho$  SPP  $\rho$  Green function and SU(3) breaking in K(13) decays. *JHEP*, 04:006, 2005.
- [387] V. Cirigliano, G. Ecker, M. Eidemuller, A. Pich, and J. Portoles. The  $\rho$  VAP  $\rho$  Green function in the resonance region. *Phys. Lett.*, B596:96–106, 2004.
- [388] Gerard 't Hooft. A Planar Diagram Theory for Strong Interactions. *Nucl. Phys. B*, 72:461, 1974.
- [389] Gerard 't Hooft. A Two-Dimensional Model for Mesons. *Nucl. Phys. B*, 75:461–470, 1974.
- [390] Edward Witten. Baryons in the  $1/n$  Expansion. *Nucl. Phys. B*, 160:57–115, 1979.
- [391] C. A. Dominguez. Pion form-factor in large N(c) QCD. *Phys. Lett. B*, 512:331–334, 2001.
- [392] Christine Bruch, Alexander Khodjamirian, and Johann H. Kuhn. Modeling the pion and kaon form factors in the timelike region. *Eur. Phys. J. C*, 39:41–54, 2005.
- [393] V. M. Aul'chenko et al. Measurement of the pion form-factor in the range 1.04-GeV to 1.38-GeV with the CMD-2 detector. *JETP Lett.*, 82:743–747, 2005.
- [394] D. Bisello et al. The Pion Electromagnetic Form-factor in the Timelike Energy Range  $1.35\text{-GeV} \leq \sqrt{s} \leq 2.4\text{-GeV}$ . *Phys. Lett. B*, 220:321–327, 1989.
- [395] A. Aloisio et al. Measurement of  $\sigma(e^+e^- \rightarrow \pi^+\pi^-\gamma)$  and extraction of  $\sigma(e^+e^- \rightarrow \pi^+\pi^-)$  below 1-GeV with the KLOE detector. *Phys. Lett. B*, 606:12–24, 2005.

- [396] M.N. Achasov et al. Study of the process  $e^+ e^- \rightarrow \pi^+ \pi^-$  in the energy region  $400 \leq s^{*1/2} \leq 1000$ -MeV. *J. Exp. Theor. Phys.*, 101(6):1053–1070, 2005.
- [397] S. Schael et al. Branching ratios and spectral functions of tau decays: Final ALEPH measurements and physics implications. *Phys. Rept.*, 421:191–284, 2005.
- [398] S. Binner, Johann H. Kuhn, and K. Melnikov. Measuring  $\sigma(e^+ e^- \rightarrow \text{hadrons})$  using tagged photon. *Phys. Lett. B*, 459:279–287, 1999.
- [399] German Rodrigo, Henryk Czyz, Johann H. Kuhn, and Marcin Szopa. Radiative return at NLO and the measurement of the hadronic cross-section in electron positron annihilation. *Eur. Phys. J. C*, 24:71–82, 2002.
- [400] Henryk Czyz, Agnieszka Grzelinska, Johann H. Kuhn, and German Rodrigo. The Radiative return at phi and B factories: Small angle photon emission at next-to-leading order. *Eur. Phys. J. C*, 27:563–575, 2003.
- [401] Henryk Czyz, Agnieszka Grzelinska, Johann H. Kuhn, and German Rodrigo. The Radiative return at Phi and B factories: FSR at next-to-leading order. *Eur. Phys. J. C*, 33:333–347, 2004.
- [402] Henryk Czyz, Agnieszka Grzelinska, Johann H. Kuhn, and German Rodrigo. The Radiative return at phi and B factories: FSR for muon pair production at next-to-leading order. *Eur. Phys. J. C*, 39:411–420, 2005.
- [403] Henryk Czyz, Agnieszka Grzelinska, Johann H. Kuhn, and German Rodrigo. Electron-positron annihilation into three pions and the radiative return. *Eur. Phys. J. C*, 47:617–624, 2006.
- [404] S. Actis et al. Quest for precision in hadronic cross sections at low energy: Monte Carlo tools vs. experimental data. *Eur. Phys. J. C*, 66:585–686, 2010.

- [405] V. P. Druzhinin, S. I. Eidelman, S. I. Serednyakov, and E. P. Solodov. Hadron Production via e+e- Collisions with Initial State Radiation. *Rev. Mod. Phys.*, 83:1545, 2011.
- [406] Michel Davier, Andreas Hoecker, Bogdan Malaescu, and Zhiqing Zhang. Reevaluation of the Hadronic Contributions to the Muon g-2 and to alpha(MZ). *Eur. Phys. J. C*, 71:1515, 2011. [Erratum: *Eur.Phys.J.C* 72, 1874 (2012)].
- [407] Markus Finkemeier and Erwin Mirkes. Tau decays into kaons. *Z. Phys. C*, 69:243–252, 1996.
- [408] Markus Finkemeier and Erwin Mirkes. The Scalar contribution to tau  $\rightarrow$  k pi tau-neutrino. *Z. Phys. C*, 72:619–626, 1996.
- [409] D. R. Boito, R. Escribano, and M. Jamin. K  $\pi$  vector form factor constrained by  $\tau^- \rightarrow K \pi \nu_\tau$  and  $K_{l3}$  decays. *JHEP*, 09:031, 2010.
- [410] Diogo R. Boito, Rafel Escribano, and Matthias Jamin. K pi vector form-factor, dispersive constraints and tau  $\rightarrow$  nu(tau) K pi decays. *Eur. Phys. J. C*, 59:821–829, 2009.
- [411] B. Moussallam. Analyticity constraints on the strangeness changing vector current and applications to tau  $\rightarrow$  K pi nu(tau), tau  $\rightarrow$  K pi pi nu(tau). *Eur. Phys. J. C*, 53:401–412, 2008.
- [412] Matthias Jamin, Jose Antonio Oller, and Antonio Pich. Strangeness changing scalar form-factors. *Nucl. Phys.*, B622:279–308, 2002.
- [413] Matthias Jamin, Jose Antonio Oller, and Antonio Pich. S wave K pi scattering in chiral perturbation theory with resonances. *Nucl. Phys.*, B587:331–362, 2000.
- [414] Paul Buettiker, S. Descotes-Genon, and B. Moussallam. A new analysis of pi K scattering from Roy and Steiner type equations. *Eur. Phys. J. C*, 33:409–432, 2004.

- [415] S. Ryu. Measurement of the branching fractions and mass spectra for  $\tau$  lepton decays including  $K_S^0$  at Belle. *Nucl. Phys. B Proc. Suppl.*, 253-255:33–37, 2014.
- [416] Daiji Kimura, Kang Young Lee, and Takuya Morozumi. The Form factors of  $\tau \rightarrow K\pi(\eta)\nu$  and the predictions for CP violation beyond the standard model. *PTEP*, 2013:053B03, 2013. [Erratum: PTEP 2013, 099201 (2013), Erratum: PTEP 2014, 089202 (2014)].
- [417] V. Bernard. First determination of  $f_+(0)|V_{us}|$  from a combined analysis of  $\tau \rightarrow K\pi\nu_\tau$  decay and  $\pi K$  scattering with constraints from  $K_{\ell 3}$  decays. *JHEP*, 06:082, 2014.
- [418] L. A. Jiménez Pérez and G. Toledo Sánchez. Absorptive corrections for vector mesons: matching to complex mass scheme and longitudinal corrections. *J. Phys. G*, 44(12):125003, 2017.
- [419] Aleksandra Adametz. Studies of hadronic states containing kaons in tau decays at BaBar. *Nucl. Phys. B Proc. Suppl.*, 218:134–139, 2011.
- [420] A. D. Sakharov. Violation of CP Invariance, C asymmetry, and baryon asymmetry of the universe. *Pisma Zh. Eksp. Teor. Fiz.*, 5:32–35, 1967.
- [421] G. Bonvicini et al. Search for CP violation in tau  $\rightarrow$  K pi tau-neutrino decays. *Phys. Rev. Lett.*, 88:111803, 2002.
- [422] M. Bischofberger et al. Search for CP violation in  $\tau \rightarrow K_S^0\pi\nu_\tau$  decays at Belle. *Phys. Rev. Lett.*, 107:131801, 2011.
- [423] J. P. Lees et al. Search for CP Violation in the Decay  $\tau^- \rightarrow \pi^- K_S^0(= 0\pi^0)\nu_\tau$ . *Phys. Rev. D*, 85:031102, 2012. [Erratum: Phys.Rev.D 85, 099904 (2012)].
- [424] I. I. Bigi and A. I. Sanda. A 'Known' CP asymmetry in tau decays. *Phys. Lett. B*, 625:47–52, 2005.



- [425] G. Calderon, D. Delepine, and G. Lopez Castro. Is there a paradox in CP asymmetries of  $\tau^{+-} \rightarrow K(L,S)\pi^{+-} \nu$  decays? *Phys. Rev. D*, 75:076001, 2007.
- [426] Yuval Grossman and Yosef Nir. CP Violation in  $\tau^{\pm} \rightarrow \pi^{\pm} K_S \nu$  and  $D^{\pm} \rightarrow \pi^{\pm} K_S$ : The Importance of  $K_S - K_L$  Interference. *JHEP*, 04:002, 2012.
- [427] Vincenzo Cirigliano, Andreas Crivellin, and Martin Hoferichter. No-go theorem for nonstandard explanations of the  $\tau \rightarrow K_S \pi \nu_{\tau}$  CP asymmetry. *Phys. Rev. Lett.*, 120(14):141803, 2018.
- [428] R. Escribano, S. Gonzalez-Solis, and P. Roig.  $\tau^{-} \rightarrow K^{-} \eta^{(\prime)} \nu_{\tau}$  decays in Chiral Perturbation Theory with Resonances. *JHEP*, 10:039, 2013.
- [429] P. del Amo Sanchez et al. Studies of  $\tau^{-} \rightarrow \eta K \nu$  and  $\tau^{-} \rightarrow \eta \pi \nu(\tau)$  at BaBar and a search for a second-class current. *Phys. Rev. D*, 83:032002, 2011.
- [430] D. Buskulic et al. A Study of tau decays involving eta and omega mesons. *Z. Phys. C*, 74:263–273, 1997.
- [431] John E. Bartelt et al. First observation of the decay  $\tau^{-} \rightarrow K^{-} \eta \tau$ -neutrino. *Phys. Rev. Lett.*, 76:4119–4123, 1996.
- [432] M. Artuso et al. Measurement of tau decays involving eta mesons. *Phys. Rev. Lett.*, 69:3278–3281, 1992.
- [433] J. P. Lees et al. Study of high-multiplicity 3-prong and 5-prong tau decays at BABAR. *Phys. Rev. D*, 86:092010, 2012.
- [434] T. D. Lee and Chen-Ning Yang. Charge Conjugation, a New Quantum Number  $G$ , and Selection Rules Concerning a Nucleon Anti-nucleon System. *Nuovo Cim.*, 10:749–753, 1956.
- [435] C. Leroy and J. Pestieau. Tau Decay and Second Class Currents. *Phys. Lett. B*, 72:398–399, 1978.

- [436] Steven Weinberg. Charge symmetry of weak interactions. *Phys. Rev.*, 112:1375–1379, 1958.
- [437] A. Pich. 'Anomalous'  $\eta$  Production in Tau Decay. *Phys. Lett. B*, 196:561–565, 1987.
- [438] A. Bramon, Stephan Narison, and A. Pich. The  $\tau \rightarrow \nu_\tau \eta \pi$  Process in and Beyond QCD. *Phys. Lett. B*, 196:543–546, 1987.
- [439] S. Tisserant and T. N. Truong. TAU  $\rightarrow$  DELTA neutrino DECAY INDUCED BY LIGHT QUARK MASS DIFFERENCE. *Phys. Lett. B*, 115:264–266, 1982.
- [440] Shmuel Nussinov and Abner Soffer. Estimate of the branching fraction tau  $\rightarrow$  eta pi-nu(tau), the a(0)-(980), and non-standard weak interactions. *Phys. Rev. D*, 78:033006, 2008.
- [441] H. Neufeld and H. Rupertsberger. Isospin breaking in chiral perturbation theory and the decays eta  $\rightarrow$  pi lepton neutrino and tau  $\rightarrow$  eta pi neutrino. *Z. Phys. C*, 68:91–102, 1995.
- [442] M. Antonelli et al. An Evaluation of  $|V_{us}|$  and precise tests of the Standard Model from world data on leptonic and semileptonic kaon decays. *Eur. Phys. J. C*, 69:399–424, 2010.
- [443] S. Descotes-Genon, E. Kou, and B. Moussallam. Dispersive evaluation of the second-class amplitude  $\tau \rightarrow \eta \pi \nu_\tau$  in the standard model. *Nucl. Phys. B Proc. Suppl.*, 253-255:65–68, 2014.
- [444] M. Derrick et al. Evidence for the Decay  $\tau^+ \rightarrow \pi^+ \eta \bar{\nu}_\tau$ -neutrino. *Phys. Lett. B*, 189:260–266, 1987.
- [445] N. Paver and Riazuddin. On meson dominance in the 'second class'  $\tau \rightarrow \eta \pi \nu_\tau$  decay. *Phys. Rev. D*, 82:057301, 2010.

- [446] B. Moussallam. Deriving experimental constraints on the scalar form factor in the second-class  $\tau \rightarrow \eta\pi\nu$  mode. In *16th International Workshop on Tau Lepton Physics*, 12 2021.
- [447] Rafel Escribano, Sergi Gonzalez-Solis, and Pablo Roig. Predictions on the second-class current decays  $\tau^- \rightarrow \pi^- \eta^{(\prime)} \nu_\tau$ . *Phys. Rev. D*, 94(3):034008, 2016.
- [448] G. Hernández-Tomé, G. López Castro, and P. Roig. G-parity breaking in  $\tau^- \rightarrow \eta^{(\prime)} \pi^- \nu_\tau$  decays induced by the  $\eta^{(\prime)} \gamma \gamma$  form factor. *Phys. Rev. D*, 96(5):053003, 2017.
- [449] Kazuya Ogawa, Michel Hernández Villanueva, and Kiyoshi Hayasaka. Search for second-class currents with the  $\tau$  decay into  $\pi\eta\nu$ . *PoS, Beauty2019:061*, 2020.
- [450] Gilberto Colangelo, Markus Finkemeier, and Res Urech. Tau decays and chiral perturbation theory. *Phys. Rev. D*, 54:4403–4418, 1996.
- [451] G. Ecker and R. Underdorfer. Four pion production in  $e^+ e^-$  annihilation. *Eur. Phys. J. C*, 24:535–545, 2002.
- [452] R. Fischer, J. Wess, and F. Wagner. Decays of the Heavy Lepton  $\tau$  and Chiral Dynamics. *Z. Phys. C*, 3:313–320, 1979.
- [453] D. Gomez Dumm, P. Roig, A. Pich, and J. Portoles.  $\tau \rightarrow \pi \pi \pi \nu(\tau)$  decays and the  $a(1)(1260)$  off-shell width revisited. *Phys. Lett. B*, 685:158–164, 2010.
- [454] D. Gomez Dumm, A. Pich, and J. Portoles.  $\tau \rightarrow \pi \pi \pi \nu(\tau)$  decays in the resonance effective theory. *Phys. Rev. D*, 69:073002, 2004.
- [455] R. Barate et al. Measurement of the spectral functions of axial - vector hadronic tau decays and determination of  $\alpha(S)(M^{**2}(\tau))$ . *Eur. Phys. J. C*, 4:409–431, 1998.
- [456] D. Buskulic et al. Measurement of the strong coupling constant using tau decays. *Phys. Lett. B*, 307:209–220, 1993.

- [457] T. E. Browder et al. Structure functions in the decay  $\tau \rightarrow \pi^+ \pi^0 \nu_\tau$ . *Phys. Rev. D*, 61:052004, 2000.
- [458] M. Feindt. Measuring Hadronic Currents and Weak Coupling Constants in  $\tau \rightarrow \text{Neutrino } 3 \pi$ . *Z. Phys. C*, 48:681–688, 1990.
- [459] D. Gomez Dumm, P. Roig, A. Pich, and J. Portoles. Hadron structure in  $\tau \rightarrow \text{KK } \pi \nu$  (tau) decays. *Phys. Rev. D*, 81:034031, 2010.
- [460] Pablo Roig. *Hadronic and radiative decays of the tau lepton*. PhD thesis, Valencia U., 2010.
- [461] Daniel Gomez Dumm and Pablo Roig. Resonance Chiral Lagrangian analysis of  $\tau^- \rightarrow \eta^{(\prime)} \pi^- \pi^0 \nu_\tau$  decays. *Phys. Rev. D*, 86:076009, 2012.
- [462] J. J. Gomez-Cadenas, M. C. Gonzalez-Garcia, and A. Pich. The decay  $\tau^- \rightarrow K^- K^+ \pi^- \nu_\tau$  and the tau-neutrino mass. *Phys. Rev. D*, 42:3093–3099, 1990.
- [463] M. Finkemeier, Johann H. Kuhn, and E. Mirkes. Theoretical aspects of  $\tau \rightarrow K h$  (h) tau-neutrino decays and experimental comparisons. *Nucl. Phys. B Proc. Suppl.*, 55:169–178, 1997.
- [464] M. Davier, S. Descotes-Genon, Andreas Hocker, B. Malaescu, and Z. Zhang. The Determination of  $\alpha(s)$  from Tau Decays Revisited. *Eur. Phys. J. C*, 56:305–322, 2008.
- [465] L. Y. Dai, J. Portoles, and O. Shekhovtsova. Three pseudoscalar meson production in  $e^+e^-$  annihilation. *Phys. Rev. D*, 88:056001, 2013.
- [466] O. Shekhovtsova, T. Przedzinski, P. Roig, and Z. Was. Resonance chiral Lagrangian currents and  $\tau$  decay Monte Carlo. *Phys. Rev. D*, 86:113008, 2012.
- [467] I. M. Nugent, T. Przedzinski, P. Roig, O. Shekhovtsova, and Z. Was. Resonance chiral Lagrangian currents and experimental data for  $\tau^- \rightarrow \pi^- \pi^- \pi^+ \nu_\tau$ . *Phys. Rev. D*, 88:093012, 2013.

- [468] Stanislaw Jadach, Johann H. Kuhn, and Zbigniew Was. TAUOLA: A Library of Monte Carlo programs to simulate decays of polarized tau leptons. *Comput. Phys. Commun.*, 64:275–299, 1990.
- [469] S. Jadach, Z. Was, R. Decker, and Johann H. Kuhn. The tau decay library TAUOLA: Version 2.4. *Comput. Phys. Commun.*, 76:361–380, 1993.
- [470] R. Unterdorfer. The One loop functional of chiral SU(2). *JHEP*, 07:053, 2002.
- [471] Zhi-Hui Guo and Pablo Roig. One meson radiative tau decays. *Phys. Rev. D*, 82:113016, 2010.
- [472] A. Guevara, G. López Castro, and P. Roig. Weak radiative pion vertex in  $\tau^- \rightarrow \pi^- \nu_\tau \ell^+ \ell^-$  decays. *Phys. Rev. D*, 88(3):033007, 2013.
- [473] Adolfo Guevara, Gabriel López Castro, and Pablo Roig. Improved description of dilepton production in  $\tau^- \rightarrow \nu_\tau P^-$  decays. *Phys. Rev. D*, 105(7):076007, 2022.
- [474] A. Anastassov et al. Study of tau decays to six pions and neutrino. *Phys. Rev. Lett.*, 86:4467–4471, 2001.
- [475] R. Barate et al. Three-prong  $\tau$  decays with charged kaons. *Eur. Phys. J. C*, 1:65–79, 1998.
- [476] Bernard Aubert et al. Exclusive branching fraction measurements of semileptonic tau decays into three charged hadrons,  $\tau^- \rightarrow \phi \pi^- \nu(\tau)$  and  $\tau^- \rightarrow \phi K^- \nu(\tau)$ . *Phys. Rev. Lett.*, 100:011801, 2008.
- [477] M. J. Lee et al. Measurement of the branching fractions and the invariant mass distributions for  $\tau^- \rightarrow h^- h^+ h^- \nu_\tau$  decays. *Phys. Rev. D*, 81:113007, 2010.
- [478] Roy A. Briere et al. Branching fractions of tau leptons decays to three charged hadrons. *Phys. Rev. Lett.*, 90:181802, 2003.
- [479] R. Barate et al.  $K_0(S)$  production in tau decays. *Eur. Phys. J. C*, 4:29–45, 1998.

- [480] R. Barate et al. One prong tau decays with kaons. *Eur. Phys. J. C*, 10:1–18, 1999.
- [481] J. P. Lees et al. Measurement of the spectral function for the  $\tau^- \rightarrow K^- K_S \nu_\tau$  decay. *Phys. Rev. D*, 98(3):032010, 2018.
- [482] S. Ryu et al. Measurements of Branching Fractions of  $\tau$  Lepton Decays with one or more  $K_S^0$ . *Phys. Rev. D*, 89(7):072009, 2014.
- [483] T. E. Coan et al. Decays of tau leptons to final states containing  $K(s)0$  mesons. *Phys. Rev. D*, 53:6037–6053, 1996.
- [484] Kregg E. Arms et al. Study of tau decays to four-hadron final states with kaons. *Phys. Rev. Lett.*, 94:241802, 2005.
- [485] H. Albrecht et al. An Improved Upper Limit on the tau-neutrino Mass from the Decay  $\tau^- \rightarrow \pi^- \pi^- \pi^- \pi^+ \pi^+ \tau$ -neutrino. *Phys. Lett. B*, 202:149, 1988.
- [486] D. Gibaut et al. Study of the five charged pion decay of the tau lepton. *Phys. Rev. Lett.*, 73:934–938, 1994.
- [487] J. Abdallah et al. A Measurement of the tau hadronic branching ratios. *Eur. Phys. J. C*, 46:1–26, 2006.
- [488] B. G. Bylsma et al. LIMIT ON tau DECAY TO SEVEN CHARGED PARTICLES. *Phys. Rev. D*, 35:2269, 1987.
- [489] K. Ackerstaff et al. Measurement of tau branching ratios to five charged hadrons. *Eur. Phys. J. C*, 8:183–189, 1999.
- [490] J. P. Lees et al. The branching fraction of  $\tau^- \rightarrow \pi^- K_S^0 K_S^0 (\pi^0) \nu_\tau$  decays. *Phys. Rev. D*, 86:092013, 2012.
- [491] M. Battle et al. Measurement of Cabibbo suppressed decays of the tau lepton. *Phys. Rev. Lett.*, 73:1079–1083, 1994.

- [492] P. Abreu et al. Charged kaon production in tau decays at LEP. *Phys. Lett. B*, 334:435–449, 1994.
- [493] G. Abbiendi et al. A Study of one prong tau decays with a charged kaon. *Eur. Phys. J. C*, 19:653–665, 2001.
- [494] Bernard Aubert et al. Measurement of the  $\tau^- \rightarrow K^- \pi^0 \nu_\tau$  branching fraction. *Phys. Rev. D*, 76:051104, 2007.
- [495] G. Abbiendi et al. Measurement of the strange spectral function in hadronic tau decays. *Eur. Phys. J. C*, 35:437–455, 2004.
- [496] M. Bishai et al. First observation of the decay tau-  $\rightarrow$  K\*- eta tau-neutrino. *Phys. Rev. Lett.*, 82:281–285, 1999.
- [497] M. Acciarri et al. One prong tau decays with neutral kaons. *Phys. Lett. B*, 352:487–497, 1995.
- [498] G. Abbiendi et al. Tau decays with neutral kaons. *Eur. Phys. J. C*, 13:213–223, 2000.
- [499] R. Barate et al. Study of tau decays involving kaons, spectral functions and determination of the strange quark mass. *Eur. Phys. J. C*, 11:599–618, 1999.
- [500] W. Altmannshofer et al. The Belle II Physics Book. *PTEP*, 2019(12):123C01, 2019. [Erratum: PTEP 2020, 029201 (2020)].
- [501] Swagato Banerjee et al. Snowmass 2021 White Paper: Charged lepton flavor violation in the tau sector. 3 2022.
- [502] Antonio Pich. Workshop on Tau Lepton Physics: **30<sup>th</sup>** Anniversary. In *16th International Workshop on Tau Lepton Physics*, 12 2021.
- [503] E. Fermi. An attempt of a theory of beta radiation. 1. *Z. Phys.*, 88:161–177, 1934.

- [504] Vincenzo Cirigliano, James Jenkins, and Martin Gonzalez-Alonso. Semileptonic decays of light quarks beyond the Standard Model. *Nucl. Phys. B*, 830:95–115, 2010.
- [505] Tanmoy Bhattacharya, Vincenzo Cirigliano, Saul D. Cohen, Alberto Filipuzzi, Martin Gonzalez-Alonso, Michael L. Graesser, Rajan Gupta, and Huey-Wen Lin. Probing Novel Scalar and Tensor Interactions from (Ultra)Cold Neutrons to the LHC. *Phys. Rev. D*, 85:054512, 2012.
- [506] Vincenzo Cirigliano, Susan Gardner, and Barry Holstein. Beta Decays and Non-Standard Interactions in the LHC Era. *Prog. Part. Nucl. Phys.*, 71:93–118, 2013.
- [507] Hsi-Ming Chang, Martin González-Alonso, and Jorge Martin Camalich. Nonstandard Semileptonic Hyperon Decays. *Phys. Rev. Lett.*, 114(16):161802, 2015.
- [508] Aurore Courtoy, Stefan Baeßler, Martín González-Alonso, and Simonetta Liuti. Beyond-Standard-Model Tensor Interaction and Hadron Phenomenology. *Phys. Rev. Lett.*, 115:162001, 2015.
- [509] Martín González-Alonso and Jorge Martin Camalich. Global Effective-Field-Theory analysis of New-Physics effects in (semi)leptonic kaon decays. *JHEP*, 12:052, 2016.
- [510] Martín González-Alonso and Jorge Martin Camalich. New Physics in  $s \rightarrow u\ell^-\bar{\nu}$ : Interplay between semileptonic kaon and hyperon decays. 6 2016.
- [511] S. Alioli, V. Cirigliano, W. Dekens, J. de Vries, and E. Mereghetti. Right-handed charged currents in the era of the Large Hadron Collider. *JHEP*, 05:086, 2017.
- [512] Vincenzo Cirigliano, Adam Falkowski, Martín González-Alonso, and Antonio Rodríguez-Sánchez. Hadronic  $\tau$  Decays as New Physics Probes in the LHC Era. *Phys. Rev. Lett.*, 122(22):221801, 2019.
- [513] S. Descotes-Genon and B. Moussallam. Analyticity of  $\eta\pi$  isospin-violating form factors and the  $\tau \rightarrow \eta\pi\nu$  second-class decay. *Eur. Phys. J. C*, 74:2946, 2014.



- [514] I. Baum, V. Lubicz, G. Martinelli, L. Orifici, and S. Simula. Matrix elements of the electromagnetic operator between kaon and pion states. *Phys. Rev. D*, 84:074503, 2011.
- [515] Stanley J. Brodsky and Glennys R. Farrar. Scaling Laws at Large Transverse Momentum. *Phys. Rev. Lett.*, 31:1153–1156, 1973.
- [516] G. Peter Lepage and Stanley J. Brodsky. Exclusive Processes in Perturbative Quantum Chromodynamics. *Phys. Rev. D*, 22:2157, 1980.
- [517] V. Mateu and J. Portoles. Form-factors in radiative pion decay. *Eur. Phys. J. C*, 52:325–338, 2007.
- [518] O. Cata and V. Mateu. Chiral perturbation theory with tensor sources. *JHEP*, 09:078, 2007.
- [519] J. A. Miranda and P. Roig. Effective-field theory analysis of the  $\tau^- \rightarrow \pi^- \pi^0 \nu_\tau$  decays. *JHEP*, 11:038, 2018.
- [520] A. Sirlin. Radiative corrections to  $g(v)/g(\mu)$  in simple extensions of the  $su(2) \times u(1)$  gauge model. *Nucl. Phys. B*, 71:29–51, 1974.
- [521] A. Sirlin. Current Algebra Formulation of Radiative Corrections in Gauge Theories and the Universality of the Weak Interactions. *Rev. Mod. Phys.*, 50:573, 1978. [Erratum: *Rev.Mod.Phys.* 50, 905 (1978)].
- [522] A. Sirlin. Large  $m(W)$ ,  $m(Z)$  Behavior of the  $O(\alpha)$  Corrections to Semileptonic Processes Mediated by  $W$ . *Nucl. Phys. B*, 196:83–92, 1982.
- [523] W. J. Marciano and A. Sirlin. Radiative Corrections to beta Decay and the Possibility of a Fourth Generation. *Phys. Rev. Lett.*, 56:22, 1986.
- [524] Kenneth M. Watson. The Effect of final state interactions on reaction cross-sections. *Phys. Rev.*, 88:1163–1171, 1952.

- [525] M. J. Losty, V. Chaloupka, A. Ferrando, L. Montanet, E. Paul, D. Yaffe, A. Zieminski, J. Alitti, B. Gandois, and J. Louie. A Study of  $\pi^- \pi^-$  scattering from  $\pi^- p$  interactions at 3.93-GeV/c. *Nucl. Phys. B*, 69:185–204, 1974.
- [526] W. Hoogland et al. Measurement and Analysis of the  $\pi^+ \pi^+$  System Produced at Small Momentum Transfer in the Reaction  $\pi^+ p \rightarrow \pi^+ \pi^+ n$  at 12.5-GeV. *Nucl. Phys. B*, 126:109–123, 1977.
- [527] K. Ackerstaff et al. Measurement of the strong coupling constant  $\alpha(s)$  and the vector and axial vector spectral functions in hadronic tau decays. *Eur. Phys. J. C*, 7:571–593, 1999.
- [528] W. Ochs. Ph. d. thesis, münchen university. 1974.
- [529] B. Hyams et al.  $\pi\pi$  Phase Shift Analysis from 600-MeV to 1900-MeV. *Nucl. Phys. B*, 64:134–162, 1973.
- [530] P. Estabrooks and Alan D. Martin.  $\pi^+ \pi^+$  Phase Shift Analysis Below the K anti-K Threshold. *Nucl. Phys. B*, 79:301–316, 1974.
- [531] Johan Bijnens, Gilberto Colangelo, and Gerhard Ecker. The Mesonic chiral Lagrangian of order  $p^6$ . *JHEP*, 02:020, 1999.
- [532] Sidney R. Coleman, J. Wess, and Bruno Zumino. Structure of phenomenological Lagrangians. 1. *Phys. Rev.*, 177:2239–2247, 1969.
- [533] Curtis G. Callan, Jr., Sidney R. Coleman, J. Wess, and Bruno Zumino. Structure of phenomenological Lagrangians. 2. *Phys. Rev.*, 177:2247–2250, 1969.
- [534] Dao-Neng Gao. Angular distribution asymmetry in  $\tau^- \rightarrow \pi^- \pi^0 \nu(\tau)$  decay in the two-Higgs-doublet model with large  $\tan \beta$ . *Phys. Rev. D*, 71:051301, 2005.
- [535] Francisco Guerrero and Jose Antonio Oller.  $K\bar{K}$  scattering amplitude to one loop in chiral perturbation theory, its unitarization and pion form-factors. *Nucl. Phys. B*, 537:459–476, 1999. [Erratum: *Nucl.Phys.B* 602, 641–643 (2001)].

- [536] J. A. Oller, E. Oset, and J. E. Palomar. Pion and kaon vector form-factors. *Phys. Rev. D*, 63:114009, 2001.
- [537] A. Gomez Nicola and J. R. Pelaez. Meson meson scattering within one loop chiral perturbation theory and its unitarization. *Phys. Rev. D*, 65:054009, 2002.
- [538] David J. Wilson, Raul A. Briceño, Jozef J. Dudek, Robert G. Edwards, and Christopher E. Thomas. Coupled  $\pi\pi, K\bar{K}$  scattering in  $P$ -wave and the  $\rho$  resonance from lattice QCD. *Phys. Rev. D*, 92(9):094502, 2015.
- [539] Martin González-Alonso, Oscar Naviliat-Cuncic, and Nathal Severijns. New physics searches in nuclear and neutron  $\beta$  decay. *Prog. Part. Nucl. Phys.*, 104:165–223, 2019.
- [540] Javier Rendón. *Exclusive hadronic  $\tau$  decays as probes of non-SM interactions*. PhD thesis, CINVESTAV, IPN, 10 2021.
- [541] M. Tanabashi et al. Review of Particle Physics. *Phys. Rev. D*, 98(3):030001, 2018.
- [542] Sergi González-Solís, Alejandro Miranda, Javier Rendón, and Pablo Roig. Effective-field theory analysis of the  $\tau^- \rightarrow K^-(\eta^{(\prime)}, K^0)\nu_\tau$  decays. *Phys. Rev. D*, 101(3):034010, 2020.
- [543] F. Ambrosino et al. Measurement of the pseudoscalar mixing angle and eta-prime gluonium content with KLOE detector. *Phys. Lett. B*, 648:267–273, 2007.
- [544] G. Peter Lepage and Stanley J. Brodsky. Exclusive Processes in Quantum Chromodynamics: Evolution Equations for Hadronic Wave Functions and the Form-Factors of Mesons. *Phys. Lett. B*, 87:359–365, 1979.
- [545] H. Leutwyler. On the  $1/N$  expansion in chiral perturbation theory. *Nucl. Phys. B Proc. Suppl.*, 64:223–231, 1998.
- [546] Roland Kaiser and H. Leutwyler. Large  $N(c)$  in chiral perturbation theory. *Eur. Phys. J. C*, 17:623–649, 2000.

- [547] Rafel Escribano, Sergi González-Solís, Pere Masjuan, and Pablo Sanchez-Puertas.  $\eta'$  transition form factor from space- and timelike experimental data. *Phys. Rev. D*, 94(5):054033, 2016.
- [548] A. Guevara, P. Roig, and J. J. Sanz-Cillero. Pseudoscalar pole light-by-light contributions to the muon ( $g - 2$ ) in Resonance Chiral Theory. *JHEP*, 06:160, 2018.
- [549] Sébastien Descotes-Genon, Adam Falkowski, Marco Fedele, Martín González-Alonso, and Javier Virto. The CKM parameters in the SMEFT. *JHEP*, 05:172, 2019.
- [550] Diogo Boito, Maarten Golterman, Kim Maltman, James Osborne, and Santiago Peris. Strong coupling from the revised ALEPH data for hadronic  $\tau$  decays. *Phys. Rev. D*, 91(3):034003, 2015.
- [551] Antonio Pich and Antonio Rodríguez-Sánchez. Determination of the QCD coupling from ALEPH  $\tau$  decay data. *Phys. Rev. D*, 94(3):034027, 2016.
- [552] K. Maltman, C. E. Wolfe, Swagato Banerjee, J. M. Roney, and I. Nugent. Status of the Hadronic Tau Determination of  $|V_{us}|$ . *Int. J. Mod. Phys. A*, 23:3191–3195, 2008.
- [553] Renwick J. Hudspith, Randy Lewis, Kim Maltman, and James Zanotti. A resolution of the inclusive flavor-breaking  $\tau |V_{us}|$  puzzle. *Phys. Lett. B*, 781:206–212, 2018.
- [554] K. G. Chetyrkin, Johann H. Kuhn, and A. A. Pivovarov. Determining the strange quark mass in Cabibbo suppressed tau lepton decays. *Nucl. Phys. B*, 533:473–493, 1998.
- [555] Antonio Pich and Joaquim Prades. Strange quark mass determination from Cabibbo suppressed tau decays. *JHEP*, 10:004, 1999.
- [556] Joachim Kambor and Kim Maltman. The Strange quark mass from flavor breaking in hadronic tau decays. *Phys. Rev. D*, 62:093023, 2000.

- [557] S. Chen, M. Davier, E. Gamiz, Andreas Hocker, A. Pich, and J. Prades. Strange quark mass from the invariant mass distribution of Cabibbo suppressed tau decays. *Eur. Phys. J. C*, 22:31–38, 2001.
- [558] E. Gamiz, M. Jamin, A. Pich, J. Prades, and F. Schwab. Determination of  $m(s)$  and  $-V(us)$ — from hadronic tau decays. *JHEP*, 01:060, 2003.
- [559] Elvira Gamiz, Matthias Jamin, Antonio Pich, Joaquim Prades, and Felix Schwab.  $V(us)$  and  $m(s)$  from hadronic tau decays. *Phys. Rev. Lett.*, 94:011803, 2005.
- [560] P. A. Baikov, K. G. Chetyrkin, and Johann H. Kuhn. Strange quark mass from tau lepton decays with  $O(\alpha(s)^3)$  accuracy. *Phys. Rev. Lett.*, 95:012003, 2005.
- [561] J. Alcaraz et al. A Combination of preliminary electroweak measurements and constraints on the standard model. 12 2006.
- [562] Alberto Filipuzzi, Jorge Portoles, and Martin Gonzalez-Alonso.  $U(2)^5$  flavor symmetry and lepton universality violation in  $W \rightarrow \tau\nu_\tau$ . *Phys. Rev. D*, 85:116010, 2012.
- [563] Georges Aad et al. Test of the universality of  $\tau$  and  $\mu$  lepton couplings in  $W$ -boson decays with the ATLAS detector. *Nature Phys.*, 17(7):813–818, 2021.
- [564] Armen Tumasyan et al. Precision measurement of the  $W$  boson decay branching fractions in proton-proton collisions at  $\sqrt{s} = 13$  TeV. *Phys. Rev. D*, 105(7):072008, 2022.
- [565] Zhi-Hui Guo and J. A. Oller. Resonances from meson-meson scattering in  $U(3)$  CHPT. *Phys. Rev. D*, 84:034005, 2011.
- [566] Zhi-Hui Guo, J. A. Oller, and J. Ruiz de Elvira. Chiral dynamics in form factors, spectral-function sum rules, meson-meson scattering and semi-local duality. *Phys. Rev. D*, 86:054006, 2012.

- [567] Zhi-Hui Guo, Liuming Liu, Ulf-G. Meißner, J. A. Oller, and A. Rusetsky. Chiral study of the  $a_0(980)$  resonance and  $\pi\eta$  scattering phase shifts in light of a recent lattice simulation. *Phys. Rev. D*, 95(5):054004, 2017.
- [568] Martin Hoferichter, Bastian Kubis, Jacobo Ruiz de Elvira, and Peter Stoffer. Nucleon Matrix Elements of the Antisymmetric Quark Tensor. *Phys. Rev. Lett.*, 122(12):122001, 2019. [Erratum: Phys.Rev.Lett. 124, 199901 (2020)].
- [569] Jonathan L. Rosner, Sheldon Stone, and Ruth S. Van de Water. Leptonic Decays of Charged Pseudoscalar Mesons - 2015. 9 2015.
- [570] Vincenzo Cirigliano, David Díaz-Calderón, Adam Falkowski, Martín González-Alonso, and Antonio Rodríguez-Sánchez. Semileptonic tau decays beyond the Standard Model. *JHEP*, 04:152, 2022.
- [571] P.A.M. Dirac. A Theory of Electrons and Protons. *Proc. Roy. Soc. Lond. A*, 126(801):360–365, 1930.
- [572] Pablo Roig Garces. The anomalous magnetic moment of the muon: short overview. *Rev. Mex. Fis. Suppl.*, 3(2):020706, 2022.
- [573] Bogdan Malaescu. Theory of Muon  $g-2$ . In *24th International Symposium on Spin Physics*, 6 2022.
- [574] Stefano Laporta. High-precision calculation of the 4-loop contribution to the electron  $g-2$  in QED. *Phys. Lett. B*, 772:232–238, 2017.
- [575] Tatsumi Aoyama, M. Hayakawa, Toichiro Kinoshita, and Makiko Nio. Tenth-Order Electron Anomalous Magnetic Moment — Contribution of Diagrams without Closed Lepton Loops. *Phys. Rev. D*, 91(3):033006, 2015. [Erratum: Phys.Rev.D 96, 019901 (2017)].
- [576] Tatsumi Aoyama, Toichiro Kinoshita, and Makiko Nio. Theory of the Anomalous Magnetic Moment of the Electron. *Atoms*, 7(1):28, 2019.

- [577] Sergey Volkov. Calculating the five-loop QED contribution to the electron anomalous magnetic moment: Graphs without lepton loops. *Phys. Rev. D*, 100(9):096004, 2019.
- [578] A. L. Kataev. Renormalization group and the five loop QED asymptotic contributions to the muon anomaly. *Phys. Lett. B*, 284:401–409, 1992. [Erratum: *Phys.Lett.B* 710, 710 (2012)].
- [579] S. Laporta. Analytical and numerical contributions of some tenth order graphs containing vacuum polarization insertions to the muon  $(g-2)$  in QED. *Phys. Lett. B*, 328:522–527, 1994.
- [580] P. A. Baikov, A. Maier, and P. Marquard. The QED vacuum polarization function at four loops and the anomalous magnetic moment at five loops. *Nucl. Phys. B*, 877:647–661, 2013.
- [581] Richard H. Parker, Chenghui Yu, Weicheng Zhong, Brian Estey, and Holger Müller. Measurement of the fine-structure constant as a test of the Standard Model. *Science*, 360:191, 2018.
- [582] Andrzej Czarnecki, William J. Marciano, and Arkady Vainshtein. Refinements in electroweak contributions to the muon anomalous magnetic moment. *Phys. Rev. D*, 67:073006, 2003. [Erratum: *Phys.Rev.D* 73, 119901 (2006)].
- [583] C. Gnendiger, D. Stöckinger, and H. Stöckinger-Kim. The electroweak contributions to  $(g - 2)_\mu$  after the Higgs boson mass measurement. *Phys. Rev. D*, 88:053005, 2013.
- [584] Bai-Long Hoid, Martin Hoferichter, and Bastian Kubis. Hadronic vacuum polarization and vector-meson resonance parameters from  $e^+e^- \rightarrow \pi^0\gamma$ . *Eur. Phys. J. C*, 80(10):988, 2020.
- [585] Martin Hoferichter, Bai-Long Hoid, and Bastian Kubis. Three-pion contribution to hadronic vacuum polarization. *JHEP*, 08:137, 2019.

- [586] Alexander Kurz, Tao Liu, Peter Marquard, and Matthias Steinhauser. Hadronic contribution to the muon anomalous magnetic moment to next-to-next-to-leading order. *Phys. Lett. B*, 734:144–147, 2014.
- [587] M. Ablikim et al. Future Physics Programme of BESIII. *Chin. Phys. C*, 44(4):040001, 2020.
- [588] M. Passera, W. J. Marciano, and A. Sirlin. The Muon  $g-2$  and the bounds on the Higgs boson mass. *Phys. Rev. D*, 78:013009, 2008.
- [589] Andreas Crivellin, Martin Hoferichter, Claudio Andrea Manzari, and Marc Montull. Hadronic Vacuum Polarization:  $(g - 2)_\mu$  versus Global Electroweak Fits. *Phys. Rev. Lett.*, 125(9):091801, 2020.
- [590] Alexander Keshavarzi, William J. Marciano, Massimo Passera, and Alberto Sirlin. Muon  $g - 2$  and  $\Delta\alpha$  connection. *Phys. Rev. D*, 102(3):033002, 2020.
- [591] Eduardo de Rafael. Constraints between  $\Delta\alpha_{\text{had}}(M_Z^2)$  and  $(g_\mu - 2)_{\text{HVP}}$ . *Phys. Rev. D*, 102(5):056025, 2020.
- [592] Bogdan Malaescu and Matthias Schott. Impact of correlations between  $a_\mu$  and  $\alpha_{\text{QED}}$  on the EW fit. *Eur. Phys. J. C*, 81(1):46, 2021.
- [593] C. M. Carloni Calame, M. Passera, L. Trentadue, and G. Venanzoni. A new approach to evaluate the leading hadronic corrections to the muon  $g-2$ . *Phys. Lett. B*, 746:325–329, 2015.
- [594] G. Abbiendi et al. Measuring the leading hadronic contribution to the muon  $g-2$  via  $\mu e$  scattering. *Eur. Phys. J. C*, 77(3):139, 2017.
- [595] Marco Cè et al. Window observable for the hadronic vacuum polarization contribution to the muon  $g - 2$  from lattice QCD. 6 2022.



- [596] G. Colangelo, A. X. El-Khadra, M. Hoferichter, A. Keshavarzi, C. Lehner, P. Stoffer, and T. Teubner. Data-driven evaluations of Euclidean windows to scrutinize hadronic vacuum polarization. 5 2022.
- [597] Kirill Melnikov and Arkady Vainshtein. Hadronic light-by-light scattering contribution to the muon anomalous magnetic moment revisited. *Phys. Rev. D*, 70:113006, 2004.
- [598] Joaquim Prades, Eduardo de Rafael, and Arkady Vainshtein. The Hadronic Light-by-Light Scattering Contribution to the Muon and Electron Anomalous Magnetic Moments. *Adv. Ser. Direct. High Energy Phys.*, 20:303–317, 2009.
- [599] Andreas Nyffeler. Hadronic light-by-light scattering in the muon  $g-2$ : A New short-distance constraint on pion-exchange. *Phys. Rev. D*, 79:073012, 2009.
- [600] Fred Jegerlehner and Andreas Nyffeler. The Muon  $g-2$ . *Phys. Rept.*, 477:1–110, 2009.
- [601] Josef Leutgeb and Anton Rebhan. Axial vector transition form factors in holographic QCD and their contribution to the anomalous magnetic moment of the muon. *Phys. Rev. D*, 101(11):114015, 2020.
- [602] Luigi Cappiello, Oscar Catà, Giancarlo D’Ambrosio, David Greynat, and Abhishek Iyer. Axial-vector and pseudoscalar mesons in the hadronic light-by-light contribution to the muon  $(g - 2)$ . *Phys. Rev. D*, 102(1):016009, 2020.
- [603] Pere Masjuan, Pablo Roig, and Pablo Sanchez-Puertas. The interplay of transverse degrees of freedom and axial-vector mesons with short-distance constraints in  $g - 2$ . *J. Phys. G*, 49(1):015002, 2022.
- [604] Johan Bijnens, Nils Hermansson-Truedsson, Laetitia Laub, and Antonio Rodríguez-Sánchez. The two-loop perturbative correction to the  $(g - 2)_\mu$  HLbL at short distances. *JHEP*, 04:240, 2021.
- [605] Igor Danilkin, Martin Hoferichter, and Peter Stoffer. A dispersive estimate of scalar contributions to hadronic light-by-light scattering. *Phys. Lett. B*, 820:136502, 2021.

- [606] Luigi Cappiello, Oscar Catà, and Giancarlo D’Ambrosio. Scalar resonances in the hadronic light-by-light contribution to the muon  $(g-2)$ . *Phys. Rev. D*, 105(5):056020, 2022.
- [607] Martin Hoferichter and Thomas Teubner. Mixed Leptonic and Hadronic Corrections to the Anomalous Magnetic Moment of the Muon. *Phys. Rev. Lett.*, 128(11):112002, 2022.
- [608] Pere Masjuan and Pablo Sanchez-Puertas. Pseudoscalar-pole contribution to the  $(g_\mu - 2)$ : a rational approach. *Phys. Rev. D*, 95(5):054026, 2017.
- [609] Gilberto Colangelo, Martin Hoferichter, Massimiliano Procura, and Peter Stoffer. Dispersion relation for hadronic light-by-light scattering: two-pion contributions. *JHEP*, 04:161, 2017.
- [610] Martin Hoferichter, Bai-Long Hoid, Bastian Kubis, Stefan Leupold, and Sebastian P. Schneider. Dispersion relation for hadronic light-by-light scattering: pion pole. *JHEP*, 10:141, 2018.
- [611] Antoine Gérardin, Harvey B. Meyer, and Andreas Nyffeler. Lattice calculation of the pion transition form factor with  $N_f = 2+1$  Wilson quarks. *Phys. Rev. D*, 100(3):034520, 2019.
- [612] Johan Bijnens, Nils Hermansson-Truedsson, and Antonio Rodríguez-Sánchez. Short-distance constraints for the HLbL contribution to the muon anomalous magnetic moment. *Phys. Lett. B*, 798:134994, 2019.
- [613] Gilberto Colangelo, Franziska Hagelstein, Martin Hoferichter, Laetitia Laub, and Peter Stoffer. Longitudinal short-distance constraints for the hadronic light-by-light contribution to  $(g - 2)_\mu$  with large- $N_c$  Regge models. *JHEP*, 03:101, 2020.
- [614] Vladyslav Pauk and Marc Vanderhaeghen. Single meson contributions to the muon’s anomalous magnetic moment. *Eur. Phys. J. C*, 74(8):3008, 2014.

- [615] Igor Danilkin and Marc Vanderhaeghen. Light-by-light scattering sum rules in light of new data. *Phys. Rev. D*, 95(1):014019, 2017.
- [616] M. Knecht, S. Narison, A. Rabemananjara, and D. Rabetiariivony. Scalar meson contributions to a  $\mu$  from hadronic light-by-light scattering. *Phys. Lett. B*, 787:111–123, 2018.
- [617] Gernot Eichmann, Christian S. Fischer, and Richard Williams. Kaon-box contribution to the anomalous magnetic moment of the muon. *Phys. Rev. D*, 101(5):054015, 2020.
- [618] Pablo Roig and Pablo Sanchez-Puertas. Axial-vector exchange contribution to the hadronic light-by-light piece of the muon anomalous magnetic moment. *Phys. Rev. D*, 101(7):074019, 2020.
- [619] Thomas Blum, Norman Christ, Masashi Hayakawa, Taku Izubuchi, Luchang Jin, Chulwoo Jung, and Christoph Lehner. Hadronic Light-by-Light Scattering Contribution to the Muon Anomalous Magnetic Moment from Lattice QCD. *Phys. Rev. Lett.*, 124(13):132002, 2020.
- [620] En-Hung Chao, Renwick J. Hudspith, Antoine Gérardin, Jeremy R. Green, Harvey B. Meyer, and Konstantin Ottnad. Hadronic light-by-light contribution to  $(g - 2)_\mu$  from lattice QCD: a complete calculation. *Eur. Phys. J. C*, 81(7):651, 2021.
- [621] D. Giusti and S. Simula. Lepton anomalous magnetic moments in Lattice QCD+QED. *PoS, LATTICE2019:104*, 2019.
- [622] Gilberto Colangelo, Martin Hoferichter, Andreas Nyffeler, Massimo Passera, and Peter Stoffer. Remarks on higher-order hadronic corrections to the muon  $g-2$ . *Phys. Lett. B*, 735:90–91, 2014.
- [623] Stanley J. Brodsky and Eduardo De Rafael. SUGGESTED BOSON - LEPTON PAIR COUPLINGS AND THE ANOMALOUS MAGNETIC MOMENT OF THE MUON. *Phys. Rev.*, 168:1620–1622, 1968.

- [624] B.E. Lautrup and E. De Rafael. Calculation of the sixth-order contribution from the fourth-order vacuum polarization to the difference of the anomalous magnetic moments of muon and electron. *Phys. Rev.*, 174:1835–1842, 1968.
- [625] Bernd Krause. Higher order hadronic contributions to the anomalous magnetic moment of leptons. *Phys. Lett. B*, 390:392–400, 1997.
- [626] R.R. Akhmetshin et al. Reanalysis of hadronic cross-section measurements at CMD-2. *Phys. Lett. B*, 578:285–289, 2004.
- [627] R.R. Akhmetshin et al. Measurement of  $e^+e^- \rightarrow \rho \rightarrow \pi^+\pi^-$  cross-section with CMD-2 around rho meson. *Phys. Lett. B*, 527:161–172, 2002.
- [628] V.M. Aul’chenko et al. Measurement of the pion form-factor in the range 1.04-GeV to 1.38-GeV with the CMD-2 detector. *JETP Lett.*, 82:743–747, 2005.
- [629] R.R. Akhmetshin et al. High-statistics measurement of the pion form factor in the rho-meson energy range with the CMD-2 detector. *Phys. Lett. B*, 648:28–38, 2007.
- [630] M. N. Achasov et al. Study of the reaction  $e^+e^- \rightarrow \pi^0\gamma$  with the SND detector at the VEPP-2M collider. *Phys. Rev. D*, 93(9):092001, 2016.
- [631] M. N. Achasov et al. Measurement of the  $e^+e^- \rightarrow \pi^0\gamma$  cross section in the energy range 1.075-2 GeV at SND. *Phys. Rev. D*, 98(11):112001, 2018.
- [632] R. R. Akhmetshin et al. Measurement of  $\phi$  meson parameters in  $K_L^0 K_S^0$  decay mode with CMD-2. *Phys. Lett. B*, 466:385, 1999. [Erratum: *Phys.Lett.B* 508, 217–218 (2001)].
- [633] M. N. Achasov et al. Measurement of the  $e^+e^- \rightarrow K^+K^-$  process cross-section in the energy range  $s^{**}(1/2) = 1.04 - 1.38$  GeV with the SND detector in the experiment at VEPP-2M  $e^+e^-$  collider. *Phys. Rev. D*, 76:072012, 2007.

- [634] M. N. Achasov et al. Measurement of the  $e^+e^- \rightarrow \mathbf{K}^+\mathbf{K}^-$  cross section in the energy range  $\sqrt{s} = 1.05 - 2.0$  GeV. *Phys. Rev. D*, 94(11):112006, 2016.
- [635] Bernard Aubert et al. A Study of  $e^+e^- \rightarrow p\bar{p}$  using initial state radiation with BABAR. *Phys. Rev. D*, 73:012005, 2006.
- [636] J. P. Lees et al. Study of  $e^+e^- \rightarrow p\bar{p}$  via initial-state radiation at BABAR. *Phys. Rev. D*, 87(9):092005, 2013.
- [637] J. P. Lees et al. Measurement of the  $e^+e^- \rightarrow p\bar{p}$  cross section in the energy range from 3.0 to 6.5 GeV. *Phys. Rev. D*, 88(7):072009, 2013.
- [638] R. R. Akhmetshin et al. Study of the process  $e^+e^- \rightarrow p\bar{p}$  in the c.m. energy range from threshold to 2 GeV with the CMD-3 detector. *Phys. Lett. B*, 759:634–640, 2016.
- [639] M. N. Achasov et al. Study of the process  $e^+e^- \rightarrow n\bar{n}$  at the VEPP-2000  $e^+e^-$  collider with the SND detector. *Phys. Rev. D*, 90(11):112007, 2014.
- [640] R. R. Akhmetshin et al. Study of  $\phi \rightarrow \pi^+ \pi^- \pi^0$  with CMD-2 detector. *Phys. Lett. B*, 642:203–209, 2006.
- [641] M. N. Achasov et al. Precise measurements of the hadronic cross sections with the CMD-3 and SND detectors at the VEPP-2000  $e^+e^-$  collider. *EPJ Web Conf.*, 71:00121, 2014.
- [642] A. Antonelli et al. Measurement of the  $e^+ e^- \rightarrow \pi^+ \pi^- \pi^0$  and  $e^+ e^- \rightarrow \omega \pi^+ \pi^-$  reactions in the energy interval 1350-MeV - 2400-MeV. *Z. Phys. C*, 56:15–20, 1992.
- [643] Akio Sugamoto. An Attempt to study pentaquark baryons in string theory. In *2nd International Symposium on New Developments of Integrated Sciences*, 4 2004.
- [644] M. N. Achasov et al. Analysis of  $e^+ e^- \rightarrow \pi^+ \pi^- \pi^+ \pi^-$  and  $e^+ e^- \rightarrow \pi^+ \pi^- \pi^0$  processes in the energy range of  $s^{*(1/2)} = 0.98\text{--}1.38\text{-GeV}$  in experiments with a spherical neutral detector. *J. Exp. Theor. Phys.*, 96:789–800, 2003.

- [645] R. R. Akhmetshin et al.  $\rho(1)(1260)$  pi dominance in the process  $e^+e^- \rightarrow 4\pi$  at energies 1.05-GeV - 1.38-GeV. *Phys. Lett. B*, 466:392–402, 1999.
- [646] R. R. Akhmetshin et al. Study of the process  $e^+e^- \rightarrow \pi^+\pi^-\pi^+\pi^-$  in the c.m. energy range 920–1060 MeV with the CMD-3 detector. *Phys. Lett. B*, 768:345–350, 2017.
- [647] Bernard Aubert et al. The  $e^+e^- \rightarrow 3(\pi^+\pi^-), 2(\pi^+\pi^-\pi^0)$  and  $K^+K^-2(\pi^+\pi^-)$  cross sections at center-of-mass energies from production threshold to 4.5-GeV measured with initial-state radiation. *Phys. Rev. D*, 73:052003, 2006.
- [648] R. R. Akhmetshin et al. Study of the process  $e^+e^- \rightarrow 3(\pi^+\pi^-)$  in the c.m. energy range 1.5–2.0 GeV with the cmd-3 detector. *Phys. Lett. B*, 723:82–89, 2013.
- [649] M. N. Achasov et al. Measurement of the  $e^+e^- \rightarrow \eta\pi^+\pi^-$  cross section with the SND detector at the VEPP-2000 collider. *Phys. Rev. D*, 97(1):012008, 2018.
- [650] S. S. Gribov et al. Measurement of the  $e^+e^- \rightarrow \eta\pi^+\pi^-$  cross section with the CMD-3 detector at the VEPP-2000 collider. *JHEP*, 01:112, 2020.
- [651] J. P. Lees et al. Study of the reactions  $e^+e^- \rightarrow \pi^+\pi^-\pi^0\pi^0\pi^0\gamma$  and  $\pi^+\pi^-\pi^0\pi^0\eta\gamma$  at center-of-mass energies from threshold to 4.35 GeV using initial-state radiation. *Phys. Rev. D*, 98(11):112015, 2018.
- [652] D. N. Shemyakin et al. Measurement of the  $e^+e^- \rightarrow K^+K^-\pi^+\pi^-$  cross section with the CMD-3 detector at the VEPP-2000 collider. *Phys. Lett. B*, 756:153–160, 2016.
- [653] M. N. Achasov et al. Measurement of the  $e^+e^- \rightarrow \mathbf{K}_S\mathbf{K}_L\pi^0$  cross section in the energy range  $\sqrt{s} = 1.3 - 2.0$  GeV. *Phys. Rev. D*, 97(3):032011, 2018.
- [654] Medina Ablikim et al. Measurement of the leptonic decay width of  $J/\psi$  using initial state radiation. *Phys. Lett. B*, 761:98–103, 2016.
- [655] Michel Davier, Andreas Höcker, Bogdan Malaescu, Chang-Zheng Yuan, and Zhiqing Zhang. Update of the ALEPH non-strange spectral functions from hadronic  $\tau$  decays. *Eur. Phys. J. C*, 74(3):2803, 2014.

- [656] Ricard Alemany, Michel Davier, and Andreas Hocker. Improved determination of the hadronic contribution to the muon ( $g-2$ ) and to alpha ( $M(z)$ ) using new data from hadronic tau decays. *Eur. Phys. J. C*, 2:123–135, 1998.
- [657] M. Acciarri et al. Measurement of exclusive branching fractions of hadronic one space prong tau decays. *Phys. Lett. B*, 345:93–102, 1995.
- [658] Julian S. Schwinger. *PARTICLES, SOURCES, AND FIELDS. VOL. 3.* 1989.
- [659] Manuel Drees and Ken-ichi Hikasa. Scalar top production in  $e^+e^-$  annihilation. *Phys. Lett. B*, 252:127–134, 1990.
- [660] F. V. Flores-Baez, G. Lopez Castro, and G. Toledo Sanchez. The Width difference of rho vector mesons. *Phys. Rev. D*, 76:096010, 2007.
- [661] G. J. Gounaris and J. J. Sakurai. Finite width corrections to the vector meson dominance prediction for  $\rho \rightarrow e^+e^-$ . *Phys. Rev. Lett.*, 21:244–247, 1968.
- [662] J. Grange et al. Muon ( $g-2$ ) Technical Design Report. 1 2015.
- [663] Khépani Raya, Adnan Bashir, and Pablo Roig. Contribution of neutral pseudoscalar mesons to  $a_\mu^{HLbL}$  within a Schwinger-Dyson equations approach to QCD. *Phys. Rev. D*, 101(7):074021, 2020.
- [664] Marc Knecht. On some short-distance properties of the fourth-rank hadronic vacuum polarization tensor and the anomalous magnetic moment of the muon. *JHEP*, 08:056, 2020.
- [665] Jan Lüdtke and Massimiliano Procura. Effects of longitudinal short-distance constraints on the hadronic light-by-light contribution to the muon  $g - 2$ . *Eur. Phys. J. C*, 80(12):1108, 2020.
- [666] B. Ananthanarayan, Irinel Caprini, and Diganta Das. Test of analyticity and unitarity for the pion form-factor data around the  $\rho$  resonance. *Phys. Rev. D*, 102(9):096003, 2020.

- [667] Christopher Aubin, Thomas Blum, Maarten Golterman, and Santiago Peris. Application of effective field theory to finite-volume effects in  $a_\mu^{HVP}$ . *Phys. Rev. D*, 102(9):094511, 2020.
- [668] Johan Bijnens, Nils Hermansson-Truedsson, Laetitia Laub, and Antonio Rodríguez-Sánchez. Short-distance HLbL contributions to the muon anomalous magnetic moment beyond perturbation theory. *JHEP*, 10:203, 2020.
- [669] Wen Qin, Ling-Yun Dai, and Jorge Portoles. Two and three pseudoscalar production in  $e^+e^-$  annihilation and their contributions to  $(g - 2)_\mu$ . *JHEP*, 03:092, 2021.
- [670] Ángel Miramontes, Adnan Bashir, Khépani Raya, and Pablo Roig. Pion and Kaon box contribution to  $a_\mu$ HLbL. *Phys. Rev. D*, 105(7):074013, 2022.
- [671] Gilberto Colangelo, Franziska Hagelstein, Martin Hoferichter, Laetitia Laub, and Peter Stoffer. Short-distance constraints for the longitudinal component of the hadronic light-by-light amplitude: an update. *Eur. Phys. J. C*, 81(8):702, 2021.
- [672] Jing-Yu Yi, Zhong-Yu Wang, and C. W. Xiao. Study of the pion vector form factor and its contribution to the muon  $g-2$ . *Phys. Rev. D*, 104(11):116017, 2021.
- [673] Josef Leutgeb and Anton Rebhan. Hadronic light-by-light contribution to the muon  $g-2$  from holographic QCD with massive pions. *Phys. Rev. D*, 104(9):094017, 2021.
- [674] Christopher L. James, Randy Lewis, and Kim Maltman. ChPT estimate of the strong-isospin-breaking contribution to the anomalous magnetic moment of the muon. *Phys. Rev. D*, 105(5):053010, 2022.
- [675] Gilberto Colangelo, Martin Hoferichter, Bastian Kubis, Malwin Niehus, and Jacobo Ruiz de Elvira. Chiral extrapolation of hadronic vacuum polarization. *Phys. Lett. B*, 825:136852, 2022.
- [676] M. Abe et al. A New Approach for Measuring the Muon Anomalous Magnetic Moment and Electric Dipole Moment. *PTEP*, 2019(5):053C02, 2019.



- [677] F. Flores-Baez, A. Flores-Tlalpa, G. Lopez Castro, and G. Toledo Sanchez. Long-distance radiative corrections to the di-pion tau lepton decay. *Phys. Rev. D*, 74:071301, 2006.
- [678] A. Flores-Tlalpa, F. Flores-Baez, G. Lopez Castro, and G. Toledo Sanchez. Model-dependent radiative corrections to tau-  $\rightarrow$  pi- pi0 nu revisited. *Nucl. Phys. B Proc. Suppl.*, 169:250–254, 2007.
- [679] Sergi González-Solís, Alejandro Miranda, Javier Rendón, and Pablo Roig. Exclusive hadronic tau decays as probes of non-SM interactions. *Phys. Lett. B*, 804:135371, 2020.
- [680] Mattia Bruno, Taku Izubuchi, Christoph Lehner, and Aaron Meyer. On isospin breaking in  $\tau$  decays for  $(g - 2)_\mu$  from Lattice QCD. *PoS, LATTICE2018*:135, 2018.
- [681] Fred Jegerlehner. Muon  $g - 2$  theory: The hadronic part. *EPJ Web Conf.*, 166:00022, 2018.
- [682] P. D. Ruiz-Femenia, A. Pich, and J. Portoles. Odd intrinsic parity processes within the resonance effective theory of QCD. *JHEP*, 07:003, 2003.
- [683] Zhi-Hui Guo. Study of tau-  $\rightarrow$  V P- nu(tau) in the framework of resonance chiral theory. *Phys. Rev. D*, 78:033004, 2008.
- [684] Karol Kampf and Jiri Novotny. Resonance saturation in the odd-intrinsic parity sector of low-energy QCD. *Phys. Rev.*, D84:014036, 2011.
- [685] Yun-Hua Chen, Zhi-Hui Guo, and Han-Qing Zheng. Study of  $\eta$ - $\eta'$  mixing from radiative decay processes. *Phys. Rev. D*, 85:054018, 2012.
- [686] P. Colangelo, J. J. Sanz-Cillero, and F. Zuo. Holography, chiral Lagrangian and form factor relations. *JHEP*, 11:012, 2012.
- [687] Pablo Roig and Juan José Sanz Cillero. Consistent high-energy constraints in the anomalous QCD sector. *Phys. Lett.*, B733:158–163, 2014.

- [688] Yun-Hua Chen, Zhi-Hui Guo, and Han-Qing Zheng. Radiative transition processes of light vector resonances in a chiral framework. *Phys. Rev. D*, 90(3):034013, 2014.
- [689] P. Roig, A. Guevara, and G. López Castro.  $VV'P$  form factors in resonance chiral theory and the  $\pi - \eta - \eta'$  light-by-light contribution to the muon  $g - 2$ . *Phys. Rev. D*, 89(7):073016, 2014.
- [690] Yun-Hua Chen, De-Liang Yao, and Han-Qing Zheng. A study of  $\rho - \omega$  mixing in resonance chiral theory. *Commun. Theor. Phys.*, 69(1):50, 2018.
- [691] Ling-Yun Dai, Javier Fuentes-Martín, and Jorge Portolés. Scalar-involved three-point Green functions and their phenomenology. *Phys. Rev. D*, 99(11):114015, 2019.
- [692] Tomáš Kadavý, Karol Kampf, and Jiri Novotny. OPE of Green functions of chiral currents. *JHEP*, 10:142, 2020.
- [693] B. Moussallam. A Sum rule approach to the violation of Dashen's theorem. *Nucl. Phys. B*, 504:381–414, 1997.
- [694] Santiago Peris, Michel Perrottet, and Eduardo de Rafael. Matching long and short distances in large  $N(c)$  QCD. *JHEP*, 05:011, 1998.
- [695] M. Knecht, S. Peris, M. Perrottet, and E. de Rafael. Decay of pseudoscalars into lepton pairs and large  $N(c)$  QCD. *Phys. Rev. Lett.*, 83:5230–5233, 1999.
- [696] S. Peris, B. Phily, and E. de Rafael. Tests of large  $N(c)$  QCD from hadronic tau decay. *Phys. Rev. Lett.*, 86:14–17, 2001.
- [697] Marc Knecht and Andreas Nyffeler. Resonance estimates of  $O(p^{**6})$  low-energy constants and QCD short distance constraints. *Eur. Phys. J. C*, 21:659–678, 2001.
- [698] Johan Bijnens, Elvira Gamiz, Edisher Lipartia, and Joaquim Prades. QCD short distance constraints and hadronic approximations. *JHEP*, 04:055, 2003.

- [699] B. Ananthanarayan and B. Moussallam. Four-point correlator constraints on electromagnetic chiral parameters and resonance effective Lagrangians. *JHEP*, 06:047, 2004.
- [700] A. Guevara, G. López-Castro, and P. Roig.  $\tau^- \rightarrow \eta^{(\prime)} \pi^- \nu_\tau \gamma$  decays as backgrounds in the search for second class currents. *Phys. Rev.*, D95(5):054015, 2017.
- [701] J. Bijnens, G. Ecker, and J. Gasser. Radiative semileptonic kaon decays. *Nucl. Phys.*, B396:81–118, 1993.
- [702] F. E. Low. Bremsstrahlung of very low-energy quanta in elementary particle collisions. *Phys. Rev.*, 110:974–977, 1958.
- [703] J. L. Gutiérrez Santiago, G. López Castro, and P. Roig. Lepton-pair production in dipion  $\tau$  lepton decays. *Phys. Rev. D*, 103(1):014027, 2021.
- [704] I. Rosell, P. Ruiz-Femenia, and J. Portoles. One-loop renormalization of resonance chiral theory: Scalar and pseudoscalar resonances. *JHEP*, 12:020, 2005.
- [705] Ignasi Rosell, Juan Jose Sanz-Cillero, and Antonio Pich. Towards a determination of the chiral couplings at NLO in  $1/N(C)$ :  $L^{**r}(8)(\mu)$ . *JHEP*, 01:039, 2007.
- [706] Jorge Portoles, Ignasi Rosell, and Pedro Ruiz-Femenia. Vanishing chiral couplings in the large- $N(C)$  resonance theory. *Phys. Rev. D*, 75:114011, 2007.
- [707] A. Pich, I. Rosell, and J. J. Sanz-Cillero. Form-factors and current correlators: Chiral couplings  $L(10)\mu) **r(\mu)$  and  $C(87)**r(\mu)$  at NLO in  $1/N(C)$ . *JHEP*, 07:014, 2008.
- [708] J. J. Sanz-Cillero. Renormalization group equations in resonance chiral theory. *Phys. Lett. B*, 681:100–104, 2009.
- [709] Steven Weinberg. Precise relations between the spectra of vector and axial vector mesons. *Phys. Rev. Lett.*, 18:507–509, 1967.

- [710] Maarten F. L. Golterman and Santiago Peris. The 7/11 Rule: An Estimate of  $m(\rho) / f(\pi)$ . *Phys. Rev.*, D61:034018, 2000.
- [711] Yun-Hua Chen, Zhi-Hui Guo, and Bing-Song Zou. Unified study of  $J/\psi \rightarrow PV, P\gamma^{(*)}$  and light hadron radiative processes. *Phys. Rev. D*, 91:014010, 2015.
- [712] T. H. Burnett and Norman M. Kroll. Extension of the low soft photon theorem. *Phys. Rev. Lett.*, 20:86, 1968.
- [713] Alain Flores-Tlalpa. *Modelo de dominancia de mesones para decaimientos semileptónicos de sabores pesados*. PhD thesis, CINVESTAV, IPN, 2008.
- [714] J. J. Sakurai. Theory of strong interactions. *Annals Phys.*, 11:1–48, 1960.
- [715] M. Gourdin and E. De Rafael. Hadronic contributions to the muon  $g$ -factor. *Nucl. Phys. B*, 10:667–674, 1969.
- [716] M. Benayoun, P. David, L. DelBuono, and F. Jegerlehner. Upgraded Breaking Of The HLS Model: A Full Solution to the  $\tau^- e^+ e^-$  and  $\phi$  Decay Issues And Its Consequences On  $g-2$  VMD Estimates. *Eur. Phys. J. C*, 72:1848, 2012.
- [717] M. Benayoun, P. David, L. DelBuono, and F. Jegerlehner. An Update of the HLS Estimate of the Muon  $g-2$ . *Eur. Phys. J. C*, 73:2453, 2013.
- [718] M. Benayoun, P. David, L. DelBuono, and F. Jegerlehner. Muon  $g - 2$  estimates: can one trust effective Lagrangians and global fits? *Eur. Phys. J. C*, 75(12):613, 2015.
- [719] E. Borie and G. A. Rinker. THE ENERGY LEVELS OF MUONIC ATOMS. *Rev. Mod. Phys.*, 54:67–118, 1982.
- [720] A. E. Dorokhov, A. P. Martynenko, F. A. Martynenko, and A. E. Radzhabov. The proton size puzzle: experiment vs theory. *EPJ Web Conf.*, 191:04001, 2018.
- [721] Michael I. Eides, Howard Grotch, and Valery A. Shelyuto. Theory of light hydrogen - like atoms. *Phys. Rept.*, 342:63–261, 2001.

- [722] Krzysztof Pachucki. Theory of the Lamb shift in muonic hydrogen. *Phys. Rev. A*, 53:2092–2100, 1996.
- [723] Krzysztof Pachucki. Proton structure effects in muonic hydrogen. *Phys. Rev. A*, 60:3593–3598, 1999.
- [724] E. Borie. Lamb shift in muonic hydrogen. *Phys. Rev. A*, 71:032508, 2005.
- [725] E. Borie. Lamb Shift in Light Muonic Atoms. *Z. Phys. A*, 275:347–349, 1975.
- [726] E. Borie and G. A. Rinker. Improved calculation of the muonic-helium Lamb shift. *Phys. Rev. A*, 18:324–327, 1978.
- [727] E. Borie. Hyperfine Structure of Light Exotic Atoms. *Z. Phys. A*, 278:127, 1976.
- [728] E. Borie. LAMB SHIFT IN MUONIC HE-3. *Z. Phys. A*, 297:17–18, 1980.
- [729] A. Di Giacomo. A sensitive test of quantum electrodynamics. the 2s-2p energy difference of muonic hydrogen. *Nucl. Phys. B*, 11:411–427, 1969.
- [730] G. Carboni. Lamb shift in muonic deuterium. *Lett. Nuovo Cim.*, 7S2:160–162, 1973.
- [731] Carl E. Carlson. The Proton Radius Puzzle. *Prog. Part. Nucl. Phys.*, 82:59–77, 2015.
- [732] Jean-Philippe Karr, Dominique Marchand, and Eric Voutier. The proton size. *Nature Rev. Phys.*, 2(11):601–614, 2020.
- [733] Haiyan Gao and Marc Vanderhaeghen. The proton charge radius. *Rev. Mod. Phys.*, 94(1):015002, 2022.
- [734] Clara Peset, Antonio Pineda, and Oleksandr Tomalak. The proton radius (puzzle?) and its relatives. *Prog. Part. Nucl. Phys.*, 121:103901, 2021.

- [735] U.D. Jentschura, A. Matveev, C.G. Parthey, J. Alnis, R. Pohl, Th. Udem, N. Kolachevsky, and T.W. Hänsch. Hydrogen-deuterium isotope shift: From the  $1s - 2s$ -transition frequency to the proton-deuteron charge-radius difference. *Phys. Rev. A*, 83:042505, Apr 2011.
- [736] Julian J. Krauth et al. Measuring the  $\alpha$ -particle charge radius with muonic helium-4 ions. *Nature*, 589(7843):527–531, 2021.
- [737] M. Mihovilovič et al. The proton charge radius extracted from the initial-state radiation experiment at MAMI. *Eur. Phys. J. A*, 57(3):107, 2021.
- [738] Steffen Strauch. The MUon Scattering Experiment (MUSE) at the Paul Scherrer Institute. *PoS*, NuFACT2018:136, 2018.
- [739] Christian Dreisbach et al. Measuring the Proton Radius in High-Energy Muon-Proton Scattering. *PoS*, DIS2019:222, 2019.
- [740] A. Gasparian et al. PRad-II: A New Upgraded High Precision Measurement of the Proton Charge Radius. 9 2020.
- [741] Simon Scheidegger and Frédéric Merkt. Spectroscopy of highly excited states of the hydrogen atom. *CHIMIA*, 74(4):285, Apr. 2020.
- [742] J. J. Krauth, L. S. Dreissen, C. Roth, E. L. Gründeman, M. Collombon, M. Favier, and K. S. E. Eikema. Paving the way for fundamental physics tests with singly-ionized helium. *PoS*, FFK2019:049, 2020.
- [743] M. Herrmann, M. Haas, U. D. Jentschura, F. Kottmann, D. Leibfried, G. Saathoff, C. Gohle, A. Ozawa, V. Batteiger, S. Knünz, N. Kolachevsky, H. A. Schüssler, T. W. Hänsch, and Th. Udem. Feasibility of coherent xuv spectroscopy on the  $1s-2s$  transition in singly ionized helium. *Phys. Rev. A*, 79:052505, May 2009.

- [744] S. Alighanbari, G.S. Giri, F.L. Constantin, Korobov V. I., and S. Schiller. Precise test of quantum electrodynamics and determination of fundamental constants with  $HD^+$  ions. *Nature*, 581:152–158, 2020.
- [745] Maxim Pospelov and Yu-Dai Tsai. Light scalars and dark photons in Borexino and LSND experiments. *Phys. Lett. B*, 785:288–295, 2018.
- [746] Savely G. Karshenboim, David McKeen, and Maxim Pospelov. Constraints on muon-specific dark forces. *Phys. Rev. D*, 90(7):073004, 2014. [Addendum: *Phys.Rev.D* 90, 079905 (2014)].
- [747] Yu-Sheng Liu, Ian C. Cloët, and Gerald A. Miller. Eta Decay and Muonic Puzzles. *Nucl. Phys.*, B:114638, 2019.
- [748] Carl E. Carlson and Michael Freid. Extending theories on muon-specific interactions. *Phys. Rev. D*, 92(9):095024, 2015.
- [749] Masaharu Sato et al. Laser spectroscopy of the hyperfine splitting energy in the ground state of muonic hydrogen. In *20th International Conference on Particles and Nuclei*, pages 460–463, 9 2014.
- [750] Andrzej Adamczak. Muonic Molecule Formation in Condensed Deuterium. *Hyperfine Interact.*, 138(1-4):343–350, 2001.
- [751] Dimitar Bakalov, Andrzej Adamczak, Mihail Stoilov, and Andrea Vacchi. Toward the measurement of the hyperfine splitting in the ground state of muonic hydrogen. *Hyperfine Interact.*, 233(1-3):97–101, 2015.
- [752] C. Pizzolotto et al. Measurement of the muon transfer rate from muonic hydrogen to oxygen in the range 70-336 K. *Phys. Lett. A*, 403:127401, 2021.
- [753] C. Pizzolotto et al. The FAMU experiment: muonic hydrogen high precision spectroscopy studies. *Eur. Phys. J. A*, 56(7):185, 2020.

- [754] E. Borie. Lamb shift in light muonic atoms: Revisited. *Annals Phys.*, 327:733–763, 2012.
- [755] Paul Indelicato. Nonperturbative evaluation of some QED contributions to the muonic hydrogen  $n=2$  Lamb shift and hyperfine structure. *Phys. Rev. A*, 87(2):022501, 2013.
- [756] S. G. Karshenboim, E. Y. Korzinin, V. A. Shelyuto, and V. G. Ivanov. Theory of Lamb Shift in Muonic Hydrogen. *Journal of Physical and Chemical Reference Data*, 44:031202, 2015.
- [757] Hans A. Bethe and Edwin E. Salpeter. *Quantum Mechanics of One- and Two-Electron Atoms*. 1957.
- [758] Aldo Antognini, Franz Kottmann, Francois Biraben, Paul Indelicato, Francois Nez, and Randolph Pohl. Theory of the 2S-2P Lamb shift and 2S hyperfine splitting in muonic hydrogen. *Annals Phys.*, 331:127–145, 2013.
- [759] A. P. Martynenko. Fine and hyperfine structure of P-levels in muonic hydrogen. *Phys. Atom. Nucl.*, 71:125–135, 2008.
- [760] U. D. Jentschura. Lamb Shift in Muonic Hydrogen. I. Verification and Update of Theoretical Predictions. *Annals Phys.*, 326:500–515, 2011.
- [761] Michael C. Birse and Judith A. McGovern. Proton polarisability contribution to the Lamb shift in muonic hydrogen at fourth order in chiral perturbation theory. *Eur. Phys. J. A*, 48:120, 2012.
- [762] James H. Wilson. Measuring Zitterbewegung predicted by the Dirac equation for a free electron. *Phys. Essays*, 31(1):59–67, 2018.
- [763] James Lewis Friar. Nuclear Finite Size Effects in Light Muonic Atoms. *Annals Phys.*, 122:151, 1979.



- [764] A. C. Zemach. Proton Structure and the Hyperfine Shift in Hydrogen. *Phys. Rev.*, 104:1771–1781, 1956.
- [765] Carl E. Carlson, Vahagn Nazaryan, and Keith Griffioen. Proton structure corrections to hyperfine splitting in muonic hydrogen. *Phys. Rev. A*, 83:042509, 2011.
- [766] Y. Prok et al. Moments of the Spin Structure Functions  $g_p^{**}(1)$  and  $g_d^{**}(1)$  for  $0.05 < Q^{**2} < 3.0\text{-GeV}^{**2}$ . *Phys. Lett. B*, 672:12–16, 2009.
- [767] P. L Anthony et al. Measurements of the  $Q^{**2}$  dependence of the proton and neutron spin structure functions  $g(1)^{**p}$  and  $g(1)^{**n}$ . *Phys. Lett. B*, 493:19–28, 2000.
- [768] Frank R. Wesselmann et al. Proton spin structure in the resonance region. *Phys. Rev. Lett.*, 98:132003, 2007.
- [769] Carl E. Carlson, Vahagn Nazaryan, and Keith Griffioen. Proton structure corrections to electronic and muonic hydrogen hyperfine splitting. *Phys. Rev. A*, 78:022517, 2008.
- [770] Kaushik Borah, Richard J. Hill, Gabriel Lee, and Oleksandr Tomalak. Parametrization and applications of the low- $Q^2$  nucleon vector form factors. *Phys. Rev. D*, 102(7):074012, 2020.
- [771] Franziska Hagelstein and Vladimir Pascalutsa. Proton structure in the hyperfine splitting of muonic hydrogen. *PoS*, CD15:077, 2016.
- [772] P. Amaro et al. Laser excitation of the 1s-hyperfine transition in muonic hydrogen. 11 2021.
- [773] Helmut Hellwig, Robert F. C. Vessot, Martin W. Levine, Paul W. Zitzewitz, David W. Allan, and David J. Glaze. Measurement of the unperturbed hydrogen hyperfine transition frequency. *IEEE Transactions on Instrumentation and Measurement*, 19(4):200–209, 1970.

- [774] Savely G. Karshenboim. Some possibilities for laboratory searches for variations of fundamental constants. *Can. J. Phys.*, 78:639–678, 2000.
- [775] Savely G. Karshenboim. Nuclear structure dependent radiative corrections to the hydrogen hyperfine splitting. *Phys. Lett. A*, 225:97, 1997.
- [776] Clara Peset and Antonio Pineda. Model-independent determination of the two-photon exchange contribution to hyperfine splitting in muonic hydrogen. *JHEP*, 04:060, 2017.
- [777] Oleksandr Tomalak. Hyperfine splitting in ordinary and muonic hydrogen. *Eur. Phys. J. A*, 54(1):3, 2018.
- [778] Savely G. Karshenboim and Valery A. Shelyuto. Hadronic vacuum-polarization contribution to various QED observables. *Eur. Phys. J. D*, 75(2):49, 2021.
- [779] M. S. Safronova, D. Budker, D. DeMille, Derek F. Jackson Kimball, A. Derevianko, and C. W. Clark. Search for New Physics with Atoms and Molecules. *Rev. Mod. Phys.*, 90(2):025008, 2018.
- [780] Matthew P. A. Jones, Robert M. Potvliege, and Michael Spannowsky. Probing new physics using Rydberg states of atomic hydrogen. *Phys. Rev. Res.*, 2(1):013244, 2020.
- [781] Claudia Frugiuele and Clara Peset. Muonic vs electronic dark forces: a complete EFT treatment for atomic spectroscopy. *JHEP*, 05:002, 2022.
- [782] Antoni Szczurek. Production of axial-vector mesons at  $e^+e^-$  collisions with double-tagging as a way to constrain the axial meson light-by-light contribution to the muon  $g-2$  and the hyperfine splitting of muonic hydrogen. *Phys. Rev. D*, 102(11):113015, 2020.
- [783] Marvin Zanke, Martin Hoferichter, and Bastian Kubis. On the transition form factors of the axial-vector resonance  $f_1(1285)$  and its decay into  $e^+e^-$ . *JHEP*, 07:106, 2021.

- [784] A. E. Dorokhov, N. I. Kochelev, A. P. Martynenko, F. A. Martynenko, and A. E. Radzhabov. The contribution of axial-vector mesons to hyperfine structure of muonic hydrogen. *Phys. Lett. B*, 776:105–110, 2018.
- [785] A. E. Dorokhov, A. P. Martynenko, F. A. Martynenko, and A. E. Radzhabov. Effects of light-by-light scattering in the Lamb shift and hyperfine structure of muonic hydrogen. *EPJ Web Conf.*, 222:03010, 2019.
- [786] Alejandro Miranda, Pablo Roig, and Pablo Sanchez-Puertas. Axial-vector exchange contribution to the hyperfine splitting. *Phys. Rev. D*, 105(1):016017, 2022.
- [787] A. S. Rudenko.  $f_1(1285) \rightarrow e^+e^-$  decay and direct  $f_1$  production in  $e^+e^-$  collisions. *Phys. Rev. D*, 96(7):076004, 2017.
- [788] Martin Hoferichter and Peter Stoffer. Asymptotic behavior of meson transition form factors. *JHEP*, 05:159, 2020.
- [789] L. D. Landau. On the angular momentum of a system of two photons. *Dokl. Akad. Nauk SSSR*, 60(2):207–209, 1948.
- [790] Chen-Ning Yang. Selection Rules for the Dematerialization of a Particle Into Two Photons. *Phys. Rev.*, 77:242–245, 1950.
- [791] Pere Masjuan and Pablo Sanchez-Puertas.  $\eta$  and  $\eta'$  decays into lepton pairs. *JHEP*, 08:108, 2016.
- [792] P. Achard et al.  $f(1)(1285)$  formation in two photon collisions at LEP. *Phys. Lett. B*, 526:269–277, 2002.
- [793] P. Achard et al. Study of resonance formation in the mass region 1400-MeV to 1500-MeV through the reaction  $\gamma\gamma \rightarrow K_0(S) K^\pm \pi^\mp$ . *JHEP*, 03:018, 2007.
- [794] Pere Masjuan, Enrique Ruiz Arriola, and Wojciech Broniowski. Meson dominance of hadron form factors and large- $N_c$  phenomenology. *Phys. Rev. D*, 87(1):014005, 2013.

- [795] Meng-Chuan Du and Qiang Zhao. Comprehensive study of light axial vector mesons with the presence of triangle singularity. *Phys. Rev. D*, 104(3):036008, 2021.
- [796] Leendert Hayen. Radiative corrections to nucleon weak charges and Beyond Standard Model impact. 2 2021.
- [797] C. Alexandrou, S. Bacchio, M. Constantinou, J. Finkenrath, K. Hadjiyiannakou, K. Jansen, G. Koutsou, and A. Vaquero Aviles-Casco. Nucleon axial, tensor, and scalar charges and  $\sigma$ -terms in lattice QCD. *Phys. Rev. D*, 102(5):054517, 2020.
- [798] P.A. Zyla et al. Review of Particle Physics. *PTEP*, 2020(8):083C01, 2020.
- [799] Pere Masjuan, Enrique Ruiz Arriola, and Wojciech Broniowski. Systematics of radial and angular-momentum Regge trajectories of light non-strange  $q\bar{q}$ -states. *Phys. Rev. D*, 85:094006, 2012.
- [800] Veronique Bernard, Latifa Elouadrhiri, and Ulf-G. Meissner. Axial structure of the nucleon: Topical Review. *J. Phys. G*, 28:R1–R35, 2002.
- [801] Jeremy Green, Nesreen Hasan, Stefan Meinel, Michael Engelhardt, Stefan Krieg, Jesse Laeuchli, John Negele, Kostas Orginos, Andrew Pochinsky, and Sergey Syritsyn. Up, down, and strange nucleon axial form factors from lattice QCD. *Phys. Rev. D*, 95(11):114502, 2017.
- [802] Eigo Shintani, Ken-Ichi Ishikawa, Yoshinobu Kuramashi, Shoichi Sasaki, and Takeshi Yamazaki. Nucleon form factors and root-mean-square radii on a  $(10.8 \text{ fm})^4$  lattice at the physical point. *Phys. Rev. D*, 99(1):014510, 2019. [Erratum: *Phys.Rev.D* 102, 019902 (2020)].
- [803] Yong-Chull Jang, Rajan Gupta, Boram Yoon, and Tanmoy Bhattacharya. Axial Vector Form Factors from Lattice QCD that Satisfy the PCAC Relation. *Phys. Rev. Lett.*, 124(7):072002, 2020.

- [804] C. Alexandrou et al. Nucleon axial and pseudoscalar form factors from lattice QCD at the physical point. *Phys. Rev. D*, 103(3):034509, 2021.
- [805] Gunnar S. Bali, Lorenzo Barca, Sara Collins, Michael Gruber, Marius Löffler, Andreas Schäfer, Wolfgang Söldner, Philipp Wein, Simon Weishäupl, and Thomas Wurm. Nucleon axial structure from lattice QCD. *JHEP*, 05:126, 2020.
- [806] Sungwoo Park, Rajan Gupta, Boram Yoon, Santanu Mondal, Tanmoy Bhattacharya, Yong-Chull Jang, Bálint Joó, and Frank Winter. Precision nucleon charges and form factors using (2+1)-flavor lattice QCD. *Phys. Rev. D*, 105(5):054505, 2022.
- [807] Stanley J. Brodsky, G. Peter Lepage, and S. A. A. Zaidi. Weak and Electromagnetic Form-factors of Baryons at Large Momentum Transfer. *Phys. Rev. D*, 23:1152, 1981.
- [808] Carl E. Carlson and J. L. Poor. ISOSCALAR AXIAL FORM-FACTOR AT HIGH  $Q^{*2}$ . *Phys. Rev. D*, 36:2169, 1987.
- [809] Carl E. Carlson and J. L. Poor. Determining Probabilities and Momentum Fractions From Distribution Amplitudes. *Phys. Rev. D*, 36:2070, 1987.
- [810] R. N. Faustov, E. V. Cherednikova, and A. P. Martynenko. Proton polarizability contribution to the hyperfine splitting in muonic hydrogen. *Nucl. Phys. A*, 703:365–377, 2002.
- [811] A. P. Martynenko. 2S hyperfine splitting of muonic hydrogen. *Phys. Rev. A*, 71:022506, 2005.
- [812] Nguyen Thu Huong, Emi Kou, and Bachir Moussallam. Single pion contribution to the hyperfine splitting in muonic hydrogen. *Phys. Rev. D*, 93(11):114005, 2016.
- [813] G. Ecker and C. Zauner. Tensor meson exchange at low energies. *Eur. Phys. J.*, C52:315–323, 2007.

- [814] Oscar Cata and Vicent Mateu. Novel patterns for vector mesons from the large- $N(c)$  limit. *Phys. Rev. D*, 77:116009, 2008.
- [815] D. Garcá Gudiño and G. Toledo Sánchez. Determination of the magnetic dipole moment of the rho meson using four-pion electroproduction data. *Int. J. Mod. Phys.*, A30(18n19):1550114, 2015.
- [816] Kaoru Hagiwara, R. D. Peccei, D. Zeppenfeld, and K. Hikasa. Probing the Weak Boson Sector in  $e^+ e^- \rightarrow W^+ W^-$ . *Nucl. Phys.*, B282:253–307, 1987.
- [817] Jose F. Nieves and Palash B. Pal. Electromagnetic properties of neutral and charged spin 1 particles. *Phys. Rev.*, D55:3118–3130, 1997.
- [818] Shao-Zhou Jiang, Zhen-Long Wei, Qing-Sen Chen, and Qing Wang. Computation of the  $O(p^6)$  order low-energy constants: An update. *Phys. Rev. D*, 92:025014, 2015.
- [819] J. Gasser, M.E. Sainio, and A. Svarc. Nucleons with Chiral Loops. *Nucl. Phys. B*, 307:779–853, 1988.
- [820] Veronique Bernard, Norbert Kaiser, Joachim Kambor, and Ulf G. Meissner. Chiral structure of the nucleon. *Nucl. Phys. B*, 388:315–345, 1992.
- [821] M. Morita, R. Morita, and K. Koshigiri. Induced terms of weak nucleon currents in light nuclei. *Nucl. Phys. A*, 577:387–392, 1994.
- [822] Thomas Gutsche, Astrid N. Hiller Blin, Sergey Kovalenko, Serguei Kuleshov, Valery E. Lyubovitskij, Manuel J. Vicente Vacas, and Alexey Zhevlakov. CP-violating decays of the pseudoscalars eta and eta' and their connection to the electric dipole moment of the neutron. *Phys. Rev. D*, 95(3):036022, 2017.
- [823] M.L. Goldberger and S.B. Treiman. Form-factors in Beta decay and muon capture. *Phys. Rev.*, 111:354–361, 1958.

- [824] A.E. Dorokhov, N.I. Kochelev, A.P. Martynenko, F.A. Martynenko, A.E. Radzhabov, and R.N. Faustov. The contribution of pseudoscalar and axial-vector mesons to hyperfine structure of muonic hydrogen. *J. Phys. Conf. Ser.*, 938(1):012042, 2017.
- [825] Pablo Sanchez-Puertas.  $CP$  violation in  $\eta$  muonic decays. *JHEP*, 01:031, 2019.
- [826] Vanamali Shastry, Enrico Trotti, and Francesco Giacosa. Constraints imposed by the partial wave amplitudes on the decays of  $J=1, 2$  mesons. *Phys. Rev. D*, 105(5):054022, 2022.